frontiers | Research Topics

Modeling in ecology and epidemiology

Edited by
Md. Shahidul Islam, Md. Kamrujjaman and Uttam Ghosh

Published in
Frontiers in Applied Mathematics and Statistics
Frontiers in Public Health
Frontiers in Ecology and Evolution

ISSN 1664-8714
ISBN 978-2-8325-5594-1
DOI 10.3389/978-2-8325-5594-1

About Frontiers

Frontiers is more than just an open access publisher of scholarly articles: it is a pioneering approach to the world of academia, radically improving the way scholarly research is managed. The grand vision of Frontiers is a world where all people have an equal opportunity to seek, share and generate knowledge. Frontiers provides immediate and permanent online open access to all its publications, but this alone is not enough to realize our grand goals.

Frontiers journal series

The Frontiers journal series is a multi-tier and interdisciplinary set of open-access, online journals, promising a paradigm shift from the current review, selection and dissemination processes in academic publishing. All Frontiers journals are driven by researchers for researchers; therefore, they constitute a service to the scholarly community. At the same time, the *Frontiers journal series* operates on a revolutionary invention, the tiered publishing system, initially addressing specific communities of scholars, and gradually climbing up to broader public understanding, thus serving the interests of the lay society, too.

Dedication to quality

Each Frontiers article is a landmark of the highest quality, thanks to genuinely collaborative interactions between authors and review editors, who include some of the world's best academicians. Research must be certified by peers before entering a stream of knowledge that may eventually reach the public - and shape society; therefore, Frontiers only applies the most rigorous and unbiased reviews. Frontiers revolutionizes research publishing by freely delivering the most outstanding research, evaluated with no bias from both the academic and social point of view. By applying the most advanced information technologies, Frontiers is catapulting scholarly publishing into a new generation.

What are Frontiers Research Topics?

Frontiers Research Topics are very popular trademarks of the *Frontiers journals series*: they are collections of at least ten articles, all centered on a particular subject. With their unique mix of varied contributions from Original Research to Review Articles, Frontiers Research Topics unify the most influential researchers, the latest key findings and historical advances in a hot research area.

Find out more on how to host your own Frontiers Research Topic or contribute to one as an author by contacting the Frontiers editorial office: frontiersin.org/about/contact

Modeling in ecology and epidemiology

Topic editors

Md. Shahidul Islam — University of Dhaka, Bangladesh

Md. Kamrujjaman — University of Dhaka, Bangladesh

Uttam Ghosh — University of Calcutta, India

Citation

Islam, M. S., Kamrujjaman, M., Ghosh, U., eds. (2024). *Modeling in ecology and epidemiology*. Lausanne: Frontiers Media SA. doi: 10.3389/978-2-8325-5594-1

Table of contents

frontiers | Frontiers in Applied Mathematics and Statistics

TYPE Original Research
PUBLISHED 09 August 2022
DOI 10.3389/fams.2022.949585

OPEN ACCESS

EDITED BY
Roberto Barrio,
University of Zaragoza, Spain

REVIEWED BY
Sahabuddin Sarwardi,
Aliah University, India
Aatif Ali,
Abdul Wali Khan University Mardan, Pakistan
Md Afsar Ali,
York University, Canada

*CORRESPONDENCE
Md. Kamrujjaman
kamrujjaman@du.ac.bd

SPECIALTY SECTION
This article was submitted to Dynamical Systems, a section of the journal Frontiers in Applied Mathematics and Statistics

RECEIVED 21 May 2022
ACCEPTED 19 July 2022
PUBLISHED 09 August 2022

CITATION
Zahan I, Kamrujjaman M, Alim MA, Mohebujjaman M and Khan T (2022) Dynamics of heterogeneous population due to spatially distributed parameters and an ideal free pair. *Front. Appl. Math. Stat.* 8:949585. doi: 10.3389/fams.2022.949585

Dynamics of heterogeneous population due to spatially distributed parameters and an ideal free pair

Ishrat Zahan[1], Md. Kamrujjaman [2]*, Md. Abdul Alim[1], Muhammad Mohebujjaman[3] and Taufiquar Khan[4]

[1]Department of Mathematics, Bangladesh University of Engineering and Technology, Dhaka, Bangladesh, [2]Department of Mathematics, University of Dhaka, Dhaka, Bangladesh, [3]Department of Mathematics and Physics, Texas A&M International University, Laredo, TX, United States, [4]Department of Mathematics and Statistics, University of North Carolina at Charlotte, Charlotte, NC, United States

Population movements are necessary to survive the individuals in many cases and depend on available resources, good habitat, global warming, climate change, supporting the environment, and many other issues. This study explores the spatiotemporal effect on the dynamics of the reaction-diffusion model for two interacting populations in a heterogeneous habitat. Both species are assumed to compete for different fundamental resources, and the diffusion strategies of both organisms follow the resource-based diffusion toward a positive distribution function for a large variety of growth functions. Depending on the values of spatially distributed interspecific competition coefficients, the study is conducted for two cases: weak competition and strong competition, which do not perform earlier in the existing literature. The stability of global attractors is studied for different conditions of resource function and carrying capacity. We investigated that in the case of weak competition, coexistence is attainable, while strong competition leads to competitive exclusion. This is an emphasis on how resource-based diffusion in the niche impacts selection. When natural resources are in sharing, either competition or predator-prey interaction leads to competitive exclusion or coexistence of competing species. However, we concentrate on the situation in which the ideal free pair is achieved without imposing any other additional conditions on the model's parameters. The effectiveness of the model is accomplished by numerical computation for both one and two space dimension cases, which is very important for biological consideration.

KEYWORDS

dispersal dynamics, competition, spatial functions, directed distribution, global stability

1. Introduction

The life history of most organisms depends on their dispersal strategy and resource distribution, which is the most important and obvious feature of ecology. Most of the time, their ecological impact and progression remain inadequately understood. The question that attracts most researchers is how individual organisms choose their

habitat in the ecological niche. At this point, reaction-diffusion models can be used for interacting biological species in an isolated confined habitat that is highly adapted for capturing species' bio-geographic properties. Numerous new theoretical research in the field of mathematical ecology have been conducted on the reaction-diffusion problem (refer to, e.g., [1–6] and references therein) that suggest in many cases the uniform and non-uniform ideal free distribution. The key idea of ideal free distribution is that the individual has an extensive understanding of the environment. They can freely diffuse where they evaluate them-self in order to optimize their fitness, without any cost. The concept of ideal free distribution was laid out in Cantrell et al. [5], which signifies any movement from this dispersed system will diminish the fitness of the moving organism. Spatially heterogeneous, but temporary constant ideal free distribution is estimated as the solution of the model. In this context, for model dispersal, there were various promising approaches (refer to, e.g., [4–6]) that provide the ideal free distribution as the equilibrium solution of the dynamical model.

However, the most crucial problem in heterogeneous environments is that the strategy of diffusion, which is adopted from any physical system, presumes enormous migration of organisms to the areas of poor available resources [3, 7]. The migration transport is considered proportional to the gradient of population density itself. In this situation, species can be preordained to extinction. As in classical diffusion, species are uniformly distributed over the space with the increase of the diffusion coefficient. However, ideal free distribution corresponds to the equal distribution of available resources at each spatial location. Classical diffusion cannot correspond to the ideal free dispersal in a spatially non-homogeneous environment. As a remedy to this, in our study, we have considered an alternative take out type of diffusion strategy, named resource-based diffusion [8, 9] along with a positive and smooth distribution function, which is individual for each population. In this migration pattern, the diffusive transport is considered proportional to the gradient of population density per unit resource instead of the carrying capacity studied in Braverman and Braverman [4] and Korobenko and Braverman [10].

The evolutionary advantage of various diffusion tactics on the outcome of competition coefficients on the model parameters was studied in Kamrujjaman [11]. The major outcome of this study was that the mutual coexistence of species and destruction of one by others, as well as considering the case for which both species are managed confirms the ideal free pair. The case of weak competition for two competing species was studied in Kamrujjaman [12] where the diffusion strategy of two competing species is considered different, the first species following the resource-base diffusion, whereas others disperse randomly. The study concluded that the resource-based diffusion strategy has an evolutionary advantage compared to regular diffusion. Also, it was found that when two strategies, adopted by the competing species, were combined, both species were able to coexist and an ideal free pair was attained.

Moreover, competition between organisms is usually depicted by the predator-prey and Lotka system. The Lotka-Volterra system with random diffusion has been discussed in the literature [7, 13, 14] throughout the last two decades. Partial resource sharing described by a Lotka system with competition parameters between zero and one was studied in Braverman and Kamrujjaman [15]. They investigated how the diffusion coefficients, as well as the competition coefficients, can affect whether a possible interaction is a coexistence or competitive exclusion. Furthermore, two species striving for the same resource are unable to coexist. Spatial heterogeneity, which is defined by the environment's resource capacity, intrinsic growth rate, inter-specific competition coefficient, and spatially distributed diffusion strategies, can alter the scenario.

Inspired by the overhead discussion, in this study, we have studied a two species compete model, where the main aim behind it is based on different imposed diffusion strategies and the tensity of competition coefficient on their growth function. We will study the existence of global stability both for competitive exclusion and coexistence of the model, without imposing additional conditions on the model parameter in which ideal free pair exists in competition.

2. Mathematical model

Let us now define the well known growth functions that we want to define in our generalized reaction-diffusion system:

$$\text{Gilpin-Ayala growth [16]}: F(x,u,K(x)) = r(x)\left(1-\left(\frac{u(t,x)}{K(x)}\right)^{\theta}\right), \quad 0<\theta\leq 1; \tag{2.1}$$

For $\theta = 1$, the logistic growth is a particular case;

$$\text{Gompertz growth [17]}: F(x,u,K(x)) = r(x)\ln\left(\frac{K(x)}{u(t,x)}\right); \tag{2.2}$$

$$\text{Food-limited growth [18]}: F(x,u,K(x)) = r(x)\frac{1-u(t,x)/K(x)}{1+\beta u(t,x)/K(x)}, \quad \beta>0. \tag{2.3}$$

In this study, we contemplate a couple of species competition models in mathematical ecology. Both species compete for the same basic resources at time t and location x, and early define the notation, $\Lambda = \Omega\times(0,\infty)$ and $\partial\Lambda = \partial\Omega\times(0,\infty)$. Both species are competing for the available natural resources in an isolated domain Ω and their diffusion strategies are similar according to two spatially distribution functions. This corresponds to the

following non-linear system of equations with zero Neumann boundary conditions:

$$\begin{cases} u_t = d_1\Delta\left(\frac{u(t,x)}{M(x)}\right) + r_1(x)u(t,x)f(x,u,v,M,N,K), & \text{in } \Lambda, \\ v_t = d_2\Delta\left(\frac{v(t,x)}{N(x)}\right) + r_2(x)v(t,x)f(x,v,u,N,M,K), & \text{in } \Lambda, \\ \nabla(u/M)\cdot n = \nabla(v/N)\cdot n = 0, & \text{on } \partial\Lambda, \\ u(0,x) = u_0(x),\ v(0,x) = v_0(x), & \text{in } \Omega. \end{cases} \tag{2.4}$$

For spatially distributed positive functions $M(x)$, $N(x)$, and $K(x)$, we assume that $M(x) < K(x)$ and $N(x) < K(x)$ for any x in a non-empty open domain. However, $K(x)$ is the ultimate population density which is well known as the natural carrying capacity. The habitat Ω is defined as a bounded region in $\mathbb{R}^n$, where $n = 1, 2, \text{or } 3$ with $\partial\Omega \in C^{2+\beta}$, $\beta > 0$. The population densities of the two competing species are represented, respectively by the functions $u(t,x)$ and $v(t,x)$, where their migration rates are $d_1 > 0$ and $d_2 > 0$, respectively. The intrinsic growth rate of species is represented by the function $r_i(x)$, $(i = 1, 2)$, and it is bounded. We suppose that all functions belong to the class of $C^{1+\beta}(\overline{\Omega})$, $\beta > 0$ for any $x \in \overline{\Omega}$. As well as, throughout this study, we will assume that $M(x)$ and $N(x)$ satisfy

- distribution functions $M(x) > 0$ and $N(x) > 0$ are non-constant and Hölder continuous in Ω.

In the case of logistic growth, the system (2.4) can be presented in the following pattern

$$\begin{cases} u_t = d_1\Delta\left(\frac{u(t,x)}{M(x)}\right) + r_1(x)u(t,x) \\ \qquad (1 - \frac{u(t,x)+\mu(x)v(t,x)}{K(x)}), & \text{in } \Lambda, \\ v_t = d_2\Delta\left(\frac{v(t,x)}{N(x)}\right) + r_2(x)v(t,x) \\ \qquad (1 - \frac{v(x)u(t,x)+v(t,x)}{K(x)}), & \text{in } \Lambda, \\ \nabla(u/M)\cdot n = \nabla(v/N)\cdot n = 0, & \text{on } \partial\Lambda, \\ u(0,x) = u_0(x),\ v(0,x) = v_0(x), & \text{in}\Omega. \end{cases} \tag{2.5}$$

where

$$\mu(x) = \frac{K(x) - M(x)}{N(x)}, \quad \nu(x) = \frac{K(x) - N(x)}{M(x)}. \tag{2.6}$$

In the past periods, most of the study of the competition model has been accomplished by considering constant competition coefficients [12, 15, 19] which belong to either 0 and 1 or greater than 1. In our study, we have designed our model by considering non-constant space dependent competition coefficient $\mu(x)$ and $\nu(x)$, which makes this study extremely novel and to the best of the authors' knowledge, until now no literature is available considering this type of space dependent competition coefficients. However, considering resource-based diffusion as a strategy for both competing species for generalized growth function is not investigated earlier in the literature.

Let us consider the growth functions as, $g_1(x,u,v) = r_1 u f(x,u,v,M,N,K)$ and $g_2(x,u,v) = r_2 v f(x,v,u,N,M,K)$. We next list the following assumptions on g_1 and g_2 which will be used throughout the article:

h1 $\mathbf{g} = (g_1, g_2)$ is quasimonotone nonincreasing in $l_1 \times l_2$;
h2 $g_i(\cdot,u,v)$ is Hölder continuous in Ω and $f_i(x,\cdot,\cdot) \in C^2(l_1 \times l_2)$, $i = 1, 2$;
h3 $f(x,u,v,M,N,K) = F(x, u + \frac{K-M}{N}v, K)$, and $f(x,v,u,N,M,K) = F(x, v + \frac{K-N}{M}u, K)$;
h4 $f(x,M,N,M,N,K) = f(x,N,M,N,M,K) = F(x,K,K) = 0$;
h5 $F(x,u,M,N,K)$ is decreasing in u in a strictly monotonic manner;
h6 $F(x,u,M,N,K)$ is increasing in K precisely in a strictly monotonic manner;

The most common instances of $F(x,u,K)$ that satisfy the following properties are defined in (2.1)-(2.3). The property h5 of growth for the model's population densities does not satisfy for growth laws with the Allee effect [20].

Let us now introduce two new variables $m(t,x) = \frac{u(t,x)}{M(x)}$ and $w(t,x) = \frac{v(t,x)}{N(x)}$, and we get the above equivalent system of (2.4)

$$\begin{cases} M(x)m_t = d_1\Delta m(t,x) + r_1(x)M(x)m(t,x)h(x,m,w,M,N,K), \\ \qquad \text{in } \Lambda, \\ N(x)w_t = d_2\Delta w(t,x) + r_2(x)N(x)w(t,x)h(x,w,m,N,M,K), \\ \qquad \text{in } \Lambda, \\ \nabla m\cdot n = \nabla w\cdot n = 0, & \text{on } \partial\Lambda, \\ m(0,x) = u_0(x)/M(x),\ w(0,x) = v_0(x)/N(x), & \text{in } \Omega. \end{cases} \tag{2.7}$$

where h is a new function instead of f for new substitutions. For further analysis, we can consider either the problem (2.4) or (2.7) since both systems are equivalent.
In the present study, the main findings are as follows:

1. We demonstrate the global existence and uniqueness of the solution of the initial value system under some assumptions on the model parameters.
2. We investigate the global existence of the competition model in which the first species' resource function is proportional to its carrying capacity and the other is following a resource-based diffusion strategy by considering two main cases of competition coefficient: weak competition and strong competition.
3. We will find when $M(x) + N(x) > K(x)$ i.e., $\mu(x)$, $\nu(x) < 1$ (weak competition) then both species should survive in the competition and as $t \to \infty$ the solution move toward (M, N) and form an ideal free pair.
4. Also, when $M(x) + N(x) < K(x)$ i.e., $\mu(x)$, $\nu(x) > 1$ (strong competition) no coexistence solution is possible and

depending on the values of proportionally constant one of the species will survive in the battle.
5. In the case when both species follow the resource-based diffusion strategy, along with their positive distribution function and $M(x) + N(x) \geq K(x)$, they will attain an ideal free pair and both species should coexist.
6. We also present some numerical results both in one- and two-dimensional cases. In addition, we present the case of time periodic state with the same time period numerically to compare the time periodic cases which may occur for seasonal variation with the steady state case.

The manuscript is arranged as follows: the existence of the solution of the competition model for generalized growth functions is provided in Section 3. Section 4, reveals the existence of global and local stability under some conditions on the resource functions. Here, we have considered two cases: weak competition and strong competition, based on the values of space dependent competition coefficients. The main result of this study is also presented in this section. To see the efficacy of the model, the numerical computation both for the case of one dimension and two dimensions are presented in Section 5 in terms of a line graph, surface plots, trajectory plots, contour plots, and heat maps. Some numerical results for the time periodic state are also presented since it is very important for ecological consideration. Section 6, provides the concluding remarks of the study.

3. Existence and distinctiveness

To delineate the existence and uniqueness of $u = u(t,x)$ with zero Neumann boundary conditions consider the following boundary value problem for the first equation of (2.4)

$$\begin{cases} u_t = d_1 \Delta \left(\frac{u(t,x)}{M(x)} \right) + r_1(x) u(t,x) f(x,u,v,M,N,K), & \text{in } \Lambda, \\ \nabla(u/M) \cdot n = 0, & \text{on } \partial\Lambda, \\ u(0,x) = u_0(x), & \text{in } \Omega. \end{cases} \tag{3.1}$$

The following results are also discussed in Cantrell and Cosner [7] and Korobenko and Braverman [21]. It is to be mentioned that the proof of Lemma 1 and Lemma 2 are analogous to the proofs of Korobenko and Braverman [21], Theorem 1 and Theorem 2, where the authors considered two competing species competing for similar basic resources in the heterogeneous habitat with different diffusion strategies. The study was as follows: one species followed the carrying capacity-driven diffusion while others dispersed by the random movement for generalized symmetric growth function with $\mu(x) = \nu(x) = 1$.

Lemma 1. *Korobenko and Braverman [21] Let $g_1(x,u,v) = r_1 u f(x,u,v,M,N,K)$ satisfy the property h2, h4, h5 and the initial condition of 3.1 be $u_0(x) \in C(\Omega)$, $u_0(x) \geq 0$ in Ω and $u_0(x) > 0$ in some open, bounded, and non-empty domain $\Omega_s \subset \Omega$. Also let, all the the parameters are positive on $\overline{\Omega}$. Then there exists a unique positive solution $u^*(x)$ of the system 3.1. Furthermore, if $\frac{M(x)}{K(x)} \equiv$ Constant, then the only solution of problem 3.1 is $u^*(x) = K(x)$, and as $t \to \infty$ the solution converges to $K(x)$, otherwise $u^*(x)$ is different from $K(x)$.*

Similarly, we can also establish the existence and unique results for the second equation of (2.4) for $v = v(t,x)$ with homogeneous Neumann boundary conditions as

$$\begin{cases} v_t = d_2 \Delta \left(\frac{u(t,x)}{N(x)} \right) + r_2(x) v(t,x) f(x,v,u,N,M,K), & \text{in } \Lambda, \\ \nabla(v/N) \cdot n = 0, & \text{on } \partial\Lambda, \\ v(0,x) = v_0(x), & \text{in } \Omega. \end{cases} \tag{3.2}$$

Lemma 2. *Korobenko and Braverman [21] Let $g_2(x,u,v) = r_2 v f(x,v,u,N,M,K)$ satisfy the property h2, h4, h5 and the initial condition of 3.1 be $u_0(x) \in C(\Omega)$, $v_0(x) \geq 0$ in Ω and $v_0(x) > 0$ in some open, bounded, and non-empty domain $\Omega_s \subset \Omega$. Also let, all the parameters are positive on $\overline{\Omega}$. Then there exists a unique positive solution $v^*(x)$ of the problem (3.2). Furthermore, if $\frac{N(x)}{K(x)} \equiv$ Constant, then $\lim_{t\to\infty} v(t,x) = K(x)$ otherwise $\lim_{t\to\infty} v(t,x) = v^*(x)$ evenly in $x \in \overline{\Omega}$.*

The following Theorem 1 establishes the existence and uniqueness of (2.4) for coupled systems of equations. Model (2.4) is a paragon that follows the monotone dynamical system [7, 22, 23]. Once substituting, $m = u/M$, and $w = v/N$ it reduces into a system of regular diffusion. Where d_1/M and d_2/N represent space dependent positive smooth diffusion coefficients. Note that the following proof for (2.4) is analogous with Korobenko and Braverman [21] in Theorem 10, for $\mu = \nu = 1$.

Theorem 1. *Let $K(x), M(x), N(x) > 0$ where $M(x), N(x) < K(x)$ for any x in a non-empty open domain so that $\mu(x), \nu(x) > 0$ and $g_1(x,u,v) = r_1 u f(x,u,v,M,N,K)$ and $g_2(x,u,v) = r_2 v f(x,v,u,N,M,K)$ satisfy the property h1, h2, and h5 on $x \in \overline{\Omega}$. Then for any $u_0(x)$, $v_0(x) \in C(\Omega)$ the problem (2.4) has a unique solution (u,v). Furthermore, if both initial functions are non-negative and non-trivial, then $u(t,x) > 0$ and $v(t,x) > 0$ for any $t > 0$.*

Proof: To prove this, we enacted ([22], Theorem 8.7.2) to the problem (2.7) , which is obtained after substitution $m = \frac{u(t,x)}{M(x)}$, and $w = \frac{v(t,x)}{N(x)}$, respectively.

To show the existence of non-trivial solutions, let us choose the following constants ρ_m and ρ_w such that

$$\rho_m \geq \sup_{(t,x)\in\mathbb{A}_1} u_0(t,x)/M(x), \quad \text{and} \quad \rho_w \geq \sup_{x\in\omega} v_0(t,x)/N(x).$$

Then it is simple to check that the subsequent conditions of the theorem are satisfied.

$$g_1(t,x,\rho_m,0,M,N,K) \le 0 \le g_1(t,x,0,\rho_w,M,N,K). \quad (3.3)$$

$$g_2(t,x,0,\rho_w,N,M,K) \le 0 \le g_2(t,x,\rho_m,0,N,M,K). \quad (3.4)$$

So that $f(t,x,\rho_m,0,M,N,K) < 0$ and $f(t,x,0,\rho_w,N,M,K) < 0$, since $f(x,Mm,Nw,M,N,K)$ and $f(x,Nw,Mm,N,M,K)$ are monotonically nonincreasing in $\mathbb{R}^+$. However, $u(0,x)$ and $v(0,x)$ are bounded in $\overline{\Omega}$, and $M(x)$ and $N(x)$ are bounded from below, so we have $\sup_{x\in\Omega} \frac{u(0,x)}{M(t,x)} < \infty$, and $\sup_{x\in\Omega} \frac{v(0,x)}{N(x)} < \infty$, respectively.

The conditions (3.3) and (3.4) satisfy the conditions (refer to, [22], Theorem 8.7.2, Equation 8.7.4) for the functions g_1 and g_2 defined above. Therefore, we arrive at the conclusion of the theorem that for any non-trivial and non-negative $(u_0(x), v_0(x))$ such that ρ_m and ρ_w specified above satisfy

$$\left(\frac{u_0(x)}{M(x)}, \frac{v_0(x)}{N(x)}\right) \in \mathbf{S}_\rho := \{(m,w) \in C\left([0,\infty)\times\overline{\Omega}\right) \times C\left([0,\infty)\times\overline{\Omega}\right) : (0,0) \le (m,w) \le (\rho_m,\rho_w)\}.$$

Where $C\left([0,\infty)\times\overline{\Omega}\right)$ denotes the class of continuous functions on $[0,\infty)\times\overline{\Omega}$. Accordingly, from (refer to, [22], Theorem 8.7.2) all of the requirements have been met, so the unique solution (m,w) of (2.7) has existed and it is positive. Apparently, the unique positive solution of (2.4) is $(u,v) = (Mm, Nw)$. Thus, the solution (u,v) is positive and unique. □

As a system (2.4) as well as (2.7) is a sample of the monotone dynamical system [7, 22, 23]. For further analysis of the model's equilibrium solutions, we will apply the following theorem of the monotone dynamical system that is provided in Korobenko and Braverman [21], Theorem 16.

Lemma 3. *If the trivial equilibrium of (2.4) is not stable as well as the repeller, then certainly one of the subsequent three situations are stand from a specified set:*

(i) a positive and stable coexistence of (2.4) will sustain,
(ii) all positive and stable solution either converges to $(u^*, 0)$ *as* $t \to \infty$,
(iii) all positive and stable solution either converges to $(0, v^*)$ *as* $t \to \infty$.

4. Analysis of steady states

In this part of the study, we will explore the stability of the following equilibrium states of the system (2.4): $(u^*(x), 0)$, $(0, v^*(x))$ named semi-trivial equilibria, which corresponds to a situation where only one species survives in the competition and the other species dies out. The trivial equilibrium $(0,0)$, when both species leave the area and the coexistence equilibria $(u_e(x), v_e(x))$ while both semi-trivial, as well as the trivial solution, are unstable. As we know, $u(t,x)$ and $v(t,x)$ are the solutions of (2.4) for all $t > 0$. Also, we describe our main results.

Lemma 4. *The* $(0,0)$ *equilibrium of the system (2.4) is unstable and repelling.*

Proof: Let us consider the system (2.7) around the origin and the associated eigenvalue problem of the corresponding problem is

$$\begin{cases} d_1\Delta\phi(x) + r_1\phi(x)M(x)h(x,0,0,M,N,K) = \sigma\phi(x), \\ \quad \text{in } \Omega, \quad \nabla\phi\cdot n = 0, \quad \text{on } \partial\Omega, \\ d_2\Delta\psi(x) + r_2\psi(x)N(x)h(x,0,0,N,M,K) = \sigma\psi(x), \\ \quad \text{in } \Omega, \quad \nabla\psi\cdot n = 0, \quad \text{on } \partial\Omega. \end{cases} \quad (4.1)$$

The principal eigenvalue of the first equation of (4.1) is expressed by following the variational characterization of the eigenvalues ([7], Theorem 2.1) as

$$\sigma_1 = \sup_{\phi\neq 0,\phi\in W^{1,2}} \frac{-\int_\Omega d_1|\nabla\phi(x)|^2\,dx + \int_\Omega r_1M(x)\phi^2(x)h(x,0,0,M,N,K)\,dx}{\int_\Omega \phi^2(x)dx}.$$

For non-trivial positive constant function $\phi(x)$, we get

$$\sigma_1 \ge \frac{1}{|\Omega|}\int_\Omega r_1M(x)h(x,0,0,M,N,K)dx > 0,$$
since $h(x,0,0,M,N,K) > 0$.

and the zero equilibrium $(0,0)$ of (2.4) is not stable.

To prove that $(0,0)$ of (2.4) is a repeller, i.e., assuming u_0, v_0 being the neighborhood of the equilibrium point $(0,0)$, then all solutions move away from $(0,0)$ as t approaches infinity.

Let $\delta = \min\left\{\inf_{x\in\Omega}\frac{K}{4}, \inf_{x\in\Omega}\frac{KN}{4(K-M)}, \inf_{x\in\Omega}\frac{MK}{4(K-N)}\right\} > 0$, $u_0(x) \ge 0$ and $v_0(x) \ge 0$ be such that $u_0(x) < \delta$, $v_0(x) < \delta$ for $(u_0(x), v_0(x)) \neq (0,0)$. Adding the foremost equations of the system (2.4) and integrate over Ω and applying homogeneous Neumann boundary conditions, we get

$$\frac{d}{dt}\int_\Omega (u(t,x)+v(t,x))dx = \int_\Omega [r_1(x)uf(x,u,v,M,N,K) + r_2(x)vf(x,v,u,N,M,K)]dx. \quad (4.2)$$

Note that, $\gamma = \min\left\{\inf_{x\in\Omega} r_1(x), \inf_{x\in\Omega} r_2(x)\right\} > 0$ and on condition, $u \le \delta$ and $v \le \delta$ there holds

$$\frac{d}{dt}\int_\Omega (u(t,x)+v(t,x))dx \ge \frac{\gamma}{2}\int_\Omega (u(t,x)+v(t,x))dx.$$

Now applying Gronwall's lemma we have

$$\int_\Omega (u(t,x)+v(t,x))dx \ge e^{\gamma t/2}\int_\Omega (u_0(x)+v_0(x))dx.$$

As $\int_\Omega (u_0(x)+v_0(x))dx > 0$, then $\int_\Omega (u(t,x)+v(t,x))dx$ expands exponentially with time goes as far as $u \le \delta$ and $v \le \delta$. Hence there exists $t_0 > 0$ so that $u(t_0,x) > \delta$ and $v(t_0,x) > \delta$ for some $x \in \Omega$ and the equilibrium point $(0,0)$ is a repeller. □

The functions u^* and v^* are the solutions to the preceding elliptic boundary value problems, which are straightforward to understand:

$$d_1\Delta\left(\frac{u^*(x)}{M(x)}\right) + r_1(x)u^*(x)f(x,u^*,0,M,N,K) = 0,$$
$$\text{in } \Omega, \quad \frac{\partial(u^*/M)}{\partial n} = 0, \quad \text{on } \partial\Omega, \tag{4.3}$$

$$d_2\Delta\left(\frac{v^*(x)}{N(x)}\right) + r_2(x)v^*(x)f(x,v^*,0,N,M,K) = 0,$$
$$\text{in } \Omega, \quad \frac{\partial(v^*/N)}{\partial n} = 0, \quad \text{on } \partial\Omega, \tag{4.4}$$

respectively.

Lemma 5. *Let f satisfy h1-h6, $r_1(x) \equiv r_1$, $r_2(x) \equiv r_2$ are constant and $K(x) \not\equiv$ constant. Then a unique positive solution $v^*(x)$ of (4.4) will exist, so that*

$$r_2\int_\Omega f(x,v^*,0,N,M,K)K(x)\,dx \equiv r_2\int_\Omega F(x,v^*(x),K(x))K(x)\,dx > 0. \tag{4.5}$$

Proof: Integrating (4.4) over the domain Ω and applying the corresponding boundary conditions which implies $d_2\int_\Omega \Delta v^*(x)dx = 0$ and we obtain using h3 for g

$$\int_\Omega r_2 v^*(x)F(x,v^*,K)\,dx = 0. \tag{4.6}$$

Integrating the equality and using the Mean Value Theorem with property h4

$$\begin{aligned} r_2v^*(x)F(x,v^*,K) &= r_2(v^*-K)(F(x,v^*,K)-F(x,K,K)) \\ &\quad + r_2K(x)F(x,v^*,K) \\ &= r_2(v^*-K)^2F_v(x,\xi,K) \\ &\quad + r_2K(x)F(x,v^*,K) \end{aligned}$$

we have

$$r_2\int_\Omega K(x)F(x,v^*(x),K(x))\,dx = -\int_\Omega F_v(x,\xi,K(x))(v^*(x)-K(x))^2\,dx > 0. \tag{4.7}$$

where $\xi(x)$ lies in between $v^*(x)$ and $K(x)$. Here the right-hand side is positive unless $v^*(x) \equiv K(x) \equiv$ *constant*, since $F_v < 0$ due to h5, which completes the proof. □

Remark 1. *Note that for any $v \le K$ the properties h4 and h5 result in $f(x,v,0,N,M,K) \ge 0$. As a result, in an integral sense the inequality (4.5) can be regarded as the condition $v^* < K(x)$.*

Lemma 6. *Let f satisfies h1-h6 and $r_1(x) \equiv r_1$, $r_2(x) \equiv r_2$ are constant and $\frac{K(x)}{M(x)} \equiv \beta > 0$. Then the semi-trivial equilibrium $(0,v^*(x))$ of (2.4) is unstable if there exists non-constant $M(x)$, $N(x)$, and $K(x)$ such that $(M(x)+N(x)) \ge K(x)$ i.e., $\mu(x) \le 1$ in a non-empty open domain $\Omega_s \subseteq \Omega$.*

Proof: First taking the linearization of (2.4) over $(0,v^*(x))$.

$$\begin{cases} \frac{\partial u}{\partial t} = d_1\Delta\left(\frac{u(t,x)}{M(x)}\right) + r_1u(t,x)f(x,0,v^*,M,N,K), \\ \quad (t,x)\in\Lambda, \quad \frac{\partial(u/M)}{\partial n} = 0, \quad x\in\partial\Omega, \\ \frac{\partial v}{\partial t} = d_2\Delta\left(\frac{v(t,x)}{N(x)}\right) \\ \quad + r_2v(t,x)f(x,v^*,0,N,M,K) \\ \quad + r_2v^*f_u(x,v^*,0,N,M,K)u(t,x) \\ \quad + r_2v^*f_v(x,v^*,0,M,N,K)v(t,x), \quad (t,x)\in\Lambda, \\ \quad \frac{\partial(v/N)}{\partial n} = 0, \quad x\in\partial\Omega. \end{cases}$$

and study the corresponding eigenvalue problem for u

$$\begin{cases} d_1\Delta\left(\frac{\phi(x)}{M(x)}\right) + r_1\phi(x)f(x,0,v^*,M,N,K) = \sigma\phi(x), \quad x\in\Omega, \\ \frac{\partial(\phi/M)}{\partial n} = 0, \quad x\in\partial\Omega. \end{cases} \tag{4.8}$$

If the principal eigenvalue is positive then $(0,v^*)$ is unstable. Consider (4.8) and according to Cantrell and Cosner [7], Theorem 2.1, its principal eigenvalue is presented as

$$\sigma_1 = \sup_{\phi\neq 0,\phi\in W^{1,2}} \frac{-\int_\Omega d_1|\nabla(\phi/M)|^2dx + \int_\Omega \frac{r_1}{M}\phi^2(x)f(x,0,v^*,M,N,K)dx}{\int_\Omega\left(\frac{\phi^2}{M}\right)dx}.$$

Letting $\phi(x) = K(x)$ and using the property h3

$$\sigma_1 \geq \frac{\int_\Omega r_1 K(x) F(x, \frac{K-M}{N} v^*, K) dx}{\int_\Omega K(x) dx} \quad (4.9)$$
$$\geq \frac{r_1 \int_\Omega K(x) F(x, v^*, K)\, dx}{\int_\Omega K(x)\, dx}, \text{ since } \mu(x) \equiv \frac{K(x) - M(x)}{N(x)}$$
$$\leq 1 \text{ for any } x \in \Omega_s \subseteq \Omega.$$

Thus, $\sigma_1 > 0$ using (4.5) in Lemma 5, which completes the proof. □

Lemma 7. *Let f satisfies h1-h6 and $r_1(x) \equiv r_1$, $r_2(x) \equiv r_2$ are constant and $\frac{K(x)}{M(x)} \equiv \beta > 0$. Then the semi-trivial equilibrium $(K, 0)$ of (2.4) is unstable if there exists non-constant $M(x)$, $N(x)$, and $K(x)$ such that $(M(x) + N(x)) \geq K(x)$ i.e., $\nu(x) \leq 1$ in a non-empty open domain $\Omega_s \subseteq \Omega$.*

Proof: Analogous to Lemma 6, examine the associated eigenvalue problem of the linearized second equations of (2.4) around $(K, 0)$ and we obtain

$$d_2 \Delta \left(\frac{\psi(x)}{N(x)} \right) + r_2 \psi(x) f(x, 0, K, N, M, K) = \sigma \psi(x), \quad x \in \Omega,$$
$$\frac{\partial(\psi/N)}{\partial n} = 0, \quad x \in \partial\Omega. \quad (4.10)$$

Consider the Equation (4.10) and according to Cantrell and Cosner [7], the corresponding principal eigenvalue is stated as

$$\sigma_1 = \sup_{\psi \neq 0, \psi \in W^{1,2}} \frac{d_2 - \int_\Omega |\nabla \psi(x)/N|^2 dx + \int_\Omega r_2 \frac{\psi^2}{N} f(x, 0, K, N, M, K) dx}{\int_\Omega \left(\frac{\psi^2}{N} \right) dx}.$$

On substituting $\psi(x) = N(x)$ and using h3, the principal eigenvalue is

$$\sigma_1 \geq \frac{r_2 \int_\Omega N F(x, \frac{K-N}{M} K, K)\, dx}{\int_\Omega K^2(x) dx}.$$

Since, $F(x, \frac{K-N}{M} K, K) = \frac{M(x) - K(x) + N(x)}{M(x)} > 0$ for $M(x) + N(x) > K(x)$, also $N(x) > 0$. Therefore, $\sigma_1 > 0$ and $(K, 0)$ of (2.4) is unstable. □

Since $(0, v^*(x))$ and $(K(x), 0)$ are not stable as far as $(M(x) + N(x)) > K(x)$ (refer to, Lemma 6 and Lemma 7), they are not asymptotically stable. Also from Lemma 4, $(0, 0)$ or trivial equilibrium is unstable and repeller. Therefore, according to strong monotone dynamical system [7, 22, 23] the coexistence equilibrium $(u_e(x), v_e(x))$ is globally asymptotically stable so as to $(M(x) + N(x)) \geq K(x)$ for all x. Since system (2.4) is an example of a strongly monotone dynamical system, which represents the following Theorem 2.

Theorem 2. *Let the functions $g_1(x, u, v) = r_1 u f(x, u, v, M, N, K)$ and $g_2(x, u, v) = r_2 v f(x, v, u, N, M, K)$ satisfy h1-h6. Also, let $r_1(x) \equiv r_1$, $r_2(x) \equiv r_2$ are constant and $\frac{K(x)}{M(x)} \equiv \beta > 0$. Then the coexistence equilibrium $(u_e(x), v_e(x))$ of the system of Equations (2.4) is globally asymptotically stable if $(M(x) + N(x)) > K(x)$ for any x in a non-empty open domain. Also if $K \equiv$ constant then the equilibrium $(u_e(x), v_e(x))$ is globally asymptotically stable when $M(x) + N(x) \equiv K$. That is, for any $u_0, v_0 \in C(\overline{\Omega})$ which is non-negative and non-trivial, the solution (u, v) of (2.4) satisfies*

$$(u, v) \to (u_e(x), v_e(x)), \quad as \quad t \to \infty.$$

Corollary 1. *Let the functions $g_1(x, u, v) = r_1 u f(x, u, v, M, N, K)$ and $g_2(x, u, v) = r_2 v f(x, v, u, M, N, K)$ satisfy h1-h6. Also if M, N, K all are constants and $(M + N) > K$ then the coexistence equilibrium (M, N) of the system of equations (2.4) is globally asymptotically stable. That is, for any $u_0, v_0 \in C(\overline{\Omega})$ which is non-negative and non-trivial, the solution (u, v) of (2.4) satisfies*

$$(u, v) \to (M, N), \quad as \quad t \to \infty$$

uniformly in $x \in \overline{\Omega}$.

Next, in the following result, it is shown that there is no coexistence for strong competition, depending on the relations between $M(x)$, $N(x)$, and $K(x)$. In this case, competitive exclusion is expected.

Lemma 8. *Let f satisfies h1-h6 and $M(x)$, $N(x)$, $K(x)$ are non-constant. If $(M(x) + N(x)) \leq K(x)$ for any $x \in \Omega$, i.e., $\mu(x), \nu(x) \geq 1$ in a non-empty open domain $\Omega_s \subseteq \Omega$ with $r_1(x) \equiv r_1$, $r_2(x) \equiv r_2$ are constant, $\frac{K(x)}{M(x)} \equiv \beta > 0$, then there is no coexistence steady state (u_e, v_e) of the system (2.4).*

Proof: Suppose to the contrary, let us assume there exists a strictly positive equilibrium solution $(u_e(x), v_e(x))$ of (2.4) and we will present that the assumption provides a conflict. So, the solution $(u_e(x), v_e(x))$ satisfies the governing equations

$$\begin{cases} d_1 \Delta \left(\frac{u_e(x)}{M(x)} \right) + r_1 u_e(x) f(x, u_e, v_e, M, N, K) = 0, & \text{in } \Omega, \\ \frac{\partial(u_e/M)}{\partial n}, & \text{on } \partial\Omega, \\ d_2 \Delta \left(\frac{v_e(x)}{N(x)} \right) + r_2 v_e(x) f(x, v_e, u_e, N, M, K) = 0, & \text{in } \Omega, \\ \frac{\partial(v_e/N)}{\partial n} = 0, & \text{on } \partial\Omega. \end{cases} \quad (4.11)$$

After dividing by $r_1 r_2$ in each of the first two equations in (4.11) and adding them as well as imposing h3 for f, we get

$$\frac{d_1}{r_1} \Delta \left(\frac{u_e(x)}{M(x)} \right) + \frac{d_2}{r_2} \Delta \left(\frac{v_e(x)}{N(x)} \right) + u_e(x) F\left(x, u_e + \mu(x) v_e, K\right) + v_e(x) F(x, v_e + \nu(x) u_e, K) = 0.$$

Integrating over Ω and applying Numann boundary conditions in (4.11), we have

$$\begin{aligned}0 &= \int_\Omega \left[u_e F\left(x, u_e+\mu(x)v_e, K\right) + v_e F\left(x, v_e+\nu(x)u_e, K\right)\right] dx\\ &< \int_\Omega \left[u_e F\left(x, u_e+\mu(x)v_e, K\right) + \mu(x)v_e F\left(x, u_e+\mu(x)v_e, K\right)\right] dx\\ &= \int_\Omega (u_e+\mu(x)v_e) F\left(x, u_e+\mu(x)v_e, K\right) dx.\end{aligned}$$

since $\mu(x)F(x, u_e+\mu(x)v_e, K) > F(x, v_e+\nu(x)u_e, K)$, for $\nu(x) > \mu(x)$. Thus

$$\int_\Omega (u_e+\mu(x)v_e) F\left(x, u_e+\mu(x)v_e, K\right) dx > 0. \tag{4.12}$$

Integrating the equality

$$\begin{aligned}&(u_e+\mu(x)v_e) F\left(x, u_e+\mu(x)v_e, K\right) = F\left(x, u_e+\mu(x)v_e, K\right)\\ &(u_e+\mu(x)v_e - K)\\ &+ K(x) F\left(x, u_e+\mu(x)v_e, K\right)\end{aligned}$$

over Ω using (4.12) we get,

$$\begin{aligned}0 < &\int_\Omega F\left(x, u_e+\mu(x)v_e, K\right)(u_e+\mu(x)v_e - K)\, dx\\ &+ \int_\Omega K(x) F\left(x, u_e+\mu(x)v_e, K\right)\, dx.\end{aligned} \tag{4.13}$$

The Mean Value Theorem and $F(x, K, K) = 0$ by h4 imply

$$\begin{aligned}F\left(x, u_e+\mu(x)v_e, K\right) &= F\left(x, u_e+\mu(x)v_e, K\right) - F(x, K, K)\\ &= F_v(x, \xi, K)(u_e+\mu(x)v_e - K)\end{aligned} \tag{4.14}$$

where ξ is between $u_e+\mu(x)v_e$ and K for each $(t, x) \in \Lambda$. Using (4.14), inequality (4.15) can be rewritten as

$$\begin{aligned}&\int_\Omega K(x) F\left(x, u_e+\mu(x)v_e, K\right) dx >\\ &\qquad -\int_\Omega F_v(x, \xi, K)(u_e+\mu(x)v_e - K)^2\, dx.\end{aligned} \tag{4.15}$$

and the last inequality is strictly positive and excludes the possibility of $u_e+\mu(x)v_e \equiv K$ where $F_v < 0$ due to h5. Thus, we have to consider the following case.

Let $u_e+\mu(x)v_e \not\equiv K$ in some nonempty open domain, where $\mu(x), \nu(x) \geq 1$. Consider the eigenvalue problem

$$\begin{aligned}&d_1 \Delta\left(\frac{\phi(x)}{M(x)}\right) + r_1\phi(x) F\left(x, u_e+\mu(x)v_e, K\right) = \sigma\phi(x), \quad x \in \Omega,\\ &\frac{\partial(\phi/M)}{\partial n} = 0, \quad x \in \partial\Omega.\end{aligned} \tag{4.16}$$

According to Cantrell and Cosner [7], Theorem 2.1, the corresponding principal eigenvalue is presented as

$$\sigma_1 = \sup_{\phi\neq 0, \phi\in W^{1,2}} \frac{-\int_\Omega d_1 |\nabla(\phi/M)|^2 dx + r_1 \int_\Omega \frac{\phi^2}{M} F\left(x, u_e+\mu(x)v_e, K\right) dx}{\int_\Omega (\phi^2/M) dx}$$

Letting $\phi(x) = K(x)$ and applying (4.15), we obtain

$$\begin{aligned}\sigma_1 &\geq \frac{r_1 \int_\Omega K(x) F\left(x, u_e+\mu(x)v_e, K\right) dx}{\int_\Omega K(x) dx} > 0,\\ &\text{since } K/M \equiv \textit{constant}.\end{aligned} \tag{4.17}$$

Since 0 is always a principal eigenvalue of (4.16) along with a positive principal eigenfunction, which contradicts the positivity of $\sigma_1 > 0$. □

Remark 2. *The Lemma 8 is also valid for proportional growth rates* $\frac{r_1(x)}{r_2(x)} = \alpha > 0$, *since* $r_2(x)$ *can be involved as a part of function F.*

Remark 3. *If all the functions M, N, and K are constants then always there exists a coexistence solution* (M, N) *of the system (2.4) and the solution is globally stable.*

Lemma 9. *Let f satisfy h1-h6 and* $M(x), N(x)$, $K(x)$ *are non-constant. If* $(M(x)+N(x)) \leq K(x)$ *for any* $x \in \Omega$, *i.e.,* $\mu(x) \geq 1$ *in a non-empty open domain* $\Omega_s \subseteq \Omega$ *with* $r_1(x) \equiv r_1$, $r_2(x) \equiv r_2$ *are constant,* $\frac{K(x)}{M(x)} \equiv \beta > 0$, *then the semi-trivial steady state* $(K, 0)$ *of the system (2.4) is locally asymptotically stable.*

Proof: Similar to the proof of Lemma 7, let us study the associated eigenvalue problem of the linearized second equations of (2.4) around $(K, 0)$, then according to Cantrell and Cosner [7], Theorem 2.1 the principal eigenvalue is given by

$$\sigma_1 = \sup_{\psi\neq 0, \psi\in W^{1,2}} \frac{d_2 - \int_\Omega |\nabla\psi(x)/N|^2 dx + \int_\Omega r_2 \frac{\psi^2}{N} f(x, 0, K, N, M, K) dx}{\int_\Omega \left(\frac{\psi^2}{N}\right) dx}.$$

Upon putting $\psi(x) = N(x)$ and using h3, the principal eigenvalue is

$$\sigma_1 \geq \frac{r_2 \int_\Omega NF(x, \frac{K-N}{M}K, K)\, dx}{\int_\Omega N(x)\, dx}.$$

Since, $F(x, \frac{K-N}{M}K, K) = 1 - \frac{(\frac{K-N}{M})K}{K} = \frac{M(x)-K(x)+N(x)}{M(x)} < 0$ for $M(x)+N(x) < K(x)$, also $N(x) > 0$. Therefore, $\sigma_1 < 0$ and semi-trivial equilibrium $(K, 0)$ of (2.4) is locally stable. □

In a similar way, we can prove $(0, v^*)$ is locally stable if $(M(x) + N(x)) \leq K(x)$ for any $x \in \Omega$, i.e., $v(x) \geq 1$ in a non-empty open domain $\Omega_s \subseteq \Omega$ with $r_1(x) \equiv r_1$, $r_2(x) \equiv r_2$ are constant, $\frac{K(x)}{M(x)} \equiv \beta > 0$.

As Lemma 4 is still valid. From Lemma 8 and Lemma 9, we can state the consequent Theorem 3, represents the local existence of one semi-trivial steady state controlling the initial conditions.

Theorem 3. *Let the functions $g_1(x, u, v) = r_1 uf(x, u, v, M, N, K)$ and $g_2(x, v, u) = r_2 vf(x, v, u, N, M, K)$ satisfy h1-h6 and $K(x) \not\equiv$ constant. Also, let $r_1(x) \equiv r_1$, $r_2(x) \equiv r_2$ are constant and $\frac{K(x)}{M(x)} \equiv \beta > 0$. Then either the equilibrium $(K(x), 0)$ or the equilibrium $(0, v^*(x))$ of the system of equations (2.4) is locally asymptotically stable if $(M(x) + N(x)) \leq K(x)$ for any $x \in \Omega$. That is, depending on $u_0, v_0 \in C(\overline{\Omega})$, the solution (u, v) of (2.4) satisfies*

$$\text{either } (u, v) \to (K, 0), \quad \text{or } (u, v) \to (0, v^*), \quad \text{as} \quad t \to \infty$$

uniformly in $x \in \overline{\Omega}$.

Corollary 2. *Let the functions $g_1(x, u, v) = r_1 uf(x, u, v, M, N, K)$ and $g_2(x, v, u) = r_2 vf(x, v, u, N, M, K)$ satisfy h1-h6 and $K(x) \equiv$ constant. Then either the equilibrium $(K(x), 0)$ or the equilibrium $(0, v^*(x))$ of the system of equations (2.4) is locally asymptotically stable if $M(x) + N(x) < K$ for any $x \in \Omega$. That is, depending on $u_0, v_0 \in C(\overline{\Omega})$, the solution (u, v) of (2.4) satisfies*

$$\text{either } (u, v) \to (K, 0), \quad \text{or } (u, v) \to (0, v^*), \quad \text{as} \quad t \to \infty$$

uniformly in $x \in \overline{\Omega}$.

Lemma 10. *Let the growth function f satisfy h1-h6, $r_1(x) \equiv r_2(x) \equiv r$ are constant and $K(x) \not\equiv$ constant. If $(u^*, 0)$ and $(0, v^*)$ are the semi-trivial solution of (4.3) and (4.4), respectively and $\mu, \nu \in (0, 1)$ then*

$$r \int_\Omega f(x, 0, v^*, 0, M, N, K) M(x)\, dx \equiv r \int_\Omega F(x, v^*(x), M, N, K) M(x)\, dx > 0, \tag{4.18}$$

and

$$r \int_\Omega f(x, 0, u^*, N, M, K) N(x)\, dx \equiv r \int_\Omega F(x, v^*(x), N, M, K) N(x)\, dx > 0. \tag{4.19}$$

Proof: Let us assume, $N_1 = \int_\Omega M(x)\, dx$ and $N_2 = \int_\Omega N(x)\, dx$ where $r_1(x) \equiv r_2(x) \equiv r$.
Denote,

$$a^* = \min \left\{ \frac{N_1}{\int_\Omega (\frac{M(x)v^*(x)}{K(x)})\, dx}, 1 \right\} \in (0, 1)$$

If $\mu \in (0, a^*)$ then,

$$\int_\Omega \frac{M(x)v^*(x)\mu(x)}{K(x)}\, dx < N_1$$

$$\Rightarrow \int_\Omega r\frac{M(x)v^*(x)\mu(x)}{K(x)}\, dx < r \int_\Omega M(x)\, dx,$$

where $\mu(x) \in (0, 1)$ and r is constant

$$\Rightarrow r \int_\Omega \left(1 - \frac{\mu v^*}{K}\right) M\, dx > 0$$

$$\Rightarrow r \int_\Omega g(x, v^*, 0, M, N, K) M\, dx > 0.$$

Applying property h3 for f, we get, $r \int_\Omega F(x, v^*, M, N, K) M\, dx > 0$.

Now if $(u^*, 0)$ is a semi-trivial equilibrium of (4.3) and $a^{**} = \min \left\{ \frac{N_2}{\int_\Omega \left(\frac{N(x)v^*(x)}{K(x)}\right) dx}, 1 \right\} \in (0, 1)$ than for $\nu \in (0, a^{**}) \in (0, 1)$, applying the same procedure as before we can find,

$$r \int_\Omega F(x, u^*, N, M, K) N\, dx > 0.$$

□

Now we will analyze the case of the ideal free pair when $M(x), N(x)$, and $K(x)$ are space dependent and non-proportional to each other. By direct substitution of $\mu(x) = \frac{K(x)-M(x)}{N(x)}$ and $\nu(x) = \frac{K(x)-N(x)}{M(x)}$ it is easy to check that (M, N) is the solution of the system (2.4). Now we will establish this coexistence steady state *via* the instability of both $(u^*, 0)$ and $(0, v^*)$.

Lemma 11. *Let f satisfies h1-h6 and $M(x), N(x)$, and $K(x)$ are non-constant and linearly independent. If $r_1(x) \equiv r_2(x) \equiv r$ are constant and $(M(x) + N(x)) \geq K(x)$ for any $x \in \Omega$, then the semi-trivial steady state $(0, v^*)$ of the system (2.4) is unstable.*

Proof: Assume the linearized equations of the problem (2.4) for the first equation around $(0, v^*)$, then the associated eigenvalue problem for u is,

$$d_1 \Delta \left(\frac{\phi(x)}{M(x)}\right) + r_1 \phi(x) f(x, 0, v^*, M, N, K) = \sigma \phi(x), \quad \in \Omega, \quad \frac{\partial(\phi/M)}{\partial n} = 0, \quad x \in \partial\Omega. \tag{4.20}$$

According to Cantrell and Cosner [7], Theorem 2.1, the principal eigenvalue of (4.20) is represented as

$$\sigma_1 = \sup_{\phi\neq 0,\phi\in W^{1,2}} \frac{-\int_\Omega d_1|\nabla(\phi/M)|^2dx + \int_\Omega \frac{r_1}{M}\phi^2(x)f(x,0,v^*,M,N,K)dx}{\int_\Omega \left(\frac{\phi^2}{M}\right)dx}.$$

Selecting $\phi(x) = M(x)$ and using the property h3

$$\sigma_1 \geq \frac{\int_\Omega r_1 M(x)F(x,\frac{K-M}{N}v^*,K)dx}{\int_\Omega M(x)\,dx} \tag{4.21}$$

$$= \frac{r}{N_1}\int_\Omega M(x)F(x,v^*,M,N,K)dx > 0,$$

$$\text{where } N_1 = \int_\Omega M(x)dx > 0 \text{ for any } x\in\Omega. \tag{4.22}$$

Thus, $\sigma_1 > 0$ using (4.18) in Lemma 10 for $\mu \in (0,1)$, which concludes the proof. □

Lemma 12. *Let f satisfies h1-h6 and $M(x), N(x), K(x)$ are non-constant and linearly independent. If $r_1(x) \equiv r_2(x) \equiv r$ are constant and $(M(x) + N(x)) \geq K(x)$ for any $x \in \Omega$, then the semi-trivial steady state $(u^*, 0)$ of the system (2.4) is unstable.*

Proof: Analogous to Lemma 11 assumes the linearization of the second equation of the problem (2.4) around $(u^*, 0)$ and examine the related eigenvalue problem for v,

$$d_2\Delta\left(\frac{\psi(x)}{N(x)}\right) + r_2\psi(x)f(x,u^*,N,M,K) = \sigma\psi(x), \quad x\in\Omega,$$
$$\frac{\partial(\psi/N)}{\partial n} = 0, \quad x\in\partial\Omega. \tag{4.23}$$

and its principal eigenvalues according to Cantrell and Cosner [7], Theorem 2.1 is given by

$$\sigma_1 = \sup_{\psi\neq 0,\phi\in W^{1,2}} d_2 \frac{-\int_\Omega |\nabla(\psi/N)|^2dx + \int_\Omega \frac{r_2}{N}\phi^2(x)f(x,u^*,0,N,M,K)\,dx}{\int_\Omega \left(\frac{\psi^2}{N}\right)dx}.$$

Choosing $\phi(x) = N(x)$ and imposing the property h3

$$\sigma_1 \geq \frac{\int_\Omega r_2 N(x)F(x,\frac{K-N}{M}u^*,K)\,dx}{\int_\Omega N(x)dx} \tag{4.24}$$

$$= \frac{r}{N_2}\int_\Omega N(x)F(x,u^*,N,M,K)dx > 0,$$

$$\text{where } N_2 = \int_\Omega N(x)dx > 0 \text{ for any } x\in\Omega. \tag{4.25}$$

Thus, $\sigma_1 > 0$, using (4.19) from Lemma 10 for $v \in (0,1)$, which concludes the proof. □

Right now, we are prepared to give a conclusion about the existence of stable coexistence steady state (M, N) of (2.4) with the help of Lemma 11 and Lemma 12. It is noted that Lemma 4 is still true for the system (2.4).

Theorem 4. *Let the functions $g_1(x,u,v) = r_1uf(x,u,v,M,N,K)$ and $g_2(x,v,u) = r_2vf(x,v,u,N,M,K)$ satisfy h1-h6 and $M(x), N(x), K(x)$ are non-constant and linearly independent. If $(M(x) + N(x)) \geq K(x)$ for any $x \in \Omega$, and $r_1(x) \equiv r_2(x) \equiv r$ are constant, then for any non-negative and non-trivial $u_0, v_0 \in C(\overline{\Omega})$ the coexistence of steady state (M,N) of the system of equations (2.4) is globally asymptotically stable.*

The uniqueness of the coexistence solution $(u_e, v_e) = (M, N)$ can be proved similarly according to Braverman and Kamrujjaman [9, 15], where they consider carrying capacity as equal to the linear combination of the corresponding resource functions.

5. Numerical methods and applications

Consider the system of (2.5) for numerical simulations with the generalized logistic growth laws. To implement the numerical test, we consider the domain $\Omega = [0,1]$ for one space dimension and $\Omega = [0,1]\times[0,1]$ for two space dimensions, throughout the paper. In this study, for simplicity taking a uniform rectangular grid of spacing $\Delta x \times \Delta y \equiv h_x \times h_y$ on Ω with $h_x = (x_f - x_0)/N_x$ and $h_y = (y_f - y_0)/N_y$, where N_x and N_y are the number of grid points along x and y directions, respectively. Also, partition the time T by a distance $\Delta t \equiv h_t = T/N_t$. To discretize the system of partial differential equations into a continuous space and temporal domain we have imposed the Crank-Nicolson method for the case of 1-D whereas the ADI method has been applied for the case of 2D. Thus, we can write as $u_i^n = u(ih_x, nh_t)$, $v_i^n = v(ih_x, nh_t)$ for 1-D and $u_{i,j}^n = u(ih_x, jh_y, nh_t)$, $v_{i,j}^n = v(ih_x, ih_y, nh_t)$ for 2D, respectively. Also, for the discretized equation the result was considered to have converged when successive iterations are within 10^{-7} of each other.

5.1. When K, M, N, μ, and v are time independent

5.1.1. Case of one- space dimension

In this segment of the numerical computation, we will discuss the model (2.5) when K, M, and N are merely functions of one space dimension.

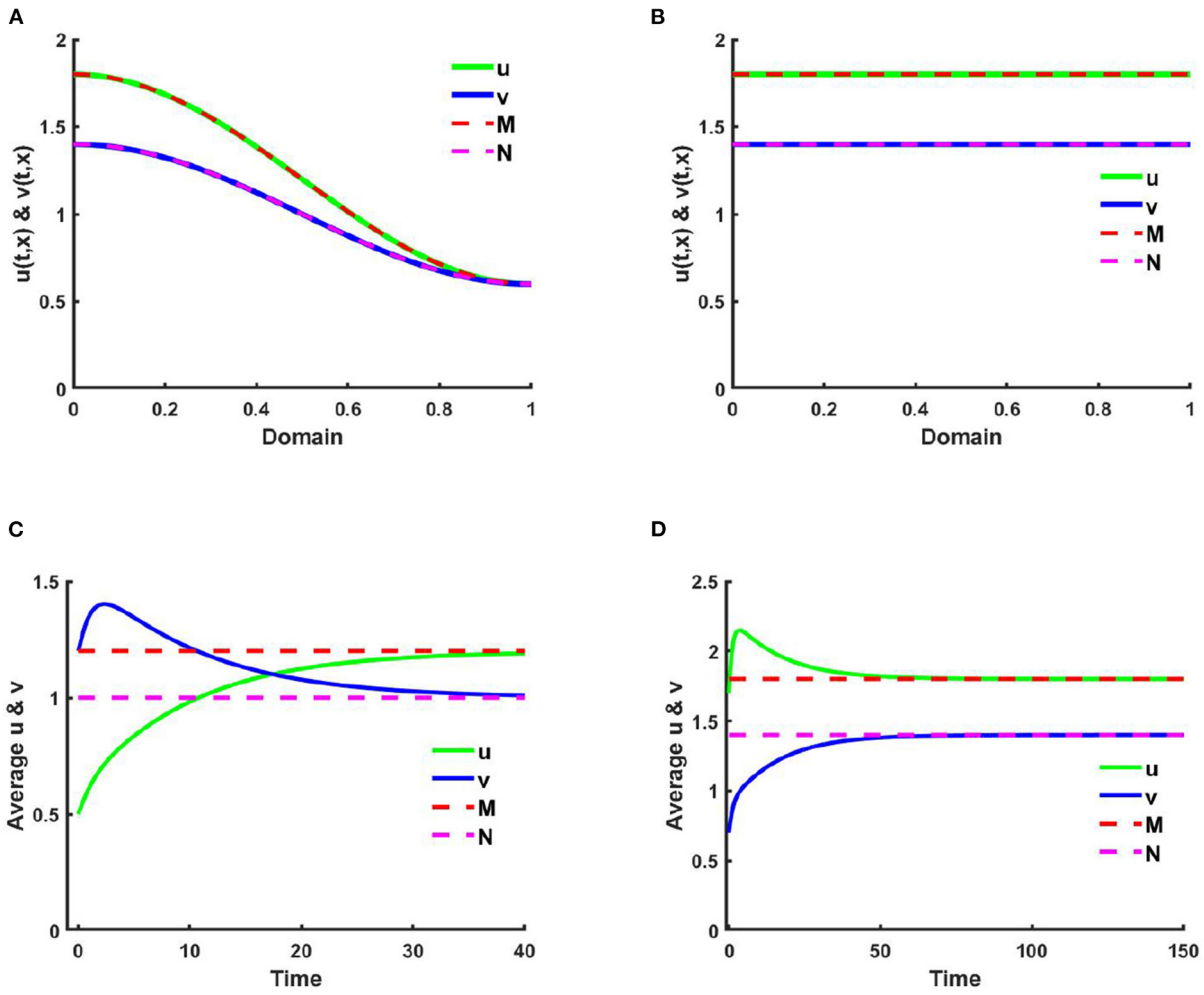

FIGURE 1
The solutions and space average density of (2.5) when $M + N > K$ where $d_1 = d_2 = 1.0$, $r_1 = r_2 = 1.0$ for **(A,C)** $K = 2.0 + \cos(\pi x)$, $M = 0.6K = 1.2 + 0.6\cos(\pi x)$, $N = 1.0 + 0.4\cos(\pi x)$, $\mu(x) = \frac{0.8+0.4\cos(\pi x)}{1.5+0.6\cos(\pi x)} \in [0.66, 0.85]$, $\nu(x) = \frac{1.0+0.4\cos(\pi x)}{0.8+0.4\cos(\pi x)} \in [0.66, 0.88]$, $(u_0, v_0) = (0.5, 1.2)$, and **(B,D)** $K = 3.0$, $M = 0.6K = 1.8$, $N = 1.5$, $\mu(x) = 0.85$, $\nu(x) = 0.89$, $(u_0, v_0) = (1.7, 0.7)$ on $\Omega = (0, 1)$.

Example 1. *Consider the case of (2.5) when* $M + N > K$ *on* $\Omega = (0, 1) \subset \mathbb{R}$, *where u is diffusing according to their carrying capacity and v is followed by the resource-based diffusion strategy. Here, in Figures 1, 2A,C consider* $K(x) = 2.0 + \cos(\pi x)$, $M(x) = 0.6K$, *where* $N(x) = 1.0 + 0.4\cos(\pi x)$, $\mu(x) = \frac{0.8+0.4\cos(\pi x)}{1.5+0.6\cos(\pi x)} \in [0.66, 0.85]$, $\nu(x) = \frac{1.0+0.4\cos(\pi x)}{0.8+0.4\cos(\pi x)} \in [0.66, 0.88]$ *and in Figures 1, 2B,D* $K = 3.0$, $M = 0.6K$, *and* $N = 1.5$ *with* $\mu(x) = 0.85$, $\nu(x) = 0.89$. *Additionally, let,* $r_1 = r_2 = 1.0$, $(u_0, v_0) = (0.5, 1.2)$, *and* $d_1 = d_2 = 1.0$. *Figures 1A,B characterizes the population density profiles of u and v over domain x and Figures 1C,D represents the space average density profiles of u and v against time for different values of competition coefficients* $(\mu(x), \nu(x))$. *We perceive from Figures 1A,C that when K, M, and N are space dependent then there exists a non-trivial coexistence solution that converges to M and N with time grows which is expected as in Theorem 2 and Corollary 1. Here, it is mentioned that the values of* (u, v) *coincide with* (M, N), *respectively which provide the existence of ideal free pair while M is proportional to K and* N/K *are non-constant.*

Since $\mu(x) \in [0.66, 0.85]$ *and* $\nu(x) \in [0.66, 0.88]$ *in Figures 1A,C, due to the nearly higher impact of* $\nu(x)$ *on v the density of u is found higher than v. Which is also found analogous in Figures 1B,D where K is constant and* $\mu(x) = 0.85$, $\nu(x) = 0.89$. *It is likewise noted that when K, M, and N are space dependent spatial functions then space average density converges faster to the steady state compared to letting constant values of K, M, and N. It is also observed that density profiles correlate with their corresponding resource*

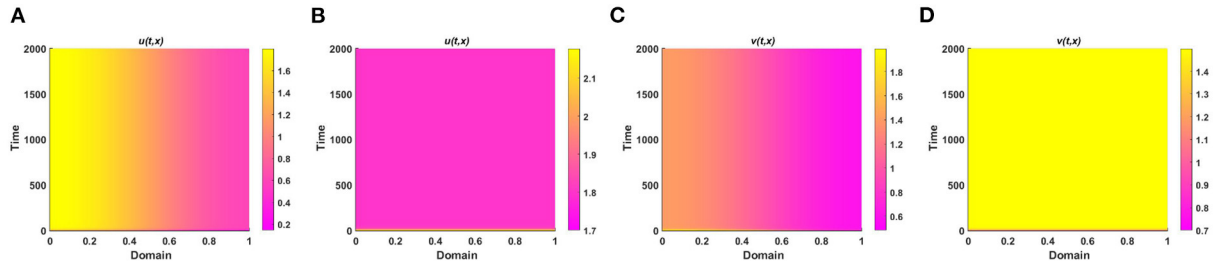

FIGURE 2
The population density of u and v for (2.5) when $M + N > K$ with $d_1 = d_2 = 1.0$, $r_1 = r_2 = 1.0$ for **(A,C)** $K = 2.0 + \cos(\pi x)$, $M = 0.6K = 1.2 + 0.6\cos(\pi x)$, $N = 1.0 + 0.4\cos(\pi x)$, $\mu(x) = \frac{0.8+0.4\cos(\pi x)}{1.5+0.6\cos(\pi x)} \in [0.66, 0.85]$, $\nu(x) = \frac{1.0+0.4\cos(\pi x)}{0.8+0.4\cos(\pi x)} \in [0.66, 0.88]$, $(u_0, v_0) = (0.5, 1.2)$, and **(B,D)** $K = 3.0$, $M = 0.6K = 1.8$, $N = 1.5$, $\mu(x) = 0.85$, $\nu(x) = 0.89$, $(u_0, v_0) = (1.7, 0.7)$ on $\Omega = (0, 1)$.

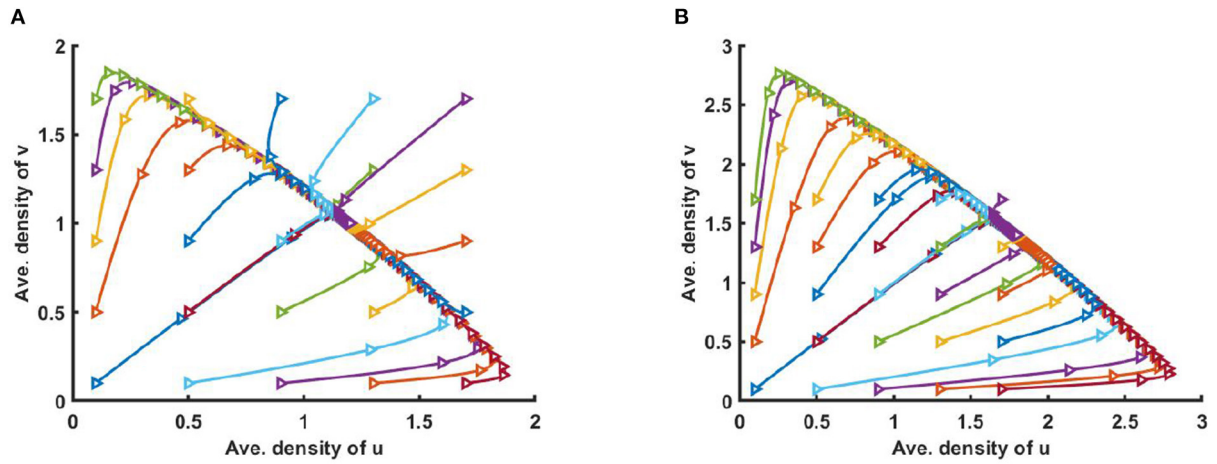

FIGURE 3
Solution trajectories of space average density of u and v for different initial values (u_0, v_0) on $\Omega = (0, 1)$ when $M + N > K$ where $d_1 = d_2 = 1.0$, $r_1 = r_2 = 1.0$ for **(A)** $K = 2.0 + \cos(\pi x)$, $M = 0.6K = 1.2 + 0.6\cos(\pi x)$, $N = 1.0 + 0.4\cos(\pi x)$, $\mu(x) = \frac{0.8+0.4\cos(\pi x)}{1.5+0.6\cos(\pi x)} \in [0.85, 0.66]$, $\nu(x) = \frac{1.0+0.4\cos(\pi x)}{0.8+0.4\cos(\pi x)} \in [0.66, 0.88]$, and **(B)** $K = 3.0$, $M = 0.6K = 1.8$, $N = 1.5$, $\mu(x) = 0.85$, $\nu(x) = 0.89$ of (2.5) at $t = T = 100$.

functions in all cases, independent of non-negative, non-trivial initial values.

Figure 2 reveals the solution of (2.5) for u and v when $t = 2,000$. *Similar to Figure 1 an attractive coexistence equilibrium solution is noticed for different values of* μ *and* ν.

However, Figure 3 illustrates the solution trajectories for space average density of u vs. v for different initial values (u_0, v_0) *when* $M + N > K$, *wherein (a)* $K(x) = 2.0 + \cos(\pi x)$, $M(x) = 0.6K$, $N(x) = 1.0 + 0.4\cos(\pi x)$, $\mu(x) = \frac{0.8+0.4\cos(\pi x)}{1.5+0.6\cos(\pi x)} \in [0.66, 0.85]$, $\nu(x) = \frac{1.0+0.4\cos(\pi x)}{0.8+0.4\cos(\pi x)} \in [0.66, 0.88]$ *and in (b)* $K = 3.0$, $M = 0.6K$, *and* $N = 1.5$, $\mu(x) = 0.85$, $\nu(x) = 0.89$, *for allowing others parameters are fixed. We found that for different constant and non-constant values of competition coefficients both species survive in the competition which is independent of initial values* (u_0, v_0).

Example 2. *Consider (2.5) when* $M + N < K$ *for the functions* $K(x) = 2.0 + \cos(\pi x)$, *where* $d_1 = d_2 = 1.0$, $r_1 = r_2 = 1.0$, $(u_0, v_0) = (0.7, 0.7)$. *Here, setting in Figure 4A* $M = 0.3K$, *where* $N = 1.0 + 0.7\cos(\pi x)$, $\mu(x) = \frac{1.4+0.7\cos(\pi x)}{1.0+0.7\cos(\pi x)} \in [1.23, 2.33]$, $\nu(x) = \frac{1.0+0.3\cos(\pi x)}{0.6+0.3\cos(\pi x)} \in [1.44, 2.33]$, *and in Figure 4B* $M = 0.6K$, *and* $N = 0.6 + 0.4\cos(\pi x)$, *where* $\mu(x) = \frac{0.8+0.4\cos(\pi x)}{0.6+0.4\cos(\pi x)} \in [1.2, 2]$, $\nu(x) = \frac{1.4+0.6\cos(\pi x)}{1.2+0.6\cos(\pi x)} \in [1.11, 1.33]$ *on* $\Omega = (0, 1)$. *According to Theorem 3, all the solutions either converge to the equilibrium* $(K(x), 0)$ *or to the equilibrium* $(0, v^*(x))$ *which is locally asymptotically stable. Figures 4A,B represents the population density profiles of u and v vs. x for different values of competition coefficients* $(\mu(x), \nu(x))$ *at* $t = T = 2,000$ *where the solution is sufficiently large to reach the steady state. Here in all cases, we discover the existence of a competitive exclusion solution. However, in Figure 4A, we observe for small*

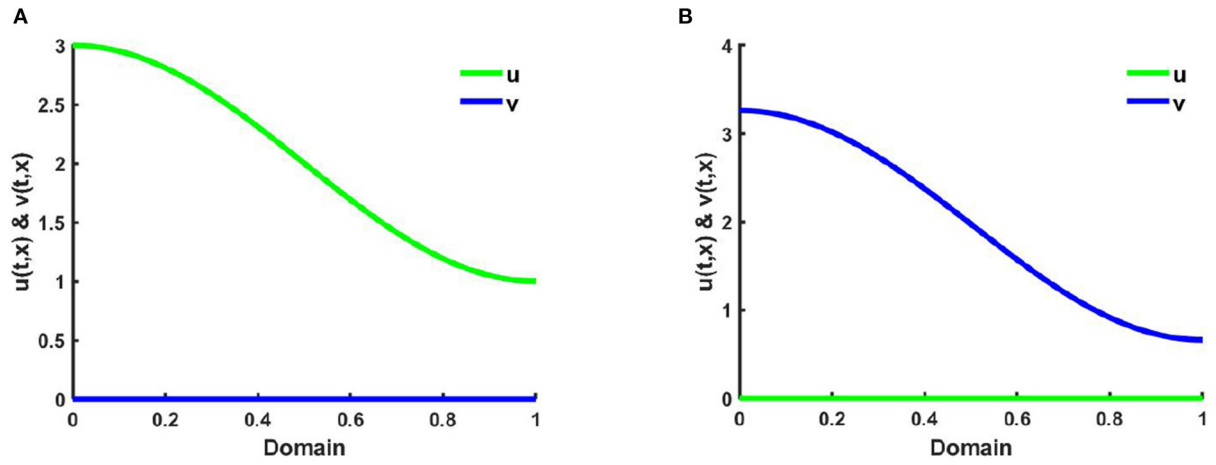

FIGURE 4
The solutions of (2.5) when $M + N < K$ where $K = 2.0 + \cos(\pi x)$, $d_1 = d_2 = 1.0$, $r_1 = r_2 = 1.0$, $(u_0, v_0) = (0.7, 0.7)$ for **(A)** $M = 0.3K = 0.6 + 0.3\cos(\pi x)$, $N = 1.0 + 0.7\cos(\pi x)$, $\mu(x) = \frac{1.4+0.7\cos(\pi x)}{1.0+0.7\cos(\pi x)} \in [1.23, 2.33]$, $\nu(x) = \frac{1.0+0.3\cos(\pi x)}{0.6+0.3\cos(\pi x)} \in [1.44, 2.33]$, and **(B)** $M = 0.6K = 1.2 + 0.6\cos(\pi x)$, $N = 0.6 + 0.4\cos(\pi x)$, $\mu(x) = \frac{0.8+0.4\cos(\pi x)}{0.6+0.4\cos(\pi x)} \in [1.2, 2]$, $\nu(x) = \frac{1.4+0.6\cos(\pi x)}{1.2+0.6\cos(\pi x)} \in [1.11, 1.33]$ on $\Omega = (0, 1)$.

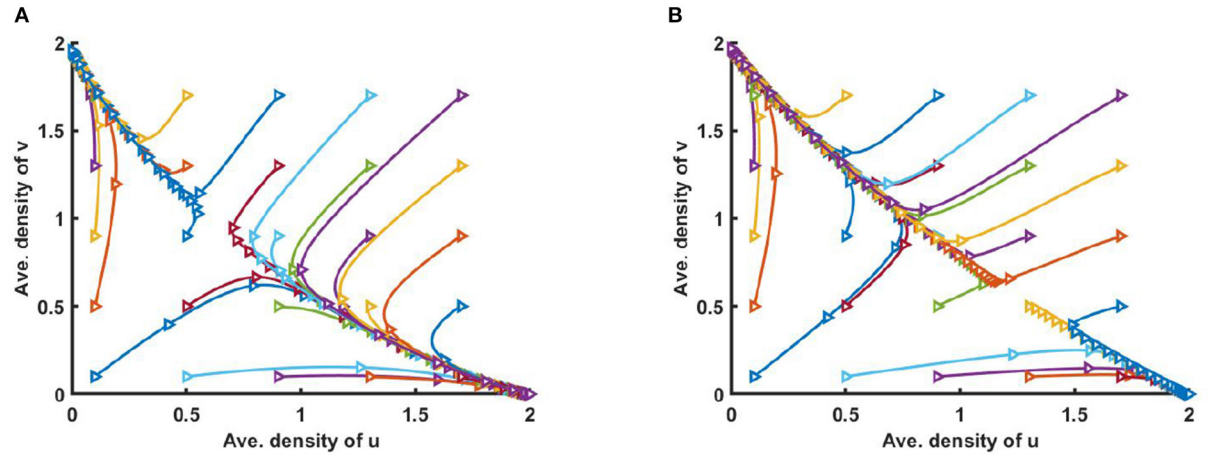

FIGURE 5
Solution trajectories of space average density of u and v for different initial values (u_0, v_0) on $\Omega = (0, 1)$ when $M + N < K$ where $K = 2.0 + \cos(\pi x)$, $d_1 = d_2 = 1.0$, $r_1 = r_2 = 1.0$ for **(A)** $M = 0.3K = 0.6 + 0.3\cos(\pi x)$, $N = 1.0 + 0.7\cos(\pi x)$, $\mu(x) = \frac{1.4+0.7\cos(\pi x)}{1.0+0.7\cos(\pi x)} \in [1.23, 2.33]$, $\nu(x) = \frac{1.0+0.3\cos(\pi x)}{0.6+0.3\cos(\pi x)} \in [1.44, 2.33]$, and **(B)** $M = 0.6K = 1.2 + 0.6\cos(\pi x)$, $N = 0.6 + 0.4\cos(\pi x)$, $\mu(x) = \frac{0.8+0.4\cos(\pi x)}{0.6+0.4\cos(\pi x)} \in [1.2, 2]$, $\nu(x) = \frac{1.4+0.6\cos(\pi x)}{1.2+0.6\cos(\pi x)} \in [1.11, 1.33]$ of (2.5) at $t = T = 100$.

values of proportionality constant ($\beta = 0.3$) the species u is endure while v goes to extinction as time raises and the solution of u converges to K with the increase of time. An opposite observation is noticed in Figure 4B where $\beta = 0.6$ and the non-trivial solution is found for v, and u turns to elimination for different values of competition coefficients.

Furthermore, Figure 5 shows the solution trajectories for space average density of u vs. v for different initial values when $M + N < K$ and $\mu(x), \nu(x) > 1$. Also let, $M = 0.3K$, where $N = 1.0 + 0.7\cos(\pi x)$ in Figure 5A, and $M = 0.6K$ where $N = 0.6 + 0.4\cos(\pi x)$ in Figure 5B. If M is proportional to K, N/K are non-constant, and $M + N < K$ then by Theorem 3, both semi-trivial equilibrium solutions are locally asymptotically stable. We find that for different non-constant values of competition coefficients one of the species survives in competition, and the solution trajectory moves either toward u or to v depending on the different values of initial values (u_0, v_0).

Example 3. *Consider (2.5) where $M + N > K$ and both species disperse according to their resource function $M = 1.2 + 0.5\cos(\pi x)$ and $N = 1.3 + 0.5\cos(\pi x)$, respectively which are not proportional to $K = 2.0 + \cos(\pi x)$ in Figures 6, 7, respectively.*

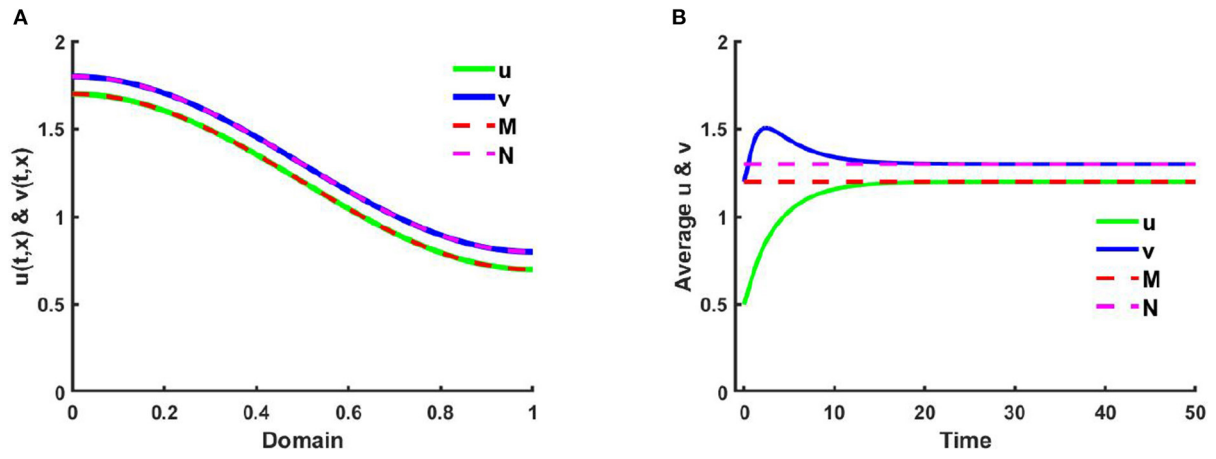

FIGURE 6
(A) The solutions, and **(B)** space average density of (2.5) when $M + N > K$ where $K = 2.0 + \cos(\pi x)$, $M = 1.2 + 0.5\cos(\pi x)$, $N = 1.3 + 0.5\cos(\pi x)$, $\mu(x) = \frac{0.8+0.5\cos(\pi x)}{1.3+0.5\cos(\pi x)} \in [0.37, 0.72]$, $\nu(x) = \frac{0.7+0.5\cos(\pi x)}{1.2+0.5\cos(\pi x)} \in [0.29, 0.70]$, $d_1 = d_2 = 1.0$, $r_1 = r_2 = 1.0$, $(u_0, v_0) = (0.5, 1.2)$ on $\Omega = (0, 1)$ at $t = T = 50$.

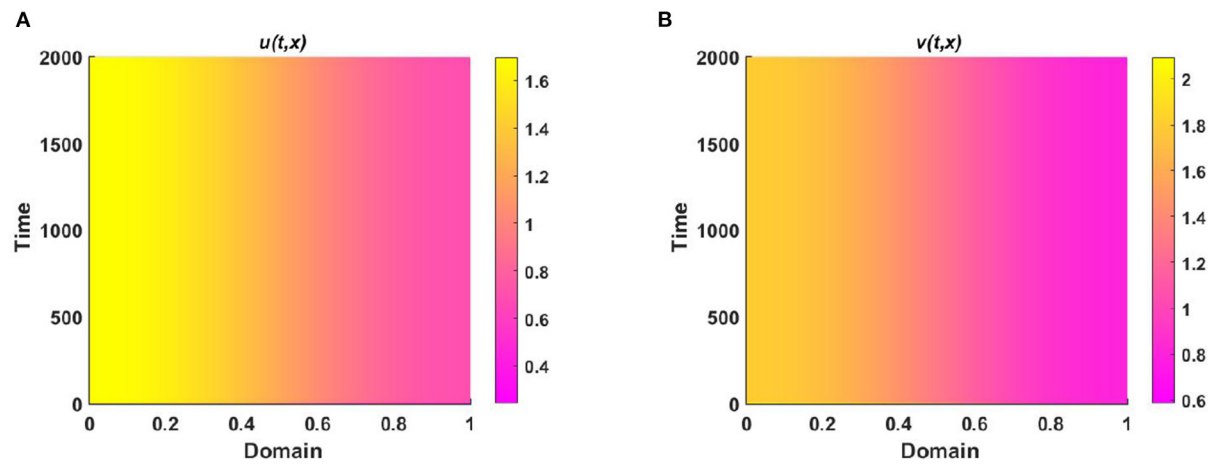

FIGURE 7
The population density of **(A)** u, and **(B)** v for (2.5) when $M + N > K$ where $K = 2.0 + \cos(\pi x)$, $M = 1.2 + 0.5\cos(\pi x)$, $N = 1.3 + 0.5\cos(\pi x)$, $\mu(x) = \frac{0.8+0.5\cos(\pi x)}{1.3+0.5\cos(\pi x)} \in (0.37, 0.72)$, $\nu(x) = \frac{0.7+0.5\cos(\pi x)}{1.2+0.5\cos(\pi x)} \in (0.29, 0.70)$, $d_1 = d_2 = 1.0$, $r_1 = r_2 = 1.0$, $(u_0, v_0) = (0.5, 1.2)$ on $\Omega = (0, 1)$.

Also let, $d_1 = d_2 = 1.0$, $r_1 = r_2 = 1.0$, $(u_0, v_0) = (0.5, 1.2)$ *on* $\Omega = (0, 1)$ *where* $\mu(x) = \frac{0.8+0.5\cos(\pi x)}{1.3+0.5\cos(\pi x)} \in [0.37, 0.72]$, $\nu(x) = \frac{0.7+0.5\cos(\pi x)}{1.2+0.5\cos(\pi x)} \in [0.29, 0.70]$. *In Figure 6, it is observed that the solution approaches the ideal pair* (M, N) *which is regardless of* (u_0, v_0)*, which is an affirmation of Theorem 4.*

Also, Figure 7 illustrates the coexistence of both species is globally asymptotically stable and $(u, v) \to (M, N)$ *with* $t \to \infty$.

5.1.2. Case of two- space dimensions

This section aims to simulate the model (2.5) when K, M, and N are functions of both x and y.

Example 4. *Consider the spatial functions for model (2.5) when* $M + N > K$ *wherein Figures 8A,C* $K = 2.0 + \cos(\pi x)\cos(\pi y)$, $M = 0.6K = 1.2 + 0.6\cos(\pi x)\cos(\pi y)$, $N = 1.0 + 0.4\cos(\pi x)\cos(\pi y)$, *and* $\mu(x) = \frac{0.8+0.4\cos(\pi x)\cos(\pi y)}{1.0+0.4\cos(\pi x)\cos(\pi y)} \in [0.67, 0.86]$, $\nu(x) = \frac{1.0+0.6\cos(\pi x)\cos(\pi y)}{1.2+0.6\cos(\pi x)\cos(\pi y)} \in [0.67, 0.89]$, *and in Figures 8B,D* $K = 3.0$, $M = 0.6K = 1.8$, $N = 1.5$, $\mu(x) = 0.8$, $\nu(x) = 0.83$. *Also let,* $d_1 = d_2 = 1.0$, $r_1 = r_2 = 1.0$, $(u_0, v_0) = (0.7, 0.7)$ *on* $\Omega = (0, 1) \times (0, 1)$ *for different values of competition coefficients. Figure 8 signifies the contour profiles of* u *and* v *while* M *is proportional to* K *and* N/K *are non-constant. We have computed the solution at* $t = T = 400$ *for which it is adequate to get a steady state. We see that for*

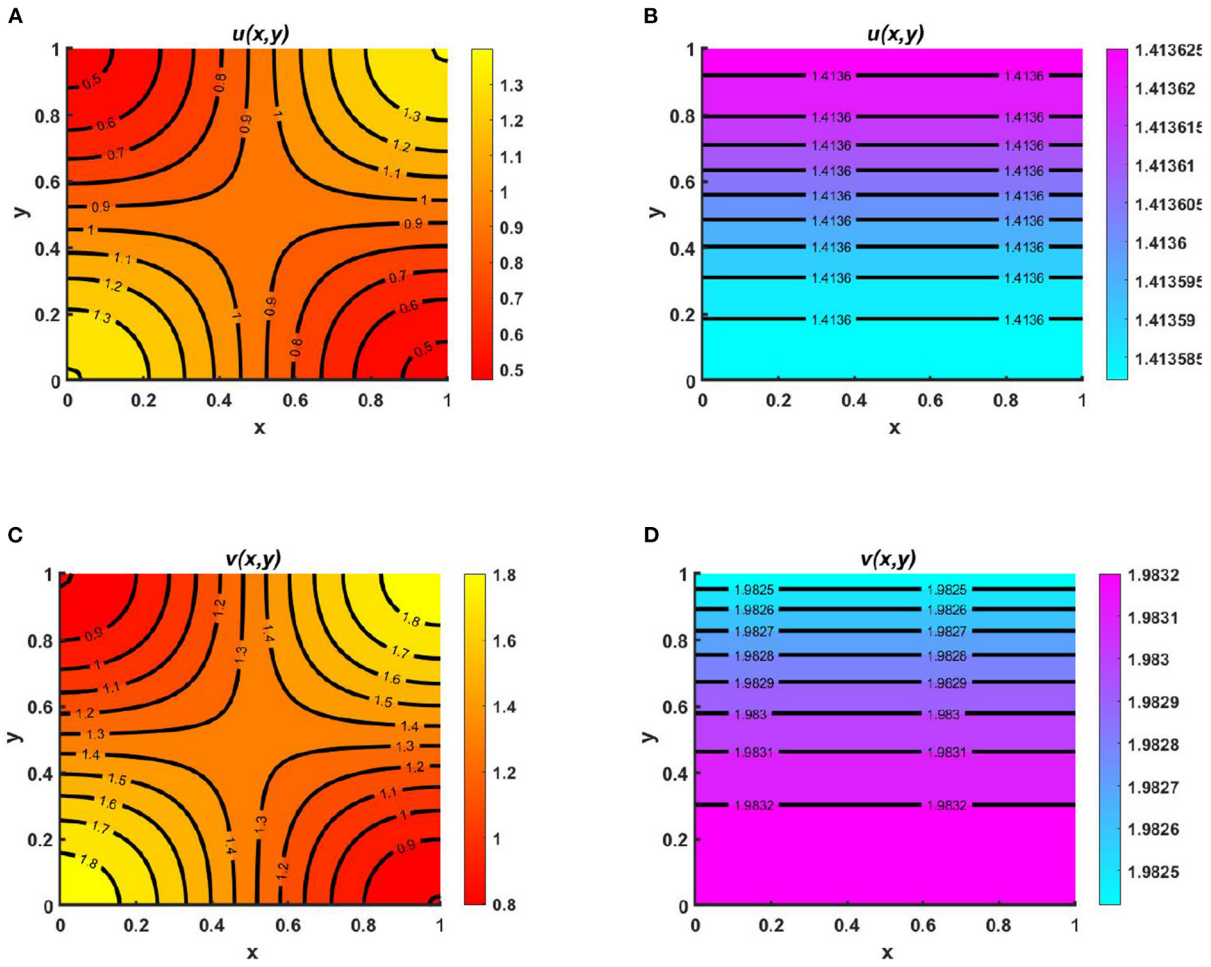

FIGURE 8
Contour plots of u and v of (2.5) at $t = T = 400$ when $M + N > K$ where $d_1 = d_2 = 1.0$, $r_1 = r_2 = 1.0$, $(u_0, v_0) = (0.7, 0.7)$ for **(A,C)** $K = 2.0 + \cos(\pi x)\cos(\pi y)$, $M = 0.6K = 1.2 + 0.6\cos(\pi x)\cos(\pi y)$, $N = 1.0 + 0.4\cos(\pi x)\cos(\pi y)$, $\mu(x) = \frac{0.8+0.4\cos(\pi x)\cos(\pi y)}{1.0+0.4\cos(\pi x)\cos(\pi y)} \in [0.67, 0.86]$, $v(x) = \frac{1.0+0.6\cos(\pi x)\cos(\pi y)}{1.2+0.6\cos(\pi x)\cos(\pi y)} \in [0.67, 0.89]$, and **(B,D)** $K = 3.0$, $M = 0.6K = 1.8$, $N = 1.5$, $\mu(x) = 0.8$, $v(x) = 0.83$ on $\Omega = (0, 1) \times (0, 1)$.

$\mu(x), v(x) \in (0, 1)$, both species sustain in the competition, and the contour pattern followed shows a correlation with M and N rather than K. The contour profiles in Figures 8A,C represent the saddle shape where maximum population density is located at the left and right bottom and top corners of the domain whereas minimum population density is found right and left bottom and top corner of the contour profile, respectively. Additionally, also Figures 8B,D shows the coexistence with a very small change in contour profiles. As we know, for two interacting species the outcome is either competitive exclusion or coexistence of two species. Here, we observed that for different constant and space dependent values of μ and v both species sustain (refer to, Figures 8A–D), which justified Theorem 2 and Corollary 1 while coexistence is feasible. From an ecological perspective, when the competition coefficients are less than 1 then the interspecific competition has less effect than intraspecific competition. The opposite scenario occurs when both competition coefficients are greater than 1. Due to partial resource sharing of both interacting species, competition coefficients (μ, v) between 0 and 1 stimulate cohabitation in the battle. It is also worth noting that v has a slightly greater population density than u, indicating that species which consume lower per capita accessible resources can have a slightly higher elevated population density. On the other hand, when niche differentiation occurs, most species do not utilize all of the resources available to them. The fish population is one of the most common instances of river organisms. Since one species forages mostly in shallow water and the other in deep water, they can coexist while sharing shared resources. Another example of resource sharing by grazers like zebra and wildebeest which are grazing on plants and eating typical African savanna grass (Panicum maximum) over time. The growing season of this grass begins later in the peak rain and lasts for 6 months. Among the two grazers, zebra eat the tallest

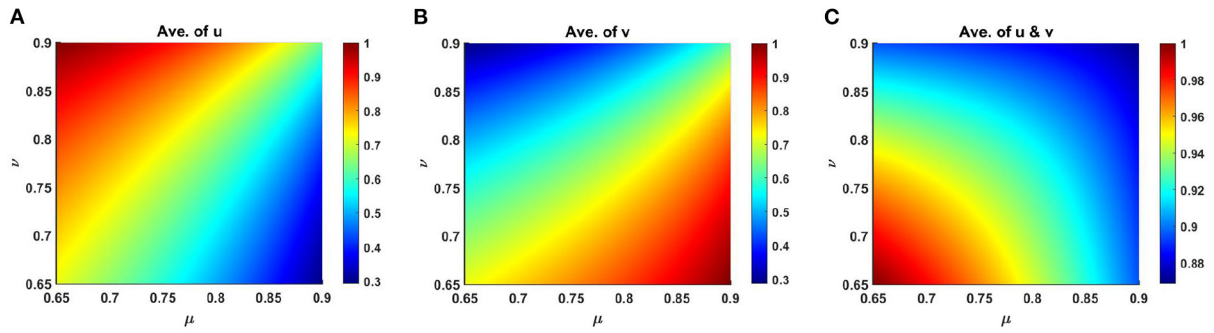

FIGURE 9
Average scaled density of (2.5) as a function of competition coefficients $\mu \in [0.65, 0.9]$ and $\nu \in [0.65, 0.9]$ on $\Omega \in (0,1) \times (0,1)$ when $M + N > K$ where $d_1 = d_2 = 1.0$, $r_1 = r_2 = 1.0$, $(u_0, v_0) = (0.7, 0.7)$ with $K = 2.0 + \cos(\pi x)\cos(\pi y)$, $M = 0.6K = 1.2 + 0.6\cos(\pi x)\cos(\pi y)$, $N = 1.0 + 0.4\cos(\pi x)\cos(\pi y)$ on $\Omega = (0,1) \times (0,1)$ for **(A)** u, **(B)** v, and **(C)** $u + v$ at $t = T = 1,000$.

grass, which is abundant but less nutritious since zebra teeth allow them to consume the taller grass. Zebras' digestive systems are also more effective than that of a ruminant grazer. However, by eating the tops of the grass, zebra make it simpler for wildebeests to access the more nutrient-dense areas of the grass close to the ground. Despite not being able to digest food as quickly as zebras, wildebeests can gain more energy since the lower portion of the grass is more nutrient-rich and soft. Thus, even though the other animals cannot obtain enough energy from it, they can survive on the shortest grass. In this way, two or more populations can sustain mutually by resource sharing.

Moreover, average scaled density of u, v and u + v of (2.5) are presented in Figure 9 as a function of competition coefficients for $M + N > K$, *where* $\mu \in [0.69, 0.9]$ *and* $\nu \in [0.65, 0.9]$ *on* $\Omega \in (0,1) \times (0,1)$ *that represents the dependency of the space average population density for* μ *and* ν. *Here, we have considered,* $K = 2.0 + \cos(\pi x)\cos(\pi y)$, $M = 0.6K = 1.2 + 0.6\cos(\pi x)\cos(\pi y)$, $N = 1.0 + 0.4\cos(\pi x)\cos(\pi y)$ *while others parameters are fixed as before. We have computed the values of* $\mu(x)$ *and* $\nu(x)$ *at each point in the domain for the range* $\mu \in [0.69, 0.9]$ *and* $\nu \in [0.65, 0.9]$ *which we have computed from equation (2.6) by the relation of* K, M, N, μ, *and* ν *at* $t = T = 1,000$. *Figure 9 demonstrates the coexistence of both species for the limited range of* μ *and* ν. *At this point, it is mentioned that with the increase of* ν, *the average density of u rise, whereas it starts to reduce with the increase of* μ *values. The opposite scenario is noticed for the scaled average population density of v.*

Example 5. *Consider the case of (2.5) at* $t = T = 400$ *when* $M + N < K$ *where* $K = 2.0 + \cos(\pi x)\cos(\pi y)$, $d_1 = d_2 = 1.0$, $r_1 = r_2 = 1.0$, $(u_0, v_0) = (0.7, 0.7)$ *on* $\Omega = (0,1) \times (0,1)$. *Here Figures 10A,C characterizes the contour profiles of u and v where we assume* $M = 0.3K = 0.6 + 0.3\cos(\pi x)\cos(\pi y)$, $N = 1.0 + 0.7\cos(\pi x)\cos(\pi y)$ *so that* $\mu(x,y) = \frac{1.4+0.7\cos(\pi x)\cos(\pi y)}{1.0+0.7\cos(\pi x)\cos(\pi y)} \in [1.24, 2.33]$, $\nu(x,y) = \frac{1.0+0.3\cos(\pi x)\cos(\pi y)}{0.6+0.3\cos(\pi x)\cos(\pi y)} \in [1.45, 2.33]$ *and in Figures 10B,D* $M = 0.6K = 1.2+0.6\cos(\pi x)\cos(\pi y)$, $N = 0.6+0.4\cos(\pi x)\cos(\pi y)$ *for which* $\mu(x,y) = \frac{0.8+0.4\cos(\pi x)\cos(\pi y)}{0.6+0.4\cos(\pi x)\cos(\pi y)} \in [1.2, 2.0]$, $\nu(x,y) = \frac{1.4+0.6\cos(\pi x)\cos(\pi y)}{1.2+0.6\cos(\pi x)\cos(\pi y)} \in [1.11, 1.33]$. *Here in both cases, competitive exclusion is observed to happen. Depending on the values of proportionally constant* β *either* $(u^*, 0)$ *or* $(0, v^*)$ *that ensure to is attained, which ensures the existence of local semi-trivial equilibrium where the diffusive migration of u followed carrying capacity K and the movement of other species is directed toward their resource distribution N. According to Theorem 3, as time increases, v dies out and the solution of u converges to K as shown in Figures 10A,C. However, in Figures 10B,D, the solution converges to v, and as time grows, u does not sustain in battle. In this case, the values of both competition coefficients are greater than 1, and interspecific competition is strong between the competing species. As we know, one possible effect of intense interspecific competition is competitive exclusion. If two species compete for a similar habitat, then one of them will eventually outcompete the others and drive them out of the environment. On the other hand, due to quite small per capita resource consumption the growth of species u increases rapidly seen in the case of Figures 10A,C, and other populations move toward extinction. A similar observation is noticed in Figures 10B,D for which v sustains in competition. For example, consider bird populations, as most birds rely on the same resources to survive in competition. It could result in fierce rivalry among the species. The more competition in the environment, the more difficult it is to sustain.*

However, Figure 11 represents the diagram of scaled average population density of u and v for different levels of competition coefficients at $t = T = 1,000$. *Here* $\mu \in [1, 2.5]$ *and* $\nu \in [1, 2.5]$ *which is obtained from equation (2.6) on* $\Omega \in (0,1) \times (0,1)$ *for* $M+N < K$ *when* $M = 0.3K$ *and* $N = 1.0+0.7\cos(\pi x)\cos(\pi y)$. *Here, we have calculated the dependency of u and v at each point for the consider fixed upper and lower estimates of* μ *and* ν *in the domain.*

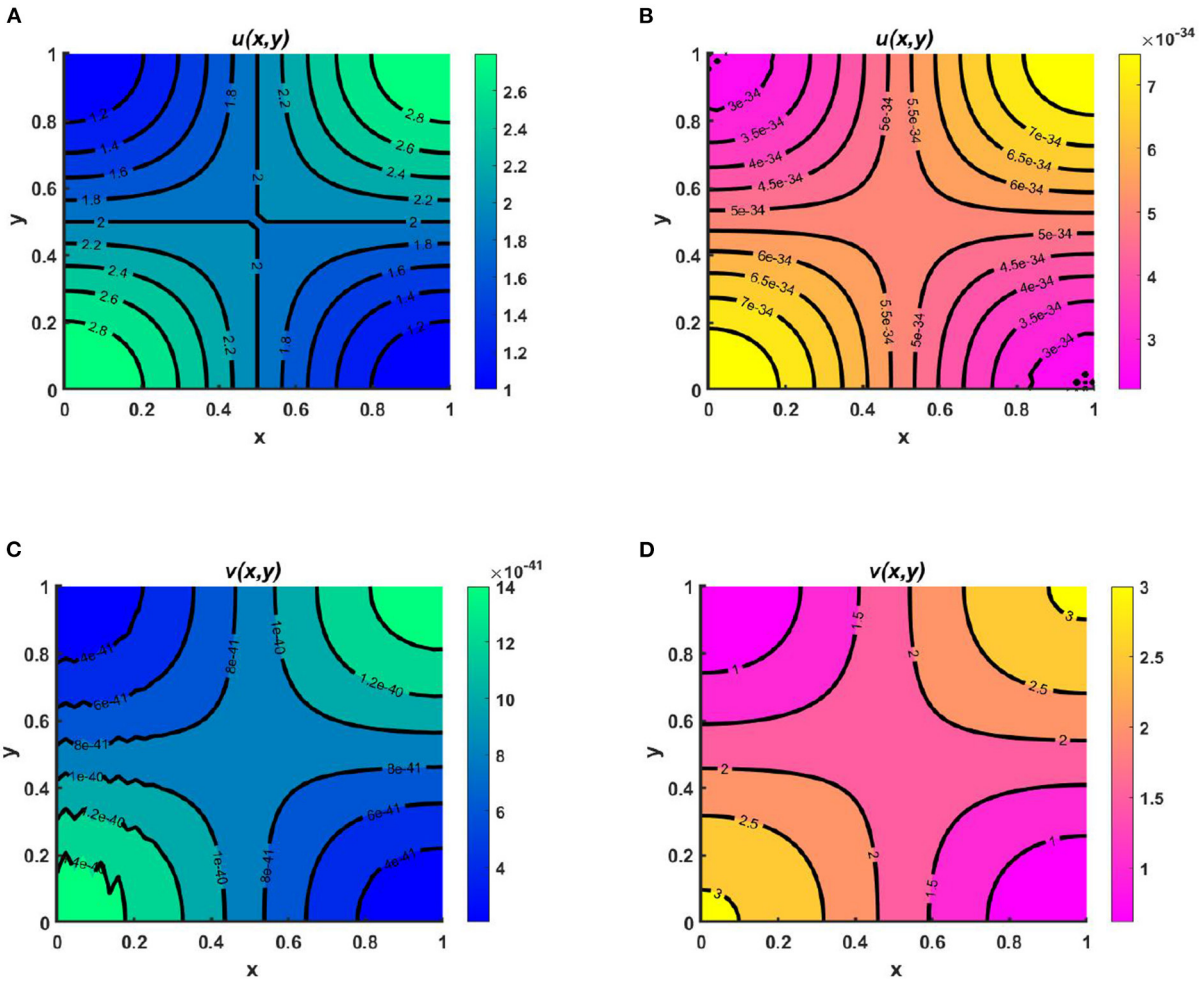

FIGURE 10
Contour plots of u and v of (2.5) at $t = T = 400$ when $M + N < K$ where $K = 2.0 + \cos(\pi x)\cos(\pi y)$, $d_1 = d_2 = 1.0$, $r_1 = r_2 = 1.0$, $(u_0, v_0) = (0.7, 0.7)$ for **(A,C)** $M = 0.3K = 0.6 + 0.3\cos(\pi x)\cos(\pi y)$, $N = 1.0 + 0.7\cos(\pi x)\cos(\pi y)$, $\mu(x, y) = \frac{1.4+0.7\cos(\pi x)\cos(\pi y)}{1.0+0.7\cos(\pi x)\cos(\pi y)} \in [1.24, 2.33]$, $v(x, y) = \frac{1.0+0.3\cos(\pi x)\cos(\pi y)}{0.6+0.3\cos(\pi x)\cos(\pi y)} \in [1.45, 2.33]$, and **(B,D)** $M = 0.6K = 1.2 + 0.6\cos(\pi x)\cos(\pi y)$, $N = 0.6 + 0.4\cos(\pi x)\cos(\pi y)$, $\mu(x, y) = \frac{0.8+0.4\cos(\pi x)\cos(\pi y)}{0.6+0.4\cos(\pi x)\cos(\pi y)} \in [1.2, 2.0]$, $v(x, y) = \frac{1.4+0.6\cos(\pi x)\cos(\pi y)}{1.2+0.6\cos(\pi x)\cos(\pi y)} \in [1.11, 1.33]$ on $\Omega = (0, 1) \times (0, 1)$.

Also, Figure 12 reveals the comparison of the average scaled population density of u and v for different levels of competition coefficients where $\mu \in [1, 2]$ *and* $\nu \in [1, 2]$ *on* $\Omega \in (0, 1) \times (0, 1)$ *at time* $t = T = 1{,}000$. *Here we set,* $M = 0.6K = 1.2 + 0.6\cos(\pi x)\cos(\pi y)$, $N = 0.6 + 0.4\cos(\pi x)\cos(\pi y)$ *and considering other parameters are fixed as before.*

Example 6. *Take* $K = 2.0 + \cos(\pi x)\cos(\pi y)$ *where* $M = 0.9 + 0.5\cos(\pi x)\cos(\pi y)$, $N = 1.1 + 0.5\cos(\pi x)\cos(\pi y)$ *in Figures 13A,B and* $M = 1.5 + 0.6\cos(\pi x)\cos(\pi y)$, $N = 0.8 + 0.7\cos(\pi x)\cos(\pi y)$ *in Figures 13C,D on* $\Omega = (0, 1) \times (0, 1)$ *for the model (2.5) when* $M + N \geq K$ *for which the contour profiles in Figure 13 form an ideal free pair. Here also let,* $d_1 = d_2 = 1.0$, $r_1 = r_2 = 1.0$, $(u_0, v_0) = (0.5, 0.5)$ *where* $\mu(x, y) = \nu(x, y) = 1.0$ *and* $\mu(x, y) = \frac{0.5+0.4\cos(\pi x)\cos(\pi y)}{0.8+0.7\cos(\pi x)\cos(\pi y)} \in [0.6, 1.0]$, $\nu(x, y) = \frac{1.2+0.3\cos(\pi x)\cos(\pi y)}{1.5+0.6\cos(\pi x)} \in [0.71, 1.0]$, *respectively in the prescribed domain. Here, we perceive that the contour profile of u follows M and the contour profiles of v correlate with N, respectively (refer to, Figures 13A,B) while* $M + N = K$. *In this case both species are diffusing in the direction of their resource functions and for the fixed values of competition coefficients, the coexistence of species appears, and they form an ideal pair. The total density for such a pair is identical to the carrying capacity. In this condition, the availability of resources for the couple species is spatially distinct, which can specialize through resource consumption. However, a similar observation is noticed for the case* $M + N > K$ *(refer to, Figures 13C,D) and the contour profile approaches toward their respective resource function that will form an ideal pair with*

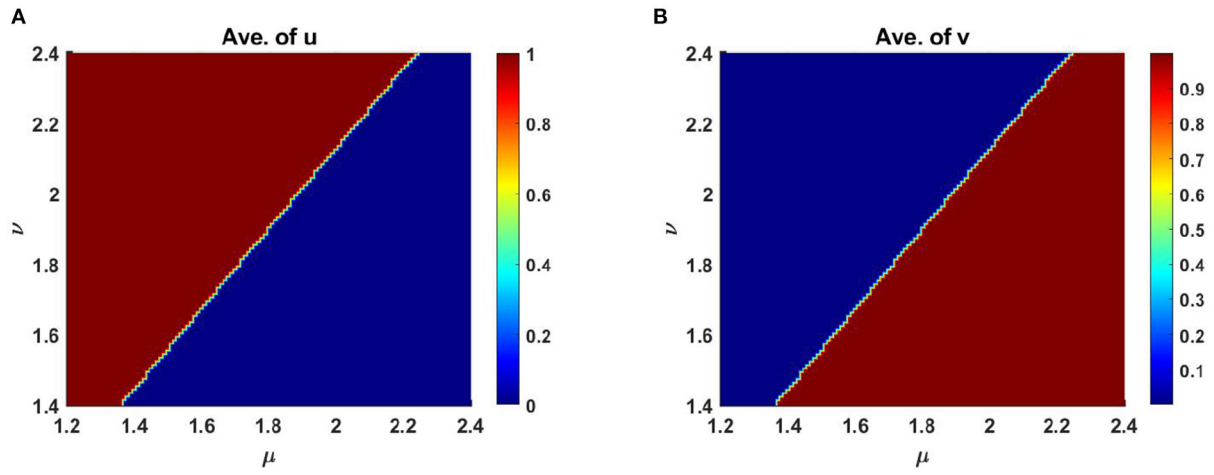

FIGURE 11
Average scaled density of u and v of (2.5) as a function of competition coefficients $\mu \in [1, 2.5]$ and $\nu \in [1, 2.5]$ on $\Omega \in (0,1) \times (0,1)$ when $M+N > K$ with $K = 2.0 + \cos(\pi x)\cos(\pi y)$, $M = 0.3K = 0.6 + 0.3\cos(\pi x)\cos(\pi y)$, $N = 1.0 + 0.7\cos(\pi x)\cos(\pi y)$, $d_1 = d_2 = 1.0$, $r_1 = r_2 = 1.0$, $(u_0, v_0) = (0.7, 0.7)$ on $\Omega = (0,1) \times (0,1)$ at $t = T = 1,000$.

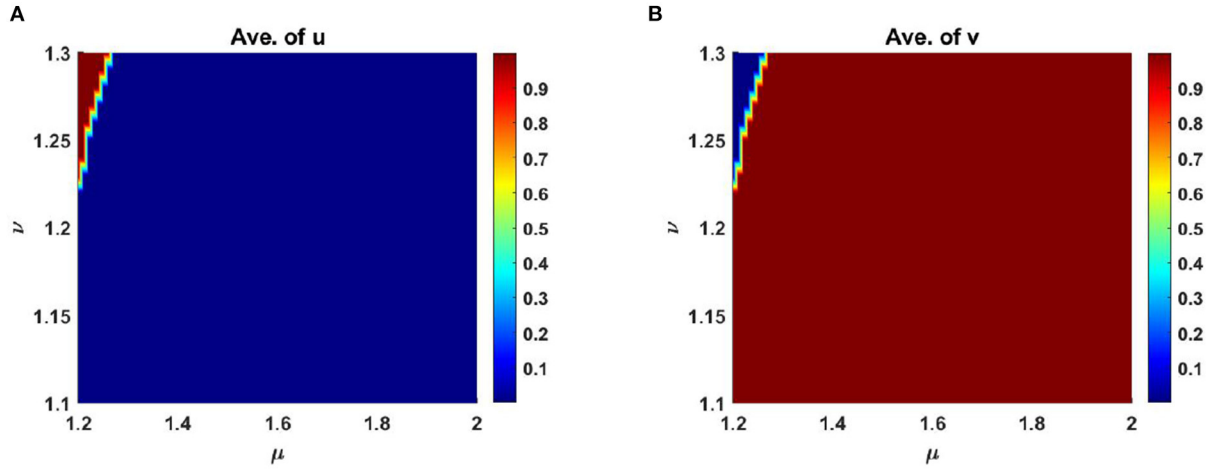

FIGURE 12
Average scaled density of u and v of (2.5) as a function of competition coefficients $\mu \in [1.2, 2]$ and $\nu \in [1.1, 1.3]$ on $\Omega \in (0,1) \times (0,1)$ when $M + N > K$ with $K = 2.0 + \cos(\pi x)\cos(\pi y)$, $M = 0.6K = 1.2 + 0.6\cos(\pi x)\cos(\pi y)$, $N = 0.6 + 0.4\cos(\pi x)\cos(\pi y)$, $d_1 = d_2 = 1.0$, $r_1 = r_2 = 1.0$, $(u_0, v_0) = (0.7, 0.7)$ on $\Omega = (0,1) \times (0,1)$ at $t = T = 1,000$.

the increase of time, which is one of the confirmations of the Theorem 4.

5.2. When K, M, N, μ, and ν are time dependent

5.2.1. Case of two-space dimensions

In this section, we will study the model (2.5) numerically when K, M, and N are two-dimensional time dependent functions, which may occur for seasonal variations. We will present the instantaneous contour profiles of $u(t,x,y)$ and $v(t,x,y)$ for $t = T$, $t = T + \frac{2\pi}{k\Omega}$ where $k = 1, 2, \ldots,$ that confirm the existence of a positive periodic state during a particular time interval. Here, T is substantially sufficient to reach the time periodicity of the population density. Furthermore, we exhibit the space averaged density profile as a function of time to show its approach to a periodic state. Here we will compare the time periodic case with the case of steady state only by including the time periodic function. The time dependent case has been

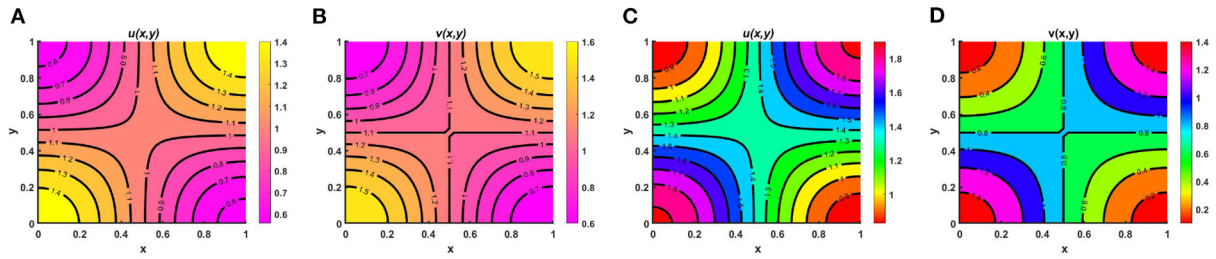

FIGURE 13
Contour plots of u and v of (2.5) at $t = T = 350$ when $M + N \geq K$ with $K = 2.0 + \cos(\pi x)\cos(\pi y)$ for **(A,B)** $M = 0.9 + 0.5\cos(\pi x)\cos(\pi y)$, $N = 1.1 + 0.5\cos(\pi x)\cos(\pi y)$, $\mu(x, y) = 1.0$, $\nu(x, y) = 1.0$, and **(C,D)** $M = 1.5 + 0.6\cos(\pi x)\cos(\pi y)$, $N = 0.8 + 0.7\cos(\pi x)\cos(\pi y)$, $\mu(x, y) = \frac{0.5+0.4\cos(\pi x)\cos(\pi y)}{0.8+0.7\cos(\pi x)\cos(\pi y)} \in [0.6, 1.0]$, $\nu(x, y) = \frac{1.2+0.3\cos(\pi x)\cos(\pi y)}{1.5+0.6\cos(\pi x)} \in [0.71, 1.0]$, $d_1 = d_2 = 1.0$, $r_1 = r_2 = 1.0$, $(u_0, v_0) = (0.5, 0.5)$ on $\Omega = (0, 1) \times (0, 1)$.

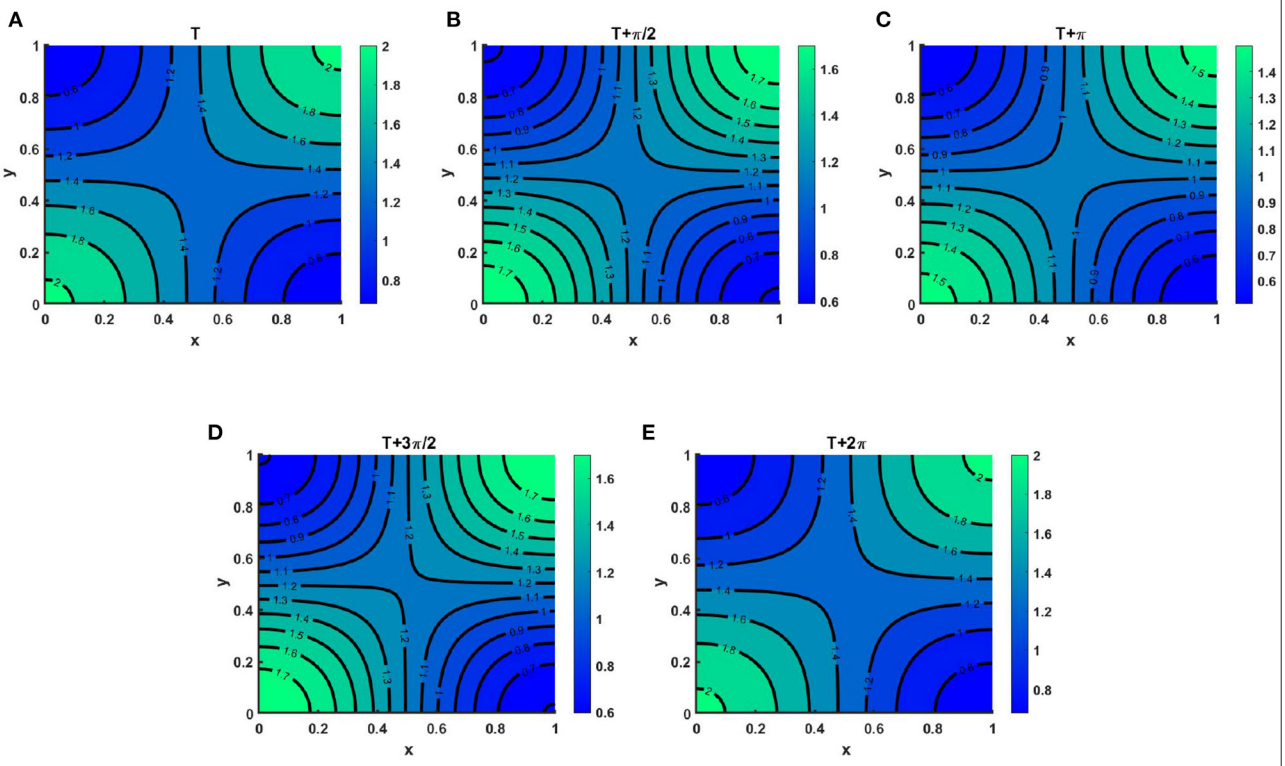

FIGURE 14
Contour plots of $u(t, x, y)$ of (2.5) when $M + N > K$ where $K = (2.0 + \cos(\pi x)\cos(\pi y))(1.0 + 0.2\cos(t))$, $M = 0.6K = (1.2 + 0.6\cos(\pi x)\cos(\pi y))(1.0 + 0.2\cos(t))$, $N = (1.0 + 0.4\cos(\pi x)\cos(\pi y))(1.0 + 0.2\cos(t))$, $\mu(t, x, y) \in [0.67, 0.86]$, $\nu(t, x, y) \in [0.67, 0.89]$, $r_1 = r_2 = r = 1.0$, $(u_0, v_0) = (0.5, 0.5)$, $d_1 = d_2 = 1.0$, $\Omega = (0, 1) \times (0, 1)$ for **(A)** T, **(B)** $T + \frac{\pi}{2}$, **(C)** $T + \pi$, **(D)** $T + \frac{3\pi}{2}$, and **(E)** $T + 2\pi$, where $T = 38.55$.

computed to examine, do the periodic state represents the same patterns as the same steady state cases studied in the earlier section? We will discover this question in this section.

Example 7. *Consider the time dependent functions for the case of (2.5) when* $M+N > K$ *where* $K = (2.0+\cos(\pi x)\cos(\pi y))(1.0+0.2\cos(t))$, $M = 0.6K = (1.2 + 0.6\cos(\pi x)\cos(\pi y))(1.0 + 0.2\cos(t))$, $N = (1.0 + 0.4\cos(\pi x)\cos(\pi y))(1.0 + 0.2\cos(t))$ *on* $\Omega = (0, 1) \times (0, 1)$. *Here* $\mu(t, x, y) \in [0.67, 0.86]$, $\nu(t, x, y) \in [0.67, 0.89]$ *with* $r_1 = r_2 = r = 1.0$, $(u_0, v_0) = (0.5, 0.5)$, $d_1 = d_2 = 1.0$. *Here, Figure 14 demonstrates the instantaneous change in population development of* $u(t, x, y)$ *and* $v(t, x, y)$ *through contour profiles for a specific time period. At this point, we have computed the instantaneous contour profiles of u for (Figure 14A)* T, *(Figure 14B)* $T+\frac{\pi}{2}$, *(Figure 14C)* $T+\pi$, *(Figure 14D)* $T+\frac{3\pi}{2}$, *and (Figure 14E)* $T + 2\pi$, *where* $t = T = 38.55$, *which is large*

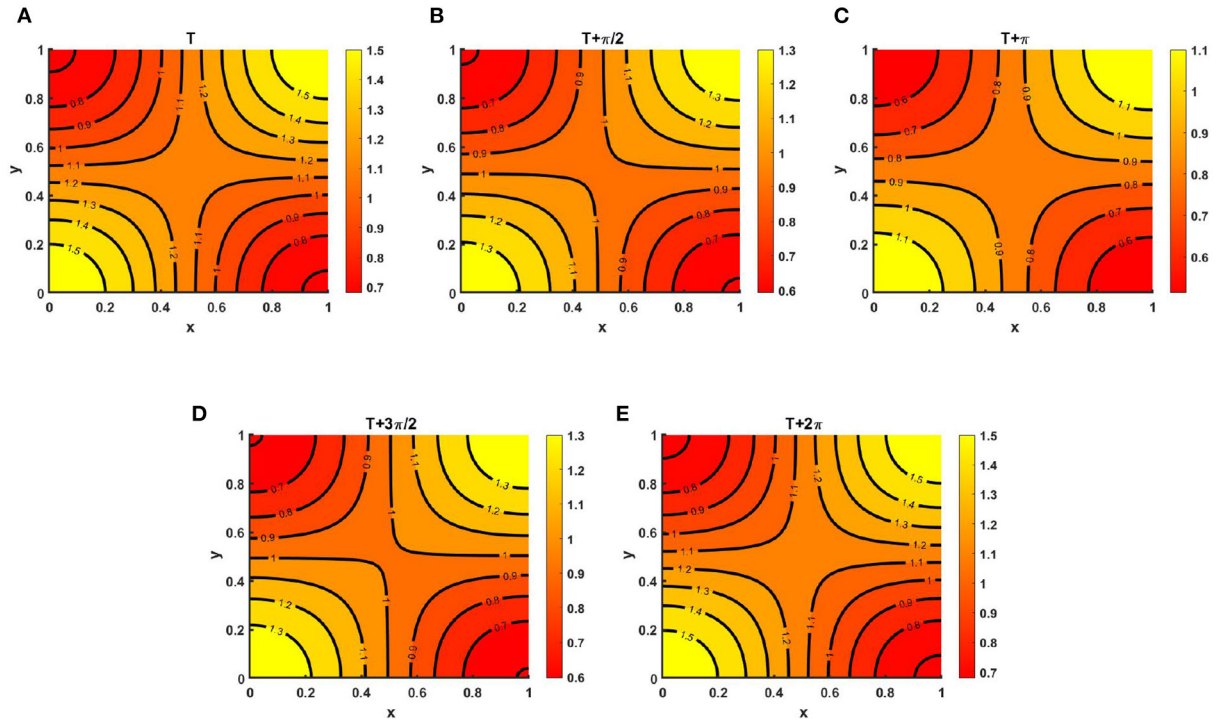

FIGURE 15
Contour plots of $v(t,x,y)$ of (2.5) when $M+N>K$ where $K=(2.0+\cos(\pi x)\cos(\pi y))(1.0+0.2\cos(t))$, $M=0.6K=(1.2+0.6\cos(\pi x)\cos(\pi y))(1.0+0.2\cos(t))$, $N=(1.0+0.4\cos(\pi x)\cos(\pi y))(1.0+0.2\cos(t))$, $\mu(t,x,y)\in[0.67,0.86]$, $v(t,x,y)\in[0.67,0.89]$, $r_1=r_2=r=1.0$, $(u_0,v_0)=(0.5,0.5)$, $d_1=d_2=1.0$, $\Omega=(0,1)\times(0,1)$ for **(A)** T, **(B)** $T+\frac{\pi}{2}$, **(C)** $T+\pi$, **(D)** $T+\frac{3\pi}{2}$, and **(E)** $T+2\pi$, where $T=19.71$.

enough to reach the steady state. As we know, due to seasonal variation or any other periodic factors during a time phase, the population growth is not always even everywhere, its growth rises and falls during specific seasons. There are many reasons, such as food availability, space, water supply, climate change, diseases, and predators that influence the growth of population during a time interval.

Thus, at all times during a period, we will not get the same population density. As we have shown in Figure 14. We observe that at $T=38.55$ and $T=38.55+2\pi$ the instantaneous contours plots correspond to identical values that provide the existence of positive periodic solutions. It is also noted that Figure 14 corresponds to Figure 8A of the steady state case for which both species survive in competition. Here, we have only included the time periodic function with the same steady state function to see the existence of the periodic state.

However, Figure 15 represents the instantaneous contour profiles of $v(t,x,y)$ for (Figure 15A) T, (Figure 15B) $T+\frac{\pi}{2}$, (Figure 15C) $T+\pi$, (Figure 15D) $T+\frac{3\pi}{2}$, and (Figure 15E) $T+2\pi$, where $t=T=19.71$ for which species v is found to survive. Similar to Figure 14, we observe that at $T=19.71$ and $T=19.71+2\pi$ the instantaneous contours plots of $v(t,x,y)$ resemble indistinguishable values which corresponds to Figure 8C of the steady state case.

Example 8. *Consider $K=(2.0+\cos(\pi x)\cos(\pi y))(1.0+0.2\cos(t))$ when $M+N<K$ where $M=0.3K=(0.6+0.3\cos(\pi x)\cos(\pi y))(1.0+0.2\cos(t))$, $N=(1.0+0.7\cos(\pi x)\cos(\pi y))(1.0+0.2\cos(t))$, $\mu(t,x,y)\in[1.23,2.33]$, $v(t,x,y)\in[1.44,2.33]$ in Figures 16A,B and $M=0.6K=(1.2+0.0.6\cos(\pi x)\cos(\pi y))(0.6+0.4\cos(t))$, $N=(0.6+0.4\cos(\pi x)\cos(\pi y))(1.0+0.2\cos(t))$, $\mu(t,x,y)\in[1.2,2.0]$, $v(t,x,y)\in[1.11,1.33]$ in Figures 16C,D. Also let, $r_1=r_2=r=1.0$, $(u_0,v_0)=(0.5,0.5)$, $d_1=d_2=1.0$ on $\Omega=(0,1)\times(0,1)$. The time average over a specific time interval are $\langle u(.,x,y)\rangle=\frac{1}{2\pi}\int_T^{2\pi+T}u(t,x,y)dt$ and $\langle v(.,x,y)\rangle=\frac{1}{2\pi}\int_T^{2\pi+T}v(t,x,y)dt$, respectively. It is noticed that the time average profiles in Figures 16A,B is similar to the steady pattern in Figures 10A,C. We found that due to intense interspecific competition and slightly higher values of v compared to μ species u is persist and v dies out (refer to, Figures 16A,B), which is expected according to Theorem 3. Also, the contour profile of u corresponds to the contour pattern of K with the increase of time. Opposite observation is found while considering $M=0.6K$, and $N=(0.6+0.4\cos(\pi x)\cos(\pi y))(1.0+0.2\cos(t))$ for $\mu,v>1$ and it is observed that the time average for periodic time dependent function the patterns*

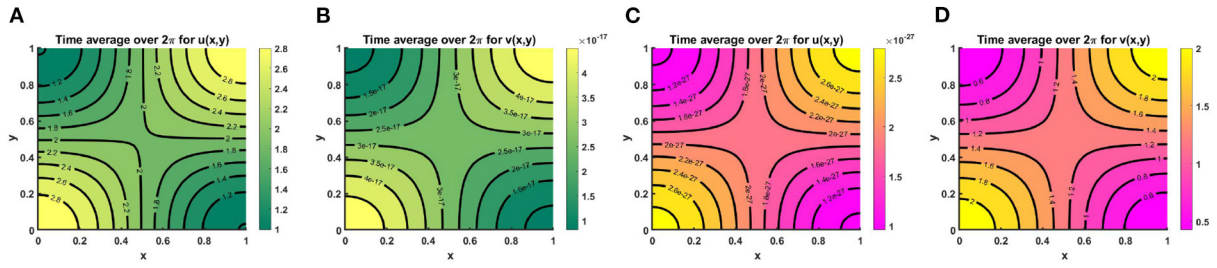

FIGURE 16
Contour plots of $\langle u(.,x,y)\rangle$, and $\langle v(.,x,y)\rangle$ of (2.5) when $M+N<K$ where $K=(2.0+\cos(\pi x)\cos(\pi y))(1.0+0.2\cos(t))$, $r_1=r_2=r=1.0$, $(u_0,v_0)=(0.5,0.5)$, $d_1=d_2=1.0$, for **(A,B)** $M=0.3K=(0.6+0.3\cos(\pi x)\cos(\pi y))(1.0+0.2\cos(t))$, $N=(1.0+0.7\cos(\pi x)\cos(\pi y))(1.0+0.2\cos(t))$, $\mu(t,x,y)\in[1.23,2.33]$, $\nu(t,x,y)\in[1.44,2.33]$, and **(C,D)** $M=0.6K=(1.2+0.0.6\cos(\pi x)\cos(\pi y))(0.6+0.4\cos(t))$, $N=(0.6+0.4\cos(\pi x)\cos(\pi y))(1.0+0.2\cos(t))$, $\mu(t,x,y)\in[1.2,2.0]$, $\nu(t,x,y)\in[1.11,1.33]$ on $\Omega=(0,1)\times(0,1)$.

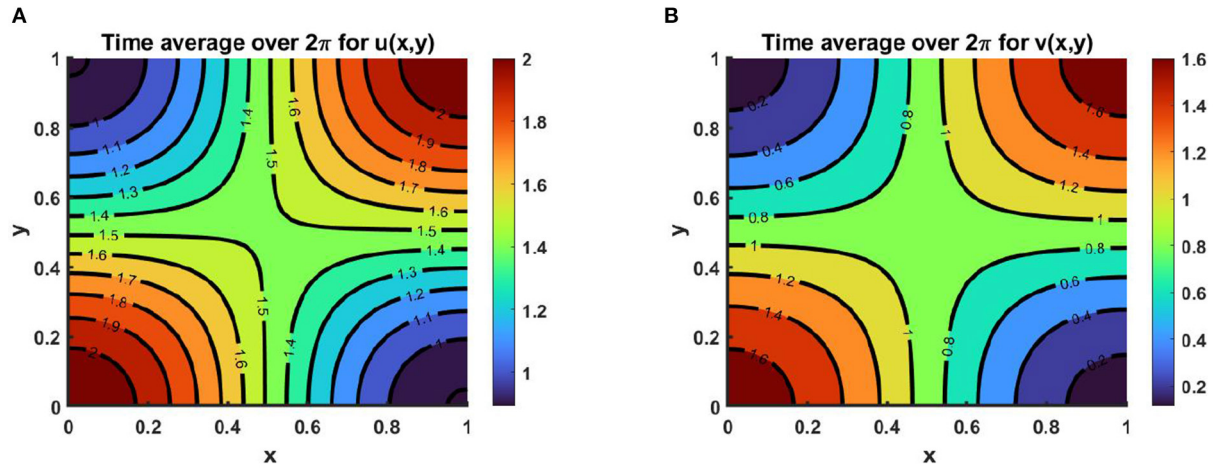

FIGURE 17
Contour plots of $\langle u(.,x,y)\rangle$, and $\langle v(.,x,y)\rangle$ of (2.5) when $M+N\geq K$ where $K=(2.0+\cos(\pi x)\cos(\pi y))(1.0+0.2\cos(t))$, $M=(1.5+0.0.6\cos(\pi x)\cos(\pi y))(1.0+0.2\cos(t))$, $N=(0.8+0.7\cos(\pi x)\cos(\pi y))(1.0+0.2\cos(t))$, $\mu(t,x,y)\in[0.6,1.0]$, $\nu(t,x,y)\in[0.71,1.0]$, $r_1=r_2=r=1.0$, $(u_0,v_0)=(0.5,0.5)$, $d_1=d_2=1.0$ on $\Omega=(0,1)\times(0,1)$.

in Figures 16C,D correspond to the steady state patterns in Figures 10B,D.

Example 9. *Consider the time dependent function for model (2.5) when* $M+N\geq K$ *on* $\Omega=(0,1)\times(0,1)$. *Assume* $K=(2.0+\cos(\pi x)\cos(\pi y))(1.0+0.2\cos(t))$, $M=(1.5+0.0.6\cos(\pi x)\cos(\pi y))(1.0+0.2\cos(t))$, $N=(0.8+0.7\cos(\pi x)\cos(\pi y))(1.0+0.2\cos(t))$ *for which* $\mu(t,x,y)\in[0.6,1.0]$, $\nu(t,x,y)\in[0.71,1.0]$. *Also let,* $r_1=r_2=r=1.0$, $(u_0,v_0)=(0.5,0.5)$, $d_1=d_2=1.0$. *We get the time average contour profiles of* $u(t,x,y)$ *and* $v(t,x,y)$ *produce ideal pair for the time dependent function which converges to M and N as time grows up. Also, the time average contour profiles in Figure 17 relate to the steady state pattern in Figure 13. We find that while both M and N are non-proportional with K than for* $\mu,\nu\in(0,1)$ *both species survive and pick up the finest solution* (M,N) *known as the ideal free pair.*

6. Summary of the study

We studied two species' competition dynamics that describe the competition and cooperation of both species in a heterogeneous environment with different imposed diffusion strategies. Several results have been established, considering the weak and strong competition, based on the intensity of spatially dependent competition coefficients. For a generalized non-symmetric growth function, we have discovered that if the first species follow $K-$ driven diffusion and at the same time, the other species diffuse according to their resource

distribution, then in the case of weak competition ($\mu(x), \nu(x) < 1$) both species sustain in the competition. Additionally, rising over time, its solution converges to the resource functions, forming an ideal free pair. However, in the case of strong competition ($\mu(x), \nu(x) > 1$), no coexistence is possible and there exists at least one semi-trivial solution. Furthermore, if both organisms follow the resource base diffusion, then once again, for $\mu(x), \nu(x) < 1$ ideal pair is guaranteed to be attained in battle. The model's efficacy for the case of one and two space dimensions is presented *via* numerical computation both for space and time-dependent cases, which is very effective from an ecological perspective. The findings may provide insight into the management of species invasions. If a more efficient diffuser is an invader, and all other factors remain constant, the invasive species' higher competitive coefficient may drive the local species to extinction. In addition, the enforced diffusion tactics are essential for researching grazing animals, marine organisms, and various winter birds. On the other hand, the population always moves in a good environment and leaves an unfavorable one, which can lead to unpredictable habits, like human behavior. The idea of different diffusion strategies is often closely connected to the creation and diffusion of knowledge as well as to the technological evolution of society. For more current advanced study on the model of human dynamical analysis, refer to Ali et al. [24]. The outcomes of the investigation can be extended by considering three species' population dynamics while they follow similar diffusion strategies with different competition coefficients.

Data availability statement

The original contributions presented in the study are included in the article/supplementary material, further inquiries can be directed to the corresponding authors.

Author contributions

IZ and MK: conceptualization, formal analysis, software, and original draft preparation. IZ, MK, and MA: methodology. MM and TK: validation and investigation. TK and MA: resources. IZ: data curation. MA, MM, and TK: review and editing. MK: supervision. All the authors have read and agreed to the published version of the manuscript.

Funding

The authors acknowledged the reviewers for their comments and suggestions which significantly improve the quality of the manuscript. The author MM, research was supported by National Science Foundation grant DMS-2213274, and University Research grant, TAMIU. Also, the author, MK's research, was partially supported by the Ministry of Science and Technology (MOST), EAS 488 for the year 2021-2022, Bangladesh.

Conflict of interest

The authors declare that the research was conducted in the absence of any commercial or financial relationships that could be construed as a potential conflict of interest.

Publisher's note

All claims expressed in this article are solely those of the authors and do not necessarily represent those of their affiliated organizations, or those of the publisher, the editors and the reviewers. Any product that may be evaluated in this article, or claim that may be made by its manufacturer, is not guaranteed or endorsed by the publisher.

References

1. Averill I, Lou Y, Munther D. On several conjectures from evolution of dispersal. *J Biol Dyn*. (2012) 6:117–30. doi: 10.1080/17513758.2010.529169

2. Chen X, Lam KY, Lou Y. Dynamics of a reaction-diffusion-advection model for two competing species. *Discrete Contin Dyn Syst*. (2012) 32:3841–59. doi: 10.3934/dcds.2012.32.3841

3. Dockery J, Hutson V, Mischaikow K, Pernarowski M. The evolution of slow dispersal rates: a reaction diffusion model. *J Math Biol*. (1998) 37:61–83. doi: 10.1007/s002850050120

4. Braverman E, Braverman L. Optimal harvesting of diffusive models in a nonhomogeneous environment. *Nonlinear Anal Theory Meth Appl*. (2009) 71:e2173–81. doi: 10.1016/j.na.2009.04.025

5. Cantrell RS, Cosner C, Lou Y. Approximating the ideal free distribution via reaction-diffusion-advection equations. *J Differ Equat*. (2008) 245:3687–707. doi: 10.1016/j.jde.2008.07.024

6. Cantrell RS, Cosner C, Lou Y. Evolution of dispersal and the ideal free distribution. *Math Biosci Eng*. (2010) 7:17–36. doi: 10.3934/mbe.2010.7.17

7. Cantrell RS, Cosner C. *Spatial Ecology via Reaction-diffusion Equations, Wiley Series in Mathematical and Computational Biology*. Chichester: John Wiley & Sons (2003).

8. Braverman E, Ilmer I. On the interplay of harvesting and various diffusion strategies for spatially heterogeneous population. *J Theor Biol*. (2019) 466:106–18. doi: 10.1016/j.jtbi.2019.01.024

9. Braverman E, Kamrujjaman M. Competitive-cooperative models with various diffusion strategies. *Comput Math Appl*. (2016) 72:653–62. doi: 10.1016/j.camwa.2016.05.017

10. Korobenko L, Braverman E. A logistic model with a carrying capacity driven diffusion. *Can Appl Math Quart*. (2009) 17:85–104.

11. Kamrujjaman M. Directed vs regular diffusion strategy: evolutionary stability analysis of a competition model and an ideal free pair. *Differ Equat Appl*. (2019) 11:267–90. doi: 10.7153/dea-2019-11-11

12. Kamrujjaman M. Weak competition and ideally distributed population in a cooperative diffusive model with crowding effects. *Phy Sci I J*. (2018) 18:1–16. doi: 10.9734/PSIJ/2018/42472

13. Morita Y, Tachibana K. An entire solution to the Lotka-Volterra competition-diffusion equations. *SIAM J Math Anal*. (2009) 40:2217–40. doi: 10.1137/080723715

14. He X, Ni MW. The effects of diffusion spatial variation in Lotka—Volterra competition–diffusion system I: heterogeneity vs. homogeneity. *J Differ Equat*. (2013) 254:528–46. doi: 10.1016/j.jde.2012.08.032

15. Braverman E, Kamrujjaman M. Lotka systems with directed dispersal dynamics: competition and influence of diffusion strategies. *Math Biosci*. (2016) 279:1–12. doi: 10.1016/j.mbs.2016.06.007

16. Gilpin ME, Ayala FJ. Global models of growth and competition. *Proc Natl Acad Sci USA*. (1973) 70:3590–3. doi: 10.1073/pnas.70.12.3590

17. Gompertz B. On the nature of the function expressive of human mortality and on a a new mode of determining the value of life contingencies. *Philo Trans R Soc Lond*. (1825) 115:513–83. doi: 10.1098/rstl.1825.0026

18. Smith FE. Population dynamics in Daphnia Magna and a new model for population, *Ecology*. (1963) 44:651–63. doi: 10.2307/1933011

19. Wang Q. Some global dynamic of a Lotka-Volterra competition-diffusion-advection system. *Commun Pure Appl. Math*. (2020) 19:3245–55. doi: 10.3934/cpaa.2020142

20. Kot M. *Elements of Mathematical Ecology*. Cambridge: Cambridge University Press (2001).

21. Korobenko L, Braverman E. On evolutionary stability of carrying capacity driven dispersal in competition with regularly diffusing populations. *J Math Biol*. (2014) 69:1181–206. doi: 10.1007/s00285-013-0729-8

22. Pao CV. *Nonlinear Parabolic and Elliptic Equations*. New York, NY: Plenum (1992).

23. Smith HL. Monotone dynamical systems: an introduction to the theory of competitive and cooperative system. *Amer Math Soc*. (2008) 33:41. doi: 10.1090/surv/041

24. Ali A, Alshammari SF, Islam S, Khan MA, Ullah S. Modeling and analysis of the dynamics of novel coronavirus (COVID-19) with Caputo fractional derivative. *Results Phys*. (2021) 20:103669. doi: 10.1016/j.rinp.2020.103669

frontiers | Frontiers in Applied Mathematics and Statistics

TYPE Original Research
PUBLISHED 03 April 2023
DOI 10.3389/fams.2023.1151270

OPEN ACCESS

EDITED BY
Md. Kamrujjaman,
University of Dhaka, Bangladesh

REVIEWED BY
Olumuyiwa James Peter,
University of Medical Sciences, Ondo, Nigeria
Pankaj Tiwari,
University of Kalyani, India

*CORRESPONDENCE
Baba Seidu
✉ bseidu@cktutas.edu.gh

SPECIALTY SECTION
This article was submitted to Mathematical Biology, a section of the journal Frontiers in Applied Mathematics and Statistics

RECEIVED 25 January 2023
ACCEPTED 07 March 2023
PUBLISHED 03 April 2023

CITATION
Kailan Suhuyini A and Seidu B (2023) A mathematical model on the transmission dynamics of typhoid fever with treatment and booster vaccination.
Front. Appl. Math. Stat. 9:1151270.
doi: 10.3389/fams.2023.1151270

A mathematical model on the transmission dynamics of typhoid fever with treatment and booster vaccination

Abdulai Kailan Suhuyini and Baba Seidu*

Department of Mathematics, School of Mathematical Sciences, C. K. Tedam University of Technology and Applied Sciences, Navrongo, Ghana

Typhoid fever is a potentially fatal illness that is caused by the bacteria *Salmonella typhi*. In this study, a deterministic mathematical model was formulated to look into transmission dynamics of typhoid fever with treatment and booster vaccination. The reproduction number $\mathcal{R}_0$ is calculated using the next-generation matrix approach. Then, a stability analysis on the equilibrium points was performed using Routh–Hurwitz criteria. It was revealed that the disease-free equilibrium point is locally asymptotically stable whenever $\mathcal{R}_0$ is less than 1 together with other conditions. We also showed that $\mathcal{R}_0 \leq 1$ does not guarantee global stability of the typhoid-free equilibrium point and corroborated the result by showing the possible existence of backward bifurcation at $\mathcal{R}_0 = 1$. The model parameters in $\mathcal{R}_0$ were also subjected to sensitivity analysis, which revealed that the transmission rate, infection through an exposed person, and bacteria are the most influential parameters of the reproduction number $\mathcal{R}_0$. Numerical simulations were run to determine the impact of various parameters on the dynamics of typhoid.

KEYWORDS

booster vaccination, bifurcation, mathematical modeling, typhoid fever, vaccination, basic reproduction number

1. Introduction

Typhoid fever, also known as enteric fever, is an enfeebling infectious disease that infects humans. It is normally high in children below the age of 6 years of age and is relatively average in adults. Bacteria, known as *Salmonella typhi (S. typhi)*, are the primary cause of typhoid fever. The disease is usually contracted by infecting humans through the intake of fecal discharges from an infected person, contaminated water or food, and by sharing basic utensils, such as cups, spoons, bowls, and others, with an infected person. Some express it bluntly by saying that a person who has contracted typhoid fever has eaten the feces of a carrier or another infected person. These gram-negative bacteria find their way into the body through the aforementioned ways into the small intestine and then shed into the bloodstream by macrophages in the reticuloendothelial system [1]. The symptoms of typhoid fever include prolonged low to high fever, severe headache, loss of appetite, body pain and weight loss, dry cough, diarrhea or constipation, itching or rashes, and also, to some extent nausea, and abdominal pain. At the chronic stage of typhoid, perforation of the intestine and neurological complications are observed in the patient [2]. Endemic cases of typhoid fever are recorded in both developed and developing countries, thereby making it a public health concern. This disease still remains a concern, even despite the recent improvements in water sanitation [3]. Usually, it takes 7–14 days for the disease to manifest in an infected person. The patient is given antibiotic treatment, after which the person

may feel better a few days later. Still, in the worse case, an infected person without a proper treatment could develop complications resulting in death. Vaccines against typhoid fever are only partially effective. The said vaccines are usually manufactured only for those persons who are prone or are exposed to hotspot areas of the disease [4]. Hence, the jabs of typhoid fever vaccines are seen as one of the core factors in curbing the transmission of the disease. The available vaccines in the system now are of two types that are oral and injectable. Among the injectable types, we have: typhoid conjugate vaccine, Tya, and Vi capsular polysaccharide vaccine. They are about 30% to 80% effective within the first 2 years of the specific vaccine in question. When a person takes on the drug-resistant strain of typhoid fever and is not properly managed with effective antibiotics, then there is a high chance of it resulting in complications [5]. It is estimated that typhoid fever cases have risen from 11 million to 21.5 million and five million cases of paratyphoid fever worldwide, with 200,000 deaths occurring each year [6]. It is also estimated that African countries have not been left out with an increasing number of cases between 10 and 100 per 100,000 individuals, with children being the most infected due to poor hygiene and sanitation. As a result of the high rate of infection and the rising spirit of the disease strain, typhoid has become a burden that has turned into a major world health problem. However, vaccination seems to be the essential method for controlling the transmission of the disease [7]. Several mathematical models have been proposed to study the dynamics of infectious diseases. Among the diseases that have gained much attention from mathematical modelers are HIV/AIDS [8–10, and references therein], malaria [11, and references therein], and tuberculosis [12, and references therein]. With the advent of coronavirus disease (COVID-19), several models have been proposed to study the dynamics and control of the disease [13, 14, and references therein]. González-Guzmán [15] appears to be from among the first researchers to have developed a mathematical model to study the spread of typhoid fever. Following González-Guzmán [15], several models have been proposed to help increase the understanding of the spread and control of typhoid fever. Specifically, Wameko et al. [16] proposed a deterministic ODE compartmental model for the dynamics of typhoid fever with a susceptible-carrier-infected-recovered (ESCIR) pattern for the human population and a pathogen compartment B(t). The recent study of Ayoola et al. [17] analyzed a similar compartmental model for the spread of typhoid fever by incorporating optimal education and vaccination control strategies. A six-class compartmental model by Ogunlade et al. [18] describes the application of deterministic and stochastic models to the dynamics of typhoid fever. They first analyzed the deterministic model and then transformed it into a stochastic model where the mean and variance were determined. The stochastic model simulations were done using the Euler–Maruyama numerical scheme. Even though the research indicates that controls, such as vaccination, screening, and treatments, are effective enough to reduce the spread of the disease, hospitalization and personal hygiene could not be considered to help control the disease. Other interesting models of typhoid fever can be seen in Peter et al. [19], Peter et al. [20, 21], and Musa et al. [7].

To the best of our knowledge, no typhoid fever model that incorporates treatment and booster vaccination as control measures has been proposed. Therefore, this research seeks to develop a mathematical fever model that incorporates vaccination, treatment, booster vaccine, and pathogen populations.

The rest of the article is arranged as follows: In Section 2, the model of interest is formulated. In Section 3, basic qualitative properties, including positivity and boundedness of model solutions, stability of equilibrium points of the model, are discussed. In Section 4, the model is numerically simulated to illustrate the analytical results obtained and to study the impact of model parameters on model output behavior. Finally, in Section 5, the main conclusions drawn from the study are presented.

2. Formulation of the mathematical model

Based on the model proposed by Ayoola et al. [17], we incorporate double-dose vaccination with treatment and a compartment to monitor the concentration of the bacteria in the environment. The said model consists of six human compartments and one pathogen compartment. These are: the singly vaccinated population V, the susceptible population, S, the exposed E, infected, I, recovered R, and those who have received the booster vaccine V_B. The pathogen concentration is given by B. Therefore, the total human population is given by $N = V + S + E + I + R + V_B + B$. The susceptible represents the people who are uninfected but stand the chance of getting infected with the disease. This compartment increases through the following:

- Recruitment at rate $n\Lambda_h$, where Λ_h is the recruitment rate into the population and n is the proportion of the recruits who are susceptible,
- Loss of immunity of the single-vaccinated individuals. The rate of loss of immunity by the single-vaccinated individuals is taken to be ν_1, The recovered population may lose their temporal immunity and join the susceptible at rate θ.

The susceptible population also reduces due to the following:

- Infection as a result of effective contact with the exposed and infected persons at the rate of $(1-\eta)\beta S\lambda$, where $\lambda = \beta(\gamma_1 E + \gamma_2 I + \gamma_3 B)$. A proportion η of those susceptible become exposed, while the remainder become infectious right away due to compromised immune system,
- Vaccination at rate ϕ.
- Natural death at rate μ.

The single-dose vaccinated population increases through recruitment at a rate $(1-\eta)\Lambda_h$, vaccination of the susceptible and recovered at rates of ν_1, and ν_2, respectively. The vaccinated population also reduces as a result of: the loss of immunity at rate ϕ, going in for booster vaccine at a rate ρ, and through natural death at a rate μ. The exposed compartment increases through some fraction η of susceptible population following effective contact with infected, exposed persons and the pathogen at a rate $\eta S\lambda$, and decreases as a result of the natural recovery rate of w, the natural mortality rate of μ, and the development of clinical symptoms at a rate of ψ. The infected compartment grows through infection following the effective contact with exposed, infected persons and the shed pathogen in the environment at rate $(1-\eta)\lambda S$, and

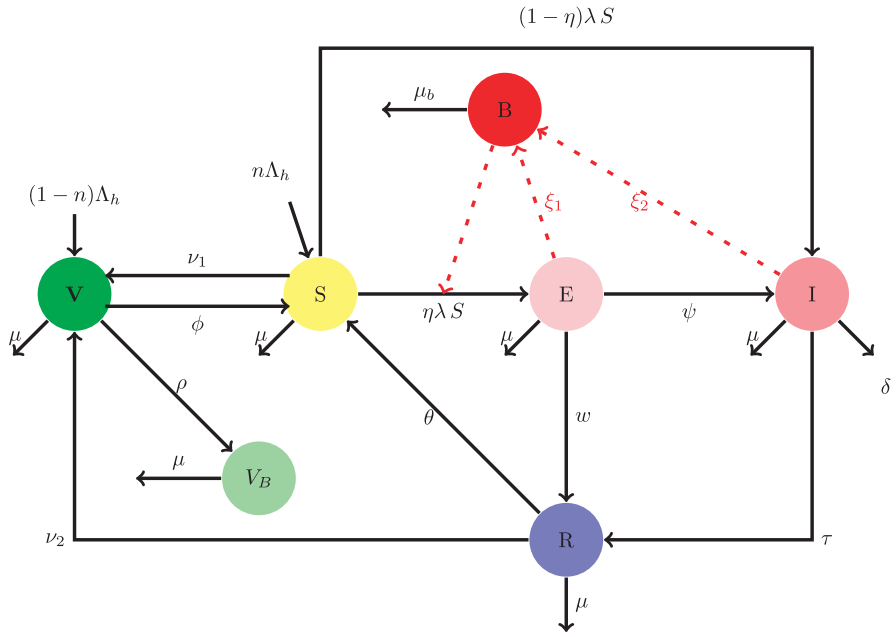

FIGURE 1
Compartmental diagram of the model.

progression of exposed individuals into the infected class at rate ψ. The infected population diminishes in the following manner: a successful treatment at rate τ, a disease-induced mortality at rate of δ, and natural mortality rate of μ. The recovered compartment population increases through a successful treatment of infected persons at the rate of τ and natural self-recovery of the exposed at the rate of w. The recovered compartment also reduces as a result of temporal immunity loss at the rate θ, rate of vaccination ν_2, and natural mortality rate μ. The booster vaccinated compartment grows through the intake of booster vaccine by the vaccinated compartment at the rate ρ and reduces as a result of the natural mortality rate μ and the Pathogen concentration increases through the shedding of pathogens by exposed and infectious persons at rates ξ_1 and ξ_2, respectively. The decay rate of pathogens is taken to be μ_b.

The schematic diagram that represents the model described thus far is presented in Figure 1.

The following set of differential equations therefore describes the dynamics of typhoid spread with double-dose vaccination scheme:

$$\left.\begin{aligned}
\frac{dV}{dt} &= (1-n)\,\Lambda_h + \nu_1 S + \nu_2 R - (\phi+\rho+\mu)\,V;\\
\frac{dS}{dt} &= n\Lambda_h + \phi V + \theta R - (\nu_1+\mu+\lambda)\,S;\\
\frac{dE}{dt} &= \eta\lambda S - (\mu+\psi+w)\,E;\\
\frac{dI}{dt} &= (1-\eta)\,\lambda S + \psi E - (\delta+\tau+\mu)I;\\
\frac{dR}{dt} &= \tau I + wE - (\theta+\nu_2+\mu)R;\\
\frac{dV_B}{dt} &= \rho V - \mu V_B;\\
\frac{dB}{dt} &= \xi_1 E + \xi_2 I - \mu_b B.
\end{aligned}\right\} \quad (1)$$

Where necessary, we use the following conventions in subsequent discussions.

$$k_1 = (\phi+\rho+\mu)\,,\ k_2 = (\nu_1+\mu)\,,\qquad k_3 = (\mu+\psi+w)\,,$$
$$k_4 = (\delta+\tau+\mu)\,,\ k_5 = (\theta+\nu_2+\mu)\,.$$

In Table 1, the model parameters and their baseline values are presented.

3. Qualitative properties

3.1. Positivity of solutions

Theorem 1. Let $\Omega = \left\{(V_B, V, S, E, I, R) \in \mathbb{R}^6_+\right\}$. If positive conditions and initial conditions are provided for Equation (1), then all its solutions remain positive for $t > 1$.

Thus, $V(t) > 0$, $S(t) \geq 0$, $E(t) \geq 0$, $I(t) \geq 0$, $R(t) \geq 0$, $V_B(t) \geq 0$, $B(t) \geq 0$ of the system is positive for all $t > 1$.

Proof. Considering the first of Equation (1), we have

$$\frac{dV}{dt} = (1-n)\,\Lambda_h + \nu_1 S + \nu_2 R - (\phi+\rho+\mu)\,V$$

$$\frac{dV}{dt} \geq -(\phi+\rho+\mu)\,V$$

$$\int \frac{1}{V} dV \geq -\int (\phi+\rho+\mu)\,dt$$

Integrating both sides gives

$$\ln|V| \geq -(\phi+\rho+\mu)\,t + c$$

TABLE 1 Description and values of parameters for model (Equation 1).

Parameter	Description	Baseline value	Source
Λ_h	Human recruitment rate	100	[22]
ν_1	Rate of vaccination	0.260	Assumed
ν_2	Rate of vaccination	0.220	Assumed
ϕ	Loss of vaccination	0.130	Estimated
n	Fraction of recruited susceptible	0.670	Estimated
ρ	Booster vaccination	0.75	Estimated
μ	Natural mortality rate	0.0041	Estimated
η	proportion of susceptible	0.650	Assumed
τ	Treatment rate	0.851	[22]
w	Recovery rate from exposed	0.676	[23]
δ	Typhoid-induced mortality rate	0.0022	[22]
ψ	Rate of progression into Infection	0.142	Estimated
θ	Loss of Immunity upon recovery	0.7204	[24]
β	Transmission rate	0.714	Estimated
ξ_1	Rate of bacteria excretion (Exposed)	0.0818	[25]
ξ_2	Rate of bacteria excretion (Infected)	0.0712	[25]
γ_1	Infectiousness from exposed	0.02	[19]
γ_2	Infectiousness from infected	0.01	[19]
γ_3	Infectiousness from bacteria	0.01	[19]
μ_b	Rate of bacteria decay	0.0645	[25]

$$V \geq C_1 e^{-(\phi+\rho+\mu)t}$$

Where C_1 is the integration constant, i.e., $V(0) = C_1$. Therefore, $V(0) \geq 0 \, \forall \, t > 0$. □

Similarly, we can show this for $\{S(0) \geq 0, E(0) \geq 0, I(0) \geq 0, R(0) \geq 0, V_B(0) \geq 0, B(0) \geq 0\}$ model variables. As a result, the model's solution is positive.

3.2. Boundedness of solutions

Adding all equations consisting of human compartments from model system (1) gives;

$$\frac{\mathrm{d}N}{\mathrm{d}t} = \Lambda_h - N\mu - \delta I$$

$$\frac{\mathrm{d}N}{\mathrm{d}t} \leq \Lambda_h - N\mu \tag{2}$$

Solving Equation (2) yields

$$N(t) \geq, N(0)e^{-ut} + \frac{\Lambda_h}{\mu}\left(1 - e^{-ut}\right)$$

Now,

$$\lim_{t\to\infty} N(t) \leq \frac{\Lambda_h}{\mu} \tag{3}$$

Thus, $N(t)$ is bounded.

With use of the inequality (Equation 3), we obtained from the seventh equation of system (Equation 1) that,

$$\frac{dB(t)}{dt} \leq \frac{\Lambda_h(\xi_1 + \xi_2)}{\mu} - \mu_b B(t) \tag{4}$$

Solving inequality (Equation 4), we have

$$B(t) \leq B(0)e^{-\mu_b t} + \frac{\Lambda_h(\xi_1 + \xi_2)}{\mu\mu_b}\left(1 - e^{-\mu_b t}\right) \tag{5}$$

Taking the limits will give

$$\lim_{t\to\infty} B(t) \leq \frac{\Lambda_h(\xi_1 + \xi_2)}{\mu\mu_b} \tag{6}$$

Hence, B(t) is bounded as well. Thus, the aforementioned results indicate that the solutions of system (Equation 1) are positive and bounded in the region.

$$\Omega = \left\{\left(V, S, E, I, R, V_B\right) \in \mathbb{R}^6_+ | V + S + E + I + R + V_B \leq \frac{\Lambda_h}{\mu}; B(t) \leq \frac{\Lambda_h(\xi_1 + \xi_2)}{\mu\mu_b}\right\}$$

3.3. Equilibrium points of model

3.3.1. Typhoid-free equilibrium point and basic reproduction number

The typhoid-free equilibrium $\mathcal{E}_{T0} = \left(V^0, S^0, 0, 0, 0, V_B^0, 0\right)$ is obtained by equating the dynamic system of Equation (1) to zero together with the conditions $E = 0, I = 0, R = 0$, and $B = 0$. Then, we have;

$$\left.\begin{aligned} S^0 &= \frac{\Lambda_h((1-n)\phi + nk_1)}{k_1k_2 - \phi\nu_1}, \\ V^0 &= \frac{\Lambda_h((1-n)k_2 + n\nu_1)}{k_1k_2 - \phi\nu_1}, \\ V_b^0 &= \frac{\rho\Lambda_h((1-n)k_2 + n\nu_1)}{\mu(k_1k_2 - \phi\nu_1)}. \end{aligned}\right\} \tag{7}$$

The basic reproduction number, which is often denoted by $\mathcal{R}_0$, is an epidemiological quantity which is used to describe the average number of secondary infections that are recorded as a result of introducing an infected individual into an otherwise completely susceptible population. Several techniques have been developed to determine this threshold for deterministic ODE models. In this article, we employ the method of Driessche et al. [26] to obtain $\mathcal{R}_0$ for the typhoid fever model. Following the technique in Driessche

et al. [26], the infected sub-system of model system (Equation 1) is given by the following set of equations.

$$\left.\begin{array}{l} \frac{dE}{dt} = \eta\, S\lambda - k_3 E; \\ \frac{dI}{dt} = (1-\eta)\, S\lambda + \psi\, E - k_4 I; \\ \frac{dB}{dt} = \xi_1 E + \xi_2 I - \mu_b B. \end{array}\right\} \tag{8}$$

According to Driessche and Watmough [26], the, matrix F represents the component consisting of the infection terms (transmission) and V contains all other terms (transitions). The transmission and transition matrices are then given by

$$\mathcal{F} = \beta\, S^0 \begin{bmatrix} \eta\gamma_1 & \eta\gamma_2 & \eta\gamma_3 \\ (1-\eta)\,\gamma_1 & (1-\eta)\,\gamma_2 & (1-\eta)\,\gamma_3 \\ 0 & 0 & 0 \end{bmatrix},$$

$$\text{and } \mathcal{V} = \begin{bmatrix} k_3 & 0 & 0 \\ -\psi & k_4 & 0 \\ -\xi_1 & -\xi_2 & \mu_b \end{bmatrix}.$$

Therefore,

$$\mathcal{F}\mathcal{V}^{-1} = \frac{\beta\, S^0}{\mu_b\, k_3\, k_4} \begin{bmatrix} \eta\zeta_1 & \eta\, k_3\,(\gamma_2\mu_b + \gamma_3\xi_2) & \eta\gamma_3\, k_3\, k_4 \\ (1-\eta)\,\zeta_1 & (1-\eta)\, k_3\,(\gamma_2\mu_b + \gamma_3\xi_2) & (1-\eta)\,\gamma_3\, k_3\, k_4 \\ 0 & 0 & 0 \end{bmatrix},$$

Where $\zeta_1 = \mu_b\left(\gamma_1\, k_4 + \gamma_2\psi\right) + \gamma_3\left(\psi\xi_2 + \xi_1\, k_4\right)$.

It is easy to determine that the basic reproduction number taken as the spectral radius of $\mathcal{F}\mathcal{V}^{-1}$ [26] is given by

$$\mathcal{R}_0 = \frac{\beta\, S^0\left[\gamma_1\mu_b\eta\, k_4 + \gamma_2\left[\mu_b\eta\psi + (1-\eta)\, k_3\mu_b\right] + \gamma_3\left[(1-\eta)\, k_3\xi_2 + \eta\left(\psi\xi_2 + \xi_1 k_4\right)\right]\right]}{\mu_b k_3 k_4}.$$

3.3.2. Endemic equilibrium point

At a typical non-trivial equilibrium point $\mathcal{E}^* = \left(V_B^*, V^*, S^*, E^*, I^*, R^*, B^*\right)$, we have the following.

$$\frac{dV}{dt} = 0, \frac{dS}{dt} = 0, \frac{dE}{dt} = 0, \frac{dI}{dt} = 0, \frac{dR}{dt} = 0, \frac{dV_B}{dt} = 0, \frac{dB}{dt} = 0.$$

Solving the set of equations above, the endemic equilibrium point can be explicitly expressed in terms of λ^* and other model parameters as follows:

$$\left.\begin{array}{l} S^* = \frac{(\phi(1-n)+nk_1)\Lambda_h}{\Phi\lambda^* k_1 + k_1 k_2 - \phi\nu_1}, \\ E = \frac{\eta(\phi(1-n)+nk_1)\Lambda_h\lambda^*}{k_3(\Phi\lambda^* k_1 + k_1 k_2 - \phi\nu_1)}, \\ I^* = \left(\frac{\psi\eta}{k_3 k_4} + \frac{1-\eta}{k_4}\right)\lambda^* S^*, \\ R^* = \left[\frac{\eta\omega}{k_3 k_5} + \left(\frac{\psi\eta}{k_3 k_4 k_5} + \frac{1-\eta}{k_4 k_5}\right)\tau\right]\lambda^* S^*, \\ B^* = \left[\frac{\eta\xi_1}{k_3\mu_b} + \left(\frac{\psi\eta}{k_3 k_4\mu_b} + \frac{1-\eta}{k_4\mu_b}\right)\xi_2\right]\lambda^* S^*, \\ V^* = \frac{(1-n)\Lambda_h}{k_1} + \left[\frac{\nu_1}{k_1} + \nu_2\left(\frac{\eta\omega}{k_1 k_3 k_5} + \left(\frac{\psi\eta}{k_1 k_3 k_4 k_5} + \frac{1-\eta}{k_1 k_4 k_5}\right)\tau\right)\lambda^*\right] S^*, \\ V_b^* = \frac{\rho}{\mu}\left[\frac{\nu_1}{k_1} + \nu_2\left(\frac{\eta\omega}{k_1 k_3 k_5} + \left(\frac{\psi\eta}{k_1 k_3 k_4 k_5} + \frac{1-\eta}{k_1 k_4 k_5}\right)\tau\right)\lambda^*\right] S^* \\ + \frac{\rho(1-n)\Lambda_h}{\mu\, k_1}, \\ \Phi = 1 - \frac{(\phi\nu_2 + \theta k_1)}{k_1 k_3 k_4 k_5}\left[\tau\,(1-\eta)\, k_3 + \eta\left(\omega k_4 + \psi\tau\right)\right]. \end{array}\right\} \tag{9}$$

Where

$$\lambda^* = \beta\left(\gamma_1 E^* + \gamma_2 I^* + \gamma_3 B^*\right) \tag{10}$$

Substituting E^*, I^*, and B^* into (10) and simplifying give

$$\lambda^*\left[\lambda^* - \frac{\left(k_1 k_2 - \phi\nu_1\right)}{\Phi}\left(\mathcal{R}_0 - 1\right)\right] = 0. \tag{11}$$

Solutions of Equation (11) are $\lambda^* = 0$, corresponding to the typhoid-free equilibrium, and $\lambda^* = \frac{(k_1 k_2 - \phi\nu_1)}{\Phi}(\mathcal{R}_0 - 1)$, corresponding to the typhoid-persistent equilibrium. The following result is easily established.

Lemma 1. The typhoid fever model (Equation 12) has an epidemiologically reasonable disease-free equilibrium point only when $\mathcal{R}_0 > 1$.

Proof. It is easy to notice that $\frac{(k_1 k_2 - \phi\nu_1)}{\Phi} > 0$ by substituting the expressions for k_1, $k_2, \ldots$ k_5, and simplifying. This implies that the $\lambda^* > 0$ if $\mathcal{R}_0 > 0$ and $\lambda^* \leq 0$ if $\mathcal{R}_0 \leq 1$. We note that $\lambda^* > 0$ is associated with a positive endemic equilibrium. This concludes the proof. □

3.4. Stability of equilibrium points

We investigate the local stability of the typhoid-free equilibrium and the endemic equilibrium of the basic reproduction number, in this section, using the Lyapunov second technique, which states that an equilibrium point is locally asymptotically stable if all eigenvalues of the associated Jacobian have negative real parts and unstable otherwise.

3.4.1. Local stability of equilibrium points

The typhoid-free equilibrium $\mathcal{E}_{T0}$ is locally asymptotically stable, if and only if all eigenvalues of the Jacobian matrix of system (Equation 1) at the $\mathcal{E}_{T0}$ have negative real parts. Now, let $X = (S, E, I, R, V, V_B, B)$. Then, model (Equation 1) can be written in the form $\frac{dX}{dt} = f(X)$, where $f_i(X) = \frac{dX_i}{dt}$, where X_i is the ith component of X.

The Jacobian matrix of the model evaluated at typhoid-free equilibrium we have $\mathcal{J}_{(\mathcal{E}_{T0})}$ is given by

$$\mathcal{J}_{(\mathcal{E}_{T0})} = \begin{bmatrix} -k_1 & \nu_1 & 0 & 0 & \nu_2 & 0 & 0 \\ \phi & -k_2 & -\gamma_1\beta\, S^0 & -\gamma_2\beta\, S^0 & \theta & 0 & -\gamma_3\beta\, S^0 \\ 0 & 0 & \eta\gamma_1\beta\, S^0 - k_3 & \eta\gamma_2\beta\, S^0 & 0 & 0 & \eta\gamma_3\beta\, S^0 \\ 0 & 0 & (1-\eta)\,\gamma_1\beta\, S^0 + \psi & (1-\eta)\,\gamma_2\beta\, S^0 - k_4 & 0 & (1-\eta)\,\gamma_3\beta\, S^0 & \\ 0 & 0 & w & & -k_5 & 0 & 0 \\ \rho & 0 & 0 & 0 & 0 & -\mu & 0 \\ 0 & 0 & \xi_1 & \xi_2 & 0 & 0 & -\mu_b \end{bmatrix}$$

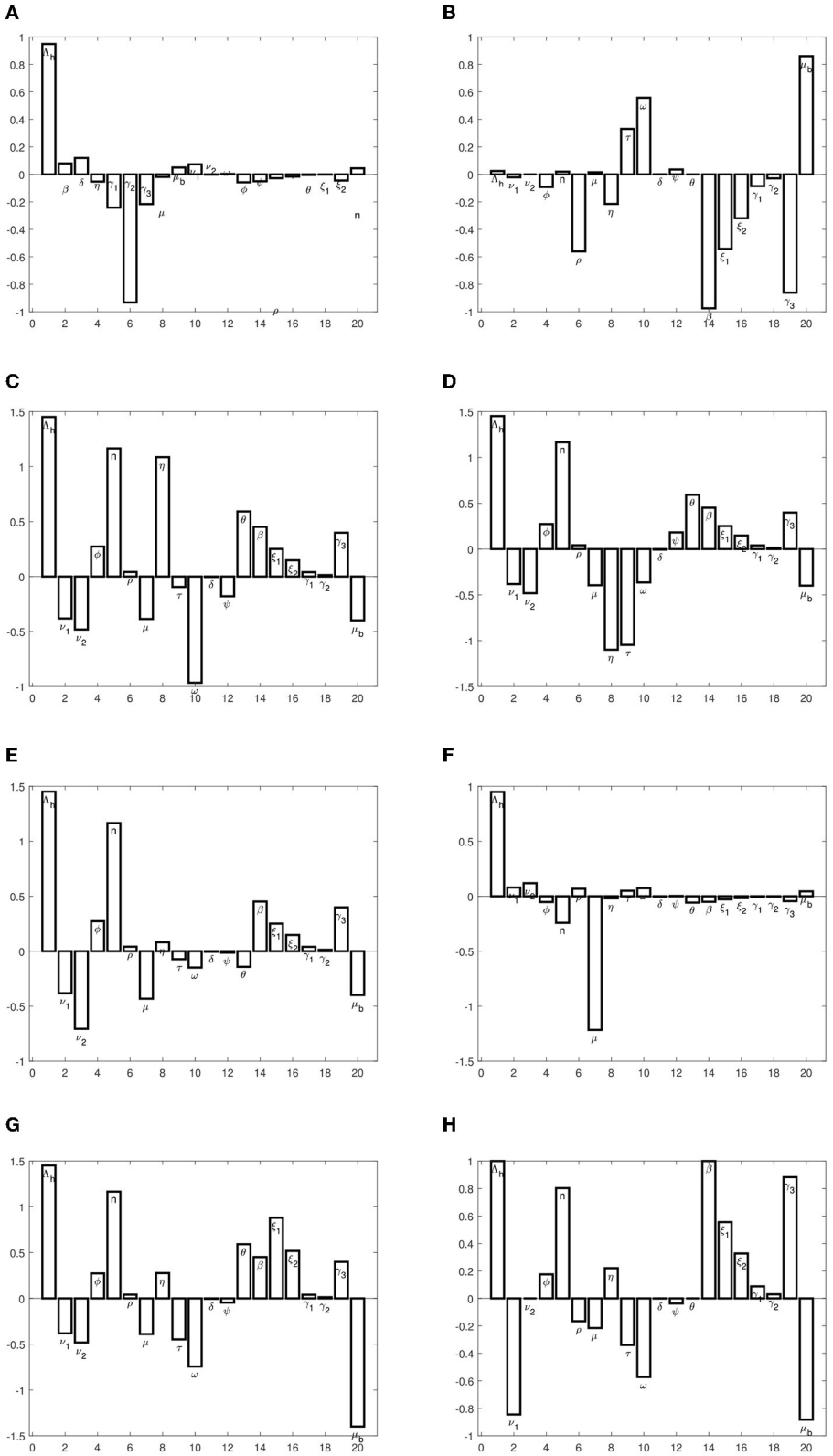

FIGURE 2
(A–H) Graphs of sensitivity indices of endemic equilibrium point, and $\mathcal{R}_0$.

TABLE 2 Sensitivity indices of endemic equilibrium and $\mathcal{R}_0$.

Par	V^*	S^*	E^*	I^*	R^*	V_b^*	B^*	$\mathcal{R}_0$
Λ_h	0.94967	0.025017	1.4518	1.4518	1.4518	0.94967	1.4518	1.0000
ν_1	0.079707	−0.021137	−0.38175	−0.38175	−0.38175	0.079707	−0.38175	−0.84487
ν_2	0.11923	0.0000	−0.48209	−0.48209	−0.70626	0.11923	−0.48209	0.0000
ϕ	−0.052327	−0.092072	0.27321	0.27321	0.27321	−0.052327	0.27321	0.17508
n	−0.24147	0.020089	1.1659	1.1659	1.1659	−0.24147	1.1659	0.80302
ρ	−0.93200	−0.56061	0.041211	0.041211	0.041211	0.068004	0.041211	−0.16601
μ	−0.21621	0.015254	−0.38595	−0.39528	−0.43201	-1.2162	−0.3894	−0.21526
η	−0.018594	−0.21486	1.0862	−1.0999	0.081086	−0.018594	0.27634	0.22037
τ	0.049869	0.33092	−0.094795	−1.0465	−0.072583	0.049869	−0.44736	−0.33941
ω	0.073227	0.55791	−0.96616	−0.36404	−0.14909	0.073227	−0.7431	−0.57222
δ	−0.00163	0.00086	−0.00338	−0.00584	−0.00451	−0.00163	−0.00429	−0.00088
ψ	0.0030737	0.035518	−0.17955	0.18182	−0.013404	0.0030737	−0.045681	−0.036429
θ	−0.057561	0.0000	0.59224	0.59224	−0.14181	−0.057561	0.59224	0.0000
β	−0.050327	−0.97498	0.45184	0.45184	0.45184	−0.050327	0.45184	1.0000
ξ_1	−0.027968	−0.54182	0.2511	0.2511	0.2511	−0.027968	0.88064	0.55572
ξ_2	−0.016458	−0.31884	0.14776	0.14776	0.14776	−0.016458	0.51822	0.32702
γ_1	−0.0044106	−0.085445	0.039598	0.039598	0.039598	−0.0044106	0.039598	0.087638
γ_2	−0.0014909	−0.028883	0.013386	0.013386	0.013386	−0.0014909	0.013386	0.029625
γ_3	−0.044426	−0.86065	0.39886	0.39886	0.39886	−0.044426	0.39886	0.88274
μ_b	0.044426	0.86065	−0.39886	−0.39886	−0.39886	0.044426	−1.3989	−0.88274

If Y is a typical eigenvalue, then the characteristic polynomial of $\mathcal{J}$ is given by

$$(\mu + Y)\left(Y + k_5\right)\left(Y^2 + \left(k_1 + k_2\right)Y + k_1 k_2 - \nu_1 \phi\right)\Psi(Y) = 0$$

where

$$\begin{aligned}
&\Psi(Y) = Y^3 + \Delta_1 Y^2 + \Delta_2 Y + \Delta_3,\\
&\Delta_1 = \mu_b + k_3 + k_4 - \beta S^0\left(\eta\gamma_1 + (1-\eta)\gamma_2\right),\\
&\Delta_2 = \beta S^0\Big[k_4\gamma_1\eta + \eta\psi\gamma_2 + \xi_2(1-\eta)\gamma_3\\
&-\left(\mu_b\gamma_1\eta + \gamma_2(1-\eta)\left(\mu_b + k_3\right)\right) + \eta\xi_1\gamma_3\Big]\\
&\quad +\mu_b\left(k_3 + k_4\right) + k_3 k_4,\\
&\Delta_3 = k_3\, k_4\,\mu_b\left(1 - \mathcal{R}_0\right),
\end{aligned}$$

$$\begin{aligned}
\Delta_2 = \beta S^0\Big[&k_4\gamma_1\eta + \eta\psi\gamma_2 + \xi_2(1-\eta)\gamma_3\\
&-\left(\mu_b\gamma_1\eta + \gamma_2(1-\eta)\left(\mu_b + k_3\right)\right)\\
&+\eta\xi_1\gamma_3\Big] + \mu_b\left(k_3 + k_4\right) + k_3 k_4
\end{aligned}$$

Clearly, two of the eigenvalues of $\mathcal{J}$ ($\mathcal{E}_{T0}$), namely, $-\mu$ and $-k$ are negative. Two other eigenvalues can be determined as,

$$Y_{3,4} = \frac{\left(k_1 + k_2\right) \pm \sqrt{\left(k_1 + k_2\right)^2 - 4\left(k_1 k_2 - \nu_1\phi\right)}}{2},$$

which clearly have negative real parts since $\left(k_1 k_2 - \nu_1\phi\right) > 0$, and $\left(k_1 + k_2\right) > 0$. Now, the condition for stability of typhoid-free equilibrium point rests on the zeros of $\Psi(Y)$. These roots have negative real parts if $\Delta_1 > 0,\ \Delta_2 > 0,\ \Delta_3 > 0,$ and $\Delta_1\Delta_2 > \Delta_3$. Clearly, $\Delta_3 > 0$ whenever $\mathcal{R}_0 < 1$. Therefore, the local stability of $\mathcal{E}_{T0}$ is characterized in the following result.

Lemma 2. The typhoid-free equilibrium point $\mathcal{E}_{T0}$ is locally asymptotically stable whenever $\mathcal{R}_0 < 1$ and the conditions $\Delta_1 > 0,\ \Delta_2 > 0,$ and $\Delta_1\Delta_2 > \Delta_3$ also hold. The equilibrium point is unstable otherwise.

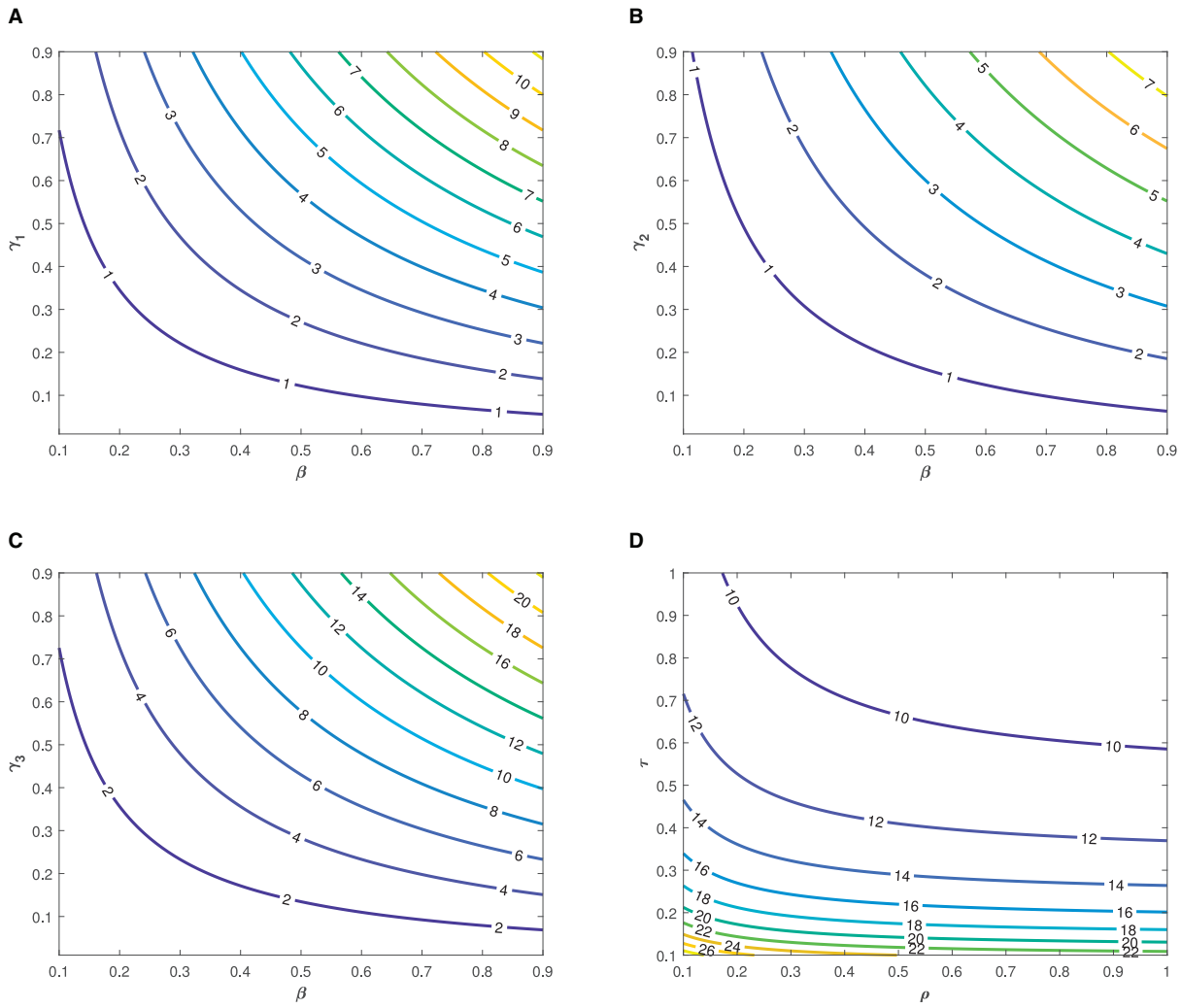

FIGURE 3
Contour plots showing the impact of various parameters on the basic reproduction number $\mathcal{R}_0$ as functions of **(A, B)**, β and γ_2, **(C)** β and γ_3, and **(D)** τ and ρ.

3.5. Global stability of typhoid-free equilibrium points

To study the global stability of the typhoid-free equilibrium point, we define the Lyapunov function

$$\mathcal{L} = \left[\gamma_1 k_4 \mu_b + \psi\gamma_2\mu_b + \left(\psi\xi_2 + k_4\xi_1\right)\gamma_3\right]E + k_3\left(\gamma_2\mu_b + \gamma_3\xi_2\right)I + \gamma_3 k_3 k_4 B.$$

The time derivative of $\mathcal{L}$ is given by

$$\frac{\mathrm{d}\mathcal{L}}{\mathrm{d}t} = \left[\gamma_1 k_4 \mu_b + \psi\gamma_2\mu_b + \left(\psi\xi_2 + k_4\xi_1\right)\gamma_3\right]\frac{\mathrm{d}E}{\mathrm{d}t} + k_3\left(\gamma_2\mu_b + \gamma_3\xi_2\right)\frac{\mathrm{d}I}{\mathrm{d}t} + \gamma_3 k_3 k_4\frac{\mathrm{d}B}{\mathrm{d}t}.$$

Upon substituting the expressions for $\frac{\mathrm{d}E}{\mathrm{d}t}$, $\frac{\mathrm{d}I}{\mathrm{d}t}$, and $\frac{\mathrm{d}B}{\mathrm{d}t}$ into the aforementioned equation and simplifying, we obtain the following.

$$\frac{\mathrm{d}\mathcal{L}}{\mathrm{d}t} = k_3 k_4 \mu_b\left(\frac{S}{S^0}\mathcal{R}_0 - 1\right)\left(\gamma_1 E + \gamma_2 I + \gamma_3 B\right);$$
$$\leq k_3 k_4 \mu_b\left(\frac{\Lambda_h}{\mu S^0}\mathcal{R}_0 - 1\right)\left(\gamma_1 E + \gamma_2 I + \gamma_3 B\right), \text{since } S \leq N \leq \frac{\Lambda_h}{\mu}.$$

Now, $\frac{\Lambda_h}{\mu S^0}\mathcal{R}_0 = \frac{(k_1k_2 - \phi\nu_1)\mathcal{R}_0}{\mu\left((1-n)\phi + nk_1\right)}$, and hence, $\frac{\mathcal{L}}{t} \leq 0$ if $\mathcal{R}_0 \leq \frac{\mu\left((1-n)\phi + nk_1\right)}{(k_1k_2 - \phi\nu_1)}$.
Therefore, even though $\mathcal{R}_0 \leq 1$ is required for local stability, it is not sufficient for global stability. This suggests the existence of backward bifurcation, which will be explored in the next section.

3.6. Sensitivity analysis

Mathematical models have always been proposed and used to make predictions. The reliability of the predictions from these

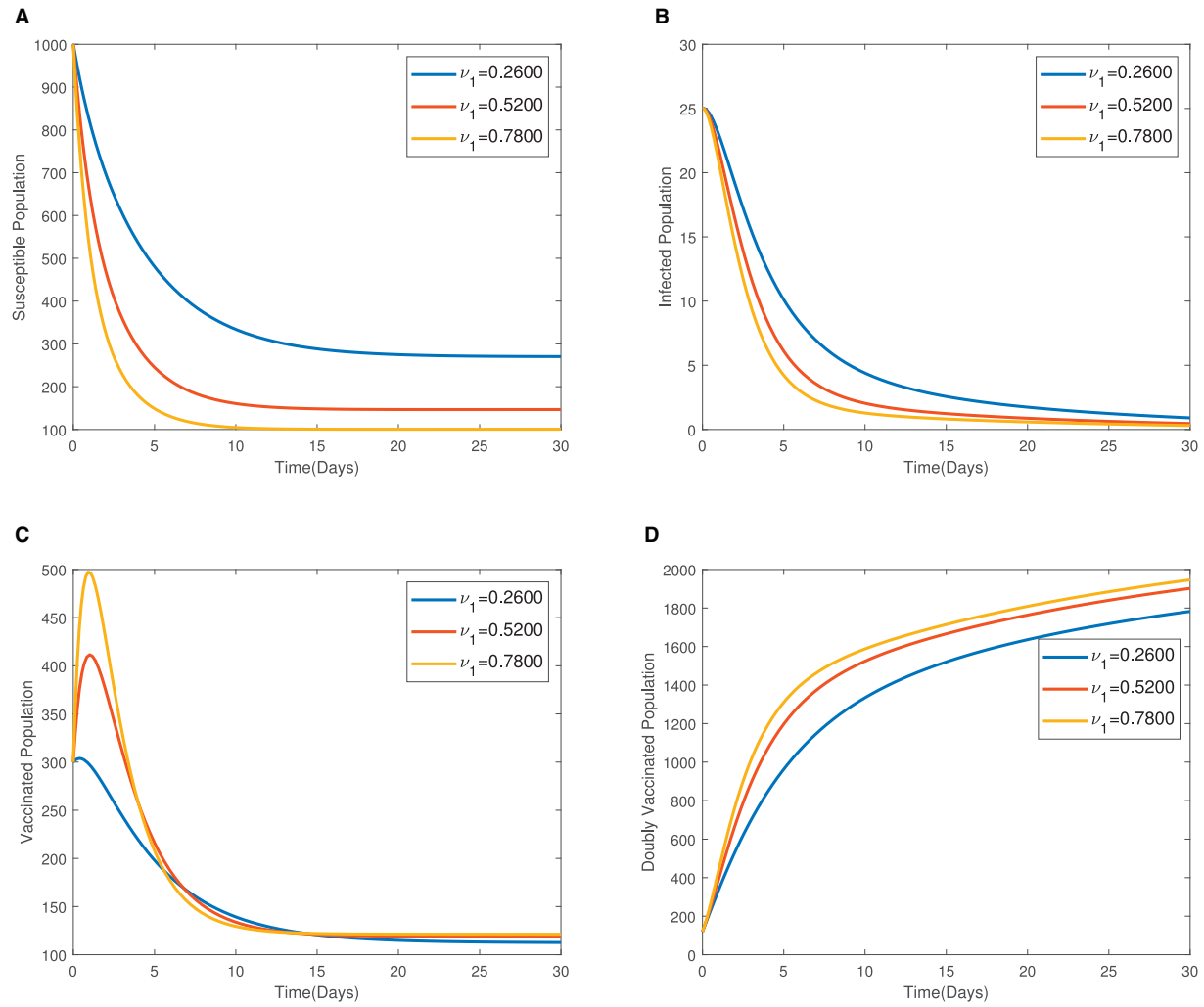

FIGURE 4
(A–D) Time series plots of model variables showing the impact of varying the rate of administration of the first dose of vaccine.

models depends not only on the precision or accuracy of the models, but also on the precision or accuracy of the model inputs, which are mostly in the form of model parameters. Data on these model parameters are often uncertain. Thus, the measurement of model parameters can affect predictions by models. It is therefore important to study the impact of variations in model parameters on the model output. This is done through sensitivity analysis. In this section, we adopt the forward normalized sensitivity index to study the effect of small changes in model parameters on model predictions. This index allows us to determine the parameters with the maximum impact on the model output, so that these models can be targeted for an accurate or precise measurement and also to optimize model predictions. The normalized sensitivity index is defined as follows:

$$\Upsilon_z^p = \frac{\partial z}{\partial p} \times \frac{p}{z}.$$

Where z is an output that depends differentiably on the model input p. Using this index, we determined the sensitivity indices of endemic equilibrium and the basic reproduction number and evaluated them using the model parameter values given in Table 1. The sensitivity indices are presented in Table 2.

The sensitivity indices indicate the percentage change in the given model output that follows from a percentage change in the model input. Positive indices indicate that a percentage increase (decrease) in the model input leads to a corresponding decrease (increase) in the model output. The graphs in Figure 2 present the sensitivity indices.

We observe that the recruitment rate, Λ_h, has a high impact on all, except the susceptible population at equilibrium. The proportion of immigrants who are susceptible also has a high impact on exposed and infected populations. This implies that the inflow of persons into the population should be checked, so as to ensure that they are all vaccinated against typhoid. The transmission rate, β, also has a high impact on disease progression. We also observe that the rate at which individuals who come into contact with the pathogen sources remain exposed and not become

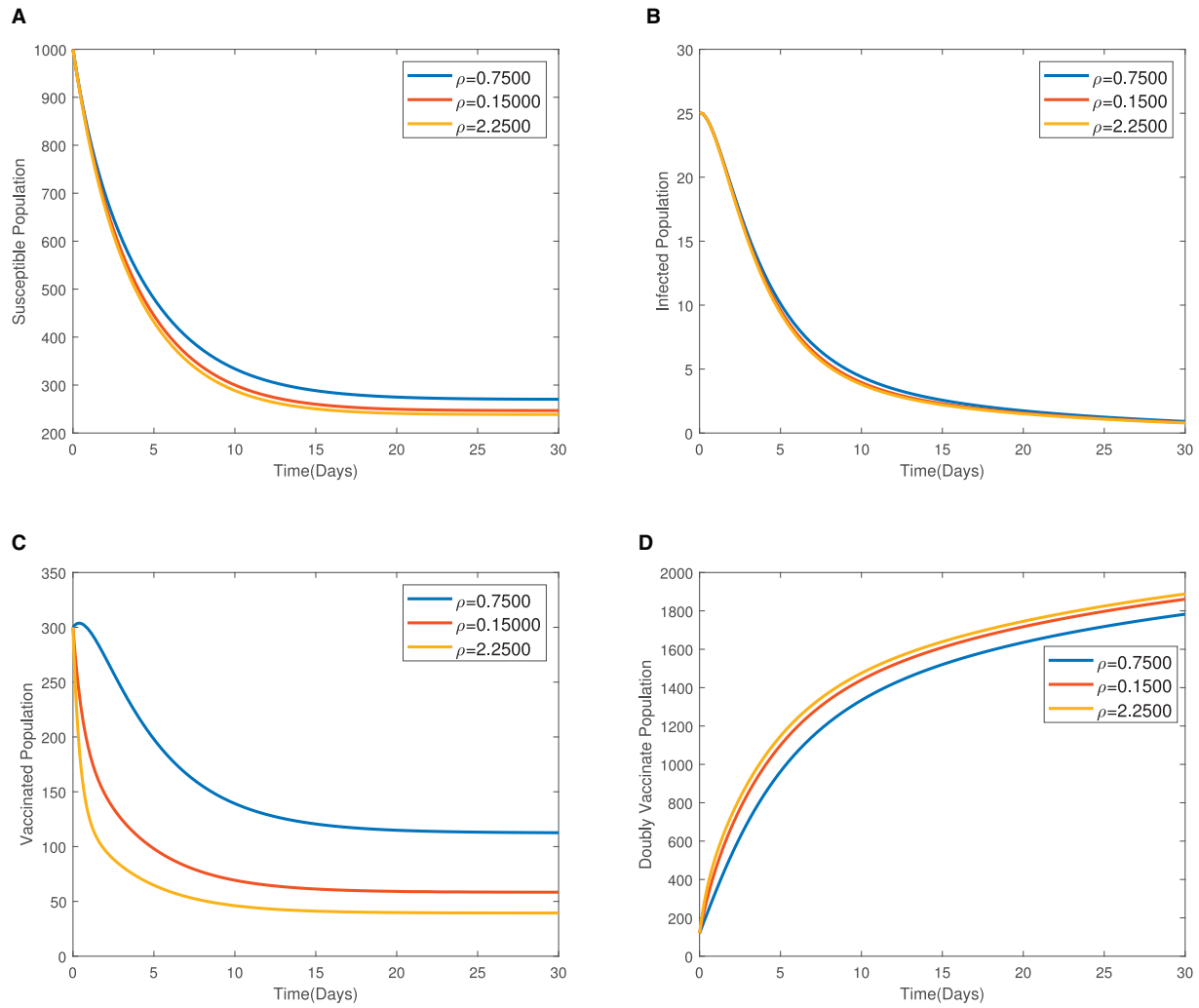

FIGURE 5
(A–D) Time series plots showing the impact of administration of the booster dose of vaccine.

infected has a high impact on disease spread. These parameters should be targeted to ensure that they are reduced or increased (whichever is appropriate) to keep the infections low. Specifically, to reduce or eradicate typhoid, the following measures should be carried out:

- The parameters, Λ_h,ϕ, n, β, ξ_1, ξ_2, γ_1, γ_2, and γ_3, should be reduced.
- The parameters, ν_1, μ, τ, ω, δ, ψ, and μ_b, should be increased. We note however that increasing death rate in humans is not a good option and should hence be ignored.

3.7. Bifurcation analysis

In this section, we study the existence and direction of bifurcation in model (Equation 1). It is easy to show that the Jacobian of the model evaluated at the typhoid-free equilibrium point $\mathcal{E}_{T0}$ has a simple eigenvalue (i.e., a zero eigenvalue) when $\mathcal{R}_0 = 1$. Therefore, the center manifold theory [27] can be employed to study the nature of the bifurcation of the model.

To do this, we set $x_1 = V, x_2 = S, x_3 = E, x_4 = I, x_5 = R, x_6 = V_B$, and $x_7 = B$, so that the model can be written as follows:

$$\left.\begin{aligned}
0 &= (1-n)\,\Lambda_h + \nu_1 x_1 + \nu_2 x_5 - k_1 x_1;\\
0 &= n\Lambda_h + \phi\, x_1 + \theta\, x_5 - k_2 \lambda\, x_2;\\
0 &= \eta\lambda\, x_2 - k_3 x_3;\\
0 &= (1-\eta)\,\lambda\, x_2 + \psi\, x_3 - k_4 x_4;\\
0 &= \tau\, x_4 + w\, x_3 - k_5 x_5;\\
0 &= \rho\, x_1 - \mu\, x_6;\\
0 &= \xi_1 x_3 + \xi_2 x_4 - \mu_b x_7.
\end{aligned}\right\} \tag{12}$$

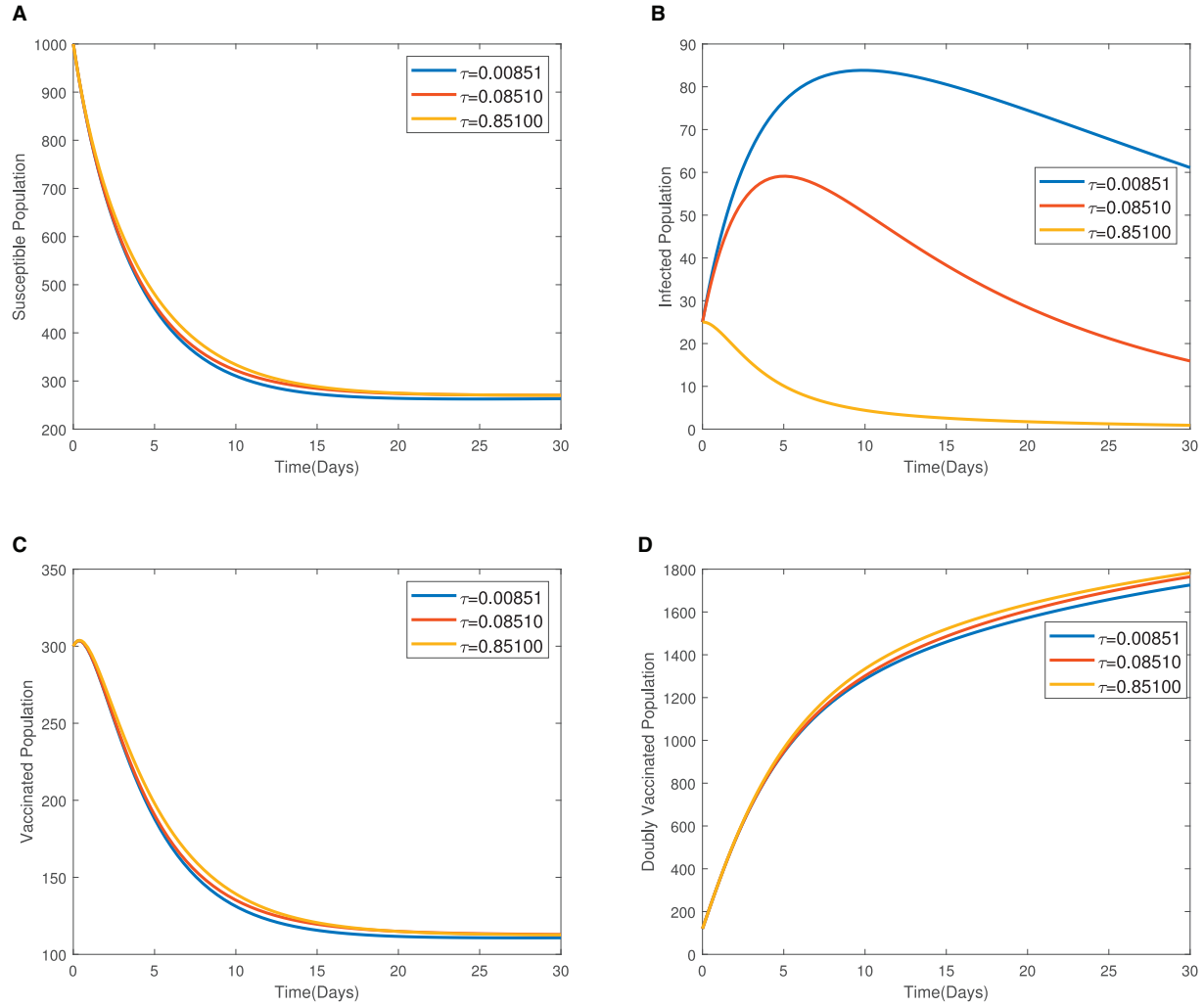

FIGURE 6
(A–D) Time series plots of model variables for varying values showing the impact of treatment rate.

The left and right eigenvectors ($\mathbf{v}$ and $\mathbf{w}$, respectively) associated with the simple eigenvalue are given as follows:

$$
\begin{aligned}
w_1 &= \frac{w_4\left[\left((\tau(\gamma_1\mu_b+\gamma_3\xi_1)-(\gamma_2\mu_b+\gamma_3\xi_2)\omega)(\theta\nu_1+k_2\nu_2)\eta+k_3k_5\nu_1(\gamma_2\mu_b+\gamma_3\xi_2)\right)\beta S^0-k_3\mu_b\tau(\theta\nu_1+k_2\nu_2)\right]}{(k_1k_2-\phi\nu_1)\left(\beta\eta S^0(\gamma_1\mu_b+\gamma_3\xi_1)-k_3\mu_b\right)k_5},\\
w_2 &= \frac{w_4\left[\left((\phi\nu_2+\theta k_1)(\tau(\gamma_1\mu_b+\gamma_3\xi_1)-(\gamma_2\mu_b+\gamma_3\xi_2)\omega)\eta+k_3k_5k_1(\gamma_2\mu_b+\gamma_3\xi_2)\right)\beta S^0-k_3\mu_b\tau(\phi\nu_2+\theta k_1)\right]}{(k_1k_2-\phi\nu_1)\left(\beta\eta S^0(\gamma_1\mu_b+\gamma_3\xi_1)-k_3\mu_b\right)k_5},\\
w_3 &= \frac{\beta\eta S^0(\gamma_2\mu_b+\gamma_3\xi_2)w_4}{k_3\mu_b-\beta\eta S^0(\gamma_1\mu_b+\gamma_3\xi_1)},\\
w_5 &= \left(\frac{\omega\beta\eta S^0(\gamma_2\mu_b+\gamma_3\xi_2)}{k_5\left(k_3\mu_b-\beta\eta S^0(\gamma_1\mu_b+\gamma_3\xi_1)\right)}+\frac{\tau}{k_5}\right)w_4,\\
w_6 &= \frac{\rho w_1}{\mu},\\
w_7 &= \left(\frac{\xi_1\beta\eta S^0(\gamma_2\mu_b+\gamma_3\xi_2)}{\left(k_3\mu_b-\beta\eta S^0(\gamma_1\mu_b+\gamma_3\xi_1)\right)\mu_b}+\frac{\xi_2}{\mu_b}\right)w_4,\\
\nu_1 &= \nu_2=\nu_5=\nu_6=0,\ \nu_3=\frac{\left[k_4\mu_b-\beta S^0(1-\eta)(\gamma_2\mu_b+\gamma_3\xi_2)\right]\nu_4}{(\gamma_2\mu_b+\gamma_3\xi_2)\beta\eta S^0},\nu_7=\frac{\gamma_3k_4\nu_4}{\gamma_2\mu_b+\gamma_3\xi_2}.
\end{aligned}
$$

as a bifurcation parameter, the nature and direction of bifurcation are determined by the bifurcation coefficients

Taking

$$
\beta^*=\frac{\mu_bk_3k_4}{S^0\left[\gamma_1\mu_b\eta\,k_4+\gamma_2\left[\mu_b\eta\psi+(1-\eta)\,k_3\mu_b\right]+\gamma_3\left[(1-\eta)\,k_3\xi_2+\eta\left(\psi\xi_2+\xi_1k_4\right)\right]\right]}
$$

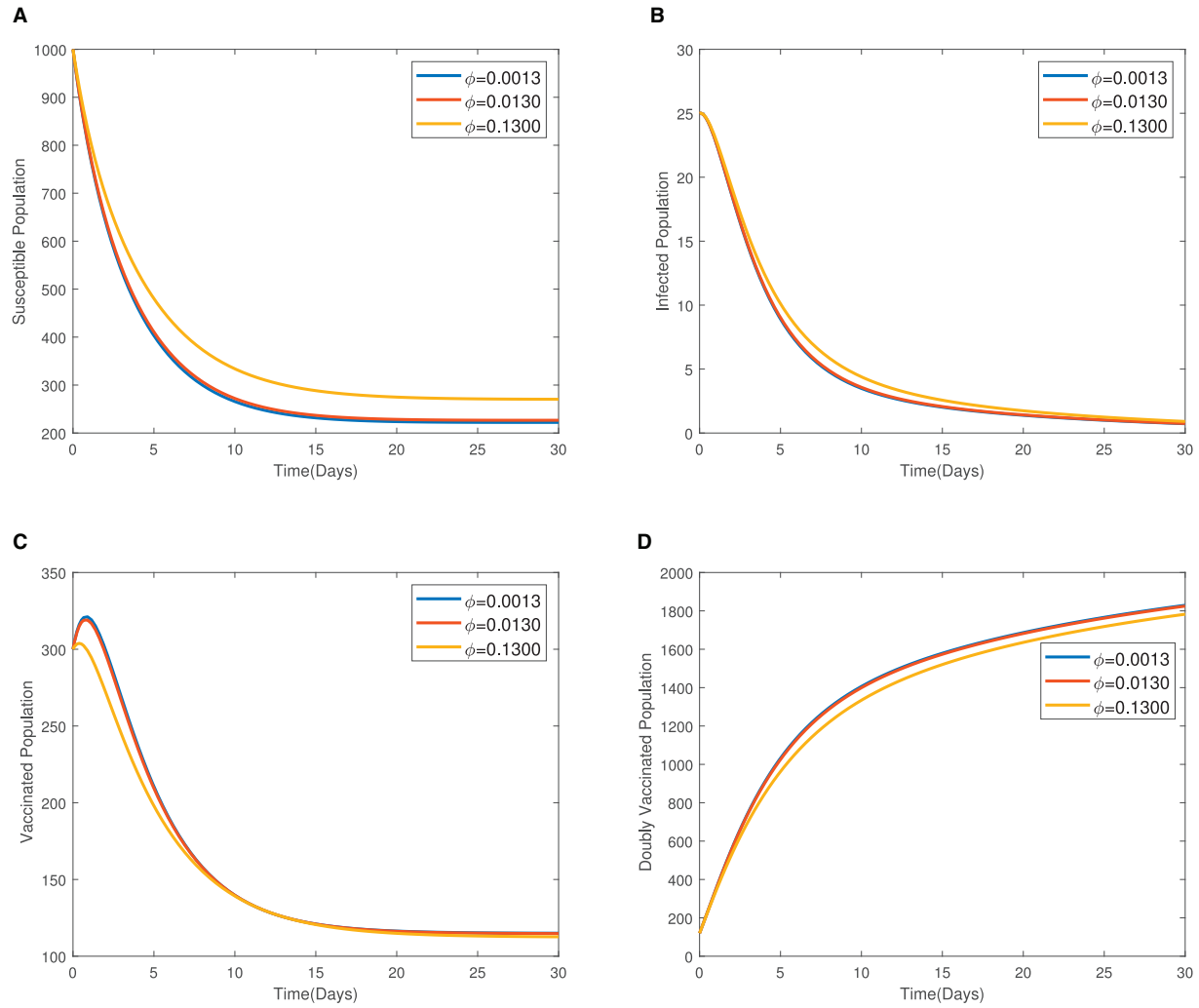

FIGURE 7
(A–D) Time series plots showing the impact of loss of immunity after the first vaccination.

defined by

$$\mathbf{a} = \sum_{i,j,k=1}^{n} v_k w_i w_j \frac{\partial^2 f_k}{\partial x_i \partial x_j} \left(\mathcal{E}_{T0}, \beta^*\right),$$
$$\mathbf{b} = \sum_{i,k=1}^{n} v_k w_i \frac{\partial^2 f_k}{\partial x_i \partial \beta} \left(\mathcal{E}_{T0}, \beta^*\right).$$

Direct computation and simplification yield the following.

$$\mathbf{a} = \frac{2k_4\mu_b}{(\gamma_2\mu_b+\gamma_3\xi_2)S^0}\left(\frac{k_3(\gamma_2\mu_b+\gamma_3\xi_2)}{k_3\mu_b-\beta^*\eta S^0(\gamma_1\mu_b+\gamma_3\xi_1)}\right)w_4w_2v_4;$$
$$\mathbf{b} = \frac{k_4k_3\mu_b w_4v_4}{\beta^*(k_3\mu_b-\beta^*\eta S^0(\gamma_1\mu_b+\gamma_3\xi_1))}.$$

where w_4 and v_4 satisfy

$$\left(\frac{k_4\mu_b - (\gamma_2\mu_b+\gamma_3\xi_2)\,\beta\,(1-\eta)\,S^0}{k_3\mu_b - \beta\eta S^0\,(\gamma_1\mu_b+\gamma_3\xi_1)} + 1 + \frac{\left(\eta\beta\,(-\gamma_1\xi_2+\gamma_2\xi_1)\,S^0 + k_3\xi_2\right)\gamma_3k_4}{\left(k_3\mu_b - \beta\eta S^0\,(\gamma_1\mu_b+\gamma_3\xi_1)\right)(\gamma_2\mu_b+\gamma_3\xi_2)}\right)w_4v_4 = 1.$$

Since the signs of the bifurcation coefficients are not clearly known, the system exhibits backward bifurcation at $\mathcal{R}_0 = 1$ whenever $\mathbf{a} > 0$ and $\mathbf{b} > 0$ [27].

4. Numerical simulation

In this section, we perform numerical simulations of the proposed model (Equation 1). The dynamic model system is simulated using the `ode45` routine in MATLAB. The initial conditions used are given by

$$N(0) = 1,548,\ V(0) = 300,\ S(0) = 1,000,\ E(0) = 50,\ I(0) = 25,$$
$$R(0) = 23,\ V_B(0) = 120,\ B(0) = 500.$$

The the parameter values listed in Table 1 were used in the simulation. The simulation was performed to demonstrate the impact of each parameter on the transmission of typhoid fever. Contour plots, showing the impact of various parameters on the basic reproduction number $\mathcal{R}_0$, are presented in Figure 3.

In Figure 4, the time series plots of model variables, showing the impact of varying the rate of administration of the first dose of typhoid vaccine, are presented. It is observed that increasing the rate of vaccine administration has the potential of driving infections downward. A similar effect of booster vaccine administration is observed from Figure the time series plots given in Figure 5. However, the booster vaccine is observed to have a far lesser impact on driving infections than the single dose. In Figure 6, the time series plots of model variables for varying values of the treatment rate are presented. It is observed that increasing the treatment rate has a very significant impact on infections but not so much for the other compartments. In Figure 7, time series plots showing the impact of loss of immunity after the first vaccination are presented. It is observed that an increased loss of immunity leads to an increase in the susceptible population and an increase in the Infected population.

5. Conclusions

This study formulated and analyzed a mathematical model for the transmission dynamics of typhoid fever disease, taking into account, both the booster vaccination and treatment. The region within which the analysis of the model is reasonable was determined. The typhoid-free and endemic equilibrium points were also determined. The basic reproduction number, $\mathcal{R}_0$, was then calculated using the next-generation matrix method of Driessche and Watmough [26]. The local and global stability conditions for the equilibrium points were investigated. We demonstrated that the model may exhibit backward bifurcation when $\mathcal{R}_0 = 1$ under some conditions. Therefore, the condition $\mathcal{R}_0 < 1$ may not be sufficient to eradicate typhoid fever in the community. A sensitivity analysis of the model parameters was conducted to determine the relative impact of changes in those model parameters on endemic equilibrium values and $\mathcal{R}_0$. It was observed that the most influential parameters include the transmission rate, β, recruitment rate, Λ_h, and the fraction of recruits who are susceptible, n. A numerical simulation was then conducted to illustrate the impact of various model parameters on the state variables. The results largely agree with the sensitivity index results. However, the results show that the booster vaccination may not be very effective in endemic areas.

Data availability statement

The original contributions presented in the study are included in the article/supplementary material, further inquiries can be directed to the corresponding author.

Author contributions

All authors listed have made a substantial, direct, and intellectual contribution to the work and approved it for publication.

Acknowledgments

This article was produced from the M.Phil. thesis of the first author under supervision of the co-author.

Conflict of interest

The authors declare that the research was conducted in the absence of any commercial or financial relationships that could be construed as a potential conflict of interest.

Publisher's note

All claims expressed in this article are solely those of the authors and do not necessarily represent those of their affiliated organizations, or those of the publisher, the editors and the reviewers. Any product that may be evaluated in this article, or claim that may be made by its manufacturer, is not guaranteed or endorsed by the publisher.

References

1. Parry CM, Hien TT, Dougan G, White NJ, Farrar JJ. Typhoid fever. *N Engl J Med.* (2002) 347:1770–82. doi: 10.1056/NEJMra020201

2. Antillón M, Warren JL, Crawford FW, Weinberger DM, Kürüm E, Pak GD, et al. The burden of typhoid fever in low- and middle-income countries: a meta-regression approach. *PLoS Neglect Trop Dis.* (2017) 11:e0005376. doi: 10.1371/journal.pntd.0005376

3. Dougan Baker GS. Salmonella enterica serovar typhi and the pathogenesis of typhoid fever. *Ann Rev Microbiol.* (2014) 68:317–36. doi: 10.1146/annurev-micro-091313-103739

4. Näsström E. *Diagnosis of acute and chronic enteric fever using metabolomics* (Ph.D. thesis). Umeå Universitet (2017).

5. Nthiiri J, Lawi G, Akinyi C, Oganga D, Muriuki W, Musyoka M, et al. Mathematical modelling of typhoid fever disease incorporating protection against infection. *J Adv Math Comput Sci.* (2016) 14:1–10. doi: 10.9734/BJMCS/2016/23325

6. CDC-US X. *Typhoid and Paratyphoid fever: Information for Healthcare Professionals.* Washington, DC: U.S. Department of Health and Human Services (2019).

7. Musa SS, Zhao S, Hussaini N, Usaini S, He D. Dynamics analysis of typhoid fever with public health education programs and final epidemic size relation. *Results Appl Math.* (2021) 10:100153. doi: 10.1016/j.rinam.2021.100153

8. Daabo MI, Makinde OD, Seidu B. Modeling the combined effects of careless susceptible and infective immigrants on the transmission dynamics of hiv/aids epidemics. *J Public Health Epidemiol.* (2013) 5:362–9.

9. Daabo MI, Makinde OD, Seidu B. Modelling the spread of HIV/AIDS epidemic in the presence of irresponsible infectives. *Afr J Biotechnolo.* (2012) 11:11287–95. doi: 10.5897/AJB12.786

10. Ghosh I, Tiwari PK, Samanta S, Elmojtaba IM, Al-Salti N, Chattopadhyay J. A simple si-type model for HIV/AIDS with media and self-imposed psychological fear. *Math Biosci.* (2018) 306:160–9. doi: 10.1016/j.mbs.2018.09.014

11. Seidu B, Makinde OD, Seini IY. Mathematical analysis of the effects of hiv-malaria co-infection on workplace productivity. *Acta Biotheoretica*. (2015) 63:151–82. doi: 10.1007/s10441-015-9255-y

12. Gumel AB, Song B. Existence of multiple-stable equilibria for a multi-drug-resistant model of mycobacterium tuberculosis. *Math Biosci Eng*. (2008) 5:437–55. doi: 10.3934/mbe.2008.5.437

13. Seidu B. Optimal strategies for control of covid-19: a mathematical perspective. *Scientifica*. (2020) 2020:4676274. doi: 10.1155/2020/4676274

14. Tiwari PK, Rai RK, Khajanchi S, Gupta RK, Misra AK. Dynamics of coronavirus pandemic: effects of community awareness and global information campaigns. *Eur Phys J Plus*. (2021) 136:994. doi: 10.1140/epjp/s13360-021-01997-6

15. González-Guzmán J. An epidemiological model for direct and indirect transmission of typhoid fever. *Math Biosci*. (1989) 96:0–46. doi: 10.1016/0025-5564(89)90081-3

16. Wameko M, Koya P, Wodajo A. Mathematical model for transmission dynamics of typhoid fever with optimal controlâĂŐ strategiesâĂŐ. *Int J Ind Math*. (2020) 12:283–96.

17. Ayoola TA, Edogbanya HO, Peter OJ, Oguntolu FA, Oshinubi K, Olaosebikan ML. Modelling and optimal control analysis of typhoid fever. *J Math Comput Sci*. (2021) 11:6666–82. doi: 10.28919/jmcs/6262

18. Ogunlade TO, Ogunmiloro OM, Fatoyinbo GE. On the deterministic and stochastic model applications to typhoid fever disease dynamics. *J Phys Conf Ser*. (2020) 1734:012048. doi: 10.1088/1742-6596/1734/1/012048

19. Peter O, Afolabi O, Oguntolu F, Ishola C, Victor A. Solution of a deterministic mathematical model of typhoid fever by variational iteration method. *Sci World J*. (2018) 13:64–8.

20. Peter OJ, Ibrahim MO, Edogbanya HO, Oguntolu FA, Oshinubi K, Ibrahim AA, et al. Direct and indirect transmission of typhoid fever model with optimal control. *Results Phys*. (2021) 27:104463. doi: 10.1016/j.rinp.2021.104463

21. Peter OJ, Adebisi AF, Ajisope MO, Ajibade FO, Abioye AI, Oguntolu FA. Global stability analysis of typhoid fever model. *Adv Syst Sci Appl*. (2020) 20:20–31. doi: 10.1016/j.imu.2020.100419

22. Abboubakar Racke HR. Mathematical modeling, forecasting, and optimal control of typhoid fever transmission dynamics. *Chaos Solitons Fractals*. (2021) 149:111074. doi: 10.1016/j.chaos.2021.111074

23. Bailey NT. The structural simplification of an epidemiological compartment model. *J Math Biol*. (1982) 14:101–16. doi: 10.1007/BF02154756

24. Adetunde I. Mathematical models for the dynamics of typhoid fever in Kassena-Nankana district of upper east region of Ghana. *J Modern Math Stat*. (2008) 2: 45–9.

25. Mutua JM, Wang FB, Vaidya NK. Modeling malaria and typhoid fever co-infection dynamics. *Math Biosci*. (2015) 264:128–44. doi: 10.1016/j.mbs.2015.03.014

26. Driessche Watmough VJ. Reproduction numbers and sub-threshold endemic equilibria for compartmental models of disease transmission. *Math. Biosci*. (2002) 180:29–48. doi: 10.1016/S0025-5564(02)00108-6

27. Castillo-Chavez Song CB. Dynamical models of tuberculosis and their applications. *Math Biosci Eng*. (2004) 1:361. doi: 10.3934/mbe.2004.1.361

frontiers | Frontiers in Public Health

TYPE Original Research
PUBLISHED 18 May 2023
DOI 10.3389/fpubh.2023.1154944

OPEN ACCESS

EDITED BY
Shahidul Islam,
University of Dhaka, Bangladesh

REVIEWED BY
Dawei Cui,
Zhejiang University School of Medicine, China
Ze Chen,
Hunan Normal University, China

*CORRESPONDENCE
Haocheng Wu
✉ hchwu@cdc.zj.cn
Junfen Lin
✉ 594791158@qq.com
Qinbao Lu
✉ hesiran@126.com

†These authors have contributed equally to this work

RECEIVED 31 January 2023
ACCEPTED 28 April 2023
PUBLISHED 18 May 2023

CITATION
Wu H, Xue M, Wu C, Ding Z, Wang X, Fu T, Yang K, Lin J and Lu Q (2023) Estimation of influenza incidence and analysis of epidemic characteristics from 2009 to 2022 in Zhejiang Province, China.
Front. Public Health 11:1154944.
doi: 10.3389/fpubh.2023.1154944

Estimation of influenza incidence and analysis of epidemic characteristics from 2009 to 2022 in Zhejiang Province, China

Haocheng Wu[1*†], Ming Xue[2†], Chen Wu[1], Zheyuan Ding[1], Xinyi Wang[1], Tianyin Fu[1], Ke Yang[1], Junfen Lin[1*] and Qinbao Lu[1*]

[1]Center for Disease Control and Prevention (Zhejiang CDC), Zhejiang, Hangzhou, China, [2]Hangzhou Center for Disease Control and Prevention (HZCDC), Hangzhou, China

Background: Influenza infection causes a huge burden every year, affecting approximately 8% of adults and approximately 25% of children and resulting in approximately 400,000 respiratory deaths worldwide. However, based on the number of reported influenza cases, the actual prevalence of influenza may be greatly underestimated. The purpose of this study was to estimate the incidence rate of influenza and determine the true epidemiological characteristics of this virus.

Methods: The number of influenza cases and the prevalence of ILIs among outpatients in Zhejiang Province were obtained from the China Disease Control and Prevention Information System. Specimens were sampled from some cases and sent to laboratories for influenza nucleic acid testing. Random forest was used to establish an influenza estimation model based on the influenza-positive rate and the percentage of ILIs among outpatients. Furthermore, the moving epidemic method (MEM) was applied to calculate the epidemic threshold for different intensity levels. Joinpoint regression analysis was used to identify the annual change in influenza incidence. The seasonal trends of influenza were detected by wavelet analysis.

Results: From 2009 to 2021, a total of 990,016 influenza cases and 8 deaths were reported in Zhejiang Province. The numbers of estimated influenza cases from 2009 to 2018 were 743,449, 47,635, 89,026, 132,647, 69,218, 190,099, 204,606, 190,763, 267,168 and 364,809, respectively. The total number of estimated influenza cases is 12.11 times the number of reported cases. The APC of the estimated annual incidence rate was 23.33 (95% CI: 13.2 to 34.4) from 2011 to 2019, indicating a constant increasing trend. The intensity levels of the estimated incidence from the epidemic threshold to the very high-intensity threshold were 18.94 cases per 100,000, 24.14 cases per 100,000, 141.55 cases per 100,000, and 309.34 cases per 100,000, respectively. From the first week of 2009 to the 39th week of 2022, there were a total of 81weeks of epidemics: the epidemic period reached a high intensity in 2weeks, the epidemic period was at a moderate intensity in 75weeks, and the epidemic period was at a low intensity in 2weeks. The average power was significant on the 1-year scale, semiannual scale, and 115-week scale, and the average power of the first two cycles was significantly higher than that of the other cycles. In the period from the 20th week to the 35th week, the Pearson correlation coefficients between the time series of influenza onset and the positive rate of pathogens, including A(H3N2), A (H1N1)pdm2009, B(Victoria) and B(Yamagata), were−0.089 (p=0.021), 0.497 (p<0.001), −0.062 (p=0.109) and−0.084 (p=0.029), respectively. In the period from the 36th week of

the first year to the 19th week of the next year, the Pearson correlation coefficients between the time series of influenza onset and the positive rate of pathogens, including A(H3N2), A (H1N1)pdm2009, B(Victoria) and B(Yamagata), were 0.516 (p<0.001), 0.148 (p<0.001), 0.292 (p<0.001) and 0.271 (p<0.001), respectively.

Conclusion: The disease burden of influenza has been seriously underestimated in the past. An appropriate method for estimating the incidence rate of influenza may be to comprehensively consider the influenza-positive rate as well as the percentage of ILIs among outpatients. The intensity level of the estimated incidence from the epidemic threshold to the very high-intensity threshold was calculated, thus yielding a quantitative standard for judging the influenza prevalence level in the future. The incidence of influenza showed semi-annual peaks in Zhejiang Province, including a main peak from December to January of the next year followed by a peak in summer. Furthermore, the driving factors of the influenza peaks were preliminarily explored. While the peak in summer was mainly driven by pathogens of A(H3N2), the peak in winter was alternately driven by various pathogens. Our research suggests that the government urgently needs to address barriers to vaccination and actively promote vaccines through primary care providers.

KEYWORDS

estimation, influenza, random forest, moving epidemic method, Joinpoint regression

Background

Influenza is an acute respiratory infectious disease caused by influenza virus, which is an RNA virus that is divided into three types: A, B and C (1, 2). The types of A, B and C not only reflect the order in which the virus was discovered but also, more importantly, reflect the order of harm to human beings (3, 4). Influenza A virus is the main epidemic strain and can lead to a global influenza pandemic. It is widely transmitted among animals, which can lead to a flu epidemic among animals and cause a large number of animal deaths (5, 6). Compared with influenza A virus, influenza B virus causes only local outbreaks and does not cause pandemics. Influenza C virus generally appears in a scattered form; it mainly affects infants and does not cause epidemics (7). Subtypes of influenza A–i.e., H3N2 virus and H1N1pdm2009 virus–and influenza B virus are the main viruses circulating in the population (8).

Influenza is mainly transmitted by droplets, and people are generally susceptible to infection (2). Influenza virus can cause different degrees of infection, ranging from mild illness requiring hospitalization to severe illness and sometimes even death (9, 10). Each year, a substantial disease burden is attributed to seasonal influenza (11). Influenza infections annually affect approximately 8% of adults and approximately 25% of children, resulting in approximately 400,000 respiratory-related deaths worldwide according to the World Health Organization (WHO) (12). From 2006 to 2019, the annual number of outpatient visits for influenza-related influenza-like diseases (ILIs), number of hospitalizations for severe acute respiratory infections (SARIs) and number of excessive respiratory deaths in mainland China were 3 million, 2.34 million and 90,000,000, respectively, leading to a total economic burden of 26.38 billion yuan and accounting for 0.266 ‰ of the 2019 GDP (13). However, compared with the number of reported cases of influenza, the actual prevalence of influenza may be greatly underestimated (14). From 2005 to 2010, the number of reported influenza cases in mainland China was only 45,672, 57,557, 36,434, 41,692, 198,381 and 64,502, respectively; however, the estimated incidence of influenza in Guangzhou city in 2006 was 2,382/100,000, approximately equal to 237,413 cases, which was far more than the reported number of cases in the whole country (15). Therefore, reports of influenza-like illness (ILIs) are usually used to estimate the trend of disease instead of reports of influenza alone (14, 16). However, according to a previous study, the specificity of ILIs for estimating the incidence of influenza is only 77%, thus leading to an overestimate of the incidence of influenza (14). The purpose of this study is to establish an influenza estimation model based on the percentage of ILIs among outpatients and the influenza-positive rate and to correct the reported incidence level. Furthermore, the moving epidemic method (MEM) was applied to calculate the epidemic threshold for different intensity levels based on the estimated weekly incidence. Joinpoint regression analysis was used to identify the annual change in estimated influenza incidence. The seasonal periodicity of weekly incidence of influenza was detected by wavelet analysis.

Materials and methods

Data collection

Data regarding newly diagnosed influenza cases and the prevalence of ILIs among outpatients in Zhejiang Province were collected between week 1 in 2009 and week 39 in 2022 from the China Disease Control and Prevention Information System. The population data used to calculate the incidence rate was updated by the company responsible for system operation and maintenance and the new

population data was imported into the system every December. The incidence rate of influenza was computed by the system and can be exported. Data on the influenza A (H1N1)pdm2009 subtype from 2009 to 2013 were reported separately, and these cases were added to the total number of influenza cases in the corresponding year. Specimens were sampled from some cases and sent to laboratories for A(H3N2), A (H1N1)pdm2009, B(Victoria) and B(Yamagata) influenza nucleic acid testing or antigen testing. The diagnosis of influenza virus is based on the diagnosis and treatment criteria, including 'Diagnostic criteria for influenza' (Version 2008), 'Guidelines for diagnosis and treatment of influenza A (H1N1)pdm2009' (3rd Edn 2009) and 'Guidelines for diagnosis and treatment of influenza' (Version 2019) (17–19). When a symptomatic case has positive results of any of the following pathogenic tests, it is diagnosed as a confirmed case, including positive influenza virus nucleic acid test, positive influenza antigen test, positive influenza virus culture isolation, and the level of influenza virus-specific IgG antibody in the double sera of acute and convalescent patients increased by 4 times or more.

Random forest analysis

Random forest is a widely used method for data prediction and classification calculation. Random forest is a combinatorial classification intelligent algorithm based on statistical learning theory. The basic idea of this method is to combine multiple weak classifiers with complementary functions to form a strong classifier. By reducing the impact of single classifier errors, the accuracy and stability of model classification can be improved. The main step is to randomly select k subtraining sample sets from the total training sample set through bootstrap sampling and establish a decision classification subtree model. Then, m is randomly selected from the n indices of each node in the classification tree and segment according to the optimal segmentation index. The previous step is repeated to traverse K classification subtrees to determine multiple classification results. Then, the final classification result is determined by voting. Approximately 36.8% of the samples in this model will not appear in the bootstrap sampling set. This part of the data is called OOB (Out Of Bag) data. OOB data can be used to evaluate the decision subtree model and determine the error classification rate of the decision subtree, namely, the OOB error (20).

We established the training model based on the reported influenza cases as a dependent variable and the observed weekly percentage of ILIs among outpatients and influenza-positive rate during 2019–2022 as the independent variables. In the next step, we estimated the weekly number of influenza cases from 2009 to 2018.

Joinpoint regression

Joinpoint regression is also called piecewise regression, broken-line regression or multiphase regression. This model does not require the data series itself to show an obvious trend, and it is increasingly used to determine the degree of change in time series data. Joinpoint regression analysis software uses the Z score to test the hypothesis of segmentation points to determine whether the data have sufficient evidence to add how many segmentation points. The first step assumes that there is no segmentation point, that is, H_0. If H_0 is rejected, then the analysis is used to test whether there is statistical significance between 1 segmentation point and n segmentation points, and so on (21).

The objective indicator was the annual percent change (APC) of each period segment, estimated according to the following formula:

$$APCi = \left[\exp\left(\beta_i\right) - 1\right] \times 100, \quad (1)$$

where β_i represents the slope of the period segment (22).

Wavelet analysis (22)

The wavelet method is a reasonable method for studying periodic phenomena in time series, especially when the existence of potential frequency changes with time. Morlet wavelet is used to analyze the frequency structure of univariate and bivariate time series. This continuous complex wavelet leads to the continuous complex wavelet transform of the time series at hand, so the information can be saved by carefully selecting the time and frequency resolution parameters. The transformation can be divided into a real part and an imaginary part to provide information about the local amplitude and instantaneous phase of any periodic process in time, which is a prerequisite for studying the correlation between two time series (22).

Moving epidemic method (23)

The MEM includes three main steps. The first step is to determine the time length of the epidemic season and the time nodes of the beginning and end of the epidemic season from a professional perspective based on the epidemic law of the disease and to divide the epidemic season into the pre-epidemic period (from the beginning of the epidemic season to the end of the epidemic season), the epidemic period (from the beginning of the epidemic season to the end of the epidemic season) and the post-epidemic period (from the end of the epidemic season to the end of the epidemic season). The second step is to calculate the pre-epidemic baseline, pre-epidemic threshold (epidemic start threshold), post-epidemic baseline and post-epidemic threshold (epidemic end threshold) by using the pre-epidemic and post-epidemic monitoring index values of historical data. The pre-epidemic/post-epidemic baseline is calculated using the arithmetic mean of all its monitoring indicators. For the calculation of the pre-epidemic/post-epidemic threshold of the current epidemic season, the n maximum monitoring indicators ($n = 30/\mathrm{N}$, N is the number of epidemic seasons) of each historical epidemic season are taken, for a total of $n \times N = 30$ values, and the upper limit of its one-sided 95% confidence interval is calculated. The third step is to calculate the different-intensity thresholds of the current epidemic period by using the monitoring index values of the epidemic period in the historical epidemic season for monitoring and warning. The specific method is as follows: select the maximum value of n monitoring indicators in the historical epidemic period, totaling $n \times N = 30$ values; then, define the upper limit of the one-sided 40, 90 and 97.5% confidence intervals of the geometric mean of the 30 maximum monitoring index values, which correspond with the medium, high and extremely high intensity thresholds, respectively.

Influenza epidemic intensity level is defined as ① baseline: weekly monitoring index value < epidemic start/end threshold; ② low-intensity epidemic: epidemic threshold ≤ weekly monitoring index value < medium-intensity threshold; ③ moderate-intensity epidemic: moderate-intensity threshold ≤ weekly monitoring index value < high-intensity threshold; ④ high-intensity epidemic: high-intensity threshold ≤ weekly monitoring index value < extremely high-intensity threshold; ⑤ extremely high-intensity epidemic: weekly monitoring index value ≥ extremely high-intensity threshold.

Statistical analysis

The joinpoint regression model was constructed using joinpoint software (version 4.5.0.1). The random forest modeling, MEM model and wavelet analysis were run by R Studio (version 1.2.5001). A p value less than 0.05 indicated statistical significance for all the tests.

Results

Basic information

From 2009 to 2021, a total of 990,016 influenza cases and 8 related deaths were reported in Zhejiang Province. The annual influenza incidence varies widely from 4.9498 cases per 100,000 to 850.2056 cases per 100,000. The percentage of ILIs among outpatients fluctuated across years and followed a bimodal seasonal pattern, where the peak epidemic period was always from the 51st week of a year to the 8th week of the next year; additionally, there was sometimes a small peak in summer. The highest prevalence of ILIs among outpatients was 12.11%, which was observed in the 48th week of 2009 and was mainly affected by the influenza A (H1N1)pdm2009 subtype. The lowest prevalence was 1.69%, which was observed in the 49th week of 2010 (Figure 1A). The intensity levels of the prevalence of ILIs among outpatients from the epidemic threshold to the very high-intensity

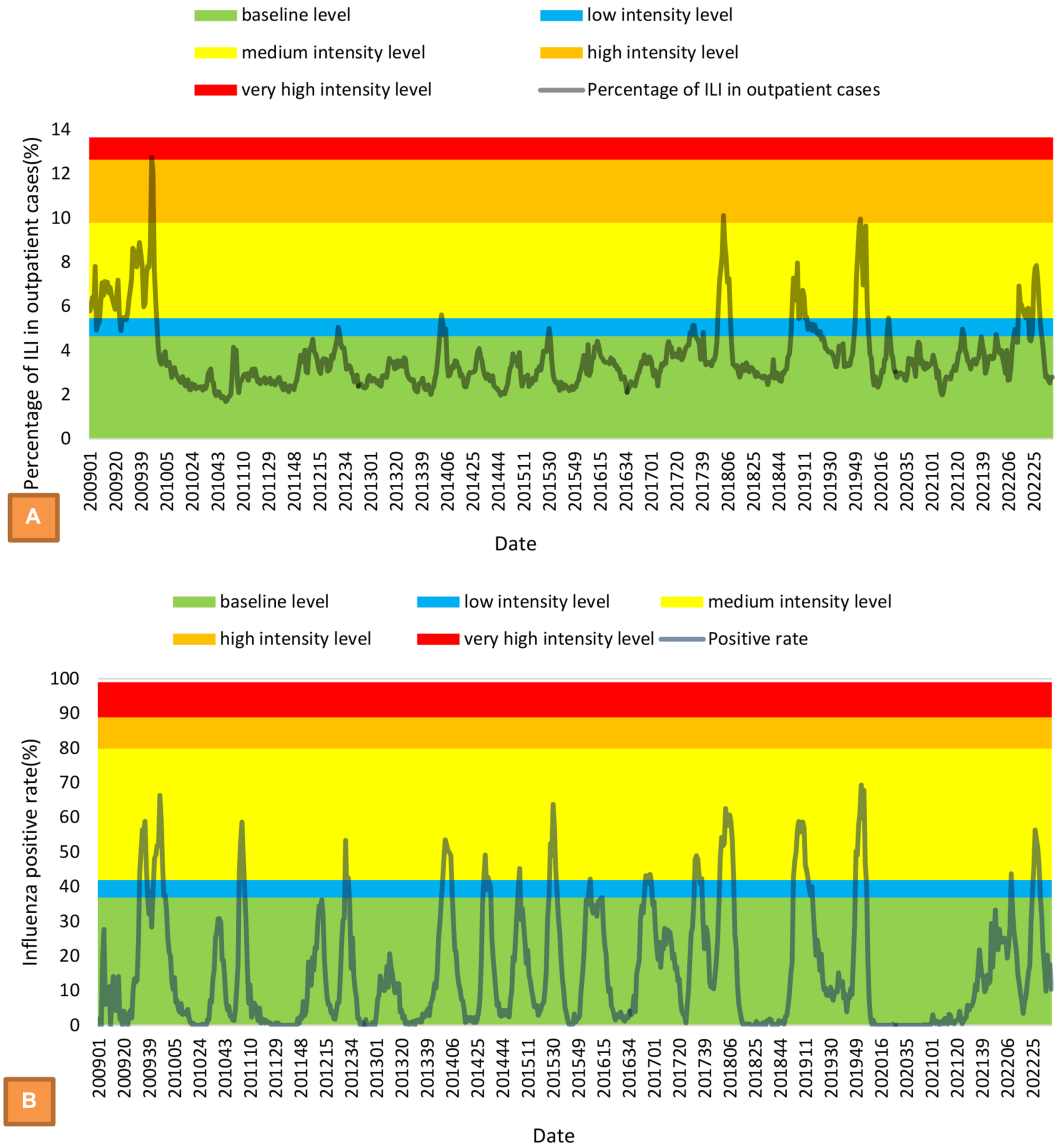

FIGURE 1
MEM model with intensity levels and time-series of weekly percentage of ILIs among outpatients **(A)** and weekly influenza-positive rate **(B)**.

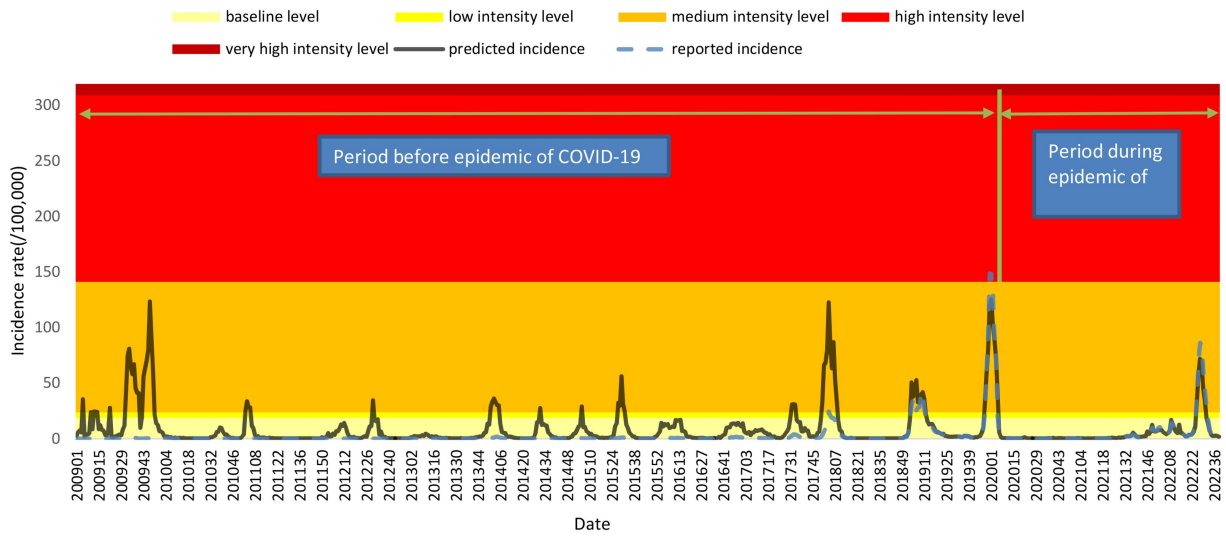

FIGURE 2
MEM model with intensity levels and time series of weekly estimated incidence and reported incidence.

threshold were 4.66, 5.48, 9.79, and 12.65%, respectively. The weekly influenza-positive rate was similar across different years, and the peak of the epidemic was driven by the alternation of different influenza subtypes into dominant strains. The lowest weekly influenza-positive rate was 0%, and the highest rate was 69.33%, which was observed in the first week of 2020 (Figure 1B). The intensity levels of the influenza-positive rate from the epidemic threshold to the very high-intensity threshold were 37.01, 42.23, 80.33 and 89.64%, respectively.

Estimation of the incidence of influenza and the trend from 2009 to 2021

Based on the observed weekly percentage of ILIs among outpatients and the influenza-positive rate during 2019–2022, the training model was established. The mean absolute percentage error (MAPE) of the model was 26.10%. The raw predicted data and the actual data were well matched (Figure 2). The numbers of estimated influenza cases from 2009 to 2018 were 743,449, 47,635, 89,026, 132,647, 69,218, 190,099, 204,606, 190,763, 267,168 and 364,809, respectively. However, the number of reported cases during the same periods was only 20,385, 4,063, 2,694, 2,908, 3,302, 9,700, 7,970, 14,394, 30,434 and 94,091, respectively. The total number of estimated influenza cases is 12.11 times the number of reported cases.

The time series of the estimated annual incidence rate is significantly different from the curve of the reported annual incidence rate. The final selected model of the reported annual incidence rate was the 2 joinpoints relative to the 0 joinpoint ($p < 0.001$) and 1 joinpoint ($p < 0.001$). The APCs were −17.70 (95% CI: −31.40 to −1.20) from 2009 to 2016, 349.99 (95% CI: 206.40 to 560.80) from 2016 to 2019, and −51.91 (95% CI: −62.00 to −39.20) from 2019 to 2021, which were significant differences at the 0.05 level (test statistic = −2.70, 10.10, −8.00, respectively, $p < 0.001$). The APC indicated a gradual decreasing trend from 2009 to 2016; then, it showed a sharp upward trend from 2016 to 2019 and decreased again after 2019 (Figure 3A). The final selected model of the estimated annual incidence rate was also the 2 joinpoints relative to the 0 joinpoint ($p < 0.001$) and 1 joinpoint ($p = 0.01$). The APC was 23.33 (95% CI: 13.2 to 34.4) from 2011 to 2019, indicating a monotonically increasing trend, but the APC before 2011 and after 2019 was not significantly different from zero(Figure 3B).

Intensity level of influenza, seasonal periodicity and driving factors

The inner parameters of the model was set from 1.5 to 3%, increasing by 0.1% each time, and the fitted Youden index of all models was between 0.4709 and 0.5450, of which the parameter corresponding to the maximum Youden index is 1.8%, and the correspondingspecificity, sensitivity, positive predictive value and negative predictive value, were 0.95, 0.56, 0.75 and 0.89, respectively. The intensity levels of the estimated incidence from the epidemic threshold to the very high-intensity threshold were 18.94 cases per 100,000, 24.14 cases per 100,000, 141.55 cases per 100,000, and 309.34 cases per 100,000, respectively. According to the estimated time series of influenza incidence, the influenza incidence level is at the baseline level in most of the time periods, and most of the peaks of the influenza epidemic corresponded to a the moderate intensity level. From the first week of 2009 to the 39th week of 2022, there were a total of 81 weeks of epidemics, of which the epidemic period reached a high intensity in 2 weeks, the epidemic period was at a moderate intensity in 75 weeks, and the epidemic period was at a low intensity in 2 weeks. The epidemic reached a high intensity in the 52nd week of 2019 and the first week of 2020; the respective incidence rates were 148.89 cases per 100,000 and 148.20 cases per 100,000. Based on the reported incidence, the number of influenza cases reported in the week before 2018 was very low and fluctuated very little between different weeks, making it impossible to detect the peak epidemic (Figure 2).

For the incidence rate of reported cases, it is almost impossible to observe obvious seasonal characteristics before 2017. After adjusting the reported incidence rate, an obvious peak of incidence in winter and

spring can be observed, which usually occurs from December to March of the next year from 2009 to 2022. In addition, there was also a peak incidence in summer in 2009, 2014, 2015, 2017 and 2022. Figure 4 shows the wavelet power spectrum for the estimated incidence of influenza. The average power was significant on the semiannual scale, 1-year scale, and 115-week scale, and the average power of the first two cycles was significantly higher than that of the other cycles. The average power indicated that this disease showed half a year peaks, including a main peak from December to January of the next year followed by a peak in summer. This periodicity is not significant at all times. From the 47th week of 2010 to the 40th week of 2013 and from the 8th week of 2020 to the 32nd week of 2021, there was no obvious semiannual periodicity of the incidence. The 1-year scale was also relatively weak from the 44th week of 2011 to the 41st week of 2013.

Because the influenza season has two waves, it was divided into two periods: the first section is from the 20th week to the 35th week, and the second section is from the 36th week of the first year to the 19th week of the next year. In the first period, the Pearson correlation coefficients between the time series of influenza onset and the positive rate of pathogens, including A(H3N2), A (H1N1)pdm2009, B(Victoria) and B(Yamagata), were 0.497 ($p < 0.001$), −0.089 ($p = 0.021$), −0.062 ($p = 0.109$) and −0.084 ($p = 0.029$), respectively. In the second period, the Pearson correlation coefficients between the time series of influenza onset and the positive rate of pathogens, including A (H1N1)pdm2009, A (H3N2), B (Victoria) and B (Yamagata), were 0.516 ($p < 0.001$), 0.148 ($p < 0.001$), 0.292 ($p < 0.001$) and 0.271 ($p < 0.001$), respectively.

Discussion

Influenza virus infections are very common worldwide, and the incidence of influenza can only be estimated (14, 24). Two major surveillance subsystems under the China Disease Control and

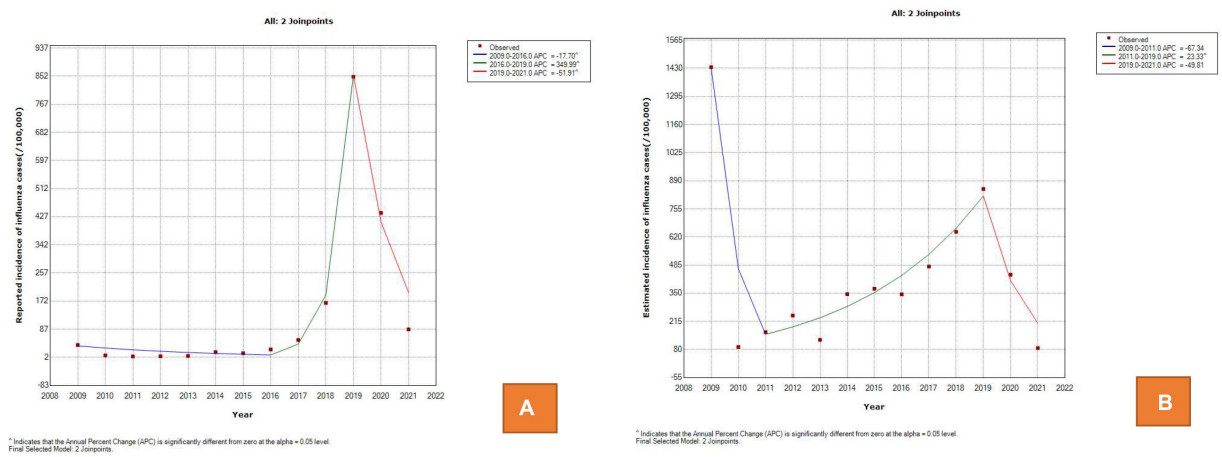

FIGURE 3
Trend of influenza incidence between 2009 and 2021 in the joinpoint regression model. **(A)** The reported annual incidence rate. **(B)** The estimated annual incidence rate.

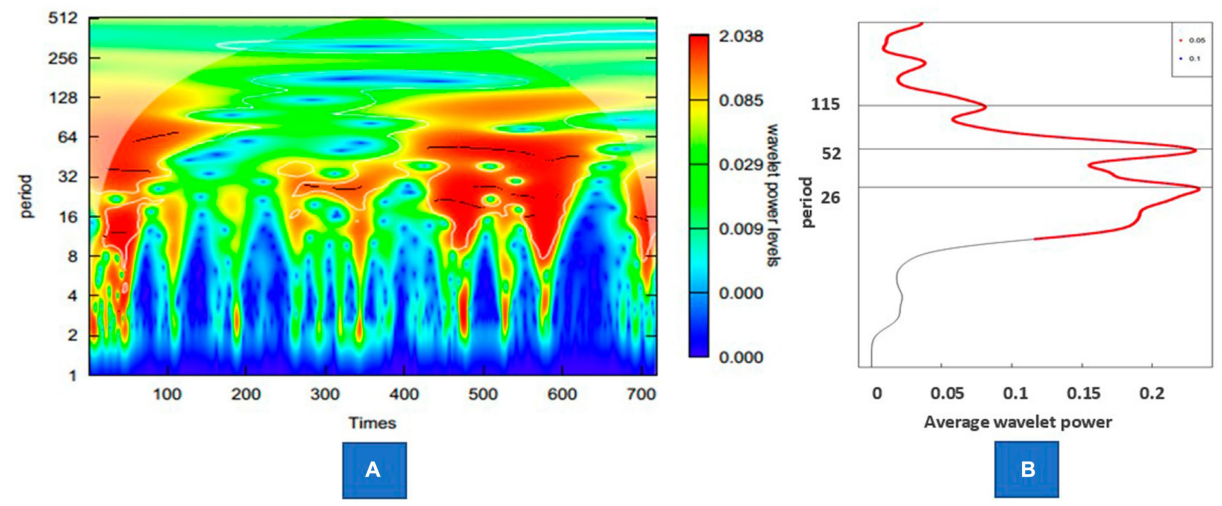

FIGURE 4
Wavelet power of the estimated incidence of influenza. **(A)** Wavelet power spectrum of the series. **(B)** The average power of the whole period.

Prevention Information System, including the Infectious Disease Monitoring and Reporting System and the Influenza-Like Illness (ILI) Surveillance System, have been officially used for the monitoring and analysis of influenza in China (25). However, due to the limitations of diagnostic criteria and the fact that not everyone was tested for influenza, the reported incidence of influenza differs greatly from the actual incidence level (14, 15). Therefore, influenza-like illness (ILI) is usually used to estimate the trend of disease instead of influenza (14, 16). However, a previous study showed that the level of influenza-like cases is important for monitoring influenza infection and had the best sensitivity (86%) and specificity (77%) values (26). However, based on the percentage of ILIs among outpatients, the actual prevalence of influenza may be overestimated. In our study, from the 11th week of 2020 to the 53rd week of 2020, the weekly median level of the percentage of ILIs among outpatients was 3.21, which was higher than the weekly median level from 2010 to 2016; however, the weekly average level of influenza-positive rate in the same period was almost 0. This suggests that the level of influenza incidence during this period is very low, and the use of the percentage of ILIs among outpatients instead of measuring influenza cases will lead to significant overestimation. Therefore, an appropriate method for estimating the incidence rate of influenza may be to comprehensive consider the influenza-positive rate in addition to the percentage of ILIs among outpatients.

According to our research, the actual incidence level of influenza is far higher than the current reported number, which also indicates that the disease burden of influenza has been seriously underestimated in the past. The reported incidence of influenza increased rapidly in 2019, mainly due to the revision of the Guidelines for the Diagnosis and Treatment of Influenza, in which the rapid antigen detection method was added as the diagnostic standard. Compared with previous studies, only a few samples were reported with positive nucleic acid detection. According to the number of reported cases, the incidence of influenza from 2011 to 2016 showed a downward trend, but after estimation with the model, we found that the incidence of influenza in this period actually showed an upward trend, which suggested that incomplete diagnosis and inaccurate reporting would lead to misunderstanding of the epidemic trend. The result of a rapid increasing trend of influenza is similar to several previous studies (25, 27). There are several reasons that may be related to the increasing trend of influenza during this period. Influenza vaccination is the most effective way to prevent influenza infection and reduce severe influenza-related complications (28). The reductions in the numbers of vaccine supplements and low vaccination coverage rate might be an important factor for the increased incidence of influenza. The lack of an influenza vaccine may be mainly due to the vaccine scandal caused by improper vaccine storage and production in 2016 and 2018, respectively (25, 29). In addition, the use of automatic data acquisition and reporting systems, which improved both the quantity and quality of data collection, might be another reason (30). In addition, the rapid increase in the number of airlines and high-speed rail transport in recent years will make it easier for influenza virus to spread on a larger scale and in a shorter time across the country (31). The outbreak growth of influenza cases in 2009 is obviously attributable to the spread and widespread impact of influenza A (H1N1) pdm2009 (25). Due to the response to the COVID-19 pandemic, some prevention and control measures, including the improvement of self-protection, the isolation of cases and close contacts, and the reduction in social activities of the population, have led to a reduction in several infectious diseases, including influenza and tuberculosis transmission, in 2020, and this effect may last until 2021 (8, 32). During the period of this study, Chinese Mainland adopted the strategy of containment and elimination of the COVID-19 epidemic. Once cases with suspicious symptoms were found, nucleic acid testing and strict diagnosis were required, and all possible close contacts were tracked and managed to achieve the goal of clearing cases in a short period of time. Therefore, the context of each case of COVID-19 is very clear, and there will be no misclassification with influenza cases. According to the model of the estimated annual incidence rate, the decreasing trend was not significantly different from zero after 2019, which suggests that influenza incidence is gradually returning to the level before 2020 (8).

The epidemic threshold is affected by the regional heterogeneity of monitoring data, and the intensity thresholds vary according to the historical rates (33). Through the correction of the influenza incidence level, we calculated the influenza incidence intensity grading threshold, which provides a quantitative standard for judging the influenza prevalence level in the future. Before the winter peak in 2019–2020, the epidemic level of influenza in Zhejiang Province was at the middle or lower level. Influenced by the prevention and control of COVID-19, the winter peak of 2019–2020 was interrupted, during which the influenza epidemic was at the baseline level. This impact lasted for nearly 2 years until the summer peak of influenza reappeared in 2022. In general, the established influenza grading model has good performance, especially its specificity, which reaches 95%. According to previous studies, compared with sensitivity, specificity is a more important indicator for detecting influenza epidemics because false-positives will cause excessive public concern and trigger unnecessary influenza prevention and control measures, such as antiviral use, enhanced vaccination or nondrug intervention (23).

According to wavelet analysis, the influenza epidemic in Zhejiang Province mainly experiences semiannual peaks – one in winter and the other in summer–while the periodicity of the long cycle across the year is relatively less significant, which is similar to previous studies (34, 35). Further research shows that the peak of influenza incidence in Zhejiang Province in summer was mainly driven by pathogens of A(H3N2), while the peak in winter was alternately driven by various pathogens, including A(H3N2),A (H1N1)pdm2009, B(Victoria) and B(Yamagata). However, the summer influenza epidemic peak in southern China may not always occur regularly (34). In our study, the summer epidemic was not obvious in two periods, and the latter period was mainly due to the decline in the overall incidence level caused by the management and control of the COVID-19 pandemic. Another reason for the summer epidemic is the impact of relative humidity (RH) on the survival and transmission of influenza virus (36). In summer, influenza activity is mainly driven by high humidity rather than high temperature because contact transmission might be predominant due to the increasingly large droplets produced in a high RH environment (37). Furthermore, the high incidence in winter is affected by many reasons, including the inhibition of mucociliary clearance, the low RH environment where aerosol transmission is predominant, the decreased activities of proteases and increased indoor crowding (3).

In conclusion, the total number of estimated influenza cases is 12.11 times the number of reported cases. The actual incidence level of influenza is far higher than the current reported number,

which also indicates that the disease burden of influenza has been seriously underestimated in the past. An appropriate method for estimating the incidence rate of influenza may be to comprehensively consider the percentage of ILIs among outpatients as well as the influenza-positive rate. The APC was 23.33 (95% CI: 13.2 to 34.4) from 2011 to 2019, indicating a constant increasing trend during this period. The intensity level of the estimated incidence from the epidemic threshold to the very high-intensity threshold was calculated, which provides a quantitative standard for judging the influenza prevalence level in the future. The incidence of influenza showed half a year peaks, including a main peak from December to January of the next year followed by a peak in summer in Zhejiang Province. Furthermore. The driving factors of the influenza peak have been preliminarily explored, while the peak in summer was mainly driven by pathogens of A(H3N2), and the peak in winter was alternately driven by various pathogens. According to previous studies, the average annual influenza vaccination rate for the entire population in China was only 2%, while the vaccination rate for the old adult aged over 60 was 3.8%, the overall influenza vaccination rate in the Chinese population is still very low (38). As influenza vaccination is the most important measure of preventing influenza infections, our research suggests that the government urgently needs to address barriers to vaccination and actively promote vaccines through primary care providers (28).

Limitations

There are several limitations in our research that need to be acknowledged. First, because pathogenic surveillance cannot be carried out in all cases, the positive samples only represent a portion of cases, which may lead to bias to some degree. Second, the influenza incidence data were reported from the case visit report system, which might be affected by many factors, such as the case visit rate, the type of medical institution, and the detection rate of influenza pathogens. In future research, it should be considered to include mild and asymptomatic cases without medical treatment as much as possible to obtain a more complete infection spectrum. For example, it is possible to actively detect close contacts in school cluster outbreaks, or use positive results from community residents' self-testing to supplement infection spectrum data. Third, data on factors influencing the peak incidence of different influenza subtypes have not been collected, and the driving factors causing the conversion between subtypes have not been resolved. Fourth, due to inaccurate classification of causes of death, the actual number of deaths caused by influenza cannot be estimated and the case fatality rate of influenza is significantly underestimated. Fifth, the model established in this study is black box, so the specific relationship between the incidence rate of influenza and the predicted independent variable is still unclear.

Data availability statement

The raw data supporting the conclusions of this article will be made available by the authors, without undue reservation.

Ethics statement

The studies involving human participants were reviewed and approved by the Ethics Committee of the Zhejiang Provincial Centers for Disease Control and Prevention. Written informed consent to participate in this study was provided by the participants' legal guardian/next of kin.

Author contributions

JL and HW: conceived and designed the research. QL, ZD, CW, XW, TF, and KY: data collection. HW: data analysis and wrote the paper. JL and MX: reviewed and revised the paper. All authors read and approved the final manuscript.

Funding

This work was supported by the Major Science and Technology Project of the Science and Technology Department of Zhejiang Province (2021C03038, 2022C03109, 2022C03183). The funders had no role in study design, data collection and analysis, decision to publish, or preparation of the manuscript.

Conflict of interest

The authors declare that the research was conducted in the absence of any commercial or financial relationships that could be construed as a potential conflict of interest.

Publisher's note

Supplementary material

The Supplementary material for this article can be found online at: https://www.frontiersin.org/articles/10.3389/fpubh.2023.1154944/full#supplementary-material

References

1. Wang J, Jiang L, Yunan X, He W, Zhang C, Bi F, et al. Epidemiology of influenza virus reinfection in Guangxi, China: a retrospective analysis of a nine-year influenza surveillance data Characteristics of influenza virus reinfection. *Int J Infect Dis*. (2022) 120:135–41. doi: 10.1016/j.ijid.2022.04.045

2. Meng P, Huang J, Kong D. Prediction of incidence trend of inlfuenza-like illness in Wuhan based on ARIMA model. *Comput Math Methods Med*. (2022) 2022:1–7. doi: 10.1155/2022/6322350

3. Zhang S, Sun Z, He J, Li Z, Han L, Shang J, et al. The influences of the East Asian Monsoon on the spatio-temporal pattern of seasonal influenza activity in China. *Sci Total Environ*. (2022) 843:157024. doi: 10.1016/j.scitotenv.2022.157024

4. Zhou N, Dai H, Zha WT, Lv Y. The development trend of inflenza in China from 2010 to 2019. *Hum Vaccin Immunother*. (2022) 18:e2071558. doi: 10.1080/21645515.2022.2071558

5. Peng Z, Feng L, Carolyn GM, Wang K, Zhu G, Zhang Y, et al. Characterizing the epidemiology, virology, and clinical features of inflenza in China's fist severe acute respiratory infection sentinel surveillance system, February 2011 –October 2013. *BMC Infect Dis*. (2015) 15:143. doi: 10.1186/s12879-015-0884-1

6. Paul Glezen W, Schmier JK, Kuehn CM, Ryan KJ, Oxford J. The burden of infuenza B: a structured literature review. *Am J Public Health*. (2013) 103:e43–51. doi: 10.2105/AJPH.2012.301137

7. Tafalla M, Buijssen M, Geets R, Vonk N-S. A comprehensive review of the epidemiology and disease burden of Infuenza B in 9 European countries. *Hum Vaccin Immunother*. (2016) 12:993–1002. doi: 10.1080/21645515.2015.1111494

8. Huang WJ, Cheng YH, Tan MJ, Liu J, Li XY, Zeng XX, et al. Epidemiological and virological surveillance of Infuenza viruses in China during 2020–2021. *Infect Dis Poverty*. (2022) 11:74. doi: 10.1186/s40249-022-01002-x

9. Li J, Wang C, Ruan L, Jin S, Ye C, Huiting Y, et al. Development of inflenza-associated disease burden pyramid in Shanghai, China, 2010–2017: a Bayesian modelling study. *BMJ Open*. (2021) 11:e047526. doi: 10.1136/bmjopen-2020-047526

10. Tempia S, Walaza S, Moyes J, Cohen AL, McMorrow ML, Treurnicht FK, et al. Quantifying How Different Clinical Presentations, Levels of Severity, and Healthcare Attendance Shape the Burden of Influenza-associated Illness: A Modeling Study From South Africa. *Clin Infect Dis*. (2019) 69:1036–48. doi: 10.1093/cid/ciy1017

11. Lafond KE, Porter RM, Whaley MJ, Suizan Z, Ran Z, Aleem MA, et al. Global burden of infuenza-associated lower respiratory tract infections and hospitalizations among adults: a systematic review and meta-analysis. *PLoS Med*. (2021) 18:e1003550. doi: 10.1371/journal.pmed.1003550

12. Paget J, Spreeuwenberg P, Charu V, Taylor RJ, Iuliano AD, Bresee J, et al. Global mortality associated with seasonal influenza epidemics: new burden estimates and predictors from the GLaMOR Project. *J Glob Health*. (2019) 9:2047–986. doi: 10.7189/jogh.09.020421

13. Gong H, Shen X, Yan H, Lu WY, Zhong GJ, Dong KG, et al. Estimating the disease burden of seasonal influenza in China, 2006-2019. *Natl Med J China*. (2021) 101:560–6. doi: 10.3760/cma.j.cn112137-20201210-03323

14. Song Z, Jia X, Bao J, Yang Y, Zhu H, Shi X. Spatio-Temporal Analysis of Influenza-Like Illness and Prediction of Incidence in High-Risk Regions in the United States from 2011 to 2020. *Int J Environ Res Public Health*. (2021) 18:7120. doi: 10.3390/ijerph18137120

15. Chuntao Z, Ren Q. Epidemiology and disease burden analysis of influenza in China. *Chin J Viral Dis*. (2013) 3:423–6. doi: 10.16505/j.2095-0136.2013.06.004

16. Pei S, Kandula S, Yang W, Shaman J. Forecasting the spatial transmission of influenza in the United States. *Proc Natl Acad Sci U S A*. (2018) 115:2752–7. doi: 10.1073/pnas.1708856115

17. National Health and Family Planning Commission of the People's Republic of China. *Diagnostic criteria for influenza Version*. (2008) Available at: (http://www.nhc.gov.cn/zwgkzt/s9491/200802/38820.shtml). Accessed February 28, 2008.

18. National Health Commission of the People's Republic of China. *Guidelines for diagnosis and treatment of influenza A (H1N1)pdm2009*. (2009). Available at: http://www.nhc.gov.cn/yzygj/s3593g/201306/5fc4b2d158d7475fa0da32e959f9a7ac.shtml. (Accessed October 12, 2009).

19. National Health Commission of the People's Republic of China. *Guidelines for diagnosis and treatment of influenza, Version*. (2019) Available at: http://www.nhc.gov.cn/yzygj/s7653p/201911/a577415af4e5449cb30ecc6511e369c7.shtml. (Accessed November 13, 2019).

20. Haocheng W, Chen W, Qinbao L, Ding Z, Xue M, Lin J. Spatial-temporal characteristics of severe fever with thrombocytopenia syndrome and the relationship with meteorological factors from 2011 to 2018 in Zhejiang Province, China. *PLoS Negl Trop Dis*. (2020) 14:e0008186. doi: 10.1371/journal.pntd.0008186

21. Yang SG, Wu J, Ding C, Cui Y, Zhou Y, Li Y, et al. Epidemiological features of and changes in incidence of infectious diseases in China in the first decade after the SARS outbreak: an observational trend study. *Lancet Infect Dis*. (2017) 17:716–25. doi: 10.1016/S1473-3099(17)30227-X

22. Wu H, Xue M, Wu C, Lu Q, Ding Z, Wang X, et al. Trend of hand, foot, and mouth disease from 2010 to 2021 and estimation of the reduction in enterovirus 71 infection after vaccine use in Zhejiang Province, China. *PLoS One*. (2022) 17:e0274421. doi: 10.1371/journal.pone.0274421

23. Vega T's, Lozano JE, Meerhoff T, Snacken R, Mott J, Ortiz de Lejarazu R, et al. Influenza surveillance in Europe: establishing epidemic thresholds by the Moving Epidemic Method. *Influenza Other Respir Viruses*. (2013) 7:546–58. doi: 10.1111/j.1750-2659.2012.00422.x

24. Tokars JI, Olsen SJ, Reed C. Seasonal Incidence of Symptomatic Influenza in the United States. *Clin Infect Dis*. (2018) 66:1511–8. doi: 10.1093/cid/cix1060

25. Zhang Y, Wang X, Ma YLJ. Spatiotemporal Analysis of Infuenza in China, 2005–2018. *Sci Rep*. (2019) 9:19650. doi: 10.1038/s41598-019-56104-8

26. Humiston SG, Pham TN. Influenza-like illness diagnosis and management in the acute care setting. *Pediatric Emerg Care*. (2016) 32:875–82. doi: 10.1097/PEC.0000000000000974

27. Mao Y, He R, Zhu B, Liu J, Zhang N. Notifiable respiratory infectious diseases in china: a spatial–temporal epidemiology analysis. *Int J Environ Res Public Health*. (2020) 17:2301. doi: 10.3390/ijerph17072301

28. Ma C, Pan Y, Zhang L, Zhang Y, Wu S, Sun Y, et al. Influenza vaccine effectiveness against medically attended influenza illness in Beijing, China, 2014/15 season. *Hum Vaccin Immunother*. (2017) 13:2379–84. doi: 10.1080/21645515.2017.1359364

29. Phillips N. Chinese vaccine scandal unlikely to dent childhood immunization rates. *Nature*. (2018) 560:14–5. doi: 10.1038/d41586-018-05835-1

30. Ye Q, Deng Z, Chen Y, Liao J, Li G. Using Electronic Health Records Data to Evaluate the Impact of Information Technology on Improving Health Equity: Evidence from China. *J Med Syst*. (2019) 43:176. doi: 10.1007/s10916-019-1322-5

31. Chen Y, Wen Y. Spatiotemporal distributions and dynamics of human infections with the A H7N9 avian Infuenza virus. *Comput Math Methods Med*. (2019) 2019:1–20. doi: 10.1155/2019/9248246

32. Xiao JP, Dai JY, Hu JX, Liu T, Gong DX, Li X, et al. Co-benefits of nonpharmaceutical intervention against COVID-19 on infectious diseases in China: a large population-based observational study. *Lancet Reg Health Western Pac*. (2021) 17:100282. doi: 10.1016/j.lanwpc.2021.100282

33. Vega T, Lozano JE, Meerhoff T, Snacken R, Beauté J, Jorgensen P, et al. Influenza surveillance inEurope: comparing intensity levels calculated using the moving epidemic method. *Influenza Other Respir Viruses*. (2015) 9:234–46. doi: 10.1111/irv.12330

34. Diamond C, Gong H, Sun FY, Liu Y, Quilty BJ, Jit M, et al. Regional-based within-year seasonal variations in influenza-related health outcomes across mainland China: a systematic review and spatio-temporal analysis. *BMC Med*. (2022) 20:58. doi: 10.1186/s12916-022-02269-5

35. Dai Q, Ma W, Huang H, Xu K, Qi X, Yu H, et al. The effect of ambient temperature on the activity of influenza and influenza like illness in Jiangsu Province, China. *Sci Total Environ*. (2018) 645:684–91. doi: 10.1016/j.scitotenv.2018.07.065

36. Irwin CK, Yoon KJ, Wang C, Hoff SJ, Zimmerman JJ, Denagamage T, et al. Using the systematic review methodology to evaluate factors that influence the persistence of influenza virus in environmental matrices. *Appl Environ Microbiol*. (2011) 77:1049–60. doi: 10.1128/AEM.02733-09

37. Moriyama M, Hugentobler WJ, Iwasaki A. Seasonality of respiratory viral infections. *Annu Rev Virol*. (2020) 7:83–101. doi: 10.1146/annurev-virology-012420-022445

38. Chen C, Liu G, Zeng G. Influenza-related burden in China: current situation, challenges and response strategies. *Chin J Public Health*. (2022) 38:1494–7. doi: 10.11847/zgggws1140026

frontiers | Frontiers in Applied Mathematics and Statistics

TYPE Original Research
PUBLISHED 26 June 2023
DOI 10.3389/fams.2023.1157992

OPEN ACCESS

EDITED BY
Dumitru Trucu,
University of Dundee, United Kingdom

REVIEWED BY
Pankaj Tiwari,
University of Kalyani, India
Andrey Cherstvy,
University of Potsdam, Germany

*CORRESPONDENCE
Md. Kamrujjaman
✉ kamrujjaman@du.ac.bd

RECEIVED 03 February 2023
ACCEPTED 29 May 2023
PUBLISHED 26 June 2023

CITATION
Zahan I, Kamrujjaman M, Abdul Alim M, Shahidul Islam M and Khan T (2023) The evolution of resource distribution, slow diffusion, and dispersal strategies in heterogeneous populations.
Front. Appl. Math. Stat. 9:1157992.
doi: 10.3389/fams.2023.1157992

The evolution of resource distribution, slow diffusion, and dispersal strategies in heterogeneous populations

Ishrat Zahan [1], Md. Kamrujjaman [2]*, Md. Abdul Alim[1], Md. Shahidul Islam[2] and Taufiquar Khan[3]

[1]Department of Mathematics, Bangladesh University of Engineering and Technology, Dhaka, Bangladesh, [2]Department of Mathematics, University of Dhaka, Dhaka, Bangladesh, [3]Department of Mathematics and Statistics, University of North Carolina at Charlotte, Charlotte, NC, United States

Population diffusion in river-ocean ecologies and for wild animals, including birds, mainly depends on the availability of resources and habitats. This study explores the dynamics of the resource-based competition model for two interacting species in order to investigate the spatiotemporal effects in a spatially distributed heterogeneous environment with no-flux boundary conditions. The main focus of this study is on the diffusion strategy, under conditions where the carrying capacity for two competing species is considered to be unequal. The same growth function is associated with both species, but they have different migration coefficients. The stability of global coexistence and quasi-trivial equilibria are also studied under different conditions with respect to resource function and carrying capacity. Furthermore, we investigate the case of competitive exclusion for various linear combinations of resource function and carrying capacity. Additionally, we extend the study to the instance where a higher migration rate negatively impacts population growth in competition. The efficacy of the model in the cases of one- and two-dimensional space is also demonstrated through a numerical study.

AMS subject classification 2010: 92D25, 35K57, 35K50, 37N25, 53C35.

KEYWORDS

resource-based diffusion, global analysis, competition, numerical analysis, slow diffusion

1. Introduction

The study of spatial effects in a heterogeneous environment for two competing or cooperating species provides a vital tool for use in population ecology that is well-suited to capturing real-world phenomena for geographies with different attributes. The reaction-diffusion equations [1–6] are typically and widely used as a model of spatial effect incorporating parameters such as local growth rate, dispersal rate, and carrying capacity, which may vary over time and space. These reaction-diffusion equations have been improved continuously to enhance their ability to explain real-world situations. In practice, many biological events show that population density and the dynamics of population behaviors are greatly affected by the reaction and diffusion terms of the model. For population dispersion, not only is the diffusion speed relevant, but the strategy by which species diffuse in nature is also a vital issue that has recently become a critically important element of in-depth analysis. In the implementation of diffusion models, numerous dispersal strategies have appeared in models using biological particles; these strategies should be specified for species' improved survival. In a model with regular diffusion terms, when resources are distributed

unequally or in the case of a non-constant carrying capacity, a non-feasible system may appear when very high levels of migration are observed from a location with higher per-capita available resources to a less fruitful region. Moreover, the ideal free distribution has been approximated in [7] for a spatially dispersed population. This exhibits a property of diffusion toward the direction of improved fitness to produce a stable equilibrium that can be expected to represent a solution in a temporally fixed but spatially heterogeneous environment. However, any individual deviation from the ideal population distribution will reduce the fitness of the species. The fitness pattern is presented in Figure 1.

The concepts of different diffusion strategies, predator–prey systems, nutrient–phytoplankton systems with toxic effects on phytoplankton, and pest control are often closely connected to the creation and diffusion of knowledge and the technological evolution of society. For more advanced work on the dynamics of species management, see [8, 9]. Additionally, in most scenarios, resources are not unlimited and environmental conditions are not optimal. Population growth may be resisted by environmental resources due to issues like food, climate, water availability, and others. Naturally, species tend to move toward superior locations in terms of food, safety, or any other survival instinct. Thus, they do not simply diffuse randomly; instead, they choose to migrate to attain a better existence. Along with the aforementioned observation, Braverman and Braverman [10] were the first to introduce the notion of carrying-capacity–driven diffusion, inspired by the selection of optimal harvesting strategies, which have major biological significance. The stability properties of the model were first studied in [11] with logistic-type growth. In this type of diffusion strategy, the diffusive transport of the population is considered proportional to the gradient of population density per unit capacity instead of simply the population density. The advantage of the carrying-capacity–driven diffusion strategy relative to classical diffusion in terms of completion was initially delineated in [12] considering logistic growth, and further explored in [13] for a wide variety of growth functions. The latest modification to species migration strategy was first introduced in 2016 by Braverman and Kamrujjaman in [14, 15] and is known as the resource-based diffusion strategy. Under this type of diffusion strategy, species diffuse according to their respective resource-based dispersal function, in which the diffusive movement of species is considered proportional to the gradient of population density per unit resource rather than simply to carrying capacity. Compared to random diffusion, the main advantage of using this type of diffusion is that its solution coincides with the ideal free distribution under certain conditions with respect to carrying capacity and resource function. In this context, we can mention several fields studied on the basis of a single species: for example, studies of grazing animal populations [16], invasive weeds or plants like *Solanum carolinense* in Europe [17], or North American Prairie duck [18]; these studies were conducted in the experimental field, and the experimental results show that the dispersion of these species is directed toward the area of higher per-capita available resources. Similar observations will be noted when considering a pair of species in a heterogeneous environment.

It is most significant for the dynamics of two competing populations to examine how the density of one organism or species changes relative to others in space and time to survive under this competitive scenario. In a competition, the main possible outcomes are that both species triumph or one survives as the other goes extinct. Additionally, in ecology, operating under some instinct, both species may leave the area in a competition that yields neither extinction nor coexistence. For a historical discussion of the proposed models, readers are referred to [2, 7, 12, 13, 15, 19–22]. It should also be mentioned that lower diffusion rates were favored by [2] in a heterogeneous environment, since the authors found that the fitness levels of species differ only according to their dispersal rate, and population growth falls as the diffusion coefficient increases. Accordingly, in our study, the results of [2] have been extended to a scenario where the strategy of dispersion is the same for both species, rather than random, which is dissimilar from [11]. This paper focuses on estimating the possible benefits to a species adopting a strategy based on the availability of resources, in contrast with the well-established study of other diffusion strategies. We also examine the significance of higher diffusion and intrinsic growth rates in a heterogeneous environment for two competing species. These are the central facets of our interest in studying a pair of species with various resource distributions. See additionally [23], where a single-species population was studied by considering Gilpin-Ayla growth and harvesting; this study was mostly concerned with diffusion strategy, migration coefficient, and harvesting. The present, in contrast, study explores population distribution under an approach that has many applications in various areas of ecology and economics; readily applicable examples are applications in river and ocean ecology relating to observations of the seasonal behaviors of various species, including wild animals and winter birds. Three critical issues are primarily considered: (i) diffusion strategies for scenarios in which the competing species have equal and unequal carrying capacities; (ii) slow dispersal effects; and (iii) resource distributions, with corresponding demonstrations for each issue. Additionally, we demonstrate that there are certain evolutionary advantages of employing a carrying-capacity- and resource-based diffusion strategy despite classical diffusion.

The main findings of the present study are as follows:

1. We study the global existence of solutions to the competition model by considering two main ecological settings: Case I, in which the carrying capacities of the interacting species are unequal, and Case II, in which carrying capacity is equal with different diffusion strategies. We find effects of diffusion speed as well as interactions between resources and capacity function.
2. For unequal carrying capacity, if the first species follows a carrying-capacity–driven diffusion strategy while the other adopts resource-based diffusion, then the first species always survives in competition in cases of an equal intrinsic growth rate. We also observe that more resource consumption by the species with the greater carrying capacity will drive the one with the lower capacity to extinction in the competition.
3. When both species adopt the same resource-based diffusion strategy, the species that consumes more, with a higher carrying capacity ratio, is guaranteed to survive in the competition.
4. In addition, in cases of the same diffusion strategy, a species that diffuses slowly has an evolutionary advantage compared to

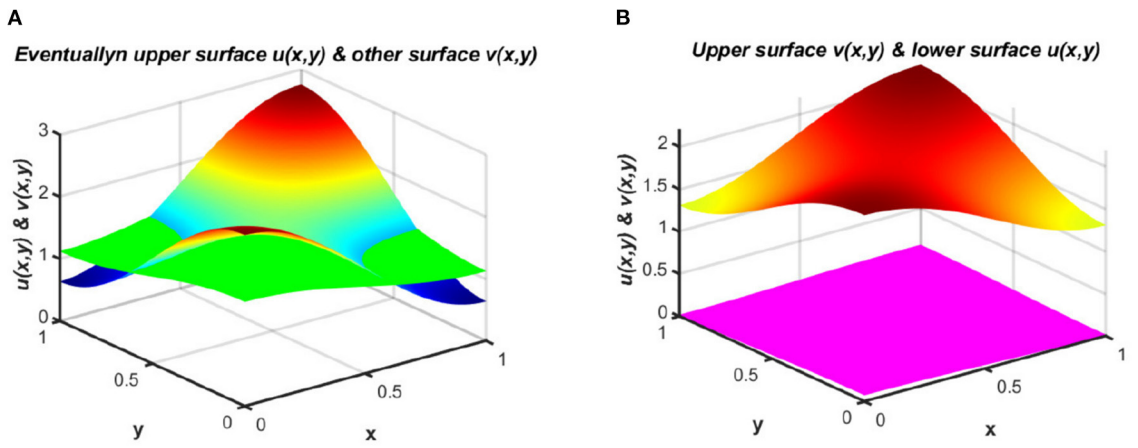

FIGURE 1
Population densities under (2.1) for **(A)** coexistence signature, and **(B)** extinction vs. survival.

others; this extends the result of [2] to resource-based diffusion. We find that a higher diffusion coefficient is unconducive to sustained competition.

5. In cases of species with different proportions of carrying capacity and intrinsic growth rates, coexistence is also evident. In this situation, the species' elevated growth rate is noted, incorporating a higher proportion of the available resources in competition.
6. When the carrying capacity of both species is equal, we study the case of competitive exclusion as an abbreviation of carrying capacity and one of the resource functions for which the globally stable semi-trivial equilibrium is observed to obtain.
7. We also present some numerical results for both one- and two-dimensional cases. As we know, the theory does not give any idea of the shape of the non-zero equilibrium profiles, which we explore numerically.
8. We show via numerical computation that the existence of a state of coexistence is also possible due to the influence of migration coefficients. Intrinsic growth rates can also play an important role in sustaining both species in competition.
9. Furthermore, for the case of time-periodic parameters, numerical results suggest the existence of a time-periodic state with the same period.

The manuscript is organized as follows. A description of the mathematical model is provided in Section 2. Section 3 describes the results of the model in terms of the existence and uniqueness of solutions for non-negative and non-trivial initial conditions; these results also justify the positivity of the solution. A coexistence analysis and quasi-trivial equilibrium with some preliminary results for the case of unequal carrying capacity that are applicable in the remainder of the discussion are presented in Section 4. Moreover, Section 4 also presents the main results and proof of the study: the global existence of an equilibrium for competitive exclusion and coexistence analysis for $K_u \not\equiv K_v$. Section 5 considers the competitive exclusion of population for the case of $K_u \equiv K_v$ with some auxiliary results. Section 6 presents a numerical simulation and illustrates the application of this study for ecological implementations. The numerical computation for the case of two spatial dimensions is presented in Section 6.1 in the form of contour plots for both space- and time-dependent functions. This is highly novel to our study; it captures the ecological impact of this study in a more biologically feasible way and justifies the theoretical underpinnings of the main result through numerical assertion. Finally, Section 7 provides a summary and discussion of the model presented in this study.

2. Mathematical model

In our model, we consider the two species [notionally, $u(t,x)$ and $v(t,x)$] as a competitive system, isolated and spatially distributed in a heterogeneous environment. Here, $u(t,x)$ and $v(t,x)$ represent the population densities of two striving species, each undergoing diffusion under similar resource-based diffusion strategies while the most troubling situation for them is when they fight for the same fundamental resources. The dispersal strategies of the species are also considered to stipulate two positive distribution functions with different carrying capacity proportions; i.e., the system considers the carrying capacities of the competing species to be dissimilar, with no-flux/zero Neumann boundary conditions contemplated through the domain boundary. The use of homogeneous Neumann boundary conditions represents a scenario in which (i) the populations are isolated in a closed area and there is no movement across the boundaries of this area, and (ii) spatial immigration is compensated through emigration to the domain. Under these assumptions, the corresponding competitive model with homogeneous Neumann boundary conditions associated with positive and non-trivial initial conditions is defined as follows:

$$\begin{cases} \frac{\partial u}{\partial t} = d_1 \Delta\left(\frac{u(t,x)}{M(x)}\right) + r_1(x)u(t,x)\left(1 - \frac{u+v}{K_u(x)}\right), & t > 0,\ x \in \omega, \\ \frac{\partial v}{\partial t} = d_2 \Delta\left(\frac{v(t,x)}{N(x)}\right) + r_2(x)v(t,x)\left(1 - \frac{v+u}{K_v(x)}\right), & t > 0,\ x \in \omega, \\ \mathbf{n} \cdot \nabla\left(\frac{u(t,x)}{M(x)}\right) = \mathbf{n} \cdot \nabla\left(\frac{v(t,x)}{N(x)}\right) = 0, & x \in \partial\omega, \\ u_0(x) = u(0,x), \quad v_0(x) = v(0,x), & x \in \omega. \end{cases} \tag{2.1}$$

We assume that $K_u > 0$, $K_v > 0$; these expressions represent the carrying capacity of the environment for the corresponding species, where $r_i > 0$, $i = 1, 2$ are the intrinsic growth rates, and M, N are the species resource functions. All fall within the class of $C^{1+\alpha}(\overline{\omega})$, where ω is an open non-empty isolated bounded domain in $\mathbb{R}^n$ with $\partial\omega \in C^{2+\alpha}$, and $0 < \alpha < 1$ for any $x \in \omega$, which means that $r_1(x), r_2(x), K_u(x), K_v(x), M(x)$, and $N(x)$ are all positive in an open non-empty sub-domain of ω. Here, $d_1 > 0$ and $d_2 > 0$ are the migration rates that describe the corresponding dispersal rates of each species. The range of the solutions to (2.1) corresponds to the set $p_1 \times p_1$, which is determined by the corresponding upper and lower solutions.

Suppose u^* and v^* are the stationary solutions of the first and second equation corresponding to (2.1) when only one species survives, so that the semi-trivial equilibria $(u^*, 0)$ and $(0, v^*)$ satisfy

$$d_1\Delta\left(\frac{u^*(x)}{M(x)}\right) + r_1(x)u^*\left(1 - \frac{u^*}{K_u(x)}\right) = 0,$$
$$x \in \omega,\ \mathbf{n}\cdot\nabla\left(\frac{u^*}{M}\right) = 0,\ x \in \partial\omega; \tag{2.2}$$

$$d_2\Delta\left(\frac{v^*(x)}{N(x)}\right) + r_2(x)v^*\left(1 - \frac{v^*}{K_v(x)}\right) = 0,$$
$$x \in \omega,\ \mathbf{n}\cdot\nabla\left(\frac{v^*}{N}\right) = 0,\ x \in \partial\omega. \tag{2.3}$$

Model (2.1) is a specimen of a monotone dynamical system [5, 24, 25]. That is, when the zero equilibrium is not stable, no coexistence equilibrium occurs for the system (2.1), and one of the semi-trivial equilibria is also unstable, the remaining semi-trivial equilibrium solution will be globally asymptotically stable; on the other hand, if both semi-trivial equilibria are unstable, then (2.1) possesses at least one stable coexistence equilibrium.

Resource-based competition model (2.1), with unequal carrying capacities and intrinsic growth rates, is a prevalent ecological model for inter-specific competition that captures the reality observed in nature. Many organisms follow our stated types of diffusion strategy, such as grazing animals [16], marine organisms [26], zooplankton-like protozoa, and wild birds (owls, sparrows, etc., and all kinds of winter birds).

For further analysis, it is also convenient to substitute $w = \frac{u(t,x)}{M(x)}$ and $z = \frac{v(t,x)}{N(x)}$, respectively. Then, system (2.1) is reduced to

$$\begin{cases} \frac{\partial w(t,x)}{\partial t} = \left(\frac{d_1}{M(x)}\right)\Delta w + r_1(x)w\left(1 - \frac{M}{K_u}w - \frac{N}{K_u}z\right), \\ t > 0,\ x \in \omega, \\ \frac{\partial z(t,x)}{\partial t} = \left(\frac{d_2}{N(x)}\right)\Delta z + r_2(x)z\left(1 - \frac{M}{K_v}w - \frac{N}{K_v}z\right), \\ t > 0,\ x \in \omega, \\ \mathbf{n}\cdot\nabla w = \mathbf{n}\cdot\nabla z = 0,\ \ x \in \partial\omega, \\ w_0(x) = w(0,x),\ \ z_0(x) = z(0,x),\ \ x \in \omega. \end{cases} \tag{2.4}$$

The model then reduces to a couple of equations with classical diffusion through smooth and positive space-dependent coefficients $\frac{d_1}{M(x)}$ and $\frac{d_2}{N(x)}$. Next, we analyze the existence, uniqueness, and positivity of solutions to the system (2.4). To do this, we initially confine our observations to a model that represents the action of the system for a single species and for a pair of species.

3. Existence, uniqueness, and positivity of solution

Consider the following directed diffusion model with homogeneous Neumann boundary and positive initial conditions:

$$\begin{cases} \frac{\partial u}{\partial t} = d_1\Delta\left(\frac{u(t,x)}{M(x)}\right) + r_1(x)u\left(1 - \frac{u}{K_u(x)}\right), \ \ t > 0,\ x \in \omega, \\ \mathbf{n}\cdot\nabla\left(\frac{u}{M}\right) = 0, \ \ x \in \partial\omega, \ \ u_0(x) = u(0,x), \ \ x \in \omega. \end{cases} \tag{3.1}$$

Existence and uniqueness results for species u in the form of the Equation (3.1) are well-established for $K_u = M$ in [13, 20, 27], indicating that the system (3.1) has a unique and stable positive solution. According to [5, 13, 20, 24, 27] the proof of the following Lemma can proceed in the same way as far as $M \equiv K_u$ or $M \not\equiv K_u$.

Lemma 1. [20, 27] For any $u_0(x) \geq 0$ in ω and $u_0(x) \not\equiv 0$ in some open and bounded sub-domain $\omega_l \subset \omega$, there is a unique solution $u(t,x)$ of model (3.1) and it is positive. If $\frac{M(x)}{K_u(x)} \equiv Constant$, then $u^*(x) = K_u(x)$ is the only solution of (3.1), and as $t \to \infty$ the solution converges to $K_u(x)$, otherwise $u^*(x)$ is different from $K_u(x)$.

Similarly, we can construct the existence and uniqueness result for the species v.

The system (2.1) is an example of a monotone dynamical system [15, 28, 29]. According to [1, 13, 15], the system has a unique and positive solution for $K_u = K_v = K$. The same procedure can be applied to (2.1), which affords the existence and uniqueness of a solution for a coupled system of the Equation (2.1).

Theorem 1. [13] Let $u_0(x)$ and $v_0(x)$ be non-negative on ω. Then for any $u_0(x), v_0(x) \in C(\omega)$, the system (2.1) has a unique solution (u, v). Furthermore, if $(u_0(x), v_0(x))$ is non-trivial and non-negative, then for any $T > 0$, both $u(t,x) > 0$ and $v(t,x) > 0$.

In the next section, we express the result based upon the stability of all steady-state solutions of the model (2.1), which are two semi-trivial equilibria $(u^*, 0)$ and $(0, v^*)$, in which only a single species persists, as well as a coexistence state (u^*, v^*), in which both species coexist in the same environment, and finally the trivial equilibrium $(0, 0)$, in which both species leave the area due to competition. The stated results are for the monotone dynamical system that originated in [5]; for the system (2.1), we use a modification in the form previously described in [20] [see [20], Theorem 09, pp. 73 for more details], since system (2.1) follows a monotone dynamical system. Additionally, a few preliminary consequences for the existence of an equilibrium are presented in Section 4.

4. Steady state and global analysis: case I, $K_u \not\equiv K_v$

For further analysis of system (2.1), we have extended the following three auxiliary results (to be applied in completing the following discussion), which are already established in [12–15], for $K_u = K_v = K$.

Lemma 2. [13–15] Suppose $M(x), N(x), K_u(x) \not\equiv K_v(x)$ are non-constant and $r_1(x) \equiv r_2(x) \equiv r(x)$. If $\frac{M}{K_u} \equiv$ *Constant*, while $\frac{N}{K_u} \not\equiv$ *Constant* and $\frac{N}{K_v} \not\equiv$ *Constant* or $K_u > K_v$ in a non-empty open domain $x \in \omega$, then a unique and positive stationary solution $(0, v^*)$ to (2.1) occurs, so that

$$\int_\omega r(x)K_u\left(1-\frac{v^*}{K_u}\right)dx > 0. \tag{4.1}$$

Lemma 3. [13–15] Assume that (u_c, v_c) is a positive steady state solution of system (2.1), and $K_u > K_v$, so that $u_c + v_c \not\equiv K_u$; then

$$\int_\omega r(x)K_u(x)\left(1-\frac{u_c+v_c}{K_u}\right)dx > 0.$$

Lemma 4. The zero equilibrium $(0, 0)$ of the model (2.1) is unstable and repelling.

The proof is available in [12, 13], so we have omitted it here.

Next, we examine our key results for the system 2.1 by inspecting the stability of two semi-trivial or quasi-trivial equilibria, namely $(u^*, 0)$ and $(0, v^*)$, that occur when a single species endures alone, as well as a coexistence equilibrium (u^*, v^*), which is a neither quasi-trivial nor trivial equilibrium that satisfies $u^*(x) > 0, v^*(x) > 0$. If $M(x) = K_u(x)$ and $N(x) = K_v(x)$, then the semi-trivial equilibria will converge to $(K_u, 0)$, and $(0, K_v)$. However, we also confirm that, in this case, the species that survives in the competition will always be the one adopting a carrying-capacity–driven diffusion strategy. After considering all these possibilities, we prove our main results.

Lemma 5. Assume that the functions $M(x), N(x), K_u(x), K_v(x)$ are non-constant and $r_1(x) \equiv r_2(x) \equiv r(x)$. If $K_u \geq K_v$ for all $x \in \omega$, and $\frac{M}{K_u} \equiv$ *Constant* while $\frac{N}{K_u} \not\equiv$ *Constant* or $\frac{N}{K_v} \not\equiv$ *Constant* or $K_u(x) > K_v(x)$ in a non-empty, bounded, and open domain ω, then no coexistence state (u_c, v_c) of the system (2.1) will exist.

Proof. We are now interested only in cases where $K_u(x) > K_v(x)$, because the result for $K_u(x) \equiv K_v(x)$ was already established in [13] for all $x \in \omega_l \subseteq \omega$. First, let us speculate to the contrary that there prevails a strictly positive equilibrium state (u_c, v_c) of (2.1), and we will prove that this assumption leads to a contradiction. Under this assumption, the solution (u_c, v_c) satisfies

$$\begin{cases} d_1\Delta\left(\frac{u_c(x)}{M(x)}\right) + r(x)u_c\left(1-\frac{u_c(x)+v_c(x)}{K_u(x)}\right) = 0, & x \in \omega, \\ \mathbf{n}\cdot\nabla\left(\frac{u_c}{M}\right) = 0, & x \in \partial\omega. \\ d_2\Delta\left(\frac{v_c(x)}{N(x)}\right) + r(x)v_c\left(1-\frac{u_c(x)+v_c(x)}{K_v(x)}\right) = 0, & x \in \omega, \\ \mathbf{n}\cdot\nabla\left(\frac{v_c}{N}\right) = 0, & x \in \partial\omega. \end{cases} \tag{4.2}$$

Adding the first two equations in (4.2), integrating over ω, and applying the Neumann boundary conditions, we obtain:

$$\int_\omega r(x)u_c\left(1-\frac{u_c+v_c}{K_u}\right)dx + \int_\omega r(x)v_c\left(1-\frac{u_c+v_c}{K_v}\right)dx = 0. \tag{4.3}$$

Since $K_u > K_v$, it follows that $\left(1-\frac{u_c+v_c}{K_v}\right) < \left(1-\frac{u_c+v_c}{K_u}\right)$. Thus, (4.3) implies:

$$\int_\omega r(x)\left(u_c(x)+v_c(x)\right)\left(1-\frac{u_c+v_c}{K_u}\right)dx > 0. \tag{4.4}$$

Now, $(u_c+v_c)\left(1-\frac{u_c+v_c}{K_u}\right) = K_u\left(1-\frac{u_c+v_c}{K_u}\right) + (u_c+v_c-K_u)\left(1-\frac{u_c+v_c}{K_u}\right)$.

Multiplying by $r(x)$ and integrating the above inequality over ω gives:

$$\int_\omega r(x)K_u\left(1-\frac{u_c+v_c}{K_u}\right)dx > \int_\omega r(x)\frac{(u_c+v_c-K_u)^2}{K_u}dx > 0$$

Therefore,

$$\int_\omega r(x)K_u\left(1-\frac{u_c+v_c}{K_u}\right)dx > 0, \tag{4.5}$$

which is only valid if $u_c + v_c \not\equiv K_u(x)$. Hence, we need to consider the above two cases for $K_u(x) > K_v(x)$.

Case 1: When $u_c + v_c \equiv K_u(x)$, $w_c = \frac{u_c}{M}$ satisfies $\Delta w_c = 0, x \in \omega$, $\nabla w_c = 0$; and therefore, by the Maximum Principle [30], we have $w_c \equiv$ *Constant*.

This implies that $\frac{u_c}{M} \equiv$ *Constant*, so $u_c \equiv c_m K_u$ such that $v_c = K_u - c_m K_u = (1-c_m)K_u$, which is constant only when $c_m = 1$, since $K_u(x)$ is variable.

Case 2: Thus, we have to impose only one condition when $u_c + v_c \not\equiv K_u(x)$ or $K_u > K_v$ in some non-empty open domain. Examine the following eigenvalue problem:

$$\begin{aligned} d_1\Delta\left(\frac{\phi}{M}\right) + r(x)\phi\left(1-\frac{u_c+v_c}{K_u}\right) &= \sigma\phi, \quad x \in \omega, \\ \mathbf{n}\cdot\nabla\left(\frac{\phi}{M}\right) &= 0, \quad x \in \partial\omega. \end{aligned}$$

Following from the fact of variational characterization of eigenvalues [[5], Theorem 2.1], its principal eigenvalue is conferred by

$$\sigma_1 = \sup_{\phi\neq 0, \phi\in W^{1,2}} \frac{\int_\omega -d_1\left|\nabla\left(\frac{\phi}{M}\right)\right|^2 dx + \int_\omega r(x)\left(\frac{\phi^2}{M(x)}\right)\left(1-\frac{u_c+v_c}{K_u}\right)dx}{\int_\omega\left(\frac{\phi^2}{M(x)}\right)dx}. \tag{4.6}$$

Upon substituting $\phi = M(x)$, and using (4.5), we obtain:

$$\sigma_1 \geq \frac{\int_\omega r(x)K_u\left(1-\frac{u_c+v_c}{K_u}\right)dx}{\int_\omega K_u(x)dx} > 0.$$

However, (w_c, z_c) is a steady state solution of (2.1); w_s satisfies

$$\begin{aligned} d_1\Delta w_c + r(x)w_c K_u(x)\left(1-\frac{M}{K_u}w_c - \frac{N}{K_u}z_c\right) &= 0, \quad x \in \omega, \\ \nabla w_c &= 0, \quad x \in \partial\omega. \end{aligned}$$

and is therefore a positive principal eigenfunction of (4.6) along with principal eigenvalue 0. This contradicts $\sigma_1 > 0$, which concludes the proof. □

Lemma 6. Suppose the functions $M(x), N(x), K_u(x), K_v(x)$ are non-constant and $r_1(x) \equiv r_2(x) \equiv r(x)$. If $K_u \geq K_v$ for all $x \in \omega$, and $\frac{M}{K_u} \equiv$ *Constant* while $\frac{N}{K_u} \not\equiv$ *Constant* or $\frac{N}{K_v} \not\equiv$ *Constant* or $K_u(x) > K_v(x)$ in a non-empty, bounded, and open domain ω, then $(0, v^*)$ is unstable for the system (2.1).

Proof. Taking the linearization of (2.1) over $(0, v^*)$ for the case $K_u > K_v$, we obtain:

$$\frac{\partial u}{\partial t} = d_1 \Delta \left(\frac{u}{M}\right) + r(x)u\left(1 - \frac{v^*}{K_u}\right), \quad t > 0, \quad x \in \omega,$$
$$\frac{\partial v}{\partial t} = d_2 \Delta \left(\frac{v}{N}\right) + r(x)v\left(1 - \frac{2v^*}{K_v}\right) - rv^*\frac{u(t,x)}{K_u(x)}, \quad t > 0, \quad x \in \omega;$$

and studying the associative eigenvalue problem of the equation u,

$$d_1 \Delta \left(\frac{\phi}{M}\right) + r(x)\phi\left(1 - \frac{v^*}{K_u}\right) = \sigma\phi, \quad x \in \omega,$$
$$\mathbf{n} \cdot \nabla \left(\frac{\phi}{M}\right) = 0, \quad x \in \partial\omega. \tag{4.7}$$

The quasi-trivial equilibrium $(0, v^*)$ will not be stable if the principal eigenvalue is positive. Next, considering (4.7): according to [5] (Theorem 2.1), the principal eigenvalue is stated by

$$\sigma_1 = \sup_{\phi \neq 0, \phi \in W^{1,2}} \frac{\int_\omega -d_1 \left|\nabla\left(\frac{\phi}{M}\right)\right|^2 dx + \int_\omega r(x)\left(\frac{\phi^2}{M(x)}\right)\left(1 - \frac{v^*}{K_u}\right) dx}{\int_\omega \left(\frac{\phi^2}{M(x)}\right) dx}.$$

upon substituting $\phi = M(x)$ and using (4.1) from Lemma 2 for $K_u > K_v$ we obtain:

$$\sigma_1 \geq \frac{\int_\omega r(x)K_u\left(1 - \frac{v^*}{K_u}\right) dx}{\int_\omega K_u dx} > 0.$$

Thus, $\sigma_1 > 0$, which concludes the proof. □

Theorem 2. Suppose the functions $M(x), N(x), K_u(x), K_v(x)$ are non-constant and $r_1(x) \equiv r_2(x) \equiv r(x)$. If $K_u \geq K_v$ for all $x \in \omega$, and $\frac{M}{K_u} \equiv$ *Constant* while $\frac{N}{K_u} \not\equiv$ *Constant* or $\frac{N}{K_v} \not\equiv$ *Constant* or $K_u(x) > K_v(x)$ in a non-empty, bounded, and open domain ω, then $(K_u, 0)$ of (2.1) is globally asymptotically stable.

Proof. According to Lemma 4, $(0, 0)$ is a repeller. By Lemma 5, no coexistence equilibrium exists for the system (2.1); additionally, by Lemma 6, $(0, v^*)$ is unstable as far as $K_u > K_v$. Therefore, for a strong monotone dynamical system [15, 28, 29], the other quasi-trivial equilibrium $(K_u, 0)$ is globally asymptotically stable. □

Similarly, under the assumption of Lemma 6 with $\frac{M(x)}{K_u(x)} \not\equiv$ *Constant* as well as $\frac{M(x)}{K_v(x)} \not\equiv$ *Constant* while $\frac{N(x)}{K_v(x)} \equiv$ *Constant*, and for $K_u < K_v$ in a non-empty open domain, we can establish that $(u^*, 0)$ is also unstable.

The following remark follows the proof of Theorem 2.

Remark 1. Suppose the functions $M(x), N(x), K_u(x), K_v(x)$ are non-constant and $r_1(x) \equiv r_2(x) \equiv r(x)$. If $K_u \leq K_v$ for all $x \in \omega$, and $\frac{N}{K_v} \equiv$ *Constant* while $\frac{M}{K_u} \not\equiv$ *Constant* or $\frac{M}{K_v} \not\equiv$ *Constant* or $K_u(x) < K_v(x)$ in a non-empty, bounded, and open domain ω, then $(0, K_v)$ of (2.1) is globally asymptotically stable.

Similar results are presented in Appendix A for the case of $K_u \not\equiv K_v$, when both resource functions are proportional to their respective carrying capacity. At this point, we have identified the global existence of competitive exclusion, considering cases of unequal carrying capacity while other parameters are fixed.

Remark 2. Suppose the functions M, K_u, K_v are constant and $r_1 \equiv r_2 \equiv r$, $d_1 \equiv d_2 \equiv d$, while $\frac{M}{K_u} \equiv$ *Constant* and $\frac{N(x)}{K_v} \not\equiv$ *Constant*. Then, for $K_u > K_v$ and $K_u < K_v$ in an open, bounded, and non-empty domain $x \in \omega$, one of the semi-trivial equilibria is globally asymptotically stable. However, for $K_u \equiv K_v$, a coexistence equilibrium is possible.

Lemma 7. Suppose $\frac{M(x)}{K_u(x)} \not\equiv$ *Constant*, $\frac{N(x)}{K_v(x)} \not\equiv$ *Constant*, and $K_u(x), K_v(x)$ are non-constant. If $K_u(x) \geq K_v(x)$ for some non-empty open domain $x \in \omega$ and $r_1(x) \equiv r_2(x) \equiv r(x)$, then for fixed $r(x)$, there exists such d^* that for $d_1 < d^*$, the quasi-trivial equilibrium $(0, v^*)$ of (2.1) is not stable.

Proof. Assuming that the eigenvalue problem associates to the foremost equation of (2.1) around $(0, v^*)$, we have:

$$d_1 \Delta \left(\frac{\phi}{M}\right) + r(x)\phi\left(1 - \frac{v^*}{K_u}\right) = \sigma\phi, \quad x \in \omega,$$
$$\mathbf{n} \cdot \nabla \left(\frac{\phi}{M}\right) = 0, \quad x \in \partial\omega. \tag{4.8}$$

According to [5] (Theorem 2.1), the principal eigenvalue of (4.8) is given by

$$\sigma_1 = \sup_{\phi \neq 0, \phi \in W^{1,2}} \frac{\int_\omega -d_1 \left|\nabla\left(\frac{\phi}{M}\right)\right|^2 dx + \int_\omega r(x)\left(\frac{\phi^2}{M(x)}\right)\left(1 - \frac{v^*}{K_u}\right) dx}{\int_\omega \left(\frac{\phi^2}{M}\right) dx}. \tag{4.9}$$

$(0, v^*)$ will not be stable if we can execute such a ϕ that the expression of the right-hand side is positive. Since $K_u > K_v$, from Lemma 2 we obtain $\int_\omega r(x)K_u\left(1 - \frac{v^*}{K_u}\right) dx > 0$.

Taking $\phi = \sqrt{K_u(x)M(x)}$, and using the fact for linearly independent M, K_u and N, K_v, let $P := \int_\omega rK_u\left(1 - \frac{v^*}{K_u}\right) dx > 0$; then, we achieve from (4.9):

$$-\int_\omega d_1 \left|\nabla\left(\sqrt{\frac{K_u}{M}}\right)\right|^2 dx + \int_\omega r(x)K_u\left(1 - \frac{v^*}{K_u}\right) dx$$
$$= -\int_\omega d_1 \left|\nabla\left(\sqrt{\frac{K_u}{M}}\right)\right|^2 dx + P > 0,$$

unless $\frac{K_u}{M} \equiv$ *Constant*, when

$$d_1 < d^* := P\left[\int_\omega \left|\nabla\left(\sqrt{\frac{K_u}{M}}\right)\right|^2 dx\right]^{-1},$$

which concludes the proof. □

Lemma 8. Suppose $\frac{M(x)}{K_u(x)} \not\equiv$ *Constant*, $\frac{N(x)}{K_v(x)} \not\equiv$ *Constant*, and $K_u(x), K_v(x)$ are non-constant. If $K_u(x) \geq K_v(x)$ for some non-empty open domain $x \in \omega$ and $r_1(x) \equiv r_2(x) \equiv r(x)$, then for fixed $r(x)$, there exists such d^* that for $d_1 < d^*$, no coexistence equilibrium (u_c, v_c) of (2.1) exists.

Proof. We initially suppose that there exists a coexistence equilibrium (u_c, v_c) such that (u_c, v_c) satisfies the system (2.1) as

$$\begin{cases} d_1\Delta\left(\frac{u_c(x)}{M(x)}\right) + r(x)u_c\left(1-\frac{u_c(x)+v_c(x)}{K_u(x)}\right) = 0, \quad x\in\omega, \\ \mathbf{n}\cdot\nabla\left(\frac{u_c}{M}\right) = 0, \quad x\in\partial\omega. \\ d_2\Delta\left(\frac{v_c(x)}{N(x)}\right) + r(x)v_c\left(1-\frac{u_c(x)+v_c(x)}{K_v(x)}\right) = 0, \quad x\in\omega, \\ \mathbf{n}\cdot\nabla\left(\frac{v_c}{N}\right) = 0, \quad x\in\partial\omega. \end{cases} \tag{4.10}$$

Next, adding both the equations of (4.10), integrating over ω, and applying the Neumann boundary conditions, we obtain:

$$\int_\omega r(x)u_c\left(1-\frac{u_c+v_c}{K_u}\right)dx + \int_\omega r(x)v_c\left(1-\frac{u_c+v_c}{K_v}\right)dx = 0. \tag{4.11}$$

Since $K_u > K_v$, we have from (4.11):

$$\int_\omega r(x)\,(u_c+v_c)\left(1-\frac{u_c+v_c}{K_u}\right)dx > 0, \tag{4.12}$$

which is only possible if $u_c + v_c \not\equiv K_u$. Now we must impose only the case where $u_c + v_c \not\equiv K_u$ or $K_u > K_v$ in $x \in \omega$.

Consider the associate eigenvalue problem

$$\begin{aligned} d_1\Delta\left(\frac{\phi}{M}\right) + r(x)\phi\left(1-\frac{u_c+v_c}{K_u}\right) = \sigma\phi, \quad x\in\omega, \\ \mathbf{n}\cdot\nabla\left(\frac{\phi}{M}\right) = 0, \quad x\in\partial\omega. \end{aligned} \tag{4.13}$$

Its principal eigenvalue is obtained according to [5] (Theorem 2.1) as

$$\sigma_1 = \sup_{\phi\neq 0,\ \phi\in W^{1,2}} \frac{\int_\omega -d_1\left|\nabla\left(\frac{\phi}{M}\right)\right|^2 dx + \int_\omega r(x)\left(\frac{\phi^2}{M}\right)\left(1-\frac{u_c+v_c}{K_u}\right)dx}{\int_\omega\left(\frac{\phi^2}{M}\right)dx}, \tag{4.14}$$

and it will be unstable if there appears such ϕ that the expression of the right-hand side is positive. Holding $\phi = \sqrt{K_u M}$ for linearly independent M, N, K_u, K_v, if we also let $Q := \int_\omega r(x)K_u\left(1-\frac{u_c+v_c}{K_u}\right)dx > 0$, we obtain from (4.14):

$$\begin{aligned} -\int_\omega d_1\left|\nabla\left(\sqrt{\frac{K_u}{M}}\right)\right|^2 dx + \int_\omega r(x)K_u\left(1-\frac{u_c+v_c}{K_u}\right)dx \\ = -\int_\omega d_1\left|\nabla\left(\sqrt{\frac{K_u}{M}}\right)\right|^2 dx + Q > 0, \end{aligned}$$

unless $\frac{K_u}{M} \equiv$ *Constant*, when

$$d_1 < d^* := Q\left[\int_\omega\left|\nabla\left(\sqrt{\frac{K_u}{M}}\right)\right|^2 dx\right]^{-1},$$

which concludes the proof. □

For a strong monotone dynamical system [15, 28, 29], for $K_u > K_v$, the following outcome is sketched by Lemma 4, Lemma 7, and Lemma 8.

Theorem 3. Let $\frac{M(x)}{K_u(x)} \not\equiv$ *Constant* and $\frac{N(x)}{K_v(x)} \not\equiv$ *Constant*, while $M(x), N(x), K_u(x), K_v(x)$ are non-constant and $r_1(x) \equiv r_2(x) \equiv r(x)$. If $K_u(x) \geq K_v(x)$ for some open, non-empty, and bounded domain ω, then for fixed d_2 and $r(x)$ there exists d^* such that $d_1 < d^*$ and the quasi-trivial state $(u^*, 0)$ of (2.1) is globally asymptotically stable.

The following remark follows the proof of Theorem 3.

Remark 3. Let $\frac{M(x)}{K_u(x)} \not\equiv$ *Constant* and $\frac{N(x)}{K_v(x)} \not\equiv$ *Constant*, while $M(x), N(x), K_u(x), K_v(x)$ are non-constant and $r_1(x) \equiv r_2(x) \equiv r(x)$. If $K_u(x) \leq K_v(x)$ for some open, non-empty, and bounded domain ω, then for fixed d_1 and $r(x)$, there exists d^* such that $d_2 < d^*$ and the quasi-trivial state $(0, v^*)$ of (2.1) is globally asymptotically stable.

5. Steady state and global analysis: case II, $K_u \equiv K_v \equiv K$

Let u^* and v^* be the steady-state solutions corresponding to the first and second equation in (2.1) for the single species model:

$$\begin{aligned} d_1\Delta\left(\frac{u^*(x)}{M(x)}\right) + r_1(x)u^*\left(1-\frac{u^*}{K(x)}\right) = 0, \quad x\in\omega, \\ \mathbf{n}\cdot\nabla\left(\frac{u^*}{M}\right) = 0, \ x\in\partial\omega, \end{aligned} \tag{5.1}$$

$$\begin{aligned} d_2\Delta\left(\frac{v^*(x)}{M(x)}\right) + r_1(x)v^*\left(1-\frac{v^*}{K(x)}\right) = 0, \quad x\in\omega, \\ \mathbf{n}\cdot\nabla\left(\frac{v^*}{N}\right) = 0, \ x\in\partial\omega, \end{aligned} \tag{5.2}$$

respectively. We now present some auxiliary statements for the equal resource distribution that justify the results in [13]. This means when $K_u \equiv K_v \equiv K$, here we consider $r_1(x) \equiv r_2(x) \equiv r(x)$.

Lemma 9. [13] Suppose $N(x) \not\equiv$ *Constant*, $K(x) \not\equiv$ *Constant*, and $\frac{N(x)}{K(x)} \not\equiv$ *Constant*. If the positive solution of (5.2) is v^*, then

$$\int_\omega r(x)K\left(1-\frac{v^*}{K}\right)dx > 0. \tag{5.3}$$

Lemma 10. [13] Suppose $M(x) \not\equiv$ *Constant*, $K(x) \not\equiv$ *Constant*, and $\frac{M(x)}{K(x)} \not\equiv$ *Constant*. If the positive solution of (5.1) is u^*, then

$$\int_\omega r(x)M\left(\frac{u^*}{K}-1\right)dx > 0. \tag{5.4}$$

Lemma 11. [14, 22] Suppose $\frac{M(x)}{K(x)} \not\equiv$ *Constant* and $\frac{N(x)}{K(x)} \not\equiv$ *Constant*, while $M(x), N(x), K(x)$ are non-constant and $r_1(x) \equiv r_2(x) \equiv r(x)$. If $K(x) = \alpha M + \beta N$ for some $\alpha > 0, \beta > 0$ in ω, then the coexistence state (u_c, v_c) of system (2.1) is globally asymptotically stable.

Lemma 12. Suppose $\frac{M(x)}{K(x)} \not\equiv$ *Constant* and $\frac{N(x)}{K(x)} \not\equiv$ *Constant*, while $M(x), N(x), K(x)$ are non-constant and $r_1(x) \equiv r_2(x) \equiv r(x)$. If $M(x) = \alpha K + \beta N$ for some $\alpha > 0, \beta > 0$ with $\alpha K, \beta N < M(x)$ in ω, then $(0, v^*)$ of (2.1) is not stable.

Proof. Considering the eigenvalue problem in (2.1) for the first equation around $(0, v^*)$ with the usual boundary conditions, we obtain:

$$d_1\Delta\left(\frac{\phi}{M}\right) + r(x)\phi\left(1-\frac{v^*}{K}\right) = \sigma\phi, \quad x\in\omega,$$
$$\mathbf{n}\cdot\nabla\left(\frac{\phi}{M}\right) = 0, \ x\in\partial\omega. \tag{5.5}$$

The principal eigenvalue of (5.5) is defined as in [5] (Theorem 2.1), giving:

$$\sigma_1 = \sup_{\phi\neq 0,\phi\in W^{1,2}} \frac{\int_\omega -d_1\left|\nabla\left(\frac{\phi}{M}\right)\right|^2 dx + \int_\omega r(x)\left(\frac{\phi^2}{M}\right)\left(1-\frac{v^*}{K}\right)dx}{\int_\omega\left(\frac{\phi^2}{M}\right)dx}. \tag{5.6}$$

Choosing $\phi = M(x)$ such that for $M(x) = \alpha K + \beta N$ we obtain using (5.3) and (5.4):

$$\sigma_1\int_\omega M dx \geq \int_\omega rM\left(1-\frac{v^*}{K}\right)dx,$$

now,

$$\begin{aligned}\int_\omega rM\left(1-\frac{v^*}{K}\right)dx &= \int_\omega r(\alpha K+\beta N)\left(1-\frac{v^*}{K}\right)dx\\ &= \alpha\int_\omega rK\left(1-\frac{v^*}{K}\right)dx\\ &+ \beta\int_\omega rN\left(1-\frac{\alpha v^*}{M-\beta N}\right)dx\\ &> \alpha\int_\omega rK\left(1-\frac{v^*}{K}\right)dx\\ &+ \beta\int_\omega rN\left(1+\frac{\alpha v^*}{\beta N}\right)dx,\end{aligned}$$

where $M(x) = \alpha K+\beta N$, and for positive $M(x), N(x), r(x)$ with $\beta > 0$, $M(x) - \beta N(x) > -\beta N(x)$. Therefore, the principal eigenvalue is positive, as the foremost term is positive by Lemma 9 and the second term is non-negative, so $\sigma_1 > 0$. □

Lemma 13. Suppose $\frac{M(x)}{K(x)} \not\equiv$ *Constant* and $\frac{N(x)}{K(x)} \not\equiv$ *Constant*, while $M(x), N(x), K(x)$ are non-constant and $r_1(x) \equiv r_2(x) \equiv r(x)$. If $M(x) = \alpha K + \beta N$ for some $\alpha > 0, \beta > 0$ with $\alpha K, \beta N < M(x)$ in ω, then no coexistence equilibrium (u_c, v_c) for the system (2.1) holds.

Proof. First, suppose to the contrary that there exists a strictly positive coexistence equilibrium (u_c, v_c) of (2.1), such that the solution (u_c, v_c) satisfies

$$\begin{cases} d_1\Delta\left(\frac{u_c(x)}{M(x)}\right) + r(x)u_c\left(1-\frac{u_c(x)+v_c(x)}{K(x)}\right) = 0, & x\in\omega,\\ \mathbf{n}\cdot\nabla\left(\frac{u_c}{M}\right) = 0, \ x\in\partial\omega.\\ d_2\Delta\left(\frac{v_c(x)}{N(x)}\right) + r(x)v_c\left(1-\frac{u_c(x)+v_c(x)}{K(x)}\right) = 0, & x\in\omega,\\ \mathbf{n}\cdot\nabla\left(\frac{v_c}{N}\right) = 0, \ x\in\partial\omega.\end{cases} \tag{5.7}$$

Adding the first two equations in (5.7), and integrating over the domain ω, while also applying the homogeneous Neumann boundary conditions,

$$\int_\omega r(u_c+v_c)\left(1-\frac{u_c+v_c}{K}\right)dx = 0$$
$$\Rightarrow \int_\omega rK\left(1-\frac{u_c+v_c}{K}\right)dx = \frac{r}{K}(K-u_c-v_c)^2\,dx > 0,$$

unless $u_c + v_c \not\equiv K$.

So, we have

$$\int_\omega r(x)K\left(1-\frac{u_c+v_c}{K}\right)dx > 0. \tag{5.8}$$

Thus we have two cases:

Case 1: For $u_c + v_c \equiv K(x)$, by the Maximum Principle[30], $w_c \equiv$ *Constant* and $z_c \equiv$ *Constant* on ω in (2.1) where $\frac{u_c}{M} = w_c$ and $\frac{v_c}{N} = z_c$. Therefore,

$$u_c + v_c \equiv K$$
$$\Rightarrow Mw_c + Nz_c \equiv \frac{1}{\alpha}(M-\beta N).$$

Thus, $w_c = 1/\alpha$, and $z_c = -\left(\frac{\beta}{\alpha}\right)$, which is a contradiction, since $v_c > 0$.

Case 2: For $u_c + v_c \not\equiv K(x)$, taking the eigenvalue problem

$$d_1\Delta\left(\frac{\phi}{M}\right) + r(x)\phi\left(1-\frac{u_c+v_c}{K}\right) = \sigma\phi, \quad x\in\omega,$$
$$\mathbf{n}\cdot\nabla\left(\frac{\phi}{M}\right) = 0, \ x\in\partial\omega,$$

according to [5] (Theorem 2.1), the corresponding principal eigenvalue is stated as

$$\sigma_1 = \sup_{\phi\neq 0,\phi\in W^{1,2}} \frac{\int_\omega -d_1\left|\nabla\left(\frac{\phi}{M}\right)\right|^2 dx + \int_\omega r(x)\left(\frac{\phi^2}{M(x)}\right)\left(1-\frac{u_c+v_c}{K}\right)dx}{\int_\omega\left(\frac{\phi^2}{M(x)}\right)dx}. \tag{5.9}$$

Upon substituting $\phi = M(x)$, and for $M(x) = \alpha K + \beta N$, we have:

$$\begin{aligned}&\int_\omega r(x)M\left(1-\frac{u_c+v_c}{K}\right)dx\\ &= \int_\omega r(x)(\alpha K+\beta N)\left(1-\frac{u_c+v_c}{K}\right)dx\\ &> \alpha\int_\omega rK\left(1-\frac{u_c+v_c}{K}\right)dx + \beta\int_\omega rN\left(1+\frac{u_c+v_c}{N\beta}\right)dx.\end{aligned}$$

For the last integral, we have $M(x) = \alpha K + \beta N > 0$ and $M(x) - \beta N(x) > -\beta N(x)$ for non-negative $N(x)$; and, using (5.8), the first term of the last integral is positive. Hence, the eigenvalue σ_1 is positive for non-negative $N(x), r(x)$ and $\beta > 0$. However, the equilibrium solution (u_c, v_c) of (2.1) gives the positive eigenfunction with 0 eigenvalues, which is contradictory with $\sigma_1 > 0$. Therefore, no coexistence equilibrium (u_c, v_c) exists. □

The following Theorem follows Lemma 4, Lemma 12, and Lemma 13, since according to Lemma 12, the quasi-trivial equilibrium $(0, v^*)$ is not stable; by Lemma 13, no coexistence equilibrium (u_c, v_c) exists for the combined effect of spatial functions; and Lemma 4 is also still valid.

Theorem 4. Suppose $\frac{M(x)}{K(x)} \not\equiv$ *Constant* and $\frac{N(x)}{K(x)} \not\equiv$ *Constant*, while $M(x), N(x), K(x)$ are non-constant and $r_1(x) \equiv r_2(x) \equiv r(x)$. If $M(x) = \alpha K + \beta N$, for some $\alpha > 0, \beta > 0$ with $\alpha K, \beta N < M(x)$ in ω, then $(u^*, 0)$ of system (2.1) is globally asymptotically stable.

Following a similar procedure to Lemma 12 and Lemma 13, and also to Lemma 4, if $N(x) = \alpha K + \beta M$, for some $\alpha > 0, \beta > 0$ with $\alpha K, \beta M < N(x)$ in ω and for non-constant $M(x), N(x)$, and $K(x)$, we obtain the following remark.

Remark 4. Suppose $\frac{M(x)}{K(x)} \not\equiv$ *Constant* and $\frac{N(x)}{K(x)} \not\equiv$ *Constant*, while $M(x), N(x), K(x)$ are non-constant and $r_1(x) \equiv r_2(x) \equiv r(x)$. If $N(x) = \alpha K + \beta M$, for some $\alpha > 0$ and $\beta > 0$ with $\alpha K, \beta M < N(x)$ in ω, then $(0, v^*)$ of system (2.1) is globally asymptotically stable.

Lemma 14. Suppose that $M(x) \equiv N(x)$ satisfying $\frac{N(x)}{K(x)} \not\equiv$ *Constant* for $x \in \omega$, and $M(x), N(x), K(x)$ are non-constant and $r_1(x) \equiv r_2(x) \equiv r(x)$. If $d_1 > d_2$, then the problem (2.1) has no coexistence state (u_c, v_c).

Proof. We initially suppose that there exists (u_c, v_c) such that (u_c, v_c) satisfies the system (2.1) as

$$\begin{cases} d_1 \Delta\left(\frac{u_c(x)}{M(x)}\right) + r(x) u_c \left(1 - \frac{u_c(x)+v_c(x)}{K(x)}\right) = 0, & x \in \omega, \\ \mathbf{n} \cdot \nabla\left(\frac{u_c}{M}\right) = 0, & x \in \partial\omega. \\ d_2 \Delta\left(\frac{v_c(x)}{M(x)}\right) + r(x) v_c \left(1 - \frac{u_c(x)+v_c(x)}{K(x)}\right) = 0, & x \in \omega, \\ \mathbf{n} \cdot \nabla\left(\frac{v_c}{M}\right) = 0, & x \in \partial\omega. \end{cases} \tag{5.10}$$

Consider the eigenvalue problem of (5.10):

$$\begin{cases} d_1 \Delta\left(\frac{\phi}{M(x)}\right) + r(x)\phi \left(1 - \frac{u_c(x)+v_c(x)}{K(x)}\right) = \sigma\phi, \\ \mathbf{n} \cdot \nabla\left(\frac{\phi}{M}\right) = 0, & x \in \omega. \\ d_2 \Delta\left(\frac{\Phi}{M(x)}\right) + r(x)\Phi \left(1 - \frac{u_c(x)+v_c(x)}{K(x)}\right) = \sigma\Phi, \\ \mathbf{n} \cdot \nabla\left(\frac{\Phi}{M}\right) = 0, & x \in \omega. \end{cases} \tag{5.11}$$

Taking the principal eigenvalues of the first equation of (5.11) according to [5] (Theorem 2.1), we have

$$\overline{\sigma}_1 = \sup_{\phi \neq 0,\ \phi \in W^{1,2}} \frac{\int_\omega -d_1 \left|\nabla\left(\frac{\phi}{M}\right)\right|^2 dx + \int_\omega r(x)\left(\frac{\phi^2}{M}\right)\left(1 - \frac{u_c+v_c}{K}\right) dx}{\int_\omega \left(\frac{\phi^2}{M}\right) dx}, \tag{5.12}$$

and taking the principal eigenvalues of the second equation of (5.11) in a similar way,

$$\sigma_1 = \sup_{\Phi \neq 0,\ \Phi \in W^{1,2}} \frac{\int_\omega -d_2 \left|\nabla\left(\frac{\Phi}{M}\right)\right|^2 dx + \int_\omega r(x)\left(\frac{\Phi^2}{M}\right)\left(1 - \frac{u_c+v_c}{K}\right) dx}{\int_\omega \left(\frac{\Phi^2}{M}\right) dx}. \tag{5.13}$$

Since (u_c, v_c) is the steady-state solution of (5.10), u_c satisfies the first equation of (5.10):

$$d_1 \Delta\left(\frac{u_c}{M}\right) + r u_c \left(1 - \frac{u_c + v_c}{K}\right) = 0, \quad x \in \omega,$$
$$\mathbf{n} \cdot \nabla\left(\frac{u_c}{M}\right) = 0, \ x \in \partial\omega,$$

and so, from the eigenvalues problem (5.11), a positive principal eigenfunction corresponds to the principal eigenvalues $\overline{\sigma}_1 \equiv 0$. Now, from (5.12),

$$-\int_\omega d_1 \left|\nabla\left(\frac{u_c}{M}\right)\right|^2 dx + \int_\omega r(x)\left(\frac{u_c^2}{M(x)}\right)\left(1 - \frac{u_c + v_c}{K}\right) dx = 0. \tag{5.14}$$

Substituting $\Phi = u_c$ in (5.13) and using (5.14), we obtain:

$$\begin{aligned} &\int_\omega -d_2 \left|\nabla\left(\frac{u_c}{M}\right)\right|^2 dx + \int_\omega r(x)\left(\frac{u_c^2}{M(x)}\right)\left(1 - \frac{u_c + v_c}{K}\right) dx \\ &= (d_1 - d_2) \int_\omega \left|\nabla\left(\frac{u_c}{M}\right)\right|^2 dx \\ &+ \int_\omega r(x)\left(\frac{u_c^2}{M(x)}\right)\left(1 - \frac{u_c + v_c}{K}\right) dx - d_1 \int_\omega \left|\nabla\left(\frac{u_c}{M}\right)\right|^2 dx \\ &= (d_1 - d_2) \int_\omega \left|\nabla\left(\frac{u_c}{M}\right)\right|^2 dx \\ &+ \left[-d_1 \int_\omega \left|\nabla\left(\frac{u_c}{M}\right)\right|^2 dx + \int_\omega r(x)\left(\frac{u_c^2}{M(x)}\right)\left(1 - \frac{u_c + v_c}{K}\right) dx\right] \\ &= (d_1 - d_2) \int_\omega \left|\nabla\left(\frac{u_c}{M}\right)\right|^2 dx + 0 > 0, \end{aligned}$$

unless $\frac{u_c}{M(x)} \equiv$ *Constant*. If $\frac{u_c}{M} \equiv C$, then $u_c + v_c \equiv K$ on ω. So, $v_c = K - MC$. Replacing $v_c = K - MC$ in the second equation of (2.1) on ω implies:

$$0 = d_2 \Delta\left[\frac{K - MC}{N}\right] = d_2 \Delta\left(\frac{K}{N}\right)$$

for $M \equiv N$, which contradicts $\frac{N(x)}{K(x)} \not\equiv$ *Constant* in the hypothesis of this Lemma. Hence, the principal eigenvalue $\sigma_1 > 0$. Additionally, v_s satisfies

$$d_2 \Delta\left(\frac{v_c}{M(x)}\right) + r(x) v_c \left(1 - \frac{u_c + v_c}{K(x)}\right) = 0, \quad \mathbf{n} \cdot \nabla\left(\frac{v_c}{M}\right) = 0, \quad x \in \omega,$$

and hence the positive principal eigenfunctions of the second equation of (5.11) correspond to principal eigenvalues $\sigma_1 \equiv 0$. This proves that there is no (u_c, v_c). □

Lemma 15. Suppose that $M(x) \equiv N(x)$ satisfying $\frac{N(x)}{K(x)} \not\equiv$ *Constant* for $x \in \omega$, and $M(x), N(x), K(x)$ are non-constant and $r_1(x) \equiv r_2(x) \equiv r(x)$. Then, for $d_1 > d_2$, the semi-trivial state $(u^*, 0)$ of (2.1) is not stable.

Proof. Consider the eigenvalue problem of (2.1) about $(u^*, 0)$ for the second equation with boundary conditions:

$$d_2 \Delta\left(\frac{\phi}{M(x)}\right) + r(x)\phi \left(1 - \frac{u^*}{K(x)}\right) = \sigma\phi, \quad \mathbf{n} \cdot \nabla\left(\frac{\phi}{M}\right) = 0, \ x \in \omega. \tag{5.15}$$

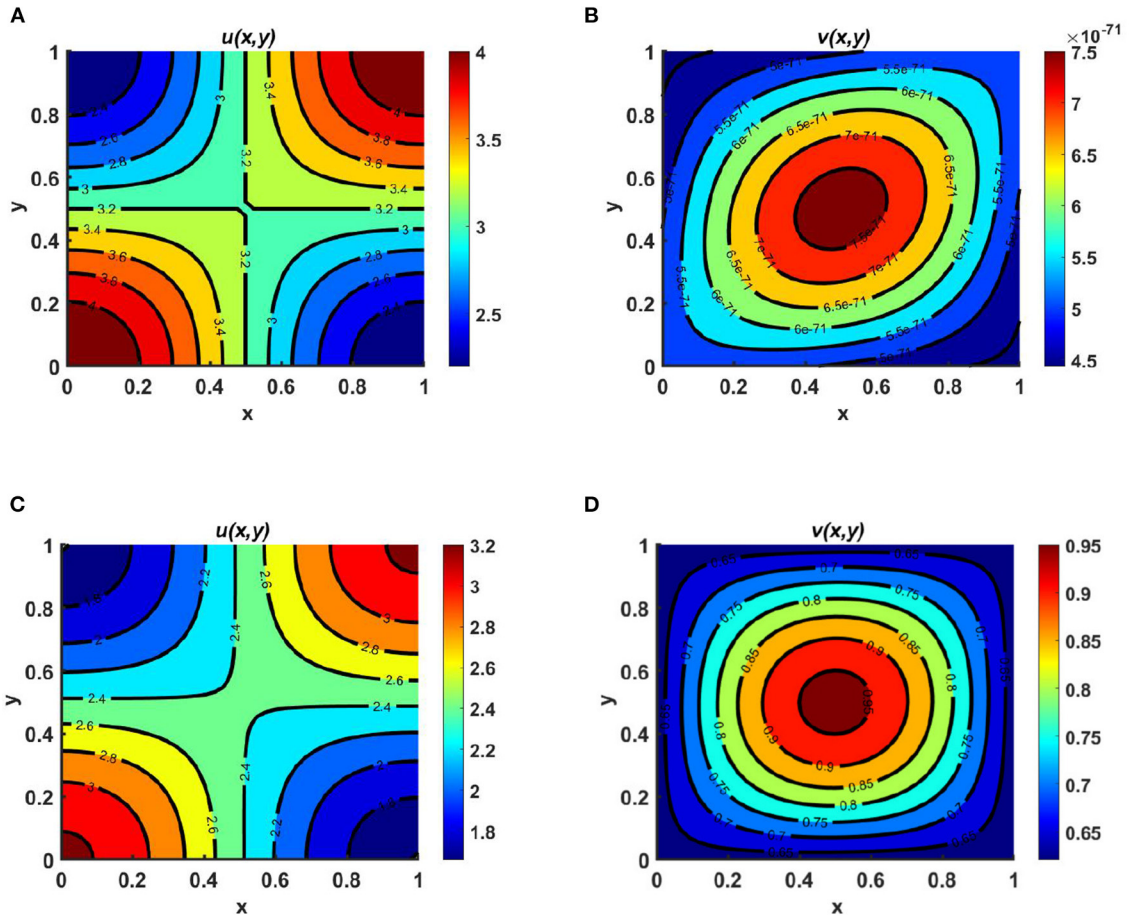

FIGURE 2
Contour plots for (2.1) with $N = 1.8 + \sin(\pi x)\sin(\pi y)$, $r_1 \equiv r_2 \equiv 1.0$, $d_1 \equiv d_2 \equiv 1.0$, $(u_0, v_0) = (0.5, 1.75)$ on $\omega = (0, 1) \times (0, 1)$ for **(A, B)** $K_u = M = (3.2 + \cos(\pi x)\cos(\pi y)) > K_v = (1.6 + \cos(\pi x)\cos(\pi y))$, and **(C, D)** $K_u = K_v = M = 3.2 + \cos(\pi x)\cos(\pi y)$.

The principal eigenvalues of (5.15) are given, according to [5] (Theorem 2.1), by:

$$\sigma_1 = \sup_{\phi \neq 0, \phi \in W^{1,2}} \frac{\int_\omega -d_2 \left|\nabla\left(\frac{\phi}{M}\right)\right|^2 dx + \int_\omega r(x)\left(\frac{\phi^2}{M(x)}\right)\left(1 - \frac{u^*}{K}\right) dx}{\int_\omega \left(\frac{\phi^2}{M(x)}\right) dx}. \tag{5.16}$$

Since $(u^*, 0)$ is a solution, we obtain the following:

$$d_1 \Delta\left(\frac{u^*}{M}\right) + r u^*\left(1 - \frac{u^*}{K}\right) = 0, \quad x \in \omega, \ \mathbf{n}\cdot\nabla\left(\frac{u^*}{M}\right) = 0, \quad x \in \partial\omega. \tag{5.17}$$

Thus, u^* is the positive principal eigenfunction of (5.17), which corresponds to zero eigenvalues of the problem. Integrating (5.17) over the domain and applying the boundary conditions, we obtain:

$$\int_\omega -d_1 \left|\nabla\left(\frac{u^*}{M}\right)\right|^2 dx + \int_\omega r\left(\frac{u^{*2}}{M}\right)\left(1 - \frac{u^*}{K}\right) dx = 0. \tag{5.18}$$

Substituting $\phi = u^*$ in (5.16), we obtain:

$$\sigma_1 \geq \frac{\int_\omega -d_2 \left|\nabla\left(\frac{u^*}{M}\right)\right|^2 dx + \int_\omega r(x)\left(\frac{u^{*2}}{M}\right)\left(1 - \frac{u^*}{K}\right) dx}{\int_\omega \left(\frac{u^{*2}}{M}\right) dx}. \tag{5.19}$$

However, using (5.18) implies that

$$\begin{aligned}
&\int_\omega -d_2 \left|\nabla\left(\frac{u^*}{M}\right)\right|^2 dx + \int_\omega r(x)\left(\frac{u^{*2}}{M(x)}\right)\left(1 - \frac{u^*}{K}\right) dx \\
&= (d_1 - d_2)\int_\omega \left|\nabla\left(\frac{u^*}{M}\right)\right|^2 dx \\
&+ \left[-d_1 \int_\omega \left|\nabla\left(\frac{u^*}{M}\right)\right|^2 dx + \int_\omega r(x)\left(\frac{u^{*2}}{M(x)}\right)\left(1 - \frac{u^*}{K}\right) dx\right] \\
&= (d_1 - d_2)\int_\omega \left|\nabla\left(\frac{u^*}{M}\right)\right|^2 dx + 0 > 0,
\end{aligned}$$

unless $\frac{u^*}{M} \not\equiv$ *Constant*. If $\frac{u^*}{M} \equiv C_1$ then we obtain from (5.18) $r u^*\left(1 - \frac{u^*}{K}\right) = 0$; this implies that $u^* \equiv K \equiv C_1 M$,

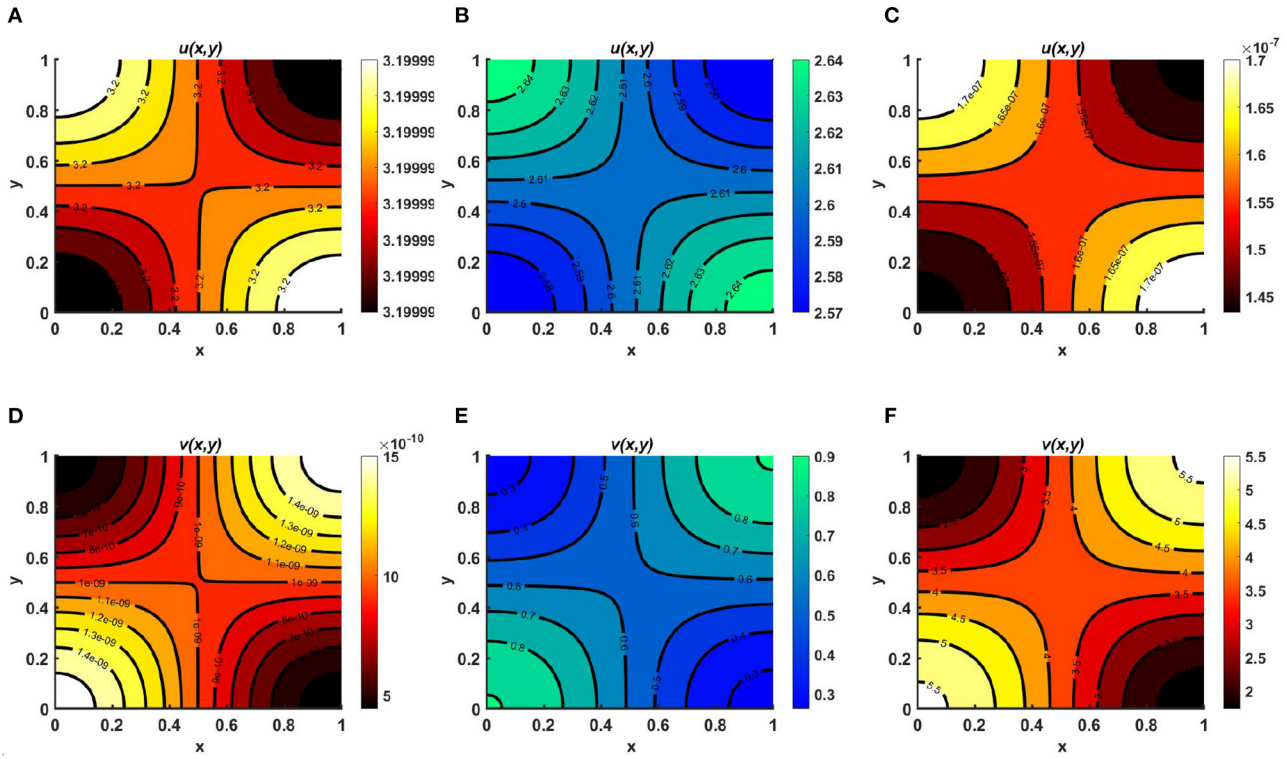

FIGURE 3
Contour plots for (2.1) with $N = 1.8 + \cos(\pi x)\cos(\pi y)$, $r_1 \equiv r_2 \equiv 1.0$, $d_1 \equiv d_2 \equiv 1.0$, $(u_0, v_0) = (0.5, 1.75)$ on $\omega = (0, 1) \times (0, 1)$ for **(A, D)** $K_u = M = 3.2 > K_v = 2.6$, **(B, E)** $K_u = K_v = M = 3.2$, and **(C, F)** $K_u = M = 3.2 < K_v = 4.0$.

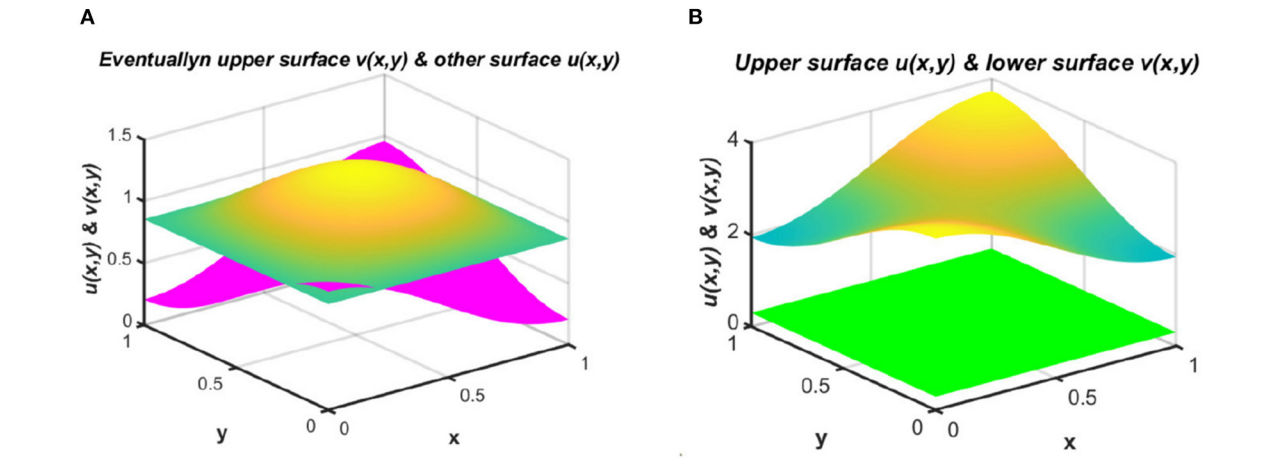

FIGURE 4
Equilibrium population densities for (2.1) with $N = 1.8 + \sin(\pi x)\sin(\pi y)$, $d_1 \equiv d_2 \equiv 1.0$, $(u_0, v_0) = (1.75, 0.5)$ when $r_1 = 1.0 >> r_2 = 0.01$ on $\omega = (0, 1) \times (0, 1)$ for **(A)** $K_u = M = (1.6 + \cos(\pi x)\cos(\pi y)) < K_v = (3.2 + \cos(\pi x)\cos(\pi y))$, and **(B)** $K_u = M = (3.2 + \cos(\pi x)\cos(\pi y)) > K_v = (1.6 + \cos(\pi x)\cos(\pi y))$.

which contradicts the hypothesis of this Lemma that M is non-proportional to K on ω. Hence, the principal eigenvalue σ_1 is non-negative. This suggests that $(u^*, 0)$ is unstable, which concludes the proof. □

By Lemma 4, Lemma 14, and Lemma 15, the following results can be confirmed.

Theorem 5. Suppose $M(x) \equiv N(x)$ satisfying $\frac{N(x)}{K(x)} \not\equiv Constant$ for $x \in \omega$, and $M(x), N(x), K(x)$ are non-constant and $r_1(x) \equiv r_2(x) \equiv r(x)$. If $d_1 > d_2$, then $(0, v^*)$ of (2.1) is globally asymptotically stable.

Here we also note that, for the case of two species, Theorem 5 extrapolates the outcome of [2] to a more realistic pattern in terms of diffusion strategy.

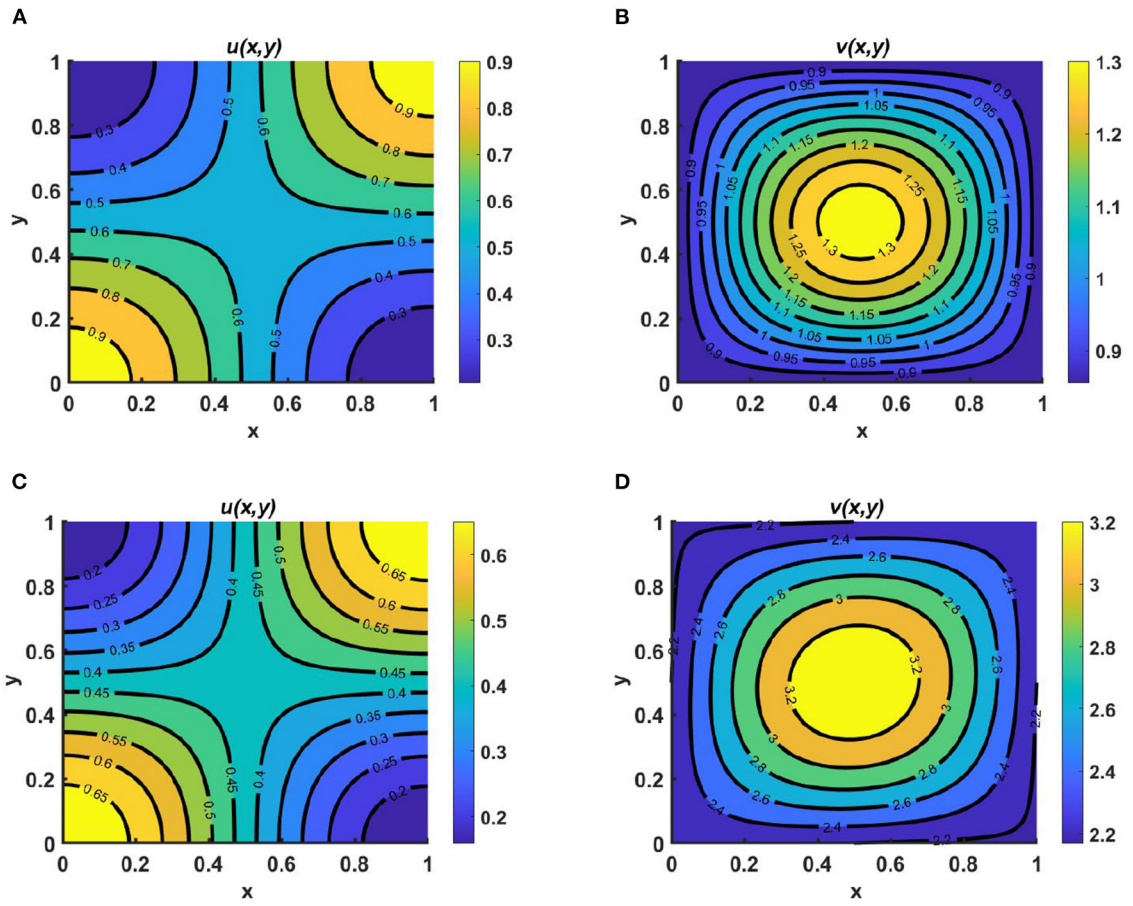

FIGURE 5
Contour plots for (2.1) for $K_u = M = (1.6 + \cos(\pi x)\cos(\pi y)) < K_v = (3.2 + \cos(\pi x)\cos(\pi y))$, $N = 1.8 + \sin(\pi x)\sin(\pi y)$, $d_1 \equiv d_2 \equiv 1.0$, $(u_0, v_0) = (1.75, 0.5)$; in **(A, B)** $r_1 = 1.0 >> r_2 = 0.01$, and in **(C, D)** $r_1 = 0.01 << r_2 = 1.0$ on $\omega = (0, 1) \times (0, 1)$.

6. Numerical examples and applications

The aim of this section is to present a series of numerical examples illustrating population density profiles for different diffusion strategies as well as different parametric values of functions that complement the extinction of one species by others, as well the coexistence of populations in competition. Both temporal and spatial effects for the case of two spatial dimensions are examined in Section 6.1. In the case of a time-dependent function, which may occur due to seasonal change, we display the average population density profile to indicate its existence over the periodic state and present a snapshot contour plot of population density during a period of the functions. In all the examples, we consider the logistic growth function for two interacting species with similar and dissimilar carrying capacities and migration rates. To perform the numerical computation, we employed the alternating-direction implicit (ADI) method with uniform discretization in space and time as we advanced each time step. The solution of the discretized system was regarded as having converged when successive iterations were within 10^{-9} of one another. We considered solutions to have converged to the PDE solution when halving the space and time steps resulted in solutions that were within 10^{-4} of each other at common grid points. Although we could consider a more complex domain, we selected a spatial domain of $[0, 1] \times [0, 1]$ for simplicity.

6.1. 2-dimensional space

This section presents a numerical investigation of the model for two-dimensional cases, both in space and in time.

Example 1. Consider the functions $K_u = M = (3.2 + \cos(\pi x)\cos(\pi y)) > K_v = (1.6 + \cos(\pi x)\cos(\pi y))$, with the same diffusion coefficients and intrinsic growth rates, where the species u follows the carrying-capacity–driven diffusion scheme and the other diffuses according to resource distribution. From the contour plots of Figures 2A, B, we observe that for cases of unequal carrying capacity, the species which follows a carrying-capacity–driven distribution will survive, and according to Theorem 2, the value of u should tend to K_u, while the other species goes to extinction. On the other hand, in Figures 2C, D, we observe that for cases of equal carrying capacity, the population density

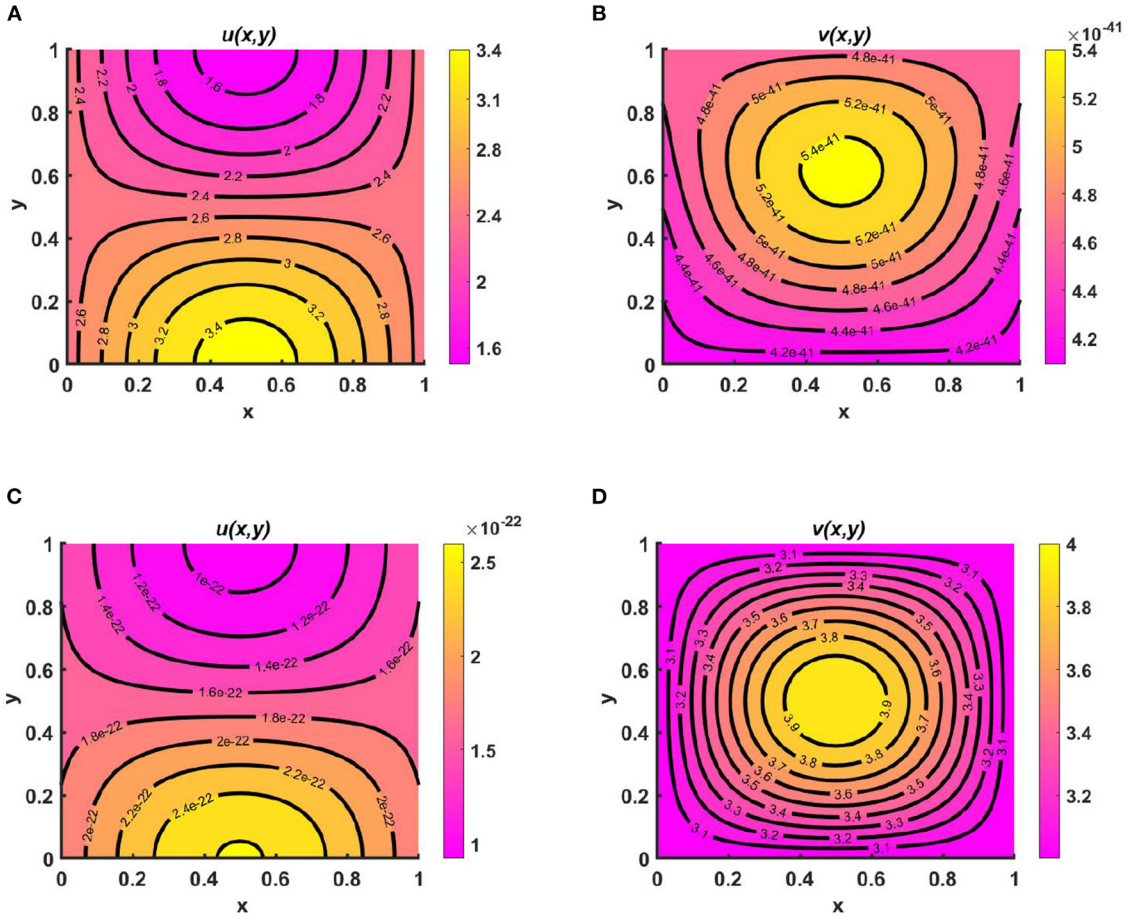

FIGURE 6
Contour plots for (2.1) with $K_u = M = 2.5 + \sin(\pi x)\cos(\pi y)$, $d_1 \equiv d_2 \equiv 1.0$, $(u_0, v_0) = (0.5, 0.5)$, $r_1 \equiv r_2 \equiv 1.0$ on $\omega = (0, 1) \times (0, 1)$ for **(A, B)** $K_v = N = 1.4 + 0.3\sin(\pi x)\sin(\pi y)$, and **(C, D)** $K_v = N = 3.0 + \sin(\pi x)\sin(\pi y)$.

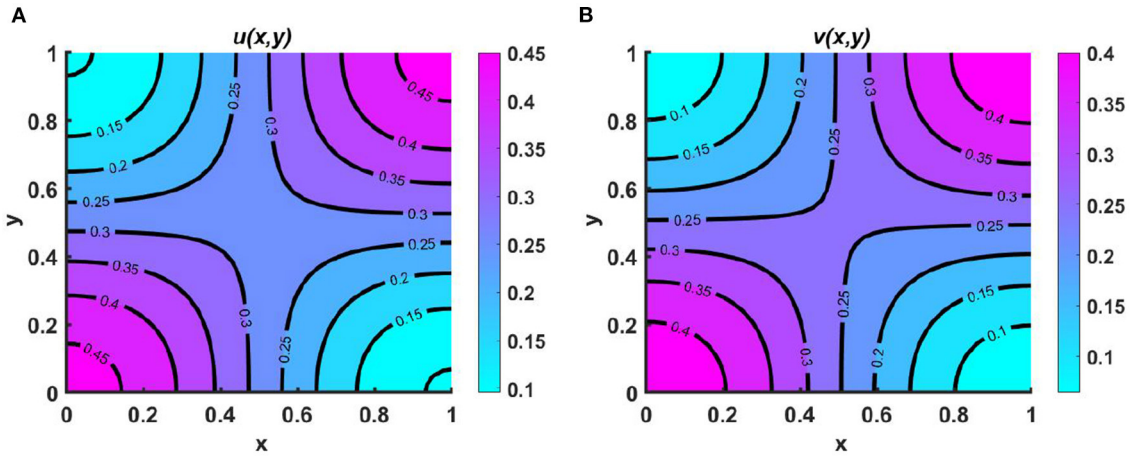

FIGURE 7
Contour plots of **(A)** u, and **(B)** v for (2.1) with $K_u = K_v = 0.5 + 0.3\sin(\pi x)\sin(\pi y)$, $M = 0.3 + 0.2\cos(\pi x)\cos(\pi y)$, $N = 0.4 + 0.3\cos(\pi x)\cos(\pi y)$, $(u_0, v_0) = (0.5, 1.75)$, $r_1 \equiv r_2 \equiv 1.0$, $d_1 \equiv d_2 \equiv 1.0$ on $\omega = (0, 1) \times (0, 1)$.

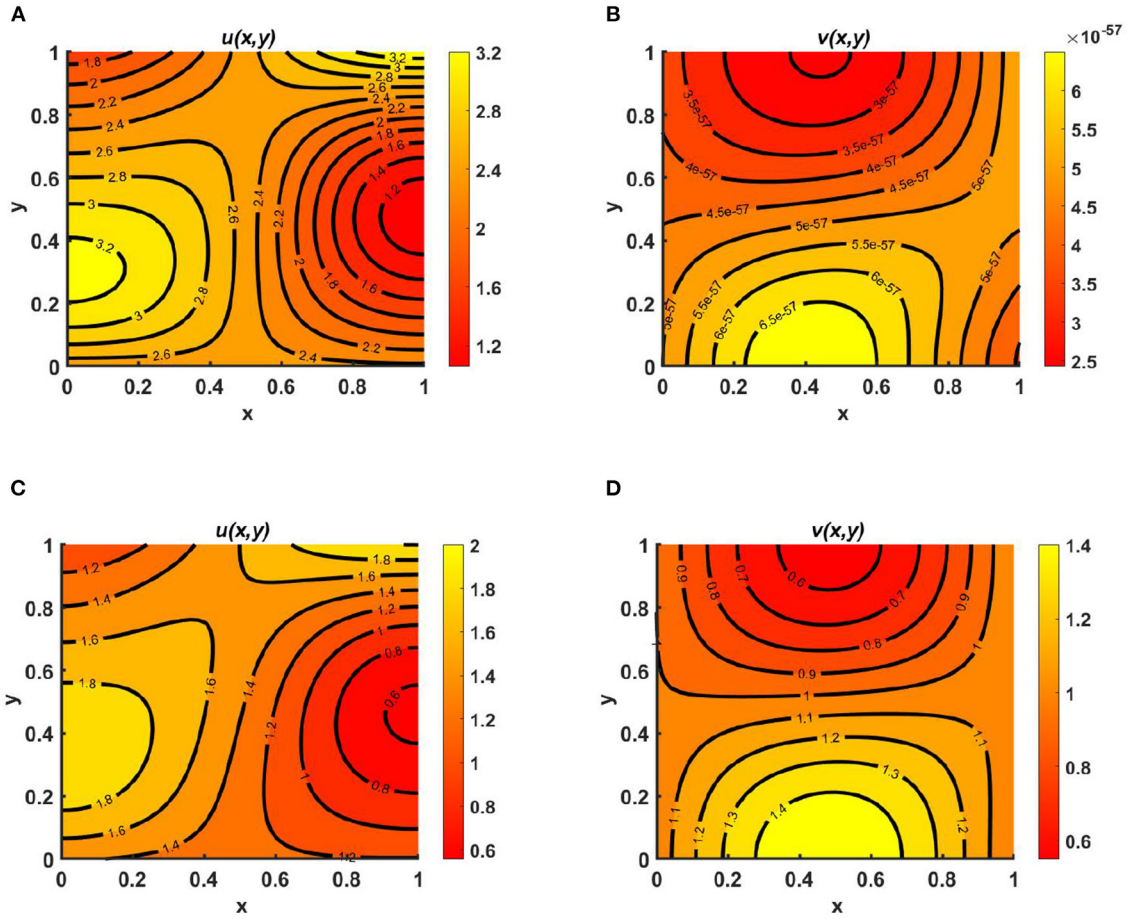

FIGURE 8
Contour plots for (2.1) with $M = 1.5 + \cos(\pi x)\sin(\pi y)$, $N = 2.1 + \sin(\pi x)\cos(\pi y)$, $d_1 = 0.1$, $d_2 = 1.0$, $(u_0, v_0) = (0.5, 0.5)$, $r_1 \equiv r_2 \equiv 1.0$ on $\omega = (0, 1) \times (0, 1)$ for **(A, B)** $K_u = 2.5 + \cos(\pi x)\cos(\pi y) > K_v = 1.4 + \cos(\pi x)\cos(\pi y)$, and **(C, D)** $K_u = K_v = 2.5 + \cos(\pi x)\cos(\pi y)$.

of u is higher. Furthermore, when K_v and N are randomly selected, the population density of v is found to be very low compared to that of u. Based on a diffusion strategy and carrying capacity, the species can survive in competition. Partial sharing of resources may cause the coexistence of populations when both follow the same diffusion strategy. We observe that the species with less efficient consumer carrying capacity goes to extinction, while the higher consumers become the only survivors of the battle.

Example 2. Consider the case of a homogeneous environment as $K_u = M = 3.2$, $d_1 \equiv d_2 = 1.0$, $r_1 \equiv r_2 = 1.0$, for fixed $N = 1.8 + \cos(\pi x)\cos(\pi y)$, where in Figures 3A, D $K_u = 3.2 > K_v = 2.6$, in Figures 3B, E $K_u = K_v = 3.2$, and in Figures 3C, F $K_u = 3.2 < K_v = 4.0$. We find that when the carrying capacities are homogeneous and do not depend on the spatial domain, for cases of unequal carrying capacity, one of the semi-trivial equilibrium solutions prevails; in contrast, for cases of equal carrying capacity, scenario with coexistence of the competing species is observed, as mentioned in Remark 2, which correlates with the case of space-dependent carrying capacities, as shown in Figure 2. As we know, carrying capacity is the key element for population growth. In fact, a constant environment can be modeled in the laboratory environment, such as by considering the yeast population in a fixed jar. However, if resources are unevenly distributed over space, spatial diffusion of the species can raise the equilibrium of the total abundance of the population of the environment.

Example 3. We next consider the cases for $K_u = M = (1.6 + \cos(\pi x)\cos(\pi y)) < K_v = (3.2 + \cos(\pi x)\cos(\pi y))$ with $N = 1.8 + \sin(\pi x)\sin(\pi y)$, $d_1 \equiv d_2 \equiv 1.0$, $(u_0, v_0) = (1.75, 0.5)$ on $\omega = (0, 1) \times (0, 1)$ when the intrinsic growth rates of the two species are unequal. If we consider a case of competition between a native and an invasive species, such that $r_1 >> r_2$ and vice versa, then it is possible to establish additional theoretical results, since the growth of the invasive population is very high. Here, Figure 4 represents equilibrium population density profiles under (2.1). We observe in Figure 4A that when K_v and M are randomly selected, carrying capacity also functions as an important factor that may enable coexistence even in cases of unequal resource distribution between the species. On the other hand, as shown in Figure 4B, when $K_u = M > K_v$, we find that species u survives and tends

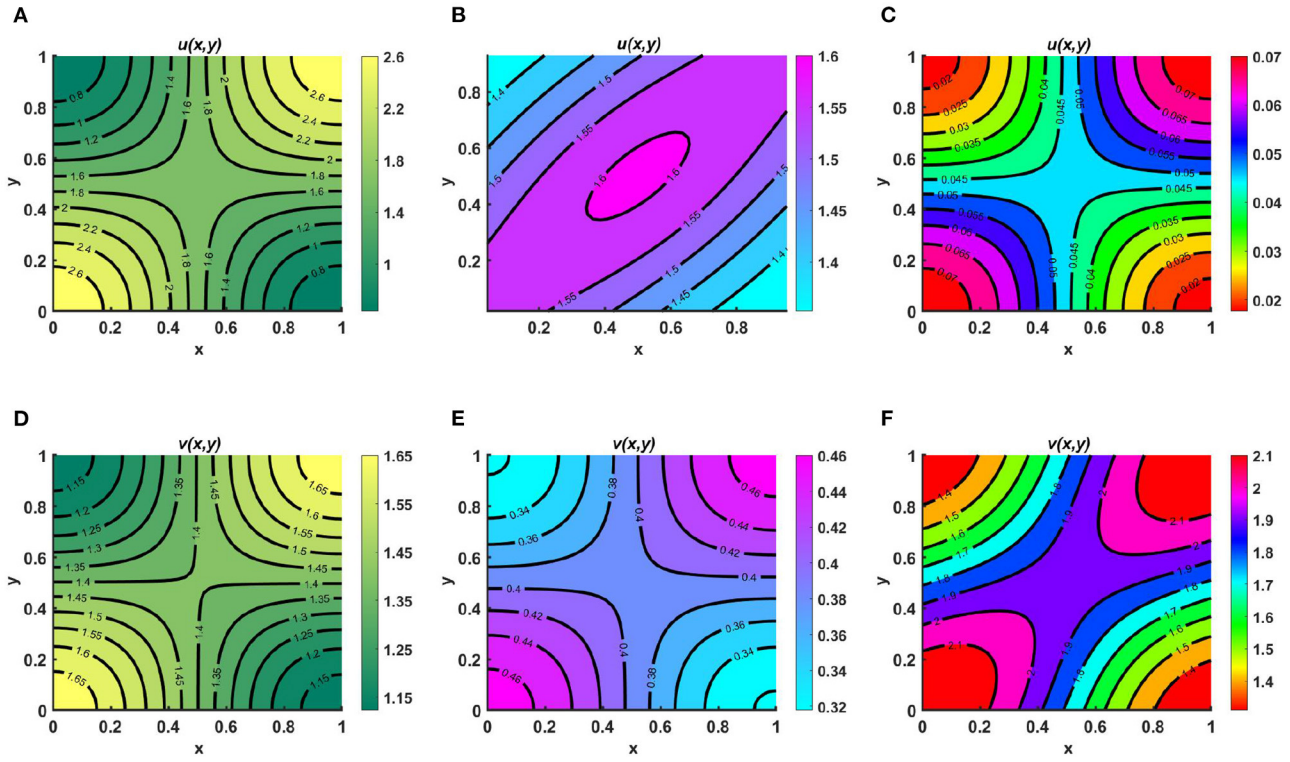

FIGURE 9
Contour plots for (2.1) with $M = 1.6 + \cos(\pi x)\cos(\pi y)$, $N = 1.5 + 0.3\cos(\pi x)\cos(\pi y)$, $K_u = K_v = K = 1.8 + 0.3\sin(\pi x)\sin(\pi y)$, $d_1 \equiv d_2 \equiv 1.0$, $r_1 \equiv r_2 \equiv 1.0$, $(u_0, v_0) = (1.95, 0.9)$ on $\omega = (0, 1) \times (0, 1)$ for **(A, D)** $K_u = K_v = K = M + N$, **(B, E)** $M = K + N$, and **(C, F)** $N = K + M$.

to K_u as $t \to \infty$, while the other species v has a very low population density that may go to extinction as time continues.

Example 4. We now consider $K_u = M = (1.6 + \cos(\pi x)\cos(\pi y)) < K_v = (3.2 + \cos(\pi x)\cos(\pi y))$, with $N = 1.8 + \sin(\pi x)\sin(\pi y)$ where the diffusion coefficients are same. Figure 5 presents contour plots for u and v for non-negative initial values $(u_0, v_0) = (1.75, 0.5)$, while u is distributed according to per-capita carrying capacity and v follows a resource-based diffusion strategy. We observe in Figures 5A, B that when $r_1 = 1.0 >> r_2 = 0.01$, the population density of u is notably higher compared to v, and coexistence may occur in cases of higher r_1 as compared to r_2. We also observe that higher population densities of u are found at the bottom-left and top-right corners, while the population density of v is higher in the middle of the contour domain, analogous to N. In contrast, when $r_1 << r_2$ and $K_u < K_v$, due to the higher consumption of resources and greater intrinsic growth rate, the population density of v is higher than that of u; see Figures 5C, D.

Example 5. In the next example, we consider cases of unequal carrying capacity while u and v diffuse according to K_u and K_v, respectively, where $K_u = M = 2.5 + \sin(\pi x)\cos(\pi y)$, $d_1 \equiv d_2 \equiv 1.0$, $(u_0, v_0) = (0.5, 0.5)$, $r_1 \equiv r_2 \equiv 1.0$ on $\omega = (0, 1) \times (0, 1)$, with $K_v = N = 1.4 + 0.3\sin(\pi x)\sin(\pi y)$ in Figures 6A, B, and $K_v = N = 3.0 + \sin(\pi x)\sin(\pi y)$ in Figures 6C, D. We observe that, in all cases, the species which utilizes more resources survives, and the other tends to extinction as time continues, which is justified theoretically in Theorem A1 and Remark A1, respectively (see Appendix). We also find that the population density of u is higher in the bottom-middle region of the contour plot because the values of $K_u = M$ are higher in this region, whereas the population density of v is higher at the center of the domain, as in $K_v = N$.

Example 6. We now turn to the scenario in a numerical setting where resources are limited and both populations are competing for the same food sources in Figures 7A, B. Here, $K_u = K_v = 0.5 + 0.3\sin(\pi x)\sin(\pi y)$, $M = 0.3 + 0.2\cos(\pi x)\cos(\pi y)$, $N = 0.4 + 0.3\cos(\pi x)\cos(\pi y)$, $(u_0, v_0) = (0.5, 1.75)$, $r_1 \equiv r_2 \equiv 1.0$, $d_1 \equiv d_2 \equiv 1.0$.We find that coexistence only occurs when both species use the resource-based approach to diffusion. This shows that when two species share certain resources, competitive exclusion can be avoided by using a more advantageous dispersal strategy. However, the contour patterns for both u and v mimic the resource functions, whose maximum and minimum are located at the left and right bottom and top corners of the profile regime. In our forthcoming work, the theoretical outcome of this finding will be presented.

Example 7. Assume different non-constant carrying capacities, unequal as in Figures 8A, B $K_u = 2.5 + \cos(\pi x)\cos(\pi y) > K_v = 1.4 + \cos(\pi x)\cos(\pi y)$, or equal as in Figures 8C, D $K_u = K_v = 2.5 + \cos(\pi x)\cos(\pi y)$, where $M = 1.5 + \cos(\pi x)\sin(\pi y)$,

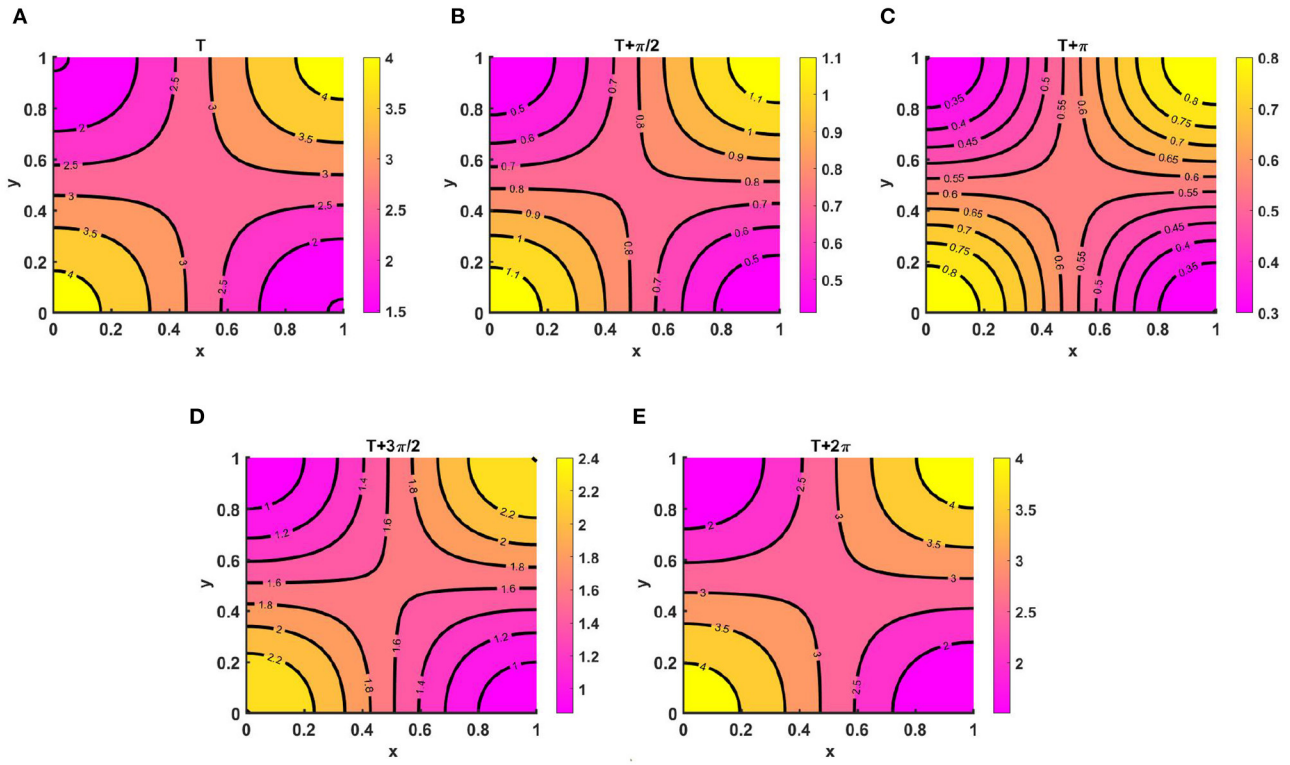

FIGURE 10
Contour plots of $u(t, x, y)$ for (2.1) with $K_u = M = (2.1 + \cos(\pi x)\cos(\pi y))(1.1 + \cos(t)) > K_v = (1.5 + \cos(\pi x)\cos(\pi y))(1.1 + \cos(t))$, $N = (2.0 + \sin(\pi x)\sin(\pi y))(1.2 + \sin(t))$, $r_1 \equiv r_2 \equiv 1.0$, $d_1 \equiv d_2 \equiv 1.0$, $(u_0, v_0) = (0.5, 1.5)$ on $\omega = (0, 1) \times (0, 1)$ at $T = 13.8$ for **(A)** T, **(B)** $T + \frac{\pi}{2}$, **(C)** $T + \pi$, **(D)** $T + \frac{3\pi}{2}$, and **(E)** $T + 2\pi$.

$N = 2.1 + \sin(\pi x)\cos(\pi y)$, $d_1 = 0.1$, $d_2 = 1.0$, $(u_0, v_0) = (0.5, 0.5)$, $r_1 \equiv r_2 \equiv 1.0$ on $\omega = (0, 1) \times (0, 1)$. Here, both species u and v diffuse according to their resource function, which is non-proportional to carrying capacity. Here, the carrying capacity of both species is more prominent in the left and right corners, whereas more resources are found for u in the bottom-left and middle-left regions of the domain and for v in the bottom-middle region and right corner of the contour profile. Nevertheless, we observe that in the case of slow diffusion of u, a higher population density is found at the bottom-left and -right corners of the domain, analogous to K_u. This means that, for small values of the diffusion coefficient, the growth of the species depends on the carrying capacity, and a species that undergoes slow diffusion relative to the other will survive in the competition, as stated in Theorem 3; see Figures 8A, B. In contrast, in Figures 8C, D, we observe that if the carrying capacity of both species is equal, then if the species disperse according to resource distribution, they may coexist with unequal diffusion coefficients. It can also be noted that the population density of u is higher in all cases than that of v, which demonstrates that the species that diffuses slowly can survive in the long run as time continues. As we know, when the species diffusion rate is very high, members of the species have a very hard time finding each other and sustaining the population. Under this scenario, it is also difficult for them to protect one another through cooperative defense. This results in notable decline in the species' growth in competition.

Example 8. Consider the case of $M = 1.6 + \cos(\pi x)\cos(\pi y)$, $N = 1.5 + 0.3\cos(\pi x)\cos(\pi y)$, $K_u = K_v = K = 1.8 + 0.3\sin(\pi x)\sin(\pi y)$, with equal diffusion coefficients and growth rates for both species, where $(u_0, v_0) = (1.95, 0.9)$. Here, in Figures 9A, D we assume $K_u = K_v = K = M + N$ and we observe that coexistence occurrs; this is globally attractive, as stated in Lemma 11, and is known as an ideal free pair. Additionally, in Figures 9B, E we let $M = N + K$ and observe that the population density profile of u is higher compared to that of v and the maximum population densities are found in the middle region or along the saddle point of the contour plot of u which confirms the global existence of $(u^*, 0)$ as stated in Theorem 4. Similarly, in Figures 9C, F we consider $N = M + K$, for which a higher population density is observed found for v, distributed symmetrically, and the population density of u is found to be very low across the entire domain. This ensures the global existence of $(0, v^*)$, as defined in Remark 4, as time continues. Here, in particular, we have focused on $\alpha = \beta = 1.0$.

Next, we consider time-dependent functions to demonstrate the existence of periodic solutions and also analyze the model 2.1 for periodic as well as seasonal changes from an ecological perspective.

Example 9. Figures 10A–E represents the periodic behavior of density profiles for u by considering time-varying functions when

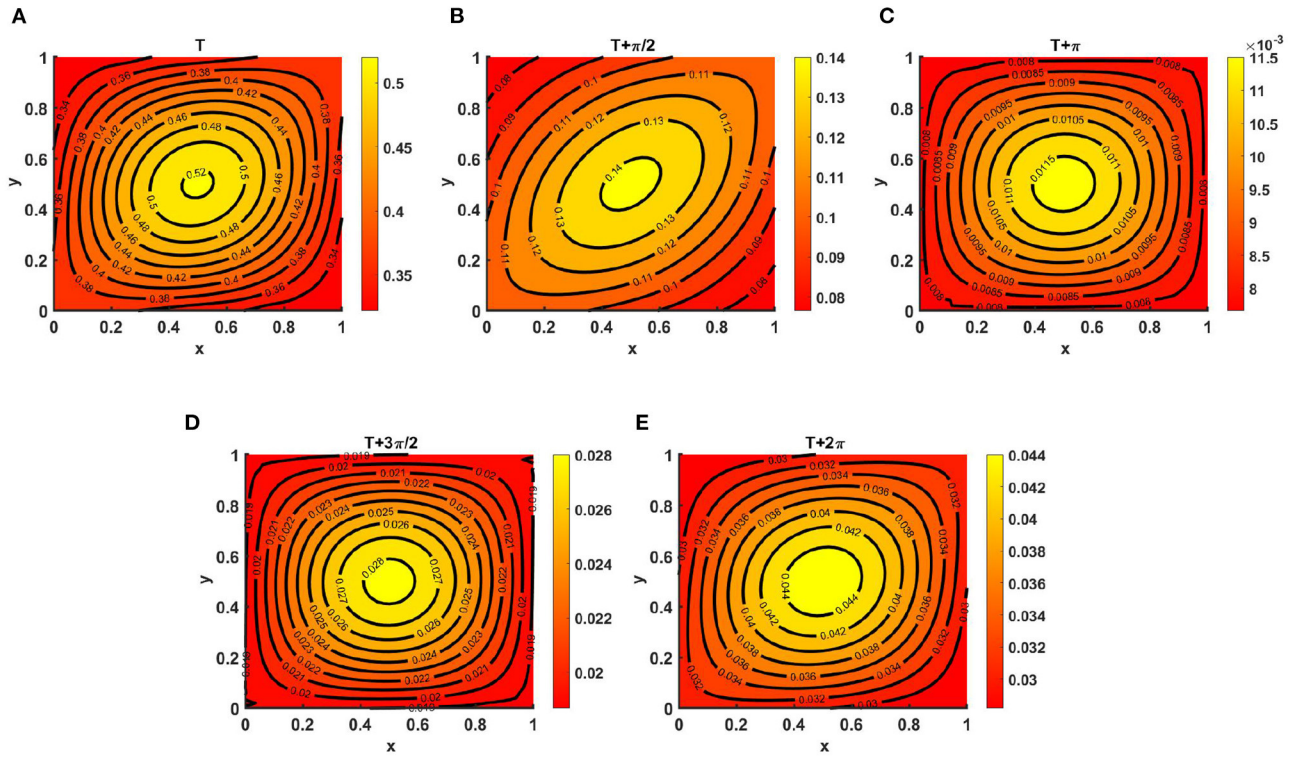

FIGURE 11
Contour plots of $v(t, x, y)$ for (2.1) with $K_u = M = (2.1 + \cos(\pi x)\cos(\pi y))(1.1 + \cos(t)) > K_v = (1.5 + \cos(\pi x)\cos(\pi y))(1.1 + \cos(t))$, $N = (2.0 + \sin(\pi x)\sin(\pi y))(1.2 + \sin(t))$, $r_1 \equiv r_2 \equiv 1.0$, $d_1 \equiv d_2 \equiv 1.0$, $(u_0, v_0) = (0.5, 1.5)$ on $\omega = (0, 1) \times (0, 1)$ at $T = 7.1$ for **(A)** T, **(B)** $T + \frac{\pi}{2}$, **(C)** $T + \pi$, **(D)** $T + \frac{3\pi}{2}$, and **(E)** $T + 2\pi$.

the carrying capacity of two species are unequal, as in $K_u = M = (2.1 + \cos(\pi x)\cos(\pi y))(1.1 + \cos(t)) > K_v = (1.5 + \cos(\pi x)\cos(\pi y))(1.1 + \sin(t))$, $N = (2.0 + \sin(\pi x)\sin(\pi y))(1.2 + \sin(t))$, with equal growth rates and diffusion coefficients for u and v at $T = 13.8$. Here, for non-negative initial population densities $(u_0, v_0) = (1.95, 0.9)$, u disperses according to per-capita carrying capacity, whereas v is distributed according to its time-dependent resource availability function N. As we know, population growth depends on natural resources, water supply, climate change, land, etc. The population will not have access to the same types of resources at all times during a given time interval; as a result, their growth will not be similar everywhere for a certain period. We notice that at $T = 13.6$ and $T = 13.6 + 2\pi$, the population density profiles represent identical values, and the existence of a unique periodic solution is evident with time growth, which ensures the existence of an attractive positive periodic solution.

Example 10. As illustrated in Figure 10, consider the time-dependent functions for $K_u = M > K_v$ (noted in the caption to Figures 11A–E) and N with $d_1 \equiv d_2 \equiv 1.0$ and $r_1 \equiv r_2 \equiv 1.0$. We observed the periodic behavior of v at $T = 7.1$, which is long enough for a time-periodic pattern to emerge. As species v diffuses according to its time-dependent resource function N, the maximum of the density profile is located at the center and is also found to be very low compared to that of u, as stated in Theorem 2, which ensures the global existence of $(K_u, 0)$ as $t \to \infty$.

Example 11. Assume time-dependent functions of the form $M = (1.7 + \sin(\pi x)\cos(\pi y))(1.1 + \sin(t))$ and $N = (1.5 + \cos(\pi x)\sin(\pi y))(1.2 + \sin(t))$, with $d_1 \equiv d_2 \equiv 1.0$, $(u_0, v_0) = (0.6, 0.6)$ on $\omega = (0, 1) \times (0, 1)$, where the carrying capacity of both species is considered to be $K_u = K_v = (2.5 + \cos(\pi x)\cos(\pi y))(1.1 + \sin(t))$. In this case, we observe that there is scope for coexistence in the case of unequal intrinsic growth rates, when the species are distributed according to their available resource functions. Additionally, in the contour plots, we note that for both $r_1 = 1.0 >> r_2 = 0.01$ and $r_1 = 0.01 << r_2 = 1.0$, the maximum value of u is found in the middle of the bottom region, whereas the maximum for v occurs in the left middle region of the contour profiles. As for the case of relatively large and equal diffusion coefficient values, the dispersion of species depends on the resource function, as both species are diffusing in the direction of their resource functions, which is evident in Figures 12A–D.

Example 12. Consider $M = N = (1.5 + \sin(\pi x)\sin(\pi y))(1.1 + \cos(t))$, $r_1 \equiv r_2 \equiv 1.0$ when the carrying capacities of u and v are equal at $K_u = K_v = (2.1 + \cos(\pi x)\cos(\pi y))(1.3 + \cos(t))$ and $(u_0, v_0) = (0.6, 0.6)$ on $\omega = (0, 1) \times (0, 1)$. We observe from Figures 13A, B that, for fixed $d_1 = 1.0$ when $d_2 = 0.1$, species v survives; it is also highlighted here that, for slow diffusion, the growth of the population is dominated by the carrying capacity of the environment. This is evident in Figure 13B, and according to Theorem 5, the global existence of $(0, v^*)$ is clear in the numerical result of Figures 13A, B. On the other hand, when the diffusion

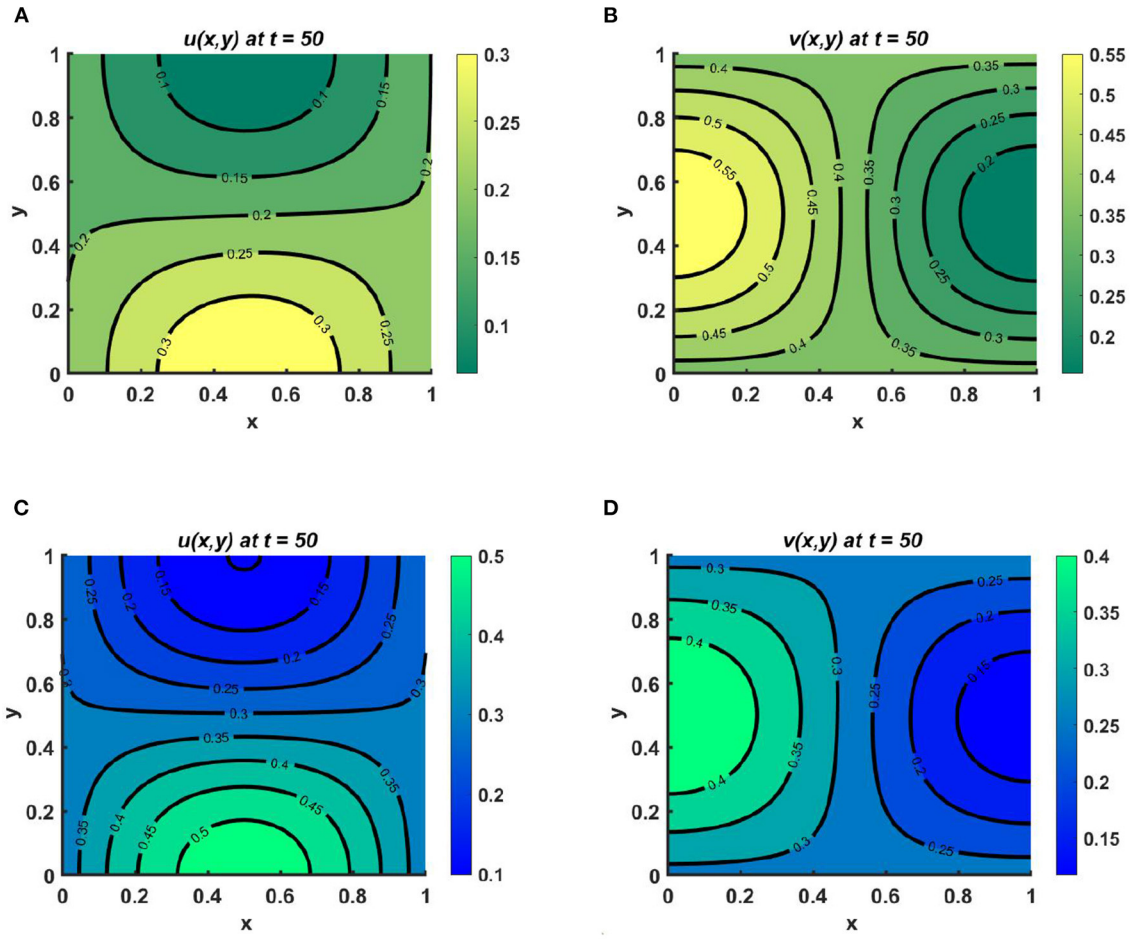

FIGURE 12
Contour plots for (2.1) with $K_u = K_v = (2.5 + \cos(\pi x)\cos(\pi y))(1.1 + \sin(t))$, $M = (1.7 + \sin(\pi x)\cos(\pi y))(1.1 + \cos(t))$, $N = (1.5 + \cos(\pi x)\sin(\pi y))(1.2 + \sin(t))$, $d_1 \equiv d_2 \equiv 1.0$, $(u_0, v_0) = (0.6, 0.6)$ on $\omega = (0, 1) \times (0, 1)$ for **(A, B)** $r_1 = 1.0 >> r_2 = 0.01$, and **(C, D)** $r_1 = 0.01 << r_2 = 1.0$.

coefficients are taken to be $d_1 = 1.0$ and $d_2 = 1.6$—that is, for quite large diffusion coefficient values for both species—the diffusion strategies of u and v will depend on the resource functions M and N. However, the maximum population density is found at the center, which is analogous to result for the function $M = N$, and in this situation, it can also be noted that coexistence is also possible for non-trivial initial population densities on the domain.

7. Conclusion

In this paper, we have reported on the design of a model of competition between a pair of species, in which both species are modeled according to their resource function, which we expect to be more realistic in some scenarios than in others. We examined the global existence of solutions to the model for cases of two species with unequal carrying capacity. We have also considered cases of different dispersion strategies for the two species based on their resource function and carrying capacity. We found that when the resource function is non-proportional to carrying capacity for one species while members of the other are diffusing according to their carrying capacity, the species that consumes more resources will survive in the competition (see Figure 2). However, for the case of both species adopting the same diffusion strategy, while the resource function varies, coexistence is not possible unless the entire environment is homogeneous, which is also valid for the case of proportionality (see Figure 6). The global existence of competitive exclusion in the model is also found to obtain when the carrying capacities and migration strategies of both species are the same, directed toward the individual resource function (see Figure 6). We have also found, based on numerical investigation, that the intrinsic growth rate can play an important factor in population growth for populations that may coexist whether or not resource distributions are unequal (see Figure 5). However, if the competing species select identical dispersal strategies, and dispersal is not proportional to carrying capacity, it appears that the effect of a higher migration rate is to impact the growth rate of the species negatively (see Figure 8). In contrast, an elevated intrinsic growth rate is an optimistic sign that a species may survive in competition (see Figure 4). The temporal and periodic effects on species growth rate that may occur due to seasonal changes have also been illustrated numerically here via contour plots for the

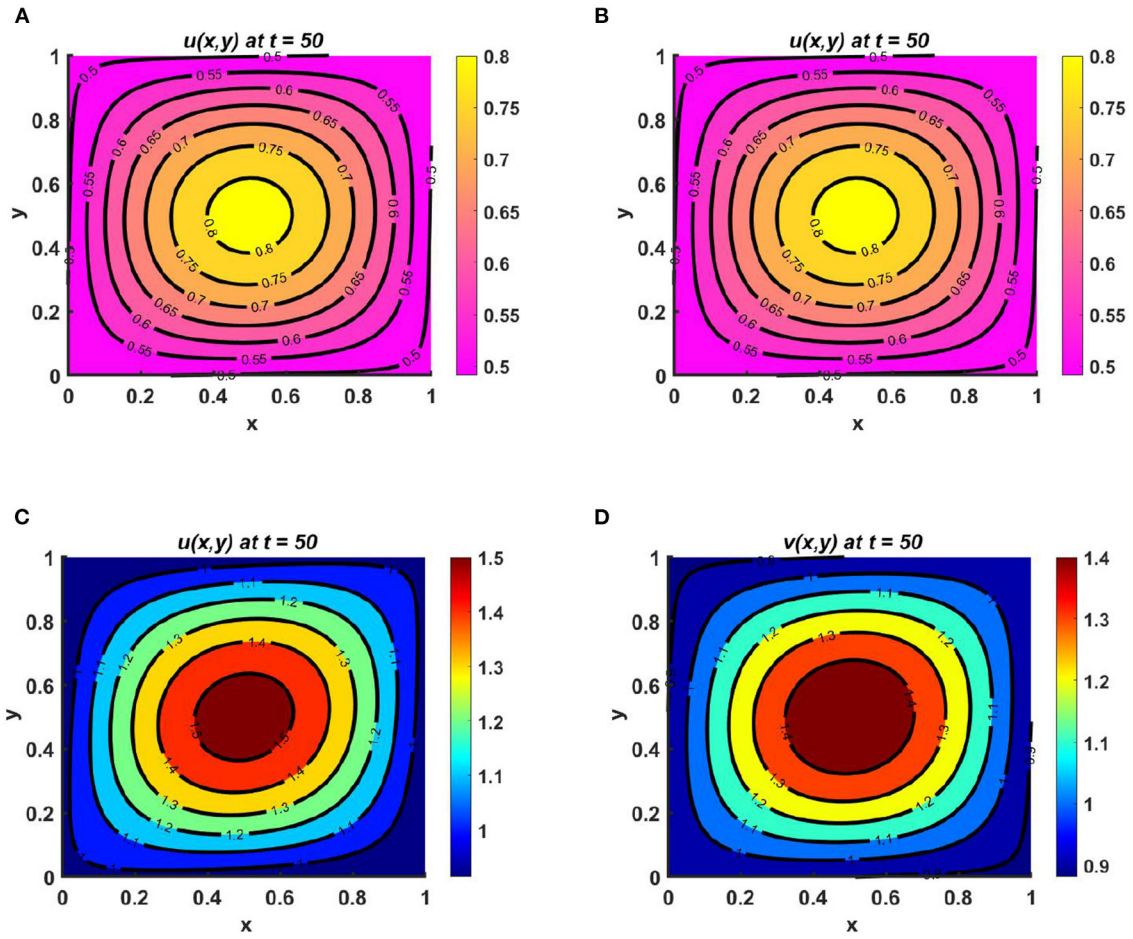

FIGURE 13
Contour plots for (2.1) with $K_u = K_v = (2.1 + \cos(\pi x)\cos(\pi y))(1.3 + \cos(t))$, $M = N = (1.5 + \sin(\pi x)\sin(\pi y))(1.1 + \cos(t))$, $r_1 \equiv r_2 \equiv 1.0$, $d_1 = 1.0$, $(u_0, v_0) = (0.6, 0.6)$ on $\omega = (0, 1) \times (0, 1)$ for **(A, B)** $d_2 = 0.01$, and **(C, D)** $d_2 = 1.6$.

model; these plots demonstrate the advantage of selecting different diffusion strategies. The results of the current study can be extended by considering cases of three competing species in symmetric competition. Additionally, harvesting effects could be included in the model in order to show the outcomes for the stability of two competing species in a heterogeneous environment. Finally, one could also study the modified problem for the cases of anomalous diffusion, nonergodicity, and Brownian motion for heterogeneous populations [31, 32].

Data availability statement

The original contributions presented in the study are included in the article/Supplementary material, further inquiries can be directed to the corresponding author.

Author contributions

MK and IZ: conceptualization, software, and formal analysis. IZ, TK, and MK: methodology. IZ: validation, data curation, and original draft preparation. MA and MS: investigation. MA and TK: resources. MK, MS, TK, and MA: review and editing. MK: supervision. All authors have read and agreed to the published version of the manuscript.

Funding

The work by MK was partially supported by the University Grants Commission (UGC) and by the Bose Center for Advanced Study and Research in Natural Sciences, University of Dhaka.

Acknowledgments

The authors acknowledge the reviewers for their comments and suggestions, which significantly improved the quality of the manuscript.

Conflict of interest

The authors declare that the research was conducted in the absence of any commercial or financial relationships that could be construed as a potential conflict of interest.

Publisher's note

All claims expressed in this article are solely those of the authors and do not necessarily represent those of their affiliated organizations, or those of the publisher, the editors and the reviewers. Any product that may be evaluated in this article, or claim that may be made by its manufacturer, is not guaranteed or endorsed by the publisher.

Supplementary material

The Supplementary Material for this article can be found online at: https://www.frontiersin.org/articles/10.3389/fams.2023.1157992/full#supplementary-material

References

1. Conser C. Reaction-diffusion equations and ecological modelling. In: Friedman AA, editor. Book Chapter of the Book: (Evolution and Ecology). Berlin; Heidelberg: Springer (2008).

2. Dockery J, Hutson V, Mischaikow K, Pernarowski M. The evolution of slow dispersal rates: a reaction diffusion model. *J Math Biol*. (1998) 37:61–83. doi: 10.1007/s002850050120

3. Belgacem F, Cosner C. The effects of dispersal along environmental gradients on the dynamics of populations in heterogeneous environment. *Can Appl Math Quart*. (1995) 3:379–97.

4. Cantrell RS, Cosner C, Lou Y. Advection-mediated coexistence of competing species. *Proc R Soc Edinburgh Sect A*. (2007) 137:497–58. doi: 10.1017/S0308210506000047

5. Cantrell RS, Cosner C. *Spatial Ecology via Reaction-Diffusion Equations*. Wiley Series in Mathematical and Computational Biology. Chichester: John Wiley & Sons (2003).

6. Williams S, Chow P. Nonlinear reaction-diffusion models for interacting population. *J Math Anal Appl*. (1978) 62:157–9. doi: 10.1016/0022-247X(78)90227-5

7. Cantrell RS, Cosner C, Lou Y. Approximating the ideal free distribution via reaction-diffusion-advection equations. *J Differ Eq*. (2008) 245:3687–703. doi: 10.1016/j.jde.2008.07.024

8. Chakraborty S, Tiwari PK, Misra AK, Chattopadhyay J. Spatial dynamics of a nutrient phytoplankton system with toxic effect on phytoplankton. *Math Biosci*. (2015) 264:94–100. doi: 10.1016/j.mbs.2015.03.010

9. Chakraborty SP, Tiwari K, Sasmal SK, Biswas S, Bhattacharya S, Chattopadhyay J. Interactive effects of prey refuge and additional food for predator in a diffusive predator-prey system. *Appl Math Model*. (2017) 47:128–40. doi: 10.1016/j.apm.2017.03.028

10. Braverman E, Braverman L. Optimal harvesting of diffusive models in a non-homogeneous environment. *Nonlinear Anal Theory Methods Appl*. (2009) 71:e2173–81. doi: 10.1016/j.na.2009.04.025

11. Korobenko L, Braverman E, A. logistic model with a carrying capacity driven diffusion. *Can Appl Math Quart*. (2009) 17:85–104.

12. Zahan I, Kamrujjaman M, Alim M, Mohebujjaman M, Khan T. Dynamics of heterogeneous population due to spatially distributed parameters and an ideal free pair. *Front Appl Math Stat*. (2022) 8:949585. doi: 10.3389/fams.2022.949585

13. Korobenko L, Braverman E. On evolutionary stability of carrying capacity driven dispersal in competition with regular diffusing populations. *J Math Biol*. (2014) 69:1181–206. doi: 10.1007/s00285-013-0729-8

14. Braverman E, Kamrujjaman M. Competitive-cooperative models with various diffusion strategies. *Comput Math Appl*. (2016) 72:653–62. doi: 10.1016/j.camwa.2016.05.017

15. Braverman E, Kamrujjaman M. Lotka systems with directed dispersal dynamics: Competition and influence of diffusion strategies. Math Biosci. (2016) 279:1–12. doi: 10.1016/j.mbs.2016.06.007

16. Oesterheld M, Semmartin M. Impact of grazing on species composition: adding complexity to a generalized model. Austral Ecol. (2011) 36:881–90. doi: 10.1111/j.1442-9993.2010.02235.x

17. Follak S, Strauss G. Potential distribution and management of the invasive weed Solanum Carolinense in Central Europe. *Weed Res*. (2010) 50:544–52. doi: 10.1111/j.1365-3180.2010.00802.x

18. Saether BE, Lillegard M, Groton V, Derever MC, Engen S, Nudds TD, et al. Geographical gradients in the population dynamics of North-America Prairie ducks. *Anim Ecol J*. (2008) 77:869–82. doi: 10.1111/j.1365-2656.2008.01424.x

19. Cantrell RS, Cosner C, Lou Y. Evolution of dispersal and the ideal free distribution. *Math Biosci Eng*. (2010) 7:17–36. doi: 10.3934/mbe.2010.7.17

20. Braverman E, Kamrujjaman M, Korobenko L. Competitive spatially distributed population dynamics model: does diversity in diffusion strategies promote coexistance? *Math Biosci*. (2015) 264:63–73. doi: 10.1016/j.mbs.2015.03.004

21. Kamrujjaman M. Directed vs. regular diffusion strategy: evolutionary stability analysis of a competition model and an ideal free pair. *Differ Eq Appl*. (2019) 11:267–90. doi: 10.7153/dea-2019-11-11

22. Kamrujjaman M. Interplay of resource distributions and diffusion strategies for spatially heterogeneous populations. *J Math Model*. (2019) 7:175–98. doi: 10.22124/jmm.2019.11734.1208

23. Zahan I, Kamrujjaman M, Tanveer S. Mathematical study of a resource-based diffusion model with Gilpin Ayala growth and harvesting. *Bull Math Biol*. (2022) 84:1202022. doi: 10.1007/s11538-022-01074-8

24. Pao CV. Nonlinear Parabolic and Elliptic Equations. New York, NY: Plenum (1992).

25. Smith HL. Monotone dynamical systems: an Introduction to the theory of competitive and cooperative system. Am Math Soc. (2008) 41. doi: 10.1090/surv/041

26. Lam KY, Liu S, Lou Y. Selected topics on reaction-diffusion-advection models from spatial ecology. *Math Appl Sci Eng*. (2020) 1:150–80. doi: 10.5206/mase/10644

27. Korobenko L, Kamrujjaman M, Braverman E. Persistence and extinction in spatial model with a carrying capacity driven diffusion and harvesting. *J Math Anal Appl*. (2013) 399:352–68. doi: 10.1016/j.jmaa.2012.09.057

28. Dancer EN. Positivity of maps and applications. *Topol Nonlinear Anal*. (1995) 15:303–40. doi: 10.1007/978-1-4612-2570-6_4

29. Hsu S, Smith H, Waltman P. Competitive exclusion and coexistence for competitive systems on ordered Banach spaces. *Trans Am Math Soc*. (1996) 348:4083–94. doi: 10.1090/S0002-9947-96-01724-2

30. Gilbarg D, Trudinge NS. Elliptic Partial Differential Equations of Second Order. 2nd ed. Berlin: Springer (1983).

31. Wang W, Cherstvy AG, Liu X, Metzler R. Anomalous diffusion and nonergodicity for heterogeneous diffusion processes with fractional Gaussian noise. *Phys Rev E*. (2020) 102:012146. doi: 10.1103/PhysRevE.102.012146

32. Wang W, Cherstvy AG, Kantz H, Metzler R, Sokolov IM. Time averaging and emerging nonergodicity upon resetting of fractional Brownian motion and heterogeneous diffusion processes. *Phys Rev E*. (2021) 104:024105. doi: 10.1103/PhysRevE.104.024105

frontiers | Frontiers in Ecology and Evolution

TYPE Original Research
PUBLISHED 17 July 2023
DOI 10.3389/fevo.2023.1200268

OPEN ACCESS

EDITED BY
Md. Shahidul Islam,
University of Dhaka, Bangladesh

REVIEWED BY
Blai Vidiella,
Spanish National Research Council (CSIC), Spain
Arnaud Zlatko Dragicevic,
Chulalongkorn University, Thailand

*CORRESPONDENCE
Lan Wang
wanglan-8722@hotmail.com

RECEIVED 04 April 2023
ACCEPTED 23 June 2023
PUBLISHED 17 July 2023

CITATION
Bai Y, Wang L and Yuan X (2023) Pesticide control, physical control, or biological control? How to manage forest pests and diseases more effectively.
Front. Ecol. Evol. 11:1200268.
doi: 10.3389/fevo.2023.1200268

Pesticide control, physical control, or biological control? How to manage forest pests and diseases more effectively

Yuntao Bai[1], Lan Wang[2*] and Xiaolong Yuan[1]

[1]Business School, Shandong Management University, Jinan, China, [2]Center of Emergency Management, Chongqing Academy of Governance, Chongqing, China

The frequent occurrence of forest diseases and insect pests has a significant impact on the forest ecosystem. The government needs to take measures to protect the forest ecosystem. The common management modes for forest pests and diseases include pesticide control, physical control, and biological control. In the process of governance, governments need to consider not only cost-effectiveness but also the impact on the ecosystem. In this article, the differential game model under these three modes is constructed, and the equilibrium results are compared and analyzed. Finally, the research conclusion is drawn that under the biological control mode, the income generated by the unit control quantity is inversely proportional to the balanced control quantity. However, under pesticide control and physical control modes, the revenue generated by the unit control quantity is proportional to the balanced control quantity. At the same time, under the biological control mode, the unit governance cost is proportional to the balanced control quantity. Under the pesticide control and physical control modes, the unit control cost is inversely proportional to the balanced control quantity. Social forces tend to adopt pesticide control. The government prefers physical control.

KEYWORDS

forest pest, differential game, control, different modes, social benefit

1 Introduction

1.1 Background and research significance

The world's total forest area is 4.06 billion hectares (ha), or 31% of the total land area (Food and Agricultural Organization, 2020). Forests are also home to many kinds of animals and many kinds of plants. It is the most biologically active region on Earth. Forests have the functions of producing oxygen, purifying air, regulating climate, and maintaining ecological balance. Forests regulate the air and water in nature and affect climate change. At the same time, forests provide various resources for human production and life. It has played a vital role in the reproduction and survival of human civilization.

In recent years, due to the influence of human activities, the global temperature has kept rising. This causes the forest ecosystem to lose balance. This provides climatic support for forest pests to thrive. This gradually increasing temperature is suitable for the propagation and spread of forest pests. The occurrence of pests and diseases seriously endangers the health of forests. The destruction of forest ecosystems is also increasing. If the forest ecosystems are destroyed, it will cause the temperature to rise further, which will aggravate forest pests and diseases. At the same time, the world's human afforestation area keeps increasing (Bai et al., 2021). Compared with natural forests, artificial forests have the following characteristics: higher density, fewer species, and more artificial intervention. Due to limited attention to adverse environmental impacts, plantation forests are devoted almost exclusively to wood production (Dragicevic, 2019a). Therefore, plantation forests are more susceptible to pests and diseases. Strengthening the management of forest pests and diseases has become the focus of ecosystem protection.

In order to deal with forest pests and diseases, multiple approaches to management are needed. This requires the participation of the government and social forces in society. The "social power" of forest pest management refers to the support and participation of nongovernmental organizations from all aspects of society. It includes the active actions and efforts of enterprises, nongovernmental organizations, the media, academia, and the public. These forces can contribute to the management of forest pests and diseases by developing regulations, promoting pest prevention technologies and innovations, conducting information and education on forest pest control, and implementing environmental regulation (Lei et al., 2021). Government and social forces can spray pesticides in forests, set up physical facilities, release natural enemies, and invest in bioeconomic activities that are less susceptible to pests and diseases (Dragicevic, 2019b). These methods can effectively control forest pests and diseases. Although the increase in forest pests and diseases in recent years is mainly due to global temperature rise and other factors, the solution to global temperature rise cannot be achieved overnight (Tandon and Verma, 2021). Instead, more effective results can be achieved using direct measures to control forest pests and diseases. At the same time, in the process of managing forest pests and diseases, governments and social forces should not only consider cost-effectiveness but also try their best to protect forest ecosystems. How to choose an effective management mode for forest pests and diseases and protect forest resources is an important issue in this article.

1.2 Literature review

The causes of forest pests and diseases are varied. For example, Ayres and Lombardero (2018) believe that the main causes of forest diseases and pests are global climate change, land use, and biological distribution. Popkin (2020) believes that the invasion of foreign pests is the main cause of forest diseases and insect pests in the USA. Canelles et al. (2021) believed that pests and diseases in one forest were mainly transmitted by other forests. Jentsch et al. (2020) believed that wood transportation is an important cause of forest diseases and insect pests. These scholars explained the causes of forest pests, mainly global climate change, natural invasion of pests, human-caused invasion, and other factors.

Some scholars have mainly studied the effects of forest pests and diseases. For example, Ozkan (2022) believed that forest diseases and insect pests could lead to a continuous reduction of forest area. Turner et al. (2007) believed that forest pests and diseases could have adverse effects on the foreign trade of wood. Niquidet et al. (2015) believed that the effects of some diseases and pests could be controlled, while others would have persistent and disastrous effects. These scholars mainly analyzed the natural impact, economic impact, and time span of the impact of forest pests and diseases.

Some scholars have mainly studied how to control forest pests and diseases. For example, Yang et al. (2014) studied the weather hostility of pests, which plays a significant role in the control of forest pests. Sheremet et al. (2018) studied how to introduce corresponding policies to encourage private forest owners to participate in forest pest control. Lovett et al. (2016) believed that it was necessary to control the circulation channels of wood products. These scholars analyzed how to manage forest pests and diseases mainly from the perspectives of biological control, national policies, and logistics management.

In order to make up for the shortcomings of the above studies, this article studied how to protect the forest ecosystem from the perspective of different forest pest management modes. The management modes of common forest pests and diseases are mainly divided into pesticide management, physical management, and biological management. In this article, based on setting the corresponding assumptions and defining the parameters of the model, three kinds of differential game models are established. The HJB formula is then used to solve the differential game model. This article obtains the optimal governance quantity and social utility of government and social forces. Comparative analysis of social utility is carried out through numerical analysis. Finally, this article discusses the relevant conclusions. In this article, the factors influencing the amount of forest pest management and the applicable scope of different forest pest control modes are identified.

1.3 Problem description

Rising global temperatures are causing serious forest pests and diseases. The effective control of forest diseases and insect pests by the government can protect forest resources. It is very important to promote the development of forestry and maintain the balance of natural ecology. In order to clearly depict the problems of forest pests and diseases that exist all the time, this article uses a differential game, which is a game with continuous time. Pesticide control tends to damage ecosystems and lead to pest resistance, but it is low-cost and has quick results. Physical containment facilities can be reused, but they are costly and vulnerable to extreme weather. Biological control can better protect the ecosystem, but introduced natural enemies are prone to problems of adaptability and infestation.

Game theory explores what strategies each player should adopt in different situations and the consequences and effects of these strategies (Valizadeh and Gohari, 2021). There are players in game

theory. This article divides the game players into government and social forces. When there are several governments in reality, two governments can be discussed separately according to the method and conclusion of this article to get the desired result. In order to effectively control forest pests and diseases, government and social forces can adopt the following three control modes:

(1) Pesticide control. There are many kinds of pesticides, and the pesticides referred to in this article mainly refer to chemical pesticides. Compared with biological pesticides, chemical pesticides have the advantages of high efficacy and an immediate effect. In controlling forest pests, pesticides with good control effects should be selected according to the characteristics of the control objects. This can achieve targeted, tailored medicine, which is the key to good prevention and control effects. In the process of pesticide control, it is necessary to choose the weakest stage of pest development to control. In this way, pesticides can be used to achieve the best control effect. However, this type of management can also adversely affect natural enemies of forest pests (Palma-Onetto et al., 2021).

(2) Physical control. This method of prevention and control begins by placing a certain number of mechanical facilities. It mainly includes artificial killing, the use of simple devices and instruments, and even the application of modern devices and equipment. Some forest pests are sensitive to radiation, sound, electricity, light, temperature, and other physical factors. Physical management mainly uses the sensitivity of forest pests to eliminate forest pests. For example, light trapping is a physical way to control pests. This is mainly to take advantage of the phototaxis of some forest pests and then artificially set up insect lights. The trap light can be used to trap and kill pests. The use of light to induce killing is one of the most common physical control measures.

(3) Biological control. This method of control is mainly based on biological control of forest pests. Natural enemies of forest pests mainly include natural enemies of insects, microorganisms, birds, and so on. The natural enemies of insects are mainly bees, ladybugs, praying mantises, and so on. Microorganisms mainly refer to bacteria, fungi, and viruses. Birds are mainly cuckoos, woodpeckers, great tit, and so on. In addition, another approach is to cultivate plants that possess natural resistance to invasive species without necessarily being their natural enemies (Dragicevic, 2015). Biological control has a certain effect on pest control and is economical (Janssen and Rijn, 2021). At the same time, the organisms themselves can reproduce, so this method also has the characteristics of environmental protection and efficiency. Biological control is one of the important methods of forest pest control.

The relationship between the three forest pests and disease control modes is shown in Figure 1.

In Figure 1, there are two players (the government and social forces) and three forest pest and disease control modes. In order to maximize their own benefits, each player can choose the forest pest and disease control mode to be adopted. The arrows in the figure show that the players are constantly choosing between different forest pests and disease control modes.

2 Methodology

2.1 Hypothesis

(1) The pest management decisions of the government and social forces are constantly changing. With the increase in global temperature, the propagation and spreading ability of forest pests are further enhanced. In the absence of natural enemies, once the

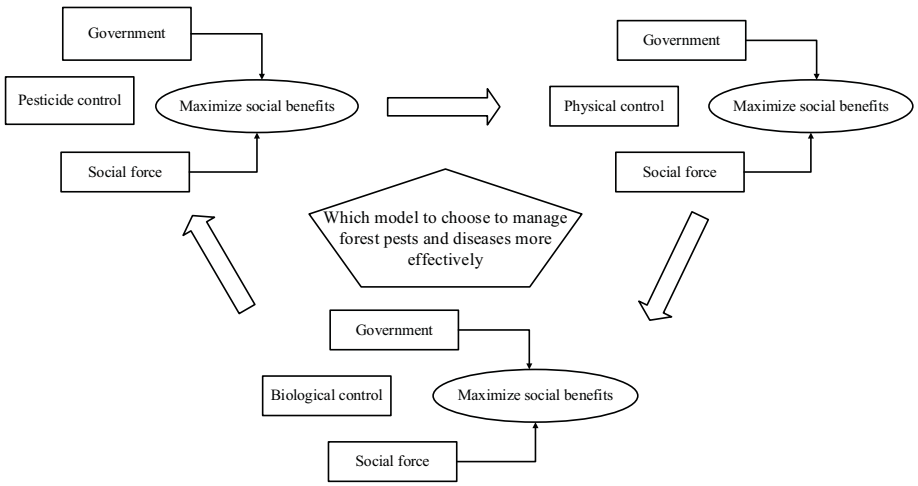

FIGURE 1
Relationship between three different forest pests and disease control modes.

forest is infected by pests and diseases, it is easy to spread such pests throughout the forest. In the face of the destruction of the forest ecosystem, the government and social forces will carry out forest pest control. After a period of management, forest pests and diseases have been reduced. At this point, the government and social forces will reduce the intensity of governance. The severity of forest pests and diseases has increased as they have been neglected. At this time, the government and social forces will increase efforts to control pests and diseases. Over time, the cycle continues. Forest pest management decisions by governments and social forces are in flux.

(2) The government and social forces can fully grasp the information about forest pests and diseases. There are many kinds of forest pests. Forests are infested by many kinds of pests and diseases. If forest pests and diseases are not dealt with in time, large areas of forest are likely to be affected. In some cases, governments do not understand some exotic insects and cannot make timely decisions conducive to forest pest management (Pirtle et al., 2021). In other cases, monitoring and early warning agencies of the government and social forces are located far from forest pests and diseases. This is not conducive to government and social forces grasping information about forest pests. In order to enable government and social forces to make optimal decisions, this article assumes that government and social forces have comprehensive access to forest pest and disease information.

(3) The forest ecosystem has an important impact on national production and management activities. Forests can conserve water, conserve soil, sequester carbon, release oxygen, and purify the atmosphere (Food and Agricultural Organization, 2020). If the forest is far from a densely populated area, then forest pests and diseases have less impact on people's lives and production and management activities. When pests and diseases occur in an area, the government does not take measures to control them. That is because forest pests and diseases cost money to control. On the other hand, if the forest is close to the country's population concentration, people will be more affected when the forest is destroyed. At this time, people will be concerned about the state of the forest ecosystem.

2.2 Variable definition

In Table 1, the discount factor ρ is a number used to calculate the value of future cash flows at the current point in time. It is a tool that reduces future cash flows to the current point in time in order to calculate the value of time. Decay of reputation δ is the process by which, over time, the quality of the reputation earned by governments and social forces as a result of environmental protection gradually declines. The decay of reputation is a natural phenomenon as people's perceptions and attitudes towards things change and evolve over time. At the same time, for governments and social forces, there can be unexpected events or negative news, which can affect the quality of their environmental reputation. The management of forest pests and diseases can protect forest resources, improve forest economic benefits, and stop the deterioration of the ecological environment. In this article, the

TABLE 1 Definition of variables and parameters used in this article.

Variables and parameters	Specific meaning
$Y = \{P, H, B\}$	Three modes of forest pest management (pesticide control, physical control, biological control)
Independent variable	
$F_{Y1}(t)$	Government control amount under forest pest control mode Y
$F_{Y2}(t)$	The number of social forces under the forest pest control mode Y
$x_{Y1}(t)$	The government's reputation under the forest pest control mode Y
$x_{Y2}(t)$	The social forces' reputation under the forest pest control mode Y
Parameter	
ρ	The discount rate occurring over time, $0 \le \rho \le 1$
δ	Decay of reputation, $\delta > 0$
b_F	The income derived from the amount of management per unit, $b_F > 0$
d	Drug resistance in forest pests, $d > 0$
k_d	The influence coefficient of pest resistance on the difficulty of control, $k_d > 0$
c_P, c_H, c_B	Unit cost of forest pest control, c_P, c_H, $c_B > 0$
c_E	Damage degree of forest ecosystem caused by unit pesticide control amount, $c_E > 0$
c_m	The added cost of inadaptability of introduced organisms, $c_m > 0$
c_o	The increased costs associated with the proliferation of introduced organisms, $c_o > 0$
k_m	Coefficient of inadaptation of introduced organisms, $k_m > 0$
k_o	Coefficient associated with the influx of introduced organisms, $k_o > 0$
s	Rate of forest pest control, $s > 0$
k_s	The effect of unit control rate, $k_s > 0$
l	The positive effect of the reputation of control or social power on earnings, $l > 0$
I_H	The positive impact of physical control on reputation, $I_H > 0$
I_E	The positive impact of biological control on reputation, $I_E > 0$
p	The proportion of subsidies to social forces, $p > 0$
a_F	Positive effect of unit forest pest control amount on reputation, $a_F > 0$
a_E	Unit number of ecological damage to the negative impact on reputation, $a_E > 0$
e_H	The number of extreme weather events, $e_H > 0$
k_e	Impact of each extreme weather event on pest management facilities, $k_e > 0$

(Continued)

TABLE 1 Continued

Variables and parameters	Specific meaning
α	The number of times physical facilities are reused, $\alpha > 0$
k_α	The impact of reuse on governance costs, $k_\alpha > 0$
Function	
$J_{Y1}(t)$	Government's social welfare function under forest pest control mode Y
$J_{Y2}(t)$	Social welfare function of social forces under forest pest control mode Y
$V_{Y1}(t)$	Government benefit function under forest pest control mode Y
$V_{Y2}(t)$	Benefit function of social forces in forest pest control mode Y

income obtained from the unit management volume is defined as b_F. Under the long-term application of insecticides, the genetic variation of pests gradually weakens their virulence to insecticides and eventually cannot be effectively controlled by insecticides. This article defines this resistance of pests as d. Once forest pests have resistance, it will increase the difficulty of controlling them, which is defined as k_d.

Each mode of forest pest management has a cost. In this article, the cost of forest pest management at the unit level is defined as c_P, c_H, c_B, respectively. Once a forest is infested with pests and diseases, it is difficult to fully recover. On the contrary, there is a certain control rate for forest pests and diseases. This article defines the control rate as s. The reputation of the government and social forces will enhance the image of the country, enhance the sense of trust and support among the people in the country, and so on. This article defines the unit impact of this reputation as l. Compared with pesticide management of forest pests and diseases, physical control and biological control can play a better role in protecting the environment. These two control modes can have an additional impact on reputation, which this article defines as $I_H$and I_E. Social forces are mainly non-governmental organizations. These organizations are often underfunded. These organizations usually receive a certain amount of subsidy in the process of managing forest pests and diseases. This article defines the proportion of these subsidies as p. Extreme weather (such as typhoons, rainstorms, heat waves, hail, etc.) will affect the effectiveness of forest pest management. In this article, the occurrence times of forest pests and diseases are defined as e_H. The impact coefficient of these extreme weather events on forest pest management facilities is k_e. Physical facilities for forest pest management (e.g., trap lights, slime boards, bark strips, infrared detectors, etc.) can be reused. The number of times these physical facilities are reused is defined as α. The number of reuses affects the cost of managing forest pests and diseases. The impact of repeated use of these physical facilities on governance costs is defined as k_α.

The social welfare function is a tool used to measure the level of social welfare. This function is the sum of utility values over a period of time to represent social welfare over that period of time. Social benefit refers to the benefits or values generated by society under a certain decision made at a certain point. These effects can be positive, negative, or neutral. This article defines the social welfare function as J. At the same time, this article defines social benefits as V.

2.3 Differential games of different forest pest control modes

The differential game has the goal of optimizing the independence and conflict of each player and can finally obtain the strategy of each player as it evolves over time and reaches the Nash equilibrium. At present, the differential game is mainly applied in the fields of advertising decisions (Viscolani and Zaccour, 2009), logistics management (Bai et al., 2022), supply chain (Zhu et al., 2021), etc. Meanwhile, some scholars also use differential games to study the field of forest protection (Fredj et al., 2004).

In the context of differential games, the strategies adopted by the government and social forces are time-dependent functions. The actions taken by each participant are influenced by the strategies employed by other participants, leading to an ongoing evolutionary process wherein participants search for optimal strategies. This dynamic interaction can be described using differential equations that capture the rate of change in the relationship between variables, typically with respect to time or space variables (Arnone et al., 2022). In the specific context of this study, both forest pests and diseases, as well as the decisions made by the government and social forces, are subject to constant change. Therefore, the application of differential game theory is highly relevant and suitable.

When compared to alternative methods such as differential equations or stochastic strategies, differential games exhibit strong applicability in this study. While differential equations fail to account for the strategic interactions and outcomes among decision-makers, differential games effectively capture the conflicts and cooperation that occur between the government and social forces in the context of forest pest management. On the other hand, stochastic game models focus primarily on probability information regarding potential future events, emphasizing randomness rather than the continuous nature of time (Wu and Zhang, 2022). As such, the applicability of stochastic strategies in this paper is limited.

Forest pests and diseases are constantly changing with the changing climate. At the same time, forest pests and diseases will be constantly changed by the governance decisions of governments and social forces. In order to describe this change clearly, this article uses differential games to study forest pest management.

In the mode of pesticide control of forest pests and diseases, the social benefits obtained by the government and social forces are composed of the benefits of pest control, economic costs, ecological costs, and reputation gained. The specific expression can be expressed as:

$$J_{P1} = \int_0^{\infty} \left[b_F F_{P1}(t) \frac{1}{\ln(e + k_d d)} - \frac{c_P}{2} F_{P1}^2(t) - \frac{c_E}{2} F_{P1}^2(t) + l x_{P1}(t) \right] e^{-\rho t} \mathrm{d}t \quad (1)$$

$$J_{P2} = \int_0^{\infty} \left[b_F F_{P2}(t) \ln(e + k_s s) - \frac{c_P}{2}(1-p) F_{P2}^2(t) + l x_{P2}(t) \right] e^{-\rho t} \mathrm{d}t \quad (2)$$

In the above formula, $b_F F_{P1}(t) \frac{1}{\ln(e+k_d d)}$ represents the benefit to the government from the pesticide control mode. $\ln(e + k_d d)$ represents the development of resistance to pesticides by forest pests. $\frac{c_P}{2} F_{P1}^2(t)$ represents how much it costs the government to buy pesticides. $\frac{c_E}{2} F_{P1}^2(t)$ represents the negative impact of pesticide use on the ecological environment. $l x_{P1}(t)$ represents the positive effect of a government's reputation on the social good. $b_F F_{P2}(t) \ln(e + k_s s)$ represents the benefits to social forces in the pesticide control mode. $\frac{c_P}{2}(1-p) F_{P2}^2(t)$ represents the cost of social forces under the pesticide control mode. $\frac{c_P}{2} p F_{P2}^2(t)$ represents government subsidies accepted by social forces. $l x_{P2}(t)$ represents the positive effect of the reputation of social power on social good.

Under the pesticide control mode, the changes in reputation gained by the government are as follows:

$$\dot{x}_{P1}(t) = (a_F - a_E) F_{P1}(t) - \delta x_{P1}(t) \quad (3)$$

Under the pesticide control mode, the changes in reputation gained by the social power are as follows:

$$\dot{x}_{P2}(t) = a_F F_{P2}(t) - \delta x_{P2}(t) \quad (4)$$

In the above formula, $a_F F_{P1}(t)$ shows the government's reputation increased in the pesticide control mode. $a_E F_{P1}(t)$ shows the government's reputation that is destroyed and reduced by biological diversity. $\delta x_{P1}(t)$ shows the attenuation of the government's reputation. $a_F F_{P2}(t)$ shows the reputation of social forces in biological control modes. $\delta x_{P2}(t)$ shows the attenuation of the reputation of social forces.

In the mode of physical control of forest diseases and insect pests, the social benefits obtained by the government and social forces are:

$$J_{H1} = \int_0^{\infty} \left[\frac{b_F}{1 + k_e e_H} F_{H1}(t) - \frac{c_H}{2} \ln(1 + k_\alpha \alpha) F_{H1}^2(t) + l x_{H1}(t) \right] e^{-\rho t} \mathrm{d}t \quad (5)$$

$$J_{H2} = \int_0^{\infty} \left[b_F F_{H2}(t) \ln(1 + k_s s) - \frac{c_H}{2}(1 + k_\alpha \alpha)(1-p) F_{H2}^2(t) + l x_{H2}(t) \right] e^{-\rho t} \mathrm{d}t \quad (6)$$

In the above formula, $\frac{b_F}{1+k_e e_H} F_{H1}(t)$ means the government gain under the physical control of forest pests. $1 + k_e e_H$ means the adverse effects of extreme weather on physical facilities. $\frac{c_H}{2} \ln(1 + k_\alpha \alpha) F_{H1}^2(t)$ means government governance costs under the physical governance of forest pests. $\ln(1 + k_\alpha \alpha)$ represents the changes in the cost caused by the repetitive use of physical facilities. $l x_{H1}(t)$ means the social benefits increased by the government's reputation. $b_F F_{H2}(t) \ln(1 + k_s s)$ represents the benefits of social forces to govern forest pests. $\frac{c_H}{2}(1 + k_\alpha \alpha)(1-p) F_{H2}^2(t)$ means the cost of governing the forest pests in social forces. $\frac{c_H}{2}(1 + k_\alpha \alpha) p F_{H2}^2(t)$ indicates subsidies obtained by social forces. $l x_{H2}(t)$ means the benefits of the reputation of social forces.

Under the physical control mode, the changes in reputation gained by the government are as follows:

$$\dot{x}_{H1}(t) = a_F \ln(e + I_H) F_{H1}(t) - \delta x_{H1}(t) \quad (7)$$

Under the physical control mode, the changes in reputation gained by the social forces are as follows:

$$\dot{x}_{H2}(t) = a_F \ln(e + I_H) F_{H2}(t) - \delta x_{H2}(t) \quad (8)$$

Among them, $a_F \ln(e + I_H) F_{H1}(t)$ indicates the increase in the government's reputation in the physical control mode. $\delta x_{H1}(t)$ shows the attenuation of the government's reputation. $a_F \ln(e + I_H) F_{H2}(t)$ shows the reputation of social forces in physical control modes. $\delta x_{H2}(t)$ shows the attenuation of the reputation of social forces.

In the mode of biological control of forest diseases and insect pests, the income obtained by the government and social forces is:

$$J_{B1} = \int_0^{\infty} \left[b_F F_{B1}^2(t) - (c_B + k_m c_m + k_o c_o) F_{B1}(t) + l x_{B1}(t) \right] e^{-\rho t} \mathrm{d}t \quad (9)$$

$$J_{B2} = \int_0^{\infty} \left[b_F F_{B2}^2(t) - c_B (1-p) F_{B2}(t) + l x_{B2}(t) \right] e^{-\rho t} \mathrm{d}t \quad (10)$$

Among them, $b_F F_{B1}^2(t)$ represents the income obtained by the government under the biological management of forest pests. $(c_B + k_m c_m + k_o c_o) F_{B1}(t)$ represents the cost of government control of forest pests under the biological control of forest pests. $k_m c_m F_{B1}(t)$ represents the loss caused by the inadaptation of introduced species. $k_o c_o F_{B1}(t)$ represents loss due to the proliferation of introduced species. $l x_{B1}(t)$ represents the social benefit increased by the government's reputation. $b_F F_{B2}^2(t)$ represents the benefits to social forces from the biological management of forest pests. $c_B(1-p) F_{B2}(t)$ represents the cost of social forces under the biological management of forest pests. $l x_{B2}(t)$ represents the increased benefit of a reputation for social power.

Under the biological control mode, the changes in reputation gained by the government are as follows:

$$\dot{x}_{B1}(t) = [a_F + a_E \ln(e + I_E)] F_{B1}(t) - \delta x_{B1}(t) \quad (11)$$

Under the biological control mode, the changes in reputation gained by the social power are as follows:

$$\dot{x}_{B2}(t) = a_F F_{B2}(t) - \delta x_{B2}(t) \quad (12)$$

Among them, $[a_F + a_E \ln(e + I_E)] F_{B1}(t)$ represents the increased government reputation under the biocontrol mode. $a_F F_{B1}(t)$ represents an increase in the government's reputation as a result of the introduction of organisms. $F_{B1}(t) a_E \ln(e + I_E)$ says improved biodiversity has led to an increase in the government's reputation. $\delta x_{B1}(t)$ represents a decline in the government's reputation. $a_F F_{B2}(t)$ represents the increased reputation of social forces under the biological control mode. $\delta x_{B2}(t)$ represents a decline in the reputation of social forces.

3 Results

In the differential game, the social welfare of the government and social forces when forest pests and diseases occur is not only affected by control variables and parameters but also changes over time. In order to better calculate the amount of control and social benefits, the HJB formula was adopted. The HJB formula is a partial differential equation, which is the core of optimal control.

3.1 HJB formula

Under the pesticide control mode, the HJB equation of the social welfare function of the government and social forces is:

$$\rho V_{P1} = \max_{F_{P1}(t)}\left\{\left[b_F F_{P1}(t)\frac{1}{\ln(e+k_d d)} - \frac{c_P}{2}F_{P1}^2(t) - \frac{c_E}{2}F_{P1}^2(t) + lx_{P1}(t)\right] + \frac{\partial V_{P1}}{\partial x_{P1}}[(a_F - a_E)F_{P1}(t) - \delta x_{P1}(t)]\right\} \tag{13}$$

$$\rho V_{P2} = \max_{F_{P2}(t)}\left\{\left[b_F F_{P2}(t)\ln(e+k_s s) - \frac{c_P}{2}(1-p)F_{P2}^2(t) + lx_{P1}(t)\right] + \frac{\partial V_{P2}}{\partial x_{P2}}[a_F F_{P2}(t) - \delta x_{P2}(t)]\right\} \tag{14}$$

Under the physical control mode, the HJB equation of the social welfare function of the government and social forces is:

$$\rho V_{H1} = \max_{F_{H1}(t)}\left\{\left[\frac{b_F}{1+k_e e_H}F_{H1}(t) - \frac{c_H}{2}\ln(1+k_\alpha\alpha)F_{H1}^2(t) + lx_{H1}(t)\right] + \frac{\partial V_{H1}}{\partial x_{H1}}[a_F\ln(e+I_H)F_{H1}(t) - \delta x_{H1}(t)]\right\} \tag{15}$$

$$\rho V_{H2} = \max_{F_{H2}(t)}\left\{\left[b_F F_{H2}(t)\ln(1+k_s s) - \frac{c_H}{2}(1+k_\alpha\alpha)(1-p)F_{H2}^2(t) + lx_{H2}(t)\right] + \frac{\partial V_{H2}}{\partial x_{H2}}[a_F\ln(e+I_H)F_{H2}(t) - \delta x_{H2}(t)]\right\} \tag{16}$$

Under the biological control mode, the HJB equation of the social welfare function of the government and social forces is:

$$\rho V_{B1} = \max_{F_{B1}(t)}\left\{\left[b_F F_{B1}^2(t) - (c_B + k_m c_m + k_o c_o)F_{B1}(t) + lx_{B1}(t)\right] + \frac{\partial V_{B1}}{\partial x_{B1}}[(a_F + a_E\ln(e+I_E))F_{B1}(t) - \delta x_{B1}(t)]\right\} \tag{17}$$

$$\rho V_{B2} = \max_{F_{B2}(t)}\left\{\left[b_F F_{B2}^2(t) - c_B(1-p)F_{B2}(t) + lx_{B2}(t)\right] + \frac{\partial V_{B2}}{\partial x_{B2}}[a_F F_{B2}(t) - \delta x_{B2}(t)]\right\} \tag{18}$$

3.2 Result of equilibrium

Proposition 1: Under the pesticide control mode, the control quantities of government and social forces are, respectively (the specific solving procedure is shown in Appendix 1):

$$F_{P1}^*(t) = \frac{b_F}{(c_P + c_E)\ln(e+k_d d)} + \frac{l}{\rho+\delta}\frac{a_F - a_E}{c_P + c_E} \tag{19}$$

$$F_{P2}^*(t) = \frac{b_F\ln(e+k_s s) + \frac{l}{\rho+\delta}a_F}{c_P(1-p)} \tag{20}$$

In Eqs. (19) and (20), the resistance d of forest pests and the degree c_E of damage of pesticides to forest ecosystems are inversely proportional to the degree $F_{P1}^*(t)$ of government control. The rate s of forest pest control is proportional to the degree $F_{P2}^*(t)$ of social force input. The cost c_P of pest control is inversely proportional to the degree $F_{Pi}^*(t)(i=1,2)$ of control by government and social forces. The amount b_F of revenue generated per unit of governance is directly proportional to the degree $F_{Pi}^*(t)(i=1,2)$ of control of both government and social forces.

Conclusion 1: Under the pesticide control mode, the stronger the resistance to forest pests, the lower the balanced management degree of the government. The higher the damage degree of pesticides to the forest ecosystem, the lower the balanced governance degree of government. The faster the pest control speed, the more balanced the control amount of social force input. The greater the cost of pest control, the smaller the amount of balanced control input of government and social forces. The greater the income generated by the amount of unit governance, the greater the amount of government and social forces invested in governance.

Proposition 2: Under the physical control mode, the control quantities of government and social forces are, respectively (the specific solving procedure is shown in Appendix 2):

$$F_{H1}^*(t) = \frac{b_F}{(1+k_e e_H)c_H\ln(1+k_\alpha\alpha)} + \frac{l}{\rho+\delta}\frac{a_F\ln(e+I_H)}{c_H\ln(1+k_\alpha\alpha)} \tag{21}$$

$$F_{H2}^*(t) = \frac{b_F\ln(1+k_s s)}{c_H(1-p)(1+k_\alpha\alpha)} + \frac{l}{\rho+\delta}\frac{a_F\ln(e+I_H)}{c_H(1-p)(1+k_\alpha\alpha)} \tag{22}$$

In Eqs. (21) and (22), the number e_H of extreme weather events is inversely proportional to the degree $F_{H1}^*(t)$ of control by the government. The number α of times physical facilities can be reused and the cost c_H of physical control are inversely proportional to the degree $F_{Hi}^*(t)$of control by government and social forces. The rate s of forest pest control is proportional to the degree $F_{Hi}^*(t)$ of balanced control of social forces. The amount b_F of revenue generated by a unit of control is proportional to the degree $F_{Hi}^*(t)$ of balanced control of government and social forces.

Conclusion 2: Under the physical control mode, the more extreme weather occurs, the lower the balanced governance degree of the government. The more physical facilities are reused, the lower the balance of government and social forces. The higher the cost of physical governance, the lower the degree of balanced governance of government and social forces. The faster the speed of forest pest control, the more balanced control amount of social forces input. The greater the income generated by the amount of unit governance, the greater the amount of government and social forces invested in governance.

Proposition 3:

$$F_{B1}^*(t) = \frac{c_B + k_m c_m + k_o c_o}{2b_F} - \frac{l}{\rho+\delta}\frac{a_F + a_E\ln(e+I_E)}{2b_F} \tag{23}$$

$$F^{\star}_{B2}(t) = \frac{c_B(1-p)}{2b_F} - \frac{l}{\rho+\delta}\frac{a_F}{2b_F} \tag{24}$$

In Eqs. (23) and (24), the cost c_m and c_o caused by the introduction of biological inadaptation or flooding is proportional to the government's balanced control degree $F^{\star}_{B1}(t)$. The income b_F generated by the amount of governance per unit is inversely proportional to the degree $F^{\star}_{Bi}(t)$ of balanced governance between government and social forces. The unit governance cost c_B is proportional to the balanced governance degree of government and social force input.

Conclusion 3: Under the biological control mode of forest pests, the more cost caused by the inadaptation or flooding of introduced organisms, the more balanced management amount the government will invest. Different from the previous two governance modes, in this biological governance mode, the greater the income generated by the unit amount of governance, the smaller the amount of balanced governance input by the government and social forces. At the same time, under the biological control mode, the larger the unit governance cost, the larger the balanced governance amount of government and social force input.

4 Numerical analysis

In order to more clearly depict the change in social benefits of government and social power, numerical analysis is used in this article. This article assumes that the discount factor ρ is 0.9. The decay δ of reputation is 0.1. The resistance d produced by forest pests is 0.2. The influence coefficient k_d of pest resistance on the difficulty of control is 1. The destruction degree c_E of forest ecosystems per unit control amount is 0.5. The added cost c_m of inadaptability of introduced organisms is 0.4. The increased cost c_o of imported organisms is 0.8. The coefficient k_m of inadaptation of introduced organisms is 0.5. The coefficient k_o associated with the influx of introduced organisms is 1. The positive impact I_H of physical governance on reputation is 1.5. The positive impact I_E of biological governance on reputation is 2. The rate s of forest pest control is 0.5. The effect k_s of unit governance speed is 2. The positive influence l of the reputation of government or social power on earnings is 1. The proportion p of subsidies to social forces is 0.3. The positive effect a_F per unit of forest pest control on reputation is 1.5. The negative impact a_E of unit number of ecological damage on reputation is 1.2. The number e_H of extreme weather events is 2. The impact k_e of each extreme weather on pest management facilities was 0.5. The number α of reuse of physical facilities is 3. The effect k_α of reuse on cost is 0.3. The state variable is 1.

Therefore, this article can calculate:

$$V^{\star}_{P1} = 1 + \frac{2.85}{c_P + 0.5} \tag{25}$$

$$V^{\star}_{H1} = 1 + \frac{1}{c_H} \times 8.68 \tag{26}$$

$$V^{\star}_{B1} = -0.14c_B^2 + 0.65c_B + 0.23 \tag{27}$$

This article can produce the graph shown in Figure 2.

If the income b_F generated by the unit control quantity is 3, this article can calculate:

$$V^{\star}_{P1} = 1 + \frac{5.84}{c_P + 0.5} \tag{28}$$

$$V^{\star}_{H1} = 1 + \frac{1}{c_H} \times 11.63 \tag{29}$$

$$V^{\star}_{B1} = -0.09c_B^2 + 0.43c_B + 0.49 \tag{30}$$

This article can produce the graph shown in Figure 3.

As can be seen from Figures 2 and 3, regardless of the change in governance benefits, the social benefits of physical control by the government are the largest. At the same time, the curve of biological governance is smoother.

Conclusion 4: When the unit management cost is the same, the government can get the maximum benefit from the physical management of forest pests. However, compared with the other two control modes, with the change of governance costs, the change of social benefits for the government under the biological control mode is relatively gentle.

If the income b_F generated by the unit control quantity is 2, this article can calculate:

$$V^{\star}_{P2} = 1 + \frac{1}{c_P} \times 13.49 \tag{31}$$

$$V^{\star}_{H2} = 1 + \frac{1}{c_H} \times 5.26 \tag{32}$$

$$V^{\star}_{B2} = -0.068c_B^2 + 0.682 \tag{33}$$

This article can produce the graph shown in Figure 4.

If the income b_F generated by the unit control quantity is 3, this article can calculate:

$$V^{\star}_{P2} = 1 + \frac{1}{c_P} \times 23.13 \tag{34}$$

$$V^{\star}_{H2} = 1 + \frac{1}{c_H} \times 7.50 \tag{35}$$

$$V^{\star}_{B2} = -0.045c_B^2 + 0.792 \tag{36}$$

This article can produce the graph shown in Figure 5.

As can be seen from Figures 4 and 5, regardless of the change of governance benefits, the social benefits of pesticide control by the social power are the largest. At the same time, the curve of biological governance is smoother.

Conclusion 5: When the unit control cost is the same, social forces gain the most benefits from pesticide control of forest pests. However, compared with the other two governance modes, with the change in governance costs, the benefits of social forces under the biological governance mode change more gently.

In Figures 2–5, this article makes a visual presentation of the change in control cost. In order to show the changes in more

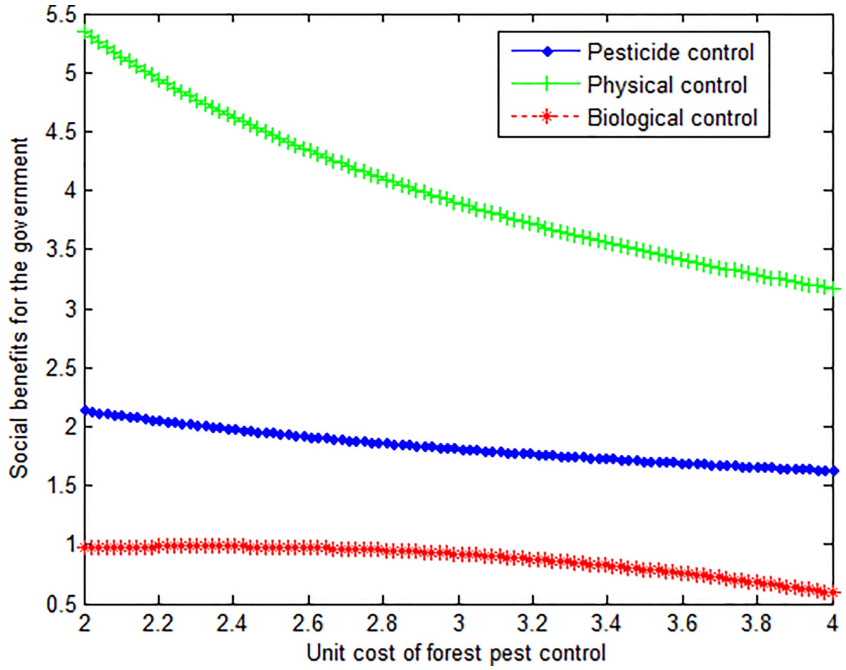

FIGURE 2
The influence of control cost on the government's social benefits.

parameters, this article then makes a visual presentation of the changes in the positive effects of control and the negative effects of ecological destruction.

Other parameters remain unchanged; redefine the following parameters. The income b_F generated by the unit control quantity is 2. The unit cost of managing forest pests and diseases is 2. That is, $c_p = c_H = c_B = 2$. The positive effect a_F per unit of forest pest control on reputation is changing. This article can calculate:

$$V_{P1}^{\star} = 0.22a_F^2 + 0.29a_F + 1.1 \tag{37}$$

$$V_{H1}^{\star} = 0.89a_F^2 + 1.24a_F + 1.43 \tag{38}$$

$$V_{B1}^{\star} = -0.14a_F^2 + 0.317a_F + 0.819 \tag{39}$$

$$V_{P2}^{\star} = 0.4a_F^2 + 2.08a_F + 3.72 \tag{40}$$

$$V_{H2}^{\star} = 0.43a_F^2 + 0.83a_F + 1.40 \tag{41}$$

$$V_{B2}^{\star} = -0.14a_F^2 + 0.39a_F + 0.73 \tag{42}$$

This article can produce the graphs shown in Figures 6 and 7.

As can be seen from Figures 6 and 7, as the reputation of controlling forest pests and diseases increases, the social benefits of both pesticide control and physical control by government and social forces increase. However, the social benefits of government and social forces change very gently under biological control.

Conclusion 6: Under pesticide control and physical control, the social benefits of government and social forces are directly proportional to the reputation generated by pest control.

Other parameters remain unchanged; redefine the following parameters: The negative impact a_E of unit number of ecological damage on reputation is changing. The income b_F generated by the unit control quantity is 2. The unit cost of managing forest pests and diseases is 2. That is, $c_p = c_H = c_B = 2$. The positive effect a_F per unit of forest pest control on reputation is 1.5. This article can calculate:

$$V_{P1}^{\star} = -0.22a_E^2 + 0.53a_E + 1.72 \tag{43}$$

$$V_{H1}^{\star} = 5.29 \tag{44}$$

$$V_{B1}^{\star} = -0.33a_E^2 + 0.67a_F + 0.69 \tag{45}$$

This article can produce the graph shown in Figure 8.

Conclusion 7: As the adverse effects of ecological damage on reputation continue to increase, the social benefits of the government under pesticide control and biological control modes are first increased and then decreased.

5 Discussion

In recent years, the global temperature has been gradually rising, and forest pests are frequently harmful and very easy to spread. Governments and social forces need to take measures to control forest pests and diseases. Pesticide control tends to damage ecosystems and lead to pest resistance, but it is low cost and has quick results. Physical containment facilities can be reused, but they are costly and vulnerable to extreme weather. Biological control can better protect the ecosystem, but introduced

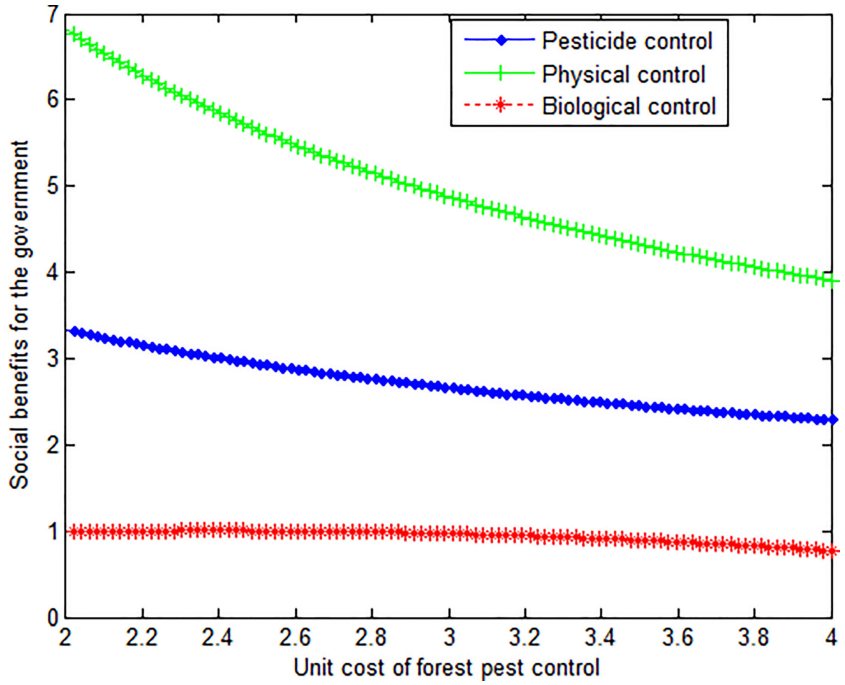

FIGURE 3
The influence of control cost on the government's social benefits.

natural enemies are prone to problems of adaptability and infestation. Therefore, how to control forest pests and diseases is an important issue in this article. As most of the existing studies use traditional methods such as data analysis and field investigation, there is no research on forest pests and diseases using differential games. In this article, the differential game is applied to forest pest management, especially considering the advantages and disadvantages of various prevention and control

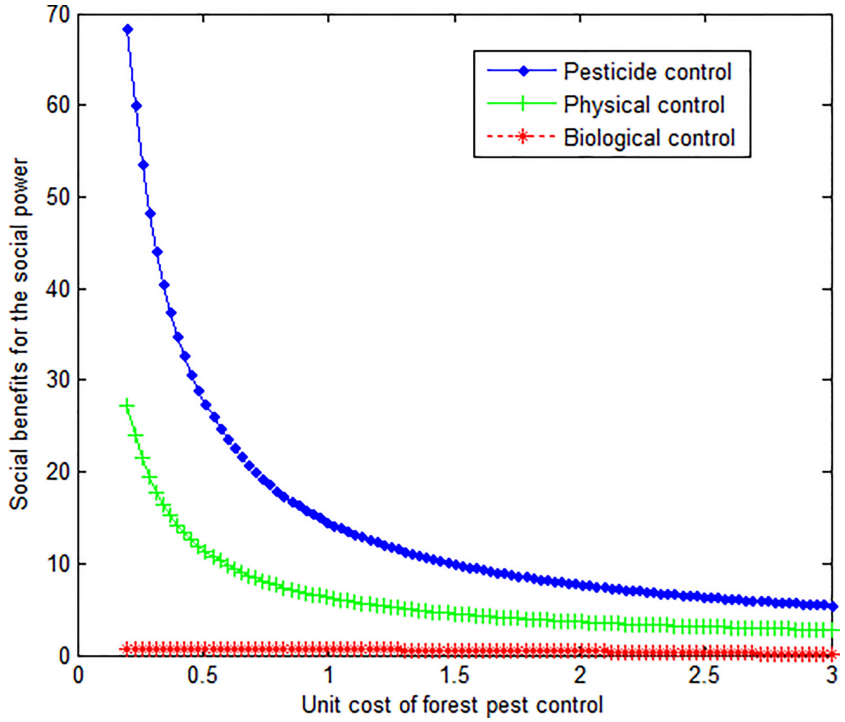

FIGURE 4
The influence of control cost on social power's social benefits.

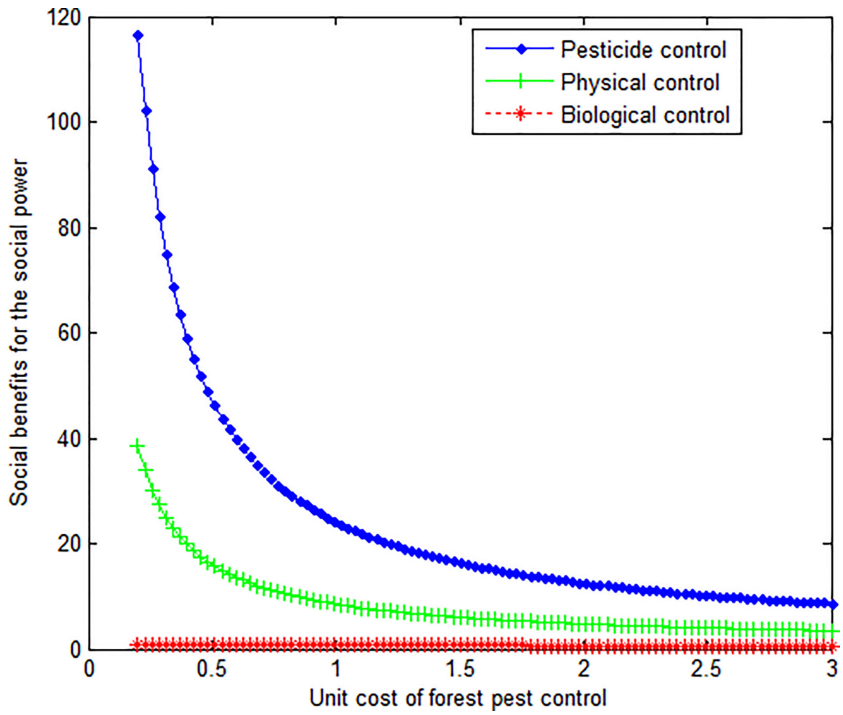

FIGURE 5
The influence of control cost on social power's social benefits.

modes and how the government and social forces achieve effective forest pest management.

In the process of forest pest management, we must pay attention to the reasonable rotation and mixing of pesticides. Long-term use of a pesticide will cause resistance to pests and diseases. Pesticide rotation and mixing can reduce the development of resistance to pests and diseases. At the same time, we also need to have a reasonable grasp of the dosage. Since reducing the number of drugs cannot reach the control effect, delay the best control period. If the amount of medicine is increased, there will be a waste of pesticides, an increase in cost, harm to the natural enemies of pests, increased environmental pollution, and other problems. In the process of pesticide use, attention should be paid to the extent of damage to the ecosystem.

Mechanical control mainly includes artificial killing, the use of simple appliances, instruments, and other devices, and even the application of modern devices and equipment. Mechanical control devices can be reused, and the more they are used, the less physical equipment is required. For example, pest traps are easy to operate, nontoxic, safe, and low-cost (Kecskeméti et al., 2021). If they can be reused after they are released, forest pests can be hunted continuously. However, in recent years, extreme weather has occurred more frequently around the world. Physical prevention and control measures are easily affected by extreme weather. When extreme weather such as typhoons and rainstorms occurs frequently, the number of physical facilities installed should be reduced to reduce the damage to physical facilities.

The goal of artificial mass breeding and release of natural enemies of insects is clear. Predators used for breeding and release should be much targeted. Only targeted natural enemies can play a better role in controlling forest pests. Moreover, predators are living things that can reproduce themselves. The offspring of natural enemies can also have an impact on forest pests. However, the more targeted the predator, the higher the cost. For example, in order to control forest pests, a variety of egg-parasitic wasps of Trichotropis (Zang, 2021) are the most studied and utilized in feeding and releasing natural enemies in China. This has been commercialized, and *Trichogramma* can be used to control major lepidopteran pests.

Pesticides are disposable and can easily affect the environment. The natural enemies of pests are easily restricted by environmental adaptability and flooding (Mandal et al., 2023). Physical facilities can be reused. As a result, governments tend to prefer physical prevention. Governments pay more attention to ecological sustainability than social forces. Governments focus on long-term interests, while social forces tend to focus on short-term interests (Dragicevic, 2019c). Social forces generally focus on the number of forest pests eliminated in the short term. The effects of pesticides on ecosystems are often not visible in the short term. As a result, social forces are more inclined to use pesticide control.

6 Conclusion

In order to study the application scope of different management modes for forest pests and diseases, differential game models of pesticide management, physical management, and biological

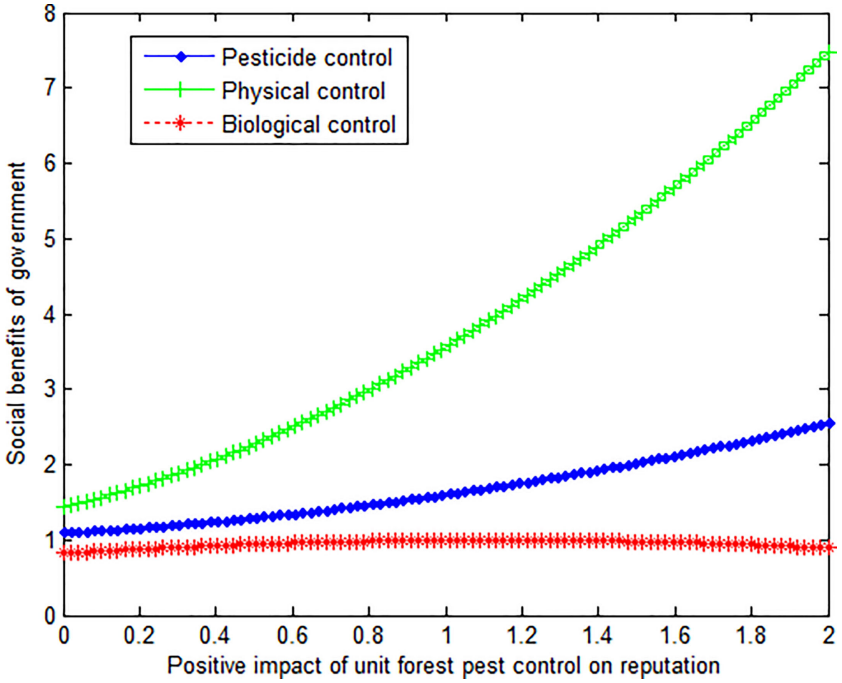

FIGURE 6
The influence of positive impact on the government's social benefits.

management were constructed in this article. Also, the equilibrium results are compared and analyzed. Finally, the research conclusion is drawn that under the biological control mode, the income generated by the unit control quantity is inversely proportional to the balanced control quantity. However, under the pesticide control and physical control modes, the income generated by the unit control quantity is proportional to the balanced control quantity. At the same time, under the biological control mode, the unit governance cost is proportional to the balanced governance quantity. Under the pesticide control and physical control modes,

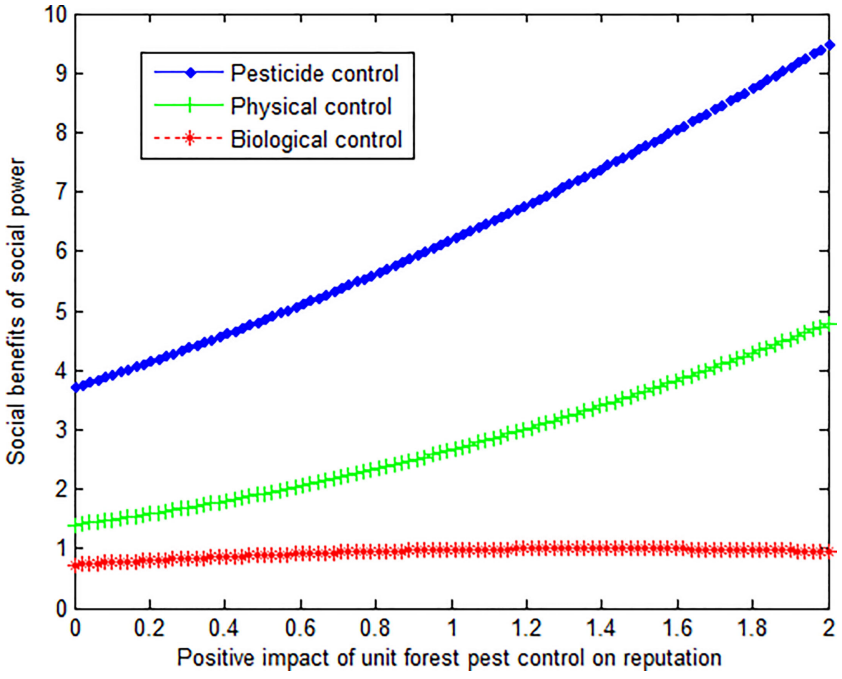

FIGURE 7
The influence of positive impact on social power's social benefits.

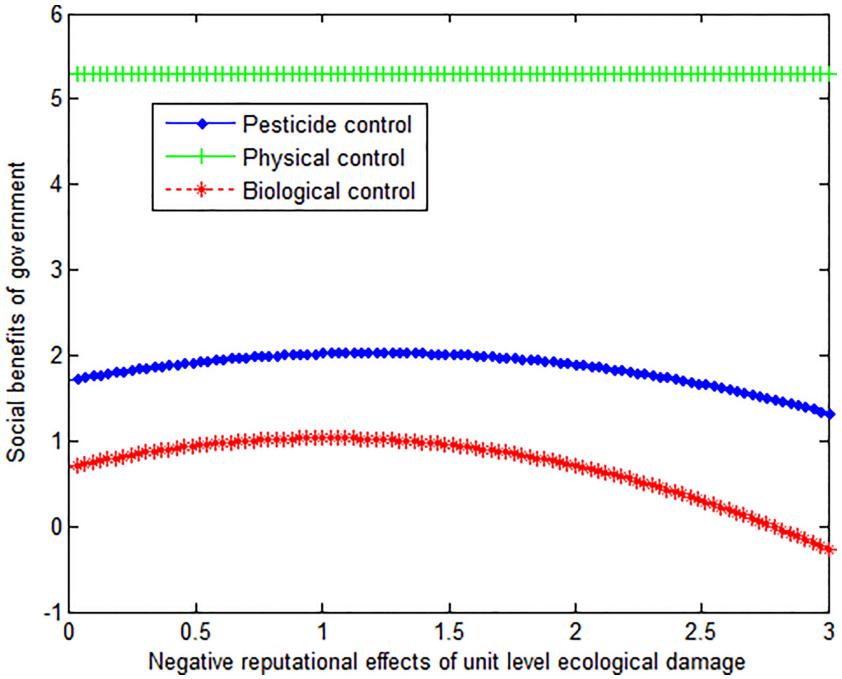

FIGURE 8
The influence of negative reputational effects on the government's social benefits.

the unit control cost is inversely proportional to the balanced control quantity. Social forces tend to adopt pesticide control. The government prefers physical control.

This article has some shortcomings. For example, this article is based on the analysis of mathematical modeling, and the relevant specific data are limited. At the same time, the problem of pests and diseases in specific forests has not been studied, and the specific conditions faced by different forests may not be exactly the same. In future studies, relevant specific data can be added to carry out research on specific forest pests and diseases. The research in this article can be extended to some extent. For example, this article only considers the situation that the government's decision-making is constantly changing, the government can grasp the information on forest diseases and pests in a more comprehensive way, and the forest affects national production and management. In future studies, it is possible to consider the situation that the government's decision is unchanged, the government cannot grasp the comprehensive information of pests and diseases, the forest has little impact on economic development, etc., and carry out relevant studies. In addition, this study is not only applicable to the study of forest pests and diseases but also has certain reference significance for forest fire control, forest wildlife protection, and other related issues.

Data availability statement

The original contributions presented in the study are included in the article/supplementary material. Further inquiries can be directed to the corresponding author.

Author contributions

YB: Model building, problem description, writing – first draft, result analysis; LW: Figure preparation, literature collection; XY: Quality control, writing – review & editing. All authors contributed to the article and approved the submitted version.

Funding

This research is funded by the Doctoral Research Foundation of Shandong Management University, sdmud2023001. This research is financially supported by Social Science Planning Foundation of Chongqing in China, 2021BS080.

Conflict of interest

The authors declare that the research was conducted in the absence of any commercial or financial relationships that could be construed as a potential conflict of interest.

Publisher's note

References

Arnone, E., Kneip, A., Nobile, F., and Sangalli, L. M. (2022). Some first results on the consistency of spatial regression with partial differential equation regularization. *Statistica Sin.* 1, 32. doi: 10.5705/ss.202019.0346

Ayres, M. P., and Lombardero, M. J. (2018). Forest pests and their management in the Anthropocene. *Can. J. For. Res.* 48, 292–301. doi: 10.1139/cjfr-2017-0033

Bai, Y., Gao, Y., Li, D., and Liu, D. (2022). Coordinated distribution or client introduce? Analysis of energy conservation and emission reduction in Canadian logistics enterprises. *Sustainability* 14, 16979. doi: 10.3390/su142416979

Bai, X., Jia, X., Zhao, C., and Shao, M. (2021). Artificial forest conversion into grassland alleviates deep-soil desiccation in typical grass zone on China's loess plateau: regional modeling. *Agriculture Ecosyst. Environ.* 320, 107608. doi: 10.1016/j.agee.2021.107608

Canelles, Q., Aquilue, N., James, P. M. A., Lawler, J., and Brotons, L. (2021). Global review on interactions between insect pests and other forest disturbances. *Landscape Ecol.* 36 (4), 945–972. doi: 10.1007/s10980-021-01209-7

Dragicevic, A. (2015). Bayesian population dynamics of spreading species. *Environ. Model. Assess.* 20, 17–27. doi: 10.1007/s10666-014-9416-4

Dragicevic, A. (2019a). Comparing forest control modes against invasive biological threats. *J. Theor. Biol.* 462, 270–282. doi: 10.1016/j.jtbi.2018.11.014

Dragicevic, A. Z. (2019b). Concentric framework for sustainability assessment. *J. Cleaner Production* 248, 119268. doi: 10.1016/j.jclepro.2019.119268

Dragicevic, A. (2019c). Rethinking the forestry in the aquitaine massif through portfolio management. *For. Policy Econo.* 109, 102020. doi: 10.1016/j.forpol.2019.102020

Food and Agricultural Organization (2020). *Global forest resources assessment 2020 – key findings* (Rome, Italy: Food and Agricultural Organization).

Fredj, K., Martín-Herrán, G., and Zaccour, G. (2004). Slowing deforestation pace through subsidies: a differential game. *Automatica* 40, 301–309. doi: 10.1016/j.automatica.2003.10.020

Janssen, A., and Rijn, P. (2021). Pesticides do not significantly reduce arthropod pest densities in the presence of natural enemies. *Ecol. Lett.* 24, 2010–2024. doi: 10.1111/ele.13819

Jentsch, P. C., Bauch, C. T., Yemshanov, D., and Anand, M. (2020). Go big or go home: a model-based assessment of general strategies to slow the spread of forest pests via infested firewood. *PloS One* 15, e0238979. doi: 10.1371/journal.pone.0238979

Kecskeméti, S., Gesel, A., Fail, J., and Egri, D. (2021). In search of the spectral composition of an effective light trap for the mushroom pest *Lycoriella ingenua* (Diptera: Sciaridae). *Sci. Rep.* 11, 12770. doi: 10.1038/s41598-021-92230-y

Lei, M., Yuan, X., and Yao, X. (2021). Synthesize dual goals: a study on China's ecological poverty alleviation system. *J. Integr. Agr.* 20, 1042–1059. doi: 10.1016/S2095-3119(21)63635-3

Lovett, G. M., Weiss, M., Liebhold, A. M., Holmes, T. P., Leung, B., Lambert, K. F., et al. (2016). Nonnative forest insects and pathogens in the united states: impacts and policy options. *Ecol. Appl.* 26, 1437–1455. doi: 10.1890/15-1176

Mandal, D. S., Samanta, S., Parshad, R. D., Chekroun, A., Helal, M., and Chattopadhyay, J. (2023). Study of a crop-pest-natural enemy model with z-type control – an approach to pest management. *Int. J. Biomathematics* 16, 2240099. doi: 10.1142/S1793524522500991

Niquidet, K., Tang, J., and Peter, B. (2015). Economic analysis of forest insect pests in Canada. *Can. Entomologist* 148, S357–S366. doi: 10.4039/tce.2015.27

Ozkan, S. N. (2022). Management of the control against forest pests in Artvin spruce forests. *Int. J. Trop. Insect Sci.* 42, 527–534. doi: 10.1007/s42690-021-00568-7

Palma-Onetto, V., Oliva, D., and González-Teuber, M. (2021). Lethal and oxidative stress side effects of organic and synthetic pesticides on the insect scale predator *Rhyzobius lophanthae*. *Entomologia Generalis* 41, 345–355. doi: 10.1127/entomologia/2021/1045

Pirtle, E. I., Umina, P. A., Hauser, C. E., and Maino, J. L. (2021). Using mock surveillance to quantify pest detectability prior to establishment of exotic leafminers. *Crop Prot.* 148, 105713. doi: 10.1016/j.cropro.2021.105713

Popkin, G. (2020). Deadly imports: in one US forest, 25% of tree loss caused by foreign pests and disease. *Science*. doi: 10.1126/science.abc7624

Sheremet, O., Ruokamo, E., Juutinene, A., Svento, R., and Hanley, N. (2018). Incentivising participation and spatial coordination in payment for ecosystem service schemes: forest disease control programs in Finland. *Ecol. Economics* 152, 260–272. doi: 10.1016/j.ecolecon.2018.06.004

Tandon, A., and Verma, P. R. (2021). Human population induced urban developments and their effects on temperature rise: a nonlinear mathematical model. *Ecol. Complexity* 47, 100947. doi: 10.1016/j.ecocom.2021.100947

Turner, J. A., Buongiorno, J., Zhu, S., Prestemon, J. P., and Bulman, L. S. (2007). Modelling the impact of the exotic forest pest nectria on the New Zealand forest sector and its major trading partners. *New Z. J. Forestry Sci.* 37, 383–411.

Valizadeh, M., and Gohari, A. (2021). Simulation of a random variable and its application to game theory. *Math. Oper. Res.* 46, 452–470. doi: 10.1287/moor.2020.1067

Viscolani, B., and Zaccour, G. (2009). Advertising strategies in a differential game with negative competitor's interference. *J. Optim. Theory Appl.* 140, 153–170. doi: 10.1007/s10957-008-9454-7

Wu, Z., and Zhang, F. (2022). Maximum principle for discrete-time stochastic optimal control problem and stochastic game. *Math. Control Related Fields* 12 (2), 475–493. doi: 10.3934/mcrf.2021031

Yang, Z., Wang, X., and Zhang, Y. (2014). Recent advances in biological control of important native and invasive forest pests in China. *Biol. Control* 68, 117–128. doi: 10.1016/j.biocontrol.2013.06.010

Zang, F. (2021). Biological control with *Trichogramma* in China: history, present status, and perspectives. *Annu. Rev. Entomology* 66, 463–484. doi: 10.1146/annurev-ento-060120-091620

Zhu, S., Xie, K., and Cui, P. (2021). Dynamic adjustment mechanism and differential game model construction of mask emergency supply chain cooperation based on covid-19 outbreak. *Sustainability* 13, 1115. doi: 10.3390/su13031115

Appendix 1

Take the derivatives of F_{P1} with respect to Eq. (13), take the derivatives of F_{P2} with respect to Eq. (14), and set them equal to zero, we can get:

$$F_{P1}^{\star}(t)=\frac{b_F}{(c_P+c_E)\ln(e+k_d d)}+\frac{\partial V_{P1}}{\partial x_{P1}}\frac{a_F-a_E}{c_P+c_E} \tag{46}$$

$$F_{P2}^{\star}(t)=\frac{b_F\ln(e+k_s s)+\frac{\partial V_{P2}}{\partial x_{P2}}a_F}{c_P(1-p)} \tag{47}$$

Substituting Eq. (46) into Eq. (13) and substituting Eq. (47) into Eq. (14), we can get:

$$\begin{aligned}\rho V_{P1}=&\left[b_F\left(\frac{b_F}{(c_P+c_E)\ln(e+k_d d)}+\frac{\partial V_{P1}}{\partial x_{P1}}\frac{a_F-a_E}{c_P+c_E}\right)\frac{1}{\ln(e+k_d d)}-\left(\frac{c_P}{2}+\frac{c_E}{2}\right)\right.\\&\left.\left(\frac{b_F}{(c_P+c_E)\ln(e+k_d d)}+\frac{\partial V_{P1}}{\partial x_{P1}}\frac{a_F-a_E}{c_P+c_E}\right)^2+lx_{P1}(t)\right]\\&+\frac{\partial V_{P1}}{\partial x_{P1}}\left[(a_F-a_E)\left(\frac{b_F}{(c_P+c_E)\ln(e+k_d d)}+\frac{\partial V_{P1}}{\partial x_{P1}}\frac{a_F-a_E}{c_P+c_E}\right)-\delta x_{P1}(t)\right]\end{aligned} \tag{48}$$

$$\begin{aligned}\rho V_{P2}=&\left[b_F\frac{b_F\ln(e+k_s s)+\frac{\partial V_{P2}}{\partial x_{P2}}a_F}{c_P(1-p)}\ln(e+k_s s)-\frac{c_P}{2}(1-p)\left(\frac{b_F\ln(e+k_s s)+\frac{\partial V_{P2}}{\partial x_{P2}}a_F}{c_P(1-p)}\right)^2+lx_{P1}(t)\right]\\&+\frac{\partial V_{P2}}{\partial x_{P2}}\left[a_F\frac{b_F\ln(e+k_s s)+\frac{\partial V_{P2}}{\partial x_{P2}}a_F}{c_P(1-p)}-\delta x_{P2}(t)\right]\end{aligned} \tag{49}$$

Let $V_{P1}^{\star}=m_1x_{P1}+m_2$ and $V_{P2}^{\star}=m_3x_{P2}+m_4$, wherein, m_1, m_2, m_3, and m_4 are all constants. The parameters of the optimal social welfare function can be obtained by calculation as follows:

$$\begin{cases}m_1=\frac{l}{\rho+\delta}\\ m_2=\frac{1}{\rho}\left[b_F\left(\frac{b_F}{(c_P+c_E)\ln(e+k_d d)}+\frac{l}{\rho+\delta}\frac{a_F-a_E}{c_P+c_E}\right)\frac{1}{\ln(e+k_d d)}-\left(\frac{c_P}{2}+\frac{c_E}{2}\right)\right.\\ \quad\left.\left(\frac{b_F}{(c_P+c_E)\ln(e+k_d d)}+\frac{l}{\rho+\delta}\frac{a_F-a_E}{c_P+c_E}\right)^2\right]\\ \quad+\frac{1}{\rho}\frac{l}{\rho+\delta}\left[(a_F-a_E)\left(\frac{b_F}{(c_P+c_E)\ln(e+k_d d)}+\frac{l}{\rho+\delta}\frac{a_F-a_E}{c_P+c_E}\right)\right]\end{cases} \tag{50}$$

$$\begin{cases}m_3=\frac{l}{\rho+\delta}\\ m_4=\frac{1}{\rho}\left[b_F\frac{b_F\ln(e+k_s s)+\frac{l}{\rho+\delta}a_F}{c_P(1-p)}\ln(e+k_s s)-\frac{c_P}{2}(1-p)\left(\frac{b_F\ln(e+k_s s)+\frac{l}{\rho+\delta}a_F}{c_P(1-p)}\right)^2\right]\\ \qquad+\frac{1}{\rho}\frac{l}{\rho+\delta}a_F\frac{b_F\ln(e+k_s s)+\frac{l}{\rho+\delta}a_F}{c_P(1-p)}\end{cases} \tag{51}$$

Therefore, it can be concluded that:

$$\begin{aligned}V_{P1}^{\star}=&\frac{l}{\rho+\delta}x_{P1}+\frac{1}{\rho}\left[b_F\left(\frac{b_F}{(c_P+c_E)\ln(e+k_d d)}+\frac{l}{\rho+\delta}\frac{a_F-a_E}{c_P+c_E}\right)\frac{1}{\ln(e+k_d d)}-\left(\frac{c_P}{2}+\frac{c_E}{2}\right)\right.\\&\left.\left(\frac{b_F}{(c_P+c_E)\ln(e+k_d d)}+\frac{l}{\rho+\delta}\frac{a_F-a_E}{c_P+c_E}\right)^2\right]\\&+\frac{1}{\rho}\frac{l}{\rho+\delta}\left[(a_F-a_E)\left(\frac{b_F}{(c_P+c_E)\ln(e+k_d d)}+\frac{l}{\rho+\delta}\frac{a_F-a_E}{c_P+c_E}\right)\right]\end{aligned} \tag{52}$$

$$\begin{aligned}V_{P2}^{\star}=&\frac{1}{\rho}\left[b_F\frac{b_F\ln(e+k_s s)+\frac{l}{\rho+\delta}a_F}{c_P(1-p)}\ln(e+k_s s)-\frac{c_P}{2}(1-p)\left(\frac{b_F\ln(e+k_s s)+\frac{l}{\rho+\delta}a_F}{c_P(1-p)}\right)^2\right]\\&+\frac{l}{\rho+\delta}x_{P2}+\frac{1}{\rho}\frac{l}{\rho+\delta}a_F\frac{b_F\ln(e+k_s s)+\frac{l}{\rho+\delta}a_F}{c_P(1-p)}\end{aligned} \tag{53}$$

In this case,

$$F_{P1}^{\star}(t)=\frac{b_F}{(c_P+c_E)\ln(e+k_d d)}+\frac{l}{\rho+\delta}\frac{a_F-a_E}{c_P+c_E} \tag{54}$$

$$F_{P2}^{\star}(t)=\frac{b_F\ln(e+k_s s)+\frac{l}{\rho+\delta}a_F}{c_P(1-p)} \tag{55}$$

Appendix 2

Take the derivatives of FH1 with respect to Eq. (15), take the derivatives of FH2 with respect to Eq. (16), and set them equal to zero, we can get:

$$F_{H1}^{\star}(t)=\frac{b_F}{(1+k_e e_H)c_H\ln(1+k_\alpha\alpha)}+\frac{\partial V_{H1}}{\partial x_{H1}}\frac{a_F\ln(e+I_H)}{c_H\ln(1+k_\alpha\alpha)} \tag{56}$$

$$F_{H2}^{\star}(t)=\frac{b_F\ln(1+k_s s)}{c_H(1-p)(1+k_\alpha\alpha)}+\frac{\partial V_{H2}}{\partial x_{H2}}\frac{a_F\ln(e+I_H)}{c_H(1-p)(1+k_\alpha\alpha)} \tag{57}$$

Substituting Eq. (56) into Eq. (15) and substituting Eq. (57) into Eq. (16), we can get:

$$\begin{aligned}\rho V_{H1}=&\left\{\frac{b_F}{1+k_e e_H}\left[\frac{b_F}{(1+k_e e_H)c_H\ln(1+k_\alpha\alpha)}+\frac{\partial V_{H1}}{\partial x_{H1}}\frac{a_F\ln(e+I_H)}{c_H\ln(1+k_\alpha\alpha)}\right]-\frac{c_H}{2}\ln(1+k_\alpha\alpha)\right.\\&\left.\left[\frac{b_F}{(1+k_e e_H)c_H\ln(1+k_\alpha\alpha)}+\frac{\partial V_{H1}}{\partial x_{H1}}\frac{a_F\ln(e+I_H)}{c_H\ln(1+k_\alpha\alpha)}\right]^2+lx_{H1}(t)\right]\\&+\frac{\partial V_{H1}}{\partial x_{H1}}a_F\ln(e+I_H)\left[\frac{b_F}{(1+k_e e_H)c_H\ln(1+k_\alpha\alpha)}+\frac{\partial V_{H1}}{\partial x_{H1}}\frac{a_F\ln(e+I_H)}{c_H\ln(1+k_\alpha\alpha)}\right]-\delta x_{H1}(t)\frac{\partial V_{H1}}{\partial x_{H1}}\}\end{aligned} \tag{58}$$

$$\begin{aligned}\rho V_{H2}=&\left\{b_F\left[\frac{b_F\ln(1+k_s s)}{c_H(1-p)(1+k_\alpha\alpha)}+\frac{\partial V_{H2}}{\partial x_{H2}}\frac{a_F\ln(e+I_H)}{c_H(1-p)(1+k_\alpha\alpha)}\right]\ln(1+k_s s)-\right.\\&\frac{c_H}{2}(1+k_\alpha\alpha)(1-p)\left[\frac{b_F\ln(1+k_s s)}{c_H(1-p)(1+k_\alpha\alpha)}+\frac{\partial V_{H2}}{\partial x_{H2}}\frac{a_F\ln(e+I_H)}{c_H(1-p)(1+k_\alpha\alpha)}\right]^2+lx_{H2}(t)\\&\left.+\frac{\partial V_{H2}}{\partial x_{H2}}a_F\ln(e+I_H)\left[\frac{b_F\ln(1+k_s s)}{c_H(1-p)(1+k_\alpha\alpha)}+\frac{\partial V_{H2}}{\partial x_{H2}}\frac{a_F\ln(e+I_H)}{c_H(1-p)(1+k_\alpha\alpha)}\right]-\delta x_{H2}(t)\frac{\partial V_{H2}}{\partial x_{H2}}\right\}\end{aligned} \tag{59}$$

Let $V_{H1}^{\star}=m_5x_{H1}+m_6$ and $V_{H2}^{\star}=m_7x_{H2}+m_8$, wherein, m_5, m_6, m_7, and m_8 are all constants. The parameters of the optimal social welfare function can be obtained by calculation as follows:

$$\begin{cases}m_5=\frac{l}{\rho+\delta}\\ m_6=\frac{1}{\rho}\left\{\frac{b_F}{1+k_e e_H}\left[\frac{b_F}{(1+k_e e_H)c_H\ln(1+k_\alpha\alpha)}+\frac{l}{\rho+\delta}\frac{a_F\ln(e+I_H)}{c_H\ln(1+k_\alpha\alpha)}\right]-\frac{c_H}{2}\ln(1+k_\alpha\alpha)\right.\\ \quad\left[\frac{b_F}{(1+k_e e_H)c_H\ln(1+k_\alpha\alpha)}+\frac{l}{\rho+\delta}\frac{a_F\ln(e+I_H)}{c_H\ln(1+k_\alpha\alpha)}\right]^2\\ \quad\left.+\frac{l}{\rho+\delta}a_F\ln(e+I_H)\left[\frac{b_F}{(1+k_e e_H)c_H\ln(1+k_\alpha\alpha)}+\frac{l}{\rho+\delta}\frac{a_F\ln(e+I_H)}{c_H\ln(1+k_\alpha\alpha)}\right]\right\}\end{cases} \tag{60}$$

$$\begin{cases} m_7 = \frac{l}{\rho+\delta} \\ m_8 = \frac{1}{\rho}\left\{ b_F\left[\frac{b_F \ln(1+k_s s)}{c_H(1-p)(1+k_\alpha\alpha)} + \frac{l}{\rho+\delta}\frac{a_F \ln(e+I_H)}{c_H(1-p)(1+k_\alpha\alpha)}\right]\ln(1+k_s s) - \right. \\ \quad \frac{c_H}{2}(1+k_\alpha\alpha)(1-p)\left[\frac{b_F \ln(1+k_s s)}{c_H(1-p)(1+k_\alpha\alpha)} + \frac{l}{\rho+\delta}\frac{a_F \ln(e+I_H)}{c_H(1-p)(1+k_\alpha\alpha)}\right]^2 \\ \quad \left. + \frac{l}{\rho+\delta} a_F \ln(e+I_H)\left[\frac{b_F \ln(1+k_s s)}{c_H(1-p)(1+k_\alpha\alpha)} + \frac{l}{\rho+\delta}\frac{a_F \ln(e+I_H)}{c_H(1-p)(1+k_\alpha\alpha)}\right]\right\} \end{cases} \tag{61}$$

Therefore, it can be concluded that:

$$\begin{aligned} V_{H1}^{\star} = {} & \frac{l}{\rho+\delta} x_{H1} + \frac{1}{\rho}\left\{ \frac{b_F}{1+k_e e_H}\left[\frac{b_F}{(1+k_e e_H)c_H \ln(1+k_\alpha\alpha)} + \frac{l}{\rho+\delta}\frac{a_F \ln(e+I_H)}{c_H \ln(1+k_\alpha\alpha)}\right] - \frac{c_H}{2}\ln(1+k_\alpha\alpha)\right. \\ & \left[\frac{b_F}{(1+k_e e_H)c_H \ln(1+k_\alpha\alpha)} + \frac{l}{\rho+\delta}\frac{a_F \ln(e+I_H)}{c_H \ln(1+k_\alpha\alpha)}\right]^2 \\ & \left. + \frac{l}{\rho+\delta} a_F \ln(e+I_H)\left[\frac{b_F}{(1+k_e e_H)c_H \ln(1+k_\alpha\alpha)} + \frac{l}{\rho+\delta}\frac{a_F \ln(e+I_H)}{c_H \ln(1+k_\alpha\alpha)}\right]\right\} \end{aligned} \tag{62}$$

$$\begin{aligned} V_{H2}^{\star} = {} & \frac{l}{\rho+\delta} x_{H2} + \frac{1}{\rho}\left\{ b_F\left[\frac{b_F \ln(1+k_s s)}{c_H(1-p)(1+k_\alpha\alpha)} + \frac{l}{\rho+\delta}\frac{a_F \ln(e+I_H)}{c_H(1-p)(1+k_\alpha\alpha)}\right]\ln(1+k_s s) - \right. \\ & \frac{c_H}{2}(1+k_\alpha\alpha)(1-p)\left[\frac{b_F \ln(1+k_s s)}{c_H(1-p)(1+k_\alpha\alpha)} + \frac{l}{\rho+\delta}\frac{a_F \ln(e+I_H)}{c_H(1-p)(1+k_\alpha\alpha)}\right]^2 \\ & \left. + \frac{l}{\rho+\delta} a_F \ln(e+I_H)\left[\frac{b_F \ln(1+k_s s)}{c_H(1-p)(1+k_\alpha\alpha)} + \frac{l}{\rho+\delta}\frac{a_F \ln(e+I_H)}{c_H(1-p)(1+k_\alpha\alpha)}\right]\right\} \end{aligned} \tag{63}$$

In this case,

$$F_{H1}^{\star}(t) = \frac{b_F}{(1+k_e e_H)c_H \ln(1+k_\alpha\alpha)} + \frac{l}{\rho+\delta}\frac{a_F \ln(e+I_H)}{c_H \ln(1+k_\alpha\alpha)} \tag{64}$$

$$F_{H2}^{\star}(t) = \frac{b_F \ln(1+k_s s)}{c_H(1-p)(1+k_\alpha\alpha)} + \frac{l}{\rho+\delta}\frac{a_F \ln(e+I_H)}{c_H(1-p)(1+k_\alpha\alpha)} \tag{65}$$

Appendix 3

Take the derivatives of FB1 with respect to Eq. (17), take the derivatives of FB2 with respect to Eq. (18), and set them equal to zero, we can get:

$$F_{B1}^{\star}(t) = \frac{c_B + k_m c_m + k_o c_o}{2b_F} - \frac{\partial V_{B1}}{\partial x_{B1}}\frac{a_F + a_E \ln(e+I_E)}{2b_F} \tag{66}$$

$$F_{B2}^{\star}(t) = \frac{c_B(1-p)}{2b_F} - \frac{\partial V_{B2}}{\partial x_{B2}}\frac{a_F}{2b_F} \tag{67}$$

Substituting Eq. (66) into Eq. (17) and substituting Eq. (67) into Eq. (18), we can get:

$$\begin{aligned} \rho V_{B1} = {} & b_F\left[\frac{c_B+k_m c_m+k_o c_o}{2b_F} - \frac{\partial V_{B1}}{\partial x_{B1}}\frac{a_F+a_E \ln(e+I_E)}{2b_F}\right]^2 - (c_B + k_m c_m + k_o c_o) \\ & \left[\frac{c_B+k_m c_m+k_o c_o}{2b_F} - \frac{\partial V_{B1}}{\partial x_{B1}}\frac{a_F+a_E \ln(e+I_E)}{2b_F}\right] + l x_{B1}(t) - \delta x_{B1}(t)\frac{\partial V_{B1}}{\partial x_{B1}} \\ & + \frac{\partial V_{B1}}{\partial x_{B1}}(a_F + a_E \ln(e+I_E))\left[\frac{c_B+k_m c_m+k_o c_o}{2b_F} - \frac{\partial V_{B1}}{\partial x_{B1}}\frac{a_F+a_E \ln(e+I_E)}{2b_F}\right] \end{aligned} \tag{68}$$

$$\begin{aligned} \rho V_{B2} = {} & b_F\left[\frac{c_B(1-p)}{2b_F} - \frac{\partial V_{B2}}{\partial x_{B2}}\frac{a_F}{2b_F}\right]^2 - c_B(1-p)\left[\frac{c_B(1-p)}{2b_F} - \frac{\partial V_{B2}}{\partial x_{B2}}\frac{a_F}{2b_F}\right] + l x_{B2}(t) \\ & + \frac{\partial V_{B2}}{\partial x_{B2}} a_F\left[\frac{c_B(1-p)}{2b_F} - \frac{\partial V_{B2}}{\partial x_{B2}}\frac{a_F}{2b_F}\right] - \delta x_{B2}(t)\frac{\partial V_{B2}}{\partial x_{B2}} \end{aligned} \tag{69}$$

Let $V_{B1}^{\star} = m_9 x_{B1} + m_{10}$ and $V_{B2}^{\star} = m_{11} x_{B2} + m_{12}$, wherein, m_9, m_{10}, m_{11}, and m_{12} are all constants. The parameters of the optimal social welfare function can be obtained by calculation as follows:

$$\begin{cases} m_9 = \frac{l}{\rho+\delta} \\ m_{10} = \frac{1}{\rho} b_F\left[\frac{c_B+k_m c_m+k_o c_o}{2b_F} - \frac{l}{\rho+\delta}\frac{a_F+a_E \ln(e+I_E)}{2b_F}\right]^2 - \frac{1}{\rho}(c_B + k_m c_m + k_o c_o) \\ \quad \left[\frac{c_B+k_m c_m+k_o c_o}{2b_F} - \frac{l}{\rho+\delta}\frac{a_F+a_E \ln(e+I_E)}{2b_F}\right] \\ \quad + \frac{1}{\rho}\frac{l}{\rho+\delta}(a_F + a_E \ln(e+I_E))\left[\frac{c_B+k_m c_m+k_o c_o}{2b_F} - \frac{l}{\rho+\delta}\frac{a_F+a_E \ln(e+I_E)}{2b_F}\right] \end{cases} \tag{70}$$

$$\begin{cases} m_{11} = \frac{l}{\rho+\delta} \\ m_{12} = \frac{1}{\rho} b_F\left[\frac{c_B(1-p)}{2b_F} - \frac{l}{\rho+\delta}\frac{a_F}{2b_F}\right]^2 - \frac{1}{\rho} c_B(1-p)\left[\frac{c_B(1-p)}{2b_F} - \frac{l}{\rho+\delta}\frac{a_F}{2b_F}\right] \\ \quad + \frac{1}{\rho}\frac{l}{\rho+\delta} a_F\left[\frac{c_B(1-p)}{2b_F} - \frac{l}{\rho+\delta}\frac{a_F}{2b_F}\right] \end{cases} \tag{71}$$

Therefore, it can be concluded that:

$$\begin{aligned} V_{B1}^{\star} = {} & \frac{l}{\rho+\delta} x_{B1} + \frac{1}{\rho} b_F\left[\frac{c_B+k_m c_m+k_o c_o}{2b_F} - \frac{l}{\rho+\delta}\frac{a_F+a_E \ln(e+I_E)}{2b_F}\right]^2 - \frac{1}{\rho}(c_B + k_m c_m + k_o c_o) \\ & \left[\frac{c_B+k_m c_m+k_o c_o}{2b_F} - \frac{l}{\rho+\delta}\frac{a_F+a_E \ln(e+I_E)}{2b_F}\right] \\ & + \frac{1}{\rho}\frac{l}{\rho+\delta}(a_F + a_E \ln(e+I_E))\left[\frac{c_B+k_m c_m+k_o c_o}{2b_F} - \frac{l}{\rho+\delta}\frac{a_F+a_E \ln(e+I_E)}{2b_F}\right] \end{aligned} \tag{72}$$

$$\begin{aligned} V_{B2}^{\star} = {} & \frac{l}{\rho+\delta} x_{B2} + \frac{1}{\rho} b_F\left[\frac{c_B(1-p)}{2b_F} - \frac{l}{\rho+\delta}\frac{a_F}{2b_F}\right]^2 - \frac{1}{\rho} c_B(1-p)\left[\frac{c_B(1-p)}{2b_F} - \frac{l}{\rho+\delta}\frac{a_F}{2b_F}\right] \\ & + \frac{1}{\rho}\frac{l}{\rho+\delta} a_F\left[\frac{c_B(1-p)}{2b_F} - \frac{l}{\rho+\delta}\frac{a_F}{2b_F}\right] \end{aligned} \tag{73}$$

In this case,

$$F_{B1}^{\star}(t) = \frac{c_B + k_m c_m + k_o c_o}{2b_F} - \frac{l}{\rho+\delta}\frac{a_F + a_E \ln(e+I_E)}{2b_F} \tag{74}$$

$$F_{B2}^{\star}(t) = \frac{c_B(1-p)}{2b_F} - \frac{l}{\rho+\delta}\frac{a_F}{2b_F} \tag{75}$$

frontiers | Frontiers in Applied Mathematics and Statistics

TYPE Original Research
PUBLISHED 07 September 2023
DOI 10.3389/fams.2023.1208774

OPEN ACCESS

EDITED BY
Uttam Ghosh,
University of Calcutta, India

REVIEWED BY
Ebenezer Bonyah,
University of Education, Winneba, Ghana
Bapin Maa Ndal,
University of Calcutta, India
Ramoshweu Solomon Lebelo,
Vaal University of Technology, South Africa
Hira Soomro,
Universiti Teknologi Petronas, Malaysia
Pankaj Tiwari,
University of Kalyani, India

*CORRESPONDENCE
Adiqa Kausar Kiani
✉ adiqa@yuntect.edu.tw

RECEIVED 19 April 2023
ACCEPTED 24 August 2023
PUBLISHED 07 September 2023

CITATION
Anwar N, Ahmad I, Kiani AK, Shoaib M and Raja MAZ (2023) Numerical treatment for mathematical model of farming awareness in crop pest management.
Front. Appl. Math. Stat. 9:1208774.
doi: 10.3389/fams.2023.1208774

Numerical treatment for mathematical model of farming awareness in crop pest management

Nabeela Anwar[1], Iftikhar Ahmad[1], Adiqa Kausar Kiani[2]*, Muhammad Shoaib[3] and Muhammad Asif Zahoor Raja[2]

[1]Department of Mathematics, University of Gujrat, Gujrat, Pakistan, [2]Future Technology Research Center, National Yunlin University of Science and Technology, Yunlin, Taiwan, [3]Artificial Intelligence (AI) Center, Yuan Ze University, Taoyuan, Taiwan

The most important factor for increasing crop production is pest and pathogen resistance, which has a major impact on global food security. Pest management also emphasizes the need for farming awareness. A high crop yield is ultimately achieved by protecting crops from pests and raising public awareness of the devastation caused by pests. In this research, we aim to investigate the intricate impacts of nonlinear delayed systems for managing crop pest management (CPM) supervised by Ordinary Differential Equations (ODEs). Our focus will be on highlighting the intricate and often unpredictable relationships that occur over time among crops, pests, strategies for rehabilitation, and environmental factors. The nonlinear delayed CPM model incorporated the four compartments: crop biomass density [B(t)], susceptible pest density [*S(t)*], infected pest density [*I(t)*], and population awareness level [*A(t)*]. The approximate solutions for the four compartments *B(t)*, *S(t)*, *I(t)*, and *A(t)* are determined by the implementation of sundry scenarios generated with the variation in crop biomass growth rate, rate of pest attacks, pest natural death rate, disease associated death rate and memory loss of aware people, by means of exploiting the strength of the Adams (ADS) and explicit Runge-Kutta (ERK) numerical solvers. Comparative analysis of the designed approach is carried out for the dynamic impacts of the nonlinear delayed CPM model in terms of numerical outcomes and simulations based on sundry scenarios.

KEYWORDS

non-linear delayed crop pest management model, public awareness, explicit Runge–Kutta method, Adams method, comparative analysis, approximate solutions, graphical illustrations

1. Introduction

In recent years, researchers have paid more attention to integrated pest management, and its use in the crop field has increased. This strategy emphasizes the implication of biological control factors to minimize the credence of pesticides. In agriculture, forest management, and population health, microbiological pesticides play a significant role in incorporated pest management. In the case of crops, biopesticides provide noticeable pest management dependability as part of incorporated pest management [1]. In North America and Europe, viruses are used as pest control agents against insect pests [2–4]. Agricultural-related awareness programs on radio, TV, mobile and other media might aid in disseminating agricultural knowledge among farmers and ranchers about the hazards of pesticide use on

human health as well as the other linked environmental concerns [5–9]. Pesticide overuse is significantly associated with farmers' lack of pesticide knowledge, the impact of pesticide retail outlets, and inaccessibility to non-synthetic pest control methods, while the tendency to overuse reduces higher levels of the learning process in Integrated Pest Management [10]. As a result, farming awareness is essential to prevent crop losses having the least amount of detrimental side effects [11, 12]. Pesticide communication campaigns made it easier for farmers to understand the substantial risks pesticides pose to public health and the ecosystem, and to limit harmful consequences. Farmers primarily learned about pesticide use and hazards through oral communication [13].

Time delay is a key feature in both natural and manmade systems. Kuang provided an example to demonstrate the significance of time delay [14]. He claimed that animals require time to digest their food before moving on to other activities and reflexes. As a result, any species model with no temporal delay is at best an approximation [15]. Many systems as well as industrial plants, including biological systems, machining, metal forming, thermal acoustic systems and many others experience time delays [16–19]. Furthermore, dynamical systems including time delay exhibit far more complex behaviors than those without delay in time [20]. There are two key reasons for the presence of temporal delays in prey-predator systems [21, 22]. The first is the gestation period, and the second is the maturation period. As a result, incorporating delays into predator-prey model is essential for ensuring the realistic nature of these models and demonstrating how well the population dynamics of such models are influenced by previous relevant information. In fact, time delays have a significant impact on the overall characteristics of dynamic systems. Many publications in the literature have described the theory-based analysis of the prey-predator model involving time delay, such as hunting delay [23], dispersal delay [24], predator gestation period [25], as well as intra-specific competitive pressure generated feedback delay [26].

There is a lack of mathematical modeling on agricultural awareness to limit plant pests as well as diseases. Daudi et al. [27] proposed a dynamic model using the fractional derivative operator for maize growth as well as interactions with fall armyworms. They described the basic reproductive number, which was the average amount of newborns generated by a single female moth over the course of a lifespan. The resilience of the trivial equilibria, as well as the positive equilibria of the dynamical system, were investigated by Li et al. [28] and the threshold requirements for pest destruction and system permanence were determined.

TABLE 1 Parameters default values used for non-linear delayed CPM model [38].

Parameters	Value	Parameters	Value
a	0.2	φ	0.5
N	50	μ	0.6
δ	0.025	μ_1	0.12
c	0.1	l	0.025
β	0.05	d	0.015
A_0	0.2	υ	0.05
τ	1	-	-

Xiang et al. [29] explored the influence of MD controls on the dynamical behavior of the pest systems by adding the gestational delay and sex pheromones. First, the system's bounds, stability, as well as bifurcation were discussed. Second, by integrating the constraint violating function, an optimized control problem depending on sex pheromone and pesticides was reduced into an analogous optimized parameter decision issue. The bifurcation control of mosaic viruses fractional order infection models for Jatropha curcas with agricultural awareness and an executing delay was examined by Liu et al. [30] Hopf bifurcation generated by executing delay was explored for the unregulated system by examining the corresponding characteristic equation. They found that changing the fractional order had a considerable impact on bifurcation dynamics. Kumari et al. [31] employed the Integrated Pest Management (IPM) technique to create a mathematical model that used a combination of chemical and biological management. The feasibility of pest eradication and non-trivial equilibria state were examined, and the local stability of the pest eradication equilibria state was investigated further. Shi et al. [32] presented a unique population Smith framework with continual delay as well as impulsive phase adaptive control and examined how it may be used in pest management. The model's singularity was first qualitatively examined, and then the presence and uniqueness of order one periodical orbits were considered in order to calculate the frequency of chemical control implementation. A Filippov prey predator model incorporating time delay was introduced by Arafa et al. [33], where the delay time indicated the changes in the natural enemy's growth rate before discharging it to fatten up pests. The bifurcation parameter time delay was used to derive the threshold constraints for the stability of the equilibrium. Utilizing Hopf bifurcation, it was proven that whenever the time delay parameter crosses through specific critical levels, a periodical oscillation phenomenon arises. They also established the equation of slipping motion and addressed the sliding phase dynamics using the Filippov convex approach. Al Basir et al. [34] presented prey predator framework for assessing the impact of delay time in crop pest management utilizing agricultural awareness-based treatments. The authors indicated that the application of biological insecticides is proportionate to the pest population density on the plantation. The presence of steady states, as well as their stability, had been examined. Allen-Perkins and Estrada [35] constructed an epidemic model to explore disease transmission and control in planted agricultural farms as a long-term pest management

Abbreviations: IPM, Integrated Pest Management; ERK, Explicit Runge-Kutta; MD, Mating disruption; TV, Television; ODEs, Ordinary differential equations; HIV, Human immunodeficiency virus; COVID-19, coronavirus disease of 2019; ADS, Adams method; CPS, Crop pest management; $B(t)$, $S(t)$, $I(t)$, $A(t)$, Crop biomass density, Susceptible density, Infected density, Aware people density; B_0, S_0, I_0 and A_0, Initial conditions for B, S, I and A; *NDSolve*, Numerical solution of differential equations; α, Crop biomass growth rate; N, Maximum crop biomass percentage; δ, Rate of pest attacks; c, Pest natural death; β, Disease associated death rate; l, Aware individuals' activity level; d, Growth rate of aware individuals; υ , Memory loss of aware people; A_0, Awareness level from a widespread source; τ , Delay in time.

TABLE 2 Illustration of scenarios for the non-linear delayed CPM model.

Scenario 1 for the crop biomass growth rate		
ADS solver		ERK solver
C-1	$a = 0.25$	$a = 0.25$
C-2	$a = 0.3$	$a = 0.3$
C-3	$a = 0.5$	$a = 0.5$
C-4	$a = 0.7$	$a = 0.7$
C-5	$a = 0.9$	$a = 0.9$
Scenario 2 for the rate of pest attacks		
ADS solver		ERK solver
C-1	$\delta = 0.015$	$\delta = 0.015$
C-2	$\delta = 0.025$	$\delta = 0.025$
C-3	$\delta = 0.035$	$\delta = 0.035$
C-4	$\delta = 0.045$	$\delta = 0.045$
C-5	$\delta = 0.055$	$\delta = 0.055$
Scenario 3 for the pest natural death rate		
ADS solver		ERK solver
C-1	$c = 0.15$	$c = 0.15$
C-2	$c = 0.25$	$c = 0.25$
C-3	$c = 0.33$	$c = 0.33$
C-4	$c = 0.45$	$c = 0.45$
C-5	$c = 0.55$	$c = 0.55$
Scenario 4 for disease associated death rate		
ADS solver		ERK solver
C-1	$\beta = 0.01$	$\beta = 0.01$
C-2	$\beta = 0.02$	$\beta = 0.02$
C-3	$\beta = 0.03$	$\beta = 0.03$
C-4	$\beta = 0.04$	$\beta = 0.04$
C-5	$\beta = 0.05$	$\beta = 0.05$
Scenario 5 for memory loss of aware people		
ADS solver		ERK solver
C-1	$\upsilon = 0.01$	$\upsilon = 0.01$
C-2	$\upsilon = 0.02$	$\upsilon = 0.02$
C-3	$\upsilon = 0.03$	$\upsilon = 0.03$
C-4	$\upsilon = 0.05$	$\upsilon = 0.05$
C-5	$\upsilon = 0.06$	$\upsilon = 0.06$

strategy. In an epidemiological susceptible, infectious and removed model, the model includes the mobility of aphids carrying a virus in an agricultural farm, the spatial dispersion of plants in a planted field, and the existence of "trapped crops." Abraha et al. [36] studied a mathematical model for crop pest control that took into account plant biomass, pests, and the impact of farmer awareness. The basic reproductive number and delays in time were used to determine the presence as well as stability of the equilibria. Whenever time delays approach critical values, stability transitions happen due to Hopf-bifurcation. The delayed system's cost-effectiveness was assessed using optimal control-theory. Rossini et al. [37] presented a mathematical framework for calculating the analytical solutions to the second variant of the distributed delay model. The researchers also investigated how the model behaved when it came to representing the population of insect pests in various environmental factors, particularly with respect to temperature. Al Basir et al. [38] proposed a mathematical model including delay to investigate the impact of public awareness on agricultural pest management using crop biomass, and pests. The basic reproductive number was used to determine the presence and stability conditions of the equilibria. The Hoph bifurcation analysis was performed at the epidemic equilibria with time delay as the bifurcation parameter.

Numerical approaches are frequently employed in science and engineering to solve mathematical problems for which exact solutions are difficult or impossible to grab. Only a limited number of differential equations can be solved analytically. There are several analytical methods to solve ordinary differential equations (ODEs). Although several ODEs have closed form solutions that can be obtained using renowned analytical methods, numerical methods must be evolved and applied to obtain numerical solutions of a differential equation under a predefined initial history. Many researchers used a variety of numerical methods to simulate the solution of mathematical models, acquiring results that were more accurate than those found in the literature, such as [39–43]. Researchers have recently focused their efforts on the numerical solutions of numerous mathematical models in the realm of epidemiology, such as the HIV model [44], COVID-19 [45], plant disease model [46], tuberculosis propagation model [47], computer virus transmission model [48]. Although the above mentioned techniques have high precision and consistency but they require considerable memory and long computational cost. Consequently, the procedures for this technique present noteworthy challenges that may be resolved in order to ensure that the solution is precise and consistent. Therefore, several efforts have been made by researchers to develop efficient techniques for solving linear and non-linear ODE systems [49–51]. The importance of numerical solutions is emphasized in the literature listed above. As a result of these considerations, the authors have decided to use the ADS (Adams) and ERK (explicit Runge–Kutta) numerical solvers to solve the delay differential system [52–56]. The Adams predictor-corrector approach [46, 57–60] is also a more efficient and straightforward numerical tool for solving delay differential systems.

In order to manage crop pests, insecticides or other preventative measures are frequently used. The emphasis is shifted to educating farmers about alternative techniques including rotation of crops, biological insect control, and cultural practices by incorporating agricultural knowledge into the pest management approach. Through integration, agricultural pest control may be approached holistically and sustainably [61]. To model and simulate the dynamics of agricultural pest populations while taking into account a variety of elements such as environmental conditions, insect life cycles, and farming practices, numerical analytic techniques such as the use of differential equations and optimization methods can be used. The model can offer

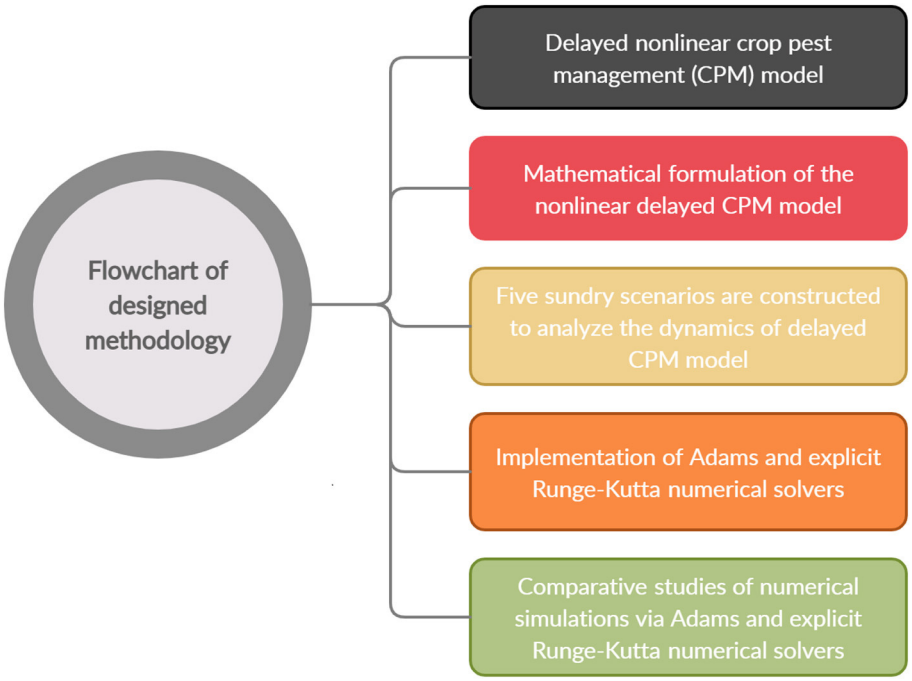

FIGURE 1
Flowchart of designed methodology for non-linear delayed CPM model.

insights to the population dynamic of pests, the effects of various management techniques, and the ideal time for putting control measures into place by using numerical analysis. By offering data-driven advice to farmers and decision-makers, this quantitative method improves the decision-making process [62]. In general, the notion is innovative since it addresses agricultural pest control by combining principles of farming awareness with numerical analytic methods. This multidisciplinary approach emphasizes eco-friendly and sustainable practices while also offering a quantitative foundation for analyzing and improving pest management tactics. Combining these factors helps researchers create agricultural pest management strategies that are both more practical and ecologically responsible. This research may help with the creation of efficient and long-lasting farming awareness campaigns, the adoption of integrated pest management techniques, and the alleviation of farmer difficulties brought on by crop pests. Time delay models really have the potential to increase complexity because of the intrinsic properties of temporal latencies and their impact on system dynamics. The implementation of numerical solutions for non-linear delayed systems may be challenging and computationally expensive. Researchers may require sophisticated software, outstanding durability computing devices, as well as expertise in both computational and mathematical modeling strategies. In this study, we used state-of-the-art numerical techniques like Adam (ADS) and explicit Runge–Kutta (ERK) to find the numerical solution of the non-linear delayed CPM model. The presented study has the following salient features:

- The dynamic impact of the non-linear delayed crop pest management (CPM) system supervised by ODEs is analyzed by incorporating awareness growth level.
- The approximate solutions for the four compartments $B(t)$, $S(t)$, $I(t)$, and $A(t)$ are determined by the implementation of sundry scenarios generated with the variation in crop biomass growth rate, rate of pest attacks, pest natural death rate, disease associated death rate and memory loss of aware people.
- The strength of the Adams and explicit Runge–Kutta numerical solvers are utilized to determine the approximate solutions for the non-linear delayed CPM model.
- Comparative analysis is carried out for the dynamic impact of the non-linear delayed CPM model in terms of numerical outcomes as well as graphical illustrations based on sundry scenarios.

The rest of the article's layout is as follows: In the second section, the non-linear delayed CPM model is formulated. The third section provides a detailed overview of the methodology. The fourth section provides the analysis, discussion, and graphical interpretation of approximate solutions. The fifth section presents the analysis-based conclusion.

2. Formulation of the mathematical model

The model [38] integrated agricultural biomass, pests, and the population's awareness. Crop biomass density, susceptible pest density, infected pest density, and aware people density are the four compartments incorporated in the model. Logistical evolution for the densities of crop biomass is assumed, since crop fields have a finite size (though it might be large), with a net growth rate a and N is carrying capacity. Pests that are susceptible to the crop are

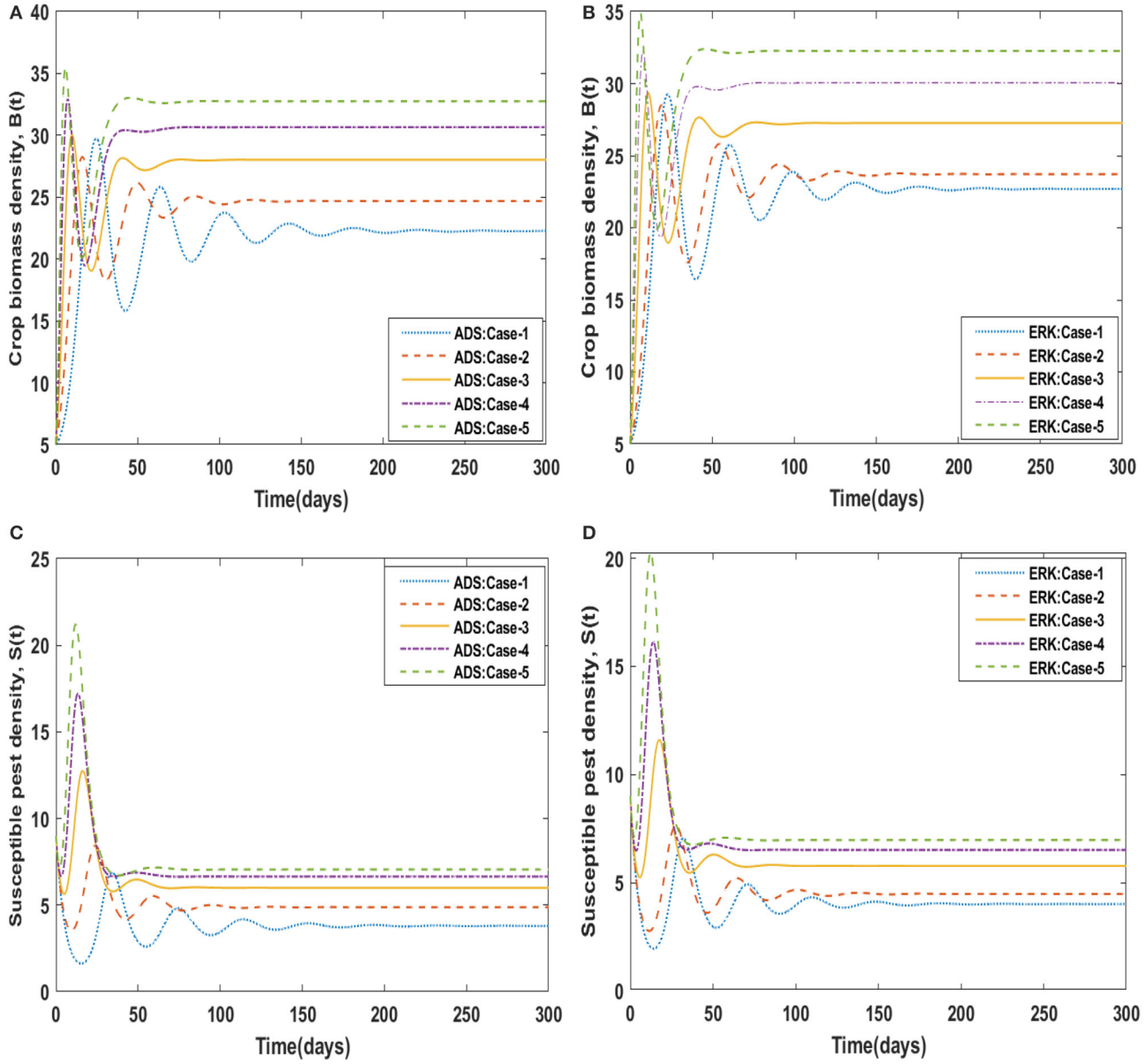

FIGURE 2
(A–D) Dynamics of *B(t), S(t)* for variation in α by ADS and ERK solvers.

attacked, significantly reducing the crop. Let λ represent the pest attack rate on crops [38].

$$\frac{dB}{dt} = aB(t)\left(1 - \frac{B(t)}{N}\right) - \delta B(t) S(t) - \varphi\delta B(t) I(t) \quad (1)$$

To take into consideration their interests as well, aware individuals may keep the crops under observation and, if properly trained, will squirt biopesticides or integrate them into fertilizer applications to manage the insect invasion. The massive term $lA(t)S(t)$ can be used to introduce the awareness action rate l, which results from deliberate human activities and control actions like the application of biopesticides [38].

$$\frac{dS}{dt} = \mu\delta B(t) S(t) - lA(t) S(t) - cS(t) \quad (2)$$

Pests that are infected can also harm the crop, $\phi\delta$, although at a much lesser rate $\phi < 1$. Here, c represents the pests' natural death rate, and the infection mortality rate β is a result of knowing human behavior, like the application of insecticides [38].

$$\frac{dI}{dt} = \mu_1\varphi\delta B(t) I(t) + lA(t) S(t) - (c + \beta) I(t) \quad (3)$$

μ and μ_1 represent the "conversion efficacy" of susceptible as well as infected pests, or how well the pests can use plant components. Since pests influenced by pesticides are less effective, $\mu > \mu_1$. Because of media initiatives and increased public awareness, farmers now have a higher level of awareness, which is denoted by A. Additionally, it is expected that the exposure of the resilient pests influences the rate at which local information is

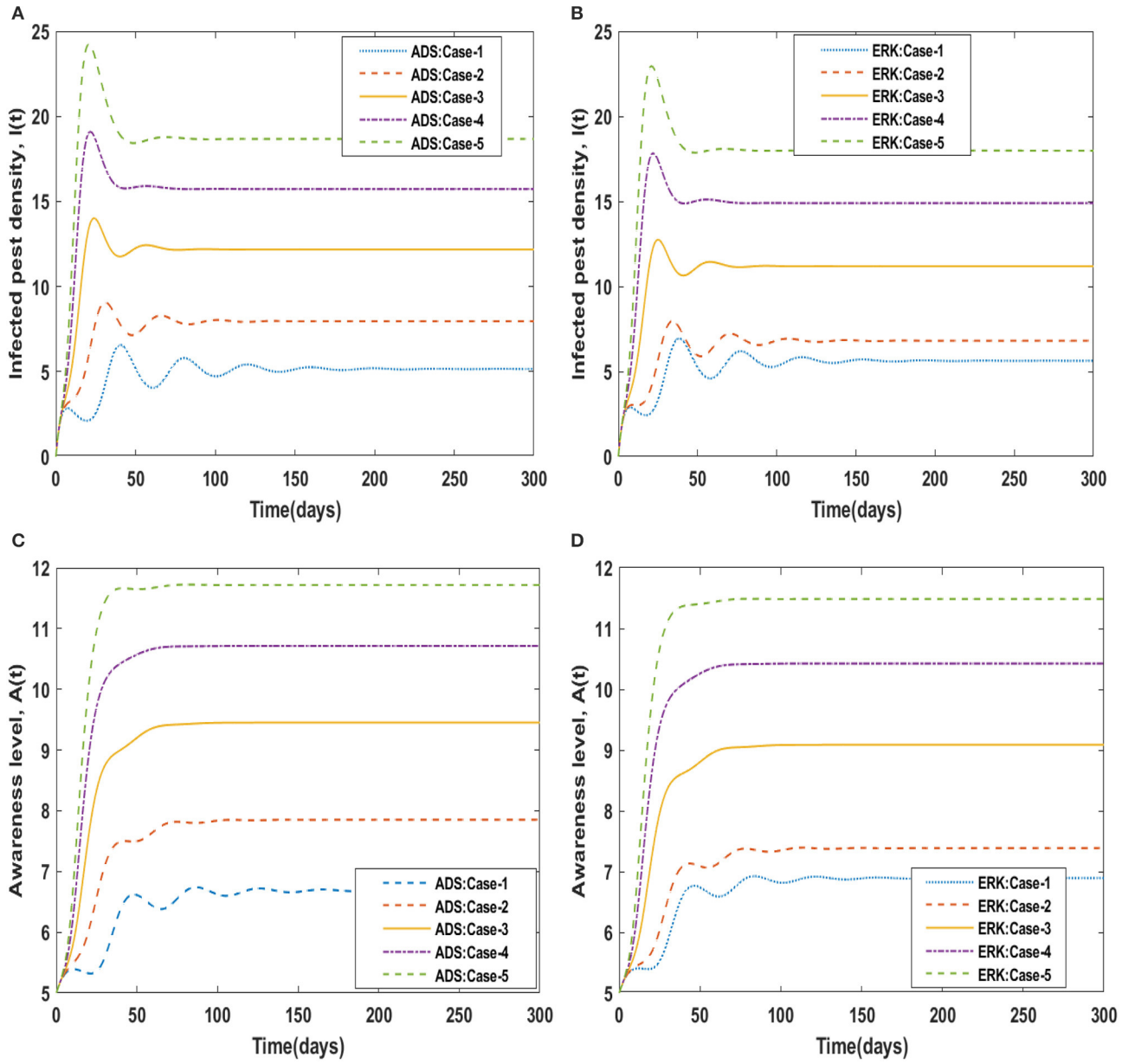

FIGURE 3
(A–D) Dynamics of *I(t), A(t)* for variation in α by ADS and ERK solvers.

increasing at a rate d. The loss of memory causes farmers' levels of consciousness to decline at a rate υ [38].

$$\frac{dA}{dt} = A_0 + d\,(S + I) - \upsilon A\,(t) \tag{4}$$

A delay in observing the number of pests or their activity might occur in a field. Typically, this prediction is produced by studying past incidences of pest prevalence. As a consequence, there are differences in the degree of awareness and the application of preventive countermeasures. Enforcement of such remedies is anticipated to be delayed. The number of pests present at time $(t-\tau)$ (or time $\tau > 0$ in some cases) will determine how intense the awareness campaigns are at time t.

The following modified mathematical model results from the abovementioned assumptions [38].

$$\begin{aligned}
\frac{dB}{dt} &= aB\,(t)\left(1 - \frac{B\,(t)}{N}\right) - \delta B\,(t)\,S\,(t) - \varphi\delta B\,(t)\,I\,(t)\,, \quad (5)\\
\frac{dS}{dt} &= \mu\delta B\,(t)\,S\,(t) - lA\,(t)\,S\,(t) - cS\,(t)\\
\frac{dI}{dt} &= \mu_1\varphi\delta B\,(t)\,I\,(t) + lA\,(t)\,S\,(t) - (c+\beta)\,I\,(t)\,,\\
\frac{dA}{dt} &= A_0 + d\,[S\,(t-\tau) + I\,(t-\tau)] - \upsilon A\,(t)\,,
\end{aligned}$$

and initial conditions are as:

$$B_0 > 0,\ S_0 > 0,\ I_0 > 0,\ A_0 > 0.$$

TABLE 3 Numerical solutions of non-linear delayed CPM model.

Time (Days)	ADS method: Case-1, scenario 1				ERK method: Case-1, scenario 1			
	B	*S*	*I*	*A*	*B*	*S*	*I*	*A*
0	5.0000	9.0000	0.0000	5.0000	5.0000	9.0000	0.0000	5.0000
30	26.1125	5.8948	3.9220	5.5834	23.3716	6.8244	5.0614	5.8591
60	25.0607	2.9136	4.0531	6.4258	25.7283	3.6210	4.6352	6.5924
90	20.9814	3.3823	5.2252	6.7278	22.5739	3.5602	5.4542	6.8884
120	21.3736	4.0253	5.4197	6.7014	21.973	4.0203	5.7923	6.9152
150	22.5170	3.9243	5.1375	6.6640	22.5754	4.1149	5.6882	6.8880
180	22.4914	3.7534	5.0876	6.6792	22.8188	4.0266	5.6053	6.8852
210	22.2127	3.7693	5.1551	6.6915	22.736	3.9931	5.6144	6.8919
240	22.2056	3.8118	5.1717	6.6890	22.6739	4.0055	5.6330	6.8939
270	22.2742	3.8102	5.1559	6.6859	22.6809	4.0143	5.6342	6.8929
300	22.2797	3.7995	5.1510	6.6864	22.6949	4.0132	5.6306	6.8924
Time (Days)	ADS method: Case-1, scenario 2				ERK method: Case-1, scenario 2			
	B	*S*	*I*	*A*	*B*	*S*	*I*	*A*
0	5.0000	9.0000	0.0000	5.0000	5.0000	9.0000	0.0000	5.0000
30	42.1137	1.4442	1.2169	4.9590	37.5666	2.4939	1.7529	5.0883
60	30.9961	4.2045	4.7578	5.9536	24.7972	3.0352	4.8875	6.4178
90	35.8779	2.8193	3.4942	6.0433	29.1146	3.9229	4.4357	6.2426
120	34.6532	3.2335	3.8803	6.0627	29.0943	3.2468	4.2783	6.3584
150	35.0477	3.0773	3.7627	6.0738	28.4761	3.5095	4.5016	6.3678
180	34.9494	3.1288	3.7958	6.0697	28.9109	3.4469	4.3903	6.3534
210	34.9740	3.1114	3.7869	6.0720	28.7450	3.4403	4.4240	6.3634
240	34.9693	3.1171	3.7891	6.0710	28.7786	3.4551	4.4215	6.3599
270	34.9697	3.1153	3.7886	6.0714	28.7857	3.4467	4.4174	6.3605
300	34.9700	3.1158	3.788	6.0713	28.7754	3.4496	4.4205	6.3607
Time (Days)	ADS method: Case-1, scenario 3				ERK method: Case-1, scenario 3			
	B	*S*	*I*	*A*	*B*	*S*	*I*	*A*
0	5.0000	9.0000	0.0000	5.0000	5.0000	9.0000	0.0000	5.0000
30	35.5348	3.2136	1.3479	4.8960	33.3640	3.5504	1.7029	5.0144
60	25.7824	2.3893	2.3939	5.8214	24.4191	2.2973	2.7589	5.9697
90	23.0944	3.4217	3.2682	5.9988	21.3008	3.46005	3.8654	6.1715
120	24.6101	3.7104	3.1689	5.9524	23.2995	3.8409	3.6906	6.0977
150	25.2161	3.5072	3.0193	5.9478	24.0785	3.5170	3.4583	6.0924
180	24.9855	3.4511	3.0346	5.9622	23.6254	3.4445	3.5082	6.1180
210	24.8747	3.4821	3.0615	5.9652	23.4641	3.5134	3.5601	6.1213
240	24.9097	3.4933	3.0603	5.9632	23.5660	3.5293	3.5490	6.1162
270	24.9307	3.4884	3.0556	5.9627	23.6013	3.5138	3.5377	6.1156
300	24.9257	3.4862	3.0556	5.9630	23.5785	3.5105	3.5402	6.1168

Each parameter used in the mathematical model is described in the nomenclature. The parameters' descriptions and default values are listed in Table 1 as per in Al Basir et al. [38]. These default parameter values are used to generate each scenario. The non-linear delayed CPM model by using numerical values can be mathematically defined for one of the cases as:

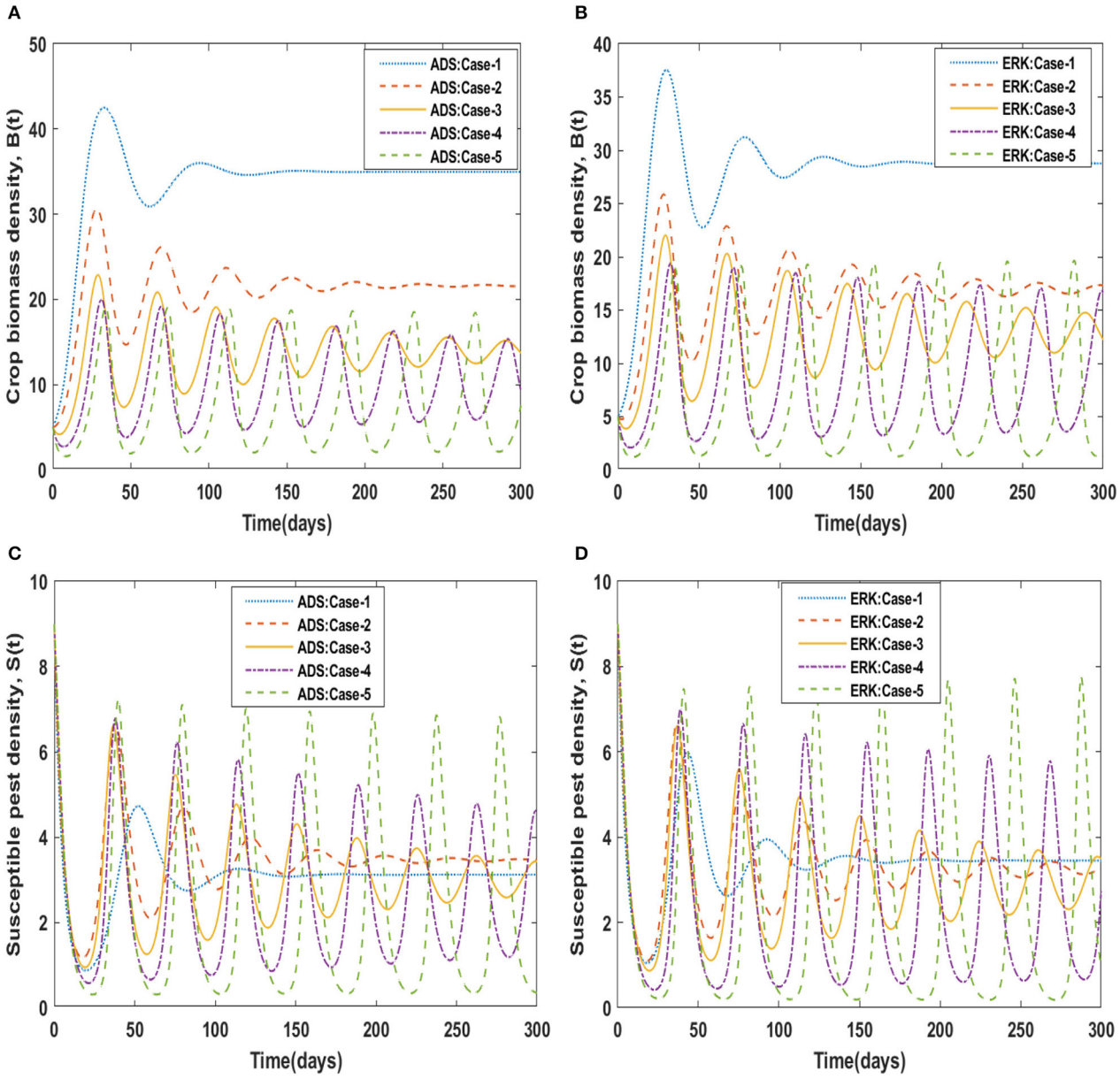

FIGURE 4
(A–D) Dynamics of *B(t), S(t)* for variation in δ by ADS and ERK solvers.

$$\begin{aligned}
\frac{dB}{dt} &= 0.2B(t)\left(1-\frac{B(t)}{50}\right) - 0.025B(t)S(t) - 0.0125B(t)I(t), \\
\frac{dS}{dt} &= 0.015B(t)S(t) - 0.025A(t)S(t) - 0.01S(t) \\
\frac{dI}{dt} &= 0.0015B(t)I(t) + 0.025A(t)S(t) - 0.15I(t), \\
\frac{dA}{dt} &= 0.2 + 0.015\left[S(t-1) + I(t-1)\right] - 0.6A(t),
\end{aligned} \tag{6}$$

3. Methodology

This section includes a detailed presentation of the learning methodologies that are used to determine the approximate solutions of the non-linear delayed CPM model.

3.1. Adams method

A two-step process called the ADS numerical solver is used to solve an ODE [63, 64]. Initially, the predictive stage provides a rough approximation of the target outcome in order to utilize an explicit technique. The corrector step uses a different method, typically an implicit one, to speed up the previous approximation.

$$\frac{dB}{dt} = H(t, B, S, I), \qquad B(t_0) = B_0 \tag{7}$$

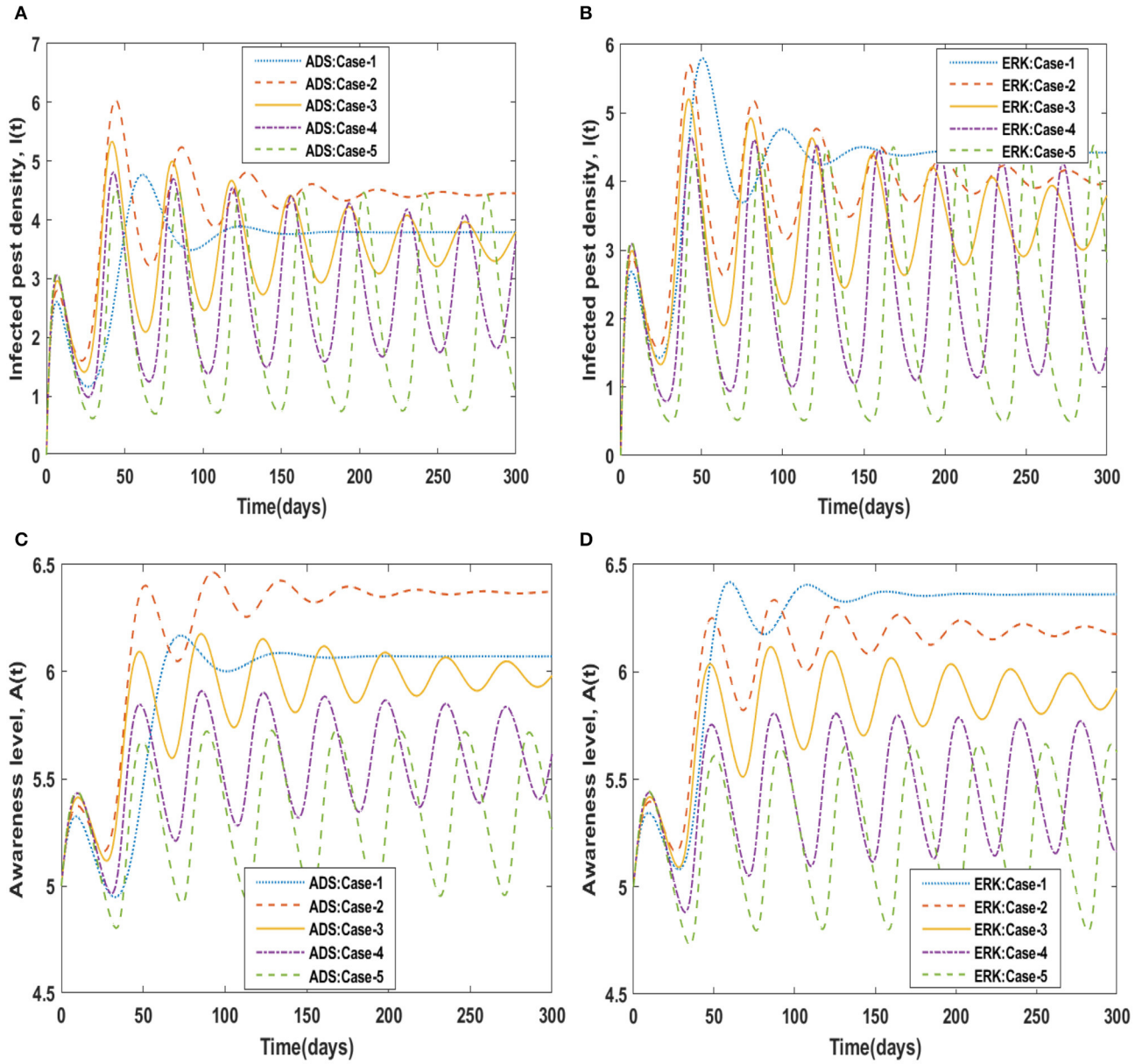

FIGURE 5
(A–D) Dynamics of *I(t), A(t)* for variation in δ by ADS and ERK solvers.

$$\frac{dS}{dt} = H(t, S, B, A), \qquad S(t_0) = S_0$$
$$\frac{dI}{dt} = H(t, I, B, S, A), \qquad I(t_0) = I_0$$
$$\frac{dA}{dt} = H(t, A, S, I), \qquad A(t_0) = A_0$$

For the very first equation in set (7) of the non-linear delayed CPM model, use the following formula to produce a two-step prediction solution:

$$B_{k+1} = B_k + \frac{6}{4}hH(t_k, B_k) - \frac{1}{2}hH\left(t_{k-1}, B_{k-1}\right), \tag{8}$$

Once the very first equation in the non-linear delayed CPM model has been evaluated, the following two step corrector formula is obtained:

$$B_{k+1} = B_k + \frac{1}{2}hH\left(t_{k+1}, B_{k+1}\right) + H(t_k, B_k). \tag{9}$$

Adams techniques may be used to solve a variety of initial value problems, including those involving delay differential equations and ODEs. They are capable of handling stiff as well as non-stiff systems. When compared to other numerical approaches, such as implicit methods, these techniques are computationally efficient. They can lead to faster computations since they require fewer function evaluations each step. Adams techniques contain stability constraints on the step-size and the ratio of step-size to time delay,

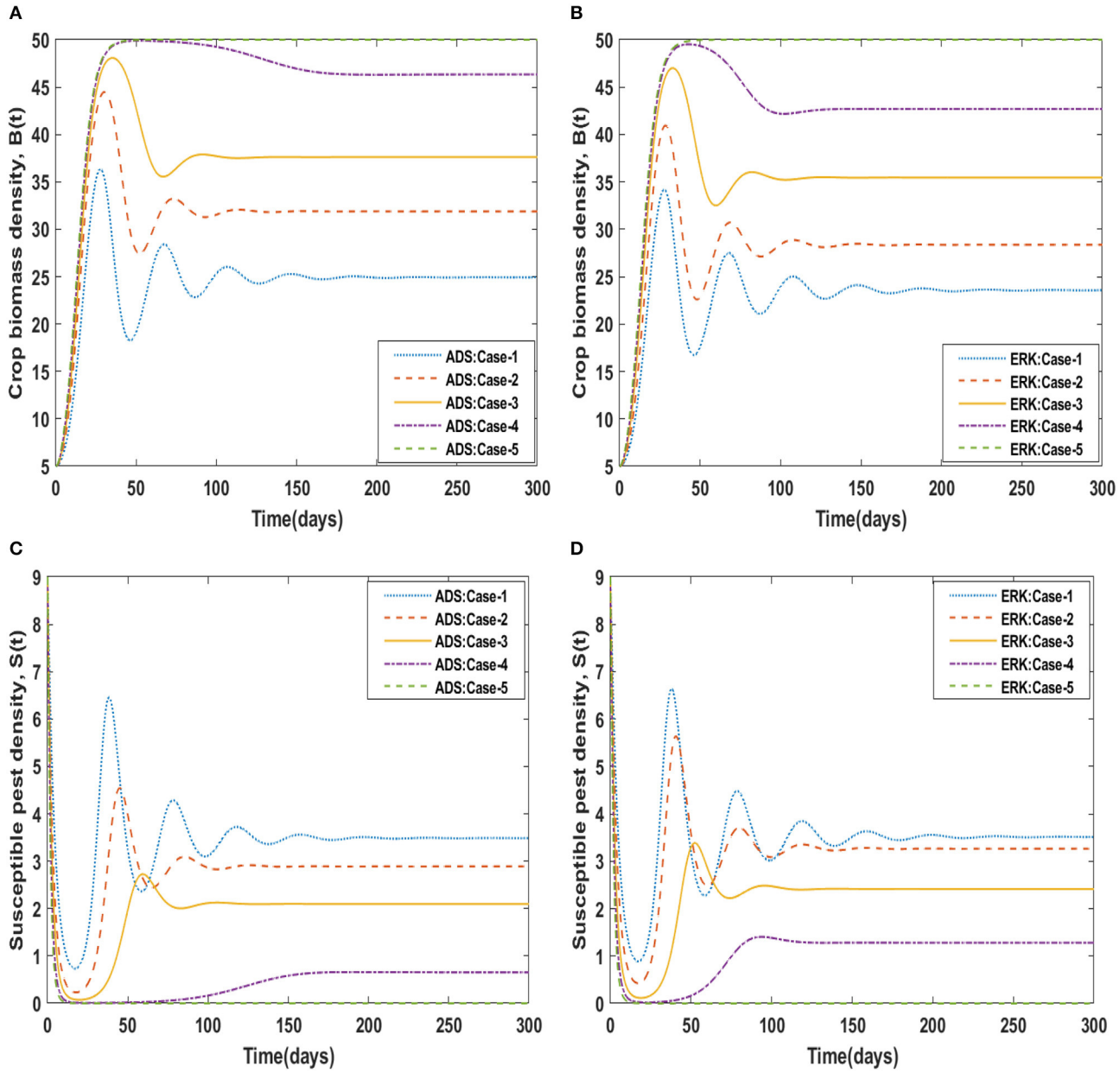

FIGURE 6
(A–D) Dynamics of *B(t)*, *S(t)* for variation in *c* by ADS and ERK solvers.

making them conditionally stable. The approach could result in unstable solutions if these requirements are not satisfied. Adams techniques need a sufficient number of starting values to begin the iteration process since they are multi-step approaches. When starting quantities are difficult to get or need further calculations, this might be difficult [65].

3.2. Runge–Kutta method

The explicit Runge–Kutta (ERK) numerical solver can be used efficiently and comprehensively to solve ODEs [66]. C. Runge and M. W. Kutta introduced the Runge–Kutta methods in the early 1900s. As time went on, this approach played a significant part in the research of iterative approaches based on explicit and implicit assumptions that were used to solve ODEs using time discretization.

The generic form of ODE is considered as:

$$\frac{dy}{dt} = f\left(t, y\right), \tag{10}$$

A generic form of ERK method is defined as:

$$m_1 = f\left(t_n, y_n\right), \tag{11}$$

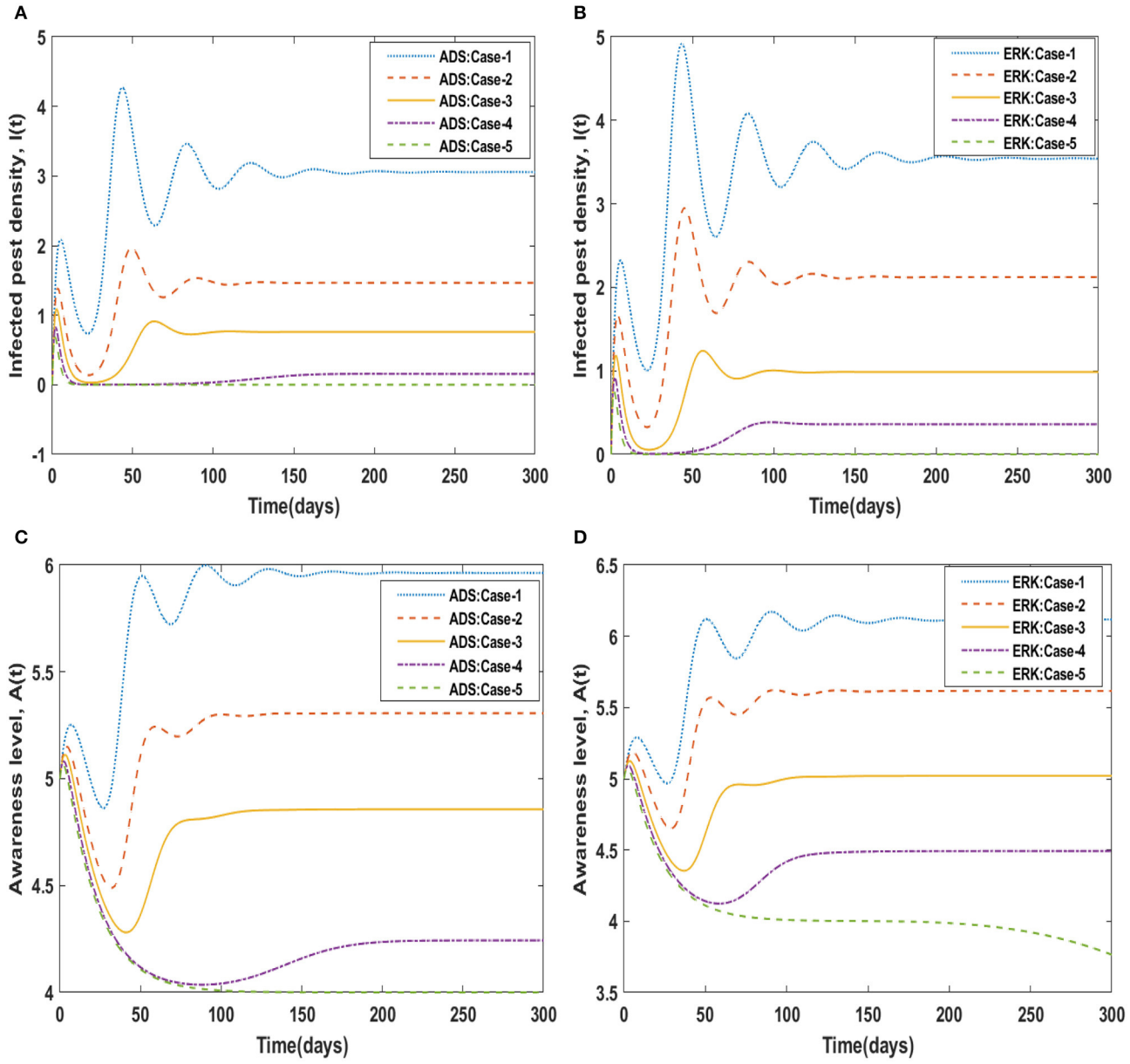

FIGURE 7
(A–D) Dynamics of *I(t)*, *A(t)* for variation in *c* by ADS and ERK solvers.

$$m_j = f\left(t_n + b_j h,\ y_n + h\sum_{i=1}^{j-1} c_{ji} m_i\right),\ j = 2, ..., l, \tag{12}$$

$$y_{n+1} = y_n + h\sum_{j=1}^{l} a_j m_j, \tag{13}$$

where the time interval is $h = \Delta t$, and y_n approximates $y(t_n)$.

The stability characteristics of Runge–Kutta techniques are well established. They can manage a variety of concerns, which includes stiff systems, without running into stability problems. Numerical simulations can be resilient and trustworthy thanks to this stability. These methods are adaptable and effective for dealing with delayed differential equations as well as regular differential equations, partially differential equations, and other forms of differential equations. They have broad applications in several fields of science and engineering [67].

4. Analysis and discussion

The approximate numerical solutions for compartments *B(t)*, *S(t)*, *I(t)*, and *A(t)* of the non-linear delayed CPM model are presented here in this section. The dynamics of the non-linear delayed CPM model are investigated for sundry scenarios each comprising of 1–5 cases by means of ADS and ERK numerical solvers with input points from 0 to

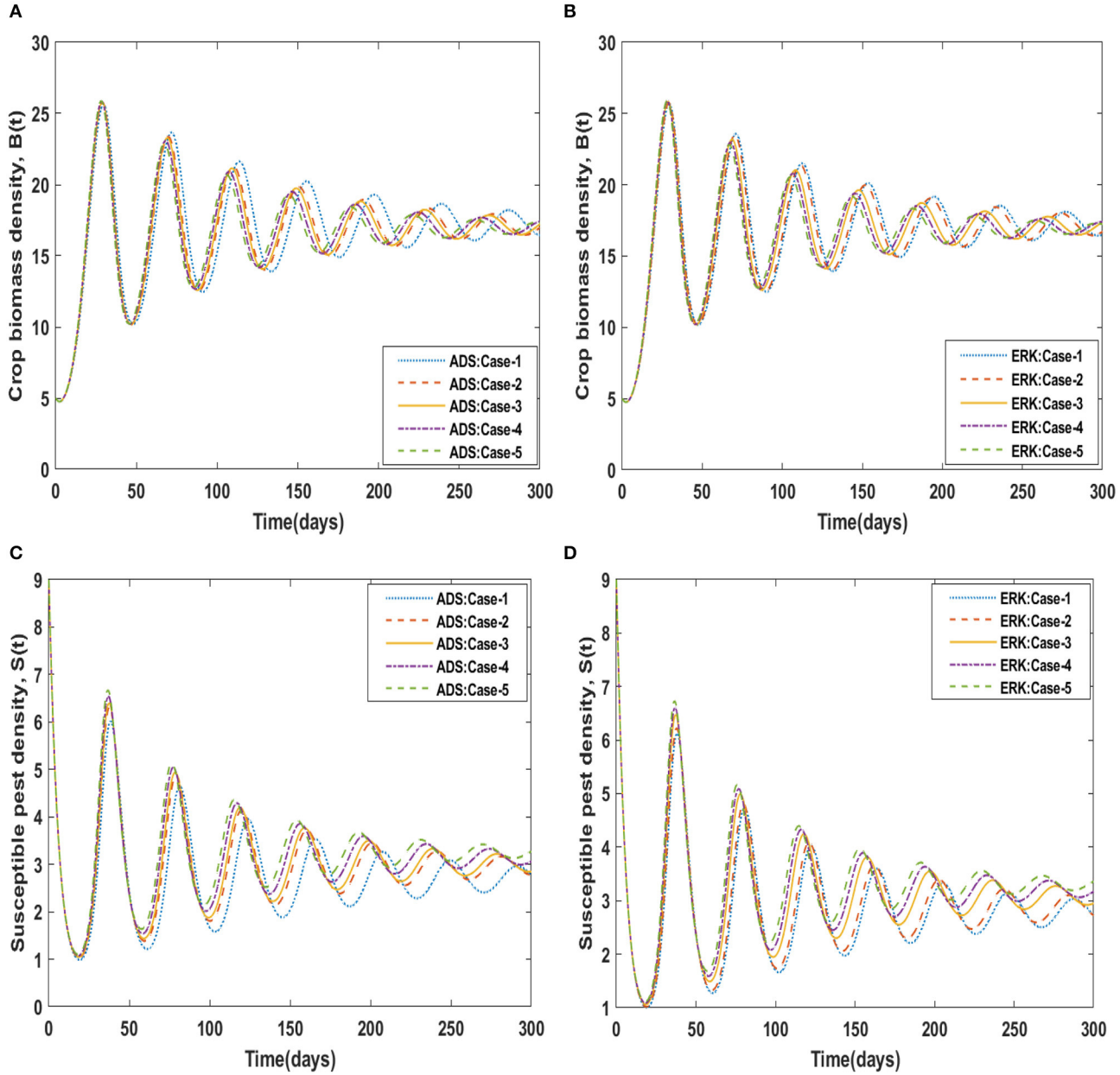

FIGURE 8
(A–D) Dynamics of *B(t)*, *S(t)* for variation in β by ADS and ERK solvers.

300 and step size 0.5. The approximate solutions for the sundry scenarios with 1–5 cases of the non-linear delayed CPM model are computed by varying the crop biomass growth rate, rate of pest attacks, pest natural death, disease associated mortality rate and memory loss of aware people.as listed in Table 2. Figure 1 presented the flowchart of the designed methodology.

The dynamics of crop biomass density are shown in Figures 2A, B, respectively, using the ADS and ERK numerical solvers for the variation in crop biomass growth rate, i.e., *a* for the non-linear delayed CPM model. The crop biomass density has been found to increase as the value of *a* increases. Figures 2C, D for various values of *a* illustrate the effects of susceptible pest density. The graph shows that as the value of *a* increases, so does the density of pests that are susceptible. Figures 3A, B show how infected pests' behavior varies as the value of *a* changes. There is an increase in the density of infected pests for larger values of *a*. The effects of people's level of awareness for various values of *a* are depicted in Figures 3C, D. The graph illustrates how increasing the value of *a* raises the level of awareness. Table 3 presents the numerical results for the classes *B(t)*, *S(t)*, *I(t)*, and *A(t)* for scenario 1, case-1 of the non-linear delayed CPM model. Using the strength of ADS and ERK numerical solvers for cases 1 to 5 of scenario 2, the dynamics of the non-linear delayed CPM model for the rate of pest attacks, i.e., δ, is investigated for all four classes *B(t)*, *S(t)*, *I(t)*, and *A(t)* and graphically shown in Figures 4, 5 respectively.

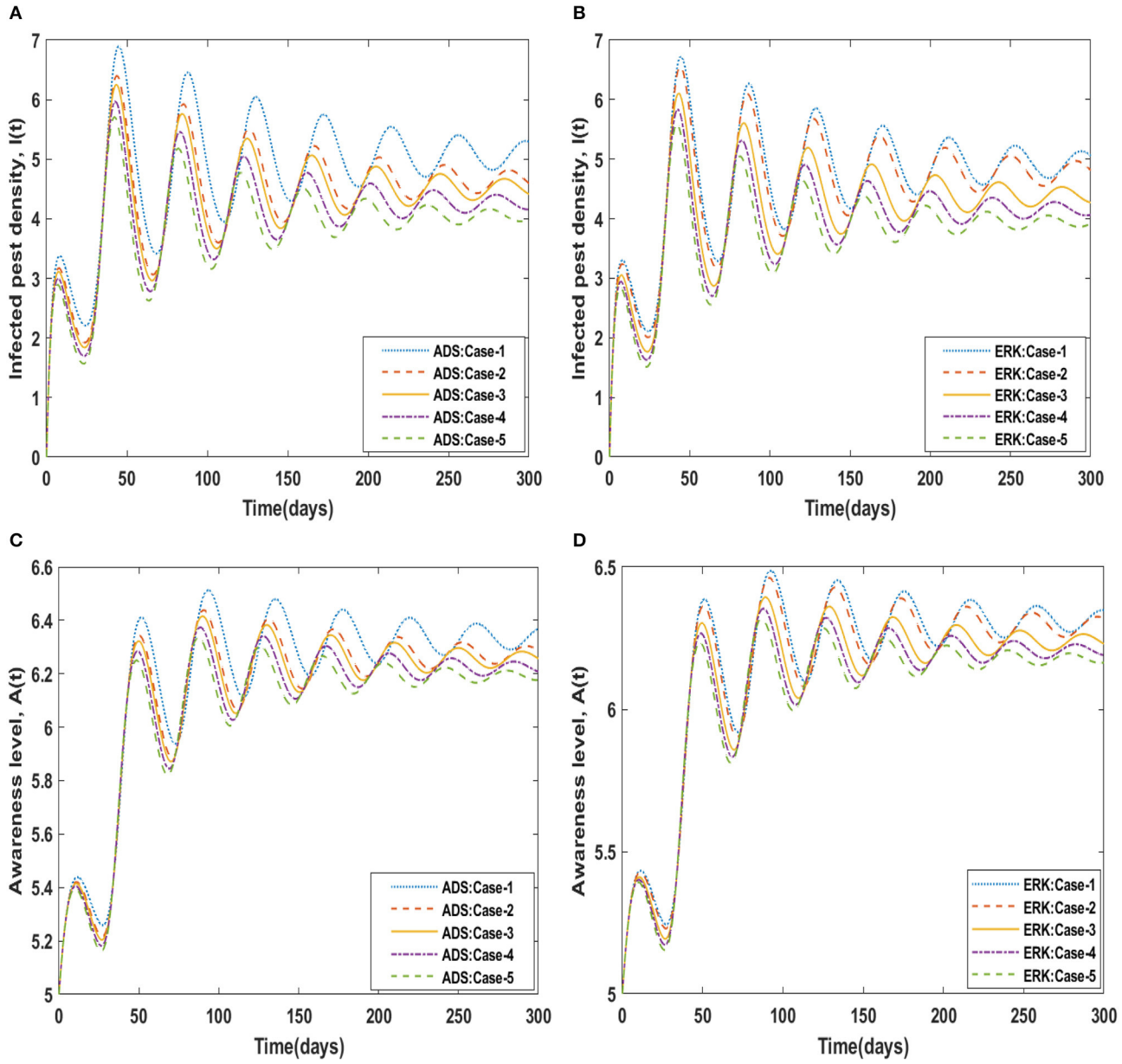

FIGURE 9
(A–D) Dynamics of *I(t)*, *A(t)* for variation in β by ADS and ERK solvers.

The numerical outcomes for the classes *B(t)*, *S(t)*, *I(t)*, and *A(t)* for scenario 2, case-1 of the non-linear delayed CPM model are shown in Table 3. Raising the value of δ increases the density of crop biomass, as presented in Figures 4A, B. For case-1 of pest attacks rate, the maximum value of *B(t)* is approximately between 5 to 45, oscillates from 0 to 150 days, and then maintains steady state behavior. The maximum value for case-2 is between 5–30 and it initially exhibits oscillating behavior in the range of 0 to 250 days before becoming stable in the range of 250 to 300 days. Cases 3 to 5, as depicted in Figures 4A, B, exhibit oscillations with varying amplitudes across the time interval. As the value of pest attacks i.e., δ expanded, the density of susceptible pests also increased, as seen in Figures 4C, D.

Susceptible pest density demonstrated oscillatory behavior from 0 to 150 days before returning to steady state behavior, whereas cases 2 to 5 exhibit oscillatory behavior with varying amplitudes from 0 to 300 days, as shown in Figures 4A, B. For compartment *I(t)* of the non-linear delayed CPM model, Figures 5A, B depict the effects of pest attacks rate. The graphs show that increasing the value of δ will result in decreasing the infected pest density. The impact of pest attacking rate, i.e., δ is also determined for compartment *A(t)* of the non-linear delayed CPM model. As seen in Figures 5C, D, the awareness level decreases as the value of pest attacks grow.

Similarly, for scenario 3 of non-linear delayed CPM model, the dynamics of the four compartments *B(t)*, *S(t)*, *I(t)*, and *A(t)*

TABLE 4 Numerical solutions of non-linear delayed CPM model.

Time (Days)	ADS method: Case-1, scenario 4				ERK method: Case-1, scenario 4			
	B	*S*	*I*	*A*	*B*	*S*	*I*	*A*
0	5.0000	9.0000	0.0000	5.0000	5.0000	9.0000	0.0000	5.0000
30	25.6352	2.7948	2.6511	5.2802	25.6454	2.9384	2.5856	5.2683
60	16.0485	1.2237	4.1627	6.2469	16.4980	1.2738	3.9219	6.2050
90	12.5031	3.1099	6.3705	6.4831	12.4801	2.9846	6.0962	6.4722
120	19.5105	3.6746	4.8757	6.1610	18.5848	3.9118	4.9691	6.1742
150	19.2204	2.0351	4.3368	6.2646	19.6539	2.2603	4.1730	6.2164
180	15.3228	2.38003	5.3581	6.4332	15.8217	2.3344	5.0070	6.3913
210	16.5595	3.2259	5.4430	6.3382	16.0291	3.1776	5.3515	6.3469
240	18.6317	2.7134	4.7792	6.2699	18.2773	2.9676	4.7624	6.2551
270	17.1624	2.407	4.9620	6.3510	17.611	2.5253	4.7201	6.3055
300	16.4349	2.7711	5.2948	6.3684	16.4975	2.7282	5.0572	6.3479
Time (Days)	ADS method: Case-1, scenario 5				ERK method: Case-1, scenario 5			
	B	*S*	*I*	*A*	*B*	*S*	*I*	*A*
0	5.0000	9.0000	0.0000	5.0000	5.0000	9.0000	0.0000	5.0000
30	33.4212	1.2608	1.7179	9.7847	32.7550	1.4497	1.7952	9.2354
60	26.8333	0.5218	3.3758	14.054	25.9310	0.6014	3.3390	12.9231
90	30.8679	1.2775	4.4344	15.9967	27.0746	1.4925	5.0180	14.4833
120	37.2066	0.5837	2.6639	17.3430	34.5850	0.9614	3.1909	15.3405
150	35.5515	0.6244	3.2161	18.1282	32.5484	0.77943	3.5441	15.9731
180	37.9167	0.5752	2.7510	18.5074	33.3100	0.9351	3.6511	16.1777
210	37.6625	0.5377	2.7981	18.7708	34.2309	0.81780	3.3647	16.3285
240	38.1941	0.5387	2.7157	18.8880	33.7867	0.8282	3.4894	16.4132
270	38.2294	0.5225	2.6998	18.9693	34.1173	0.8365	3.4408	16.4400
300	38.3414	0.5238	2.6863	19.0066	34.1219	0.8184	3.4242	16.4658

are explored by varying the value of pest natural death rate i.e., *c*, which is represented by c and graphically portrayed in Figures 6, 7 respectively. The numerical solutions for compartments *B(t)*, *S(t)*, *I(t)*, and *A(t)* for scenario 3, case-1 of the non-linear delayed model are computed and listed in Table 3. The influence of the pest's natural death rate on crop biomass density using the ADS and ERK numerical solvers respectively, is shown in Figures 6A, B. The effects of the pest natural death rate on the density of susceptible pests are shown in Figures 6C, D. It is noticed that the number of susceptible pests reduced as c increased. Figures 7A, B demonstrated how the density of infected pests decreases as the value of *c* rises. In Figures 7C, D, the level of people's awareness can be analyzed. It is worth noting that the larger value of the natural pest's death rate i.e., *c*, causes a decrease in people's awareness.

The dynamical behavior of the four compartments *B(t)*, *S(t)*, *I(t)*, and *A(t)* for cases 1 to 5 of scenario 4 with the variability in disease associated death rate, i.e., β is analyzed and graphically portrayed in Figures 8, 9 respectively. The numerical solutions for scenario 4, case-1 of the non-linear delayed CPM model are calculated for all four classes *B(t)*, *S(t)*, *I(t)*, and *A(t)* and presented in Table 4. The dynamics of crop biomass density are portrayed in Figures 8A, B exploiting the potential of the ADS and ERK numerical solvers for the variability in the disease associated death rate, i.e., β. It has been found that the crop biomass density falls as the value of β increases. Figures 8C, D show the effect of disease associated death rate on the density of susceptible pests. It is evident from Figure that raising the value of β would lead to a rise in the density of susceptible pests. The behavior of infected pest density for the variation in disease associated death rate is shown in Figures 9A, B. As the value of β is raised, it may be observed that the density of infected pests will decrease. Figures 9C, D show the impact of disease associated death rate against awareness level in people. The graphical representation presented that increasing the value of β causes the awareness level to decrease.

Using the strength of ADS and ERK numerical solvers, the dynamics for memory loss of aware people, i.e., υ , are investigated for all four compartments *B(t)*, *S(t)*, *I(t)*, and *A(t)* for scenario 5, cases 1 to 5 of the non-linear delayed CPM model. The numerical

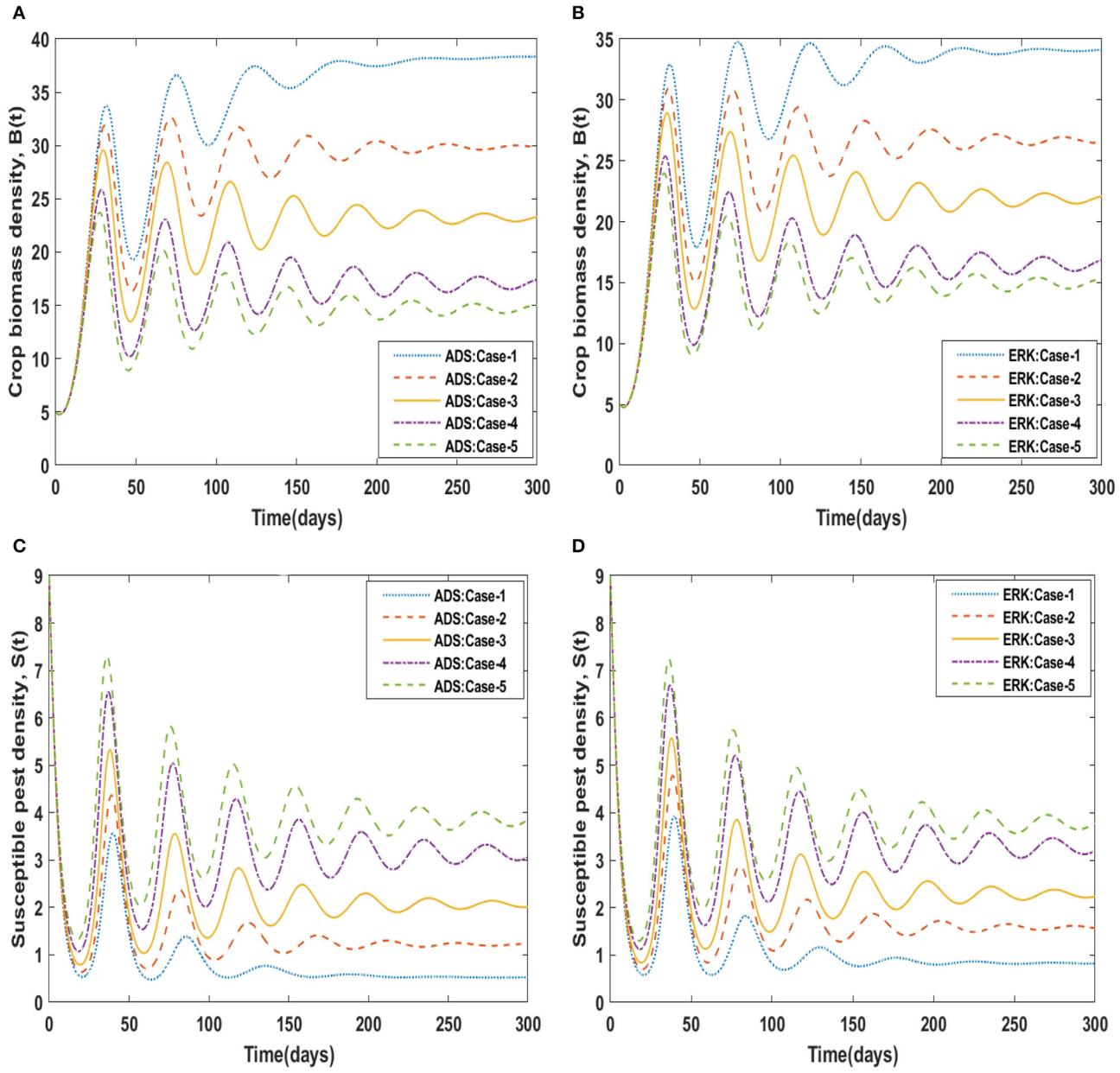

FIGURE 10
(A–D) Dynamics of *B(t), S(t)* for variation in υ by ADS and ERK solvers.

outcomes of all four compartments *B(t)*, *S(t)*, *I(t)*, and *A(t)* for case-1 of scenario 5 are provided in Table 4. The behavior of crop biomass density for the varying values of υ is depicted in Figures 10A, B, and it can be observed that crop biomass density decreases for higher values of υ. Figures 10C, D illustrated how the density of susceptible pests increases as the value of υ increases. Figures 11A, B show the dynamics of infected pest density for the variation in memory loss of aware people, i.e., υ. One may witness that the density of infected pests increases continuously in the first three cases, for $\upsilon = 0.01$, 0.02, and 0.03, and then decreases again in the subsequent two cases, for $\upsilon = 0.04$, and 0.05, in the interval of 0 to 300 days. Consequently, the density of infected pests shows varied behavior for different values of υ. Figures 11C, D portrayed the effect of memory loss in aware people, i.e., υ on awareness level compartment *A(t)*. It is clearly noticed from Figures 11C, D that the awareness level is decreased as the value $\upsilon$is increased.

5. Conclusions

In this research, the numerical approximate solution of the non-linear delayed CPM system supervised by ODEs is investigated effectively to portray the dynamic impacts of unforeseen interactions between crops and pests, rehabilitation strategies, and environmental factors across time. Based on the presented model, the dynamic nature of crop biomass density

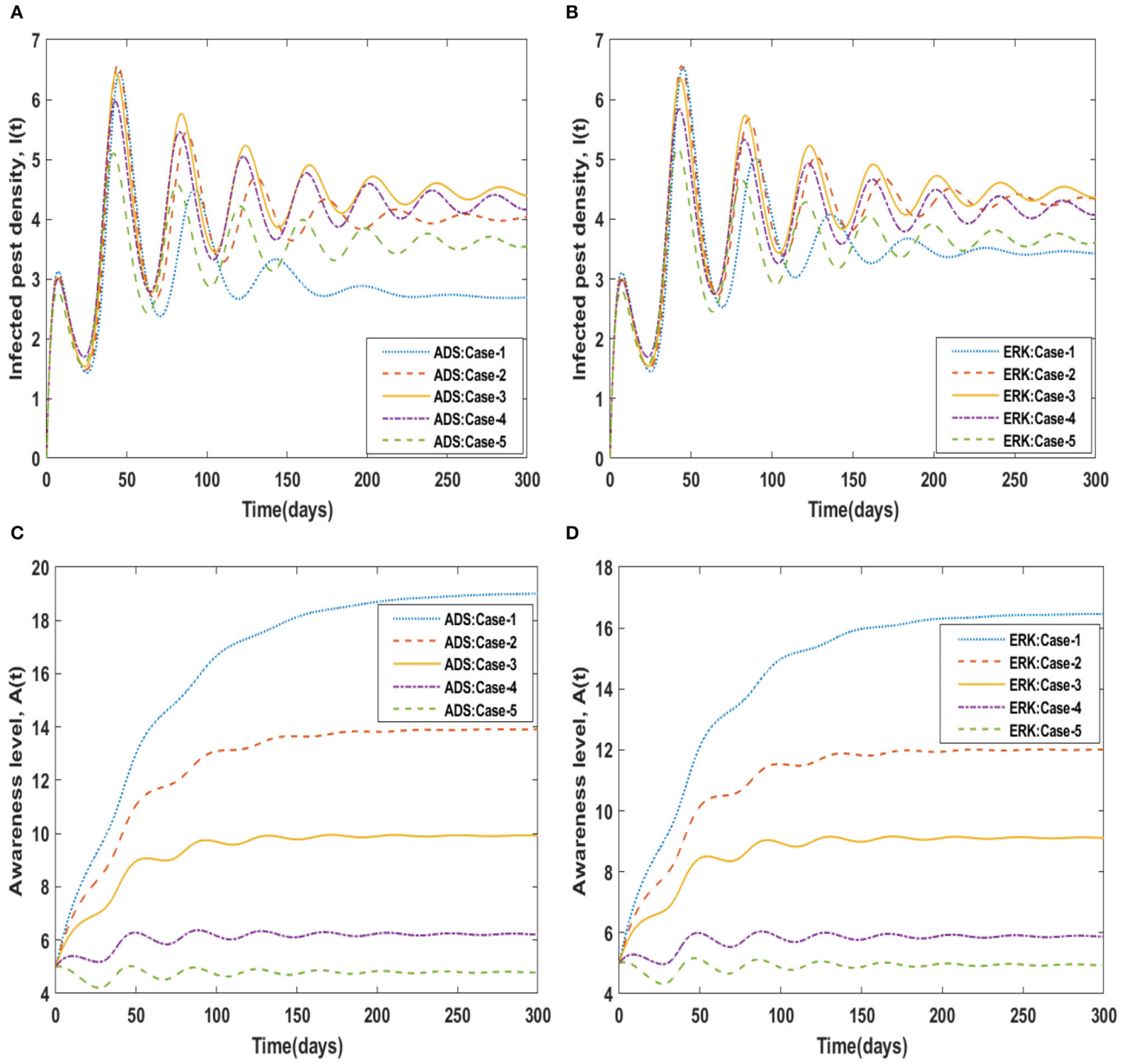

FIGURE 11
(A–D) Dynamics of *I(t)*, *A(t)* for variation in υ by ADS and ERK solvers.

[*B(t)*], susceptible pest density [*S(t)*], infected pest density [*I(t)*] and awareness level of the population [*A(t)*] may be forecasted effectively. Analysis based on the approximate numerical outcomes as well as graphic interpretations of the non-linear delayed CPM model is carried out by means of sundry scenarios by varying the different parameters utilized in the model. The approximate numerical solution of the non-linear delayed CPM model is computed by exploiting the state-of-the-art Adams (ADS) and explicit Runge–Kutta (ERK) numerical techniques. Compared with real-time models, delayed models exhibit greater realism because they take into account the interval between contact and infection. As delay affects processes along with dynamics, mathematically it impacts stability. This analysis can help to create predictive models for upcoming outbreaks and shed light on the efficacy of various pest management techniques. The numerical analysis that is being given makes it possible to optimize pest control tactics, analyze risks, educate people, and pursue continual improvement. It is essential for improving agricultural methods, reducing crop losses, and advancing environmentally friendly pest control strategies.

In the future, soft computing approaches based on artificial intelligence algorithms may be used to study the dynamics of epidemic models and other non-linear systems [68–73].

Data availability statement

The original contributions presented in the study are included in the article/supplementary material, further inquiries can be directed to the corresponding author.

Author contributions

Conceptualization, methodology, and writing—review and editing: NA and MR. Software: AK. Validation: MR. Formal analysis: MS and MR. Investigation: IA. Writing—original draft preparation: NA. Visualization: NA and MS. Project administration: AK and IA. All authors have read and agreed to the published version of the manuscript.

Conflict of interest

The authors declare that the research was conducted in the absence of any commercial or financial relationships that could be construed as a potential conflict of interest.

Publisher's note

All claims expressed in this article are solely those of the authors and do not necessarily represent those of their affiliated organizations, or those of the publisher, the editors and the reviewers. Any product that may be evaluated in this article, or claim that may be made by its manufacturer, is not guaranteed or endorsed by the publisher.

References

1. Bhattacharyya S, Bhattacharya DK. Pest control through viral disease: mathematical modeling and analysis. *J Theor Biol.* (2006) 238:177–97. doi: 10.1016/j.jtbi.2005.05.019

2. Verma D, Banjo T, Chawan M, Teli N, Gavankar R. *Microbial Control of Pests and Weeds. Natural Remedies for Pest, Disease and Weed Control.* New York, NY: Academic Press, 119–26 (2020).

3. Deebani W, Jan R, Shah Z, Vrinceanu N, Racheriu M. Modeling the transmission phenomena of water-borne disease with non-singular and non-local kernel. *Comput Methods Biomech Biomed Engin.* (2022) 26: 1–14. doi: 10.1080/10255842.2022.2114793

4. Baker BP, Green TA, Loker AJ. Biological control and integrated pest management in organic and conventional systems. *Biol Control.* (2020) 140:104095. doi: 10.1016/j.biocontrol.2019.104095

5. Kansiime MK, Alawy A, Allen C, Subharwal M, Jadhav A, Parr M, et al. Effectiveness of mobile agri-advisory service extension model: evidence from direct2farm program in India. *World Dev Persp.* (2019) 13:25–33. doi: 10.1016/j.wdp.2019.02.007

6. Al Basir FAHAD, Samanta S, Tiwari PK. Bistability, generalized and zero-hopf bifurcations in a pest control model with farming awareness. *J Biol Syst.* (2023) 31:115–40. doi: 10.1142/S0218339023500079

7. Alshemmari H, Al-Shareedah AE, Rajagopalan S, Talebi LA, Hajeyah M. Pesticides driven pollution in Kuwait: the first evidence of environmental exposure to pesticides in soils and human health risk assessment. *Chemosphere.* (2021) 273:129688. doi: 10.1016/j.chemosphere.2021.129688

8. Tripathi S, Shah KK, Tiwari I, Shrestha J. Farmers' perception about major insect pests of cucurbits and their management. *Indo J Agric Res.* (2020) 3:153–70. doi: 10.32734/injar.v3i3.4414

9. Sinan M, Shah K, Kumam P, Mahariq I, Ansari KJ, Ahmad Z, et al. Fractional order mathematical modeling of typhoid fever disease. *Results Phys.* (2022) 32:105044. doi: 10.1016/j.rinp.2021.105044

10. Mutimawurugo MC, Wagara IN, Muhinyuza JB, Ogweno JO. Virulence and characterization of isolates of potato bacterial wilt caused by *Ralstonia solanacearum* (Smith) in Rwanda. *Afr J Agric Res.* (2019) 14:311–20. doi: 10.5897/AJAR2018.13686

11. Nešić K, Habschied K, Mastanjević K. Possibilities for the biological control of mycotoxins in food and feed. *Toxins.* (2021) 13:198. doi: 10.3390/toxins13030198

12. Kumar A, Mishra AK, Saroj S, Joshi PK. Impact of traditional versus modern dairy value chains on food security: Evidence from India's dairy sector. *Food Policy.* (2019) 83:260–70. doi: 10.1016/j.foodpol.2019.01.010

13. Santoso T. The status of Oryctes rhinoceros Nudivirus (OrNV) infection in Oryctes rhinoceros (Coleoptera: Scarabaeidae) in Indonesia. *J Oil Palm Res.* (2020) 32:582–9.

14. Kuang Y. *Delay Differential Equations: With Applications in Population Dynamics*. New York, NY: Academic Press (1993). doi: 10.21894/jopr.2020.0041

15. Lotka AJ. *Elements of Physical Biology*. London: Williams & Wilkins (1925).

16. Tian Y, He G, Liu Z, Zhong L, Yang X, Stanley HE, et al. The impact of memory effect on resonance behavior in a fractional oscillator with small time delay. *Phys Stat Mech Appl.* (2021) 563:125383. doi: 10.1016/j.physa.2020.125383

17. Arafa AA, Xu Y, Mahmoud GM. Chaos suppression via integrative time delay control. *Int J Bifurc Chaos.* (2020) 30:2050208. doi: 10.1142/S0218127420502089

18. Mahmoud GM, Arafa AA, Abed-Elhameed TM, Mahmoud EE. Chaos control of integer and fractional orders of chaotic Burke–Shaw system using time delayed feedback control. *Chaos, Solitons Fractals.* (2017) 104:680–92. doi: 10.1016/j.chaos.2017.09.023

19. Mahmoud GM, Arafa AA, Mahmoud EE. Bifurcations and chaos of time delay Lorenz system with dimension 2n+1. *The Eur Phys J Plus.* (2017) 132:1–20. doi: 10.1140/epjp/i2017-11739-6

20. Rihan FA, Arafa AA, Rakkiyappan R, Rajivganthi C, Xu Y. Fractional-order delay differential equations for the dynamics of hepatitis C virus infection with IFN-α treatment. *Alexandria Eng J.* (2021) 60:4761–74. doi: 10.1016/j.aej.2021.03.057

21. Smith HL. *An Introduction to Delay Differential Equations With Applications to the Life Sciences*. New York, NY: Springer (2011).

22. Hu D, Li Y, Liu M, Bai Y. Stability and Hopf bifurcation for a delayed predator–prey model with stage structure for prey and Ivlev-type functional response. *Nonlinear Dyn.* (2020) 99:3323–50. doi: 10.1007/s11071-020-05467-z

23. Du Y, Niu B, Wei J. Two delays induce Hopf bifurcation and double Hopf bifurcation in a diffusive Leslie-Gower predator-prey system. *Chaos Interdis J Nonlin Sci.* (2019) 29:013101. doi: 10.1063/1.5078814

24. Bajeux N, Ghosh B. Stability switching and hydra effect in a predator–prey meta population model. *Biosystems.* (2020) 198:104255. doi: 10.1016/j.biosystems.2020.104255

25. Duan D, Fan Q, Guo Y. Hopf bifurcation analysis in a neutral predator–prey model with age structure in prey. *Electr J Q Theor Diff Eq.* (2019) 2019:1–13. doi: 10.14232/ejqtde.2019.1.30

26. Li Z, Dai B. Stability and Hopf bifurcation analysis in a Lotka–Volterra competition–diffusion–advection model with time delay effect. *Nonlinearity.* (2021) 34:3271. doi: 10.1088/1361-6544/abe77a

27. Daudi S, Luboobi L, Kgosimore M, Kuznetsov D, Mushayabasa S. A mathematical model for fall armyworm management on maize biomass. *Adv Diff Eq.* (2021) 2021:1–27. doi: 10.1186/s13662-021-03256-5

28. Li J, Huang Q, Liu B. A pest control model with birth pulse and residual and delay effects of pesticides. *Adv Diff Eq.* (2019) 2019:1–16. doi: 10.1186/s13662-019-1978-7

29. Xiang S, Pei Y, Liang X. Analysis and optimization based on a sex pheromone and pesticide pest model with gestation delay. *Int J Biomathematic.* (2019) 12:1950054. doi: 10.1142/S1793524519500542

30. Liu S, Huang M, Wang J. Bifurcation control of a delayed fractional Mosaic disease model for Jatropha curcas with farming awareness. *Complexity.* (2020) 2020:16. doi: 10.1155/2020/2380451

31. Kumari V, Chauhan S, Dhar J. Controlling pest by integrated pest management: a dynamical approach. *Int J Mathemati Eng Manag Sci.* (2020) 5:769. doi: 10.33889/IJMEMS.2020.5.4.061

32. Shi Z, Li Y, Cheng H. Dynamic analysis of a pest management smith model with impulsive state feedback control and continuous delay. *Mathematics.* (2019) 7:591. doi: 10.3390/math7070591

33. Arafa AA, Hamdallah SA, Tang S, Xu Y, Mahmoud GM. Dynamics analysis of a Filippov pest control model with time delay. *Commun Nonlinear Sci Num Simulation.* (2021) 101:105865. doi: 10.1016/j.cnsns.2021.105865

34. Al Basir F, Elaiw AM, Ray S. Effect of time delay in controlling crop pest using farming awareness. *Int J Appl Comput Mathematic.* (2019) 5:1–19. doi: 10.1007/s40819-019-0693-0

35. Allen-Perkins A, Estrada E. Mathematical modelling for sustainable aphid control in agriculture via intercropping. *Proc Royal Soc A.* (2019) 475:20190136. doi: 10.1098/rspa.2019.0136

36. Abraha T, Al Basir F, Obsu LL, Torres DF. Pest control using farming awareness: Impact of time delays and optimal use of biopesticides. *Chaos Soliton Fractals.* (2021) 146:110869. doi: 10.1016/j.chaos.2021.110869

37. Rossini L, Contarini M, Severini M, Speranza S. Reformulation of the Distributed Delay Model to describe insect pest populations using count variables. *Ecol Modell.* (2020) 436:109286. doi: 10.1016/j.ecolmodel.2020.109286

38. Al Basir F, Banerjee A, Ray S. Role of farming awareness in crop pest management-A mathematical model. *J Theor Biol.* (2019) 461:59–67. doi: 10.1016/j.jtbi.2018.10.043

39. Rahman MU, Arfan M, Shah Z, Kumam P, Shutaywi M. Nonlinear fractional mathematical model of tuberculosis (TB) disease with incomplete treatment under Atangana-Baleanu derivative. *Alexandria Eng J.* (2021) 60:2845–56. doi: 10.1016/j.aej.2021.01.015

40. Banu MS, Raju I, Mondal S. A comparative study on classical fourth order and butcher sixth order Runge–Kutta methods with initial and boundary value problems. *Int J Mat Math Sci.* (2021) 3:8–21. doi: 10.34104/ijmms.021.08021

41. Tang TQ, Shah Z, Jan R, Alzahrani E. Modeling the dynamics of tumor–immune cells interactions via fractional calculus. *Eur Phys J Plus.* (2022) 137:367. doi: 10.1140/epjp/s13360-022-02591-0

42. Kafle J, Thakur BK, Acharya G. Formulative visualization of numerical methods for solving non-linear ordinary differential equations. *Nepal J Mathematic Sci.* (2021) 2:79–88. doi: 10.3126/njmathsci.v2i2.40126

43. Tang TQ, Jan R, Bonyah E, Shah Z, Alzahrani E. Qualitative analysis of the transmission dynamics of dengue with the effect of memory, reinfection, and vaccination. *Comput Mathemati Methods Med.* (2022) 12:70. doi: 10.1155/2022/7893570

44. Shah Z, Jan R, Kumam P, Deebani W, Shutaywi M. Fractional dynamics of HIV with source term for the supply of new CD4+ T-cells depending on the viral load via Caputo–Fabrizio derivative. *Molecules.* (2021) 26:1806. doi: 10.3390/molecules26061806

45. Shoaib M, Raja MAZ, Sabir MT, Bukhari AH, Alrabaiah H, Shah Z, et al. A stochastic numerical analysis based on hybrid NAR-RBFs networks nonlinear SITR model for novel COVID-19 dynamics. *Comput Methods Programs Biomed.* (2021) 202:105973. doi: 10.1016/j.cmpb.2021.105973

46. Anwar N, Ahmad I, Raja MAZ, Naz S, Shoaib M, Kiani AK, et al. Artificial intelligence knacks-based stochastic paradigm to study the dynamics of plant virus propagation model with impact of seasonality and delays. *Eur Phys J Plus.* (2022) 137:144. doi: 10.1140/epjp/s13360-021-02248-4

47. Fatmawati MAK, Bonyah E, Hammouch Z, Shaiful EM. A mathematical model of tuberculosis (TB) transmission with children and adults groups: a fractional model. *Aims Math.* (2020) 5:2813–42. doi: 10.3934/math.2020181

48. Anwar N, Ahmad I, Kiani AK, Naz S, Shoaib M, Raja MAZ, et al. Intelligent predictive stochastic computing for nonlinear differential delay computer virus model. *Waves Random Complex Media.* (2022) 21:1–29. doi: 10.1080/17455030.2022.2155327

49. Städter P, Schälte Y, Schmiester L, Hasenauer J, Stapor PL. Benchmarking of numerical integration methods for ODE models of biological systems. *Sci Rep.* (2021) 11:1–11. doi: 10.1038/s41598-021-82196-2

50. Tang TQ, Jan R, Ur Rehman Z, Shah Z, Vrinceanu N, Racheriu M, et al. Modeling the dynamics of chronic myelogenous leukemia through fractional-calculus. *Fractals.* (2022) 30:2240262. doi: 10.1142/S0218348X22402629

51. Rong B, Rui X, Tao L, Wang G. Theoretical modeling and numerical solution methods for flexible multibody system dynamics. *Nonlinear Dyn.* (2019) 98:1519–53. doi: 10.1007/s11071-019-05191-3

52. Zhao J, Zhan R, Xu Y. Explicit exponential Runge–Kutta methods for semilinear parabolic delay differential equations. *Math Comput Simul.* (2020) 178:366–81. doi: 10.1016/j.matcom.2020.06.025

53. Shaalini JV, Pushpam AEK. Analysis of composite Runge Kutta methods and new one-step technique for stiff delay differential equations. *IAENG Int J Appl Mathematics.* (2019) 49:1–10. Available online at: https://api.semanticscholar.org/CorpusID:211543850

54. Bharathi DP, Jayakumar T, Vinoth S. Numerical solution of fuzzy mixed delay differential equations via Runge–Kutta method of order four. *Intervals.* (2019) 1:1–9. doi: 10.5890/DNC.2021.03.006

55. Senu N, Lee KC, Ahmadian A, Ibrahim SNI. Numerical solution of delay differential equation using two-derivative Runge–Kutta type method with Newton interpolation. *Alexandria Eng J.* (2022) 61:5819–35. doi: 10.1016/j.aej.2021.11.009

56. Hu X, Cong Y, Hu GD. Delay-dependent stability of Runge–Kutta methods for linear delay differential–algebraic equations. *J Comput Appl Math.* (2020) 363:300–11. doi: 10.1016/j.cam.2019.06.016

57. Khodabandehlo HR, Shivanian E, Abbasbandy S. Numerical solution of nonlinear delay differential equations of fractional variable-order using a novel shifted Jacobi operational matrix. *Eng Comput.* (2021) 32:1–15. doi: 10.1007/s00366-021-01422-7

58. Raja MA, Sabati M, Parveen N, Awais M, Awan SE. Integrated intelligent computing application for effectiveness of Au nanoparticles coated over MWCNTs with velocity slip in curved channel peristaltic flow. *Sci Rep.* (2021) 11:1–20. doi: 10.1038/s41598-021-98490-y

59. Cheema TN, Raja MA, Ahmad I, Naz S, Ilyas H. Intelligent computing with Levenberg–Marquardt artificial neural networks for nonlinear system of COVID-19 epidemic model for future generation disease control. *Eur Phys J Plus.* 135:1–35. doi: 10.1140/epjp/s13360-020-00910-x

60. Uddin I, Ullah I, Raja MAZ, Shoaib M, Islam S, Zobaer MS, et al. The intelligent networks for double-diffusion and MHD analysis of thin film flow over a stretched surface. *Sci Rep.* (2021) 11:1–20. doi: 10.1038/s41598-021-97458-2

61. Khan BA, Nadeem MA, Nawaz H, Amin MM, Abbasi GH, Nadeem M, et al. *Pesticides: Impacts on Agriculture Productivity, Environment, and Management Strategies. Emerging Contaminants and Plants: Interactions, Adaptations and Remediation Technologies.* Cham: Springer International Publishing (2023), 109–34.

62. Al Basir F, Adhurya S, Ray S. Impact of periodic farming awareness campaign through media for crop pest control management. *Adv Mathemat Comput Model Eng Systems.* (2023) 143:1–21. doi: 10.1201/9781003367420-6

63. Anwar N, Naz S, Shoaib M. Reliable numerical treatment with Adams and BDF methods for plant virus propagation model by vector with impact of time lag and density. *Front Appl Mathematic Stat.* (2022) 8:1001392. doi: 10.3389/fams.2022.1001392

64. Anwar N, Ahmad I, Kiani AK, Shoaib M, Raja MAZ. Intelligent solution predictive networks for non-linear tumor-immune delayed model. *Comput Methods Biomech Biomed Engin.* (2023) 25:1–28. doi: 10.1080/10255842.2023.2227751

65. Azizan FL, Sathasivam S, Velavan M, Azri NR, Manaf NIRA. Prediction of drug concentration in human bloodstream using Adams-Bashforth-Moulton method. *J Adv Res Appl Sci Eng Technol.* (2023) 29:53–71. doi: 10.37934/araset.29.2.5371

66. Citro V, D'Ambrosio R, Di Giovacchino S. A-stability preserving perturbation of Runge–Kutta methods for stochastic differential equations. *Appl Math Lett.* (2020) 102:106098. doi: 10.1016/j.aml.2019.106098

67. Shoaib M, Anwar N, Ahmad I, Naz S, Kiani AK, Raja MAZ, et al. Neuro-computational intelligence for numerical treatment of multiple delays SEIR model of worms propagation in wireless sensor networks. *Biomed Signal Process Control.* (2023) 84:104797. doi: 10.1016/j.bspc.2023.104797

68. Attia IM. Novel approach of multistate Markov chains to evaluate progression in the expanded model of non-alcoholic fatty liver disease. *Front Appl Mathematic Statistics.* (2022) 7:92. doi: 10.3389/fams.2021.766085

69. Lasri Doukkali A, Lorenzi T, Parcell BJ, Rohn JL, Bowness R. A hybrid individual-based mathematical model to study bladder infections. *Front Appl Mathematic Stat.* (2023) 5:1090334. doi: 10.3389/fams.2023.1090334

70. Netshikweta R, Garira W. A nested multiscale model to study paratuberculosis in ruminants. *Front Appl Mathematic Stat.* (2022) 79:817060. doi: 10.3389/fams.2022.817060

71. Oukouomi Noutchie SC, Mafatle NE, Guiem R, M'pika Massoukou RY. On the dynamics of sexually transmitted diseases under awareness and treatment. *Front Appl Mathematic Stat.* 8:860840. doi: 10.3389/fams.2022.860840

72. Ebrahim EA, Biru BZ. Multivariate analysis of drivers of migration, challenges, and prediction of future scenarios of female Ethiopian return migrants from the middle east. *Front Appl Mathematic Stat.* (2022) 8:870111. doi: 10.3389/fams.2022.870111

73. Haider Q, Hassan A, Eldin SM. Artificial neural network scheme to solve the hepatitis B virus model. *Front Appl Mathematic Statistics.* (2023) 9:1072447. doi: 10.3389/fams.2023.1072447

frontiers | Frontiers in Public Health

TYPE Original Research
PUBLISHED 19 October 2023
DOI 10.3389/fpubh.2023.1198356

OPEN ACCESS

EDITED BY
Md. Kamrujjaman,
University of Dhaka, Bangladesh

REVIEWED BY
Maya Santi,
State Polytechnic of Jember, Indonesia
Srigowtham Subramaniam,
Tamil Nadu Dr. M.G.R. Medical University, India

*CORRESPONDENCE
Mengcai Hu
✉ baojianbuhmc@163.com;
✉ zdsfybjb@163.com

RECEIVED 01 April 2023
ACCEPTED 09 October 2023
PUBLISHED 19 October 2023

CITATION
Zhang M, Qu H, Xia J, Hui X, Shi C, Xu F, He J, Cao Y and Hu M (2023) Trends, influencing factors and prediction analysis of under-five and maternal mortality rates in China from 1991 to 2020.
Front. Public Health 11:1198356.
doi: 10.3389/fpubh.2023.1198356

Trends, influencing factors and prediction analysis of under-five and maternal mortality rates in China from 1991 to 2020

Meng Zhang, Huimin Qu, Junfen Xia, Xiaoqing Hui, Cannan Shi, Feng Xu, Junjian He, Yuan Cao and Mengcai Hu*

Department of Health Care, The Third Affiliated Hospital of Zhengzhou University, Zhengzhou, Henan, China

Introduction: Under-five mortality rate (U5MR) and maternal mortality rate (MMR) are important indicators for evaluating the quality of perinatal health and child health services in a country or region, and are research priorities for promoting maternal and infant safety and maternal and child health. This paper aimed to analysis and predict the trends of U5MR and MMR in China, to explore the impact of social health services and economic factors on U5MR and MMR, and to provide a basis for relevant departments to formulate relevant policies and measures.

Methods: The JoinPoint regression model was established to conduct time trend analysis and describe the trend of neonatal mortality rate (NMR), infant mortality rate (IMR), U5MR and MMR in China from 1991 to 2020. The linear mixed effect model was used to assess the fixed effects of maternal health care services and socioeconomic factors on U5MR and MMR were explored, with year as a random effect to minimize the effect of collinearity. Auto regressive integrated moving average models (ARIMA) were built to predict U5MR and MMR from 2021 to 2025.

Results: The NMR, IMR, U5MR and MMR from 1991 to 2020 in China among national, urban and rural areas showed continuous downward trends. The NMR, IMR, U5MR and MMR were significantly negatively correlated with gross domestic product (GDP), the proportion of the total health expenditure (THE) to GDP, system management rate, prenatal care rate, post-natal visit rate and hospital delivery rate. The predicted values of national U5MR from 2021 to 2025 were 7.3 ‰, 7.2 ‰, 7.1 ‰, 7.1 ‰ and 7.2 ‰ and the predicted values of national MMR were 13.8/100000, 12.1/100000, 10.6/100000, 9.6/100000 and 8.3/100000.

Conclusion: China has made great achievements in reducing the U5MR and MMR. It is necessary for achieving the goals of Healthy China 2030 by promoting the equalization of basic public health services and further optimizing the allocation of government health resources. China's experience in reducing U5MR and MMR can be used as a reference for developing countries to realize the SDGs.

KEYWORDS

ARIMA, linear mixed effect model, maternal mortality rate, trends, under-five mortality rate

Introduction

Women and children make up the two-thirds of the world's population. Thus, the health of them not only exerts a strong influence on their personal and family happiness but also provides a basic premise for the sustainable development of mankind and, even more, a comprehensive index for the development of social economy and human progress (1, 2). As the important indicators to assess the service quality of national and regional perinatal care and child-care, the under-five mortality rate (U5MR) and maternal mortality rate (MMR) were the research focus for promoting the safety and health of children and women (2, 3).

According to the Millennium Development Goals (MDGs), which was formulated at the United Nations Summit in September 2000, the goals to reduce child mortality rate by two-thirds and maternal by three quarters were scheduled to be fulfilled in 2015 (4–6). The United Nations Sustainable Development Goals (SDGs) are 17 global development goals set by the United Nations to guide global development efforts from 2015 to 2030 beyond the expiration of MDGs from 2000 to 2015. Target 3 (good health and well-being) aims to reduce the global MMR to 70/100,000 and U5MR to 25‰ by 2030. Put forward by the Chinese government, outline of the Healthy China 2030 plan points out that, in the year of 2030, the infant mortality rates (IMR), U5MR and MMR will reduce to 5.0 ‰, 6.0 ‰ and 12.0/100000, respectively, (7). Over the past decades, China has made intense efforts in various ways to enhance the life quality of women and children. Besides, it is the U5MR and MMR that shows a downward trend with each passing year (8, 9). However, there are still plenty of challenges to face for the maternal and child health services. First of all, with the implementation of "Universal Two-child Policy" and the increase of high-risk pregnant women, the absolute number of maternal and child deaths is large, and which is difficult to present a continuous momentum of decline (10, 11). Apart from that, the obvious gap between urban and rural areas also poses a formidable barrier to further reduce the mortality. Additionally, the health-care level of maternal and child health care in China, especially in rural areas, still have gap with the developed countries (12, 13).

Simple as the maternal and child health indicators seem to be, they are the typical reflection of the economy, culture and policy in a country or region (14, 15). Currently, what is still unclear is to what degree these contributing factors, such as social health care services, the social economic, the total health expenditure (THE) and so on, can affect the U5MR and MMR. This paper aimed to present the U5MR and MMR, demonstrate the trends to change with time and explore the influence caused by social health-care and economic on the U5MR and MMR, about which this research also aimed to make a prediction to provide the scientific foundation for improving the quality of maternal and child health services and to supply reference for relevant policies and measures of maternal care formulated by certain departments to further reduce the mortality rates.

Methods

Data sources

The data used in this study including the data of neonatal mortality rate (NMR), IMR, U5MR, MMR, maternal system management rate, prenatal care rate, postnatal visit rate and hospital delivery rate from 1991 to 2020 were collected from the annual China Health Statistics Yearbooks (1991–2021). The data of GDP, and total health expenditure (the ratio of total health expenditure (THE) to GDP) from 1991 to 2020 were collected from official data released by the National Bureau of Statistics of China (16). The data above were shown in Additional Files 1, 2.

Definitions

NMR refers to the number of neonatal deaths that from birth to 28 days per 1,000 live births. IMR is defined as the number of infants deaths that from birth to the 1 year old per 1,000 live births. U5MR refers to the number of deaths of children under 5 years of age per 1,000 live births. MMR is defined as the number of the death caused by any pregnancy or pregnancy treatment within 42 days from pregnancy to postpartum per 100,000 live births. The number of live births are defined as the number of newborns with one of the four vital signs of heartbeat, respiration, umbilical cord fluctuation and voluntary muscle contraction after delivery after 28 weeks of pregnancy and above.

Statistical analysis

The JoinPoint regression model was established by JionPoint 4.9.1.0 software to analyze the change trend of IMR, U5MR and MMR in China from 1991 to 2020. The data of annual percent change (APC) and average annual percent change (AAPC) were the main outcome indicators of the JoinPoint model, both of which represent the percentage change of variables with the year. The former was used to evaluate the internal trend of each segment interval, and the latter was used to evaluate the overall change trend. Joinpoint pairwise comparison test was applied to compare the trend differences between urban and rural areas. The linear mixed effect model was used to explore the fixed effect of socioeconomic factors and maternal health care level on IMR, U5MR and MMR, and the year was used as a random effect to reduce the effect of col-linearity, and the socioeconomic indicators were logarithmically converted. The auto regressive integrated moving average (ARIMA) model was built using SPSS 21.0 for time series prediction. ARIMA (p, d, q) combines autoregressive analysis (AR) and moving average (MA) including three parameters: the order of AR (p), the degree of difference (d), the order of MA (q). The national data from 1991 to 2015 was used for modeling, and the data from 2016 to 2020 for evaluating the mean absolute percentage error (MAPE) of models, and the optimal model was applied to predict the rates from 2021 to 2025. A two-side p of <0.05 was considered significant in this study.

Results

Trends analysis results

The NMR, IMR, U5MR and MMR from 1991 to 2020 in China among national, urban and rural areas showed continuous downward trends (Figure 1). Table 1 shows the results of APC and AAPC

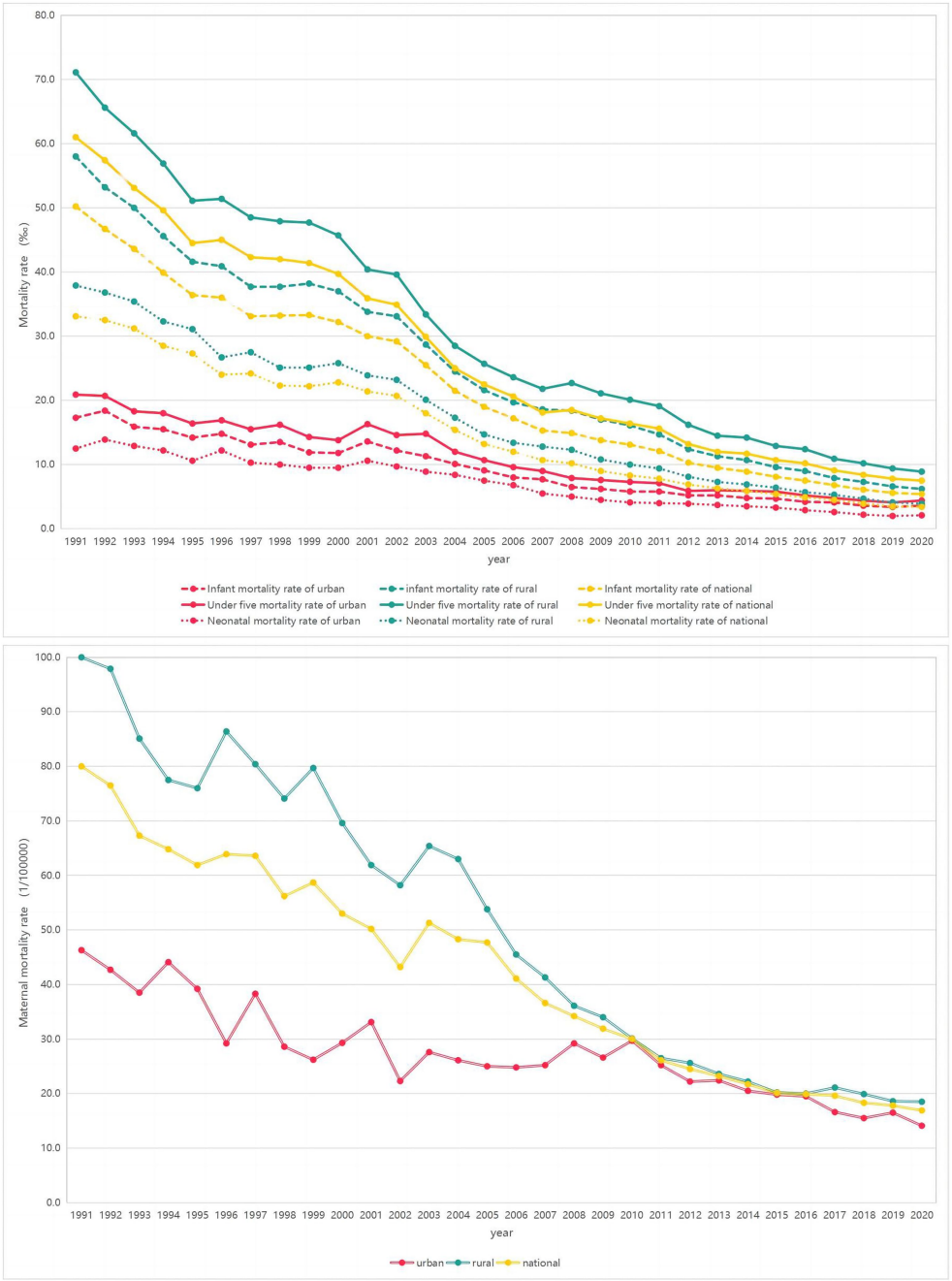

FIGURE 1
Trends of the NMR, IMR, U5MR and MMR from 1991 to 2020 of China in national, urban and rural areas.

reflecting the change trend of NMR, IMR, U5MR and MMR in the past 30 years. The results of JoinPoint pairwise comparison test showed that the AAPC differences of NMR, IMR, U5MR and MMR between urban and rural areas from 1991 to 2020 were 1.4% (95%CI = -0.7, 3.6%, $p = 0.193$), 1.8% (95%CI = 0.8, 2.8%, $p < 0.001$), 1.6% (95%CI = 0.5, 2.7%, $p = 0.003$) and 2.1% (95%CI = 0.1, 3.1%, $p = 0.005$), respectively. The data above were shown in Additional File 3.

Linear mixed model results

The results of linear mixed model (Table 2) showed that NMR, IMR, U5MR and MMR were significantly negatively correlated with GDP, the proportion of THE to GDP, system management rate, prenatal care rate, post-natal visit rate and hospital delivery rate ($p < 0.05$).

TABLE 1 JoinPoint analysis of infant mortality rate, under five mortality rate and maternal rate in national, urban and rural areas.

	Trend 1		Trend 2		Trend 3		AAPC (%)	95% CI for AAPC (%)
	Years	APC (%)	Years	APC (%)	Years	APC (%)		
National	1991–2002	−4.3	2002–2005	−12.9	2005–2020	−8.8	−7.6	(−8.5, −6.6)
Urban	1991–2004	−3.2	2004–2007	−13.8	2007–2020	−7.4	−6.2	(−8.1, −4.3)
Rural	1991–2002	−4.5	2002–2005	−11.7	2005–2020	−8.7	−7.4	(−8.5, −6.3)
National	1991–2002	−4.5	2002–2005	−12.3	2005–2020	−8.2	−7.3	(−8.3, −6.2)
Urban	1991–2003	−3.5	2003–2008	−10.0	2008–2020	−5.4	−5.5	(−6.3, −4.6)
Rural	1991–1997	−6.7	1997–2000	−0.7	2000–2020	−8.6	−7.4	(−8.6, −6.2)
National	1991–2002	−4.7	2002–2005	−13.3	2005–2020	−7.1	−6.9	(−8.0, −5.8)
Urban	1991–2003	−3.1	2003–2008	−10.2	2008–2020	−5.3	−5.3	(−6.2, −4.3)
Rural	1991–2002	−4.9	2002–2005	−11.8	2005–2020	−7.0	−6.7	(−8.0, −5.4)
National	1991–2005	−3.7	2005–2013	−8.2	2013–2020	−4.0	−5.0	(−5.7, −4.4)
Urban	1991–2002	−5.2	2002–2010	0.9	2010–2020	−6.2	−3.9	(−5.2, −2.7)
Rural	1991–2004	−3.6	2004–2012	−10.8	2012–2020	−3.3	−5.6	(−6.4, −4.8)

TABLE 2 The results of linear mixed model.

	Neonatal mortality rate		Infant mortality rate		Under five mortality rate		Maternal mortality rate	
	β	95%CI	*β*	95%CI	*β*	95%CI	*β*	95%CI
GDP[#]	−19.392	(−20.422, −18.362)	−27.386	(−28.808, −25.964)	−33.045	(−35.176, −30.914)	−38.599	(−40.607, −36.590)
Proportion of THE in GDP	−8.625	(−10.836, −6.414)	−12.057	(−15.246, −8.869)	−14.499	(−18.432, −10.567)	−17.729	(−21.776, −13.682)
System management rate	−0.854	(−1.038, −0.671)	−1.206	(−1.464, 0.949)	−1.450	(−1.773, −1.128)	−1.932	(−2.189, −1.674)
Prenatal care rate	−1.157	(−1.358, −0.957)	−1.598	(−1.883, −1.313)	−1.938	(−2.287, −1.588)	−2.244	(−2.671, −1.817)
Postpartum visit rate	−1.242	(−1.437, −1.048)	−1.720	(−1.994, −1.446)	−2.081	(−2.422, −1.740)	−2.456	(−2.832, −2.079)
Hospital delivery rate	−0.530	(−0.566, −0.494)	−0.746	(−0.801, −0.691)	−0.907	(−0.968, −0.847)	−1.039	(−1.139, −0.939)

GDP, Gross Domestic Product; THE, total health expenditure.

ARIMA models

This SPSS21.0 software was used to fit ARIMA prediction models with NMR, IMR, U5MR and MMR as dependent variables. Because most of the above time series were non-stationary, the series were stabilized after one difference transformation. The results of the selected optimal model, R^2, BIC and MAPE were shown in Table 3. All of the residual sequences were white noise sequence with the *p* values of Ljung-BoxQ tests greater than 0.05.

Prediction results of ARIMA models

The predicted results of ARIMA model were shown in Figure 2 and Additional File 3. The predicted values of national NMR in from 2021 to 2025 were 3.2 ‰, 2.9 ‰, 2.5 ‰, 2.2 ‰ and 1.8 ‰ respectively. The predicted values of the national IMR were 5.1 ‰, 4.9 ‰, 4.8 ‰, 4.7 ‰ and 4.8 ‰ respectively. The predicted values of the national U5MR are 7.3 ‰, 7.2 ‰, 7.1 ‰, 7.1 ‰ and 7.2 ‰. The predicted values of national MMR are 13.8/100000, 12.1/100000, 10.6/100000, 9.6/100000 and 8.3/100000. The predicted results of urban and rural areas were shown in the Additional File 4.

Discussion

The NMR, IMR, U5MR and MMR of China were on the decline from 1991 to 2020, and the rates in rural areas has been higher than that in urban areas, which might be caused by the imbalance of economic development and health services (17, 18). The annual average decline rates of NMR, IMR, U5MR and MMR in rural areas were greater than that in urban areas, and the differences were reduced between rural and urban, which showed that the maternal health care strategy of China, especially in rural areas, has made remarkable

progress, and the quality of maternal medical services has improved (19–21), which may be related to the development of public health services projects and the launch of basic public health services equalization projects (22, 23). In addition to increased accessibility to healthcare services, this might be related to rapid economic growth and improved transportation (24).

Since 1990, the health level of Chinese children has improved significantly, and the MDGs were achieved 8 years ahead of schedule in 2007. China's global ranking of U5MR dropped from 90th in 1990 to 133rd in 2019 (25). Currently, some progress has been made in reducing child mortality in China, but concerted efforts are still needed to avoid preventable under-five deaths in the future. Studies have shown that the distribution of causes of death varies between age groups, thus requiring preventive interventions targeting specific age groups (26, 27). Congenital diseases and accidental death account for a large proportion of under five children deaths (28–30), and it is recommended to conceive at the appropriate age, make prenatal diagnosis, improve the safety awareness and safety protection skills of the whole society (31, 32).

TABLE 3 The results of ARIMA models.

	ARIMA	R^2	BIC	MAPE
Neonatal mortality rate				
National	(1,1,2)	0.994	0.038	3.635%
Urban	(3,1,3)	0.966	0.480	6.346%
Rural	(3,1,1)	0.992	0.714	3.849%
Infant mortality rate				
National	(0,1,0)	0.993	0.398	3.387%
Urban	(2,1,2)	0.973	0.306	4.533%
Rural	(1,1,0)	0.993	0.862	3.677%
Under five mortality rate				
National	(0,1,2)	0.993	1.131	3.963%
Urban	(3,1,4)	0.973	1.071	4.752%
Rural	(2,1,0)	0.991	1.611	3.902%
Maternal mortality rate				
National	(1,1,3)	0.978	2.883	4.696%
Urban	(3,0,1)	0.850	3.264	8.624%
Rural	(3,1,4)	0.973	4.281	5.704%

At present, obstetric hemorrhage is still one of the leading causes of maternal death in China (33). Prenatal care, skilled delivery, obstetric emergency care and postnatal care can effectively reduce the risk of obstetric hemorrhage. Therefore, improving the hospital delivery rate can also be explained by an effective reduction in MMR, which was also consistent with the mixed linear model results of this study. With the adjustment of China's birth policy, the proportion of older adult and high-risk pregnant women may continue to rise, and the control of maternal deaths in the whole country and all regions is facing great challenges (34). In addition, the capacity building of medical institutions and the pregnancy and perinatal health care management of the floating population should be strengthened to ensure the safety of mothers and infants and further reduce MMR.

The results of linear mixed model suggest that NMR, IMR, U5MR and MMR were negatively correlated with GDP, the proportion of THE in GDP, system management rate, prenatal care rate, postpartum visit rate and hospital delivery rate, suggesting that the development of economic level, the investment of THE and the improvement of maternal and child health care management level would help to further reduce NMR, IMR, U5MR and MMR. Therefore, the health of children and pregnant women in poor areas should get more

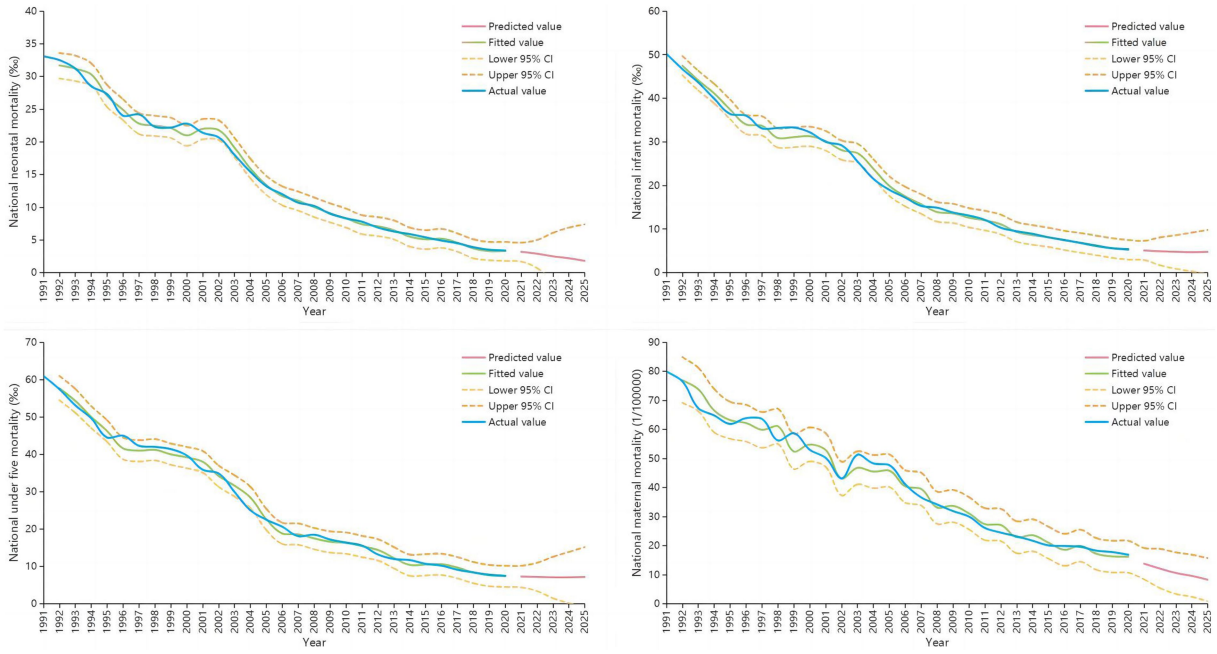

FIGURE 2
The predicted results of ARIMA model.

attention, and the relevant government departments should formulate corresponding policies and measures to implement the medical assistance system for children and pregnant women in poor areas, and effectively reduce the U5MR and MMR.

The ARIMA prediction results were that the national NMR, IMR, U5MR and MMR would be 1.8 ‰, 4.8 ‰, 7.2 ‰ and 8.3/100000 in 2025, which can meet the goals set out in the Health China 2030 planning outline (9). However, the results also showed that the rate of decline has decreased, and even in 2025, IMR and U5MR have increased from the previous year, which may be due to the following three reasons. Firstly, after IMR and U5MR have fallen to a certain level, the rate of decline may decrease. A study of IMR in Scotland showed that it had fallen from 5.75 ‰ in 2000 to 3.25 ‰ in 2018, a much slower rate of decline than the average rate of decline in China over the past 30 years (35). Secondly, the mortality rates predicted in this study are getting closer to those of developed countries. Studies have shown that IMR in Canada and the United States are 4.7 and 4.2, respectively (36, 37). However, the level of maternal and child health in rural areas of China still lags behind developed countries. Therefore, focusing on improving maternal and child health care level in rural areas remains a key factor in improving the health and quality of life of Chinese women and children. Third, few studies have analyzed the main causes and changing trends of IMR and U5MR in China. One study showed that the increase in IMR in the England since 2014 was mainly due to an increase in early NMR among preterm babies born at less than 24 weeks gestation (38). This also suggests that the causes of death in U5MR in China need to be further assessed. The predicted results in rural areas of this study were that the IMR, U5MR, and MMR would be 6.0 ‰, 8.6 ‰ and 14.0/100000, respectively, in 2025, which is higher than that in urban areas. Although the gap between urban and rural areas has narrowed, the rate of decline in rural areas is slower than in urban areas, which is also suggested that relevant departments should improve policies, strengthen the training of professional skills of grass-roots medical staff, and strive to improve the quality of rural medical and health services.

Our study has some strength. We analyzed the changing trends of long-term U5MR and MMR in China and made predictions, providing the basis for relevant departments to develop relevant child and maternal health care policies and measures. This study assessed the impact of social health services and economic factors on U5MR and MMR, which have been seldom evaluated in previous studies. This study also has some limitations, the data used in this study were from the surveillance systems and the data quality might be inconsistent in different areas such as urban and rural areas. The ARIMA model was suitable for the short-term prediction model and could not achieve the long-term trend prediction. Therefore, it is necessary to continuously collect and update the data for dynamic analysis to ensure the predictive performance of the model.

Conclusion

In the past 30 years, the U5MR and MMR of China have decreased significantly, and the gap between urban and rural areas has gradually narrowed. While it is still challenging to further reduce the U5MR and MMR with the adjustment of China's birth policy and relatively low level of primary health services in some regions. The government should continue to promote the equalization of basic public health services, improve the accessibility and fairness of health care services, focus on the health status of children and pregnant women in rural areas, and further optimize the allocation of government health resources, so as to achieve the goals set by Healthy China by 2030. The relevant experience of China in reducing U5MR and MMR is of reference significance for the improvement of maternal and child health care in less developed countries. In the context of the Belt and Road Initiative, it is suggested that China's advanced experience and applicable technologies in the field of maternal and child health be extended to developing countries to help achieve the global SDGs.

Data availability statement

The datasets presented in this study can be found in online repositories. The names of the repository/repositories and accession number(s) can be found in the article/Supplementary material.

Author contributions

MZ designed the study, conducted the data analysis, and drafted the main manuscript. HQ, JX, and XH contributed to the data collection. CS and FX contributed to writing the manuscript. JH and YC contributed to prepared figures and tables. HQ and MH provided technical support and guidance. All authors have read and agreed to the published version of the manuscript.

Funding

This work is supported by PhD research startup foundation of the Third Affiliated Hospital of Zhengzhou University (BS20230103).

Conflict of interest

The authors declare that the research was conducted in the absence of any commercial or financial relationships that could be construed as a potential conflict of interest.

Publisher's note

Supplementary material

The Supplementary material for this article can be found online at: https://www.frontiersin.org/articles/10.3389/fpubh.2023.1198356/full#supplementary-material

SUPPLEMENTARY TABLE 1
The data of neonatal mortality rate, infant mortality rate, under-five mortality rate and maternal mortality rate from 1991 to 2020 in China.

SUPPLEMENTARY TABLE 2
The maternal system management rate, prenatal care rate, postnatal visit rate, hospital delivery rate, GDP, total health expenditure and the ratio of total health expenditure to GDP from 1991 to 2020 in China.

SUPPLEMENTARY TABLE 3
The results of JoinPoint pairwise comparison test of NMR, IMR, U5MR and MMR between urban and rural areas.

SUPPLEMENTARY TABLE 4
The ARIMA predicted results of national, urban and rural areas from 2021-2025.

References

1. Bauserman M, Thorsten VR, Nolen TL, Patterson J, Lokangaka A, Tshefu A, et al. Maternal mortality in six low and lower-middle income countries from 2010 to 2018: risk factors and trends. *Reprod Health*. (2020) 17:173. doi: 10.1186/s12978-020-00990-z

2. Golding N, Burstein R, Longbottom J, Browne AJ, Fullman N, Osgood-Zimmerman A, et al. Mapping under-5 and neonatal mortality in Africa, 2000-15: a baseline analysis for the sustainable development goals. *Lancet*. (2017) 390:2171–82. doi: 10.1016/S0140-6736(17)31758-0

3. Hardelid P, Davey J, Dattani N, Gilbert R. Child deaths due to injury in the four UK countries: a time trends study from 1980 to 2010. *PLoS One*. (2013) 8:e68323. doi: 10.1371/journal.pone.0068323

4. Sachs JD, McArthur JW. The millennium project: a plan for meeting the millennium development goals. *Lancet*. (2005) 365:347–53. doi: 10.1016/S0140-6736(05)17791-5

5. Nielsen HS, Eggebø TM. Millennium development goal 5--an obstetric challenge. *Acta Obstet Gynecol Scand*. (2012) 91:1007–8. doi: 10.1111/j.1600-0412.2012.01505.x

6. Lozano R, Wang H, Foreman KJ, Rajaratnam JK, Naghavi M, Marcus JR, et al. Progress towards millennium development goals 4 and 5 on maternal and child mortality: an updated systematic analysis. *Lancet*. (2011) 378:1139–65. doi: 10.1016/S0140-6736(11)61337-8

7. Tan X, Kong S, Shao H. New strategies to improve the health of Chinese people by 2030. *Aust J Prim Health*. (2017) 23:307–8. doi: 10.1071/PY16146

8. GBD 2017. Causes of death collaborators. Global, regional, and national age-sex-specific mortality for 282 causes of death in 195 countries and territories, 1980-2017: a systematic analysis for the global burden of disease study. *Lancet*. (2017) 392:1736–88. doi: 10.1016/S0140-6736(18)32203-7

9. Tan X, Zhang Y, Shao H. Healthy China 2030, a breakthrough for improving health. *Glob Health Promot*. (2019) 26:96–9. doi: 10.1177/1757975917743533

10. Zeng Y, Hesketh T. The effects of China's universal two-child policy. *Lancet*. (2016) 388:1930–8. doi: 10.1016/S0140-6736(16)31405-2

11. Li H, Nawsherwan FC, Yin S, Haq IU, Mubarik S, Nabi G, et al. Changes in adverse pregnancy outcomes in women with advanced maternal age (AMA) after the enactment of China's universal two-child policy. *Sci Rep*. (2022) 12:5048. doi: 10.1038/s41598-022-08396-6

12. Chen Y, Wu Y, Dill S-E, Guo Y, Westgard CM, Medina A, et al. Effect of the mHealth-supported healthy future programme delivered by community health workers on maternal and child health in rural China: study protocol for a cluster randomised controlled trial. *BMJ Open*. (2023) 13:e065403. doi: 10.1136/bmjopen-2022-065403

13. Chen Y, Sylvia S, Dill S-E, Rozelle S. Structural determinants of child health in rural China: the challenge of creating health equity. *Int J Environ Res Public Health*. (2022) 19:13845. doi: 10.3390/ijerph192113845

14. Zhao Q, Chen J, Li F, Li A, Li Q. An integrated model for evaluation of maternal health care in China. *PLoS One*. (2021) 16:e0245300. doi: 10.1371/journal.pone.0245300

15. Zhang T, Lu W, Tao H. Efficiency of health resource utilisation in primary-level maternal and child health hospitals in Shanxi Province, China: a bootstrapping data envelopment analysis and truncated regression approach. *BMC Health Serv Res*. (2020) 20:179. doi: 10.1186/s12913-020-5032-y

16. National Bureau of Statistics. *The under-five and maternal mortality of surveillance region*. (2022). Available at: https://data.stats.gov.cn/easyquery.htm?cn=B01.

17. Zhao P, Diao Y, You L, Wu S, Yang L, Liu Y. The influence of basic public health service project on maternal health services: an interrupted time series study. *BMC Public Health*. (2019) 19:824. doi: 10.1186/s12889-019-7207-1

18. Zhao P, Han X, You L, Zhao Y, Yang L, Liu Y. Effect of basic public health service project on neonatal health services and neonatal mortality in China: a longitudinal time-series study. *BMJ Open*. (2020) 10:e034427. doi: 10.1136/bmjopen-2019-034427

19. Chen P, Li M, Zhu J, Wang Y, Mu Y, Li Q, et al. Provincial-level outcomes of China's 'Reducing maternal mortality and eliminating neonatal tetanus' program. *Sci Rep*. (2020) 10:13328. doi: 10.1038/s41598-020-70257-x

20. Feng XL, Shi G, Wang Y, Xu L, Luo H, Shen J, et al. An impact evaluation of the safe motherhood program in China. *Health Econ*. (2010) 19:69–94. doi: 10.1002/hec.1593

21. Jabbari Beyrami H, Doshmangir L, Ahmadi A, Asghari Jafarabadi M, Khedmati Morasae E, Gordeev VS. Impact of rural family physician programme on maternal and child health indicators in Iran: an interrupted time series analysis. *BMJ Open*. (2019) 9:e021761. doi: 10.1136/bmjopen-2018-021761

22. Li X, Krumholz HM, Yip W, Cheng KK, De Maeseneer J, Meng Q, et al. Quality of primary health care in China: challenges and recommendations. *Lancet*. (2020) 395:1802–12. doi: 10.1016/S0140-6736(20)30122-7

23. Yip W, Fu H, Chen AT, Zhai T, Jian W, Xu R, et al. 10 years of health-care reform in China: progress and gaps in universal health coverage. *Lancet*. (2019) 394:1192–204. doi: 10.1016/S0140-6736(19)32136-1

24. Mohammadi Y, Parsaeian M, Mehdipour P, Khosravi A, Larijani B, Sheidaei A, et al. Measuring Iran's success in achieving millennium development goal 4: a systematic analysis of under-5 mortality at national and subnational levels from 1990 to 2015. *Lancet Glob Health*. (2017) 5:e537–44. doi: 10.1016/S2214-109X(17)30105-5

25. United National Children's fund. *The state of the World's children*. New York: UNICEF (2021).

26. Cao H, Wang J, Li Y, Li D, Guo J, Hu Y, et al. Trend analysis of mortality rates and causes of death in children under 5 years old in Beijing, China from 1992 to 2015 and forecast of mortality into the future: an entire population-based epidemiological study. *BMJ Open*. (2017) 7:e015941. doi: 10.1136/bmjopen-2017-015941

27. Liu Z, Liu XR, He CH, Miao L, Kang LN, Li XH, et al. Analysis of mortality and leading causes of death in Chinese children under 5-year-old between 2010 and 2016. *Zhonghua Yu Fang Yi Xue Za Zhi*. (2019) 53:411–4. doi: 10.3760/cma.j.issn.0253-9624

28. Cui H, He C, Kang L, Li Q, Miao L, Shen L, et al. Under-5-years child mortality due to congenital anomalies: a retrospective study in urban and rural China in 1996-2013. *Am J Prev Med*. (2016) 50:663–71. doi: 10.1016/j.amepre.2015.12.013

29. He C, Liu L, Chu Y, Perin J, Dai L, Li X, et al. National and subnational all-cause and cause-specific child mortality in China, 1996-2015: a systematic analysis with implications for the sustainable development goals. *Lancet Glob Health*. (2017) 5:e186–97. doi: 10.1016/S2214-109X(16)30334-5

30. Xu XH, Dong H, Li L, Liu WH, Lin GZ, Ou CQ. Trends and seasonality in cause-specific mortality among children under 15 years in Guangzhou, China, 2008-2018. *BMC Public Health*. (2020) 20:1117. doi: 10.1186/s12889-020-09189-0

31. Shan D, Qiu PY, Wu YX, Chen Q, Li AL, Ramadoss S, et al. Pregnancy outcomes in women of advanced maternal age: a retrospective cohort study from China. *Sci Rep*. (2018) 8:12239. doi: 10.1038/s41598-018-29889-3

32. Wu Y, Chen Y, Shen M, Guo Y, Wen SW, Lanes A, et al. Adverse maternal and neonatal outcomes among singleton pregnancies in women of very advanced maternal age: a retrospective cohort study. *BMC Pregnancy Childbirth*. (2019) 19:3. doi: 10.1186/s12884-018-2147-9

33. Chen L, Feng P, Shaver L, Wang Z. Maternal mortality ratio in China from 1990 to 2019: trends, causes and correlations. *BMC Public Health*. (2021) 21:1536. doi: 10.1186/s12889-021-11557-3

34. Liu J, Song L, Qiu J, Jing W, Wang L, Dai Y, et al. Reducing maternal mortality in China in the era of the two-child policy. *BMJ Glob Health*. (2020) 5:e002157. doi: 10.1136/bmjgh-2019-002157

35. Harpur A, Minton J, Ramsay J, McCartney G, Fenton L, Campbell H, et al. Trends in infant mortality and stillbirth rates in Scotland by socio-economic position, 2000-2018: a longitudinal ecological study. *BMC Public Health*. (2021) 21:995. doi: 10.1186/s12889-021-10928-0

36. Fell DB, Park AL, Sprague AE, Islam N, Ray JG. A new record linkage for assessing infant mortality rates in Ontario, Canada. *Can J Public Health*. (2020) 111:278–85. doi: 10.17269/s41997-019-00265-6

37. Galan J, Mydam J, Collins JW. Infant mortality rates among US-born and foreign-born Latinx women. The effect of black race. *Matern Child Health J*. (2022) 26:511–6. doi: 10.1007/s10995-021-03366-2

38. Nath S, Hardelid P, Zylbersztejn A. Are infant mortality rates increasing in England? The effect of extreme prematurity and early neonatal deaths. *J Public Health*. (2021) 43:541–50. doi: 10.1093/pubmed/fdaa025

frontiers | Frontiers in Public Health

TYPE Original Research
PUBLISHED 26 January 2024
DOI 10.3389/fpubh.2024.1224449

OPEN ACCESS

EDITED BY
Shahidul Islam,
University of Dhaka, Bangladesh

REVIEWED BY
Myriam Boueri,
Lebanese American Univeristy, Lebanon
Linda Suwarni,
Universitas Muhammadiyah Pontianak, Indonesia
Wei Li,
Nanjing Children's Hospital, China

*CORRESPONDENCE
Emine Yaylali
✉ emineyaylali@itu.edu.tr

RECEIVED 26 May 2023
ACCEPTED 02 January 2024
PUBLISHED 26 January 2024

CITATION
Yaylali E, Erdogan ZM, Calisir F, Pullukcu H, Yildirim F, Inan A, Aydin OA, Tekin S, Sonmezer MC, Sahin T, Ozcagli TG and Ozelgun B (2024) Rapid initiation of antiretroviral therapy in Turkey: a modeling study. *Front. Public Health* 12:1224449. doi: 10.3389/fpubh.2024.1224449

Rapid initiation of antiretroviral therapy in Turkey: a modeling study

Emine Yaylali[1]*, Zikriye Melisa Erdogan[1], Fethi Calisir[1], Husnu Pullukcu[2], Figen Yildirim[3], Asuman Inan[4], Ozlem Altuntas Aydin[5], Suda Tekin[6], Meliha Cagla Sonmezer[7], Toros Sahin[8], Tahsin Gokcem Ozcagli[8] and Berna Ozelgun[8]

[1]Department of Industrial Engineering, Istanbul Technical University, Istanbul, Türkiye, [2]Infectious Diseases, Ege University, Izmir, Türkiye, [3]Infectious Diseases and Clinical Microbiology, Akdeniz Yasam Hospital, Antalya, Türkiye, [4]Infectious Diseases and Clinical Microbiology, Haydarpasa-Numune Training and Research Hospital, Istanbul, Türkiye, [5]Infectious Diseases and Clinical Microbiology, University of Health Sciences, Istanbul, Türkiye, [6]Infectious Diseases and Clinical Microbiology, Koc University, Istanbul, Türkiye, [7]Infectious Diseases and Clinical Microbiology, Hacettepe University, Ankara, Türkiye, [8]Gilead Sciences, Istanbul, Türkiye

Background: To effectively control the HIV epidemic and meet global targets, policymakers recommend the rapid initiation of antiretroviral therapy (ART). Our study aims to investigate the effect of rapid ART programs on individuals diagnosed with HIV, considering varying coverage and initiation days after diagnosis, and compare it to standard-of-care ART treatment in Turkey.

Methods: We used a dynamic compartmental model to simulate the dynamics of HIV infection in Turkey. Rapid treatment, defined as initiation of ART within 7 days of diagnosis, was contrasted with standard-of-care treatment, which starts within 30 days of diagnosis. This study considered three coverage levels (10%, 50%, and 90%) and two rapid periods (7 and 14 days after diagnosis), comparing them to standard-of-care treatment in evaluating the number of HIV infections between 2020 and 2030.

Results: Annual HIV incidence and prevalence for a 10-year period were obtained from model projections. In the absence of a rapid ART program, the model projected approximately 444,000 new HIV cases while the number of cases were reduced to 345,000 (22% reduction) with 90% of diagnosed cases included in the rapid ART program. Similarly, 10% and 50% rapid ART coverage has resulted in 3% and 13% reduction in HIV prevalence over a 10-year period.

Conclusion: Rapid ART demonstrates the potential to mitigate the increasing HIV incidence in Turkey by reducing the number of infections. The benefit of the rapid ART program could be substantial when the coverage of the program reaches above a certain percentage of diagnosed population.

KEYWORDS

HIV infections, HIV care-continuum, mathematical modeling, rapid antiretroviral treatment, infectious disease modeling

1 Introduction

As of the end of 2019, among the estimated 38 million people living with HIV globally, 67% of them had access to treatment in the world (1). With the help of global prevention and intervention efforts, the proportion of people living with HIV (PLWH) on antiretroviral therapy (ART), which is known as treatment coverage, is increasing. Consequently, HIV incidence has been decreasing or stabilizing in many countries. New HIV prevention targets aim to achieve 95% of PLWH know their HIV status, 95% of those aware of their HIV positive status accessing treatment, and 95% of people on treatment having suppressed viral loads by 2030. However, since 2020, these targets have been missed (1), with 1.5 million new HIV infections in that year. There is still much more effort to make to meet the 2030 targets.

Following the "treat all" strategy, Rapid ART Program for Individuals with an HIV Diagnosis (RAPID) is recognized as one of the key recommendations in the fight against the HIV infection. Ideally, rapid ART involves initiating treatment in the first 24 h of diagnosis, it is defined as the initiation of ART within 7 days of diagnosis (2), while some studies considered initiation within <14 days after diagnosis (3, 4). This strategy has been recommended by several guidelines, including the World Health Organization (2), the U.S. Department of Health and Human Services (5), and the International Antiviral Society (4).

The initiation of ART as early as HIV diagnosis has been an important public health strategy for HIV prevention due to two main reasons. First, rapid ART initiation enables viral load suppression (VLS) much faster (6, 7) and resulting viral suppression may prevent HIV transmission since treatment prevents up to 93–96% of infections in serodiscordant couples (i.e., treatment as prevention- TasP) (8, 9). Second, early initiation of treatment may decrease mortality and morbidity and improve the health-related quality of life (HRQoL) among people living with HIV (PLWH) (3).

Rapid ART initiation has been evaluated by randomized controlled trials and assessed by observational studies. These randomized trials [RapIt (10), START-ART (11), same day ART in Haiti (12), and CASCADE (13)] and observational studies [RAPID in San Francisco (14), TRRT in Miami (15) and CCSI in New Orleans (16)] have determined that patients in the rapid ART arm exhibit higher rates of linkage to care, retention in care and viral suppression. Similar results have been found in a systematic review on rapid ART initiation, reporting that rapid ART improves patient outcomes compared to standard-of-care treatment (3). Many countries globally have embraced rapid ART implementation in accordance with the latest guidelines. Data presented in 2023 reveal that 99 countries, corresponding to 81% of 122 reporting countries, have adopted WHO's recommendation to offer rapid ART, providing ART on the same day as HIV diagnosis. This fact represents 46% increase from 68 countries reported in 2020 worldwide (17).

Since the publication of the national guideline in 2013, ART has been the recommended as a standard treatment for all HIV-positive individuals, regardless of their CD4 cell count in Turkey. Moreover, initiation of treatment generally takes 2–4 weeks (18). However, new HIV-positive cases have been steadily increasing in the last decade in the country with nearly 60% of cases diagnosed in the last 5 years. The spread of HIV in Turkey is obscured by various contributing factors, including a lack of knowledge and awareness about the disease, being one of the most popular tourism destinations increasing the risk of exposure, high population mobility, an increasing number of unregistered sex workers, lack of prevention measures focusing on key risk groups, insufficient number of Voluntary Counseling and Testing (VCT) centers, persistent stigma, and discrimination against PLWH (19). Turkish Ministry of Health (MoH) conducted the National HIV/AIDS Control Program to enhance public health and create the roadmap for HIV in Turkey in 2019. One of the important goals in this program is to decrease the number of new HIV cases and deaths due to HIV. Moreover, it was stated that the main approach to decrease HIV transmission could be achieved by providing early diagnosis, access to care, and retention in care for PLWH, leading to viral suppression (20). Thus, we can conclude the programs that an increase in viral suppression and a decrease in transmission risk would be valuable in achieving the national goal of reduced number of new HIV positive cases. The previous studies show that the current situation in the country ranges between 48 and 50% regarding HIV diagnosis, 75.3 and 88% for ART coverage, and 85 and 87% for VLS rates (21, 22). Rapid initiation of ART would play a crucial role in improving the current continuum of care, and it should be analyzed for further consideration as it can be beneficial in reducing the total number of cases. Our motivation is to investigate the effectiveness of introducing a rapid ART initiation program in both mitigating the increasing trend of HIV and improving the current HIV prevention strategies in Turkey.

To the best of our knowledge, there are no published studies regarding rapid ART initiation in Turkey. In this study, our objective is to evaluate the differences in effects between implementing a rapid initiation of the ART program and standard care over a 10-year period in Turkey. Thus, the goal is to assess the benefit of rapid ART programs in Turkey and quantify these benefits by determining the number of prevented infections, if exists.

2 Materials and methods

2.1 Model structure

We adopted a previously developed HIV transmission and progression model of Turkey for rapid ART initiation (23). The deterministic dynamic compartmental model was tailored for a portion of diagnosed PLWH to participate in the onset of rapid ART program while the remaining diagnosed PLWH proceed with the standard treatment. The model was developed in MATLAB environment (24) and formulated using ordinary differential equations (ODEs) with details of the system as given in the Appendix.

The model population was stratified based on the disease status (HIV negative and HIV positive) and transmission risk [men who have sex with men (MSM), people who inject drugs (PWID), and heterosexuals (HET)]. PLWH in the model is further divided into subpopulations based on disease stages and continuum of care. As a

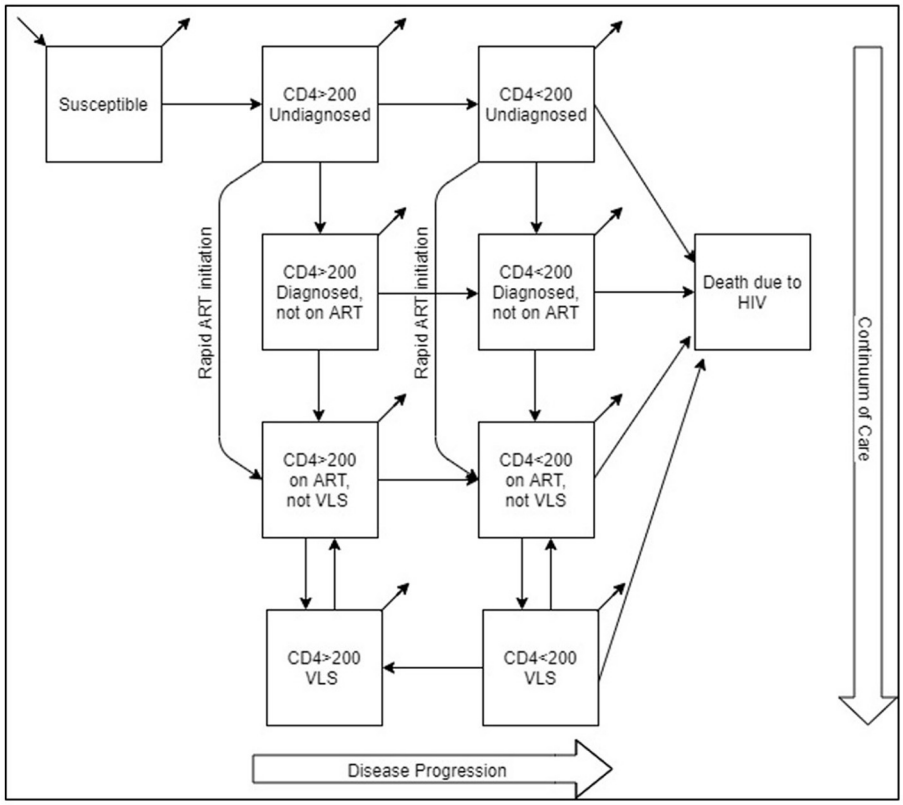

FIGURE 1
Model flow diagram including rapid ART initiation.

result, aside from susceptible (HIV negative) and death due to HIV compartments, PLWH is divided into the following compartments: CD4 count>200 cells/mm^3 and undiagnosed, CD4 count <200 cells/mm^3 and undiagnosed, CD4 count>200 cells/mm^3 diagnosed but not on ART, CD4 count <200 cells/mm^3 diagnosed but not on ART, CD4 count>200 cells/mm^3 diagnosed, on ART but no viral load suppression (VLS), CD4 count<200 cells/mm^3 diagnosed, on ART but not VLS, CD4 count>200 cells/mm^3 VLS, and CD4 count<200 cells/mm^3 VLS. Model formulation is presented in the model formulation section of Appendix and Supplementary Table A2.

Rapid ART initiation is integrated with the model via a flow between two sets of compartments. Individuals diagnosed and initiated ART in the "rapid" program move directly from undiagnosed compartments (CD4 count>200 cells/mm^3 or CD4 count<200 cells/mm^3) to the "on ART not VLS" compartments, bypassing diagnosed but not on ART compartments, which represents the standard-of-care ART initiation route (Figure 1). Since there is currently no rapid ART initiation in Turkey, we generated the "rapid" flow rates by three levels of coverage and the length of the rapid period.

Rapid ART leads to faster VLS compared to delayed treatment. In the model schematic, this is accomplished by bypassing the "Diagnosed not on ART" compartment, allowing individuals to move faster to the "on ART not VLS" compartment. The parameters for achieving VLS or drop out of VLS remain consistent across scenarios, but the time taken to reach VLS compartment decreases due to earlier entry into the on ART compartments. By achieving VLS faster, patients become less infectious, effectively curbing the spread of HIV within the population in the model. Thus, rapid ART serves as a critical component of HIV prevention efforts.

The model was validated against the number of confirmed cases reported by the Ministry of Health and considered a time horizon of 2010–2019 as its fitting (calibration) period. The prediction period extended 2020 and beyond. The primary model predictions focused on outcomes related to HIV incidence and prevalence between 2020 and 2030 and the effect on continuum of care during the same period.

2.2 Model parameters

The model is populated with demographic, epidemiological, behavioral, and clinical data. Input parameters included population size by transmission risk group, continuum of care, mortality rate (HIV-related and non-HIV related), HIV progression among disease stages, and reduction in HIV transmission after diagnosis and treatment (Supplementary Table A1). Parameters related to prevalence rates by transmission group, treatment and VLS rates, HIV-related mortality parameters, birth and natural death rates,

TABLE 1 Scenarios defined under different coverage levels and rapid ART periods.

Scenarios	Coverage level	Rapid ART period
Scenario 1	10%	7 days
Scenario 2	10%	14 days
Scenario 3	50%	7 days
Scenario 4	50%	14 days
Scenario 5	90%	7 days
Scenario 6	90%	14 days

and related population parameters are among the country-specific parameters. Due to the scarcity of behavioral parameters based on each HIV transmission group, we calibrated force of infection parameter. Parameters are estimated from several sources, such as medical literature, Turkish Statistical Institute, and three large patient cohorts. These cohorts reported around 8,000 patients, which was ∼50% of all reported cases in Turkey between 01/2010 and 12/2019 (23). Data analysis and parameter estimation were conducted using MS Excel. Data extracted from cohort databases were anonymized before access and analysis; thus, no informed consent and/or a consent waiver was obtained during the study. Ethics approval was not required for this modeling study.

Parameters related to rapid ART initiation include the rate at which PLWH diagnosed and initiated in the rapid ART program based on the disease stage and the length of rapid period. These parameters are based on rapid ART initiation scenarios developed due to lack of real-life data on the rapid initiation in Turkey. Once initiated, both rapid ART program and standard ART program have assumed to have same treatment efficacy in reducing the disease transmission and dropping out rates of ART.

2.3 Model calibration

To calibrate the model, we generated ranges for input parameters that could not be estimated from datasets and literature and applied the ranges against the reported number of cases based on the disease stage reported by MoH between 2010 and 2019. Details of the calibration procedure are provided in the Appendix.

2.4 Rapid ART initiation scenarios

To include rapid ART initiation, we considered six scenarios, which are hypothetical due to lack of real-life data on rapid ART initiation in Turkey (Table 1). In the scenarios, we assumed that different proportions of PLWH diagnosed and associated with care receive the rapid ART while the rest of diagnosed population initiate ART in the standard way. This was considered as the rapid ART coverage. Three coverage levels were 10%, 50%, and 90% of diagnosed PLWH being included in the rapid ART program. These scenarios compared to the base case scenario where no rapid ART program exists and diagnosed PLWH initiates ART ∼30 days after the diagnosis. Duration of rapid period was selected as 7 days, representing the relevant guidelines. We also evaluated a rapid ART period of 14 days to investigate the effect of the change in ART initiation time. We assumed that all diagnosed patients are eligible for the rapid ART initiation, the patients offered the rapid treatment do not refuse it, and the coverage of the rapid ART program remains constant over the time horizon. We collected annual HIV incidence, cumulative HIV cases, the number of HIV cases prevented, and the percent reduction in HIV incidence with the rapid ART intervention between 2020 and 2030. We also reported continuum of care for the base case and rapid ART scenarios.

We also applied sensitivity analysis, and further details are explained in Sensitivity Analysis section in the Appendix; then, results of two sensitivity analyses are explained in Supplementary Figures A1, A2.

3 Results

The standard-of-care ART, considered as the base case scenario, represents the current healthcare system practice, where HIV-infected persons can access ART 30 days after their diagnosis. Three rapid ART scenarios were defined based on the proportion of patients benefiting from rapid ART intervention, such as 10%, 50% and 90%.

We estimated that additionally 443,682 people would be diagnosed with HIV between 2020 and 2030 if the standard-of-care ART has been continued in Turkey. However, when 10% of diagnosed patients included in the rapid ART program, cumulative HIV incidence would be reduced to 431,858 (3% reduction). With 50% of PLWH included in the rapid ART program, total new cases for a 10-year period would drop to 368,810 (13% reduction). The benefit of the rapid ART program increases to 22% reduction in the cumulative incidence resulting with 345,252 cases when 90% of diagnosed persons receives the rapid ART instead of the standard-of-care (Figure 2).

Furthermore, we investigated the effect of the rapid ART period by analyzing the difference between the rapid ART onset at 7 days after the time of diagnosis and starting this treatment at 14 days after the diagnosis. A 7-day intervention generated less HIV incidence in all coverage scenarios, thereby preventing more infections than the 14-day option (Figure 2). While initiating rapid ART at 7 days leads to 3%, 13%, and 22% reduction in the cumulative incidence as mentioned above, the improvements for 14-days onset were 2%, 8%, and 14%, respectively. The marginal benefit of quicker initiation increases with the coverage level as 90% coverage has shown significant impact of 7-day reduction in the ART initiation. In other words, based on the model results, initiating treatment as early as possible could potentially help in preventing the disease and possibly ending the epidemic.

We determined annual HIV incidence between 2020 and 2030. Moreover, under the standard-of-care ART, 13,748 new HIV cases have been projected in 2020. HIV incidence increases to 85,130 in 2030 (Figure 3). Introducing the rapid ART program with 90% coverage would reduce HIV incidence to 13,040 and 60,560 for the same years, respectively. We can conclude that the benefits gained from the rapid initiation of ART were increased over the years.

We calculated the average of 10-year annual percentages of continuum of care for the base case and three rapid ART

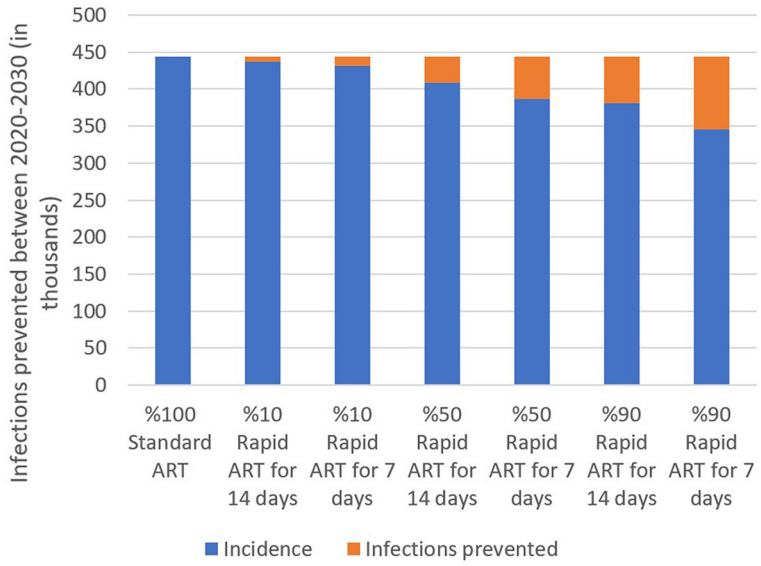

FIGURE 2
Estimated total incidence and infections prevented under three rapid ART coverage and two rapid ART period scenarios, 2020–2030.

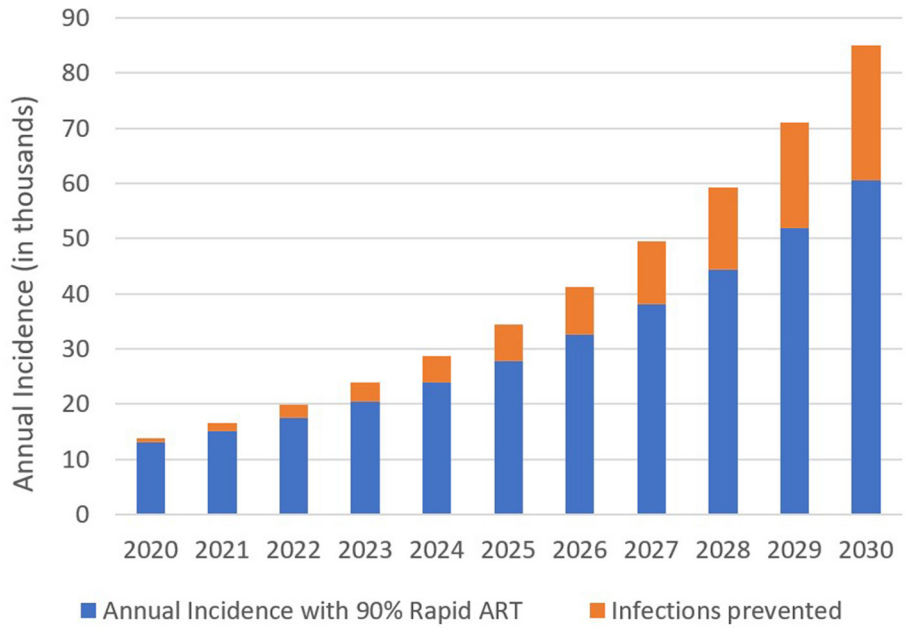

FIGURE 3
Estimated annual HIV incidence and infection prevented with 90% coverage of the rapid ART intervention, 2020–2030.

scenarios (Figure 4). As more patients were offered the rapid ART intervention, the diagnosis rate for PLWH with CD4 count>200 cells/mm^3 has increased whereas it has decreased for PLWH with CD4 count <200 cells/mm^3. On the other hand, the percentage of patients who are on ART has increased significantly for both CD4 levels with the introduction of rapid ART. The final continuum stage, the percentage of patients who achieved VLS among patients on ART, has been remained nearly the same across the different intervention scenarios.

4 Discussion

A mathematical model had been adapted to analyze the effectiveness of the rapid ART intervention compared to standard-of-care in Turkey, and the results were evaluated for HIV transmission and progression for a 10-years period. The rapid ART initiation at 7-days and at 14-days were analyzed. Although both interventions reduced the new infectious cases compared to standard care, the initiation of rapid ART at 7 days after

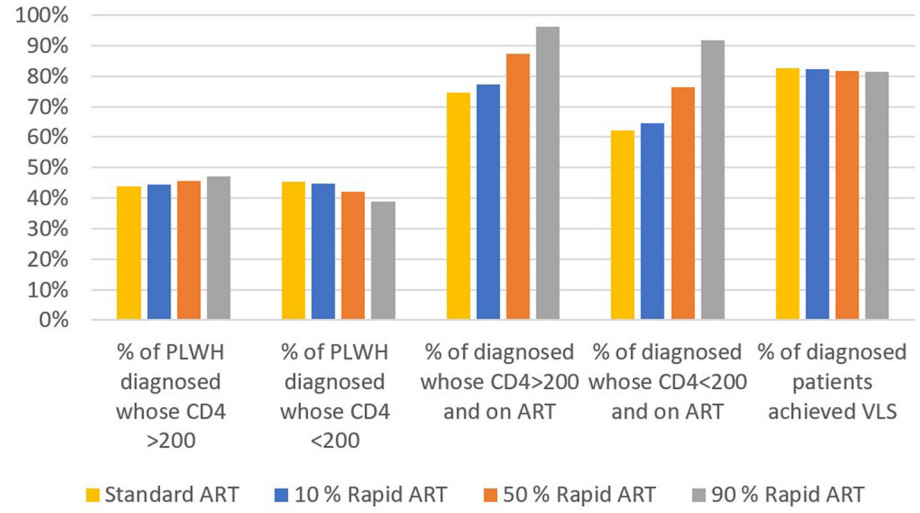

FIGURE 4
Impact of different rapid ART initiation scenarios on continuum of care.

the diagnosis had provided better reduction rate in overall HIV incidence. Although we did not analyze the same-day ART initiation, our results suggested that initiating treatment as early as possible is crucial, which is consistent with the previous studies.

In addition, we determined the effect of extending rapid treatment with three coverage levels to a large population. Since there is no current widespread practice of rapid ART programs in Turkey, we defined low, medium, and high coverage with 10%, 50%, and 90% of diagnosed cases who receive the rapid ART, respectively. As expected, the number of prevented infections increases with the increase in the coverage level. Overall, the rapid ART intervention is effective in reducing new HIV infections and it should be considered as a prevention method.

The rapid ART initiation has a positive impact on the continuum of care as the percentage of diagnosed people on ART increases significantly compared to standard care. If the rapid ART reaches 90% coverage, average percentage of PLWH on ART for CD4 count>200 cells/mm^3 and CD4 count<200 cells/mm^3 over a 10-year period was estimated as 96% and 92%, respectively. This implies that, the second part of the 95-95-95 target, i.e., 95% of diagnosed patients will be on ART by 2030 (1), is possible to achieve with the introduction and swift scaling up of the rapid ART initiation. Although the percentage of individuals on ART and achieved VLS among diagnosed did not show any significant changes, as the same efficacy is assumed for both the rapid ART and standard ART in achieving VLS, the same percentages among PLWH improved considerably.

Two sensitivity analyses demonstrated very similar conclusions regarding the most important parameters in the model. The primary drivers of HIV incidence in the model were the force of infection, and the diagnosis rates and interactions among the parameters exist. Force of infection combines the transmission risk between HIV-negative and HIV-positive individuals, mixing among risk populations and HIV prevalence rate by risk populations, and it is the one of main elements that affect the transition between susceptible and infected populations. As a result, it is expected to be one of the influential parameters. The importance of diagnosis rate in this study is probably magnified due to the introduction of rapid ART. With the rapid ART, diagnosed population has been quickly carried to the on ART and VLS compartments where the likelihood of disease transmission is very small. The benefit of compressed timeline accumulates over the time horizon, and changes in the diagnosis rate have a larger effect on the number of new cases.

In Turkey, HIV-positive patients have been eligible to receive ART irrespective of their CD4 level since 2013 guidelines (25); however, we need to take firm actions for ending the HIV due to the evident trend of rising HIV cases in Turkey. To achieve this goal, it is necessary to look for the effective interventions such as rapid ART initiation for patients and, after the careful evaluations including the cost aspect of such interventions, public health policy makers should implement the most beneficial interventions among them. This study provides the evidence on the benefit of the rapid ART intervention on cost and the prevention of new transmissions; therefore, it takes a step toward looking for the effective ways to end the HIV epidemic in Turkey and to achieve the national and international HIV targets.

This study quantifies the effectiveness of rapid ART intervention in Turkey; however, we did not include the behavioral response to the rapid ART as well as implementation barriers. Recent surveys reported that HIV-positive patients in Turkey are mostly in favor of rapid treatment initiation (26). Inclusion of patients in the decision-making process and providing information on treatment pathways to the patients would likely to increase adoption of rapid ART (27). Thus, patients should be well-informed on the process and its results during the implementation phase of the rapid ART programs (3). Barriers to delay the ART onset should be learned and eliminated, as well.

To the best of our knowledge, rapid ART initiation in Turkey has been assessed via a multi-center and retrospective study so far. Considering the lack of standard definition of rapid ART, they categorized the naive PLWH into three groups named as rapid

start (RS-ART initiation within the first 24 h after admission to the clinic), early start (ES- ART initiation between the second day and the seventh day after arriving at the clinic), and late start (LS-ART initiation on the eighth day and beyond) groups. In line with other studies, they also found that rapid ART leads to faster viral suppression. Our results are also similar in that there is no significant change in viral suppression rates with rapid ART (18).

Kroon et al. utilized a risk calculator model to estimate the effect of HIV diagnosis during acute infection and immediate initiation of ART combined with behavioral counseling in Thailand. Combining acute HIV infections and early ART with overall behavioral change could potentially result in 89% reduction in the number of onward transmissions across the cohort within the first year of infection while viral load reduction through ART was the most significant contributor to these results. However, the individual effect of early ART is not presented in the study (28). A study conducted by Dimitrov et al. developed a dynamic compartmental model of HIV in Peru and assessed the combination of prevention strategies with early detection and rapid initiation of ART by focusing on the acute HIV phase. After varying different proportions of MSM and transgender women (TW) in the model, the intervention is projected to reduce HIV incidence in 2028 by 24%−60% and new infections over 20 years by 13%−41%. The reported outcomes are common, such as fraction of HIV infections prevented and reduction in HIV incidence, whereas our model differs in assessing the impact of solely rapid initiation of ART (29). Estrada et al. designed a different methodology compared to ours by using a Markov tree to compare rapid ART initiation with current practice of ART in Spain. They had a conservative approach by considering 9 days from HIV diagnosis to rapid ART initiation. They found that rapid ART initiation would prevent about 2% of HIV infections over the 20-year period. Our study results are consistent with this study as they found that initiating ART earlier—at day 7 from diagnosis—averted more HIV cases compared to the initiation at day 9 (30). Krebs et al. investigated several HIV intervention strategies across 6 different US cities employing city-level compartmental models. Rapid ART is defined as same-day ART initiation to newly diagnosed individuals in contrast to our model. Based on the findings of the study, percentage of HIV infections averted over 10-year implementation of rapid ART initiation is estimated between 0.1% and 0.4% for the cities (31). Due to variations in HIV dynamics among different settings, direct comparisons of the magnitude of changes between studies are not feasible. Nevertheless, our findings align with the modeling studies in the literature, suggesting that rapid ART effectively reduces HIV transmission.

There are some limitations to consider when interpreting the results of this study. Since there is no available data that show a change in the parameters over time, we used the same values during the modeling period. Model parameters, such as diagnosis rates and treatment rates, remain constant over the horizon time, which considers the most significant limitation of this study. Another limitation is that we calibrated force of infection parameters due to limited data on sexual and needle sharing behaviors in Turkey. However, we validated the model results with the most recent number of confirmed cases and conducted an extensive sensitivity analysis on this parameter. Apart from these limitations, the analysis of elementary effects showed the parameters that present interactions or nonlinear effects, but it did not reveal which parameters were interacting with each other.

Basic assumption of the compartmental models is homogenous and well-mixed population. Based on this theoretical assumption, all individuals in the population have an equal probability of interacting to each other although there are complex social networks and contact patterns in reality. Our model follows the same assumptions, yet we stratified the model population based on risk groups, such as MSM, PWID, and HET, and defined different infectivity rates for each group to use different infectiousness levels in the population and decrease the limiting effects of the model. We also assumed that the time of the rapid ART initiation and coverage levels are considered the same for all risk groups. We did not consider any behavioral response to rapid ART and assumed that individuals accepted and followed the rapid ART process. Individual-based models, such as network models or agent-based models, could be used for reflecting the heterogeneity among population with the cost of additional computational efforts and increased burden of model inputs.

The strength of our model is that it represents the general dynamics of HIV and enables us to address our research questions with the acceptable number of parameters. Another benefit of our research is that data sets obtained from three largest data source regarded as the most representative data for the country so far are used to create our model. This study facilitates the understanding of the relationships between rapid ART and the number of infections and potentially quantifies the benefit of initiating ART as fast as possible. Furthermore, this study introduces the first comprehensive mathematical model to investigate the effectiveness of rapid ART programs for PLWH in Turkey. The model considers various hypothetical combinations of coverage and initiation times after diagnosis compared to the current standard-of-care ART treatment in the country.

This modeling study provides valuable insights into the significant effect of rapid ART and helps us to understand system behavior under hypothetical conditions. Nevertheless, results should be interpreted with caution due to the aforementioned limitations and methodological simplifications of the model, which do not fully capture the real-world complexities. Moreover, we did not perform any type of economic analysis in this study. The cost aspect of the rapid ART initiation should be investigated with the help of cost-effectiveness analysis before the implementation of such program, particularly for resource-limited settings. For future studies, economic analysis would extend our knowledge of the rapid ART interventions and help to shed a light on the process of selecting the right interventions that achieve the best health outcomes with the least cost for public health decision makers. For future work, the researchers have been encouraged to increase the complexity of the model enhanced by incorporating heterogeneity among the population with different CD4 levels other than 200 cells/mm^3, age levels or gender when there is available data. Rapid ART applications have recently been started in Turkey, and based on the clinical data that could be collected from these applications, our model could be updated and extended with real-life data and scenarios.

5 Conclusion

The rapid ART intervention prevents new HIV cases compared to standard-of-care ART, and the benefit of intervention increases with the coverage and faster initiation. Thus, it can be concluded that the rapid ART initiation could be an effective method to mitigate the increasing trend of HIV cases in Turkey. In other words, the practical implication of the model results is that rapid ART is a promising intervention to replace the existing standard-of-care implementation with the benefits of accelerating entry into medical care, which in turn reduces the HIV transmission in the population. Rapid ART programs demonstrate the potential to provide policy makers with a structural solution for controlling both future direction of HIV and its negative effects on the national healthcare system.

Data availability statement

The original contributions presented in the study are included in the article/Supplementary material, further inquiries can be directed to the corresponding author.

Ethics statement

Ethical approval was not required for the study involving humans in accordance with the local legislation and institutional requirements. Written informed consent to participate in this study was not required from the participants or the participants' legal guardians/next of kin in accordance with the national legislation and the institutional requirements.

Author contributions

EY: Writing – original draft, Conceptualization, Methodology, Funding acquisition, Formal analysis, Software. FC: Writing – review & editing, Conceptualization, Funding acquisition. TS: Conceptualization, Supervision. TO: Conceptualization, Supervision. BO: Conceptualization, Formal analysis, Supervision. HP: Writing – review & editing, Data curation. FY: Writing – review & editing, Data curation. AI: Writing – review & editing, Data curation. OA: Writing – review & editing, Data curation. ST: Writing – review & editing, Data curation. MS: Writing – review & editing, Data curation. ZE: Writing – original draft, Methodology, Formal analysis, Software.

Funding

The authors declare that this study received funding from Gilead Sciences. The funder was not involved in the study design, collection, analysis, interpretation of data, the writing of this article, or the decision to submit it for publication.

Conflict of interest

TS, TO, and BO were employed by Gilead Sciences.

The remaining authors declare that the research was conducted in the absence of any commercial or financial relationships that could be construed as a potential conflict of interest.

Publisher's note

Supplementary material

The Supplementary Material for this article can be found online at: https://www.frontiersin.org/articles/10.3389/fpubh.2024.1224449/full#supplementary-material

References

1. Joint United Nations Programme on HIV/AIDS (UNAIDS). *Seizing the Moment, Global AIDS Update*. Geneva: UNAIDS (2020). Available online at: https://www.unaids.org/sites/default/files/media_asset/2020_global-aids-report_en.pdf (accessed February 1, 2023).

2. World Health Organization (WHO). *World Health Organization Guidelines for Managing Advanced HIV Disease and Rapid Initiation of Antiretroviral Therapy*. Geneva: World Health Organization. (2018). p. 480.

3. Ford N, Migone C, Calmy A, Kerschberger B, Kanters S, Nsanzimana S, et al. Benefits and risks of rapid initiation of antiretroviral therapy. *AIDS*. (2018) 32:17–23. doi: 10.1097/QAD.0000000000001671

4. Gandhi RT, Bedimo R, Hoy JF, Landovitz RJ, Smith DM, Eaton EF, et al. Antiretroviral drugs for treatment and prevention of HIV infection in adults: 2022 recommendations of the international antiviral society–USA panel. *JAMA*. (2022) 329:63–84. doi: 10.1001/jama.2022.22246

5. US Department of Health and Human Services. *Guideline for Use Antiretroviral Agentes in Adults and Adolescents with HIV*. (2019).

6. Gomillia CES, Backus K V, Brock JB, Melvin SC, Parham JJ, Mena LA. Rapid Antiretroviral Therapy (ART) initiation at a community-based clinic in Jackson, MS. *AIDS Res Ther*. (2020) 17:1–6. doi: 10.1186/s12981-020-00319-7

7. Gregori N, Renzetti S, Izzo I, Faletti G, Fumarola B, Degli Antoni M, et al. Does the rapid initiation of antiretroviral therapy at HIV diagnosis impact virological response in a real-life setting? A single-centre experience in Northern Italy. *AIDS Care*. (2023) 35:1938–47. doi: 10.1080/09540121.2023.2176425

8. Cohen MS, Chen YQ, McCauley M, Gamble T, Hosseinipour MC, Kumarasamy N, et al. Prevention of HIV-1 infection with early antiretroviral therapy. *N Engl J Med*. (2011) 365:493–505. doi: 10.1056/NEJMoa1105243

9. Cohen MS, Chen YQ, McCauley M, Gamble T, Hosseinipour MC, Kumarasamy N, et al. Antiretroviral therapy for the prevention of HIV-1 transmission. *N Engl J Med*. (2016) 75:830–9. doi: 10.1056/NEJMoa1600693

10. Rosen S, Maskew M, Fox MP, Nyoni C, Mongwenyana C, Malete G, et al. Initiating antiretroviral therapy for HIV at a patient's first clinic visit: the rapit randomized controlled trial. *PLoS Med*. (2016) 13:e1002015. doi: 10.1371/journal.pmed.1002015

11. Amanyire G, Semitala FC, Namusobya J, Katuramu R, Kampiire L, Wallenta J, et al. Effects of a multicomponent intervention to streamline initiation of antiretroviral therapy in Africa: a stepped-wedge cluster-randomised trial. *Lancet HIV*. (2016) 3:e539–48. doi: 10.1016/S2352-3018(16)30090-X

12. Koenig SP, Dorvil N, Dévieux JG, Hedt-Gauthier BL, Riviere C, Faustin M, et al. Same-day HIV testing with initiation of antiretroviral therapy versus standard care for persons living with HIV: a randomized unblinded trial. *PLoS Med*. (2017) 14:e1002357. doi: 10.1371/journal.pmed.1002357

13. Labhardt ND, Ringera I, Lejone TI, Klimkait T, Muhairwe J, Amstutz A, et al. Effect of offering same-day ART vs. usual health facility referral during home-based HIV testing on linkage to care and viral suppression among adults with HIV in Lesotho: the CASCADE randomized clinical trial. In: JAMA - Journal of the American Medical Association. *Am Med Assoc*. (2018) 319:1103–12. doi: 10.1001/jama.2018.1818

14. Pilcher CD, Ospina-Norvell C, Dasgupta A, Jones D, Hartogensis W, Torres S, et al. the effect of same-day observed initiation of antiretroviral therapy on hiv viral load and treatment outcomes in a US public health setting. *J Acquir Immune Defic Syndr*. (2017) 74:44–51. doi: 10.1097/QAI.0000000000001134

15. Rodriguez AE, Wawrzyniak AJ, Tookes HE, Vidal MG, Soni M, Nwanyanwu R, et al. Implementation of an immediate hiv treatment initiation program in a Public/Academic Medical Center in the U.S. South: the Miami Test and Treat Rapid Response Program. *AIDS Behav*. (2019) 23:287–95. doi: 10.1007/s10461-019-02655-w

16. Halperin J, Butler I, Conner K, Myers L, Holm P, Bartram L, et al. *Linkage and Antiretroviral Therapy Within 72 Hours at a Federally Qualified Health Center in New Orleans*. Larchmont, NY: Mary Ann Liebert Inc. (2018) p. 39–41.

17. World Health Organization (WHO). *Policy Fact Sheet-WHO HIV Policy Adoption and Implementation Status in Countries*. (2023). Available online at: https://cdn.who.int/media/docs/default-source/hq-hiv-hepatitis-and-stis-library/who-hiv-policy-adoption-in-countries_2023.pdf?sfvrsn=e2720212_1 (accessed February 1, 2023).

18. Yildirim FS, Candevir A, Akhan S, Kaya S, Çabalak M, Ersöz G, et al. Comparison of immunological and virological recovery with rapid, early, and late start of antiretroviral treatment in naive plwh: real-world data. *Int J Gen Med*. (2023) 16:1867–77. doi: 10.2147/IJGM.S393370

19. Tumer A. Türkiye'de HIV Epidemiyolojisinin Son Durumu. In: *HIV/AIDS Kongresi 2018 – Antalya*. (2018). Available online at: https://www.klimik.org.tr/wp-content/uploads/2019/01/TÜRKIYE'DE-HIV-EPIDEMIYOLOJISININ-SON-DURUMU-Aygen-Tümer.pdf (accessed February 1, 2023).

20. Turkish Ministry of Health. *Turkey HIV/AIDS Control Program, Türkiye HIV/AIDS Kontrol Programi*. Ankara: Ministry of Health (2019). Available online at: https://hsgm.saglik.gov.tr/depo/Yayinlarimiz/Programlar/HIV_AIDS_Kontrol_Programi.pdf (accessed February 1, 2023).

21. Gokengin D, Tabak F, Korten V, Lazarus JV, Unal S. The HIV treatment cascade in Turkey. In: *HepHIV 2019 Bucharest Conference: Challenges of Timely and Integrated Testing and Care*. Bucharest: EuroTEST (2019). p. P04/09. Available online at: https://www.eurotest.org/media/usumqenv/po4_09.pdf accessed February 1, 2023).

22. Gokengin D, Cimen C, Cagatay A, Gencer S, Akalin H, Ceran N, et al. HIV cascade of care in Turkey: data from the HIV-TR cohort. In: *HIV Medicine, Vol 20, Issue S9, Special Issue: Abstracts of the 17th European AIDS Conference (EACS), Basel, Switzerland, 6–9 November 2019* (2019). doi: 10.1111/hiv.12814, PE6/22.

23. Yaylali E, Erdogan ZM, Calisir F, Gokengin D, Korten V, Tabak F, et al. Modeling the future of HIV in Turkey: cost-effectiveness analysis of improving testing and diagnosis. *PLoS ONE*. (2023) 18:e0286254. doi: 10.1371/journal.pone.0286254

24. The MathWorks Inc. *MATLAB Version: 9.13.0 (R2022b)*. Natick, Massachusetts: The MathWorks Inc. (2022). Available online at: https://www.mathworks.com (accessed February 1, 2023).

25. Turkish Ministry of Health PHI. *Guidelines on HIV/AIDS Diagnosis and Treatment, HIV/AIDS Tani Tedavi Rehberi*. Ankara: Turkish Ministry of Health PHI. (2013).

26. Karapinar A. Rapid treatment initiation, status and expectation analysis (in Turkish). In: *Ulusal HIV/AIDS Kongresi*. Antalya: KLIMIK (2021).

27. Dovel K, Phiri K, Mphande M, Mindry D, Sanudi E, Bellos M, et al. Optimizing Test and Treat in Malawi: health care worker perspectives on barriers and facilitators to ART initiation among HIV-infected clients who feel healthy. *Glob Health Action*. (2020) 13:1728830. doi: 10.1080/16549716.2020.1728830

28. Kroon EDMB, Phanuphak N, Shattock AJ, Fletcher JLK, Pinyakorn S, Chomchey N, et al. Acute HIV infection detection and immediate treatment estimated to reduce transmission by 89% among men who have sex with men in Bangkok. *J Int AIDS Soc*. (2017) 20:21708. doi: 10.7448/IAS.20.1.21708

29. Dimitrov D, Wood D, Ulrich A, Swan DA, Adamson B, Lama JR, et al. Projected effectiveness of HIV detection during early infection and rapid ART initiation among MSM and transgender women in Peru: a modeling study. *Infect Dis Model*. (2019) 4:73–82. doi: 10.1016/j.idm.2019.04.001

30. Estrada V, Górgolas M, Peña JA, Tortajada E, Castro A, Presa M, et al. Epidemiologic and economic analysis of rapid antiretroviral therapy initiation with Bictegravir/Emtricitabine/Tenofovir Alafenamide in Spain. *Pharmacoecon Open*. (2022) 6:415–24. doi: 10.1007/s41669-022-00322-w

31. Krebs E, Zang X, Enns B, Min JE, Behrends CN, Del Rio C, et al. The impact of localized implementation: determining the cost-effectiveness of HIV prevention and care interventions across six United States cities. *AIDS*. (2020) 34(3):447–58. doi: 10.1097/QAD.0000000000002455

frontiers | Frontiers in Applied Mathematics and Statistics

TYPE Conceptual Analysis
PUBLISHED 05 April 2024
DOI 10.3389/fams.2024.1360001

OPEN ACCESS

EDITED BY
Gennady Bocharov,
Marchuk Institute of Numerical Mathematics (RAS), Russia

REVIEWED BY
Teddy Lazebnik,
University College London, United Kingdom
Yafia Radouane,
Ibn Tofail University, Morocco

*CORRESPONDENCE
Chénangnon Frédéric Tovissodé
✉ chenangnon@gmail.com

RECEIVED 22 December 2023
ACCEPTED 15 March 2024
PUBLISHED 05 April 2024

CITATION
Tovissodé CF and Baumgaertner B (2024) Heterogeneous risk tolerance, in-groups, and epidemic waves.
Front. Appl. Math. Stat. 10:1360001.
doi: 10.3389/fams.2024.1360001

Heterogeneous risk tolerance, in-groups, and epidemic waves

Chénangnon Frédéric Tovissodé[1]* and Bert Baumgaertner[2]

[1]Institute for Modeling Collaboration and Innovation, University of Idaho, Moscow, ID, United States, [2]Department of Politics and Philosophy, University of Idaho, Moscow, ID, United States

There is a growing interest in the joint modeling of the dynamics of disease and health-related beliefs and attitudes, but coupling mechanisms are yet to be understood. We introduce a model where risk information, which can be delayed, comes in two flavors, including historical risk derived from perceived incidence data and predicted risk information. Our model also includes an interpretation domain where the behavioral response to risk information is subject to in-group pressure. We then simulate how the strength of behavioral reaction impacts epidemic severity as measured by epidemic peak size, number of waves, and final size. Simulated behavioral response is not effective when the level of protection that prophylactic behavior provides is as small as 50% or lower. At a higher level of 75% or more, we see the emergence of multiple epidemic waves. In addition, simulations show that different behavioral response profiles can lead to various epidemic outcomes that are non-monotonic with the strength of reaction to risk information. We also modeled heterogeneity in the response profile of a population and find they can lead to less severe epidemic outcome in terms of peak size.

KEYWORDS

standard of evidence, risk tolerance, in-group pressure, heterogeneity, behavior-disease dynamics

1 Introduction

There is a growing interest in informing public health by the joint modeling of the dynamics of disease and health-related beliefs, attitudes, and prophylactic behaviors [1–9]. A variety of factors and perspectives are likely involved in feedback loops between disease dynamics and prophylaxis. Many of these have been modeled, including, for instance, fear of infection mediated by messages from social circles or mass media [10–13], social influence [5, 14, 15], socioeconomic utility maximization [16–18], and evolutionary game theory [19–23]. Modeling such factors helps in understanding the determinants of the prophylactic responses of human populations to disease risk and is crucial for pre- or post-assessment of the effectiveness of causal interventions, including non-pharmaceutical interventions such as mask wearing, social distancing, and hand washing.

In this regard, it is well-known that risk tolerance varies in populations and largely explains the observed heterogeneity in responses to prophylactic behaviors such as mask-wearing [24–29]. To that end, Espinoza et al. [16] explored a system with adaptive behavioral responses where individuals privately adjust their contact rates by maximizing the utility of social interactions while minimizing infection risk. They found that an heterogeneous population of a risk-tolerant group with a risk-evader group can experience a more severe epidemic than an homogeneous population with no disparity in risk perception [16]. Similarly, heterogeneity in susceptibility resulting from heterogeneity in social activity can produce transient collective immunity as opposed to herd immunity, leading to multiple epidemic waves or plateau-like dynamics in

heterogeneous populations [30, 31]. Accounting for heterogeneity in risk tolerance in behavior-disease models is thus important, not just academically but also for improving the soundness of contributions to public health policy design.

In that vein, it is important to recognize that the decision to wear a mask, for instance, is not a mere combination of risk tolerance and perceived prevalence of a disease. Mask-wearing is also informed by the aggregate behaviors of others, norms that can influence how people interpret the behavior of others in relation to disease prevalence, for example, suppose you visit a foreign town to attend a conference. When you arrive, you observe that there tends to be more people wearing masks than in your hometown. There are numerous inferences you can make from this evidence. Perhaps disease prevalence is higher. Maybe the risk tolerance tends to be lower. Maybe this town has implemented a policy but there is uneven compliance. Or further still, there might be in-groups that encourage mask-wearing. Suppose you notice a correlation between mask-wearers and people with conference badges. As a conference attendee yourself, you will likely feel some pressure toward wearing a mask, and if so, this will be because of how you have come to interpret the evidence of the mask-wearers.

Stated generally, it matters whether those behaving prophylactically are part of a larger in-group, because that impacts how people (both in and out of the group) interpret what the behavior is evidence of. We refer to this aggregate of in-group and behavior as the "interpretation domain." There are few, if any, models that explore the dynamics of a system in which behavior contributes to and is a function of both perceived disease prevalence and an interpretation domain. For instance, evolutionary game theory-based models allow for individuals to engage or disengage in prophylactic behavior based on the relative importance of those already behaving prophylactically [20–22], but the decision process does not account for an interpretation domain. Interestingly, the social influence approach indirectly includes an interpretation domain: it assumes that constructive conversations between individuals with different risk tolerance levels can lead to opinion and attitude changes, and also includes an amplification mechanism by which individuals gain confidence in their health-related opinion after interaction with like-minded individuals [5]. However, social influence mechanisms cannot be directly observed [32], hence this approach lacks the perspective of directly fitting the models to observed epidemiological data and thus needs complementary methods to pair model predictions with observed data.

In this study, we propose a new behavior-disease compartmental model in which behavior contributes to and is also an explicit function of both perceived disease risk and an interpretation domain. As an example of context involving feedback loops that complicate the identification of the determinants of health-related behaviors at a population level, we consider the decision to wear a mask. For simplicity, the existing population level behavior-disease models largely consider Susceptible–Infected–Susceptible (SIS) or Susceptible–Infected–Removed (SIR) models for disease dynamic [14, 23, 33–35]. However, in a disease context with a significant proportion of asymptomatic infectives, the perceived risk of a person depends on incomplete information including the observed incidence (rather than the true incidence), and estimates of the disease prevalence publicized in media favored in the interpretation domain. Behavioral changes thus depend on the composition of the infective class, the probability to detect infectives, and testing effort, and this advises against the use of the SIR model. Furthermore, in some epidemic contexts, disease-related information, including both historical incidence and predicted trends, is discussed on a daily basis on mass media, possibly leading to risk information overload [36]. In such situations, for instance, during the COVID-19 pandemic, the decision to wear a mask may be affected by predicted trends in addition to historical risk.

Considering an hypothetical disease with COVID-19-like epidemiology, we use an extended Susceptible–Exposed–Infected–Removed (SEIR) model with differentiated infective states (asymptomatic, symptomatic, and detected infectious). Risk information from this disease dynamic comes in two flavors, namely the current disease prevalence and trends in number of new detected infectives. It flows into the behavior dynamic model with a time delay. Susceptible individuals consider this risk information along with how many individuals in their social group are already engaging to decide to (not) adopt a prophylactic behavior, which provides a certain level of protection against infection. Changes in prophylactic behaviors then flows back into the disease dynamic model through variations of the effective contact rate between infectives and the susceptible groups. The resulting model is a system of neutral delay differential equations [37], where changes in the disease state variables depend not only on the current states but also on the history of the system.

The behavior dynamic part of our model mimics a generalized logistic growth process [38] with explicit formulae (given observable disease risk information). This is an advantage over competing approaches such as the evolutionary game theory-based model [21] since, by carrying surveys before or during the early phase of an epidemic outbreak, one can obtain estimates of model parameters and derive predictions of disease-behavior co-evolution under various scenarios of interest to public health, and further iterate feedbacks between model and observable data. We do not, however, explore such an advantage here. Instead, we consider a variety of "response-profiles" inspired by work in behavioral economics and related fields [39–41]. For example, one kind of profile focuses on the current disease incidence rate. Another kind considers trends in an effort to "predict" incidence rates, thereby opening the possibility of adopting prophylactic behavior earlier when the trend moves upwards, but also giving up such behavior when the rate of change decreases. Such profiles can be further manipulated with increased (or decreased) levels of risk-aversion, as well as increased (or decreased) levels of in-group pressures (i.e., how much attention is given to pro-prophylactic behavior vs. non-prophylactic behavior in the interpretation domain).

Our purpose is to explore how differences in such response profiles affect disease dynamic. In particular, we consider epidemic severity in terms of epidemic peak time and size, time to curb the epidemic (effective reproductive number below one), final epidemic size, and the possibility of multiple epidemic waves. Under a social influence-based model, Tyson et al. [14] found that populations more responsive to risk information can experience more severe epidemics in terms of final size and undergo multiple

epidemic waves, although the epidemic peak sizes will be smaller. Here, we aim to test these results: (*i*) when the prophylactic response to risk information involves in-group pressure (which is similar to the social influence mechanism, but can account for an interpretation domain) under various response-profiles (i.e., populations responding to qualitatively different risk information); and (*ii*) when the population is heterogeneous in terms of response-profile.

The remainder of the study is organized as follows. Section 2 describes the components of the new behavior-disease compartmental model in terms of equations, motivations, and interpretations, and derives summary measures considered to assess and compare epidemic severity and overall disease dynamic. Section 3 explores various aspects of epidemics that can be generated by the proposed differential system, considering populations homogeneous or heterogeneous with respect to in-group behavior and response to historical or predicted risk information. Section 4 then discusses our findings and the limitations of the proposed model, and provides some concluding remarks.

2 Methods

This section introduces our general theoretical framework based on an SEIR model. It then describes risk information components, as well as how the proportion of prophylactic individuals in a sub-population and the effective contact rate depend on this information and in-group pressure. Finally, the section presents the behavior-disease dynamics model and related summary measures to quantify and compare epidemic severity.

2.1 Theoretical framework

It is well-known that prophylactic behavior affects disease transmissions by reducing rates of effective contacts between infectious and susceptible individuals in the target population (direct physical or indirect through shared media in which pathogens can survive) [23, 42]. In our modeling framework, change in disease dynamic affects back prophylactic behavior through observable disease prevalence (which depend, for instance, on the existence and effectiveness of a disease surveillance mechanism and testing capacity to detect infectious individuals), but disease related information is processed by a system of health beliefs and related attitudes. In other words, the feedback from disease dynamic to prophylactic behavior is mediated by health beliefs and normative attitudes in the individual's interpretation domain which determines risk tolerance. However, engagement in prophylactic behavior is also determined by how many individuals are already behaving prophylactically, and a social group can pay more attention to and mimick those behaving prophylactically than those behaving non-prophylactically, or vice-versa.

To describe disease dynamics, we consider an extended SEIR compartmental model framework [43–45] with differentiated infective states. The population size N is given at time t by

$$N(t) = S(t) + E(t) + I_a(t) + I_s(t) + I_d(t) + R(t) \tag{1a}$$

where S, E, I_a, I_s, I_d, and R are susceptible, exposed, asymptomatic infectious, symptomatic infectious, detected (tested positive and reported), and removed individuals, respectively. The disease-dependent compartments E, I_a, I_s, I_d, and R are considered homogeneous whereas the class of susceptible individuals (S) is further differentiated into two groups based on risk tolerance:

$$S(t) = S_{-1}(t) + S_1(t) \tag{1b}$$

where S_i denotes susceptibles with standard of risk $i \in \mathcal{A}$, $\mathcal{A} = \{-1, 1\}$. For instance, in a population which only responds to current risk, S_{-1} may represent individuals with low standard of evidence (the most responsive to disease prevalence), while S_1 corresponds to individuals with high standard of evidence (least responsive to disease prevalence). However, difference in standard of risk may be qualitative rather than quantitative: S_{-1} may represent individuals responsive to only historical risk while S_1 corresponds to individuals sensible to both historical and predicted risk.

2.2 Disease risk information aggregate

The primary source of disease-related information in an epidemic context is the timely number of new positive cases, denoted C. The number of individuals in the class I_d of detected infectious individuals (see Equation 1a) is related to C by

$$\dot{I}_d(t) = C(t) - \rho_d I_d(t) \tag{2}$$

where the dot notation indicates the first derivative with respect to time (i.e., $\dot{I}_d(t) = dI_d(t)/dt$), ρ_d is the removal rate of individuals from I_d, with non-negative initial condition $I_d(0) = I_{d0}$. Solving the differential Equation (2) for I_d gives

$$I_d(t) = \exp(-\rho_d t)\left[I_{d0} + \int_0^t C(u)\exp(\rho_d u)\,du\right]. \tag{3}$$

We consider the perceived disease prevalence, denoted P, and the relative rate of change of new positive cases, denoted Q, as the basic pieces of information on which susceptible individuals will decide to be prophylactic. From Equation (3), the perceived disease prevalence is given at time t by

$$P(t) = \begin{cases} \frac{I_d(t-\tau)}{N(t-\tau)} & \text{if} \quad t \geq \tau, \\ 0 & \text{otherwise} \end{cases} \tag{4a}$$

where the constant $\tau > 0$ represents a time delay in the acquisition of information on detected and reported infectious. The relative rate of change Q is the quotient of the rate of change (increase or decrease) of the number of new detected cases C to the number of new detected cases, delayed by τ time units:

$$Q(t) = \begin{cases} \frac{\dot{C}(t-\tau)}{C(t-\tau)} & \text{if} \quad C(t-\tau) > 0, \\ 0 & \text{otherwise} \end{cases}. \tag{4b}$$

Note that $Q(t) = 1$ means that the timely number of new positive cases is doubling per unit time, whereas $Q(t) = -1/2$

means that the timely number of new positive cases is halving per unit time.

We assume that based on the information pieces P and Q, each group of susceptible S_i makes up an information aggregate, denoted η_i, and which satisfies $\eta_i = 0$ before disease outbreak ($t < \tau$, $P = Q = 0$). This information aggregate is defined as a quadratic function of P and Q:

$$\eta_i = a_i P + b_i P^2 + c_i PQ + d_i Q^2 + e_i Q \tag{4c}$$

where a_i, b_i, c_i, d_i, and e_i are non-negative real coefficients expressing the weights of linear, quadratic, and interaction components of the prevalence P and the rate of change Q. It is worthwhile noticing that Equation (4c) is intended as an approximate summary of the available information that drives the decision to wear a mask. The quadratic form is indeed used as an approximation to the actual, likely non-linear mechanism by which the susceptible group S_i processes disease-related information. The non-negative signs imposed on the coefficients in η_i (a_i, b_i, c_i, d_i and e_i) ensure that when the timely number of new positive cases is non-decreasing ($Q \geq 0$), η_i is not only non-negative for any perceived disease prevalence P but also non-decreasing in P.

Equation (4c) describes how disease risk information can be differently interpreted by different tolerance groups within the same population. For instance, a group of individuals may focus on the disease incidence rate while ignoring predictions of future disease risk. For such individuals, one or both parameters a_i and b_i in the information aggregate (Equation 4c) will be positive but parameters c_i, d_i, and e_i will be zero. Another group may pay attention to trend in disease incidence, opening the possibility of adopting prophylactic behavior earlier when the trend moves upwards, and also giving up such behavior when incidence decreases. Such a group will have at least one of the parameters c_i, d_i, and e_i being greater than zero. Between these two extreme situations, there are many possibilities with various combinations of small vs. large values of parameters a_i and b_i to reflect how much attention is paid to current disease incidence by a tolerance group, and parameters c_i, d_i, and e_i related to the relative importance of trends to the group.

2.3 Prophylactic behavior dynamic

For a susceptible class with standard of evidence i, we consider for simplicity two levels of prophylactic behavior: high prophylactic behavior (i.e., individuals properly wearing mask where and when this is recommended) vs. low prophylactic behavior. The overall prophylactic behavior in the class S_i can thus be summarized by the prophylactic proportion $m_i \in [0, 1]$, i.e., the proportion of mask-wearers. We assume that change in the prophylactic proportion m_i is proportional to change in the information aggregate η_i and to the proportion of S_i individuals already wearing masks:

$$\frac{\partial m_i}{\partial t} = \left[m_i \frac{1 - m_i^{\alpha_i}}{\alpha_i} \right] \frac{\partial \eta_i}{\partial t} \tag{5}$$

where α_i is a positive real which determines the nature and strength of in-group behavior, and we have taken the proportionality constant to be one to ensure that the coefficients of the linear components of η_i (a_i and e_i) in the model are identifiable from observed data. When $\alpha_i = 1$, $\partial m_i / \partial t$ is proportional to both m_i and $1 - m_i$, and S_i individuals give the same relative importance to both mask-wearers and non-mask-wearers: for a unit increase in the information aggregate, the highest increase in m_i occurs when $m_i = 0.5$, i.e., when half of the S_i individuals have engaged in prophylactic behavior. For general α_i values, the highest increase in m_i for a unit increase in η_i occurs when $m_i = (1 + \alpha_i)^{-1/\alpha_i}$. It appears that for $\alpha_i \in (0, 1)$, the highest increase in m_i occurs when $m_i < 0.5$ (weak influence of in-group non-prophylactic behavior), and for $\alpha_i > 1$, the highest increase in m_i occurs when $m_i > 0.5$ (strong influence of in-group non-prophylactic behavior). Hence, the larger α_i, the larger impact in-group non-prophylactic behavior will have, slowing down engagement in prophylactic behavior.

Since m_i depends on time only through the information aggregate η_i, we can interpret Equation (5) as a differentiation in chain and write $\partial m_i / \partial \eta_i = m_i \left(1 - m_i^{\alpha_i}\right) / \alpha_i$, which appears to be Richards growth equation [38] with intrinsic growth rate equal to one. Solving for m_i yields the generalized logistic curve:

$$m_i = \left[1 + \exp\left\{\delta_i - \eta_i\right\}\right]^{-1/\alpha_i} \tag{6a}$$

where δ_i is a constant related to the proportion $m_{i0} \in (0, 1)$ of S_i susceptibles who would hold a high prophylactic attitude even in the absence of any evidence of disease (i.e., when $\eta_i = 0$, which happens for $t \leq \tau$) by

$$\delta_i = \log\left(m_{i0}^{-\alpha_i} - 1\right). \tag{6b}$$

Figure 1 shows the prophylactic proportion m_i as a function of time for a few selected parameter values, with a perceived disease prevalence P varying from zero to 33%. It appears that the coefficients b_i, c_i, d_i, and e_i in Equation (4c) have distinct effects on m_i and capture different reactions of susceptibles to disease risk. For instance, b_i and d_i can be described as response acceleration parameters for high and low prevalence values, respectively. Indeed, a susceptible group more responsive to large prevalence values than to low prevalence values corresponds to $b_i > 0$ (Figure 1A), whereas $d_i > 0$ corresponds to groups more responsive to low prevalence values than to high prevalence values (Figure 1C). Similarly, $c_i > 0$ corresponds to groups where engagement in prophylactic behavior is stronger (Figure 1B), and $e_i > 0$ to groups where engagement in prophylactic behavior is earlier (Figure 1D), but in both cases, disengagement also happens early, once the number of new detected case starts dropping ($Q < 0$).

The in-group behavior parameter α_i allows additional flexibility in m_i by controlling how the aggregated information is jointly used with how many individuals are already behaving prophylactically in a susceptible group. Whereas b_i and d_i can be viewed as parameters inducing behavioral response acceleration with respect to change in risk information (P and Q, respectively), α_i is an intrinsic acceleration/deceleration parameter, i.e., the acceleration of m_i happens not because of change in risk information, but rather in response to the current (low or high) value of m_i itself. Figure 2 shows m_i curves for a few selected parameter values. It can be observed that *ceteris paribus*, a larger α_i value, implies an overall

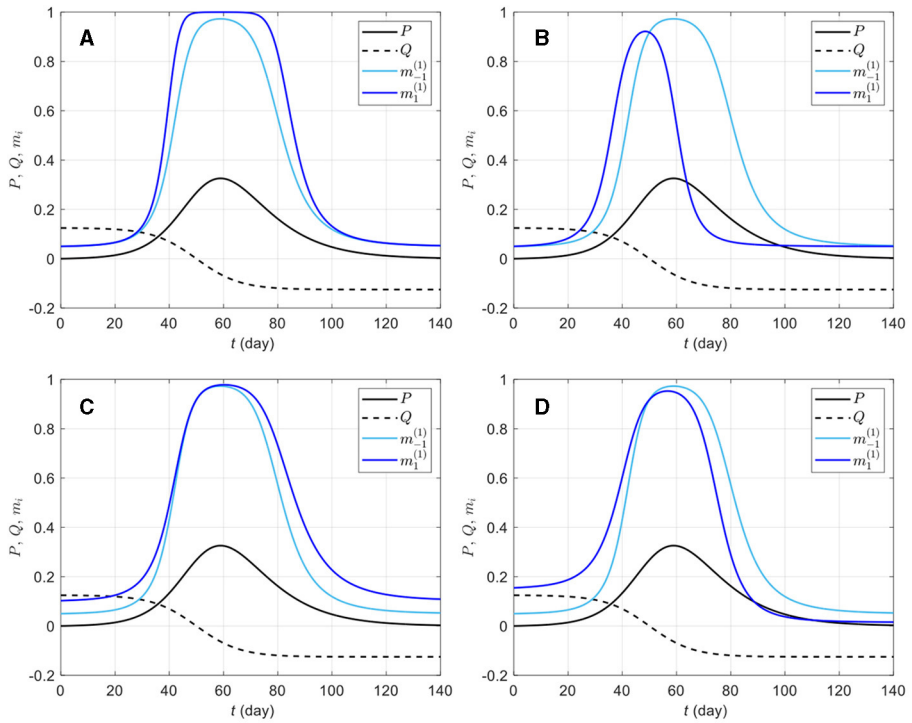

FIGURE 1
Effects of different information weights on prophylactic proportion $m_i^{(\alpha_i)}$ ($i = -1, 1$) for various parameter values. The light blue curve repeated on all plots corresponds to a response to prevalence only, i.e., only the coefficient $a_i = 20$ is non-zero in Equation (4c); the dark blue curves on plots **(A–D)** correspond to combinations of $a_i = 20$ with $b_i = 50$ **(A)**, $c_i = 150$ **(B)**, $d_i = 50$ **(C)**, and $e_i = 10$ **(D)**. The prevalence P (solid black) and the rate of change Q (dashed black) are respectively given by Equations (4a, 4b), I_d is given by Equation (3), $\rho_d = 1/14$, and the daily number of new detected cases is given by the logistic curve $C(t) = N_0 e^{\nu_t}/(1 + e^{\nu_t})^2$ with $N_0 = 100,000$, $\nu_t = (t - 50)/8$. The proportion of prophylactic individuals in disease-free conditions is $m_{i0} = 0.05$ and the in-group behavior parameter is $\alpha_i = 1$.

weaker prophylactic behavioral response. Indeed, the derivative of m_i with respect to α_i, given by

$$\frac{\partial m_i}{\partial \alpha_i} = -\frac{m_i}{\alpha_i}\left[\log\left(\frac{m_i}{m_{i0}}\right) + m_i^{\alpha_i}\left(1 - e^{-\eta_i}\right)\log\left(m_{i0}\right)\right], \qquad (7)$$

is negative (m_i decreases with α_i) for $\eta_i > 0$ (i.e., when prophylactic proportion is above the disease-free level m_{i0}). However, if information aggregate reaches zero ($\eta_i = 0$), $\partial m_i/\partial \alpha_i$ (Equation 7) vanishes, and if η_i becomes negative, $\partial m_i/\partial \alpha_i > 0$. This happens around $t = 96$ days in Figure 2D, where $e_i > 0$ (i.e., in a population where Q is given much attention) allows $\eta_i < 0$ after Q becomes negative, and as the epidemic dies out ($P \to 0$), Q dominates the information aggregate: the ordering of prophylactic proportions switches such that a lower α_i value corresponds to a weaker prophylactic behavioral response for $\eta_i < 0$. This can be interpreted as a return of the early engagement of a group with $e_i > 0$ (Figure 2D, $m_1^{(0.1)}$). In this respect, α_i appears as a parameter which exaggerates behavioral response regardless of the sign of information aggregate. But as the disease-free prophylactic proportion m_{i0} is typically low ($m_{i0} = 0.05$ in Figure 2), there will generally be less room for this exaggeration when the epidemic dies out ($\eta_i < 0$) than at disease outbreak ($\eta_i > 0$).

2.4 Contact and transmission rates

We assume for simplicity that the detected infectious individuals are isolated (e.g., hospital and home) and do not mix actively with other classes. Using the "quarantine-adjusted" incidence mechanism [46] yields the force of infection λ_i (the average number of adequate contacts of one S_i susceptible person with infectives per unit time):

$$\lambda_i(t) = \frac{\beta_{ia}(t)I_a(t) + \beta_{is}(t)I_s(t)}{N(t) - I_d(t)} \qquad (8a)$$

where β_{ia} and β_{is} are rates of effective contacts with asymptomatic and symptomatic infectious individuals, respectively. The effective contact rate β_{ij} depends on a baseline contact rate β_0 (possibly restricted by public health policies), the prophylactic attitude of S_i susceptibles, the average efficiency $\kappa \in (0, 1)$ of prophylactic behaviors in reducing transmissions, and the probability $\phi_j \in (0, 1)$ of disease transmission on contact with I_j infections:

$$\beta_{ij}(t) = \beta_0\left[1 - \kappa m_i(t)\right]\phi_j. \qquad (8b)$$

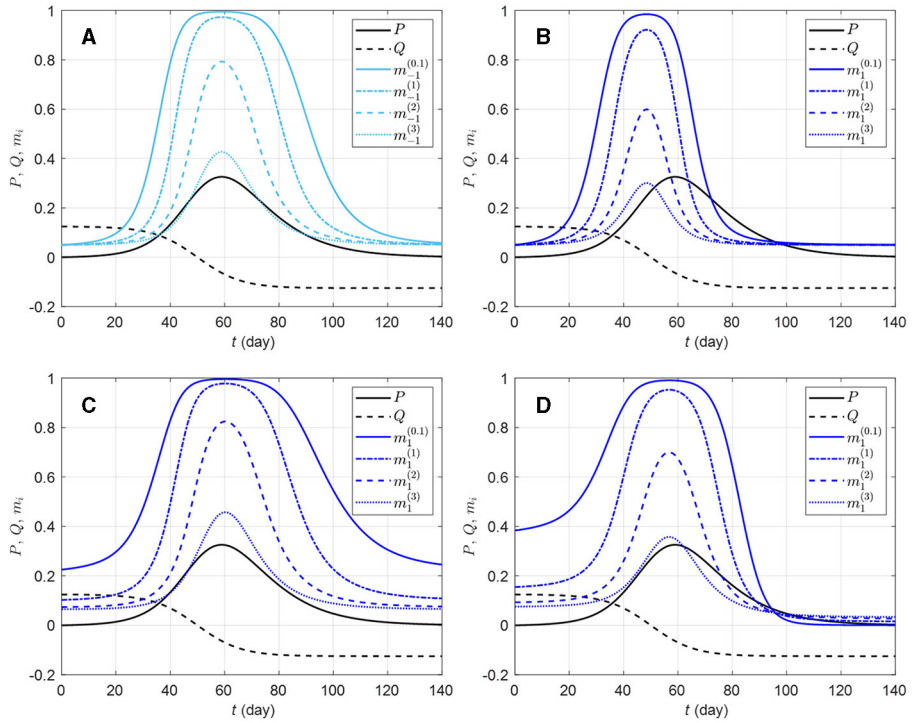

FIGURE 2
Effects of different in-group behavioral response on prophylactic proportion $m_i^{(\alpha_i)}$ ($i = -1, 1$) for various parameter values. The solid light blue curve on graphic **(A)** corresponds to a response to prevalence only, i.e., only the coefficient $a_i = 20$ is non-zero in Equation (4c); the solid dark blue curves correspond to combinations of $a_i = 20$ with $c_i = 150$ **(B)**, $d_i = 50$ **(C)**, and $e_i = 10$ **(D)**. All the solid blue curves have in-group behavior parameter $\alpha_i = 1/10$ (strong effect of in-group prophylactic behavior). On each plot, the dashed-dotted blue curve corresponds to $\alpha_i = 1$ (neutral in-group prophylactic behavior), the dashed blue curve to $\alpha_i = 2$ (strong effect of in-group non-prophylactic behavior), and the dotted blue curve to $\alpha_i = 3$ (stronger effect of in-group non-prophylactic behavior). The prevalence P (solid black) and the rate of change Q (dashed black) are respectively given by Equations (4a, 4b), I_d is given by Equation (3), $\rho_d = 1/14$, and the daily number of new detected cases is given by the logistic curve $C(t) = N_0 e^{\nu_t} / (1 + e^{\nu_t})^2$ with $N_0 = 100,000$, $\nu_t = (t - 50)/8$. The proportion of prophylactic individuals in disease-free conditions is $m_{i0} = 0.05$.

2.5 The behavior-disease dynamics model

For a target population, we consider a period of study short enough for both disease-related death and natural demographic rates (births, net immigration, and deaths) to be negligible relative to the total population size N (assumed large but finite). As a result, the population size in Equation (1a) remains constant and equal to an initial size $N_0 = N(0)$. Joining the behavior and disease dynamics mechanisms described in Sections 2.3, 2.4 gives the Behavior-SEIR model depicted on the flow diagram in Figure 3 with parameters described in Table 1. After sufficient contacts with infectious individual(s), a susceptible individual enters an incubation period (class E) lasting $1/\theta$ time units on average, in a non-infectious state, and without any disease symptom. Some of these exposed individuals are early detected with probability π thanks to contact tracing or systematic tests on target groups, and enter the class I_d. In the non-early detected exposed group, 100σ% develop symptoms and enter the class I_s, and $100(1-\sigma)$% remain asymptomatic and enter the class I_a. Individuals in the class I_s are then identified at a high rate γ_s. Thanks to contact tracing or systematic tests on target groups again, some asymptomatic individuals in the class I_a are identified at a lower rate γ_a. All exposed individuals eventually recover from the disease, entering the class R (removals).

The Behavior-SEIR dynamics model is described at time t by the following system of non-linear differential equations:

$$\dot{S}_{-1}(t) = -\lambda_{-1}(t)S_{-1}(t), \tag{9a}$$
$$\dot{S}_1(t) = -\lambda_1(t)S_1(t), \tag{9b}$$
$$\dot{E}(t) = \lambda_{-1}(t)S_{-1}(t) + \lambda_1(t)S_1(t) - \theta E(t), \tag{9c}$$
$$\dot{I}_a(t) = (1-\sigma)(1-\pi)\theta E(t) - (\gamma_a + \rho_a)I_a(t), \tag{9d}$$
$$\dot{I}_s(t) = \sigma(1-\pi)\theta E(t) - (\gamma_s + \rho_s)I_s(t), \tag{9e}$$
$$\dot{I}_d(t) = \pi\theta E(t) + \gamma_a I_a(t) + \gamma_s I_s(t) - \rho_d I_d(t), \tag{9f}$$
$$\dot{R}(t) = \rho_a I_a(t) + \rho_s I_s(t) + \rho_d I_d(t), \tag{9g}$$

with the non-negative initial conditions $S_i(0) = S_{i0}$, $E(0) = E_0$, $I_a(0) = I_{a0}$, $I_s(0) = I_{s0}$, $I_d(0) = I_{d0}$, and $R(0) = R_0$ such that $N_0 = S_{-10} + S_{10} + E_0 + I_{a0} + I_{s0} + I_{d0} + R_0$. The proposed model is a system of neutral delay differential equations [37] where the force of infection λ_i (Equation 8a) depends through m_i (Equation 8b) on the information available at time t, precisely P (dependence on state variables) and Q (dependence on first derivatives of state variables), which are delayed by τ time units.

The parameter τ accounts for two potential sources of information delay: (*i*) reporting delay, i.e., the delay between the moment exposed or infectious individuals are detected and isolated from the mixing population, and the moment the number of

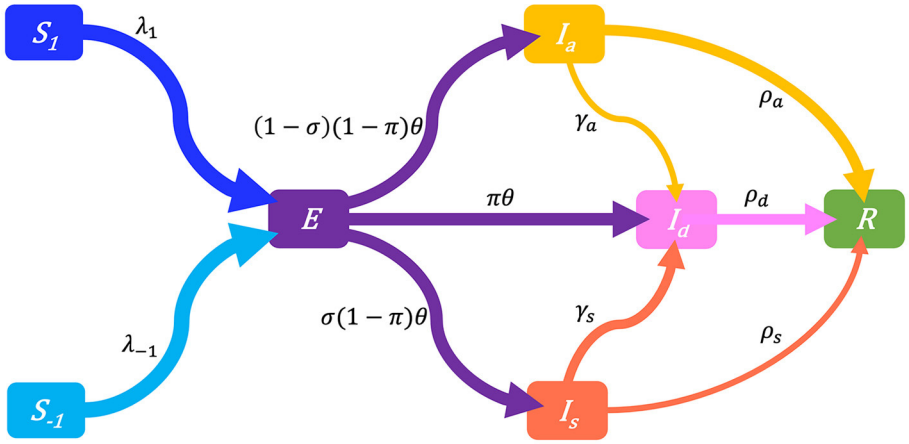

FIGURE 3
Flow-chart of a Behavior-SEIR dynamics model showing the flow of humans between different compartments. The susceptible population is distinguished in individuals with low standard of evidence (S_{-1}) and individuals with high standard of evidence (S_1). The classes E, I_a, I_s, I_d, and R denote respectively the exposed, the asymptomatic infectious, the symptomatic infectious, the detected infectious, and the removed (recoveries) populations. Recruitment (births and net immigration) and deaths (natural and disease-related) are assumed negligible relative to the population size. The parameters of the model are described in Table 1.

detected cases is publicized and can be considered by susceptible individuals to assess their risk, and (*ii*) reaction time, i.e., the delay between the moment the number of detected cases is made public and the moment susceptible individuals actually consider the information to adjust their adherence to preventive prophylactic behavior. We focus on reporting delay which can be included in public health policy design [47]. Indeed, official statistics are often reported with a time delay that may arise from a desire for thorough verification [48]. However, reporting delays can produce the dangerous illusion of an improving epidemic situation since the most recent days have the least cases accounted [48]. Including the time delay parameter τ in model (Equation 9) allows to investigate the extent to which reporting delay can affect the evolution of an epidemic through the behavioral response to delayed information. For our simulation experiments (see Section 2.8), we consider information delays ranging from 1 day to 1 week ($\tau = 1, 3, 5, 7$ days).

2.6 The effective reproductive number

We compute the effective reproductive number based on the Behavior-SEIR model (Equation 9) using the next-generation matrix approach [49]. Starting from any disease-free state $\mathbf{X}^c = (S_{-10}, S_{10}, 0, 0, 0, 0, R_0)^\top$, the basic reproductive number $\mathcal{R}(0)$ for system Equation (9) is given by

$$\mathcal{R}(0) = \mathcal{R}_o \sum_{i\in\mathcal{A}} \frac{S_{i0}}{N_0}\,(1-\kappa m_{i0})\,, \tag{10a}$$

$$\mathcal{R}_o = \beta_0(1-\pi)\left(\phi_a \frac{1-\sigma}{\gamma_a+\rho_a} + \phi_s \frac{\sigma}{\gamma_s+\rho_s}\right) \tag{10b}$$

where $N_0 = S_{-10} + S_{10} + R_0 > 0$ and $\mathcal{R}_o$ (Equation 10b) is the reproductive number when there is no differential evidentiary group, $R_0 = 0$, and all prophylactic proportions are zero ($m_{i0} = 0$). As expected, the basic reproductive number $\mathcal{R}(0)$ (Equation 10a) depends on both the distribution of the population between evidentiary groups, and the prophylactic proportion of each group when no disease evidence is available (both perceived disease prevalence P and rate of change Q are zero). Along an epidemic, the effective reproductive number is then given by

$$\mathcal{R}(t) = \sum_{i\in\mathcal{A}} \frac{S_i(t)}{S(t)}\mathcal{R}_i(t) \quad \text{with} \tag{10c}$$

$$\mathcal{R}_i(t) = \mathcal{R}_o \frac{S(t)}{N_0 - I_d(t)}\left[1-\kappa m_i(t)\right] \tag{10d}$$

where $\mathcal{R}_i(t)$ (Equation 10d) is the effective reproductive number for S_i susceptibles such that $\mathcal{R}(t)$ is the average of $\mathcal{R}_i(t)$ over all groups of susceptibles.

We would normally conduct here a stability analysis of the model, including the bifurcation diagram for interesting model parameters such as the time delay τ and the level of protection κ. However, these investigations are out of the scope of this conceptual analysis which focuses on the behavioral response to an outbreak and its impact on the dynamic of an epidemic. Such investigations can however be carried out after extending the model to represent more realistic scenarios, including, for instance, vital rates (births and immigration, natural deaths, and disease-related death), flow between susceptible compartments (S_{-1} and S_1), and immunity lost (flow from R back into S_{-1} and S_1).

2.7 Epidemic severity measures

To allow for comparison between various epidemic scenarios, we define some measures to quantify epidemic severity and overall disease dynamic.

(a) The number n_w of epidemic waves.

When the maximum number of detected cases (C_t) over the study period is less than one plus the initial number of

TABLE 1 Description and values of parameters in the behavior-disease model.

Parameter	Description	Values
τ	Time delay (days) of risk information	1, **3**, 5, 7
$a_i^{\dagger}$	Main response of S_i (susceptibles) to prevalence (P)	20
b_i	Non-linear response of S_i to P (i.e., P^2)	**0**, 50
c_i	Responsiveness of S_i to the interaction $P \times Q$	**0**, 150
d_i	Non-linear response of S_i to Q (i.e., Q^2)	**0**, 50
e_i	Main response of S_i to rate of change (Q)	0, **10**
α_i	Strength of in-group non-prophylactic behavior	0.1, **1**, 2, 3
m_{i0}	Prophylactic proportion in the absence of risk evidence	0.05
κ	Average efficiency of prophylactic behavior	$\frac{1}{2}$, $\frac{3}{5}$, $\frac{3}{4}$, $\frac{9}{10}$, $\mathbf{\frac{19}{20}}$, 1
β_0	Baseline transmission rate	1/2, **1**, 2, 3
ϕ_j^*	Probability of disease transmission by I_j infectious	1
$1/\theta$	Duration of incubation (latent) period (days)	4
π	Early detection probability for exposed individuals	$\frac{1}{4}$, $\frac{1}{2}$, $\frac{2}{3}$, $\frac{3}{4}$
σ	Proportion of symptomatic infectious	1/2
γ_j	Detection rate of I_j infectives	$\frac{2}{14\times5}$, $\frac{4}{14\times5}$
ρ_j	Removal rate of I_j infectious	$\frac{3}{14\times5}$, $\frac{1}{14\times5}$, $\frac{1}{70}$
S_{i0}	Initial number of S_i susceptibles	49, 998
E_0, I_{j0}	Initial number of exposed and infectious	2, 1, 1, 0
R_0	Initial number of recovered individuals	0
N_0	Total population size	100, 000

All parameters take non-negative values.
$^{\dagger}i$ = standard of evidence level defined in Equation (1b).
$^{*}j = a$ (asymptomatic), s (symptomatic), or d (detected) infectives.
For parameters with multiple values (τ, a_i, c_i, d_i, e_i, α_i, κ, β_0, π), the default value is bolded.

infected individuals in the population at time $t = 0$, we consider that the disease dies out and there is no epidemic wave ($n_w = 0$). Otherwise, we have $n_w \geq 1$. For $n_w \geq 1$, to cut up the epidemic period based on observable epidemiological data (C_t) and identify epidemic waves, we consider a wave detection algorithm based on five properties imposed upon the height of waves, and the troughs between waves: (*i*) the number of detected cases at the trough between two successive waves is <500, (*ii*) the duration between a trough and the preceding peak is 5 days or more, (*iii*) an epidemic wave lasts at least 1 week, (*iv*) the prominence of the peak of a wave is 10 or more detected cases (per day) above the surrounding valley (specifically the highest of the left and right troughs), and (*v*) the prominence of the peak represents at least 50% of the peak height. The algorithm is a modification [addition of properties (*i*) and (*ii*)] of Harvey et al. [50]'s epidemic wave identification algorithm. The wave detection algorithm is implemented in R freeware [51] (R package *wavefinder* with source available on the Git repository SE-SEIR).

(b) The overall peak height H_p (number of detected cases) and peak time T_p (days).

(c) The time T_{c1} to curb the first outbreak.

The duration from disease outbreak ($\mathcal{R}(0) > 1$) to the first time when the effective reproductive number $\mathcal{R}$ (Equation 10c) falls to one:

$$T_{c1} = \arg\min_t \left\{\mathcal{R}(t) = 1\right\}. \tag{11}$$

(d) The final epidemic size F_T.

For a given time horizon T, the final epidemic size is given by $F_T = 1 - S_T/N_0$, where S_T is the total number of susceptible individuals at time $t = T$ and N_0 is the total (initial) population size.

2.8 Simulation experiment

We carried out a simulation experiment to explore combinations of model parameters related to disease transmission (β_0), early detection of exposed individuals (π), delayed acquisition or reaction to risk information (τ), behavioral reaction (a_i, b_i, c_i, d_i, and e_i), in-group behavior (α_i), and efficiency of prophylactic behaviors (κ) that lead to patterns where the course of an epidemic depends more or less on differences between risk perception and related feedback loops.

2.8.1 Simulation design

We first considered a variety of basic behavioral response profiles including a reference population (*0*) responsive to prevalence only, and the four profiles of populations in Figures 1A–D: profile *0* corresponds to $a_i = 20$ ($b_i = c_i = d_i = e_i = 0$), profile *A* corresponds to $a_i = 20$ and $b_i = 50$ ($c_i = d_i = e_i = 0$), profile *B* to $a_i = 20$ and $c_i = 50$ ($b_i = d_i = e_i = 0$), profile *C* to $a_i = 20$ and $d_i = 50$ ($b_i = c_i = e_i = 0$), and profile *D* to $a_i = 20$ and $e_i = 10$ ($b_i = c_i = d_i = 0$). These five profiles are homogeneous with respect to behavioral reaction to risk information. We then included heterogeneous populations obtained as combinations of the reference profile (half of the population) with one of profiles *A*–*D*. For each profile, we varied other model parameters including β_0, π, τ, κ, and α_i (see parameter values in Table 1). Since α_i is group specific, we have the between-group difference $\Delta\alpha = \alpha_{-1} - \alpha_1$, which measures heterogeneity in in-group pressure.

For each simulation setting, we solved system (Equation 9) using the function *dede* from the R package *deSolve* [52] (code in the R package *BSEIR* with source available on the Git repository SE-SEIR), and recorded the number of epidemic waves up to $T = 1,000$ days after the first outbreak (n_w), the overall peak time (T_p) and height (H_p), the time to curb the first epidemic wave (T_{c1}), and the final epidemic size ($F_{1,000}$).

2.8.2 Statistical analyses

To summarize simulation results, we computed descriptive statistics for epidemic severity measures in R, and fitted generalized linear models [53] to the number of secondary epidemic waves (Poisson regression) and the epidemic peak size (gamma regression) as functions of population response profiles and the varied model (Equation 9) parameters (see descriptive statistics in Supplementary Table S1). We also fitted a one-inflated beta regression model [54] to the final epidemic size ($F_{1,000}$) using the R package *gamlss* [55]. For each model, we checked goodness-of-fit using a χ^2-test on residual deviance, and evaluated the explanatory power of the model using a deviance based pseudo-R^2 [56]. Supplementary Table S2 provides descriptive statistics for the different epidemic severity measures over all simulation scenarios.

3 Results

3.1 Epidemic severity across types of responses

Our simulation results indicate important variations in epidemic severity measures between levels of in-group pressure. Indeed, an increase in in-group pressure for pro-prophylactic behavior (decreasing α_i) increases the average number of secondary waves, but decreases the epidemic peak size and final size (Table 2).

Table 3 shows summaries of epidemic severity measures comparing populations with the reference response profile *0* and profiles *A*–*B*, averaged over all levels of in-group pressure ($\alpha_i \in \{0.1, 1, 2, 3\}$). All investigated parameter settings result into an epidemic, the disease quickly dying out in only 1% of settings with the homogeneous profile *B* (i.e., populations with a reaction to rate of change *Q* proportional to perceived prevalence *P*). When there is an epidemic, one secondary epidemic wave occurs in 9% of settings with the reference profile *0*. Secondary epidemic waves are the most likely (19%) under profile *A* [homogeneous populations with a strong (quadratic) reaction to *P* only], and the least likely (2%) under profile *B*. The epidemic peaks after about 64 days on average in populations responsive to *P* only (profile *0*) to ∼3,209 new reported cases. Slightly lower average peak time and size result from a stronger reaction to *P* (3,050 case after 62 days for profile *A*) or an additional response to *Q* (3,126 cases after 60 days for profile *D*). Ignoring the sign of *Q* increases the average peak time to about 72 days (profile *C*) while decreasing the peak size to ∼32,748 cases, with intermediate result for profile B (2,840 cases after 66 days). The final epidemic size is typically large, 91% on average, under profile *0* (and *C*). A stronger reaction to *P* (profile *A*) slightly reduces the final size to 90% whereas an additional response to *Q* (profiles *B* and *D*) increases the final size to 94%. In summary, a stronger reaction to *P* essentially leads to more secondary waves whereas an additional response to *Q* hastens the epidemic peak and increases the final size, with lower peak sizes in both scenarios. A response to *Q* proportional to *P* also increases average final size, but delays the peak (with a lower size).

Heterogeneity in the behavioral reaction to risk information generally leads to intermediate results half way between the two combined homogeneous profiles (Table 3). Exceptions include the time to curb the first epidemic wave (larger than expected) under profiles $0 \times C$ and $0 \times D$, and the peak time (larger than expected) and size under profile $0 \times D$ (smaller than expected). Figure 4 shows the timely number of new positive cases under profiles *0*, *D*, and $0 \times D$, exhibiting an interactive effect between in-group pressure and heterogeneity. Indeed, it appears that in an heterogeneous pro-prophylactic behavior population (Figure 4, $\alpha = 0.1$) where half of individuals are responsive to *P* and the other half is additionally responsive to *Q*, the epidemic peak size (1,380 new detected cases) is smaller than in homogeneous populations with profile *0* (1,819 new detected cases) or *D* (1,653 new detected cases).

When we restrict attention to populations where in-group pressure is neutral ($\alpha_i = 1$), we observe that a stronger reaction to *P* leads to one secondary epidemic wave in 24% of settings, as opposed to 19% across α_i values (Supplementary Table S3). Similarly, an additional response to *Q* increases the peak time and does not increase the final epidemic size (90% under profile *D*), unless the reaction to *Q* is proportional to *P* (93% under profile *B*). These discrepancies point out to important variations between levels of in-group pressure.

The results of fitted models shown in Table 4 corroborate our observations for the number of secondary waves (model coefficient estimates < 0 for α_{-1} and $\Delta\alpha$), the peak size, and the final epidemic size (coefficient estimates > 0 for α_{-1} and $\Delta\alpha$). It also appears that among the profiles *A*–*D*, only profile *B* (population with a response to the rate of change proportional to prevalence) leads to a decrease in the number of secondary epidemic waves and an increase in the final epidemic size, as compared to the reference profile *0*. In addition, the model results indicate that for an heterogeneous population, the expected number of secondary epidemic waves or the expected final epidemic size is intermediate between the outcomes for the two corresponding homogeneous populations, except when half the population has profile *D*. For the latter, after controlling for disease dynamic and in-group pressure parameters, the expected number of secondary epidemic waves is 15.9% (100×0.159) higher for the homogeneous profile *D*, but 31.8% higher for the heterogeneous profile $0 \times D$, as compared to an homogeneous profile *0*.

The fitted models also indicate that a 1-day increase in risk information delay (τ) leads to a 2.6% average increase (100×0.026) in the average odd ratio for a random individual to get infected over the course of the epidemic, a 3.3% increase in the overall peak size, and a 6.5% decrease in the number of secondary waves (Table 4). A discussion of the biological interpretation of these statistics is provided in Section 4.1. As for other varied model parameters (β_0, π, and κ), apart from in-group pressure, the variations of the number of secondary waves are mostly driven by the level of protection by prophylactic behavior, to the extent that a 1%-point increase in κ results into a 15.5% increase in the number of secondary waves. In other words, if 80% level of protection yields one epidemic wave on average, then increasing the level of protection by 10% (i.e., from 80 to 90%) results in an expected 2.55 waves ($1 + 1 \times 0.155 \times 10$). Both the peak size and the final epidemic size are mainly determined by the baseline transmission rate (β_0) and the probability of early detection of exposed individuals (π).

TABLE 2 Summary of epidemic severity measures comparing populations with various levels of in-group pressure ($\alpha_i \in \{0.1, 1, 2, 3\}$).

Statistics†	Median	Mean	SD	Median	Mean	SD
	$\alpha_{-1} = \alpha_1 = 0.1$			$\alpha_{-1} = 0.1, \alpha_1 = 1$		
Epidemic?	1.00	1.00	0.06	1.00	1.00	0.05
Nb2. waves	0.00	**0.26**	0.45	0.00	0.20	0.41
Peak time	50.50	67.26	47.88	49.50	66.95	49.11
Peak size	2,158.11	*2,293.38*	1,473.21	2,453.50	2,499.49	1,480.42
Time to curb*	48.50	65.91	50.64	49.50	67.10	51.55
Final size	0.95	*0.88*	0.15	0.96	0.89	0.15
	$\alpha_{-1} = \alpha_1 = 1$					
Epidemic?	1.00	1.00	0.03			
Nb2. waves	0.00	0.12	0.33			
Peak time	47.50	65.44	49.53			
Peak size	2,838.61	2,826.22	1,525.38			
Time to curb*	47.00	65.73	51.47			
Final size	0.97	0.91	0.13			
	$\alpha_{-1} = \alpha_1 = 2$			$\alpha_{-1} = 1, \alpha_1 = 2$		
Epidemic?	1.00	1.00	0.00	1.00	1.00	0.02
Nb2. waves	0.00	*0.02*	0.15	0.00	0.06	0.25
Peak time	46.00	65.82	52.62	46.50	65.80	50.91
Peak size	3,371.64	**3,295.01**	1,580.77	3,010.69	2,990.65	1,525.65
Time to curb*	45.50	67.00	54.03	47.50	67.12	52.48
Final size	0.99	**0.93**	0.11	0.98	0.91	0.13
	$\alpha_{-1} = \alpha_1 = 3$			$\alpha_{-1} = 1, \alpha_1 = 3$		
Epidemic?	1.00	1.00	0.00	1.00	1.00	0.00
Nb2. waves	0.00	*0.01*	0.09	0.00	0.01	0.11
Peak time	45.50	66.36	54.49	45.50	66.07	53.38
Peak size	3,551.96	**3,540.48**	1,619.83	3,459.73	3,385.74	1,587.77
Time to curb*	45.00	68.11	55.92	45.50	67.78	54.75
Final size	1.00	**0.96**	0.08	1.00	0.94	0.09

SD, standard deviation; Nb2. waves, number of secondary waves.
†The statistics are based on $n = 3,456$ simulations across the profiles *0–D*, and values of model parameters β_0, π, τ, and κ in Table 1.
*Time to curb = time to curb the first epidemic wave defined in Equation (11).
Italic (bold) figures indicate average values lower (larger) than the reference ($\alpha_i = 1$) for homogeneous populations ($\alpha_{-1} = \alpha_1$).

3.2 Epidemic severity across levels of prophylactic protection

Figures 5, 6 show the cumulative number of cases detected up to 1,000 days after the outbreak for various values of κ, π, and β_0. For $\kappa \in \{0.5, 0.6\}$, no secondary epidemic wave was observed (Figure 5). It appears that if the disease surveillance mechanism for early detection and removal is loose ($\pi = 0.25$), disease dynamic is barely sensitive to behaviors (Figure 5A). When disease surveillance is more effective ($\pi \geq 0.5$), disease dynamic (peak and observed final size) becomes more sensitive to behaviors (Figures 5B–D), especially when the baseline disease transmission rate is low ($\beta_0 = 0.25$).

When prophylactic behavior offers (almost) perfect protection ($\kappa \in \{0.95, 1\}$), secondary epidemic waves (one or two) were observed in 28% of these settings. Figure 6 shows the cumulative numbers of detected cases when there are secondary waves (see Supplementary Figure S1 for unique wave scenarios). It can be observed that at such high levels of protection by prophylactic behavior, disease dynamic is highly sensitive to behavioral changes, even when the baseline disease transmission rate is high ($\beta_0 = 3$).

TABLE 3 Summary of epidemic severity measures comparing populations with profiles A–B to the reference profile 0 under various in-group pressure ($\alpha_i \in \{0.1, 1, 2, 3\}$).

Statistics†	Median	Mean	SD	Median	Mean	SD
	0 (Prevalence only, $a_i = 20$)					
Epidemic?	1.00	1.00	0.00			
Nb2. waves	0.00	0.09	0.29			
Peak time	42.00	63.50	51.53			
Peak size	3,214.47	3,209.03	1,707.75			
Time to curb*	44.00	65.36	52.80			
Final size	0.98	0.91	0.13			
	A ($a_i = 20, b_i = 50$)			*0* × *A*		
Epidemic?	1.00	1.00	0.00	1.00	1.00	0.00
Nb2. waves	0.00	**0.19**	0.39	0.00	0.15	0.35
Peak time	41.50	61.97	4941.50	62.62	50.18	
Peak size	3,007.55	*3,049.14*	1,708.02	3,050.56	3,104.21	1,707.56
Time to curb*	43.50	63.38	50.56	43.50	64.58	51.38
Final size	0.96	0.90	0.14	0.97	0.91	0.14
	B ($a_i = 20, c_i = 150$)			*0* × *B*		
Epidemic?	1.00	0.99	0.08	1.00	1.00	0.00
Nb2. waves	0.00	0.02	0.16	0.00	0.03	0.18
Peak time	47.00	**65.77**	52.28	44.75	64.39	52.05
Peak size	2,873.28	*2,839.71*	1,509.91	2,883.91	2,890.16	1,560.58
Time to curb*	47.00	68.27	53.39	46.00	67.52	53.10
Final size	1.00	**0.94**	0.12	0.99	0.92	0.13
	C ($a_i = 20, d_i = 50$)			*0* × *C*		
Epidemic?	1.00	1.00	0.03	1.00	1.00	0.00
Nb2. waves	0.00	0.13	0.35	0.00	0.13	0.33
Peak time	54.50	**71.83**	48.81	49.00	68.01	49.99
Peak size	2,757.37	*2,747.60*	1447.82	2,886.43	2,849.68	1,468.74
Time to curb*	51.50	66.96	54.78	50.00	**69.96**	51.20
Final size	0.97	0.91	0.13	0.97	0.91	0.13
	D ($a_i = 20, e_i = 10$)			*0* × *D*		
Epidemic?	1.00	1.00	0.00	1.00	1.00	0.00
Nb2. waves	0.00	0.13	0.34	0.00	0.12	0.33
Peak time	39.75	*59.80*	40.92	49.00	**68.95**	52.40
Peak size	3,391.18	*3,126.29*	1,525.01	2,776.41	*2,805.00*	1,507.89
Time to curb*	39.50	59.28	43.90	50.50	**71.16**	53.62
Final size	1.00	**0.94**	0.10	0.97	0.91	0.13

†The statistics are based on $n = 3,840$ simulations across the values of model parameters in Table 1.
*Time to curb the first epidemic wave Equation (11).
Italic (bold) figures indicate average values lower (larger) than the reference.

When the efficiency of prophylactic behavior is between these two extremes ($\kappa \in \{0.75, 0.9\}$), secondary epidemic waves (one or two) were observed in 4% of these settings (Supplementary Figures S2, S3): with these levels of protection by prophylactic behavior, disease dynamic is already sensitive to behavioral changes, especially when the baseline disease transmission rate is $\beta_0 < 2$, and the higher the probability of early detection (π), the higher the number of secondary epidemic waves.

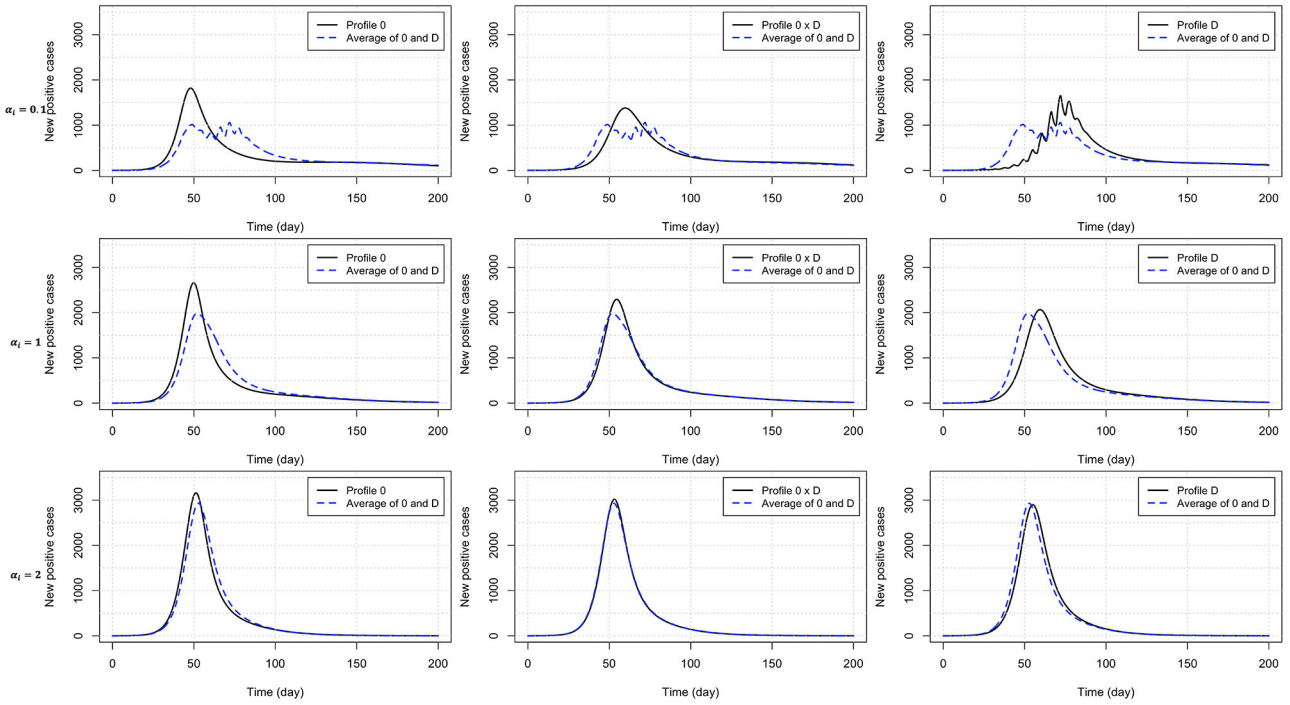

FIGURE 4
Number of new positive cases for homogeneous populations responsive to prevalence only (profile 0) or both prevalence and the rate of change of new positives (profile D), and an heterogeneous population (half profile 0 and half profile D) with pro-prophylactic behavior ($\alpha_i = 0.1$), neutral ($\alpha_i = 1$), or non-prophylactic behavior ($\alpha_i = 2$) in-group pressure. The dashed blue curve indicates for each row (each α_i value) the average of the numbers of new positive cases for profiles 0 and D. Disease-related parameters have their default (bold) values in Table 1.

4 Discussion

4.1 Main contributions

In this study, we introduce a new behavior-disease compartmental model where risk perception is a function of both perceived disease dynamic and an interpretation domain (in-group pressure). That is, the risk information derived from disease dynamics can include predicted incidence (as expressed by the rate of change Q of new positive cases) in addition to historical incidence (as expressed by the perceived prevalence P given the disease surveillance system), and the actual risk perceived by an individual can arise not only from disease dynamics but also from the pro/non-prophylactic behavior of others in the individual's social group.

Under the social influence-based model which uses true disease incidence as risk information, Tyson et al. [14] found that populations more responsive to risk information can experience more severe epidemics in terms of final size and undergo multiple epidemic waves, although the epidemic peak sizes will be smaller.

We observe similar trends when matching increase in social influence with increase in pro-prophylactic behavior in-group pressure. Considering populations responsive to historical risk information, our results regarding the number of epidemic waves and the peak size are consistent with Tyson et al.'s [14] findings, i.e., a stronger reaction to perceived disease prevalence produces more epidemic waves but smaller peak size. Indeed, a strong reaction to prevalence results in transient prophylaxis that slows down and stops disease progression (smaller peak) while many susceptible individuals are still in the population. Low disease prevalence then leads to relaxation of prophylactic behaviors and subsequently to a new outbreak (multiple waves).

A new aspect of behavior-disease dynamic captured by our model is the importance of response profiles. For instance, we considered two kinds of populations, ones that are only responsive to historical risk and ones that are additionally responsive to predicted risk. For risk predicting populations, the epidemic peak size does not monotonically decrease with increasing pro-prophylactic in-group pressure (the epidemic peak size is smallest when in-group behavior is neutral). In other words, in the context of risk information overload [36], in particular, when disease evolution curves are overly discussed on mass media and social media, stronger social influence or in-group pressure can lead to more severe epidemic outcome, at least as measured by the epidemic peak size.

Our results also indicate that erratic disease evolution curves can be explained by strong behavioral response to predicted disease curves shown on mass media or in social media. For a population paying attention to predicted risk information, a strong response reduces the time scale of the chain of reactions that leads to multiple epidemic waves, giving rise to very fast oscillations in the observed disease incidence curve (see Figure 4), both as the epidemic establishes (before peak) and as the epidemic is waning. This risk-prediction feature also makes our model quite different from others where each epidemic peak is necessarily followed by

TABLE 4 Model fit results: variations of the number of secondary epidemic waves (Poisson model, log link), the peak size (gamma model, log link), and the final epidemic size (one-inflated beta model, logit link) across response profiles.

Response	Nb. secondary waves	Peak size	Final epidemic size
Term	Coefficient (SE)	Coefficient (SE)	Coefficient (SE)
(Intercept)	−16.055 (0.362)	7.449 (0.012)	5.210 (0.027)
Profile 0	0	0	0
Profile 0 × A	0.479 (0.068)	−0.046 (0.007)	−0.138 (0.015)
Profile A	0.734 (0.065)	−0.071 (0.007)	−0.196 (0.015)
Profile 0 × B	−1.013 (0.104)	-0.113 (0.007)	0.175 (0.016)
Profile B	−1.506 (0.127)	−0.132 (0.007)	0.673 (0.016)
Profile 0 × C	0.339 (0.070)	−0.102 (0.007)	−0.066 (0.015)
Profile C	0.399 (0.070)	−0.141 (0.007)	−0.080 (0.015)
Profile 0 × D	0.318 (0.071)	−0.133 (0.007)	−0.045 (0.015)
Profile D	0.159 (0.073)	−0.146 (0.007)	−0.038 (0.015)
α_{-1}	−1.233 (0.031)	0.194 (0.002)	0.408 (0.004)
$\Delta\alpha$	−0.217 (0.017)	0.063 (0.002)	0.074 (0.004)
κ	15.524 (0.362)	−0.541 (0.010)	−3.332 (0.021)
τ	−0.065 (0.007)	0.033 (0.001)	0.026 (0.002)
π	1.161 (0.092)	−0.771 (0.009)	−4.186 (0.021)
β_0	0.012 (0.017)^{ns}	0.571 (0.002)	1.525 (0.004)
GOF: $\chi^2(df)$	7, 011.37 (34, 509)^{ns}	4, 772.52 (34, 509)^{ns}	2, 8501.19 (34, 507)^{ns}
R^2 (%)	63.59	72.46	99.69

SE, standard error.

Profiles $\boldsymbol{0}$ and $\boldsymbol{A}$ to $\boldsymbol{D}$ are defined as follows: $\boldsymbol{0}$ is the reference (hence coefficient is fixed to 0) corresponding to a population responsive to prevalence only (i.e., $a_i = 20$, with $b_i = c_i = d_i = e_i = 0$ for $i = -1, 1$), $\boldsymbol{A}$ corresponds to $a_i = 20$, $b_i = 50$, $\boldsymbol{B}$ corresponds to $a_i = 20$, $c_i = 50$, $\boldsymbol{D}$ corresponds to $a_i = 20$, $b_i = 50$, $\boldsymbol{0} \times \boldsymbol{A}$ corresponds to half of the population is $\boldsymbol{0}$ and the other half is $\boldsymbol{A}$; $\Delta\alpha = \alpha_1 - \alpha_{-1}$, α_{-1}, α_1, κ, τ, π, and β_0 are model parameters defined in Table 1 with summary statistics given in Supplementary Table S1; ^{ns} indicates a non-significant test result at 5% level (i.e., the probability to observe an effect size equal to or bigger than the observed effect by random chance only is >5%); GOF, Goodness-of-fit; df, number of residual degrees of freedom; χ^2 is the deviance statistic which is expected to be at most of the order of df if the assumed model is appropriate; R^2 is the percentage of deviance from perfect fit explained by the included predictors as compared to no predictor. The dispersion parameter of the gamma distribution for peak size is 0.1074. For the final epidemic size, the dispersion parameter of the beta distribution is 0.1982, and the probability mass at one is 0.0045.

an almost disease-free interval before emergence of the following peak [14, 57]. Because of this, which is rather frequent is real epidemic data [50], our model requires a wave delimitation method to identify epidemic waves. Also note that, unlike in Aziz-Alaoui et al. [2], our model targets a short-term dynamic, and epidemic waves in our model framework are not related to immunity lost (no flow from R back to S_i in Figure 3) but fully generated by the behavioral response to the outbreak.

Our model allows us to explore the impact of heterogeneity in the behavioral response of a population to disease risk information. In general, two-group heterogeneity in response profile (pro- vs. contra-prophylactic behavior in-group pressure, or responsiveness to predicted risk or not) leads to an intermediate epidemic outcome as compared to the two sub-populations evolving separately. One interesting finding is that under strong pro-prophylactic in-group pressure, a population consisting of two same sized sub-populations where only one group is exposed/responsive to predicted risk information can experience a less severe epidemic as measured by peak size.

Finally, we investigated the effect of delayed risk information on the severity of an epidemic in our model framework. Our simulation experiments indicate that delayed risk information slows down the behavioral response to the progression of the epidemic, contributing to a more severe epidemic outcome, i.e., larger peak and final size. For an individual with a 50% average risk to get infected in a 1-day reporting delay context, the risk to get infected becomes 54% if the reporting delay is 1 week (6 days increase). Although a 4% increase may appear small at an individual level, it would represent 4,000 more infections, given the population size in our simulations (community of 100,000 individuals). Similarly, for an epidemic that peaks to 1,500 new detected cases (see, e.g., Figure 4) under a 1-day reporting delay scenario, a reporting delay of 1 week would result into 50 additional detected cases on the peak day. These simulated results are in accordance with the work of Gutierrez et al. [47], who found that the COVID-19 epidemic in Mexico progressed much faster when delays are larger, resulting in more severe epidemic outcomes (larger death peak size and cumulative death toll). A viable solution for policymakers to reduce information delay-related increase in epidemic severity is to use a nowcasting technique to adjust the daily number of confirmed new cases for delayed reporting [48], especially in populations reactive to predicted risk, since delayed

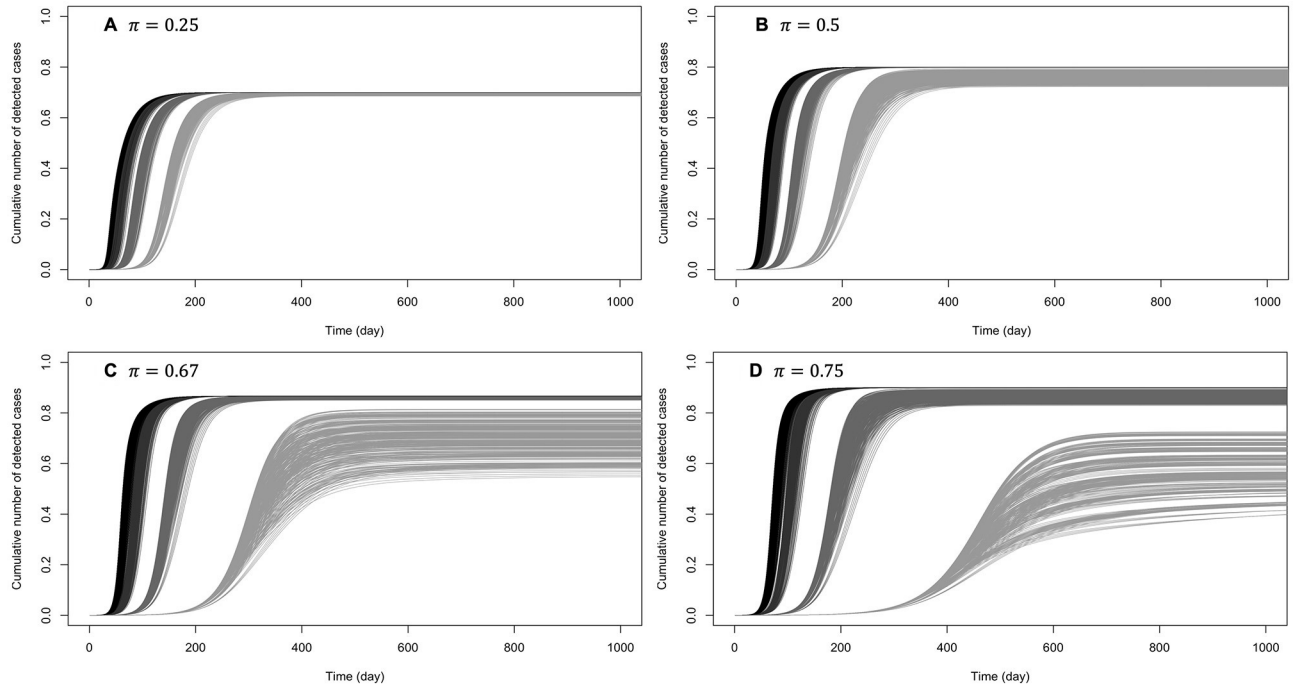

FIGURE 5
Cumulative number of detected cases when the efficiency of prophylactic behavior is medium: $\kappa \in \{0.5, 0.6\}$. The curves on **(A)** correspond to low early detection probability (loose disease surveillance mechanism), **(B)** medium early detection probability, **(C)** high early detection probability, and **(D)** very high early detection probability. For each probability of early detection of exposed individuals (π), the rightmost gray curves correspond to the lowest baseline disease transmission rate ($\beta_0 = 0.5$) and the dark curves (leftmost) correspond to the largest transmission rate ($\beta_0 = 3$). More or less gray curves have intermediate transmission rates ($\beta_0 = 1, 2$).

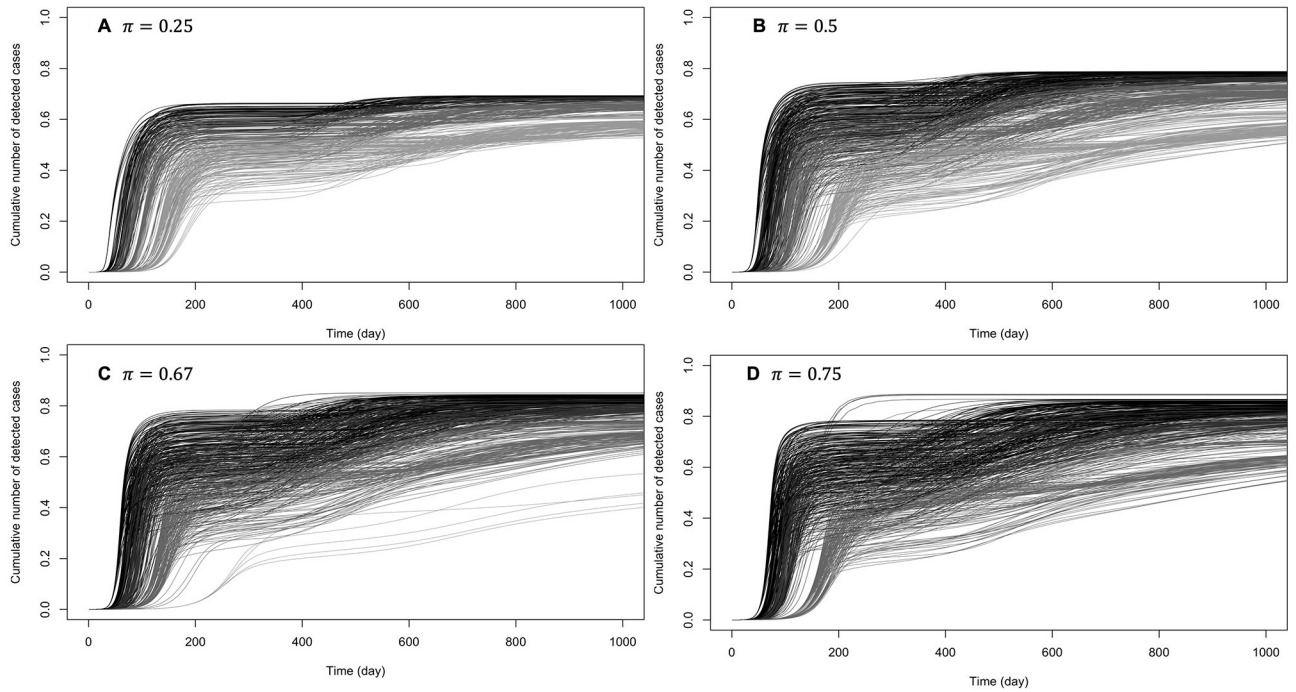

FIGURE 6
Cumulative number of detected cases when there are one or two secondary waves with (almost) perfect protection from prophylactic behavior: $\kappa \in \{0.95, 1\}$. The curves on **(A)** correspond to low early detection probability (loose disease surveillance mechanism), **(B)** medium early detection probability, **(C)** high early detection probability, and **(D)** very high early detection probability. For each probability of early detection of exposed individuals (π), the gray curves (rightmost) correspond to the lowest baseline transmission rate ($\beta_0 = 0.5$) and the dark curves (leftmost) correspond to the largest baseline transmission rate ($\beta_0 = 3$).

risk information creates an illusion of a downward trend. We must remind the reader, however, that our primary interest is to do a conceptual analysis and none of these results should be taken literally without empirical validation.

4.2 Limitations

Although the proposed model framework is quite general for coupling risk tolerance and disease dynamics, we have in our presentation limited attention to populations with relatively simple structures. In this section, we highlight and discuss the most important assumptions that may strongly affect our conclusions, and explore some potential routes to their relaxation. The prophylactic proportion defined in Equation (6) makes the strong assumption that risk information derived from in-group behavior is of no use if there is no change in risk information aggregate. However, in-group behavior can lead to change in prophylactic behavior even if risk information is constant, i.e., people can change behavior by inferring the need to engage (or the appropriateness of disengaging) based on how many individuals are already (or are still) behaving prophylactically, not because the risk has increased or decreased but because there is extant risk and in-group pressure has changed the risk perception.

Another strong assumption in Equation (6) is that the evolution of prophylactic behavior does not depend on how long people have already been engaging in prophylactic behavior, and how strong their engagement was during that time. However, prophylactic behavior is often subject to fatigue. Indeed, preventive behavior fatigue during secondary epidemic waves of a disease has been particularly well-documented since the COVID-19 pandemic event [58–75]. Failing to account for prophylactic behavior fatigue in behavior-disease model likely introduces bias in model outputs.

To account for the above two limitations of Equation (6), we propose to extend Equation (5) describing change in the proportion of prophylactic individuals in a susceptible group i as:

$$\frac{\partial m_i}{\partial t} = \left[m_i \frac{1 - m_i^{\alpha_i}}{\alpha_i}\right]\left[\frac{\partial \eta_i}{\partial t} + \omega_i \eta_i\right]\left(1 - f_i\right) \tag{12}$$

where $\omega_i \geq 0$ is the weight of "indirectly perceived change in risk" derived from in-group behavior (how informative in-group behavior is about perceived risk) and $f_i \in [0, 1]$ represents prophylactic fatigue in group i. It follows from Equation (12) that Equation (6a) can be generalized as:

$$m_i = \left[1 + \exp\left\{\delta_i - \eta_i\left(1 - f_i\right) - \zeta_i\right\}\right]^{-1/\alpha_i} \tag{13a}$$

$$\text{with} \quad f_i(t) = 1 - \exp\left\{-\epsilon M_i(t)\right\}, \quad \text{and} \tag{13b}$$

$$\zeta_i(t) = \int_0^t \eta_i(u)\left[\dot{f}_i(u) + \omega_i\left[1 - f_i(u)\right]\right] du \tag{13c}$$

where we assumed that enthusiasm for prophylactic behavior decays exponentially as experience under disease-related restrictions increases, with $\epsilon \geq 0$ expressing the extent to which prophylactic behavior is exhausting ($\epsilon = 0$ means that there is no prophylactic fatigue over time, $f_i = 0$), and the variable M_i quantifies how much effort the susceptible group i has invested in prophylactic behavior since the epidemic outbreak:

$$\dot{M}_i = \log\left(\frac{m_i^{\alpha_i}}{1 - m_i^{\alpha_i}}\right) - \log\left(\frac{m_{i0}^{\alpha_i}}{1 - m_{i0}^{\alpha_i}}\right) \tag{13d}$$

and $M_i(0) = 0$. Note from Equation (13a) that $\dot{M}_i$ can be rewritten as $\dot{M}_i = \eta_i\left(1 - f_i\right) + \zeta_i$. Equation (13a) is reduced to Equation (6a) when $\omega_i = 0$ and $f_i(t) = 0$. To solve system (9) with the prophylactic proportion m_i given by Equation (13), we can extend the differential system Equation (9) with Equation (13d) for the pseudo-state variable M_i, and an additional pseudo-state variable ζ_i whose first derivative is given by the integrand in Equation (13c), i.e., $\dot{\zeta}_i = \eta_i\left[\dot{f}_i + \omega_i\left(1 - f_i\right)\right]$, which simplifies to

$$\dot{\zeta}_i = \eta_i\left(1 - f_i\right)\left(\epsilon \dot{M}_i + \omega_i\right). \tag{14}$$

However, it appears that prophylactic fatigue, as introduced in Equations (12–14), affects equally engagement and disengagement in prophylactic behavior. A *post-hoc* but inelegant solution to that issue is to modify Equation (12) to have the form in Equation (15):

$$\frac{\partial m_i}{\partial t} = \left[m_i \frac{1 - m_i^{\alpha_i}}{\alpha_i}\right]\left[\frac{\partial \eta_i}{\partial t} + \omega_i \eta_i\right]\left(1 - f_i g_i\right) \tag{15}$$

where $g_i = 1$ if $\partial \eta_i / \partial t \geq 0$, and 0 otherwise. We leave the implementation and exploration of such speculations for future work.

Another strong hypothesis of our SEIR framework is the well-mixture assumption, i.e., for each time point, the probability of interaction between two random individuals in the population is uniformly distributed [76]. While a low standard individual might tend to interact more with low standard individuals than high standard individuals, for instance, our model assumes an homogeneous mixture of low standard and high standard groups. More generally, heterogeneity in a population goes beyond risk tolerance groups, and may be related to other factors such as geographical location [77], age [78], and behavioral risk factors [79]. In particular, the mixture of individuals from various geographical regions is generally non-uniform, and explains the large disparities among different geographical locations in the COVID-19 pandemic context [80]. Thus, to be realistic, our model should be extended to include spatial components to reveal or account for the contribution of the spatial structure of individuals to an observed epidemic dynamic. This can be achieved using, for instance, non-autonomous coupling functions between adjacent areas [6], a diffusion process [81], an agent-based infection graph [82], or a location network [83].

Finally, we point out to the possibility of an evolving pathogen, as observed for the COVID-19 pandemic [84]. For a multi-strain pathogen, a realistic epidemic model should account for mutation process occurring during infection of individuals in the population [85, 86]. As such a future direction for our study is to consider many variants of a target disease and investigate behavioral feedback loops as a pathogen strain dominates the population and is then replaced by a new pathogen, appearing through evolutionary process or interactions with adjacent geographical regions.

4.3 Conclusion

In this study, we assessed the impact of differential behavioral response profile on epidemic outcomes. Our main contributions for understanding feedback loops between transient prophylaxis and disease dynamic include (*i*) the distinction of historical risk from predicted risk information overly discussed on mass media and social media, and (*ii*) the inclusion of an interpretation domain where the collected risk information is subjected to in-group pressure. It was known that the final size of an epidemic has a non-monotonic relation with the behavioral response of a population to risk information. Our results indicate that this non-monotonicity extends to epidemic peak size as a measure of epidemic severity, in populations under strong in-group pressure.

An obvious future direction is to assess the ability of this model to predict disease dynamics, using real epidemic data (from, e.g., the world health organization, https://covid19.who.int) along with behavioral change data from surveys (e.g., adherence to COVID-19 protective measures [87, 88]). The inclusion of more than two social groups, based, for instance, on age or spatial location may be integral parts for establishing some predictive power of the model. However, our aim here was not predictive, but rather to better understand how to represent assumptions about heterogeneous risk tolerance and in-group pressures, and then in turn study their potential effects on disease dynamics.

Author contributions

CT: Conceptualization, Formal analysis, Investigation, Methodology, Software, Visualization, Writing – original draft, Writing – review & editing. BB: Conceptualization, Funding acquisition, Investigation, Methodology, Project administration, Supervision, Writing – original draft, Writing – review & editing.

Funding

The author(s) declare financial support was received for the research, authorship, and/or publication of this article. Research reported in this publication was supported by the National Institute of General Medical Sciences of the National Institutes of Health under Award Number P20GM104420.

Acknowledgments

The authors acknowledge helpful discussion with Professor Rebecca C. Tyson on modeling feedback loops between disease dynamics and prophylaxis. They also thank Craig Miller, Holly Wichman, and other members of the Institute for Modeling Collaboration and Innovation for their ongoing support of interdisciplinary collaborations.

Conflict of interest

The authors declare that the research was conducted in the absence of any commercial or financial relationships that could be construed as a potential conflict of interest.

Publisher's note

Author disclaimer

The content is solely the responsibility of the authors and does not necessarily represent the official views of the National Institutes of Health.

Supplementary material

The Supplementary Material for this article can be found online at: https://www.frontiersin.org/articles/10.3389/fams.2024.1360001/full#supplementary-material

References

1. Huang Y, Zhu Q. Game-theoretic frameworks for epidemic spreading and human decision-making: a review. *Dyn Games Appl.* (2022) 12:7–48. doi: 10.1007/s13235-022-00428-0

2. Aziz-Alaoui M, Najm F, Yafia R, SIARD. model and effect of lockdown on the dynamics of COVID-19 disease with non total immunity. *Math Model Nat Phenom.* (2021) 16:31. doi: 10.1051/mmnp/2021025

3. Bhowmick S, Panja S. Influence of opinion dynamics to inhibit epidemic spreading over multiplex network. *IEEE Control Syst Lett.* (2020) 5:1327–32. doi: 10.1109/LCSYS.2020.3035873

4. Chang SL, Piraveenan M, Pattison P, Prokopenko M. Game theoretic modelling of infectious disease dynamics and intervention methods: a review. *J Biol Dyn.* (2020) 14:57–89. doi: 10.1080/17513758.2020.1720322

5. Tyson RC, Hamilton SD, Lo AS, Baumgaertner BO, Krone SM. The timing and nature of behavioural responses affect the course of an epidemic. *Bull Math Biol.* (2020) 82:1–28. doi: 10.1007/s11538-019-00684-z

6. Ambrosio B, Aziz-Alaoui M. On a coupled time-dependent SIR models fitting with New York and New-Jersey states COVID-19 data. *Biology.* (2020) 9:135. doi: 10.3390/biology9060135

7. Alvarez-Zuzek LG, La Rocca CE, Iglesias JR, Braunstein LA. Epidemic spreading in multiplex networks influenced by opinion exchanges on vaccination. *PLoS ONE.* (2017) 12:e0186492. doi: 10.1371/journal.pone.0186492

8. Voinson M, Billiard S, Alvergne A. Beyond rational decision-making: modelling the influence of cognitive biases on the dynamics of vaccination coverage. *PLoS ONE.* (2015) 10:e0142990. doi: 10.1371/journal.pone.0142990

9. Salathé M, Bonhoeffer S. The effect of opinion clustering on disease outbreaks. *J R Soc Interface*. (2008) 5:1505–8. doi: 10.1098/rsif.2008.0271

10. Chatterjee AN, Basir FA, Ahmad B, Alsaedi A. A fractional-order compartmental model of vaccination for COVID-19 with the fear factor. *Mathematics*. (2022) 10:1451. doi: 10.3390/math10091451

11. Mpeshe SC, Nyerere N. Modeling the dynamics of coronavirus disease pandemic coupled with fear epidemics. *Comput Math Methods Med*. (2021) 2021:6647425. doi: 10.1155/2021/6647425

12. Maji C, Mukherjee D. Dynamical analysis of a fractional order model incorporating fear in the disease transmission rate of COVID-19. *Math Appl Sci Eng*. (2020) 1:207–23. doi: 10.5206/mase/10745

13. Epstein JM, Parker J, Cummings D, Hammond RA. Coupled contagion dynamics of fear and disease: mathematical and computational explorations. *PLoS ONE*. (2008) 3:e3955. doi: 10.1371/journal.pone.0003955

14. Tyson RC, Marshall ND, Baumgaertner BO. Transient prophylaxis and multiple epidemic waves. *AIMS Math*. (2022) 7:5616–33. doi: 10.3934/math.2022311

15. Giambiagi Ferrari C, Pinasco JP, Saintier N. Coupling epidemiological models with social dynamics. *Bull Math Biol*. (2021) 83:74. doi: 10.1007/s11538-021-00910-7

16. Espinoza B, Swarup S, Barrett CL, Marathe M. Heterogeneous adaptive behavioral responses may increase epidemic burden. *Sci Rep*. (2022) 12:11276. doi: 10.1038/s41598-022-15444-8

17. Arthur RF, Jones JH, Bonds MH, Ram Y, Feldman MW. Adaptive social contact rates induce complex dynamics during epidemics. *PLoS Comput Biol*. (2021) 17:e1008639. doi: 10.1371/journal.pcbi.1008639

18. Fenichel EP, Castillo-Chavez C, Ceddia MG, Chowell G, Parra PAG, Hickling GJ, et al. Adaptive human behavior in epidemiological models. *Proc Nat Acad Sci*. (2011) 108:6306–11. doi: 10.1073/pnas.1011250108

19. Frieswijk K, Zino L, Ye M, Rizzo A, Cao M. A mean-field analysis of a network behavioral-epidemic model. *IEEE Control Systems Letters*. (2022) 6:2533–8. doi: 10.1109/LCSYS.2022.3168260

20. Tori R, Tanimoto J. A study on prosocial behavior of wearing a mask and self-quarantining to prevent the spread of diseases underpinned by evolutionary game theory. *Chaos Solitons Fractals*. (2022) 158:112030. doi: 10.1016/j.chaos.2022.112030

21. Kabir KA, Risa T, Tanimoto J. Prosocial behavior of wearing a mask during an epidemic: an evolutionary explanation. *Sci Rep*. (2021) 11:12621. doi: 10.1038/s41598-021-92094-2

22. Ye M, Zino L, Rizzo A, Cao M. Game-theoretic modeling of collective decision making during epidemics. *Phys Rev E*. (2021) 104:024314. doi: 10.1103/PhysRevE.104.024314

23. Steinegger B, Arenas A, Gómez-Gardeñes J, Granell C. Pulsating campaigns of human prophylaxis driven by risk perception palliate oscillations of direct contact transmitted diseases. *Phys Rev Res*. (2020) 2:023181. doi: 10.1103/PhysRevResearch.2.023181

24. Reeves DC, Willems N, Shastry V, Rai V. Structural effects of agent heterogeneity in agent-based models: lessons from the social spread of COVID-19. *J Artif Soc Soc Simul*. (2022) 25:3. doi: 10.18564/jasss.4868

25. Shin SH Ji H, Lim H. Heterogeneity in preventive behaviors during COVID-19: health risk, economic insecurity, and slanted information. *Soc Sci Med*. (2021) 278:113944. doi: 10.1016/j.socscimed.2021.113944

26. Guenther B, Galizzi MM, Sanders JG. Heterogeneity in risk-taking during the COVID-19 pandemic: evidence from the UK lockdown. *Front Psychol*. (2021) 12:643653. doi: 10.3389/fpsyg.2021.643653

27. Arola-Fernández L, Granell C, Gómez-Gardeñes J, Arenas A. Behavioural response to heterogeneous severity of COVID-19 explains temporal variation of cases among different age groups. *Philos Trans R Soc A*. (2022) 380:20210119. doi: 10.1098/rsta.2021.0119

28. Bish A, Michie S. Demographic and attitudinal determinants of protective behaviours during a pandemic: a review. *Br J Health Psychol*. (2010) 15:797–824. doi: 10.1348/135910710X485826

29. Baumgaertner B, Ridenhour BJ, Justwan F, Carlisle JE, Miller CR. Risk of disease and willingness to vaccinate in the United States: a population-based survey. *PLoS Med*. (2020) 17:e1003354. doi: 10.1371/journal.pmed.1003354

30. Tkachenko AV, Maslov S, Elbanna A, Wong GN, Weiner ZJ, Goldenfeld N. Time-dependent heterogeneity leads to transient suppression of the COVID-19 epidemic, not herd immunity. *Proc Nat Acad Sci*. (2021) 118:e2015972118. doi: 10.1073/pnas.2015972118

31. Tkachenko AV, Maslov S, Wang T, Elbana A, Wong GN, Goldenfeld N. Stochastic social behavior coupled to COVID-19 dynamics leads to waves, plateaus, and an endemic state. *Elife*. (2021) 10:e68341. doi: 10.7554/eLife.68341

32. Shoham DA, Hammond R, Rahmandad H, Wang Y, Hovmand P. Modeling social norms and social influence in obesity. *Curr Epidemiol Rep*. (2015) 2:71–9. doi: 10.1007/s40471-014-0032-2

33. She B, Liu J, Sundaram S, Paré PE. On a networked SIS epidemic model with cooperative and antagonistic opinion dynamics. *IEEE Trans Control Netw Syst*. (2022) 9:1154–65. doi: 10.1109/TCNS.2022.3145748

34. She B, Leung HC, Sundaram S, Paré PE. Peak infection time for a networked SIR epidemic with opinion dynamics. In: *2021 60th IEEE Conference on Decision and Control (CDC)*. Austin, TX: IEEE (2021), p. 2104–9. doi: 10.1109/CDC45484.2021.9683146

35. Xuan W, Ren R, Paré PE, Ye M, Ruf S, Liu J. On a network SIS model with opinion dynamics. *IFAC-PapersOnLine*. (2020) 53:2582–7. doi: 10.1016/j.ifacol.2020.12.305

36. Mohammed M, Sha'aban A, Jatau AI, Yunusa I, Isa AM, Wada AS, et al. Assessment of COVID-19 information overload among the general public. *J Racial Ethnic Health Dis*. (2021) 9:1–9. doi: 10.1007/s40615-020-00942-0

37. Jamilla CU, Mendoza RG, Mendoza VMP. Parameter estimation in neutral delay differential equations using genetic algorithm with multi-parent crossover. *IEEE Access*. (2021) 9:131348–64. doi: 10.1109/ACCESS.2021.3113677

38. Richards F. A flexible growth function for empirical use. *J Exp Bot*. (1959) 10:290–301. doi: 10.1093/jxb/10.2.290

39. Thaler RH, Sunstein CR. Nudge: improving decisions about health, wealth, and happiness. *Penguin* (2009). p. 293.

40. Camerer CF, Loewenstein G, Rabin M. *Advances in Behavioral Economics*. Princeton, NJ: Princeton University Press (2004). doi: 10.1515/9781400829118

41. Cialdini RB, Reno RR, Kallgren CA. A focus theory of normative conduct: recycling the concept of norms to reduce littering in public places. *J Pers Soc Psychol*. (1990) 58:1015–26. doi: 10.1037//0022-3514.58.6.1015

42. Verelst F, Willem L, Beutels P. Behavioural change models for infectious disease transmission: a systematic review (2010-2015). *J R Soc Interface*. (2016) 13:20160820. doi: 10.1098/rsif.2016.0820

43. Hussain T, Ozair M, Ali F. ur Rehman S, Assiri TA, Mahmoud EE. Sensitivity analysis and optimal control of COVID-19 dynamics based on SEIQR model. *Results Phys*. (2021) 22:1–11. doi: 10.1016/j.rinp.2021.103956

44. Gerberry DJ, Milner FA. An SEIQR model for childhood diseases. *J Math Biol*. (2009) 59:535–61. doi: 10.1007/s00285-008-0239-2

45. Jumpen W, Wiwatanapataphee B, Wu Y, Tang I. A SEIQR model for pandemic influenza and its parameter identification. *Int J Pure Appl Math*. (2009) 52:247–65. doi: 10.1016/s0025-5564(02)00111-6

46. Hethcote H, Zhien M, Shengbing L. Effects of quarantine in six endemic models for infectious diseases. *Math Biosci*. (2002) 180:141–60. doi: 10.1016/S0025-5564(02)00111-6

47. Gutierrez E, Rubli A, Tavares T. Information and behavioral responses during a pandemic: evidence from delays in COVID-19 death reports. *J Dev Econ*. (2022) 154:102774. doi: 10.1016/j.jdeveco.2021.102774

48. Altmejd A, Rocklöv J, Wallin J. Nowcasting COVID-19 statistics reported with delay: a case-study of Sweden and the UK. *Int J Environ Res Public Health*. (2023) 20:3040. doi: 10.3390/ijerph20043040

49. Van den Driessche P, Watmough J. Reproduction numbers and sub-threshold endemic equilibria for compartmental models of disease transmission. *Math Biosci*. (2002) 180:29–48. doi: 10.1016/S0025-5564(02)00108-6

50. Harvey J, Chan B, Srivastava T, Zarebski AE, Dłotko P, Błaszczyk P, et al. Epidemiological waves - Types, drivers and modulators in the COVID-19 pandemic. *Heliyon*. (2023) 9:1–25. doi: 10.1101/2022.01.07.21268513

51. R Core Team. *R: A Language and Environment for Statistical Computing*. Vienna (2023). Available online at: https://www.R-project.org/ (accessed October 12, 2023).

52. Soetaert K, Petzoldt T, Setzer RW. Solving differential equations in R: package deSolve. *J Stat Softw*. (2010) 33:1–25. doi: 10.18637/jss.v033.i09

53. Nelder JA, Wedderburn RW. Generalized linear models. *J R Stat Soc A*. (1972) 135:370–84. doi: 10.2307/2344614

54. Ospina R, Ferrari SL. Inflated beta distributions. *Stat Pap*. (2010) 51:111–26. doi: 10.1007/s00362-008-0125-4

55. Rigby RA, Stasinopoulos DM. Generalized additive models for location, scale and shape (with discussion). *Appl Stat*. (2005) 54:507–54. doi: 10.1111/j.1467-9876.2005.00510.x

56. Cameron AC, Windmeijer FA. R-squared measures for count data regression models with applications to health-care utilization. *J Bus Econ Stat*. (1996) 14:209–20. doi: 10.1080/07350015.1996.10524648

57. Poletti P, Caprile B, Ajelli M, Pugliese A, Merler S. Spontaneous behavioural changes in response to epidemics. *J Theor Biol*. (2009) 260:31–40. doi: 10.1016/j.jtbi.2009.04.029

58. Chong YY, Chien WT, Cheng HY, Lamnisos D, Ļubenko J, Presti G, et al. Predictors of changing patterns of adherence to containment measures during the early stage of COVID-19 pandemic: an international longitudinal study. *Global Health*. (2023) 19:25. doi: 10.1186/s12992-023-00928-7

59. Lai DW, Jin J, Yan E, Lee VW. Predictors and moderators of COVID-19 pandemic fatigue in Hong Kong. *J Infect Public Health*. (2023) 16:645–50. doi: 10.1016/j.jiph.2023.03.003

60. Sulemana AS, Lal S, Nguyen TXT, Khan MSR, Kadoya Y. Pandemic fatigue in Japan: factors affecting the declining COVID-19 preventive measures. *Sustainability*. (2023) 15:6220. doi: 10.3390/su15076220

61. Kim JH, Kwok KO, Huang Z. Poon PKm, Hung KKC, Wong SYS, et al. A longitudinal study of COVID-19 preventive behavior fatigue in Hong Kong: a city with previous pandemic experience. *BMC Public Health*. (2023) 23:1–12. doi: 10.1186/s12889-023-15257-y

62. Zhang N, Hu T, Shang S, Zhang S, Jia W, Chen J, et al. Local travel behaviour under continuing COVID-19 waves-a proxy for pandemic fatigue? *Transp Res Interdiscip Persp*. (2023) 18:100757. doi: 10.1016/j.trip.2023.100757

63. Rodriguez-Blazquez C, Romay-Barja M, Falcon M, Ayala A, Forjaz MJ, et al. Psychometric properties of the COVID-19 pandemic fatigue scale: cross-sectional online survey study. *JMIR Public Health Surveill*. (2022) 8:e34675. doi: 10.2196/34675

64. Brankston G, Merkley E, Loewen PJ, Avery BP, Carson CA, Dougherty BP, et al. Pandemic fatigue or enduring precautionary behaviours? Canadians' long-term response to COVID-19 public health measures. *Prev Med Rep*. (2022) 30:101993. doi: 10.1016/j.pmedr.2022.101993

65. Delussu F, Tizzoni M, Gauvin L. Evidence of pandemic fatigue associated with stricter tiered COVID-19 restrictions. *PLOS Digit Health*. (2022) 1:e0000035. doi: 10.1371/journal.pdig.0000035

66. Guan M, Li Y, Scoles JD, Zhu Y. COVID-19 message fatigue: how does it predict preventive behavioral intentions and what types of information are people tired of hearing about? *Health Commun*. (2023) 38:1631–40. doi: 10.1080/10410236.2021.2023385

67. Du Z, Wang L, Shan S, Lam D, Tsang TK, Xiao J, et al. Pandemic fatigue impedes mitigation of COVID-19 in Hong Kong. *Proc Nat Acad Sci*. (2022) 119:e2213313119. doi: 10.1073/pnas.2213313119

68. Taylor S, Rachor GS, Asmundson GJ. Who develops pandemic fatigue? Insights from latent class analysis. *PLoS ONE*. (2022) 17:e0276791. doi: 10.1371/journal.pone.0276791

69. Haktanir A, Can N, Seki T, Kurnaz MF, Dilmaç B. Do we experience pandemic fatigue? current state, predictors, and prevention. *Curr Psychol*. (2022) 41:7314–25. doi: 10.1007/s12144-021-02397-w

70. Wright L, Steptoe A, Fancourt D. Trajectories of compliance with COVID-19 related guidelines: longitudinal analyses of 50,000 UK adults. *Ann Behav Med*. (2022) 56:781–90. doi: 10.1093/abm/kaac023

71. Petherick A, Goldszmidt R, Andrade EB, Furst R, Hale T, Pott A, et al. A worldwide assessment of changes in adherence to COVID-19 protective behaviours and hypothesized pandemic fatigue. *Nat Hum Behav*. (2021) 5:1145–60. doi: 10.1038/s41562-021-01181-x

72. Morgul E, Bener A, Atak M, Akyel S, Aktaş S, Bhugra D, et al. COVID-19 pandemic and psychological fatigue in Turkey. *Int J Soc Psychiatry*. (2021) 67:128–35. doi: 10.1177/0020764020941889

73. MacIntyre CR, Nguyen PY, Chughtai AA, Trent M, Gerber B, Steinhofel K, et al. Mask use, risk-mitigation behaviours and pandemic fatigue during the COVID-19 pandemic in five cities in Australia, the UK and USA: a cross-sectional survey. *Int J Infect Dis*. (2021) 106:199–207. doi: 10.1016/j.ijid.2021.03.056

74. Harvey N. Behavioral fatigue: real phenomenon, naïve construct, or policy contrivance? *Front Psychol*. (2020) 11:589892. doi: 10.3389/fpsyg.2020.589892

75. Ilesanmi OS, Bello AE, Afolabi AA. COVID-19 pandemic response fatigue in Africa: causes, consequences, and counter-measures. *Pan Afr Med J*. (2020) 37(Suppl 1):37. doi: 10.11604/pamj.supp.2020.37.1.26742

76. Lazebnik T. Computational applications of extended SIR models: a review focused on airborne pandemics. *Ecol Modell*. (2023) 483:110422. doi: 10.1016/j.ecolmodel.2023.110422

77. Callaghan T, Lueck JA, Trujillo KL, Ferdinand AO. Rural and urban differences in COVID-19 prevention behaviors. *J Rural Health*. (2021) 37:287–95. doi: 10.1111/jrh.12556

78. Urbán R, Paksi B, Miklósi Á, Saunders JB, Demetrovics Z. Non-adherence to preventive behaviours during the COVID-19 epidemic: findings from a community study. *BMC Public Health*. (2021) 21:1–11. doi: 10.1186/s12889-021-11506-0

79. Mendoza-Jiménez MJ, Hannemann TV, Atzendorf J. Behavioral risk factors and adherence to preventive measures: evidence from the early stages of the COVID-19 pandemic. *Front Public Health*. (2021) 9:674597. doi: 10.3389/fpubh.2021.674597

80. McMahon T, Chan A, Havlin S, Gallos LK. Spatial correlations in geographical spreading of COVID-19 in the United States. *Sci Rep*. (2022) 12:699. doi: 10.1038/s41598-021-04653-2

81. Viguerie A, Lorenzo G, Auricchio F, Baroli D, Hughes TJ, Patton A, et al. Simulating the spread of COVID-19 via a spatially-resolved susceptible-exposed-infected-recovered-deceased (SEIRD) model with heterogeneous diffusion. *Appl Math Lett*. (2021) 111:106617. doi: 10.1016/j.aml.2020.106617

82. Holme P. Fast and principled simulations of the SIR model on temporal networks. *PLoS ONE*. (2021) 16:e0246961. doi: 10.1371/journal.pone.0246961

83. Goel R, Sharma R. Mobility based sir model for pandemics-with case study of covid-19. In: *2020 IEEE/ACM International Conference on Advances in Social Networks Analysis and Mining (ASONAM)*. The Hague: IEEE (2020), p. 110–7. doi: 10.1109/ASONAM49781.2020.9381457

84. WHO. *Tracking SARS-CoV-2 variants: Currently Circulating Variants of Interest (VOIs) (as of 9 February 2024)*. (2024). Available online at: https://www.who.int/activities/tracking-SARS-CoV-2-variants (accessed March 10, 2024).

85. Lazebnik T, Bunimovich-Mendrazitsky S. Generic approach for mathematical model of multi-strain pandemics. *PLoS ONE*. (2022) 17:e0260683. doi: 10.1371/journal.pone.0260683

86. Shami L, Lazebnik T. Economic aspects of the detection of new strains in a multi-strain epidemiological-mathematical model. *Chaos Solitons Fractals*. (2022) 165:112823. doi: 10.1016/j.chaos.2022.112823

87. Siebenhofer A, Könczöl C, Jeitler K, Schmid D, Elliott P, Avian A. Predictors for adherent behavior in the COVID-19 pandemic: a cross-sectional telephone survey. *Front Public Health*. (2022) 10:894128. doi: 10.3389/fpubh.2022.894128

88. Sessou P, Fodjo JNS, Jérôme CS, Farougou S, Colebunders R. Assessment of adherence to public health measures and their impact on the COVID-19 outbreak in Benin Republic, West Africa. *Pan Afr Med J*. (2021) 38:293. doi: 10.11604/pamj.2021.38.293.26843

frontiers | Frontiers in Applied Mathematics and Statistics

TYPE Original Research
PUBLISHED 22 April 2024
DOI 10.3389/fams.2024.1387147

OPEN ACCESS

EDITED BY
Alain Miranville,
University of Poitiers, France

REVIEWED BY
Anibal Coronel,
University of Bío-Bío, Chile
Samson Olaniyi,
Ladoke Akintola University of Technology, Nigeria

*CORRESPONDENCE
Tesfaye Worku Gutema
✉ tesfworku21@gmail.com

RECEIVED 16 February 2024
ACCEPTED 26 March 2024
PUBLISHED 22 April 2024

CITATION
Gutema TW, Wedajo AG and Koya PR (2024) A mathematical analysis of the corruption dynamics model with optimal control strategy. *Front. Appl. Math. Stat.* 10:1387147. doi: 10.3389/fams.2024.1387147

A mathematical analysis of the corruption dynamics model with optimal control strategy

Tesfaye Worku Gutema*, Alemu Geleta Wedajo and Purnachandra Rao Koya

Department of Mathematics, College of Natural and Computational Science, Wollega University, Nekemte, Ethiopia

Corruption is a global problem that affects many countries by destroying economic, social, and political development. Therefore, we have formulated and analyzed a mathematical model to understand better control measures that reduce corruption transmission with optimal control strategies. To verify the validity of this model, we examined a model analysis showing that the solution of the model is positive and bounded. The basic reproduction number R_0 was computed by using the next-generation matrix. The formulated model was studied analytically and numerically in the context of corruption dynamics. The stability analysis of the formulated model showed that the corruption-free equilibrium is locally and globally asymptotically stable for $R_0 < 1$, but the corruption-endemic equilibrium is globally asymptotically stable for $R_0 > 1$. Furthermore, the optimal control strategy was expressed through the Pontryagin Maximum Principle by incorporating two control variables. Finally, numerical simulations for the optimal control model were performed using the Runge-Kutta fourth order forward and backward methods. This study showed that applying both mass education and law enforcement is the most efficient strategy to reduce the spread of corruption.

KEYWORDS

mathematical model, basic reproduction number, Pontryagin maximum principle, numerical simulation, optimal control strategy

1 Introduction

Corruption is an ancient and worldwide problem that destroys the economic development associated with all companies and human associations [1]. Corruption is an unlawful activity carried out for personal benefit, and the benefit of corruption is obtained by misuse of power by public or private officeholders [2]. Corruption is considered one of the frightening components for sustainable economic growth, moral values, and justice because it disturbs social life and the rule of law [3, 4]. Corruption affects the development of many countries around the world by reducing the national economy and the internal peace and security [5, 6]. Corruption is the major cause of poverty around the world, especially in Africa, and it hinders economic development, undermines democracy, and damages social justice and the rule of law [7, 8]. In Ethiopia, corruption affects political systems such as democratic power sharing, accountable and transparent institutions, and procedures. Furthermore, it is one of the causes of instability and conflict as observed in the present situations [9, 10].

The spread of corruption can be understood just as it is similar to the spread of diseases from one infected person to another susceptible individual in society, which means a non-corrupt individual gets infected with a high probability if the number of corrupt individuals in the social neighborhood exceeds a certain threshold value; in the case of mean field dependence, an individual can get corrupted because there is a high prevalence in society [10]. Introducing strong measures against the corruption is a very difficult task, since the nature of corruption practices is very secretive and illicit. However, within a society or country, it is possible to educate people and change their attitude against corruption [11]. However, it requires a thorough understanding of corruption processes to develop intervention strategies to prevent and mitigate corruption practices [12].

In epidemiology, mathematical modeling plays an important role. It is an effective tool to understand and describe the dynamics and transmission of infectious diseases [13]. Therefore, several authors, including the study mentioned in the references [14–19], have developed and analyzed mathematical models that represent the approach of corruption dynamics as a disease transmission model to evaluate the effects of corruption on national development. Furthermore, several researchers have developed mathematical models to represent corruption dynamics following the approaches adopted in epidemiology. Let us now review some of such models here.

Hathroubi [20] explained the dynamics of corruption in a closed population using the epidemiological SIR (Susceptible, Infected and Removed) model. He has determined the threshold for the transmission of corruption based on the size of the honest population. However, he did not perform stability analyses of both corruption-free and endemic equilibrium points.

Abdulrahman [11] proposed a deterministic mathematical model with constant recruitment rates and standard incidence rates for the transmission dynamics of corruption as a disease. He extended the study by Hathroubi [20] and formulated a non-linear mathematical model for describing the corruption transmission. Furthermore, he divided the total population into four compartments depending on their status of corruption: Susceptible $S(t)$, Corrupt $C(t)$, Jailed $J(t)$, and Honest $H(t)$. Employing the Jacobian matrix method and Lyapunov function approach, he examined and analyzed the stability of both corruption-free and endemic equilibrium points, respectively. Numerical simulations were also carried out and confirmed the analytical results. Additionally, these results revealed that corruption can only be reduced to a manageable level but cannot be completely eliminated.

Legesse and Shiferaw [10] proposed a mathematical model for corruption by considering awareness created by anticorruption and counseling in jail. They divided the total population into four compartments, namely, Susceptible $S(t)$, Corrupt $C(t)$, Jailed $J(t)$, and Honest $H(t)$ individuals and proved that the model is both epidemiological and mathematically well-posed. In their model, stability analyses of both corruption-free and endemic equilibrium were carried out. In addition, the simulation result shows agreement with the analytical result. However, they did not design optimal control strategies to minimize the spread of corruption. Alemneh [21] developed a mathematical model of corruption dynamics by dividing the total population into five compartments; such as Susceptible $S(t)$, Exposed to corruption $E(t)$, Corrupt $C(t)$, Recovered $R(t)$, and Honest $H(t)$ individuals. He analyzed both the local and global asymptotic stability of the corruption-free and endemic equilibrium. He extended the model to optimal control and explored its numerical simulation. He also suggested that an integrated control strategy should be taken to combat corruption.

Despite many researchers conducting mathematical modeling to control corruption transmission, this problem remains present. The present study developed a mathematical model that represents corruption dynamics by modifying the study conducted in Alemneh [21] to understand better control measures of corruption. This model is further extended to include optimal control strategy with the following two time-dependent control measures: (i) mass education of the susceptible individuals and (ii) law enforcement on the corrupted individuals. Therefore, the study is organized as follows. Section 2 explains the formulation and description of the model that represents corruption dynamics. Section 3 represents basic properties and model analysis including positivity, invariant region, existence of equilibrium, and stability of the model. In Section 4, the optimal control strategy is presented. In Section 5, the numerical simulation of the model is also analyzed. The conclusion is presented in Section 6.

2 Formulation and description of the model

The present corruption dynamics model is a modification of the existing model done by Alemneh [21] by dividing the total population $N(t)$ into six compartments based on their corruption status. These are susceptible individuals $S(t)$, exposed individuals $E(t)$, corrupted individuals $C(t)$, jailed individuals $J(t)$, recovered individuals $R(t)$, and honest individuals $H(t)$. Therefore, the total population is given as $N(t) = S(t)+E(t)+C(t)+R(t)+J(t)+H(t)$ and the six compartments are further described as follows:

(i) Susceptible individuals $S(t)$: This compartment contains individuals who have not been involved so far in any type of corruption. In addition, it contains individuals who are already involved in corruption activities but completed the jail and thus became susceptible. People enter into this compartment naturally by birth and from the jailed compartment after finishing their jail term. However, some of them can leave this compartment and move to exposed and honest compartments.

(ii) Exposed individuals $E(t)$: This compartment contains individuals who are already exposed to corruption. Although these people are already corrupted, they cannot influence or convert any susceptible individual into corrupted. People will enter from a susceptible compartment only. However, some of them can leave this compartment and move to corrupted and honest compartments.

(iii) Corrupted individuals $C(t)$: These people are capable of influencing or converting any susceptible individual to be corrupted. In other words, these individuals can encourage

and facilitate susceptible individuals to participate in corruption activities. This compartment contains individuals who are generated only from the exposed compartment. However, some of them can leave this compartment and move to jailed and recovered compartments.

(iv) Jailed individuals $J(t)$: These are the people who were already engaged in corruption activities and caught. As a result, these people are imprisoned for a specified period of time, and hence they are now in jail. People will enter into this from corrupted and recovered compartments. Similarly, after they finish their imprisonment period, people can move either to the susceptible or honest compartment as they wish.

(v) Recovered individuals $R(t)$: These are the people who had earlier participated in corruption activities but later left voluntarily. However, these individuals will move to the jailed compartment if they are proven to be involved in corrupted activities. Otherwise, they will move to the honest compartment.

(vi) Honest individuals $H(t)$: These are the people who do not participate in any corruptive activity and have no negative impact on their country's development. People in susceptible, exposed, recovered, and jailed compartments can enter this compartment.

We now describe the flow rates of individuals from one compartment to the others as follows:

Flow of susceptible individuals $S(t)$*:* Individuals are recruited with a constant birth rate Π. Furthermore, after release from jail, individuals will join susceptible individuals at a rate $(1-\varphi)\theta$. Similarly, whenever susceptible individuals contact corrupted people, they become exposed at a rate $\rho\beta$, while others can join the honest compartment at a rate γ.

Flow of exposed individuals $E(t)$*:* When influenced by corrupted people, susceptible individuals will be exposed to corruption and will enter this compartment at a rate of $\rho\beta$. However, individuals of the exposed compartment will go to the corrupt compartment at the rate of $\omega\varphi$ and to the honest compartment at a rate of $(1-\omega)\phi$.

Flow of corrupted individuals $C(t)$*:* Individuals from the exposed compartment will move into the corruption compartment at a rate of $\omega\varphi$. However, people will move out of the corrupted compartment to the jailed compartment at a rate of τ and to the recovered compartment at a rate of δ, respectively.

Flow of recovered individuals $R(t)$*:* Upon leaving corruptive activities, individuals in the corrupted compartment will move to the recovery compartment at a rate of δ. However, they move to jailed compartments at a rate of $\eta\alpha$ and honest compartment at a rate of $(1-\eta)\alpha$, respectively. Finally, we assumed the natural death rate μ in all compartments.

Depending on the assumptions and descriptions of the parameters and variables, the flow diagram of the compartmental model is shown in Figure 1.

Based on the flow diagram in Figure 1, we obtained the system of non-linear ordinary differential equations that represent the corruption dynamics as follows:

$$\begin{cases} \frac{dS}{dt} = \Pi + (1-\varphi)\theta J - \rho\beta CS - (\gamma+\mu)S, \\ \frac{dE}{dt} = \rho\beta CS - (\phi+\mu)E, \\ \frac{dC}{dt} = \omega\phi E - (\delta+\tau+\mu)C, \\ \frac{dR}{dt} = \delta C - (\alpha+\mu)R, \\ \frac{dJ}{dt} = \tau C + \eta\alpha R - (\theta+\mu)J, \\ \frac{dH}{dt} = \gamma S + (1-\omega)\varphi E + (1-\eta)\alpha R + \varphi\theta J - \mu H, \end{cases} \tag{1}$$

With the following initial condition

$$S(0) > 0, \quad E(0) \geq 0, \; C(0) \geq 0, \; R(0) \geq 0,$$
$$J(0) \geq 0, \; H(0) \geq 0. \tag{2}$$

Descriptions of the parameters in the model are presented in Table 1.

Descriptions of the variables in the model are presented in Table 2.

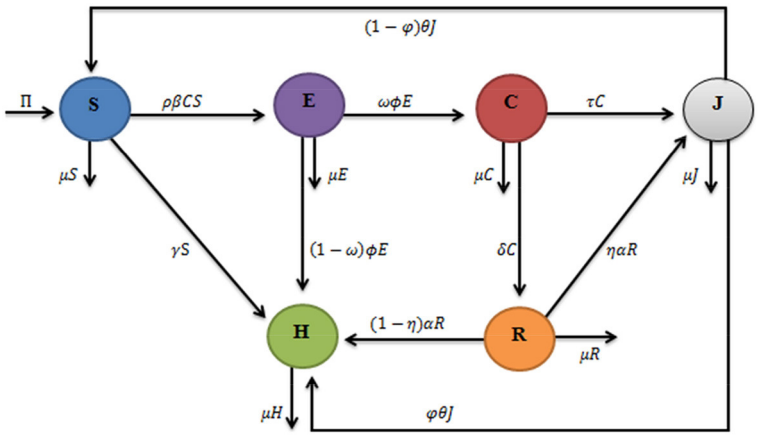

FIGURE 1
Compartmental flow diagram of corruption model.

TABLE 1 Description of the parameters in the model.

Parameter	Description
Π	Positive recruitment rate of corruption-free individuals
μ	The natural death rate of people in all compartments
ρ	Probability of corruption transmission per contact
β	The transmission rate of corruption
γ	The rate at which susceptible individuals flow into the honest compartment willingly
ω	Proportion of individuals that joins the corrupt compartment from the exposed compartment
ϕ	The rate at which exposed individuals enter the corrupt compartment
δ	The rate at which corrupt individuals move to the recovered compartment
τ	The rate at which corrupt individuals are caught and imprisoned.
α	The rate at which recovered individuals join the jailed compartment
η	Proportion of individuals that join the jailed subpopulation from the recovered compartment due to corruption prosecution
φ	Proportion of individuals that enter the honest compartment willingly from jailed compartment
θ	The average rate of a person stays in jail

TABLE 2 Description of the variables in the model.

Variables	Description
$S(t)$	Number of susceptible individuals
$E(t)$	Number of exposed individuals
$C(t)$	Number of corrupt individuals
$R(t)$	Number of recovered individuals
$J(t)$	Number of jailed individuals
$H(t)$	Number of honest individuals

3 Model analysis

In this section, we investigate the positive solution of the system (1), its boundedness, and positive invariance. In addition, the basic reproduction number, the existence of equilibrium, and the stability of the model are explored and analyzed.

3.1 Positivity solution of the model

Examining the positivity of the solution of dynamical systems is an imaginary approach to ensure the non-negativity of the solution [22]. This investigation has been carried out in several works on mathematical and epidemiological modeling. Therefore, to show that the presented model (1) is epidemiologically and mathematically meaningful, we consider the state variables of the model to be non-negative for all given time $t > 0$. Thus, we state the following result.

Theorem 1 *The initial population* $S(0) \geq 0$, $E(0) \geq 0$, $C(0) \geq 0$, $R(0) \geq 0$, $J(0) \geq 0$ *and* $H(0) \geq 0$ *such that the solutions of the system (1)* $S(t)$, $E(t)$, $C(t)$, $R(t)$, $J(t)$, $H(t)$ *are non-negative for all* $t \geq 0$.

Proof: Assume that all state variables are continuous. Then, from the third equations system of (1) which is given as follows:

$$\frac{dC}{dt} = \omega\phi E - (\delta + \tau + \mu)\, C,$$
$$\frac{dC}{C} = \left[\frac{\omega\varphi E}{C} - (\delta + \tau + \mu)\right] dt,$$

$C(t) = A_1\, e^{\int\left[\frac{\omega\varphi E}{C} - (\delta+\tau+\mu)\right] dt}$. Here, A_1 is the integral constant.

By using the initial condition of Equation (2) that is $C(0) \geq 0$, we obtain $C(0) = A_1\, e^{\left\{\int\left[\frac{\omega\varphi E}{C} - (\delta+\tau+\mu)\right] dt\right\}_{t=0}}$. Eliminating the integral constant A_1 the particular solution is obtained as follows:

$$C(t) = C(0)\; e^{\left\{\int\left[\frac{\omega\varphi E}{C} - (\delta+\tau+\mu)\right] dt - \left\{\int\left[\frac{\omega\varphi E}{C} - (\delta+\tau+\mu)\right] dt\right\}_{t=0}\right\}}$$

By using the initial condition $C(0) \geq 0$, every exponential function is a positive quantity regardless of the sign of the exponent, i.e., $e^x \geq 0$.

Hence, $C(t) = C(0)\, e^{\left\{\int\left[\frac{\omega\varphi E}{C} - (\delta+\tau+\mu)\right] dt - \left\{\int\left[\frac{\omega\varphi E}{C} - (\delta+\tau+\mu)\right] dt\right\}_{t=0}\right\}} \geq 0$, thus we conclude that $C(t)$ is positive.

Similarly, we have:

$$\begin{gathered} R(t) \geq R(0)\; e^{-(\alpha+\mu)t} \geq 0, \\ J(t) \geq J(0)\, e^{-(\theta+\mu)t} \geq 0, \\ S(t) \geq S(0)\, e^{\left\{\int[-(\rho\beta C+\gamma+\mu)]\, dt - \left\{\int[-(\rho\beta C+\gamma+\mu)]\, dt\right\}_{t=0}\right\}} \geq 0, \\ E(t) \geq E(0)\, e^{-(\phi+\mu)t} \geq 0, \\ H(t) \geq H(0)\, e^{-\mu t} \geq 0. \end{gathered} \tag{3}$$

Hence, from Equation (3) we concluded that the solutions $S(t)$, $E(t)$, $C(t)$, $R(t)$, $J(t)$, and $H(t)$ of the system (1) are positive for all $t \geq 0$. This result is very essential because the state variables denote human beings and cannot be represented by negative values.

3.2 Invariant region

Furthermore, to show that the formulated corruption model is mathematically and epidemiologically meaningful, we consider the analysis of the system (1) in the feasible region $\Omega \subseteq R_+^6$ such that

$$\Omega = \left\{ (S, E, C, R, J, H) \in R_+^6 : 0 \leq S + E + C + R + J + H = N(t) \leq \frac{\Pi}{\mu} \right\}. \tag{4}$$

Theorem 2 *The feasible solutions of system (1) all entered and bounded in the region* Ω.

Proof: The invariance region Ω of Equation (4) is obtained by adding all equations in system (1), and the simplified equation is written as follows:

$$\frac{dN}{dt} = \Pi - \mu N. \tag{5}$$

By rearranging and multiplying both sides of Equation (5) by integrating factors, and after some simplification, we obtained the following:

$$N(t) = \left(\frac{\Pi}{\mu}\right) + \left[N(0) - \left(\frac{\Pi}{\mu}\right)\right] e^{-\mu t}. \tag{6}$$

From Equation (6), we find $\lim_{t\to\infty} N(t) \leq \frac{\Pi}{\mu}$. This indicates that the total population $N(t)$ takes off from the initial value $N(0)$ at the beginning and ends up with the bounded value $\frac{\Pi}{\mu}$ as time tends to infinity. Thus, it can be concluded that $N(t)$ is bounded, i.e., $0 \leq N(t) \leq \frac{\Pi}{\mu}$. Hence, the solution set of the system (1) enters and remains in the feasible region Ω, where the model is said to be mathematically and epidemiologically well-posed [23, 24].

3.3 The point of corruption-free equilibrium of the model

To find the corruption-free equilibrium point $\mathcal{P}_0 = (S^0, E^0, C^0, R^0, J^0, H^0)$ in the model, we equate the right-hand sides of the system of Equation (1) to zero and take the corruption-free compartment $E = C = 0$. This yields $R = 0$ and $J = 0$. Thus, the corruption-free equilibrium point of system (1) is written as follows:

$$\mathcal{P}_0 = \left(\tfrac{\Pi}{(\gamma+\mu)},\ 0,\ 0,\ 0,\ 0,\ \tfrac{\gamma\Pi}{\mu(\gamma+\mu)}\right). \tag{7}$$

3.4 Basic reproduction number

The basic reproductive number R_0 is the average number of new corrupts formed after the susceptible and corrupt population contact each other [25–27]. Now, as explained in Theorem 2 in [26], we used the basic reproduction number to determine the spread of corruption. Thus, for $R_0 < 1$, the corruption will not be able to spread in the population, but if $R_0 > 1$, corruption will be able to spread in the population, which allows control measures of corruption. In the following result, we compute the basic reproduction number using the next-generation matrix technique described by the study mentioned in the reference [28]. In particular, using the notation in the study mentioned in the reference [28], the Jacobian matrix of the new infection terms (F), and the transfer terms (V), we compute the basic reproduction number. Thus, the matrix of new corrupt terms and transition terms is obtained from the corrupt compartments (i.e., E, C, R, and J) at corruption-free equilibrium and given as follows:

$$\begin{aligned}
\tfrac{dE}{dt} &= \rho\beta CS - (\phi+\mu)E,\\
\tfrac{dC}{dt} &= \omega\phi E - (\delta+\tau+\mu)C,\\
\tfrac{dR}{dt} &= \delta C - (\alpha+\mu)R,\\
\tfrac{dJ}{dt} &= \tau C + \eta\alpha R - (\theta+\mu)J.
\end{aligned} \tag{8}$$

From system Equation (8), we obtained the general transition matrix f_i and the transmission matrix $\mathcal{V}_i$ as follows:

$$f_i = \begin{bmatrix} \rho\beta CS \\ 0 \\ 0 \\ 0 \end{bmatrix}, \text{ and } \mathcal{V}_i = \begin{bmatrix} (\phi+\mu)E \\ (\delta+\tau+\mu)C - \omega\phi E \\ (\alpha+\mu)R - \delta C \\ (\theta+\mu)J - \tau C - \eta\alpha R \end{bmatrix},$$

Where the matrix $\mathcal{V}_i(x)$ is defined as $\mathcal{V}_i(x) = \mathcal{V}_i^-(x) - \mathcal{V}_i^+(x)$ with $\mathcal{V}_i^-(x) = \begin{bmatrix} (\phi+\mu)E \\ (\delta+\tau+\mu)C \\ (\alpha+\mu)R \\ (\theta+\mu)J \end{bmatrix}$, $\mathcal{V}_i^+(x) = \begin{bmatrix} 0 \\ \omega\varphi EJ \\ \delta C \\ \tau C + \eta\alpha R \end{bmatrix}$,

The Jacobian matrices at the corruption-free equilibrium point $(\mathcal{P}_0)$ yield the matrices F and V, respectively, where

$$F = \left[\frac{\partial f_c}{\partial x_j}(\mathcal{P}_0)\right] = \begin{vmatrix} 0 & \frac{\rho\beta\Pi}{(\gamma+\mu)} & 0 & 0 \\ 0 & 0 & 0 & 0 \\ 0 & 0 & 0 & 0 \\ 0 & 0 & 0 & 0 \end{vmatrix},$$

$$V = \left[\frac{\partial \mathcal{V}_c}{\partial x_j}(\mathcal{P}_0)\right] = \begin{pmatrix} (\phi+\mu) & 0 & 0 & 0 \\ -\omega\phi & (\delta+\tau+\mu) & 0 & 0 \\ 0 & -\delta & (\alpha+\mu) & 0 \\ 0 & -\tau & -\eta\alpha & (\theta+\mu) \end{pmatrix},$$

$$FV^{-1} = \begin{bmatrix} \frac{\rho\beta\Pi\omega\phi}{(\delta+\tau+\mu)(\gamma+\mu)(\phi+\mu)} & \frac{\rho\beta\Pi}{(\gamma+\mu)(\delta+\tau+\mu)} & 0 & 0 \\ 0 & 0 & 0 & 0 \\ 0 & 0 & 0 & 0 \\ 0 & 0 & 0 & 0 \end{bmatrix},$$

Thus, the basic reproduction number R_0 of the corruption model is the largest eigenvalue of the next generation matrix. Therefore,

$$R_0 = \frac{\rho\beta\Pi\omega\phi}{(\delta+\tau+\mu)(\gamma+\mu)(\phi+\mu)}. \tag{9}$$

3.5 Stability of corruption-free equilibrium point

Theorem 3 *The corruption-free equilibrium point $(\mathcal{P}_0)$ of the system (1) is locally asymptotically stable in Ω if $R_0 < 1$.*

Proof: We used the Jacobian stability techniques on system (1) to determine the corruption-free equilibrium point $(\mathcal{P}_0)$ as follows:

$$J(\mathcal{P}_0) = \begin{bmatrix} -(\gamma+\mu) & 0 & -\frac{\rho\beta\Pi}{(\gamma+\mu)} & 0 & (1-\varphi)\theta & 0 \\ 0 & -(\phi+\mu) & \frac{\rho\beta\Pi}{(\gamma+\mu)} & 0 & 0 & 0 \\ 0 & \omega\varphi & -(\delta+\tau+\mu) & 0 & 0 & 0 \\ 0 & 0 & \delta & -(\alpha+\mu) & 0 & 0 \\ 0 & 0 & \tau & \eta\alpha & -(\theta+\mu) & 0 \\ \gamma & (1-\omega)\phi & 0 & (1-\eta)\alpha & \varphi\theta & -\mu \end{bmatrix}. \tag{10}$$

From the Jacobian matrix of system Equation (10), we obtained the characteristic polynomial equation of the following form:

$$(-\mu-\lambda)(-(\gamma+\mu)-\lambda)(-(\theta+\mu)-\lambda)(-(\alpha+\mu)-\lambda)\left[\lambda^2+k_1\lambda+k_2\right]=0. \quad (11)$$

where

$$\begin{aligned} k_1 &= \phi+\delta+\tau+2\mu, \\ k_2 &= (\delta+\tau+\mu)(\phi+\mu)-\tfrac{\rho\beta\Pi\omega\varphi}{(\gamma+\mu)}. \end{aligned} \quad (12)$$

Hence, from Equation (11), we have eigenvalues,

$$\begin{aligned} \lambda_1 &= -\mu<0, \quad \lambda_2=-(\gamma+\mu)<0, \\ \lambda_3 &= -(\theta+\mu)<0, \quad \lambda_4=-(\alpha+\mu)<0. \end{aligned} \quad (13)$$

The two lasting eigenvalues are solutions of the quadratic equation $\lambda^2+k_1\lambda+k_2=0$. After substituting the value of k_1 and k_2 from the system of Equation (12), we obtain the following:

$$\lambda^2+(\phi+\delta+\tau+2\mu)\lambda+(\delta+\tau+\mu)(\phi+\mu)-\tfrac{\rho\beta\Pi\omega\varphi}{(\gamma+\mu)}=0. \quad (14)$$

Using the Routh–Hurwitz criterion principle [29], Equation (14) has negative real eigenvalues if and only if $k_1>0$, and $k_2>0$. As we observe, $k_1=(\phi+\delta+\tau+2\mu)>0$ because it is the sum of positive parameters in the model. In addition, the value of k_2 is explained as follows:

$$\begin{aligned} k_2 &= (\delta+\tau+\mu)(\phi+\mu)-\frac{\rho\beta\Pi\omega\varphi}{(\gamma+\mu)} \\ &= (\delta+\tau+\mu)(\phi+\mu)(1-R_0). \end{aligned} \quad (15)$$

From Equation (15), the value of $k_2>0$ if and only if $R_0<1$ and hence, all the determinants of the eigenvalues of Equation (11) will have negative real eigenvalues. Therefore, the corruption-free equilibrium point ($\mathcal{P}_0$) is locally asymptotically stable if $R_0<1$. The epidemiological implication of Theorem 3 is that corruption can be reduced in the population based on the initial sizes of the sub-populations.

Theorem 4 *The corruption-free equilibrium point ($\mathcal{P}_0$) of the system (1) is globally asymptotically stable in Ω if $R_0<1$.*

Proof: Let us consider the following Lyapunov function for the model (1)

$$F=r_1E+r_2C. \quad (16)$$

Differentiating the Lyapunov function of Equation (16) with respect to time t, we have:

$$\frac{dF}{dt}=r_1\frac{dE}{dt}+r_2\frac{dC}{dt}. \quad (17)$$

By substituting the value of $\frac{dE}{dt}$ and $\frac{dC}{dt}$ from the system of Equation (1) into Equation (17), we obtain the following:

$$\begin{aligned} \frac{dF}{dt} &= r_1\left[(\rho\beta\Pi CS-(\phi+\mu)E\right]+r_2\left[(\omega\phi E-(\delta+\tau+\mu)C\right], \\ &= r_1(\rho\beta\Pi CS-r_2(\delta+\tau+\mu)C-r_1(\phi+\mu)E+r_2\omega\varphi E, \\ &= \frac{\omega\varphi}{(\phi+\mu)}(\rho\beta\Pi CS-(\delta+\tau+\mu)C. \end{aligned}$$

By taking the value of $r_1=\frac{\omega\varphi}{(\phi+\mu)}r_2$ and $r_2=1$, since $S\le S^0$ we get the following:

$$\begin{aligned} \frac{dF}{dt} &\le \left[\frac{\rho\beta\Pi\omega\varphi}{(\phi+\mu)(\gamma+\mu)}-(\delta+\tau+\mu)\right]C, \\ &= \left[\left(\frac{\rho\beta\Pi\omega\varphi}{(\delta+\tau+\mu)(\phi+\mu)(\gamma+\mu)}-1\right)(\delta+\tau+\mu)\right]C, \\ &= [(R_0-1)(\delta+\tau+\mu)]C. \end{aligned} \quad (18)$$

Hence, from Equation (18) we obtained $\frac{dF}{dt}<0$ for $R_0<1$ and $\frac{dF}{dt}=0$ when $C=0$. Therefore, using LaSalle [30], corruption-free equilibrium point is globally asymptotically stable for $R_0<1$.

3.6 Corruption endemic equilibrium point

The corruption endemic equilibrium ($\mathcal{P}_1$) is the existence of corruption in a population and denoted by $(\mathcal{P}_1)=(S^*,E^*,C^*,R^*,J^*,H^*)$. It is obtained by setting the system of Equation (1) to zero as explained in the study mentioned in the reference [31].

$$\frac{dS}{dt}=\frac{dE}{dt}=\frac{dC}{dt}=\frac{dR}{dt}=\frac{dJ}{dt}=\frac{dH}{dt}=0. \quad (19)$$

Hence, the corruption-existent equilibrium point was derived as follows:

$$\begin{cases} S^*=\frac{\Pi+(1-\varphi)\theta J^*}{\rho\beta C^*+(\gamma+\mu)}, \\ E^*=\frac{\rho\beta C^*S^*}{(\phi+\mu)}, \\ R^*=\frac{\delta C^*}{(\alpha+\mu)}, \\ J^*=\frac{\delta C^*+\eta\alpha R^*}{(\theta+\mu)}, \\ H^*=\frac{\gamma S^*+(1-\omega)\phi E^*+(1-\eta)\alpha R^*+\varphi\theta\ J^*}{\mu}. \end{cases} \quad (20)$$

After some simplification of Equation (20), the value of C^* was obtained from the equation three of system (1) as follows:

$$C^*=\frac{k_1(R_0-1)}{\rho\beta\left(k_2+k_3\right)}. \quad (21)$$

where

$$\begin{aligned} k_1 &= (\theta+\mu)(\alpha+\mu)(\delta+\tau+\mu)(\phi+\mu)(\gamma+\mu), \\ k_2 &= (\theta+\mu)(\alpha+\mu)(\delta+\tau+\mu)(\phi+\mu), \\ k_3 &= (\omega\theta\tau\alpha+\omega\theta\tau\mu+\omega\theta\eta\alpha\delta)(1-\phi). \end{aligned}$$

Recalling that all the parameters of the model are positive. Hence, if $R_0>1$, from Equation (21), we obtain the value of $C^*=\frac{k_1(R_0-1)}{\rho\beta(k_2+k_3)}>0$. This indicates the existence of corruption in the entire population and the presence of corruption-endemic equilibrium point.

3.7 Stability of corruption-endemic equilibrium point

Theorem 5 *The corruption endemic equilibrium point ($\mathcal{P}_1$) of the system (1) is globally asymptotically stable in Ω if $R_0>1$.*

Proof: We used the following Lyapunov function as explained in the study mentioned in the reference [32, 33], to prove the global stability of the endemic equilibrium point.

$$L = \frac{1}{2}\left[B_1 + B_2 + B_3 + B_4 + B_5 + B_6\right]^2. \tag{22}$$

where

$$\begin{aligned} B_1 &= \left(S - S^*\right), \quad B_2 = \left(E - E^*\right), \\ B_3 &= \left(C - C^*\right), \quad B_4 = \left(R - R^*\right), \\ B_5 &= \left(J - J^*\right), \quad B_6 = \left(H - H^*\right). \end{aligned}$$

By differentiating Equation (22) with respect to time (t), we obtain the following result:

$$\begin{aligned} \frac{dL}{dt} &= \begin{pmatrix} \left[(S - S^*) + (E - E^*) + (C - C^*) + (R - R^*) + (J - J^*) + (H - H^*)\right] \\ \left[\frac{dS}{dt} + \frac{dE}{dt} + \frac{dC}{dt} + \frac{dR}{dt} + \frac{dJ}{dt} + \frac{dH}{dt}\right] \end{pmatrix}, \\ \frac{dL}{dt} &= \left[\left(S - S^{**}\right) + \left(E - E^{**}\right) + \left(C - C^{**}\right) + \left(R - R^{**}\right) + \left(J - J^{**}\right) + \left(H - H^*\right)\right]\frac{dN}{dt}. \end{aligned} \tag{23}$$

By substituting Equation (4) into Equation (23) and simplifying, we get the following expression:

$$\begin{aligned} \frac{dL}{dt} &= \left[(S + E + C + R + J + H)\right. \\ &\left. - (S^* + E^* + C^* + R^* + J^* + H^*)\right]\left[\Pi - \mu N\right]. \\ \frac{dL}{dt} &\leq \left[N - \frac{\Pi}{\mu}\right]\left[\Pi - \mu N\right]. \end{aligned} \tag{24}$$

By simplifying Equation (24), we achieve the following result:

$$\frac{dL}{dt} \leq -\frac{1}{\mu}\left[\Pi - \mu N\right]^2. \tag{25}$$

Thus, Equation (25) shows that $\frac{dL}{dt} < 0$ and also $\frac{dL}{dt} = 0$, if and only if $S = S^*$, $E = E^*$, $C = C^*$, $R = R^*$, $J = J^*$, and $H = H^*$. Then, the largest invariant set of the system (1) on the set $(S, E, C, R, J, H) \in \Omega \subset R_+^6 : \frac{dL}{dt} \leq 0$ is the endemic equilibrium point. Using the LaSalle invariance principle [30], we indicated that the endemic equilibrium point $(\mathcal{P}_1)$ is globally asymptotically stable in Ω if $R_0 > 1$. The epidemiological implication of Theorem 5 is that corruption will continue to spread in the population.

4 Optimal control strategy analysis

An optimal control strategy is another powerful mathematical tool widely used in applications that make decisions involving complex situations [34, 35]. Hence, we use an optimal control strategy to reduce the transmission of corruption and the costs associated with control strategies. In this case, the two control variables were added to system (1) to minimize the spread of corruption.

The first control variable $u_1(t)$ represents the corruption prevention mechanism (mass education). The second control variable $u_2(t)$ represents the effort rate to reduce the spread of corruption by implementing law enforcement on corrupted individuals. Adding the two control strategies to the system (1), the optimal control model is given by the following non-linear ordinary differential equations:

$$\begin{cases} \frac{dS}{dt} = \Pi + (1 - \varphi)\,\theta J - (1 - u_1)\,\rho\beta CS - (\gamma + \mu)\,S, \\ \frac{dE}{dt} = (1 - u_1)\,\rho\beta CS - (\phi + \mu)\,E, \\ \frac{dC}{dt} = \omega\phi E - (\delta + \tau + \mu + u_2)\,C, \\ \frac{dR}{dt} = \delta C - (\alpha + \mu)\,R, \\ \frac{dJ}{dt} = (\tau + u_2)\,C + \eta\alpha R - (\theta + \mu)\,J, \\ \frac{dH}{dt} = \gamma S + (1 - \omega)\,\varphi E + (1 - \eta)\,\alpha R + \varphi\theta J - \mu H. \end{cases} \tag{26}$$

With the following initial condition,

$$S(0) \geq 0,\ E(0) \geq 0,\ C(0) \geq 0,\ R(0) \geq 0,\ J(0) \geq 0,\ H(0) \geq 0. \tag{27}$$

The objective of using optimal control strategies is to find the values of $u^+ = \left(u_1{}^+,\ u_2{}^+\right)$ of the control $u = (u_1, u_2)$, which are bounded between 0 and 1 , such that the associated state trajectories S, E, C, R, J, and H are solutions of the system (26) in the fixed period of time $[0, t_f]$.

Our cost functional considers the number of exposed individuals, the number of corrupted individuals, and the implementation cost of strategies related to the controls u_i, $i = 1, 2$. Hence, we intend to examine the optimal control strategy that minimizes the following objective function:

$$\mathbb{F}(u_1, u_2) = \min_{u_1, u_2} \int_0^{t_f} \left(a_1 E + a_2 C + \frac{1}{2}\left[b_1 {u_1}^2 + b_2 {u_2}^2\right]\right). \tag{28}$$

where constants a_1, a_2, b_1, and b_2 are positive. The coefficients a_1 and a_2 represent the cost weight for exposed and corrupted individuals, respectively. The coefficients b_1 and b_2 represent the relative cost weights associated with control variables u_1 and u_2, respectively [36, 37]. t_f, represent the final time. Thus, to find the optimal control functions $u_1{}^+$ and $u_2{}^+$, we use the following:

$$\mathbb{F}\left(u_1{}^+,\ u_2{}^+\right) = \min_{(u_1, u_2) \in \Phi} \mathbb{F}\left(u_1(t), u_2(t)\right). \tag{29}$$

where the set of admissible controls functions Φ is defined as follows:

$$\begin{aligned} \Phi = \big\{&(u_1, u_2) : 0 \leq u_i(t) \leq 1,\ i = 1, 2,\ u_i \\ &(t) \text{ are Lebesgue measurable on } \left[0,\ t_f\right]\big\}. \end{aligned} \tag{30}$$

4.1 Existence of an optimal control function

In this section, we show the existence of optimal control functions that minimize the cost function over a fixed period of time. Hence, we obtain the existence of optimal control using the result of the study mentioned in the reference [38, 39]. The following result guarantees the existence of optimal control functions.

Theorem 6 *There exist optimal control functions* $u^+ = \left(u_1{}^+,\ u_2{}^+\right)$ *in* Φ *such that*

$$\mathbb{F}\left(u_1{}^+,\ u_2{}^+\right) = \min_{(u_1, u_2) \in \Phi} \mathbb{F}\left(u_1(t), u_2(t)\right). \tag{31}$$

Subject to the optimal control model of the system (26) and the initial condition of Equation (27).

Proof: All the state variables involved in the model are continuously differentiable. Therefore, we need to verify the following four conditions given in the study mentioned in the reference [38, 39].

(i) The set of controls and the corresponding solution to the system (26) and (27) are non-empty.
(ii) The admissible control set Φ is convex and closed.
(iii) The state system is bounded by a linear function in the control variables and state variables.
(iv) The integrand I of Equation (28) is convex on Φ and $I(S, E, C, R, J, H, u) \geq \mathbb{h}(u)$, where $\mathbb{h}$ is continuous and $\|u\|^{-1}\mathbb{h}(u) \to +\infty$ *as* $||u|| \to \infty$.

To prove condition (i), consider that all the state variables $S, E, C, R, J, H \in C'\left(R^{+}, R^{+}\right)$ and the total human population are defined as follows:

$$N(t) = S(t) + E(t) + C(t) + R(t) + J(t) + H(t) \tag{32}$$

Substitute the governing system (26) into Equation (32) and after some simplification, we obtain the following:

$$\frac{dN}{dt} = \Pi - \mu N. \tag{33}$$

From Equation (33), we obtain $\lim_{t\to\infty} N(t) \leq \frac{\Pi}{\mu}$.

From this, it follows that the solutions of the state system are continuous and bounded for each admissible control function in Φ. Therefore, the initial value problem (26) and (27) has a unique solution corresponding to each admissible control function Φ [40, 41].

To prove conditions (ii), consider the admissible control set $\Phi = \left\{u \in R^2 : \|u\| \leq 1 - \varepsilon\right\}$.

Let $u_1, u_2 \in \Phi$, such that $\|u_1\| \leq 1 - \varepsilon$ and $\|u_2\| \leq 1 - \varepsilon$. Then, for any $\eta \in [0, 1]$, $\|\eta u_1 + (1-\eta)u_2\| \leq \eta\|u_1\| + (1-\eta)\|u_2\| \leq 1 - \varepsilon$. This indicates that admissible control set Φ is convex and closed. The condition (iii) is explicitly verified using the algorithm as proved in Theorem 1.1 of [42]. The integrand of objective function Equation (28) $a_1E(t) + a_2C(t) + \frac{1}{2}\left[b_1{u_1}^2 + b_2{u_1}^2\right]$ is clearly convex on Φ. Moreover,

$$\begin{aligned} I(S, E, C, R, J, H, u) &= a_1E(t) + a_2C(t) + \frac{1}{2}\left[b_1{u_1}^2 + b_2{u_1}^2\right] \\ &\geq \frac{1}{2}\left[b_1{u_1}^2 + b_2{u_1}^2\right]. \end{aligned} \tag{34}$$

Let $\rho = \min\left(\frac{b_1}{2}, \frac{b_2}{2}\right) > 0$ and define a continuous function $\mathbb{h}(u) = \rho\|u\|^2$. Then, from the Equation (34), we have $I(S, E, C, R, J, H, u) \geq \mathbb{h}(u)$ and $\|u\|^{-1}\mathbb{h}(u) \to +\infty$ *as* $||u|| \to \infty$. Hence, condition (iv) is satisfied. Therefore, the existence of an optimal control pair satisfies the theorem.

4.2 Description of optimal control function

In this section, we solve the optimal control problem that satisfies the necessary conditions by using the Pontryagin maximum principle. Based on the objective function Equation (28) and the optimal control model (26), we establish the Hamiltonian function $\mathbb{Q}$ with respect to control variables $u_1(t)$ and $u_2(t)$ as follows:

$$\begin{aligned} \mathbb{Q} &= a_1E + a_2C + \tfrac{1}{2}\left[b_1{u_1}^2 + b_2{u_2}^2\right] \\ &+\pi_1\left[\Pi + (1-\varphi)\theta J - (1-u_1)\rho\beta CS - (\gamma+\mu)S\right] \\ &+\pi_2\left[(1-u_1)\rho\beta CS - (\phi+\mu)E\right] \\ &+\pi_3\left[\omega\phi E - (\delta+\tau+\mu+u_2)C\right] \\ &+\pi_4\left[\delta C - (\alpha+\mu)R\right] \\ &+\pi_5\left[(\tau+u_2)C + \eta\alpha R - (\theta+\mu)J\right] \\ &+\pi_6\left[\gamma S + (1-\omega)\varphi E + (1-\eta)\alpha R + \varphi\theta J - \mu H\right]. \end{aligned} \tag{35}$$

where $\pi_1, \pi_2, \ldots, \pi_6$ are the adjoint functions which are determined using Pontryagin's minimum principle [37], with the evidence of [38], we state the theorem as follows:

Theorem 7 *Let us consider the optimal control* $u^{+} = \left({u_1}^{+}, {u_2}^{+}\right)$ *and the unique solution of* $\left(S, E, C, R, J, \text{and } H\right)$ *from the system (26) corresponding to the state equation that minimizes* $u = (u_1, u_2)$ *over* Φ. *Then, there exist adjoint function,* $\pi_1, \pi_2, \ldots, \pi_6$ *satisfying the following established equations:*

$$\begin{aligned} \tfrac{d\pi_1}{dt} &= \pi_1\left[(1-u_1)\rho\beta C + (\gamma+\mu)\right] - \pi_2(1-u_1)\rho\beta C - \pi_6\gamma, \\ \tfrac{d\pi_2}{dt} &= -a_1 + \pi_2(\phi+\mu) - \pi_3\omega\phi - \pi_6(1-\omega)\phi, \\ \tfrac{d\pi_3}{dt} &= -a_2 + \pi_1(1-u_1)\rho\beta S - \pi_2(1-u_1)\rho\beta S \\ &+\pi_3(\delta+\tau+\mu+u_2) - \pi_4\delta - \pi_5(\tau+u_2), \\ \tfrac{d\pi_4}{dt} &= \pi_4(\alpha+\mu) - \pi_5\eta\alpha - \pi_6(1-\eta)\alpha, \\ \tfrac{d\pi_5}{dt} &= -\pi_1(1-\varphi)\theta + \pi_5(\theta+\mu) - \pi_6\varphi\theta, \\ \tfrac{d\pi_6}{dt} &= \pi_6\mu. \end{aligned} \tag{36}$$

With transversality condition

$$\pi_1(t_f) = \pi_2(t_f) = \pi_3(t_f) = \pi_4(t_f) = \pi_5(t_f) = \pi_6(t_f) = 0. \tag{37}$$

TABLE 3 Standard values for parameter of the system (1).

Parameter	Standard value	Source
Π	500	Assumed
β	0.0234	[10]
ρ	0.036	[11]
μ	0.016	[10]
γ	0.000001	[11]
ω	0.3	[18]
ϕ	0.02	[10]
δ	0.007	[18]
τ	0.000001	[11]
α	0.0001	[12]
η	0.03	[18]
φ	0.04	Assumed
θ	0.143	[11]

Moreover, for $t \in [0,\ t_f]$, the optimal controls ${u_1}^+$ and ${u_2}^+$ are given as follows:

$$\begin{aligned} {u_1}^+ &= \min\left\{1, \max\left(0, \frac{(\pi_2-\pi_1)\rho\beta CS}{b_1}\right)\right\}, \\ {u_2}^+ &= \min\left\{1, \max\left(0, \frac{(\pi_3-\pi_5)C}{b_2}\right)\right\}, \end{aligned} \tag{38}$$

Proof: The co-state equations can be computed by the Pontryagin maximum principle, which is given in the study mentioned in the reference [38]. By differentiating the Hamiltonian Equation (35), with $S,\ E,\ C,\ R, J$, and H respectively, we obtain the adjoint system as follows:

$$\begin{aligned} \frac{d\pi_1}{dt} &= -\frac{\partial \mathbb{Q}}{\partial S(t)} = \pi_1\left[(1-\ u_1)\,\rho\beta C + (\gamma+\mu)\right] - \pi_2\,(1-\ u_1) \\ &\quad \rho\beta C - \pi_6\gamma, \\ \frac{d\pi_2}{dt} &= -\frac{\partial \mathbb{Q}}{\partial E(t)} = -a_1 + \pi_2\,(\phi+\mu) - \pi_3\omega\phi - \pi_6\,(1-\omega)\,\phi, \\ \frac{d\pi_3}{dt} &= -\frac{\partial \mathbb{Q}}{\partial C(t)} = -a_2 + \pi_1\,(1-\ u_1)\,\rho\beta S - \pi_2\,(1-\ u_1)\,\rho\beta S \\ &\quad +\pi_3\,(\delta+\tau+\mu+\ u_2) - \pi_4\delta - \pi_5\,(\tau+\ u_2), \\ \frac{d\pi_4}{dt} &= -\frac{\partial \mathbb{Q}}{\partial R(t)} = \pi_4\,(\alpha+\mu) - \pi_5\eta\alpha - \pi_6\,(1-\eta)\,\alpha, \\ \frac{d\pi_5}{dt} &= -\frac{\partial \mathbb{Q}}{\partial J(t)} = -\pi_1\,(1-\varphi)\,\theta\ + \pi_5\,(\theta+\mu) - \pi_6\varphi\theta, \\ \frac{d\pi_6}{dt} &= -\frac{\partial \mathbb{Q}}{\partial H(t)} = \pi_6\mu\,. \end{aligned} \tag{39}$$

With transversality condition

$$\pi_1\left(t_f\right) = \pi_2\left(t_f\right) = \pi_3\left(t_f\right) = \pi_4\left(t_f\right) = \pi_5\left(t_f\right) = \pi_6\left(t_f\right) = 0. \tag{40}$$

Furthermore, using the optimality condition, we can find the value of optimal control functions ${u_1}^+$ and ${u_2}^+$ for $t \in [0,\ t_f\ ]$,

$$\begin{aligned} &\frac{\partial \mathbb{Q}}{\partial u_1} = 0,\ at\ u_1 = {u_1}^+, \\ \frac{\partial \mathbb{Q}}{\partial u_1} &= \frac{\partial \mathbb{Q}}{\partial {u_1}^+} = b_1u_1 + \pi_1\rho\beta CS - \pi_2\rho\beta CS = 0, \\ &{u_1}^+ = \frac{(\pi_2-\pi_1)\rho\beta CS}{b_1}\,. \end{aligned} \tag{41}$$

$$\begin{aligned} &\frac{\partial \mathbb{Q}}{\partial u_2} = 0,\ at\ u_2 = {u_2}^+, \\ \frac{\partial \mathbb{Q}}{\partial u_2} &= \frac{\partial \mathbb{Q}}{\partial {u_2}^+} = b_2u_2 - \pi_3C + \pi_5C = 0, \\ &{u_2}^+ = \frac{(\pi_3-\pi_5)C}{b_2}. \end{aligned}$$

Moreover, by using the boundary condition and simplifying the solution of Equation (41), we obtain the following optimal controls:

$$\begin{aligned} {u_1}^+ &= \min\left\{1,\ \max\left(0, \frac{(\pi_2-\pi_1)\rho\beta CS}{b_1}\right)\right\}, \\ {u_2}^+ &= \min\left\{1,\ \max\left(0, \frac{(\pi_3-\pi_5)C}{b_2}\right)\right\}, \end{aligned} \tag{42}$$

Hence, the optimal control function is described, and we can use the simulation of an optimality system to determine the best strategies that minimize corruption dynamics.

5 Numerical simulations of the model

In this section, we used the forward–backward sweep to solve the state and adjoint systems in order to obtain the optimal strategy. Therefore, to solve the state Equations (26) due to the initial value of the state variables, we used the forward fourth-order Runge–Kutta method.

Similarly, to solve the adjoint equations, we used the backward fourth-order Runge–Kutta method due to the transversality condition Equation (37) having the solution of state functions and the value of optimal controls. The initial conditions that we used for the numerical simulation of the optimality system are $S(0) = 50,000$, $E(0) = 200$, $C(0) = 500$, $R(0) = 100$, $J(0) = 50$, *and* $H(0) = 100$, as well as the weight constant values for the states and controls variables are $a_1 = 60$, $a_2 = 80$, $b_1 = 60$, *and* $b_1 = 40$. The standard parameter values of the model are displayed in Table 3, as follows.

Therefore, we consider the following three strategies to determine the impact of each control on corruption reduction.

5.1 Strategy (i): strategy with only mass education (u_1) as prevention measure

Here, to optimize the objective function of the system (26), we used only mass education (u_1) on susceptible individuals while the control strategy (u_2) is not applied. As shown in Figure 2A, the number of exposed individuals decreases and then is constant over a fixed period of time. This indicates that the number of exposed population increases if there are no control strategies. Similarly, as shown in Figure 2B, we observe that the number of corrupt population decreases as the control strategy is used over a fixed period of time. In another way, the number of populations that participate in corruption activity increases if there are no control strategies. Therefore, we conclude that the mass education strategy plays an important role in the prevention of corruption activity.

5.2 Strategy (ii): strategy with only law enforcement (u_2) as reduction measure

Here, we use only the law enforcement (u_2) strategy on corrupted individuals in order to optimize the objective function of the system (26), while the control strategy (u_1) is equal to zero. We observe in Figure 3A that due to the law enforcement control strategy, the number of exposed individuals slowly decreased. However, as shown in Figure 3B, we observed that the number of corrupt population decreases significantly as the law enforcement control strategy is used. Therefore, we conclude that the law enforcement control strategy decreases both the number of exposed and corrupted populations. However, the number of corrupt populations spreads rapidly if the law enforcement control strategy is not applied.

5.3 Strategy (iii): Using both mass education (u_1) and law enforcement (u_2) control strategy

In this strategy, we use the combination of mass education (u_1) and law enforcement (u_2) control strategy on susceptible and corrupted individuals, respectively, that can optimize the objective function of the system of the study mentioned in the reference [26]. We observe in Figure 4A that the number of exposed individuals decreases significantly if we apply the control strategies, whereas if not, the number of exposed populations increases. Similarly,

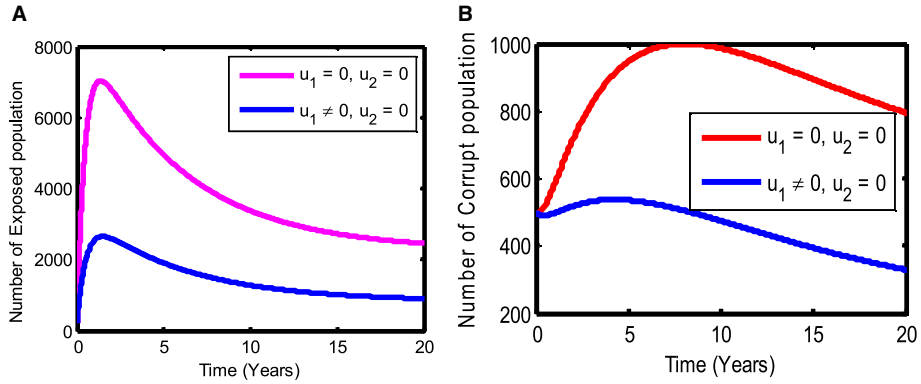

FIGURE 2
The effect of using only the mass education control strategy ($u_1 \neq 0$).

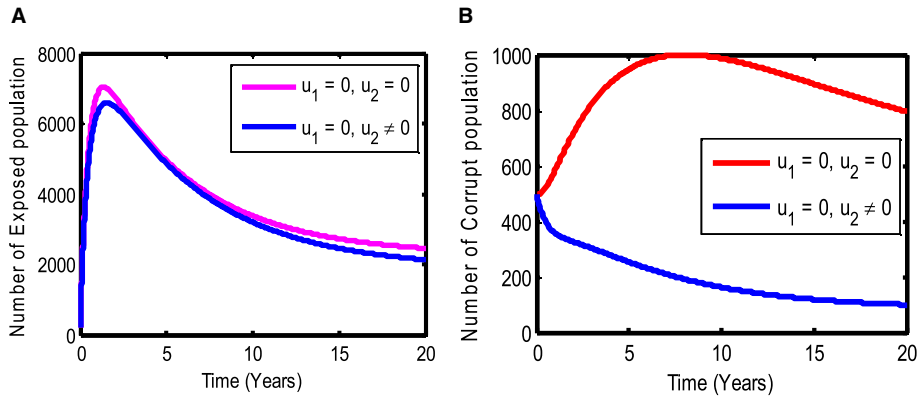

FIGURE 3
The effect of using only the law enforcement control strategy ($u_2 \neq 0$) .

as shown in Figure 4B we show that the number of corrupted populations decreases significantly as control strategies are used, while the number of corrupted populations increases if there is no control strategy. Therefore, we conclude that applying both mass education and law enforcement strategies against corruption decreases both the number of exposed and corrupted populations in a given fixed period of time. This increases the number of jailed population, as shown in Figure 4C.

6 Result, discussion, and conclusion

In this study, we develop a deterministic mathematical model for the transmission of corruption dynamics to study the effect of corruption in the population based on the corrupt status. To show that the formulated corruption model is mathematically and epidemiologically meaningful, we conducted a qualitative analysis of the model by showing that the solution of the model is positive and bounded. The basic reproduction number was calculated using the next-generation matrix method. The stability of the corruption-free and endemic equilibrium for the corruption dynamics model was analyzed in terms of the reproduction number. The analysis shows that for $R_0 < 1$, the corruption-free equilibrium point is asymptotically stable both locally and globally. It means that if the average number of new corrupted individuals generated by a single corrupted individual introduced into a susceptible population under any condition is less than one, the corruption will be minimized from the population. On the other hand, for whatever conditions if $R_0 > 1$, the corruption endemic equilibrium point is both locally and globally asymptotically stable. It means that corruption will increase in the population.

Furthermore, we extended the model to an optimal control strategy by incorporating two control variables, such as mass education and law enforcement. The necessary conditions for optimal controls such as existence and characterization were investigated with the help of Pontryagin's Maximum Principle. Finally, we have examined the numerical simulations of the optimal control model by considering individually and combining the control variables. Based on the results of the numerical analysis, we propose that using both mass education and law enforcement against corruption is the best strategy to minimize the number of exposed and corrupted populations. Therefore, anticorruption institutions and policymakers can use this finding as a good effort to reduce the corruption spread in the population. A significant and interesting aspect of the future study is to implement parameter estimation and cost-effectiveness analysis in the corruption dynamics model.

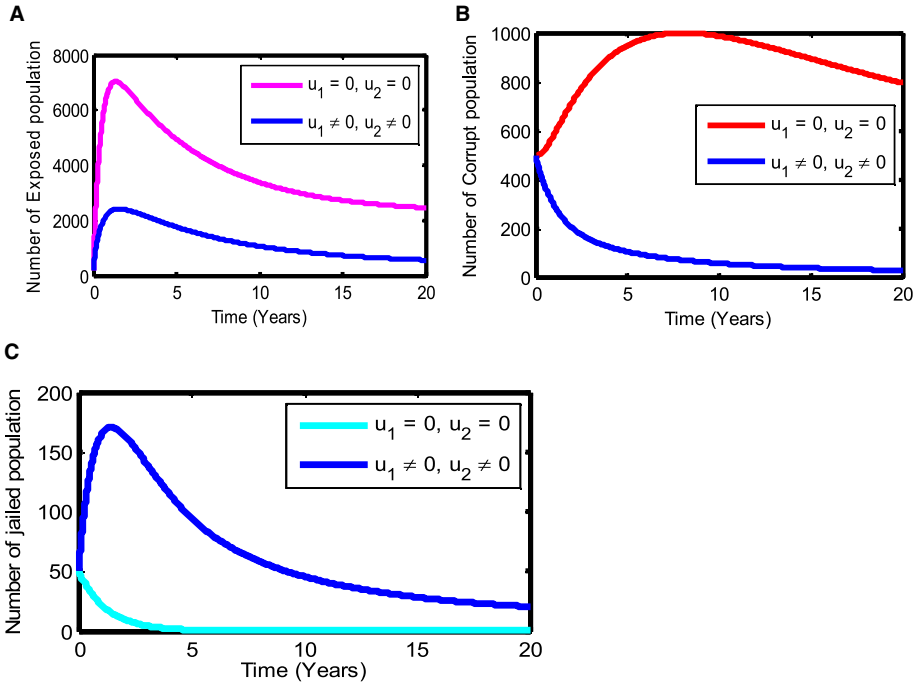

FIGURE 4
The effect of using both mass education ($u_1 \neq 0$) and law enforcement ($u_2 \neq 0$) strategies on the state variables.

Data availability statement

The original contributions presented in the study are included in the article/supplementary material, further inquiries can be directed to the corresponding author.

Author contributions

TG: Formal analysis, Methodology, Software, Visualization, Writing – original draft, Writing – review & editing. AW: Conceptualization, Investigation, Methodology, Supervision, Validation, Visualization, Writing – review & editing. PK: Conceptualization, Data curation, Investigation, Methodology, Software, Supervision, Validation, Visualization, Writing – review & editing.

Funding

The author(s) declare that no financial support was received for the research, authorship, and/or publication of this article.

Acknowledgments

The authors sincerely acknowledge the Department of Mathematics, CNCS, Wollega University, and Samara University for their support during the study.

Conflict of interest

The authors declare that the research was conducted in the absence of any commercial or financial relationships that could be construed as a potential conflict of interest.

Publisher's note

All claims expressed in this article are solely those of the authors and do not necessarily represent those of their affiliated organizations, or those of the publisher, the editors and the reviewers. Any product that may be evaluated in this article, or claim that may be made by its manufacturer, is not guaranteed or endorsed by the publisher.

References

1. Grass D, Caulkins JP, Feichtinger G, Tragler G, Behrens DA. *Optimal Control of Nonlinear Processes*. Berlin, Heidelberg: Springer (2008).

2. World Bank. *Helping Countries Combat Corruption: The Role of the World Bank* (1997).

3. Cherrier B. Gunnar Myrdal and the scientific way to social democracy. *Hist EconThought.* (2009) 31:33–55. doi: 10.1017/S105383720909004X

4. Adela S, Bernard D, Grabova P. Corruption impact on economic growth: an empirical analysis. *J Econ Dev Manag IT Finan Market*. (2014) 6:57–77. Available online at: https://api.semanticscholar.org/CorpusID:156012079

5. Saisana M, Saltelli A. *Corruption Perceptions Index 2012 - Statistical Assessment*. Luxembourg: Publications Office of the European Union (2012).

6. Andvig JC. *NUPI Working Paper Department of International Economics Crime, Poverty and Police Corruption in Non-Rich Countries* (2008).

7. Danford O, Kimathi M, Mirau S. Mathematical modelling and analysis of corruption dynamics with control measures in Tanzania. *Math Informat.* (2020) 19:57–79. doi: 10.22457/jmi.v19a07179

8. Eguda FY Oguntolu F, Ashezua T. Understanding the dynamics of corruption using mathematical modeling approach. *Int J Innovat Sci Eng Technol.* (2017) 4:190–7.

9. Kebede G. Political corruption: political and economic state capture in Ethiopia. *Eur Sci J.* (2013) 9.

10. Legesse L, Shiferaw F. Modelling corruption dynamics and its analysis. *Ethiop J Sci Sustain Dev.* (2018) 5:13–27. doi: 10.20372/ejssdastu:v5.i2.2018.34

11. Abdulrahman S. Stability analysis of the transmission dynamics and control of corruption. *Pac J Sci Technol.* (2014) 15:99–113.

12. Nathan OM, Jackob KO. Stability analysis in a mathematical model of corruption in Kenya. *Asian Res J Math.* (2019) 15:1–15. doi: 10.9734/arjom/2019/v15i430164

13. Hattaf K. A new generalized definition of fractional derivative with non-singular kernel. *Computation.* (2002) 8:49. doi: 10.3390/computation8020049

14. Blanchaed P, Krueger A, Krueger T, Martin P. The epidemics of corruption. *ArXiv*. (2005).

15. Brianzoni S, Coppier R, Michett R. Complex dynamics in a growth model with corruption in public procurement. *Discrete Dyn Nat Soc.* (2021) 2011:862396. doi: 10.1155/2011/862396

16. Athithan S, Ghosh M, Xue-Zhi L. Mathematical modeling and optimal control of corruption dynamics. *Asian Eur J Math.* (2018) 11:1850090. doi: 10.1142/S1793557118500900

17. Akanni JO, Akinpelu FO, Olaniyi S, Oladipo AT, Ogunsola AW. Modelling financial crime population dynamics: optimal control and cost-effectiveness analysis. *Int J Dynam Control.* (2020) 8:531–44. doi: 10.1007/s40435-019-00572-3

18. Akanni JO, Olaniyi S, Akinpelu FO. Global asymptotic dynamics of a nonlinear illicit drug use system. *J Appl Math Comput.* (2021) 66:39–60. doi: 10.1007/s12190-020-01423-7

19. Ibrahim OM, Okuonghae D, Ikhile MNO. A mathematical model of criminal gang rivalry: understanding the dynamics and implications. *Results Control Optimiz.* (2024) 14:100398. doi: 10.1016/j.rico.2024.100398

20. Hathroubi S. *Epidemic Corruption: A Bio-economic Homology*. Econstor (2013). Available online at: https://hdl.handle.net/10419/73558

21. Alemneh HT. Mathematical modeling, analysis, and optimal control of corruption dynamics. *Hind J Appl Math.* (2020) 2002:5109841. doi: 10.1155/2020/5109841

22. Iheonu NO, Nwajeri UK, Omame A. A non-integer order model for Zika and Dengue co-dynamics with cross-enhancement. *Healthc Anal.* (2023) 4:100276. doi: 10.1016/j.health.2023.100276

23. Peter OJ, Panigoro HS, Abidemi A, Ojo MM, Oguntolu FA. Mathematical model of COVID-19 pandemic with double dose vaccination. *Acta Biotheor.* (2023) 71:9. doi: 10.1007/s10441-023-09460-y

24. Gutema TW, Wedajo AG, Koya PR. Sensitivity and bifurcation analysis of corruption dynamics model with control measure. *Int J Math Ind.* doi: 10.1142/S2661335224500096

25. Dejene D, Worku T, Koya PR. Modeling the transmission and dynamics of COVID-19 using self-protection and isolation as control measures. *Math Model Appl.* (2020) 5:191–201. doi: 10.11648/j.mma.20200503.18

26. Van den Driessche P, Watmough J. Reproduction numbers and sub-threshold endemic equilibrium for compartmental models of disease transmission. *Math Biosci.* (2002) 180:29–48. doi: 10.1016/S0025-5564(02)00108-6

27. Hailemichael DD, Geremew KE, Koya PR. Effect of vaccination and culling on the dynamics of rabies transmission from stray dogs to domestic dogs. *Hind J Appl Math.* (2022) 2022:2769494. doi: 10.1155/2022/2769494

28. Diekmann O, Heesterbeek JAP. *Mathematical Epidemiology of Infectious Diseases: Model Building, Analysis and Integration*. New York, NY: Wiley (2000).

29. Osman M, Adu I, Isaac AK. Simple mathematical model for malaria transmission. *J Adv Math Comp Sci.* (2017) 25:1–24. doi: 10.9734/JAMCS/2017/37843

30. LaSalle JP. *The Stability of Dynamical Systems*. Philadelphia, PA: SIAM (1976).

31. Gumel A. Introduction to dynamical system in mathematical epidemiology. In: *Icmcsnuc Workshop, Abuja, Nigeria* (2007).

32. Goswami NK, Olaniyi S, Abimbade SF, Chuma FM. A mathematical model for investigating the effect of media awareness programs on the spread of COVID-19 with optimal control. *Healthc Anal.* (2024) 5:100300. doi: 10.1016/j.health.2024.100300

33. Olaniyi S, Kareem GG, Abimbade SF, Chuma FM, Sangoniyi SO. Mathematical modelling and analysis of autonomous HIV/AIDS dynamics with vertical transmission and nonlinear treatment. *Iran J Sci.* (2024) 48:181–92. doi: 10.1007/s40995-023-01565-w

34. Lenhart S, Workman JT. *Optimal Control Applied to Biological Models, 1st Edn*. Chapman and Hall/CRC (2007). p. 274

35. Fleming WH, Rishel RW. *Deterministic and Stochastic Optimal Control, Vol. 1*. New York, NY: Springer Science & Business Media (2012).

36. Wangari IM, Olaniyi S, Lebelo RS, Okosun KO. Transmission of COVID-19 in the presence of single-dose and double-dose vaccines with hesitancy: mathematical modeling and optimal control analysis. *Front Appl Math Stat.* (2023) 9:1292443. doi: 10.3389/fams.2023.1292443

37. Duressa Keno T, Mosisa Legesse, F. Modelling and optimal control strategies of corruption dynamics. *Appl Math Inform Sci.* (2023) 17:67383. doi: 10.18576/amis/170416

38. Pontryagin LS, Boltyanskii VG, Gamkrelidze RV, Mischenko EF. *The Mathematical Theory of Optimal Processes*. New York, NY: Wiley Interscience (1962).

39. Hailemichael DD, Edessa GK, Koya PR. Mathematical modeling of dog rabies transmission dynamics using optimal control analysis. *Contemp Math.* (2023) 4:296–319. doi: 10.21203/rs.3.rs-2682230/v1

40. Coddington EA, Levinson N. *Theory of Ordinary Differential Equations*. New York, NY: Tata McGraw-Hill Education (1955).

41. Fantaye AK, Birhanu ZK. Mathematical model and analysis of corruption dynamics with optimal control. *J Appl Math.* (2022) 2022:8073877. doi: 10.1155/2022/8073877

42. Abidemi A, Olaniyi S, Adepoju OA. An explicit note on the existence theorem of optimal control problem. *J Phys Conf Ser.* (2022) 2199:012021. doi: 10.1088/1742-6596/2199/1/012021

frontiers | Frontiers in Applied Mathematics and Statistics

TYPE Original Research
PUBLISHED 09 May 2024
DOI 10.3389/fams.2024.1373565

OPEN ACCESS

EDITED BY
Xiang-Sheng Wang,
University of Louisiana at Lafayette,
United States

REVIEWED BY
Kaifa Wang,
Southwest University, China
Thitiya Theparod,
Mahasarakham University, Thailand

*CORRESPONDENCE
Zhen Jin
✉ jinzhn@263.net
Junyuan Yang
✉ yjyang66@sxu.edu.cn
Yuqi Wen
✉ 18636669323@163.com

RECEIVED 20 January 2024
ACCEPTED 08 April 2024
PUBLISHED 09 May 2024

CITATION
Appiah RF, Jin Z, Yang J, Asamoah JKK and Wen Y (2024) Mathematical modeling of two strains tuberculosis and COVID-19 vaccination model: a co-infection study with cost-effectiveness analysis.
Front. Appl. Math. Stat. 10:1373565.
doi: 10.3389/fams.2024.1373565

Mathematical modeling of two strains tuberculosis and COVID-19 vaccination model: a co-infection study with cost-effectiveness analysis

Raymond Fosu Appiah[1], Zhen Jin[1]*, Junyuan Yang[1]*, Joshua Kiddy K. Asamoah[2,3] and Yuqi Wen[4]*

[1]Complex Systems Research Center, Shanxi University, Taiyuan, China, [2]Department of Mathematics, Saveetha School of Engineering SIMATS, Chennai, India, [3]Department of Mathematics, Kwame Nkrumah University of Science and Technology, Kumasi, Ghana, [4]School of Materials Science & Engineering, Beijing Institute of Technology, Beijing, China

Tuberculosis and COVID-19 co-infection is currently the major issue of public health in many nations, including Ghana. Therefore, to explore the effects of the two Tuberculosis strains on COVID-19, we suggest a Tuberculosis and COVID-19 co-infection model. The study also provides the most economical and effective control methods to reduce the co-infection of tuberculosis and COVID-19. Based on the behavioral patterns of the two Tuberculosis strains and COVID-19 reproduction numbers, the stability of the co-infection model is examined. We explore the sensitivity of the parameters to examine the effect of the drug-resistant and drug-sensitive strain of Tuberculosis on the co-infection of COVID-19. We determine the most cost-effective and optimal treatment strategies that aim to maximize outcomes while minimizing tuberculosis and/or COVID-19 incidences, cost-effectiveness, and optimization approaches. The outcomes of this work contribute to a better understanding of Tuberculosis and COVID-19 epidemiology and provide insights into implementing interventions needed to minimize Tuberculosis and COVID-19 burden in similar settings worldwide.

KEYWORDS

tuberculosis (TB), COVID-19, co-infection, optimal control, cost-effectiveness

Introduction

Over time, tuberculosis (TB) has emerged as a major public health concern due to its spread, particularly in developing nations. This is because tuberculosis is endemic in these nations, where drug-resistant tuberculosis, poverty, and insufficient diagnostic techniques are some of the factors that make the disease more difficult to treat [1]. World Health Organization (WHO) health statistics from [2] account that ∼1.4 million deaths were attributed to tuberculosis (TB) out of the 10.4 million cases reported globally in 2015 [3]. This indicates that tuberculosis (TB) affects about one-third of the world's population each year, which makes it one of the top 10 leading causes of death worldwide.

Due to vaccine inefficacy, chemotherapy has been the cornerstone of apparent control programs for TB. Antibiotic treatment for drug-resistant strains of TB patients is much more expensive and takes time compared with drug-sensitive strains of TB patients. Antibiotic-resistant tuberculosis (TB), which increases the risk of relapse and can arise

from medication treatment non-compliance, is seriously harming public health and has become a societal problem [4, 5].

Conversely, COVID-19 caused over 6 million deaths globally, and approximately, by March 2022, 480 million incidences were reported. Presently, there is growing evidence that patients with drug-sensitive TB and drug-resistant TB disease are more likely to develop a severe case of COVID-19, as reported in [6]. Even in cases where the force of reinfection is relatively weak, the COVID-19 reinfection scenario using the SIR model demonstrates that transmission could arise as a result of the immunity waning [7]. A COVID-19 model, which involves infection via items induced with SARS-CoV-2, is proposed to be made public aware [8]. The disease COVID-19 spreads swiftly, sparking a pandemic and posing a threat to world health. Other sectors, particularly the socioeconomic sector, have been significantly impacted by the pandemic [9]. According to the World Meter, as of 30 April 2022, there were 6,257,512 COVID-19 fatalities worldwide and 512,466,045 reported incidences. The results emphasize the necessity of taking steps to minimize the transmission of COVID-19 and TB. One way mathematics is essential to simulating the disease's epidemic phenomenon is by using a deterministic model to study the disease's transmission. Numerous developments have been made in analyzing the COVID-19 model with declining immunity. The natural immunity period is for the latter group, and models with symptomatic and asymptomatic infected populations show that the vaccine efficacy level determines when to begin the massive vaccination strategy [10].

The respiratory disease known as Coronavirus Disease 2019 (COVID-19) is a member of the Coronaviridae family. The α-Coronavirus, β-Coronavirus, γ-Coronavirus, and δ-Coronavirus are the four strain varieties of the virus. Humans are impacted by the first two, but bird infections are the main cause of the remaining two [11]. The source and origin of the virus are still unknown, despite the fact that COVID-19 is classified as a zoonotic disease and linked to the family of bats. After SARS and MERS, COVID-19 is the third new coronavirus of the 21st century to generate a significant outbreak that swept across 210 countries globally [12]. The variations of concern (VOC) introduce additional uncertainties and hamper efforts to prevent the disease, even as promising new vaccinations have emerged. VOCs, as described by the US Centers for Disease Control and Prevention, are more severe and highly transmissible strains of SARS-CoV-2 that significantly reduce vaccine effectiveness. Since December 2020, a number of VOCs have surfaced. Not long after the β-Coronavirus variation (B.1.351) was reported in South Africa, the α-Coronavirus variant (B.1.1.7) was initially identified with a 50% higher transmission in the United Kingdom. The δ-Coronavirus version (B.1.167.2) was originally discovered in India and classified on 11th May 2021 [13], whereas the γ-Coronavirus variant (P.1) was initially discovered in Brazil [14].

While less severe than earlier VOCs, the Omicron variety (B.1.1.529) is even more transmissible than δ-Coronavirus and was first discovered in South Africa and Botswana in 2021 [15]. Large recent increases in new COVID cases across national boundaries have been attributed to these variations. Countries with high vaccination rates experienced notable increases in incidence when the δ-Coronavirus variety emerged as the predominant virus worldwide [16]. Vaccines are less efficient in preventing δ-Coronavirus than previous forms, which made it more deadly. One dose of BNT162b2 (Pfizer-BioNTech) or ChAdOx1 (AstraZeneca) provides immunity against the δ-Coronavirus VOC, although immunity against the α-Coronavirus VOC is 45–52% [16]. Less protection against the δ-Coronavirus form was also demonstrated to be conferred by receiving two doses [16]. The enormous increases in infectious cases we saw globally in 2021 were caused by a lower mutation in the receptor-binding region of the δ-Coronavirus SARS-CoV-2 spike protein [17]. The Omicron version caused much greater worldwide spikes in cases in December 2021. Compared to the wild-type strain, Omicron was discovered to contain 33 mutations in its spike protein [18]. Given that vaccines lose their effectiveness over time and society reopens to more viral encounters, countries must reevaluate how best to implement vaccination programs in light of the significant changes that have been observed across a variety of volatile organic compounds.

While the World Health Organization and the Centers for Disease Control and Prevention have released certain health advisories and suggestions for individuals who are more susceptible to negative results from COVID-19, individuals who are co-infected with COVID-19 and have TB are at higher risk of dying [19]. A number of studies have suggested that COVID-19 may exacerbate or reactivate tuberculosis (TB), and some have even linked tuberculosis to severe COVID-19 [20–22]. Pathology-wise, diseases caused by SARS-CoV-2 and Mycobacterium tuberculosis to the immunomodulation tend to cause an imbalanced inflammatory response, which furthers the development and deterioration of both diseases [23]. In addition, patients with severe COVID-19 may be more susceptible to reactivation or new infection-related active TB [24].

The aforementioned issues motivate this study to explore the optimal control strategies incorporating cost-effectiveness analysis to mitigate TB and COVID-19. The next section illustrates the co-infection model assumptions and formulation such that people with latent TB will become active at a specific rate. Additionally, it assumes that some treated patients with active tuberculosis will not complete their course of treatment and that some of them will develop drug-resistant tuberculosis. Four control mechanisms for public education, vaccination, case finding, and case holding efforts are incorporated into this model. The article is arranged as follows: Section 2 presents the detailed framework of the epidemiological co-infection model, together with the definition of the parameters and respective values. Section 3 presents the analysis of the model's positivity of solutions, computation of the sub-models' reproduction numbers, and stability of the sub-models. Section 4 presents the model parameters estimation and sensitivity. Section 5 presents the optimal control analysis. Section 6 presents the cost-effectiveness analysis. Finally, Section 7 presents the concluding remarks of this study.

The tuberculosis (TB) and COVID-19 model

The proposed epidemiological model comprising tuberculosis and COVID-19 vaccination is characterized by two sub-models

(TB and COVID-19) with the following features. It is divided into 12 distinct compartments, namely $S(t)$: Susceptible class, $V(t)$: Vaccinated class, $E_{st}(t)$: individuals exposed to drug-sensitive (DS) strain TB only, $I_{st}(t)$: Individuals infectious with drug-sensitive (DS) TB only, $E_{rt}(t)$: Individuals exposed to drug-resistant (DR) strain of TB only, $I_{rt}(t)$: Individuals infectious with drug-resistant (DR) strain TB only, $E_c(t)$: COVID-19 exposed individuals only, $I_c(t)$: Individuals infectious with COVID-19 only, $I_{stc}(t)$: Individuals infectious with drug-sensitive (DS) strain of TB and COVID-19, $I_{rtc}(t)$: Individuals infectious with drug-resistant (DR) strain of TB and COVID-19, $T(t)$: Treated class consisting of individuals from both strains of TB, and $R(t)$: Recovered class consisting of treated individuals of TB and/or COVID-19. The dynamics of the model are as follows:

- We illustrate the TB stream of the model; susceptible and vaccinated individuals are exposed to either a drug-sensitive (DS) strain or drug-resistant (DR) strain of tuberculosis where $S(t)$ compartment recruit individuals by Λ, where individuals in $S(t)$ and $V(t)$ are infected by the two strains at the rate of $\beta_{st}SI_{st}$, $\beta_{rt}SI_{rt}$ and $\sigma\beta_{st}VI_{st}$, $\sigma\beta_{rt}VI_{rt}$ respectively, where σ belonging to [0, 1] denotes the vaccine protection rate. If $\sigma = 0$, then the vaccination protection is 100% efficient, $\sigma = 1$ implies that the vaccination protection efficiency is 0 and the immunity waning rate coefficient in the vaccinated host is ϑ, which is given as $\vartheta \geq 1$. We assume that a proportion of b and $1 - b$ of the individuals in $S(t)$ enters the drug-sensitive (DS) classes $I_{st}(t)$ and $E_{st}(t)$, respectively, and a proportion of b and $(1 - b)$ of the individuals in $V(t)$ enter $I_{st}(t)$ and $E_{st}(t)$, respectively, similar to the drug-resistant (DR) classes by $I_{rt}(t)$ and $E_{rt}(t)$, where the rate of death due to drug-sensitive (DS) strain of TB disease is given as d_1 and the rate of death due to drug-resistant (DR) strain of TB disease is given as d_2. Here, we assume that induced TB death rates are different for drug-sensitive (DS) and drug-resistant (DR) strains of TB due to differences in transmission rate and response to prophylaxis. The individuals in $E_{st}(t)$ identified to be infected move to $T(t)$ at the rate of γ_1 for prophylaxis while the rest move to $I_{st}(t)$ at the rate of δ_{st}. Individuals in $E_{rt}(t)$ moves to $I_{rt}(t)$ at the rate of δ_{rt}. A proportion of k $I_{st}(t)$ individuals move to $I_{stc}(t)$ at the rate of $k\gamma_2$ due to COVID-19 infection at the same time, while a proportion of $1 - k$ moves to $T(t)$ at the rate of $(1-k)\gamma_2$ for prophylaxis. Again, a proportion of m individuals in $I_{rt}(t)$ move to $I_{rtc}(t)$ at the rate of $m\gamma_3$ due to COVID-19 infection at the same time, while a proportion of $1 - m$ moves to $T(t)$ at the rate of $(1 - m)\gamma_3$ for prophylaxis, where k, m belong to $[0, 1]$. The individuals in $T(t)$ compartment who undergo successful prophylaxis recover at the rate of ε_5 while the rest are re-infected by $\omega\lambda_1$, where $\omega = [0, 1]$ due to unsuccessful prophylaxis.
- We illustrate the COVID-19 stream of the model; susceptible and vaccinated individuals are exposed to COVID-19 at the rate of $\beta_c SI_c$ and $\sigma\beta_c VI_c$, respectively. The individuals in $E_c(t)$ identified with mild symptoms of the disease can recover at the rate of ε_1 due to strong immunity, while the rest become infected and move to $I_c(t)$ at the rate of δ_c. The individuals in $I_c(t)$ recover at the rate of ε_2, while others may develop any strains of TB and move to $I_{stc}(t)$, $I_{rtc}(t)$ at the rate of φ_1, φ_2, respectively. A proportion of g $I_{st}(t)$ individuals move to $I_{st}(t)$ at the rate of $g\varepsilon_3$, while a proportion of $(1 - g)$ recovers at the rate of $(1 - g)\varepsilon_3$; similarly, individuals in $I_{rtc}(t)$ move to $I_{rt}(t)$ at the rate of $h\varepsilon_4$, while a proportion of $1 - h$ recovers at the rate of $(1 - h)\varepsilon_4$ where g, h belong to $[0, 1)$. The respective rate of death due to TB and/or COVID-19 infection is given as d_i, where $i = 3, 4, 5$ respectively. The meanings of the rest of the parameters illustrated in the model are tabulated. The control efforts $U_1(t), U_2(t), U_3(t)$, and $U_4(t)$ for optimal control analysis would be applied and explained in detail in the subsequent section.

The total population $N(t)$ in Equation (1) is defined based on the flowchart diagram Figure 1 as follows:

$$N(t) = S(t) + V(t) + E_{st}(t) + I_{st}(t) + E_{rt}(t) + I_{rt}(t) + E_c(t) + I_c(t) + I_{stc}(t) + I_{rtc}(t) + T(t) + R(t). \quad (1)$$

We formulate the model [see Equation (2)] as follows:

$$\begin{cases} \frac{dS}{dt} = \Lambda + \vartheta V - (1-b)\lambda_1 S - a_1 S, \\ \frac{dV}{dt} = \alpha S - (1-b)\lambda_1 \sigma V - a_2 V, \\ \frac{dE_{st}}{dt} = \frac{[(1-b)(S+\sigma V)+b\omega T]\beta_{st} I_{st}}{N} - a_3 E_{st}, \\ \frac{dI_{st}}{dt} = \frac{[b(S+\sigma V)+(1-b)\omega T]\beta_{st} I_{st}}{N} + \delta_{st} E_{st} + g\varepsilon_3 I_{stc} - a_4 I_{st}, \\ \frac{dE_{rt}}{dt} = \frac{[(1-b)(S+\sigma V)+b\omega T]\beta_{rt} I_{rt}}{N} - a_5 E_{rt}, \\ \frac{dI_{rt}}{dt} = \frac{[b(S+\sigma V)+(1-b)\omega T]\beta_{rt} I_{rt}}{N} + \delta_{rt} E_{rt} + h\varepsilon_3 I_{rtc} - a_6 I_{rt}, \\ \frac{dE_c}{dt} = \frac{(S+\sigma V)\beta_c I_c}{N} - a_7 E_c, \\ \frac{dI_c}{dt} = \delta_c E_c - a_8 I_c, \\ \frac{dI_{stc}}{dt} = \varphi_1 I_c + k\gamma_2 I_{st} - a_9 I_{stc}, \\ \frac{dI_{rtc}}{dt} = \varphi_2 I_c + m\gamma_3 I_{rt} - a_{10} I_{rtc}, \\ \frac{dT}{dt} = \gamma_1 E_{st} + (1-k)\gamma_2 I_{st} + (1-m)\gamma_3 I_{rt} - (\mu + \varepsilon_5 + \omega\lambda_1) T, \\ \frac{dR}{dt} = \varepsilon_1 E_c + \varepsilon_2 I_c + (1-g)\varepsilon_3 I_{stc} + (1-h)\varepsilon_4 I_{rtc} + \varepsilon_5 T - \mu R. \end{cases} \quad (2)$$

where $\lambda_1 = \frac{[\beta_{st} I_{st} + \beta_{rt} I_{rt}] + \beta_c [I_c + I_{stc} + I_{rtc}]}{N}$, $a_1 = \mu + \alpha$, $a_2 = \mu + \vartheta$, $a_3 = \mu + \delta_{st} + \gamma_1$, $a_4 = \mu + d_1 + \gamma_2$, $a_5 = \mu + \delta_{rt}$, $a_6 = \mu + d_2 + \gamma_3, a_7 = \mu + \delta_c + \varepsilon_1, a_8 = \mu + d_3 + \varphi_1 + \varphi_2 + \varepsilon_2, a_9 = \mu + d_4 + \varepsilon_3$, $a_{10} = \mu + d_5 + \varepsilon_4$.

With initial conditions, $S(0) \geq 0, V(0) \geq 0, E_{st}(0) \geq 0, I_{st}(0) \geq 0, E_{rt}(0) \geq 0, I_{rt}(0) \geq 0$, $E_c(0) \geq 0, I_c(0) \geq 0, I_{stc}(0) \geq 0, I_{rtc}(0) \geq 0, T(0) \geq 0, R(0) \geq 0$. All the parameters of system (2) are non-negative.

TB and COVID-19 co-infection model's positivity and boundedness

The model (2) variables and parameters are non-negative since it is based on the population with TB and COVID-19. We state the following theorems to show that all variables of model (2) are non-negative and bounded.

Theorem 1: Define $Y(t) = S(t), V(t), E_{st}(t), I_{st}(t), E_{rt}(t), I_{rt}(t), E_c(t), I_c(t), I_{stc}(t) I_{rtc}(t), T(t), R(t)$, if $Y(0) \geq 0$, then $Y(t) \geq 0$, and its solutions and initial values are non-negative for $t > 0$.

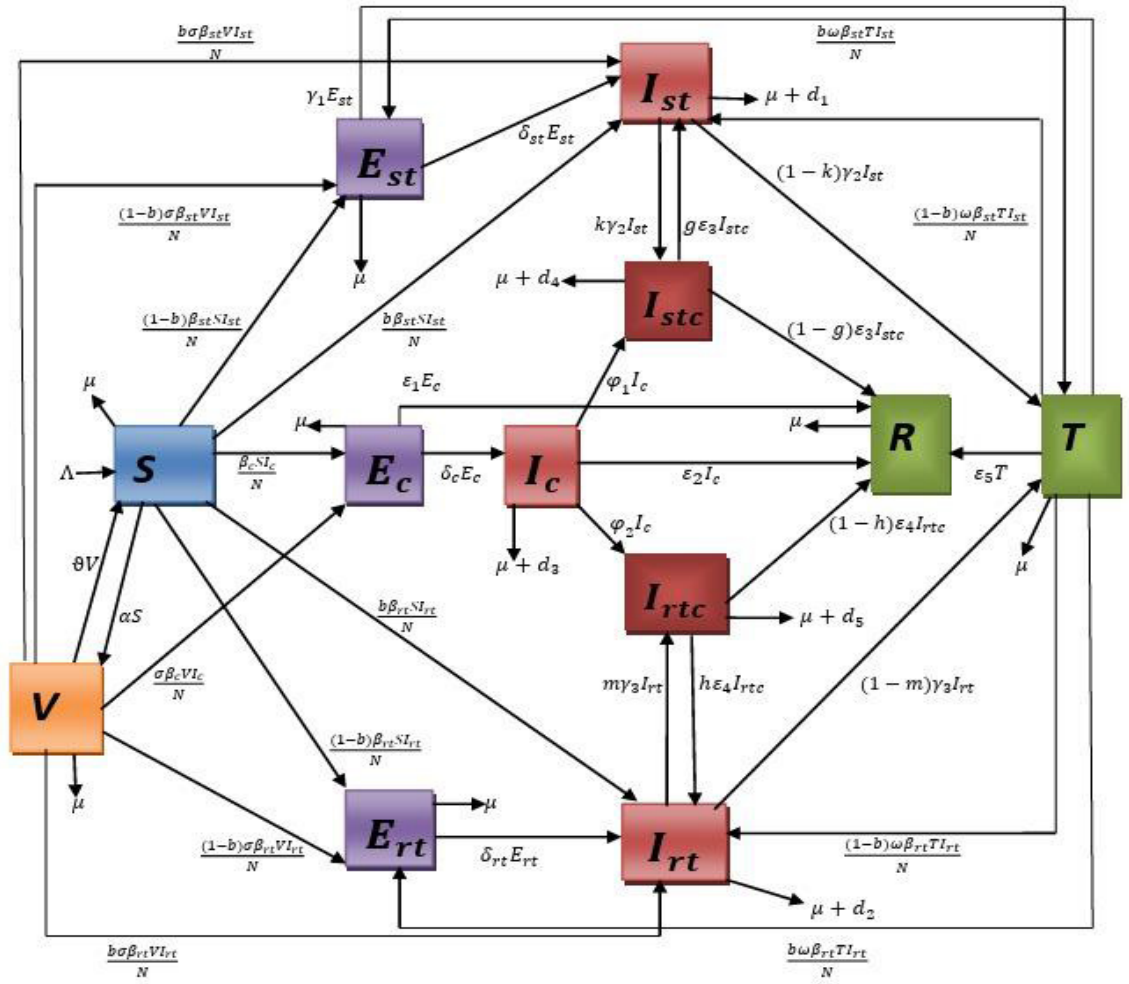

FIGURE 1
Flowchart representation of the TB-COVID-19 vaccination model.

Proof: Let us consider the following instance that there exists an initial time t_i, such that

$\min\{Y(t_i)\} > 0$ and $\min\{Y(t)\} > 0$ for all $t \in [0, t_i)$.

Here, $Y(t) = S(t), V(t), E_{st}(t), I_{st}(t), E_{rt}(t), I_{rt}(t), E_c(t), I_c(t), I_{stc}(t) I_{rtc}(t), T(t), R(t)$. Without loss of generalization, $\min\{Y(t_i)\} = S(t_i)$.

Therefore, $S(t_i) = 0$, $V(t_i) > 0$ and $S(t) > 0$ for all $t \in [0, t_i)$. However,

$\frac{dS(t_i)}{dt} = \Lambda + \vartheta V(t_i) > 0$,

Since $\Lambda \geq 0$, $S(t_i) > S(0) \geq 0$.

This contradicts the claim $S(t_i) = 0$. Therefore, $S(t) > 0$ for all $t \geq 0$. This shows that all solutions are positive for $t \geq 0$ in all other cases.

Theorem 2: To show the boundedness of solutions of model (2), define a positive invariant set as $Q = \left\{(S, V, E_{st}, I_{st}, E_{rt}, I_{rt}, E_c, I_c, I_{stc}, I_{rtc}, T, R) \in R_+^{12} : N(t) \leq \frac{\Lambda}{\mu}\right\}$, which have positive solutions.

Proof: Let us consider the total population of model (2) $N(t)$ as

$$N(t) = S(t) + V(t) + E_{st}(t) + I_{st}(t) + E_{rt}(t) + I_{rt}(t) + E_c(t) + I_c(t) + I_{stc}(t) + I_{rtc}(t) + T(t) + R(t). \quad (3)$$

The rate of change of $N(t)$ of Equation (3) is given as

$$\begin{aligned} N'(t) &= S'(t) + V'(t) + E'_{st}(t) + I'_{st} + E'_{rt} + I'_{rt} + E'_c + I'_c + I'_{stc} + I'_{rtc} + T'(t) + R'(t), \\ N'(t) &= \Lambda - \mu S - \mu V - \mu E_{st} - (\mu + d_1) I_{st} - \mu E_{rt} - (\mu + d_2) I_{rt} - \mu E_c - (\mu + d_3) I_c - (\mu + d_4) I_{stc} - (\mu + d_5) I_{rtc} - \mu T - \mu R, \\ N'(t) &= \Lambda - \mu N(t) - (d_1 I_{st} + d_2 I_{rt} + d_3 I_c + d_4 I_{stc} + d_5 I_{rtc}) \\ &\leq \Lambda - \mu N(t). \end{aligned} \quad (4)$$

This follows that from Equation (4),

$N(t) \leq \frac{\Lambda}{\mu}\left(1 - e^{-\mu t}\right) + N(0) e^{-\mu t}$.

Then, $0 < N(t) \leq \frac{\Lambda}{\mu}$, if $N(0) \leq \frac{\Lambda}{\mu}$. That is, $N(t)$ is bounded, and all solutions in Q approach enter or remain in Q. If $t \to \infty, 0 \leq N(t)$ shows that $N(t)$ is a set of positive invariant in the region R_+^{12}. Therefore, the proof is complete.

Sub-models analysis

This subsection explores the reproduction numbers and the stability of the two sub-models.

Tuberculosis (TB) sub-model

The TB sub-model's disease-free equilibrium point is achieved by setting $E_c = I_c = I_{stc} = I_{rtc} = R = 0$ of system (2) and equate it to zero, the result in Equation (5) is as follows.

$$\begin{cases} \frac{dS}{dt} = \Lambda + \vartheta V - \frac{(1-b)(\beta_{st}I_{st}+\beta_{rt}I_{rt})S}{N} - a_1 S, \\ \frac{dV}{dt} = \alpha S - \frac{(1-b)(\beta_{st}I_{st}+\beta_{rt}I_{rt})\sigma V}{N} - a_2 V, \\ \frac{dE_{st}}{dt} = \frac{[(1-b)(S+\sigma V)+b\omega T]\beta_{st}I_{st}}{N} - a_3 E_{st}, \\ \frac{dI_{st}}{dt} = \frac{[b(S+\sigma V)+(1-b)\omega T]\beta_{st}I_{st}}{N} + \delta_{st}E_{st} - a_4 I_{st}, \\ \frac{dE_{rt}}{dt} = \frac{[(1-b)(S+\sigma V)+b\omega T]\beta_{rt}I_{rt}}{N} - a_5 E_{rt}, \\ \frac{dI_{rt}}{dt} = \frac{[b(S+\sigma V)+(1-b)\omega T]\beta_{rt}I_{rt}}{N} + \delta_{rt}E_{rt} - a_6 I_{rt}, \\ \frac{dT}{dt} = \gamma_1 E_{st} + (1-k)\gamma_2 I_{st} + (1-m)\gamma_3 I_{rt} - \\ \qquad \left(\varepsilon_5 + \frac{\omega(1-b)(\beta_{st}I_{st}+\beta_{rt}I_{rt})}{N}\right) T. \end{cases} \tag{5}$$

where $N = S + V + E_{st} + I_{st} + E_{rt} + I_{rt} + T$.

The TB sub-model (5) has a positive invariant in the region R_+^7 with $Q_T = \left\{(S, V, E_{st}, I_{st}, E_{rt}, I_{rt}, T) \in R_+^7 : N(t) \leq \frac{\Lambda}{\mu}\right\}$, as shown in Theorems 2 and 3.

Tuberculosis (TB) sub-model's basic reproduction number

Here, we define the basic reproduction number and the stability of the TB sub-model.

The disease-free equilibrium E_{0T}

It is globally stable, as demonstrated under the COVID-19 sub-model. The disease-free equilibrium $E_{0T} = (S_0, V_0, 0, 0, 0, 0, 0)$ and the result is given in Equation (6).

$$S_0 = \frac{\Lambda a_2}{a_1 a_2 - \vartheta\alpha}, V_0 = \frac{\Lambda\alpha}{a_1 a_2 - \vartheta\alpha},$$
$$E_{0T} = \left(\frac{\Lambda a_2}{a_1 a_2 - \vartheta\alpha}, \frac{\Lambda\alpha}{a_1 a_2 - \vartheta\alpha}, 0, 0, 0, 0, 0\right). \tag{6}$$

The corresponding Jacobian matrix evaluated at disease-free equilibrium, $J_{E_{0T}}$ is given in Equation (7)

$$J_{E_{0T}} = \begin{pmatrix} -a_1 & \vartheta & 0 & -\frac{(1-b)\beta_{st}S_0}{N_0} & 0 & -\frac{(1-b)\beta_{rt}S_0}{N_0} & 0 \\ \alpha & -a_2 & 0 & -\frac{(1-b)\beta_{st}\sigma V_0}{N_0} & 0 & -\frac{(1-b)\beta_{rt}\sigma V_0}{N_0} & 0 \\ 0 & 0 & -a_3 & \frac{(1-b)\beta_{st}[S_0+\sigma V_0]}{N_0} & 0 & 0 & 0 \\ 0 & 0 & \delta_{st} & \frac{b\beta_{st}[S_0+\sigma V_0]}{N_0} - a_4 & 0 & 0 & 0 \\ 0 & 0 & 0 & 0 & -a_5 & \frac{(1-b)\beta_{rt}[S_0+\sigma V_0]}{N_0} & 0 \\ 0 & 0 & 0 & 0 & \delta_{rt} & \frac{b\beta_{rt}[S_0+\sigma V_0]}{N_0} - a_6 & 0 \\ 0 & 0 & \gamma_1 & (1-k)\gamma_2 & 0 & (1-m)\gamma_3 & -(\mu+\varepsilon_5) \end{pmatrix}. \tag{7}$$

where $N_0 = S_0 + \sigma V_0$ using the Jacobian at the disease-free equilibrium E_{0T}.

According to the explanation in [25], the spectral radius of the next-generation operator $G = FV^{-1}$ denotes the basic reproduction number. For sub-model (5), we have the square matrix with matrix F as the new infections and matrix V as the transition elements of the infected classes.

$$F = \begin{pmatrix} 0 & \frac{(1-b)\beta_{st}[S_0+\sigma V_0]}{N_0} & 0 & 0 \\ 0 & \frac{b\beta_{st}[S_0+\sigma V_0]}{N_0} & 0 & 0 \\ 0 & 0 & 0 & \frac{(1-b)\beta_{rt}[S_0+\sigma V_0]}{N_0} \\ 0 & 0 & 0 & \frac{b\beta_{rt}[S_0+\sigma V_0]}{N_0} \end{pmatrix},$$
$$V = \begin{pmatrix} a_3 & 0 & 0 & 0 \\ -\delta_{st} & a_4 & 0 & 0 \\ 0 & 0 & a_5 & 0 \\ 0 & 0 & -\delta_{rt} & a_6 \end{pmatrix}.$$

Hence, the reproduction numbers are

$$R_{st} = \frac{(1-b)\beta_{st}\delta_{st}[S_0+\sigma V_0]}{N_0 a_3 a_4}, R_{rt} = \frac{(1-b)\beta_{rt}\delta_{rt}[S_0+\sigma V_0]}{N_0 a_5 a_6},$$

where R_{st} and R_{rt} are the basic reproduction numbers of drug-sensitive (DS) and drug-resistant (DR) strains of TB, respectively. Substituting N_0, S_0 and V_0 give the following results:

$$R_{st} = \frac{(1-b)\beta_{st}\delta_{st}}{(\mu+\delta_{st}+\gamma_1)(\mu+d_1+\gamma_2)},$$
$$R_{rt} = \frac{(1-b)\beta_{rt}\delta_{rt}}{(\mu+\delta_{rt})(\mu+d_2+\gamma_3)},$$

The basic reproduction number is given as [see Equation (8)]

$$R_{0T} = \max\{R_{st}, R_{rt}\}. \tag{8}$$

Existence of TB sub-model endemic equilibrium

We explore the existence and uniqueness of the endemic equilibrium of sub-model (5).

If $R_{rt} > 1$, then the drug-resistant (DR) strain has the dominance in sub-model (5) with $F_{rt}^* = (S_{rt}^*, V_{rt}^*, 0, 0, E_{rt}^*, I_{rt}^*, T_{rt}^*)$ as a unique endemic equilibrium for the drug-resistant (DR) strain. Then, the endemic equilibrium follows as

$$\begin{cases} \Lambda + \vartheta V_{rt}^* - \lambda_1^* S_{rt}^* - a_1 S_{rt}^* = 0, \\ \alpha S_{rt}^* - \lambda_1^* \sigma V_{rt}^* - a_2 V_{rt}^* = 0, \\ \frac{[(1-b)(S_{rt}^*+\sigma V_{rt}^*)+b\omega T_{rt}^*]\beta_{rt}I_{rt}^*}{N_{rt}^*} - a_5 E_{rt}^* = 0, \\ \frac{[b(S_{rt}^*+\sigma V_{rt}^*)+(1-b)\omega T_{rt}^*]\beta_{rt}I_{rt}^*}{N_{rt}^*} + \delta_{rt}E_{rt}^* - a_6 I_{rt}^* = 0, \\ (1-m)\gamma_3 I_{rt}^* - (\varepsilon_5 + \omega\lambda_1^*) T_{rt}^* = 0. \end{cases} \tag{9}$$

where $\lambda_1^* = \frac{(1-b)\beta_{rt}I_{rt}^*}{N_{rt}^*}$ and $N_{rt}^* = S_{rt}^* + V_{rt}^* + E_{rt}^* + I_{rt}^* + T_{rt}^*$.

Simplifying Equation (9) gives the following.

$$\begin{cases} S_{rt}^* = \frac{(a_2+\sigma\lambda_1^*)\Lambda}{(a_1+\lambda_1^*)(a_2+\sigma\lambda_1^*)-\alpha\vartheta}, \\ V_{rt}^* = \frac{\Lambda\alpha}{(a_1+\lambda_1^*)(a_2+\sigma\lambda_1^*)-\alpha\vartheta}, \\ E_{rt}^* = \left[\frac{1}{a_5}\right]\left[\frac{\lambda_1^*\Lambda(a_2+\sigma\lambda_1^*+\sigma\alpha)}{(a_1+\lambda_1^*)(a_2+\sigma\lambda_1^*)-\alpha\vartheta} + \frac{b\omega\beta_{rt}(1-m)\gamma_3 I_{rt}^*}{(\varepsilon_5+\omega\lambda_1^*)}\right], \\ T_{rt}^* = \frac{(1-m)\gamma_3 I_{rt}^*}{(\varepsilon_5+\omega\lambda_1^*)}. \end{cases} \tag{10}$$

Simplifying Equation (10) gives the following equation for I_{rt}^*.

$$I_{rt}^* = \left(\frac{\left(\varepsilon_5 + \omega\lambda_1^*\right)\left(b\left(S_{rt}^* + \sigma V_{rt}^*\right) + a_5\right)}{\beta_{rt}^2\delta_{rt}\omega\left(1-m\right)\gamma_3}\right)\left(\frac{\left(1-b\right)\beta_{rt}\delta_{rt}}{a_5 a_6} - 1\right),$$

$$I_{rt}^* = \left(\frac{\left(\varepsilon_5 + \omega\lambda_1^*\right)\left(\frac{b\Lambda\left(a_2+\sigma\lambda_2^*+\sigma\alpha\right)}{\left(a_1+\lambda_2^*\right)\left(a_2+\sigma\lambda_2^*\right)-\alpha\vartheta} + a_5\right)}{\beta_{rt}^2\delta_{rt}\omega\left(1-m\right)\gamma_3}\right)\left(R_{rt}-1\right). \quad (11)$$

Since all the parameters associated with the model are non-negative, then from Equation (11) I_{rt}^* is always positive if and only if $R_{rt} > 1$. Hence, there exist endemic equilibrium if $R_{rt} > 1$.

Again, if $R_{st} > 1$, then the drug-sensitive (DS) strain has the dominance in sub-model (5) with $F_{st}^* = \left(S_{st}^*, V_{st}^*, E_{st}^*, I_{st}^*, 0, 0, T_{st}^*\right)$ as a unique endemic equilibrium of the drug-sensitive (DS) strain. Then, the endemic equilibrium follows as

$$\begin{cases} \Lambda + \vartheta V_{st}^* - \lambda_2^* S_{st}^* - a_1 S_{st}^* = 0, \\ \alpha S_{st}^* - \lambda_2^*\sigma V_{st}^* - a_2 V_{st}^* = 0, \\ \frac{\left[\left(1-b\right)\left(S_{st}^*+\sigma V_{st}^*\right)+b\omega T_{st}^*\right]\beta_{st}I_{st}^*}{N_{st}^*} - a_3 E_{st}^* = 0, \\ \frac{\left[b\left(S_{st}^*+\sigma V_{st}^*\right)+\left(1-b\right)\omega T_{st}^*\right]\beta_{st}I_{st}^*}{N_{st}^*} + \delta_{st}E_{st}^* - a_4 I_{st}^* = 0, \\ \gamma_1 E_{st}^* + \left(1-k\right)\gamma_2 I_{st}^* - \left(\varepsilon_5 + \omega\lambda_2^*\right)T_{st}^* = 0. \end{cases} \quad (12)$$

where $\lambda_2^* = \frac{\left(1-b\right)\beta_{st}I_{st}^*}{N_{st}^*}$ and $N_{st}^* = S_{st}^* + V_{st}^* + E_{st}^* + I_{st}^* + T_{st}^*$.

Simplifying Equation (12) gives the following.

$$\begin{cases} S_{st}^* = \frac{\left(a_2+\sigma\lambda_2^*\right)\Lambda}{\left(a_1+\lambda_2^*\right)\left(a_2+\sigma\lambda_2^*\right)-\alpha\vartheta}, \\ V_{st}^* = \frac{\Lambda\alpha}{\left(a_1+\lambda_2^*\right)\left(a_2+\sigma\lambda_2^*\right)-\alpha\vartheta}, \\ E_{st}^* = \left[\frac{1}{a_3}\right]\left[\frac{\lambda_2^*\Lambda\left(a_2+\sigma\lambda_2^*+\sigma\alpha\right)}{\left(a_1+\lambda_2^*\right)\left(a_2+\sigma\lambda_2^*\right)-\alpha\vartheta} + \frac{G_1 b\omega\beta_{st}I_{st}^*}{G_2}\right], \\ T_{st}^* = \frac{G_1}{G_2}. \end{cases} \quad (13)$$

where $G_1 = \left[\frac{\gamma_1}{a_3}\right]\left(S_{st}^* + \sigma V_{st}^*\right)\lambda_2^* + \left(1-k\right)\gamma_2 I_{st}^*, G_2 = \left(\varepsilon_5 + \omega\lambda_2^*\right) - \frac{\gamma_1 b\beta_{st}I_{st}^*}{a_3}$ and $\left(S_{st}^* + \sigma V_{st}^*\right) = \frac{\Lambda\left(a_2+\sigma\lambda_2^*+\sigma\alpha\right)}{\left(a_1+\lambda_2^*\right)\left(a_2+\sigma\lambda_2^*\right)-\alpha\vartheta}$.

Equation (13) gives the following equation for I_{st}^*.

$$I_{st}^* = \left(\frac{G_2\omega\beta_{st}a_3a_4}{G_1 b\beta_{st}\left(S_{st}^* + \sigma V_{st}^*\right)a_3 + a_3a_4 + \delta_{st}}\right)\left(\frac{\left(1-b\right)\beta_{st}\delta_{st}}{a_3a_4} - 1\right),$$

$$I_{st}^* = \left(\frac{G_2\omega\beta_{st}a_3a_4}{G_1 b\beta_{st}\left(S_{st}^* + \sigma V_{st}^*\right)a_3 + a_3a_4 + \delta_{st}}\right)\left(R_{st}-1\right). \quad (14)$$

Since all the parameters associated with the model are non-negative, then from Equation (14) I_{st}^* is always positive if and only if $R_{st} > 1$. Hence, there exist endemic equilibrium if $R_{st} > 1$.

COVID-19 sub-model

The COVID-19 sub-model's disease-equilibrium point is achieved by setting $E_{st} = I_{st} = E_{rt} = I_{rt} = I_{stc} = I_{rtc} = T = 0$ of system (2) to zero [see Equation (15)], the result is as follows.

$$\begin{cases} \frac{dS}{dt} = \Lambda + \vartheta V - \frac{\beta_c I_c S}{N} - a_1 S, \\ \frac{dV}{dt} = \alpha S - \frac{\beta_c I_c \sigma V}{N} - a_2 V, \\ \frac{dE_c}{dt} = \frac{\left(S+\sigma V\right)\beta_c I_c}{N} - a_7 E_c, \\ \frac{dI_c}{dt} = \delta_c E_c - a_8 I_c, \\ \frac{dR}{dt} = \varepsilon_1 E_c + \varepsilon_2 I_c - \mu R. \end{cases} \quad (15)$$

where $N = S + V + E_c + I_c + R$.

The COVID-19 sub-model (15) has a positive invariant in the region R_+^5 with $Q_C = \left\{(S, V, E_c, I_c, R) \in R_+^5 : N(t) \le \frac{\Lambda}{\mu}\right\}$, as shown in Theorem 2.

The COVID-19 sub-model's basic reproduction number

Here, we define the basic reproduction number and the stability of the COVID-19 sub-model.

The disease-free equilibrium E_{0C}

The disease-free equilibrium $E_{0C} = (S_0, V_0, 0, 0, 0, 0, 0)$, and the result is as follows in Equation (16):

$$S_0 = \frac{\Lambda a_2}{a_1a_2 - \vartheta\alpha}, V_0 = \frac{\Lambda\alpha}{a_1a_2 - \vartheta\alpha},$$

$$E_{0C} = \left(\frac{\Lambda a_2}{a_1a_2 - \vartheta\alpha}, \frac{\Lambda\alpha}{a_1a_2 - \vartheta\alpha}, 0, 0, 0, 0, 0\right). \quad (16)$$

The corresponding Jacobian matrix evaluated at disease-free equilibrium, $J_{E_{0C}}$, is given by Equation (17)

$$J_{E_{0C}} = \begin{pmatrix} -a_1 & \vartheta & 0 & -\frac{\beta_c S_0}{N_0} & 0 \\ \alpha & -a_2 & 0 & \frac{\beta_c\sigma V_0}{N_0} & 0 \\ 0 & 0 & -a_7 & \frac{\beta_c\left[S_0+\sigma V_0\right]}{N_0} & 0 \\ 0 & 0 & \delta_c & -a_8 & 0 \\ 0 & 0 & \varepsilon_1 & \varepsilon_2 & -\mu \end{pmatrix}. \quad (17)$$

Where $N_0 = S_0 + \sigma V_0$ using the Jacobian at the disease-free equilibrium E_{0C}. The basic reproduction number for the COVID-19 sub-model is given as

$$R_{0C} = \frac{\beta_c\delta_c\left[S_0 + \sigma V_0\right]}{N_0 a_7 a_8},$$

Substituting N_0, S_0 and V_0 give the following results in Equation (18).

$$R_{0C} = \frac{\beta_c\delta_c}{\left(\mu + \delta_c + \varepsilon_1\right)\left(\mu + d_3 + \varphi_1 + \varphi_2 + \varepsilon_2\right)}. \quad (18)$$

The COVID-19 sub-model's stability and existence of endemic equilibrium

We analyze the existence and uniqueness of the endemic equilibrium of model (15) as $D^* = \left(S^*, V^*, E_c^*, I_c^*, R^*\right)$.

$$\begin{cases} \Lambda + \vartheta V^* - \beta_c I_c^* - a_1 S^* = 0, \\ \alpha S^* - \beta_c\sigma V^* I_c^* - a_2 V^* = 0, \\ \left(S^* + \sigma V^*\right)\beta_c I_c^* - a_7 E_c^* = 0, \\ \delta_c E_c^* - a_8 I_c^* = 0, \\ \varepsilon_1 E_c^* + \varepsilon_2 I_c^* - \mu R^* = 0. \end{cases} \quad (19)$$

Simplifying Equation (19) gives the following.

$$\begin{cases} S^* = \frac{\Lambda\left(\sigma\beta_c I_c^* + a_2\right)}{\left(\beta_c I_c^* + a_1\right)\left(\sigma\beta_c I_c^* + a_2\right)-\alpha\vartheta}, \\ V^* = \frac{\Lambda\alpha}{\left(\beta_c I_c^* + a_1\right)\left(\sigma\beta_c I_c^* + a_2\right)-\alpha\vartheta}, \\ E_c^* = \frac{a_8 I_c^*}{\delta_c}, \\ R^* = \frac{1}{\mu}\left(\frac{\varepsilon_1 a_8}{\delta_c} + \varepsilon_2\right)I_c^*. \end{cases} \quad (20)$$

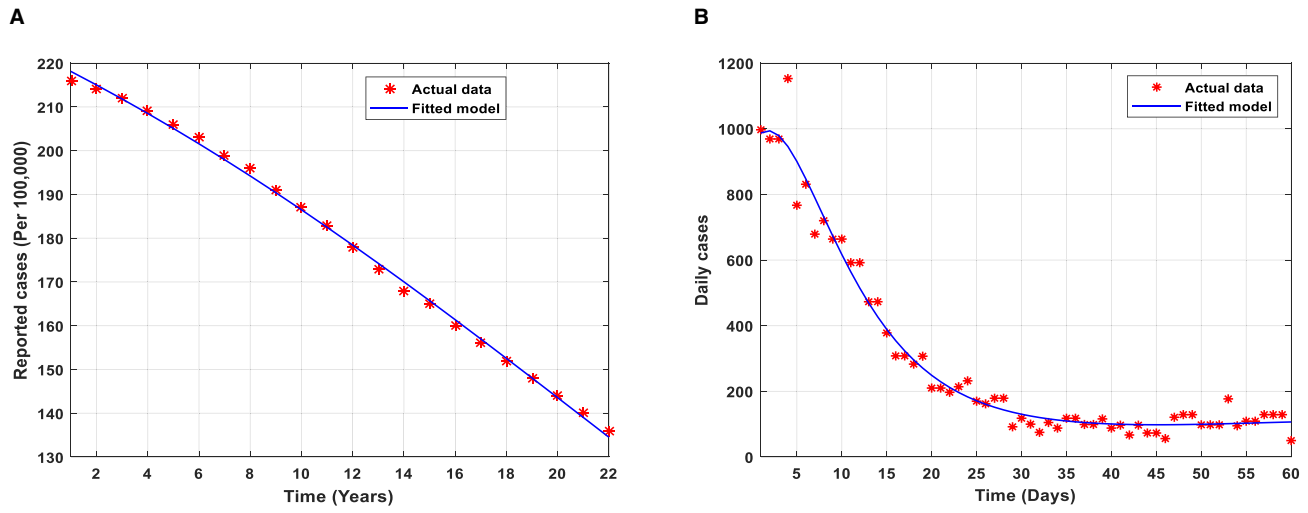

FIGURE 2
Plot of **(A)** TB stream **(B)** COVID-19 stream.

Simplifying Equation (20), the following quadratic equation is obtained in Equation (21).

$$k_2 I_c^{*2} + k_1 I_c^* + k_0 = 0. \tag{21}$$

where $k_2 = \beta_c^2 a_7 a_8, k_1 = \beta_c \delta_c \Lambda a_2 - a_7 a_8 \beta_c (a_1 + a_2), k_0 = \left(\frac{2\Lambda\beta_c^2(a_2-\alpha)}{\alpha\vartheta - a_1 a_2}\right)(R_{0C} - 1)$.

It is clear that k_2 is always positive and k_0 is positive if $R_{0C} > 1$. Hence, a unique endemic equilibrium exists if $R_{0C} > 1$.

Estimation and sensitivity of the parameters

Figure 2A illustrates the cumulative TB cases recorded within 22 years (2000 to 2022) in Ghana by the World Health Organization (WHO) [26]. Figure 2B illustrates the daily number of COVID-19 cases from 1st January 2022 to 1st March 2022 in Ghana [27]. All parameter values are illustrated in Table 1.

Now, we investigate the relationship between the parameters and I_{st}, I_{rt}, and I_c by considering the behavioral patterns of the respective parameters associated with the drug-sensitive strain of TB, drug-resistant strain of TB, and COVID-19 stream on the reproduction numbers R_{st}, R_{rt}, and R_{0c} with the graphical representations illustrated below.

Figure 3A shows the partial rank correlation coefficients (PRCC) of the parameters associated with R_{st} which depicts the transmission dynamics of individuals who are infectious with drug-sensitive (DS) strains of TB only. It is observed that $(\beta_{st}, \delta_{st})$ have a high positive effect on R_{st}. However, the vaccination protection rate σ is positive, this indicates that, the efficacy of the vaccine may be low. The parameters $(\alpha, \gamma_1, \mu, \vartheta)$ have a negative effect on R_{st}. Figure 3B shows the partial rank correlation coefficients (PRCCs) of the parameters associated with R_{rt} which depicts the transmission dynamics of the individuals infectious with drug-resistant (DR) strains of TB only. It is observed that $(\beta_{rt}, \delta_{rt}, \vartheta)$ have a high positive impact on the reproduction number R_{rt} This indicates that majority of the individuals may be resistant to the drug. The parameters (α, γ_2, μ) have a negative impact on the reproduction number R_{rt}. Figure 3C shows the partial rank correlation coefficients (PRCCs) of the parameters associated with R_{0C}, which depicts the behavioral patterns of transmission of the individuals infectious with COVID-19 only. It is observed that $(\beta_c, \delta_c, \vartheta)$ have a high positive effect on R_{0C}. Again, the vaccination protection rate σ is positive, this indicates that the efficacy of the vaccine may be low. This is determined by the associated sign; those with the positive sign indicate a perfect relationship and the negative sign indicates an imperfect relationship. If the value is high, then there exists a strong relationship, and the lower the value, the weaker the relation between the input and the output value. Once the vaccination protection rate σ increases, the reproduction numbers, and there should be measures to optimally control the transmission of TB and/or COVID-19.

To formulate control strategies to minimize the spread of TB and COVID-19, we demonstrate the transmission dynamics in different scenarios in the figures below based on the parameters that exhibit a strong relationship with the reproduction numbers, as demonstrated in Figure 4.

Figures 4A–C represent the respective contour plots of the reproduction numbers R_{st}, R_{rt}, and R_{0C} as a function of vaccination rate α and waning rate ϑ of vaccines. Figures 4D–F represent the respective contour plots of the reproduction numbers R_{st}, R_{rt}, and R_{0C} as a function of vaccination rate α and effective contact rates of TB and COVID-19. These figures suggest that to significantly minimizing the basic reproduction number to a minimum requires both pharmaceutical, such as vaccination, and non-pharmaceutical measures, such as mask usage and social distancing, to reduce the effective contact rate to prolong the period of acquiring the disease, which reduces the incubation rates.

TABLE 1 Interpretation and values of model parameters.

Parameter	Interpretation	Value	References
β_{st}	Drug-sensitive strain's effective contact rate.	0.3	[28]
β_{rt}	Drug-resistant strain's effective contact rate.	0.5	[29]
β_c	COVID-19 individuals' effective contact rate.	0.4531	[30]
α	Vaccination rate.	0.5482	[31]
ϑ	Waning rate of immunity.	0.05	[32]
σ	Rate of vaccine protection.	0.5	Fitted
δ_{st}	Drug-sensitive strain's incubation period.	0.14	[28]
δ_{rt}	Drug-resistant strain's incubation period.	0.34	[29]
δ_c	COVID-19 stream's incubation period.	0.07	Fitted
γ_1	Treatment rate of $E_{st}(t)$ individuals.	0.1	Assumed
γ_2	Treatment rate of $I_{st}(t)$ individuals.	0.2	[29]
γ_3	Treatment rate of $I_{rt}(t)$ individuals.	0.24	Assumed
φ_1	Movement rate from $I_c(t)$ to $I_{stc}(t)$.	0.015	Fitted
φ_2	Movement rate from $I_c(t)$ to $I_{rtc}(t)$.	0.015	Fitted
ε_1	Movement rate from $E_c(t)$ to $R(t)$.	0.2	Fitted
ε_2	Movement rate from $I_c(t)$ to $R(t)$.	0.023	[33]
ε_3	Movement rate from $I_{stc}(t)$ to $R(t)$.	0.02095	[31]
ε_4	Movement rate from $I_{rtc}(t)$ to $R(t)$.	0.02095	Assumed
ε_5	Movement rate from $T(t)$ to $R(t)$.	0.35	[34]
Λ	Recruitment rate.	1364	Estimated
μ	Rate of natural death.	0.000043	Estimated
ω	Treatment failure rate.	0.2	[31]
d_i	Induced death rate of TB and/or COVID-19	0.000017	[31]

All the above illustrations clearly show the pattern of the PRCC plots in Figure 3, and it is realized that all these parameters have either positive or negative effects on the transmission of TB and/or COVID-19. There should be effective interventions to reduce the rate of secondary infections; thus, R_{st}, R_{rt}, and R_{0C} of TB and COVID-19 co-infection.

Analysis of optimal control

We modify model (2) [see Equation (22)] with the following optimal control variable $U_1(t)$, as public education on the prevention of TB and COVID-19, such as mask usage and social distancing, where $U_1(t) \in [0,1]$, which reduces the force of infection, λ_1, by $1 - U_1(t)$. $U_2(t)$; control efforts to intensify vaccination of the population.$U_3(t)$; control effort for case finding to enhance prophylaxis for the population by $1 + U_3(t)$. Hence, those identified as infectious will go through prophylaxis to minimize the infections that may occur. The control effort $U_4(t)$ is control for case holding to control the failure of prophylaxis to minimize the reoccurrence of the disease by $1 - U_4(t)$. All these efforts denote the admissible control measures necessary to minimize the transmission of the diseases. The modified equation is given as

$$
\begin{cases}
\frac{dS}{dt} = \Lambda + \vartheta V - \left[(1-U_1)(\rho_1+\rho_2+\rho_3+\rho_4+\rho_5) + U_2\alpha + \mu\right] S, \\
\frac{dV}{dt} = U_2\alpha S - \left[(1-U_1)(\rho_1+\rho_2+\rho_3+\rho_4+\rho_5)\sigma + \mu + \vartheta\right] V, \\
\frac{dE_{st}}{dt} = (1-U_1)(S+\sigma V)\rho_1 + \rho_2\omega T - (\mu+\delta_{st}+(1+U_3)\gamma_1)E_{st}, \\
\frac{dI_{st}}{dt} = (1-U_1)(S+\sigma V)\rho_2 + \rho_1\omega T + \delta_{st}E_{st} + \\
g\varepsilon_3 I_{stc} - \left(\mu + d_1 + (1-U_4)\gamma_2\right) I_{st}, \\
\frac{dE_{rt}}{dt} = (1-U_1)(S+\sigma V)\rho_3 + \\
\rho_2\omega T - (\mu+\delta_{rt})E_{rt}, \\
\frac{dI_{rt}}{dt} = (1-U_1)(S+\sigma V)\rho_4 + \rho_1\omega T + \\
\delta_{rt}E_{rt} + h\varepsilon_3 I_{rtc} - \left(\mu + d_2 + (1-U_4)\gamma_3\right) I_{rt}, \\
\frac{dE_c}{dt} = (1-U_1)(S+\sigma V)\rho_5 - (\mu+\delta_c+(1+U_3)\varepsilon_1)E_c, \\
\frac{dI_c}{dt} = \delta_c E_c - (\mu + d_3 + \varphi_1 + \varphi_2 + \varepsilon_2) I_c, \\
\frac{dI_{stc}}{dt} = \varphi_1 I_c + (1-U_4)k\gamma_2 I_{st} - (\mu + d_4 + \varepsilon_3) I_{stc}, \\
\frac{dI_{rtc}}{dt} = \varphi_2 I_c + (1-U_4)m\gamma_3 I_{rt} - (\mu + d_5 + \varepsilon_4) I_{rtc}, \\
\frac{dT}{dt} = (1+U_3)\gamma_1 E_{st} + (1-U_4)(1-k)\gamma_2 I_{st} + \\
(1-U_4)(1-m)\gamma_3 I_{rt} - (\mu + \varepsilon_5 + \omega\lambda_1) T, \\
\frac{dR}{dt} = (1+U_3)\varepsilon_1 E_c + \varepsilon_2 I_c + (1-g) \\
\varepsilon_3 I_{stc} + (1-h)\varepsilon_4 I_{rtc} + \varepsilon_5 T - \mu R.
\end{cases}
\tag{22}
$$

where $\rho_1 = \frac{(1-b)\beta_{st}I_{st}}{N}, \rho_2 = \frac{b\beta_{st}I_{st}}{N}, \rho_3 = \frac{(1-b)\beta_{rt}I_{rt}}{N}, \rho_4 = \frac{b\beta_{rt}I_{rt}}{N}$, and $\rho_5 = \frac{\beta_c I_c}{N}$ are derived from Section 2 with the initial conditions given in model (2).

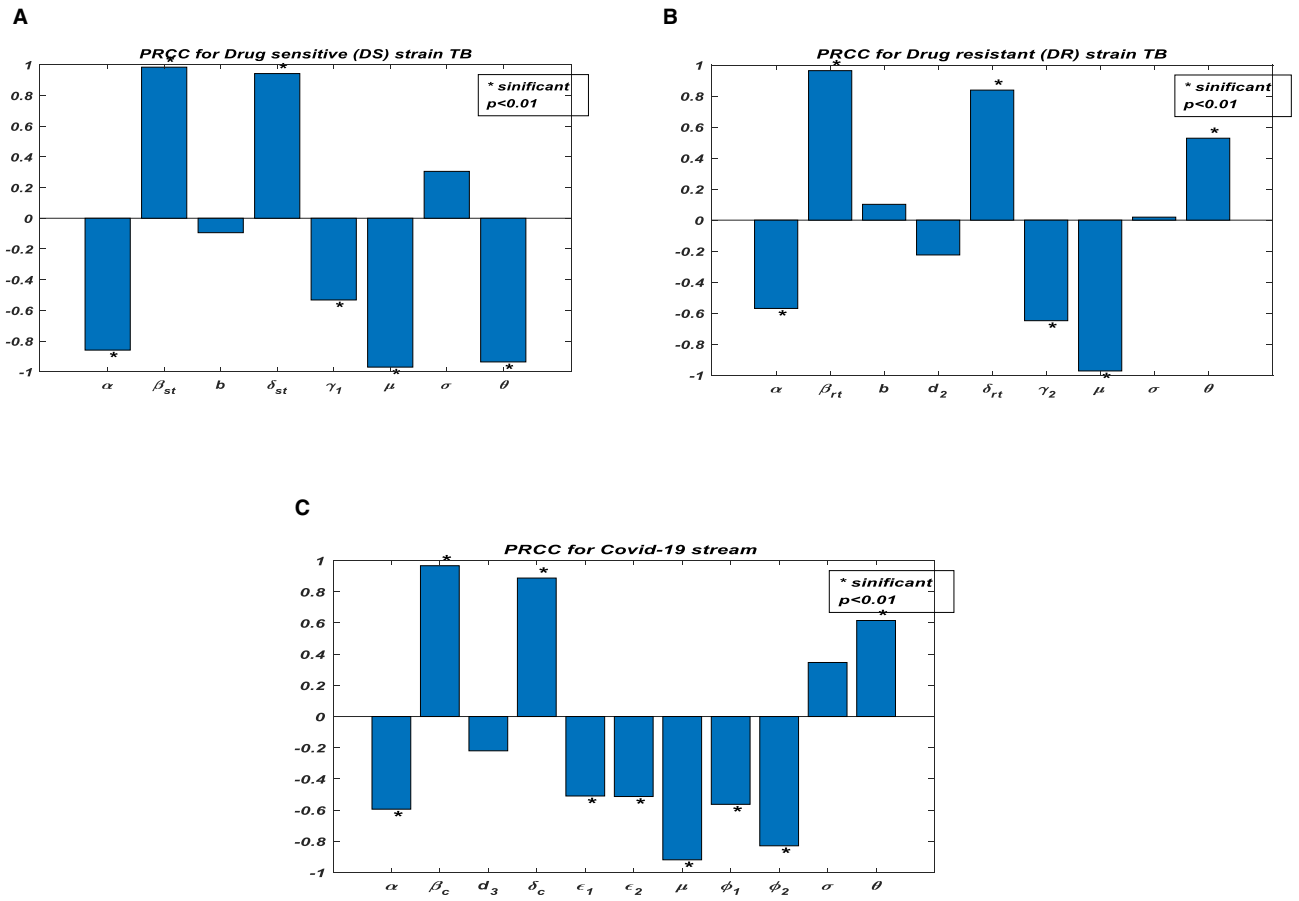

FIGURE 3
Partial rank correlation (PRCC) of the parameters in reproduction numbers. **(A)** PRCC for drug sensitive (DS) strain TB. **(B)** PRCC for drug resistant (DR) strain TB. **(C)** PRCC for COVID-19 stream.

Objective functional

We now formulate the optimal trajectories that show the effect of the control efforts $U_1(t), U_2(t), U_3(t),\ U_4(t)$ subjected to Equation (22); the objective functional M is given as,

$$M\left(U_1, U_2, U_3,\ U_4\right) = \int_0^{t_f} [m_1 E_{st} + m_2 I_{st} + m_3 E_{rt} + m_4 I_{rt} + m_5 E_c + m_6 I_c + m_7 I_{stc} + m_8 I_{rtc} + \frac{1}{2} c_1 U_1^2(t) + \frac{1}{2} c_2 U_2^2(t) + \frac{1}{2} c_3 U_3^2(t) + \frac{1}{2} c_4 U_4^2(t)\big] dt. \quad (23)$$

We focus on minimizing the cost function (23), and the total cost of implementing the optimal control is given as

$$Q = \int_0^{t_f} \left[\frac{1}{2} c_1 U_1^2(t) + \frac{1}{2} c_1 U_2^2(t) + \frac{1}{2} c_3 U_3^2(t) + \frac{1}{2} c_4 U_4^2(t)\right] dt. \quad (24)$$

The parameters $c_1,\ c_2,\ c_3$, and c_4 in Equation (24) are the balancing cost factors for $U_1(t), U_2(t), U_3(t),\ U_4(t)$, respectively. All the control efforts $U_1(t), U_2(t), U_3(t),\ U_4(t)$ are assumed to be bounded by Lebesgue measurable time-dependent functions on the interval $\left[0, t_f\right]$, where t_f is the final time.

By Pontryagin's maximum principle, system (22) and the objective functional (23) are transformed into a state of point-wise Hamiltonian H. The following optimal solution is achieved.

$$\begin{aligned} H = {} & m_1 E_{st} + m_2 I_{st} + m_3 E_{rt} + m_4 I_{rt} + m_5 E_c + m_6 I_c + m_7 I_{stc} + \\ & m_8 I_{rtc} + \tfrac{1}{2} c_1 U_1^2(t) + \tfrac{1}{2} c_2 U_2^2(t) + \\ & \tfrac{1}{2} c_3 U_3^2(t) + \tfrac{1}{2} c_4 U_4^2(t) + \\ & \lambda_S \left(\Lambda + \vartheta V - \left[(1-U_1)(\rho_1 + \rho_2 + \rho_3 + \rho_4 + \rho_5) + \right.\right. \\ & \left.\left. U_2 \alpha + \mu\right] S\right) + \lambda_V \left(U_2 \alpha S - [(1-U_1) \right. \\ & \left. (\rho_1 + \rho_2 + \rho_3 + \rho_4 + \rho_5)\sigma + \right. \\ & \left. \mu + \vartheta\right] V\big) + \lambda_{E_{st}} \left((1-U_1)\right. \\ & \left. (S + \sigma V)\rho_1 + \rho_2 \omega T - (\mu + \delta_{st} + (1+U_3)\gamma_1) E_{st}\right) + \\ & \lambda_{I_{st}} \left((1-U_1)(S+\sigma V)\rho_2 + \rho_1 \omega T + \right. \\ & \left. \delta_{st} E_{st} + g\varepsilon_3 I_{stc} - (\mu + d_1 + (1-U_4)\gamma_2) I_{st}\right) + \\ & \lambda_{E_{rt}} \left((1-U_1)(S+\sigma V)\rho_3 + \rho_2 \omega T - (\mu + \delta_{rt}) E_{rt}\right) + \\ & \lambda_{I_{rt}} \left((1-U_1)(S+\sigma V)\rho_4 + \rho_1 \omega T + \delta_{rt} E_{rt} + \right. \\ & \left. h\varepsilon_3 I_{rtc} - (\mu + d_2 + (1-U_4)\gamma_3) I_{rt}\right) + \\ & \lambda_{E_c} \left((1-U_1)(S+\sigma V)\rho_5 - (\mu + \delta_c + (1+U_3)\varepsilon_1) E_c\right) + \\ & \lambda_{I_c} \left(\delta_c E_c - (\mu + d_3 + \varphi_1 + \varphi_2 + \varepsilon_2) I_c\right) + \end{aligned} \quad (25)$$

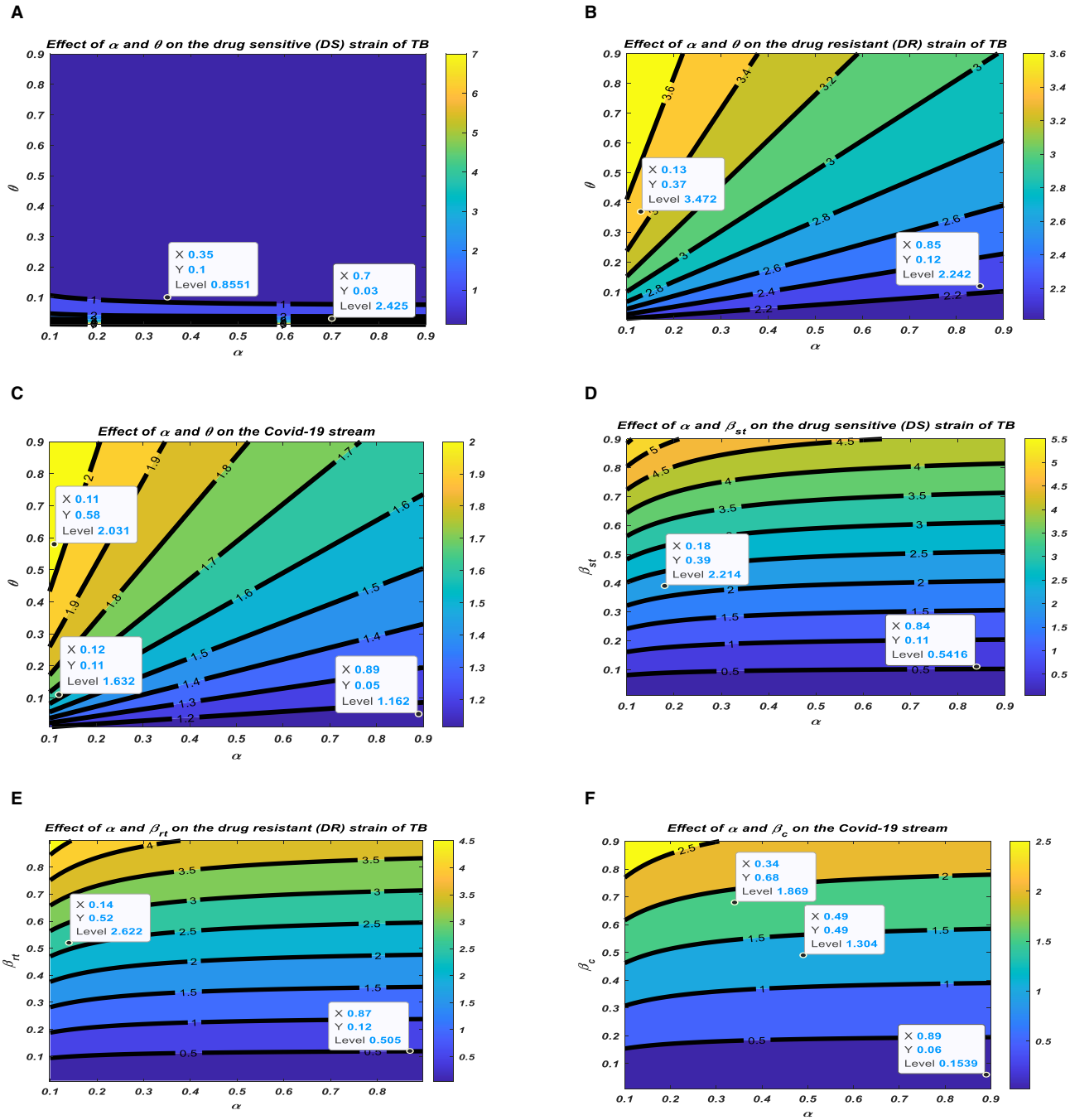

FIGURE 4
Relationship between the reproduction numbers and their corresponding parameters. **(A)** Effect of α and θ on the drug sensitive (DS) strain of TB. **(B)** Effect of α and θ on the drug resistant (DR) strain of TB. **(C)** Effect of α and θ on the COVID-19 stream. **(D)** Effect of α and β_{st} on the drug sensitive (DS) strain of TB. **(E)** Effect of α and β_{rt} on the drug resistant (DR) strain of TB. **(F)** Effect of α and β_c on the COVID-19 stream.

$$\lambda_{I_{stc}}\left(\varphi_1 I_c + (1-U_4)k\gamma_2 I_{st} - (\mu + d_4 + \varepsilon_3)I_{stc}\right) +$$
$$\lambda_{I_{rtc}}\left(\varphi_2 I_c + (1-U_4)m\gamma_3 I_{rt} - (\mu + d_5 + \varepsilon_4)I_{rtc}\right) +$$
$$\lambda_T\left((1+U_3)\,\gamma_1 E_{st} + (1-U_4)\left(1-k\right)\gamma_2 I_{st} +\right.$$
$$\left.(1-U_4)\,(1-m)\,\gamma_3 I_{rt} - (\varepsilon_5 + \omega\lambda_1)\,T\right) +$$
$$\lambda_R\left((1+U_3)\,\varepsilon_1 E_c + \varepsilon_2 I_c + \left(1-g\right)\varepsilon_3 I_{stc} +\right.$$
$$\left.\left(1-h\right)\varepsilon_4 I_{rtc} + \varepsilon_5 T - \mu R\right).$$

Where λ_S, λ_V, $\lambda_{E_{st}}$, $\lambda_{I_{st}}$, $\lambda_{E_{rt}}$, $\lambda_{I_{rt}}$, λ_{E_c}, λ_{I_c}, $\lambda_{I_{stc}}$, $\lambda_{I_{rtc}}$, λ_T, λ_R in Equation (25) are the costate variables with respect to the state variables, $S, V, E_{st}, I_{st}, E_{rt}, I_{rt}, E_c, I_c, I_{stc}, I_{rtc}, T, R$.

Theorem 3: Given $U_1^*(t), U_2^*(t), U_3^*(t), U_4^*(t)$ as the optimal controls and the corresponding solutions S^0, V^0, E_{st}^0, I_{st}^0, E_{rt}^0, I_{rt}^0, E_c^0, I_c^0, I_{stc}^0, I_{rtc}^0, T^0, R^0 of system (22), which minimizes $Q\left(U_1(t), U_2(t), U_3(t), U_4(t)\right)$, then there exist costate

variables λ_S, λ_V, $\lambda_{E_{st}}$, $\lambda_{I_{st}}$, $\lambda_{E_{rt}}$, $\lambda_{I_{rt}}$, λ_{E_c}, λ_{I_c}, $\lambda_{I_{stc}}$, $\lambda_{I_{rtc}}$, λ_T, λ_R that satisfy

$$\frac{d\lambda_j}{dt} = -\frac{\partial H}{\partial j}. \tag{26}$$

With conditions $\lambda_j(t_f) = 0$, in (27) where $j = S, V, E_{st}, I_{st}, E_{rt}, I_{rt}, E_c, I_c, I_{stc}, I_{rtc}, T, R$, the optimality conditions that minimize the Hamiltonian, H, of (25) with respect to the controls are given as

$$\begin{cases} U_1^*(t) = \\ \min\{U_1 max,\ max \\ \left(0, \frac{(S^0+\sigma V^0)((\lambda_{E_{st}}-\lambda_S)\rho_1+(\lambda_{I_{st}}-\lambda_S)\rho_2+(\lambda_{E_{rt}}-\lambda_S)\rho_3+(\lambda_{I_{rt}}-\lambda_S)\rho_4+(\lambda_{E_c}-\lambda_S)\rho_5)}{C_1}\right)\}, \\ U_2^*(t) = \min\left\{U_2 max,\ max\left(0, \frac{(\lambda_S-\lambda_V)\alpha S^0}{C_2}\right)\right\}', \\ U_3^*(t) = \min\left\{U_3 max,\ max\left(0, \frac{(\lambda_{E_{st}}-\lambda_T)\gamma_1 E_{st}^0-\varepsilon_1\lambda_{E_c}E_c^0}{C_3}\right)\right\}, \\ U_4^*(t) = \min\left\{U_4 max,\ max\left(0, \frac{(\lambda_{I_{stc}}+\lambda_T-\lambda_{I_{st}})\gamma_2 I_{st}^0+(\lambda_{I_{rtc}}+\lambda_T-\lambda_{I_{rt}})\gamma_3 I_{rt}^0}{C_4}\right)\right\}. \end{cases} \tag{27}$$

Proof: We take the partial derivative of Equation (25) with respect to the solutions of the system, optimal control, and final time conditions. The adjoint equation is demonstrated below in Equation (28).

$$\begin{cases} \frac{d\lambda_S}{dS} = [1-U_1]\left[(\lambda_{E_{st}}-\lambda_S)\rho_1 + (\lambda_{I_{st}}-\lambda_S)\rho_2 + (\lambda_{E_{rt}}-\lambda_S)\rho_3 + (\lambda_{I_{rt}}-\lambda_S)\rho_4 + (\lambda_{E_c}-\lambda_S)\rho_5\right] + \\ (\lambda_V-\lambda_S)U_2\alpha + (\lambda_S-\lambda_V)\vartheta V + \mu\lambda_S, \\ \frac{d\lambda_V}{dV} = [1-U_1]\left[(\lambda_{E_{st}}-\lambda_V)\rho_1 + (\lambda_{I_{st}}-\lambda_V)\rho_2 + (\lambda_{E_{st}}-\lambda_T)\rho_3 + (\lambda_{I_{rt}}-\lambda_V)\rho_4 + (\lambda_{E_c}-\lambda_V)\rho_5\right]\sigma + \\ (\lambda_V-\lambda_S)U_2\alpha S + (\lambda_S-\lambda_V)\vartheta + \mu\lambda_V, \\ \frac{d\lambda_{E_{st}}}{dE_{st}} = -m_1 + [1-U_1]\left[(\lambda_{E_{st}}-\lambda_S)S + (\lambda_{E_{st}}-\lambda_v)\sigma V\right]\rho_1 + (\lambda_{E_{st}}-\lambda_T)\rho_2\omega T + (\lambda_{I_{st}}-\lambda_{E_{st}})\delta_{st} + (\lambda_T-\lambda_{E_{st}}) \\ (1+U_3)\gamma_1 + \mu\lambda_{E_{st}}, \\ \frac{d\lambda_{I_{st}}}{dI_{st}} = -m_2 + [1-U_1]\left[(\lambda_{I_{st}}-\lambda_S)S + (\lambda_{I_{st}}-\lambda_v)\sigma V\right]\rho_2 + (\lambda_{I_{st}}-\lambda_T)\rho_1\omega T + (\lambda_{I_{st}}-\lambda_{E_{st}})\delta_{st}E_{st} + \\ (\lambda_T-\lambda_{I_{st}})(1-U_4)(1-k)\gamma_2 + (\lambda_{I_{st}}-\lambda_{I_{stc}})g\varepsilon_3 I_{stc} + (\lambda_{I_{stc}}-\lambda_{I_{st}})(1-U_4)k\gamma_2 + (\mu+d_1)\lambda_{I_{st}}, \\ \frac{d\lambda_{E_{rt}}}{dE_{rt}} = -m_3 + [1-U_1]\left[(\lambda_{E_{rt}}-\lambda_S)S + (\lambda_{E_{rt}}-\lambda_v)\sigma V\right]\rho_3 + (\lambda_{E_{rt}}-\lambda_T)\rho_4\omega T + (\lambda_{I_{rt}}-\lambda_{E_{rt}})\delta_{rt} + \mu\lambda_{E_{rt}}, \\ \frac{d\lambda_{I_{rt}}}{dI_{rt}} = -m_4 + [1-U_1]\left[(\lambda_{I_{rt}}-\lambda_S)S + (\lambda_{I_{rt}}-\lambda_v)\sigma V\right]\rho_4 + (\lambda_{I_{rt}}-\lambda_T)\rho_3\omega T + (\lambda_{I_{rt}}-\lambda_{I_{rtc}})h\varepsilon_4 I_{rtc} + \\ (\lambda_{I_{rtc}}-\lambda_{I_{rt}})(1-U_4)(1-m)\gamma_3 + (\lambda_T-\lambda_{I_{rt}})(1-U_4)(1-m)\gamma_3 + (\mu+d_2)\lambda_{I_{rt}}, \\ \frac{d\lambda_{E_c}}{dE_c} = -m_5 + [1-U_1]\left[(\lambda_{E_c}-\lambda_S)S + (\lambda_{E_c}-\lambda_v)\sigma V\right]\rho_5 + (\lambda_{I_c}-\lambda_{E_c})\delta_c + (\lambda_R-\lambda_{E_c})(1+U_3)\varepsilon_1 + \mu\lambda_{E_c}, \\ \frac{d\lambda_{I_c}}{dI_c} = -m_6 + (\lambda_{I_c}-\lambda_{E_c})\delta_c E_c + (\lambda_{I_{stc}}-\lambda_{I_c})\varphi_1 + (\lambda_{I_{rtc}}-\lambda_{I_c})\varphi_2 + (\lambda_R-\lambda_{I_c})\varepsilon_2 + (\mu+d_3)\lambda_{I_c}, \\ \frac{d\lambda_{I_{stc}}}{dI_{stc}} = -m_7 + (\lambda_{I_{stc}}-\lambda_{I_c})\varphi_1 I_c + (\lambda_{I_{stc}}-\lambda_{I_{st}})(1-U_4)k\gamma_2 I_{st} + (\lambda_{I_{st}}-\lambda_{I_{stc}})g\varepsilon_3 + (\lambda_R-\lambda_{I_{stc}})(1-g)\varepsilon_3 + (\mu+d_4)\lambda_{I_{stc}}, \\ \frac{d\lambda_{I_{rtc}}}{dI_{rtc}} = -m_8 + (\lambda_{I_{rtc}}-\lambda_{I_c})\varphi_2 I_c + (\lambda_{I_{rtc}}-\lambda_{I_{rt}})h\varepsilon_4 I_{rt} + (\lambda_{I_{rt}}-\lambda_{I_{rtc}})(1-U_4)m\gamma_3 + (\lambda_R-\lambda_{I_{rtc}})(1-h)\varepsilon_4 + (\mu+d_5)\lambda_{I_{rtc}}, \\ \frac{d\lambda_T}{dT} = (\lambda_T-\lambda_{E_{st}})(1+U_3)\gamma_1 E_{st} + (\lambda_T-\lambda_{I_{st}})(1-U_4)(1-k)\gamma_2 I_{st} + (\lambda_T-\lambda_{I_{rt}})(1-U_4)(1-m)\gamma_3 I_{rt} + (\lambda_{E_{st}}-\lambda_T)\rho_2\omega \\ (\lambda_{I_{st}}-\lambda_T)\rho_1\omega + (\lambda_{E_{rt}}-\lambda_T)\rho_4\omega + (\lambda_{I_{rt}}-\lambda_T)\rho_3\omega + (\lambda_R-\lambda_T)\varepsilon_5 + \mu\lambda_T, \\ \frac{d\lambda_R}{dR} = (\lambda_R-\lambda_{E_c})(1+U_3)\varepsilon_1 E_c + (\lambda_R-\lambda_{I_c})\varepsilon_2 I_c + (\lambda_R-\lambda_{I_{stc}})(1-g)\varepsilon_3 I_{stc} + (\lambda_R-\lambda_{I_{rtc}})(1-h)\varepsilon_4 I_{rtc} + (\lambda_R-\lambda_T)\varepsilon_5 T + \mu\lambda_R. \end{cases} \tag{28}$$

The control set Equation (29) below illustrates the costate system with the optimal conditions.

$$\begin{cases} \frac{\partial H}{\partial U_1} = C_1U_1 + (S^0+\sigma V^0) \\ ((\lambda_S-\lambda_{E_{st}})\rho_1 + (\lambda_S-\lambda_{I_{st}})\rho_2 + \\ (\lambda_S-\lambda_{E_{rt}})\rho_3 + (\lambda_S-\lambda_{I_{rt}})\rho_4 + (\lambda_S-\lambda_{E_c})\rho_5), \\ \frac{\partial H}{\partial U_2} = C_2U_2 + (\lambda_V-\lambda_S)\alpha S^0, \\ \frac{\partial H}{\partial U_3} = C_3U_3 + (\lambda_T-\lambda_{E_{st}})\gamma_1 E_{st}^0 + \varepsilon_1 E_c^0\lambda_{E_c}, \\ \frac{\partial H}{\partial U_4} = C_4U_4 + (\lambda_{I_{st}}-\lambda_T-\lambda_{I_{stc}})\gamma_2 I_{st}^0 + (\lambda_{I_{rt}}-\lambda_T-\lambda_{I_{rtc}})\gamma_3 I_{rt}^0. \end{cases} \tag{29}$$

We solve for $U_1(t), U_2(t), U_3(t)$, *and* $U_4(t)$ *as* $U_1^*(t)$, $U_2^*(t), U_3^*(t)$, and $U_4^*(t)$ of Equation (25), and the results are given in Equation (30):

$$\begin{cases} U_1^*(t) = \\ \frac{(S^0+\sigma V^0)((\lambda_{E_{st}}-\lambda_S)\rho_1+(\lambda_{I_{st}}-\lambda_S)\rho_2+(\lambda_{E_{rt}}-\lambda_S)\rho_3+(\lambda_{I_{rt}}-\lambda_S)\rho_4+(\lambda_{E_c}-\lambda_S)\rho_5)}{C_1}, \\ U_2^*(t) = \frac{(\lambda_S-\lambda_V)\alpha S^0{}'}{C_2} \\ U_3^*(t) = \frac{(\lambda_{E_{st}}-\lambda_T)\gamma_1 E_{st}^0-\varepsilon_1\lambda_{E_c}E_c^0}{C_3}, \\ U_4^*(t) = \frac{(\lambda_{I_{stc}}+\lambda_T-\lambda_{I_{st}})\gamma_2 I_{st}^0+(\lambda_{I_{rtc}}+\lambda_T-\lambda_{I_{rt}})\gamma_3 I_{rt}^0}{C_4}. \end{cases} \tag{30}$$

Therefore, using the bounds of the controls $U_1^*(t), U_2^*(t), U_3^*(t)$, and $U_4^*(t)$, the control efforts are in the compact form given by the optimal condition of the system in (27); hence, the proof is complete.

Optimal control results

The goal of this subsection is to study the two strains of TB; thus, drug-sensitive (DS) and drug-resistant (DR) strains of TB influence COVID-19 using the control efforts. We explore the effects of implementing the control efforts; therefore, the optimality system (21) is solved forward in time and the adjoint system backward in time with the corresponding lower and upper bounds of the controls. We use the population of Ghana to study the behavioral pattern of the co-infection of TB and COVID-19. The estimated total population of Ghana is 31732129 [35]; hence, $N(0) = 31732129$, and the assumed initial values are as follows: $S(0) = 20000000$, $V(0) = 100000$, $E_{st}(0) = 20000$, $I_{st}(0) = 10000$, $E_{rt}(0) = 20000$, $I_{rt}(0) = 10000$, $E_c(0) = 15000$, $I_c(0) = 10000$, $I_{stc}(0) = 20000$, $I_{rtc}(0) = 20000$, $T = (0)\,100000$, $R(0) = 5000$, together with parameter values illustrated in Table 1. The balance costs associated with the objective functional are assumed as $C_1 = 200$, $C_2 = 100$, $C_3 = 500, C_4 = 1000$ and weights $m_i = 100$, where $i = 1, 2, 3, 4, 5, 6, 7, 8$. The lower bound (LB) and upper bound (UB) are assumed as $LB_1 = 0$, $UB_1 = 1, LB_2 = 0$, $UB_2 = 1$, $LB_3 = 0$, $UB_3 = 1$. The results are illustrated according to the strategies to implement the control efforts.

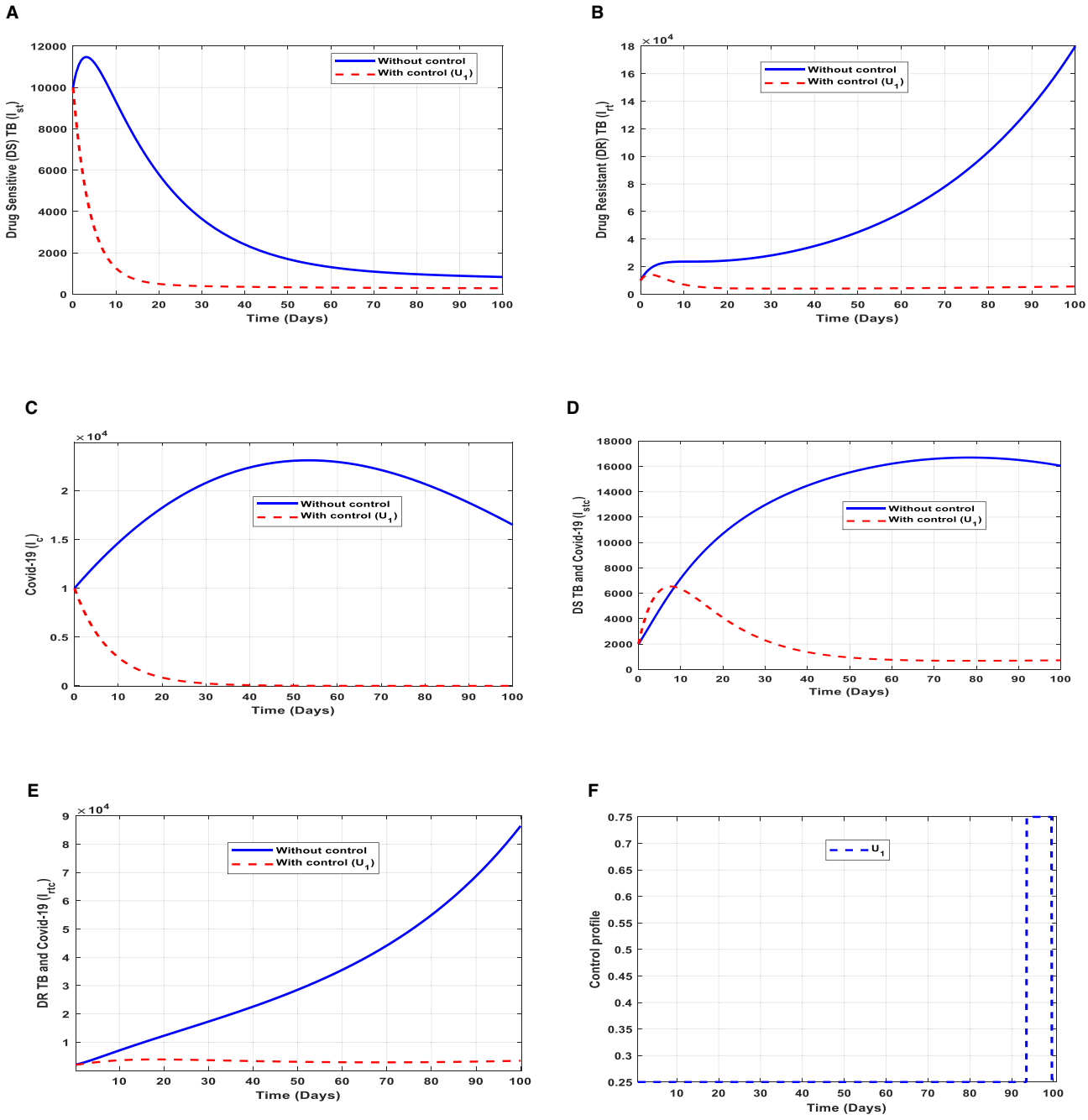

FIGURE 5
(A–E) Red dotted line is the optimal solution for implementing strategy 1. **(F)** Optimal control profile for strategy 1.

Strategy 1: implementation of public education (U_1)

This intervention is most favorable for both streams of diseases, thus halting the transmission of TB and COVID-19. The optimal solutions illustrated in Figure 5 account for the observations when the control effort U_1 is applied accordingly.

The optimal solutions illustrated above depict the following observations when public education is only applied.

(a) Figure 5A represents the effect of the control effort U_1 on the individuals infectious with drug-sensitive (DS) strain of TB only. This implies that the number of individuals will decrease to the minimum within 20 days if the control intervention is optimally implemented to halt the disease's transmission. Conversely, it will decrease but not significantly.

(b) Figure 5B represents the effect of the control effort U_1 on the individuals infectious with drug-resistant (DR) strain of TB only. This implies that the number of individuals will decrease to the minimum within 90 days if the control effort is optimally implemented to halt the disease's transmission. Conversely, if the control intervention is ignored, the number of infected

individuals will increase significantly by $> 15,000$ per 100,000 people before the 90th day, which will result in the higher transmission of the drug-resistant (DR) strain of TB only in the individuals.

(c) Figure 5C represents the effect of the control effort U_1 on the individuals infectious with COVID-19 only. This implies that the number of individuals will decrease to the minimum within 30 days if the control effort is optimally implemented to halt the disease's transmission. Conversely, it will increase significantly.

(d) Figure 5D represents the effect of the control effort U_1 on the individuals infectious with drug-sensitive (DS) strain of TB and COVID-19 at the same time. This implies that the number of individuals will decrease to the minimum within extra days if the control effort is optimally implemented to halt the disease's transmission. Conversely, it will decrease but not significantly.

(e) Figure 5E represents the effect of the control effort U_1 on the individuals infectious with drug-resistant (DR) strain of TB and COVID-19 at the same time. This implies that the number of individuals will decrease to the minimum within 90 days if the control effort is optimally implemented to halt the transmission of the disease. Conversely, if the control intervention is ignored, the number of infected individuals will increase significantly by > 90000 per 100000 people before the 90th day, which will result in higher transmission of the drug-resistant (DR) strain of TB and COVID-19 in the individuals.

(f) Figure 5F represents the profile of control efforts for public education on the prevention of TB and COVID-19, such as mask usage and social distancing. This implies that education should reach more than 25% of the population from the start of implementation and must be intensified and fully optimized to 100% after 85 subsequent days to minimize the transmission of TB and COVID-19.

Strategy 2: implementation of vaccination (U_2)

This intervention is also favorable for both streams of diseases, thus halting the spread of TB and COVID-19; however, it should be implemented with care because the proportion of the individuals may develop the drug-resistant (DR) strain of TB if treatment failure occurs, and the waning rate of the vaccine. The optimal solutions illustrated in Figure 6 account for the observations when the control effort U_2 is applied accordingly.

The optimal solutions illustrated above depict the following observations when vaccination is only applied.

(a) Figure 6A represents the effect of the control effort U_2 on the individuals infectious with drug-sensitive (DS) strain of TB only. This implies that the number of individuals will decrease to the minimum within 10 days if the control intervention is optimally implemented to halt the disease's transmission. Conversely, it will increase significantly.

(b) Figure 6B represents the effect of the control effort U_2 on the individuals infectious with drug-resistant (DR) strain of TB only. This implies that the number of individuals will decrease to the minimum within 90 days if the control intervention is optimally implemented to halt the disease's transmission. Conversely, if the control effort is ignored, the number of infected individuals will increase significantly by $> 15,000$ per 100,000 people before the 65th day, which will result in the higher transmission of the drug-resistant (DR) strain of TB only in the individuals. This is a result of drug resistance, which leads to treatment failure.

(c) Figure 6C represents the effect of the control effort U_2 on the individuals infectious with COVID-19 only. This implies that the number of individuals will decrease to the minimum within 10 days if the control effort is optimally implemented to halt the disease's transmission. Conversely, it will increase significantly.

(d) Figure 6D represents the effect of the control effort U_2 on the individuals infectious with drug-sensitive (DS) strain of TB and COVID-19 at the same time. This implies that the number of individuals will decrease to the minimum within extra days if the control effort is optimally implemented to halt the disease's transmission. Conversely, it will increase significantly.

(e) Figure 6E represents the effect of the control effort U_1 on the individuals infectious with drug-resistant (DR) strain of TB and COVID-19 at the same time. This implies that the number of individuals will decrease to the minimum within 60 days if the control intervention is optimally implemented to halt the disease's transmission. Conversely, if the control intervention is ignored, the number of infected individuals will increase significantly by $> 80,000$ per 100,000 people before the 90th day, which will result in higher transmission of the drug-resistant (DR) strain of TB and COVID-19 in the individuals. This is a result of drug resistance and vaccine inefficacy, which leads to treatment failure and/or reinfection.

(f) Figure 6F represents the profile of control efforts for vaccination to prevent TB and COVID-19. This implies that the vaccination needs to be intensified by more than 25% and reach the population from the start of implementation and must be intensified fully and optimized to 100% after some days throughout the subsequent days to halt both TB and COVID-19 transmission.

Strategy 3: implementation of case finding (U_3)

This intervention is also favorable for both streams of diseases, thus halting the spread of TB and COVID-19. The optimal solutions, illustrated in Figure 7, account for the observations when the control effort U_3 is applied accordingly.

The optimal solutions illustrated above depict the following observations when case finding is only applied. This is mostly used to detect TB infection.

(a) Figure 7A represents the effect of the control effort U_3 on the individuals infectious with drug-sensitive (DS) strain of TB only. This implies that the number of individuals will decrease to the minimum within 20 days if the control intervention is optimally implemented to halt the disease's transmission. Conversely, it will increase significantly.

(b) Figure 7B represents the effect of the control effort U_3 on the individuals infectious with drug-resistant (DR) strain of TB only. This implies that the number of individuals will decrease to the minimum within 30 days if the control effort

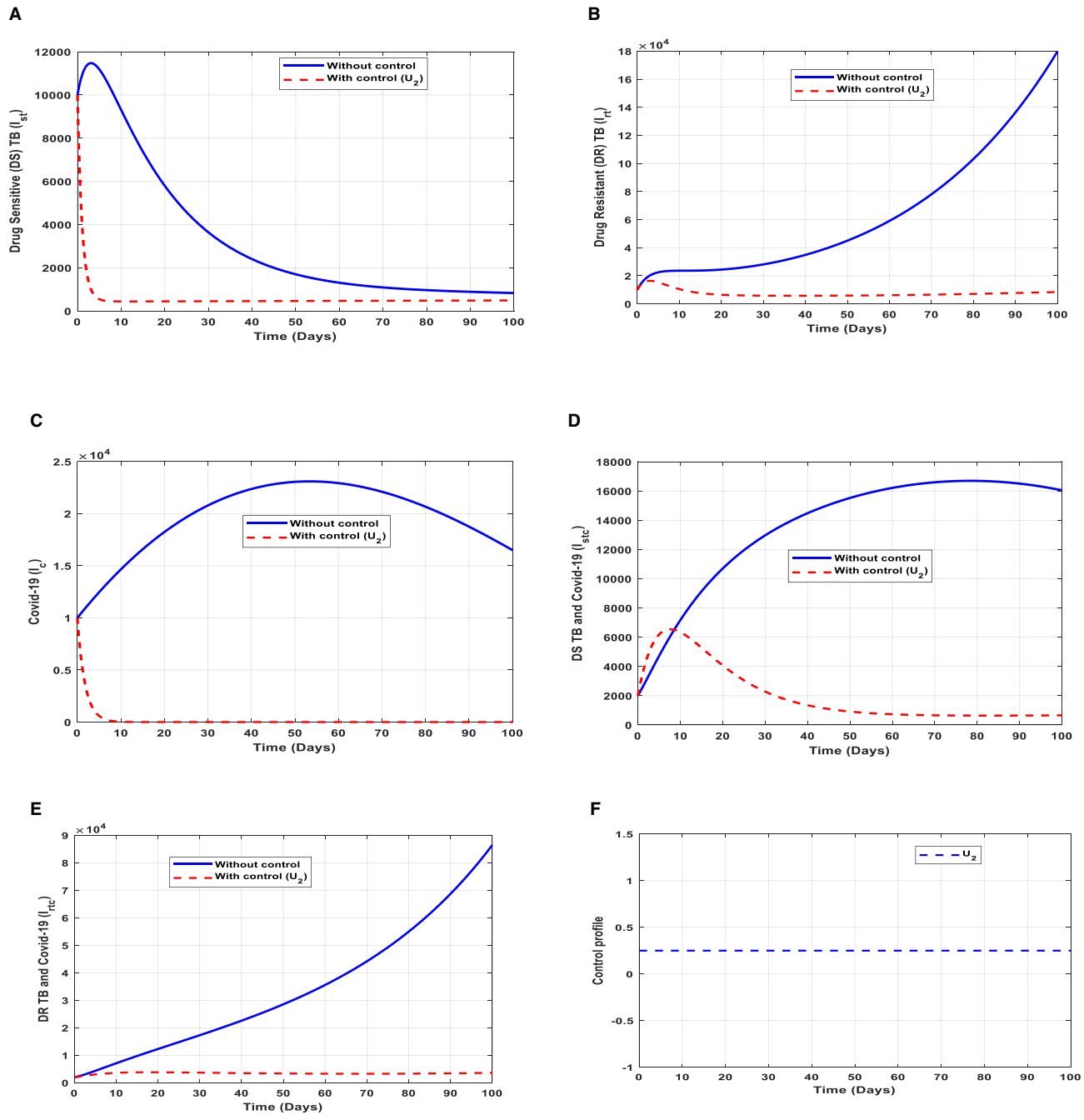

FIGURE 6
(A–E) Red dotted line is the optimal solution for implementing strategy 2. **(F)** Optimal control profile for strategy 2.

is optimally implemented to halt the transmission of the disease. Conversely, if the control intervention is ignored, the number of infected individuals will increase significantly by $> 150,000$ per 100,000 people before the 90th day, which will result in higher transmission of the drug-resistant (DR) strain of TB only in the individuals.

(c) Figure 7C represents the effect of the control effort U_3 on the individuals infectious with COVID-19 only. This implies that the number of individuals will decrease to the minimum within 30 days if the control effort is optimally implemented to halt the disease's transmission. Conversely, it will increase significantly.

(d) Figure 7D represents the effect of the control effort U_3 on the individuals infectious with drug-sensitive (DS) strain of TB and COVID-19 at the same time. This implies that the number of individuals will decrease to the minimum within 30 days if the control effort is optimally implemented to halt the disease's transmission. Conversely, it will increase significantly.

(e) Figure 7E represents the effect of the control effort U_3 on the individuals infectious with drug-resistant (DR) strain of

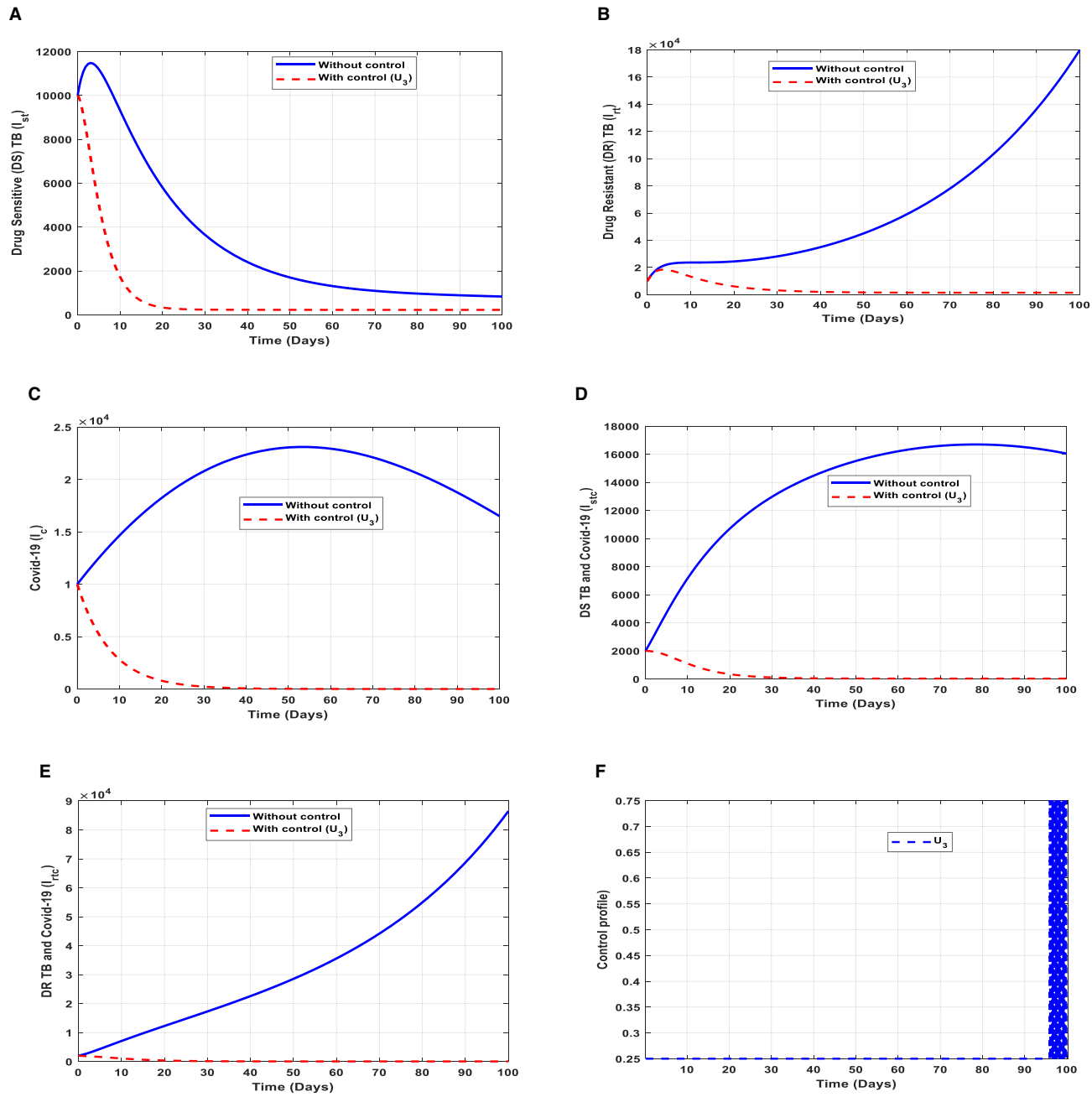

FIGURE 7
(A–E) Red dotted line is the optimal solution for implementing strategy 3. **(F)** Optimal control profile for strategy 3.

TB and COVID-19 at the same time. This implies that the number of individuals will decrease to the minimum within 90 days if the control effort is optimally implemented to halt the disease's transmission. Conversely, if the control intervention is ignored, the number of infected individuals will increase significantly by $> 180,000$ per 100,000 people before the 90th day, which will result in higher transmission of the drug-resistant (DR) strain of TB and COVID-19 in the individuals.

(f) Figure 7F represents the profile of the control effort for finding cases of TB and COVID-19. This implies that ∼25% of the cases should be identified for immediate treatment within 85 days of implementation and must be intensified to ∼75% in the subsequent days to halt both TB and COVID-19 transmission. However, the latter days of implementation vary between 25% and 75% based on the outcome of this intervention.

Strategy 4: implementation of case holding (U_4)

This intervention is also favorable for both streams of diseases, thus halting the transmission of TB and COVID-19. The optimal solutions, illustrated in Figure 8, account for the observations when the control effort U_4 is applied accordingly.

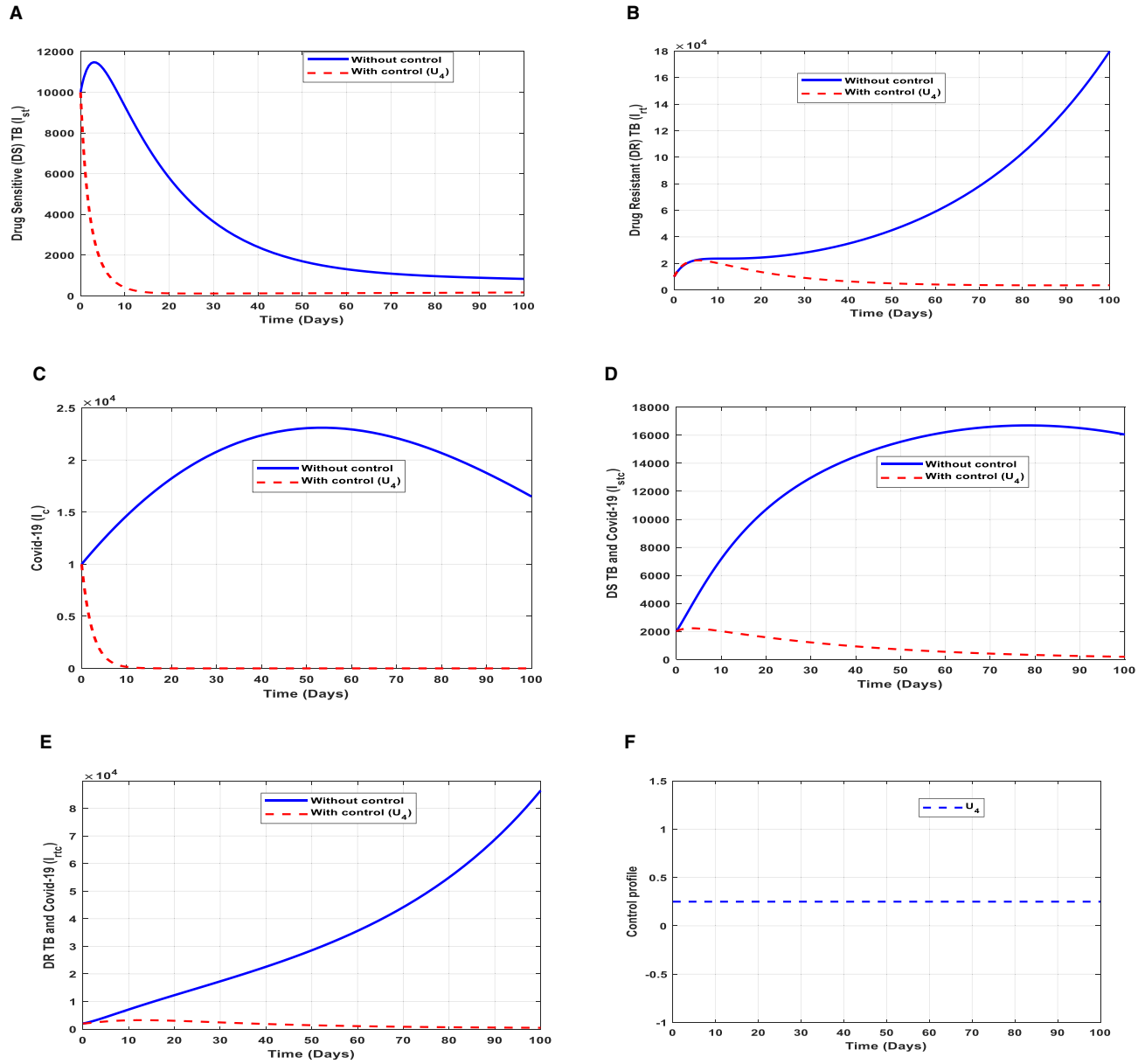

FIGURE 8
(A–E) Red dotted line is the optimal solution for implementing strategy 4. **(F)** Optimal control profile for strategy 4.

The optimal solutions illustrated above depict the following observations when case holding is only applied. This is also mostly used to handle TB infections.

(a) Figure 8A represents the effect of the control effort U_4 on the individuals infectious with drug-sensitive (DS) strain of TB only. This implies that the number of individuals will decrease to the minimum within 20 days if the control effort is optimally implemented to halt the disease's transmission. Conversely, it will increase significantly.

(b) Figure 8B represents the effect of the control effort U_4 on the individuals infectious with drug-resistant (DR) strain of TB only. This implies that the number of individuals will decrease to the minimum within 80 days if the control intervention is optimally implemented to halt the disease's transmission. Conversely, if the control effort is ignored, the number of infected individuals will increase significantly by $> 10,000$ per 100,000 people before the 90th day, which will result in higher transmission of the drug-resistant (DR) strain of TB only in the individuals.

(c) Figure 8C represents the effect of the control effort U_4 on the individuals infectious with COVID-19 only. This implies that the number of individuals will decrease to the minimum within 10 days if the control intervention is optimally implemented to halt the disease's transmission. Conversely, it will increase significantly.

(d) Figure 8D represents the effect of the control effort U_4 on the individuals infectious with drug-sensitive (DS) strain of

TB and COVID-19 at the same time. This implies that the number of individuals will decrease to the minimum within 80 days if the control intervention is optimal to halt the disease's transmission. Conversely, it will increase significantly.

(e) Figure 8E represents the effect of the control effort U_4 on the individuals infectious with drug-resistant (DR) strain of TB and COVID-19 at the same time. This implies that the number of individuals will decrease to the minimum within 90 days if the control intervention is optimally implemented to halt the disease's transmission. Conversely, if the control effort is ignored, the number of infected individuals will increase significantly by $> 50,000$ per 100,000 people before the 90th day, which will result in higher transmission of the drug-resistant (DR) strain of TB and COVID-19 in the individuals. This intervention is normally used to handle individuals infectious with (DR) strain of TB because it is very difficult to treat them. Therefore, one could realize a decrease in the number of infections.

(f) Figure 8F represents the profile of control effort for case holding for TB and COVID-19. It implies that more than 25% of the cases should be handled properly among the population from the start of implementation and must be intensified fully and optimized to 100% after some days throughout the subsequent days to halt both TB and COVID-19 transmission.

Strategy 5: implementation of all controls (U_1,U_2,U_3,U_4)

These interventions are also favorable for both streams of diseases, thus halting the transmission of TB and COVID-19. The optimal solutions, illustrated in Figure 9, account for the observations when all the control efforts are applied accordingly.

The optimal solutions illustrated above depict the following observations when all the control efforts are applied.

(a) Figure 9A represents the effect of all the control efforts U_1, U_2, U_3, U_4 on the individuals infectious with drug-sensitive (DS) strain of TB only. This implies that the number of individuals will decrease to the minimum within 20 days if the control interventions are optimally implemented to halt the disease's transmission. Conversely, it will increase significantly.

(b) Figure 9B represents the effect of all the control efforts U_1, U_2, U_3, U_4 on the individuals infectious with drug-resistant (DR) strain of TB only. This implies that the number of individuals will decrease to the minimum within 30 days if the control interventions are optimally implemented to halt the disease's transmission. Conversely, if the control effort is ignored, the number of infected individuals will increase significantly by $>$ 14000 people before the 50th day.

(c) Figure 9C represents the effect of all the control efforts U_1, U_2, U_3, U_4 on the individuals infectious with COVID-19 only. This implies that the number of individuals will decrease to the minimum within 30 days if the control effort is optimally implemented to halt the disease's transmission. Conversely, it will increase significantly.

(d) Figure 9D represents the effect of all the control efforts U_1, U_2, U_3, U_4 on the individuals infectious with drug-sensitive (DS) strain of TB and COVID-19 at the same time. This implies that the number of individuals will decrease to the minimum within 80 days if the control effort is optimally implemented to halt the disease's transmission. Conversely, it will increase significantly.

(e) Figure 9E represents the effect of all the control efforts U_1, U_2, U_3, U_4 on the individuals infectious with drug-resistant (DR) strain of TB and COVID-19 at the same time. This implies that the number of individuals will decrease to the minimum within 80 days if the control effort is optimally implemented to halt the disease's transmission. Conversely, if the control interventions are ignored, the number of infected individuals will increase significantly by $>$ 70000 per 100000 people before the 80th day, which will result in higher transmission of the drug-resistant (DR) strain of TB and COVID-19 in the individuals.

(f) Figure 9F represents the profile of control efforts for public education, vaccination, case finding, and case holding of TB and COVID-19. This implies that all the controls should be implemented at the same rate. Thus, ∼25% of the population should be educated, vaccinated, cases should be identified for immediate treatment and hold the cases within 95 days of implementation, and should be intensified to ∼70% in the subsequent days to halt both TB and COVID-19 transmission. However, the latter days of implementation vary between 25% and 70% based on the outcome of these interventions.

Strategy 6: implementation of public education and vaccination (U_1,U_2)

This intervention is also favorable for both streams of diseases, thus halting the transmission of TB and COVID-19. The optimal solutions, illustrated in Figure 10, account for the observations when the control efforts U_1, U_2 are applied accordingly.

The optimal solutions illustrated above depict the following observations when all the control efforts are applied. These interventions are normally applied to COVID-19 infection only.

(a) Figure 10A represents the effect of the control efforts U_1, U_2 on the individuals infectious with drug-sensitive (DS) strain of TB only. This implies that the number of individuals will decrease but not to the minimum within 30 days if the control interventions are optimally implemented to halt the disease's transmission. On the other hand, it will increase significantly.

(b) Figure 10B represents the effect of the control efforts U_1, U_2 on the individuals infectious with drug-resistant (DR) strain of TB only. This implies that the number of individuals will decrease to the minimum within 90 days if the control efforts are optimally implemented to halt the transmission of the disease. Conversely, if the control interventions are ignored, the number of infected individuals will increase significantly by $> 140,000$ people before the 90th day but in decreasing order of drug-resistant (DR) strain of TB-only transmission in the individuals. This is a result of the probability of the individual developing resistance to the drug.

(c) Figure 10C represents the effect of the control efforts U_1, U_2 on the individuals infectious with COVID-19 only. This implies that the number of individuals will decrease to the minimum within 10 days if the control interventions are optimally

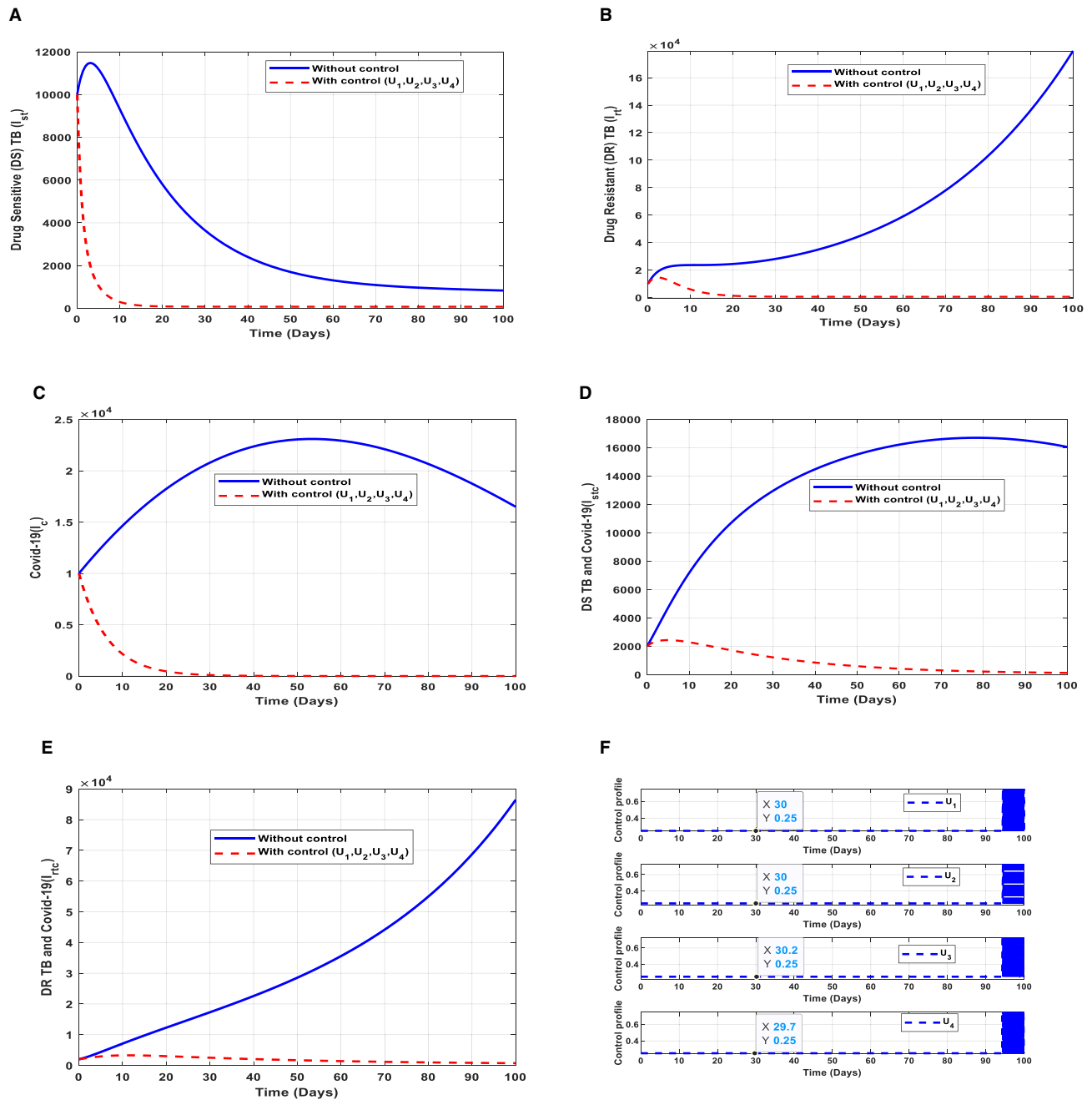

FIGURE 9
(A–E) Red dotted line is the optimal solution for implementing strategy 5. **(F)** Optimal control profile for strategy 5.

implemented to halt the disease's transmission. Conversely, it will increase significantly. These strategies are ideal for COVID-19 infection only,

(d) Figure 10D represents the effect of the control efforts U_1, U_2 on the individuals infectious with drug-sensitive (DS) strain of TB and COVID-19 at the same time. This implies that the number of individuals will decrease to the minimum within extra days and may worsen the situation if the control efforts are optimally implemented. This is a result of not identifying infectious individuals, vaccine inefficacy, and drug resistance.

(e) Figure 10E represents the effect of the control efforts U_1, U_2, U_3, U_4 on the individuals infectious with drug-resistant (DR) strain of TB and COVID-19 at the same time. This implies that the number of individuals will decrease to the minimum within 90 days if the control interventions are optimally implemented to halt the transmission of the disease. Conversely, if the control interventions are ignored, the number of infected individuals will increase significantly by $> 70,000$ per 100,000 people before the 80th day, which will result in higher transmission of the drug-resistant (DR) strain of TB and COVID-19 in the individuals.

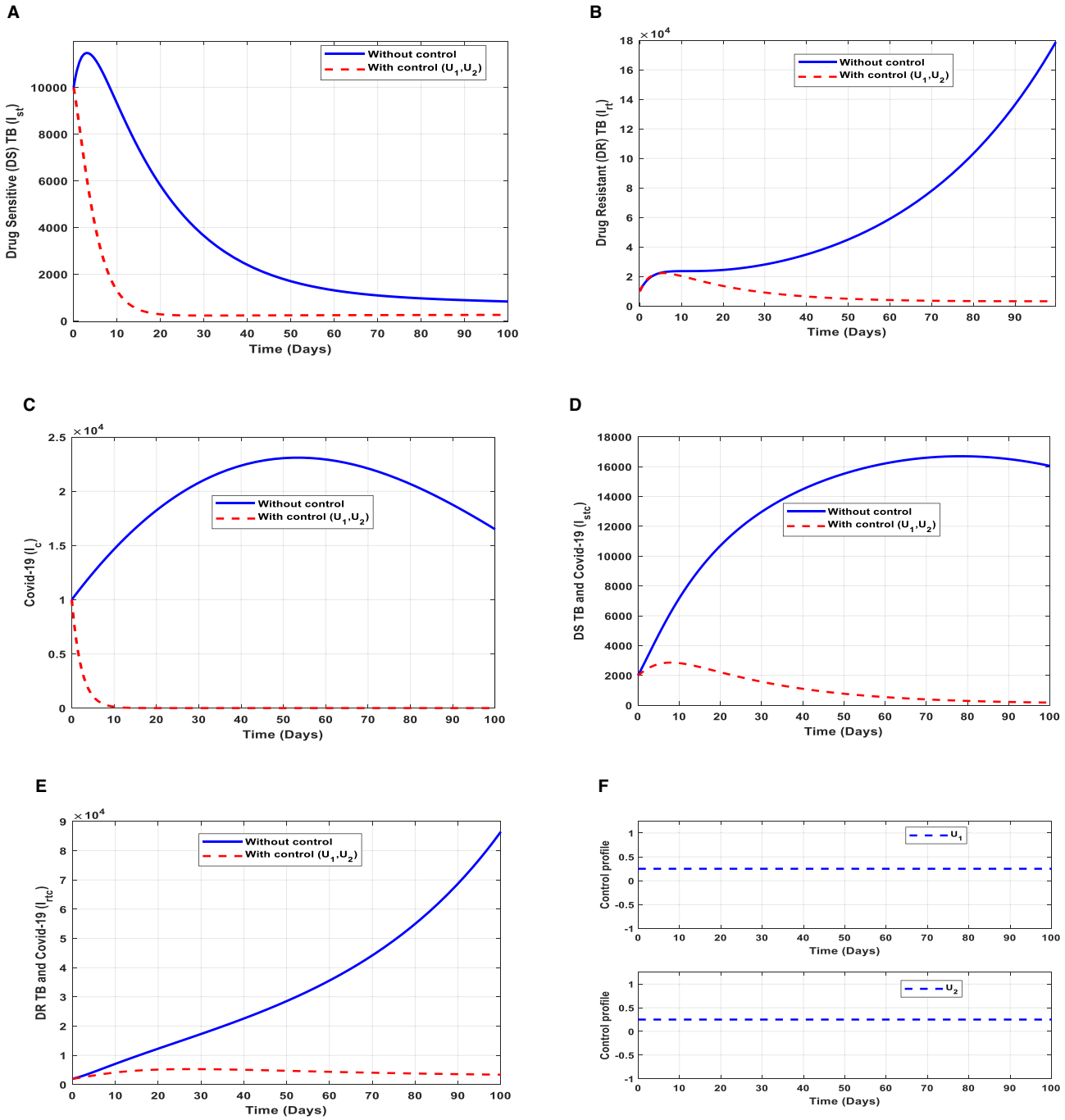

FIGURE 10
(A–E) Red dotted line is the optimal solution for implementing strategy 6. **(F)** Optimal control profile for strategy 6.

(f) Figure 10F represents the profile of control effort for public education and vaccination for TB and COVID-19. This implies that all the interventions U_1, U_2 should be more than 25% intensified in the population from the start of implementation and must be intensified fully and optimized to 100% after some days throughout the subsequent days; however, U_2 should be 25% throughout the implementation in halting both TB and COVID-19 transmission.

Strategy 7: implementation of case finding and case holding (U_3,U_4)

This intervention is also favorable for both streams of diseases, thus halting the spread of TB and COVID-19. The optimal solutions, illustrated in Figure 11, account for the observations when the control efforts U_3, U_4 are applied accordingly.

The optimal solutions illustrated above depict the following observations when public education is only

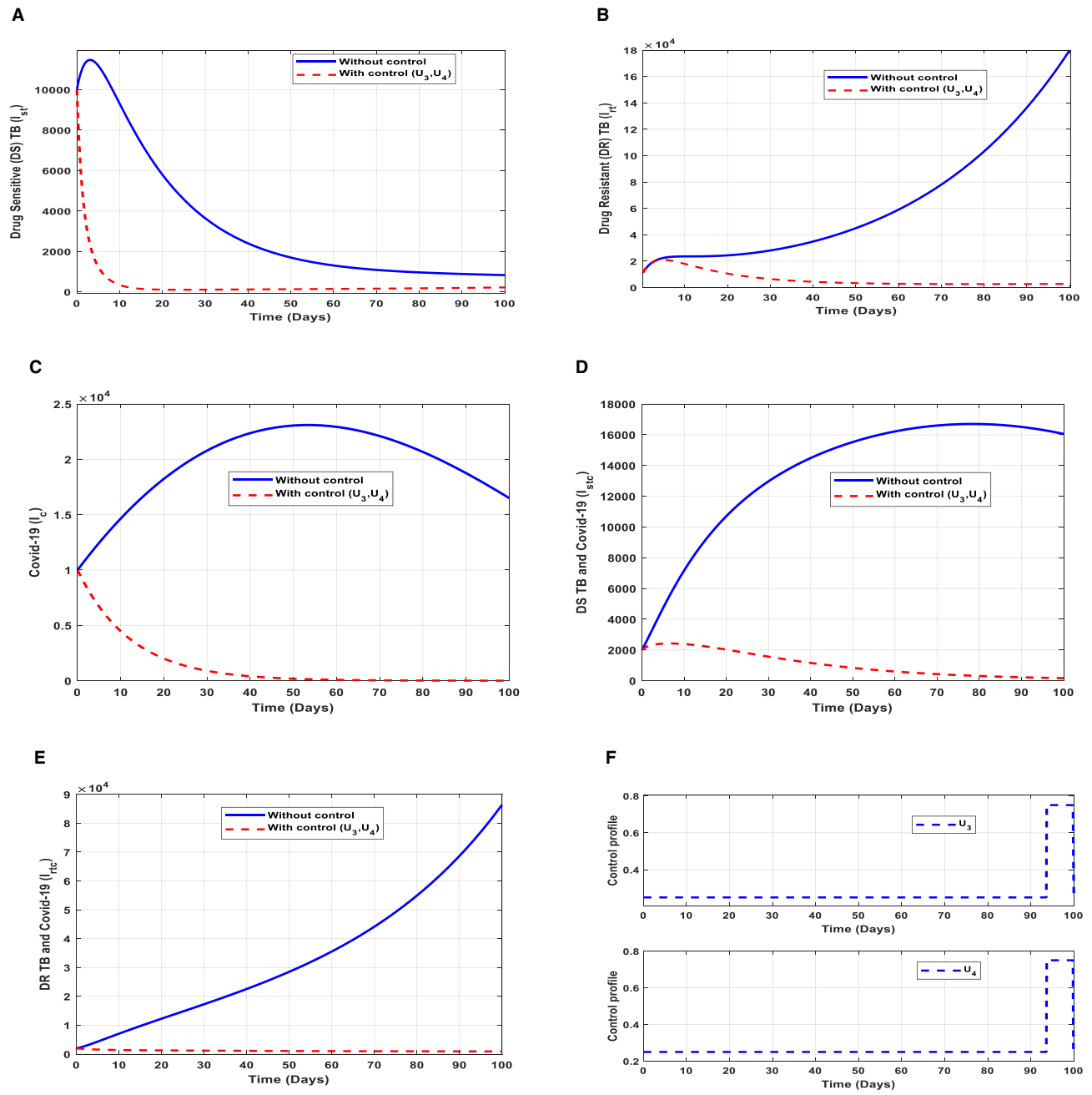

FIGURE 11
(A–E) Red dotted line is the optimal solution for implementing strategy 7. **(F)** Optimal control profile for strategy 7.

applied. These interventions are normally applied to TB infection only.

(a) Figure 11A represents the effect of the control efforts U_3, U_4 on the individuals infectious with drug-sensitive (DS) strain of TB only. This implies that the number of individuals will decrease to the minimum within 20 days if the control interventions are optimally implemented to halt the disease's transmission. Conversely, it will increase. This is a result of identifying and holding the cases as early as possible to prevent further transmission.

(b) Figure 11B represents the effect of the control efforts U_3, U_4 on the individuals infectious with drug-resistant (DR) strain of TB only. This implies that the number of individuals will decrease within 90 days if the control interventions are optimally implemented to halt the disease's transmission. Conversely, if the control interventions are ignored, the number of infected individuals will increase significantly by $> 140,000$ per 100,000 people before the 90th day, which will result in higher transmission of the drug-resistant (DR) strain of TB only in the individuals.

(c) Figure 11C represents the effect of the control efforts U_3, U_4 on the individuals infectious with COVID-19 only. This implies that the number of individuals will decrease to the minimum within 60 days if the control effort is optimally implemented to halt the disease's transmission. Conversely, it will increase significantly.

(d) Figure 11D represents the effect of the control efforts U_3, U_4 on the individuals infectious with drug-resistant (DR) strain of TB and COVID-19 at the same time. This implies that the number of individuals will decrease to the minimum within 100 days if the control interventions are optimally implemented to halt the disease's transmission. Conversely, it will decrease but not significantly. This is a result of identifying and holding the cases as early as possible to prevent further transmission.

(e) Figure 11E represents the effect of the control efforts U_3, U_4 on the individuals infectious with drug-resistant (DR) strain of TB and COVID-19 at the same time. This implies that the number of individuals will decrease to the minimum within 100 days if the control interventions are optimally implemented to halt the disease's transmission. Conversely, if the control effort is ignored, the number of infected individuals will increase significantly by $> 70,000$ per 100,000 people before the 100th day, which will result in higher transmission of the drug-resistant (DR) strain of TB and COVID-19 in the individuals.

(f) Figure 11F represents the profile of control effort for case finding and case holding of TB and COVID-19. This implies that more than 25% of the cases should be identified and held in the population from the start of implementation and must be intensified fully and optimized to 100% after 85 days throughout the subsequent days in minimizing both TB and COVID-19 transmission.

Analyzing the cost-effectiveness of the strategies

Once the strategies are given, it is imperative to know the cost associated with implementing such intervention(s). Therefore, we explore the costs associated with each control strategy to check their effectiveness. We layout some cost-effectiveness approaches to further understand the control strategies.

The average cost-effectiveness ratio (ACER) and incremental cost-effectiveness ratio (ICER)

We consider two procedures, which have been explained in [36–39], to carry out epidemiological studies.

The average cost-effectiveness ratio (ACER)

We define the average cost-effectiveness ratio (ACER) of implementing a strategy as follows Equation (31):

$$ACER = \frac{\textit{Total cost generated by applying the strategy}}{\textit{Total number of infections averted by applying the strategy}}. \quad (31)$$

TABLE 2 Strategies' ACER values with their total infection averted and total cost involved.

Strategies	Total infection averted	Total cost involved	ACER value
Strategy 1	2.7545×10^8	6.3063×10^3	2.2895×10^{-5}
Strategy 2	2.3485×10^6	3.1531×10^3	0.0013
Strategy 3	5.4017×10^5	1.6016×10^4	0.0296
Strategy 4	2.3177×10^8	3.3031×10^4	1.4252×10^{-4}
Strategy 5	3.2339×10^8	5.8506×10^4	1.8091×10^{-4}
Strategy 6	2.7566×10^8	9.4594×10^3	3.4315×10^{-5}
Strategy 7	2.3231×10^8	4.9047×10^4	2.1113×10^{-4}

The total cost Q, stated in (24), would be used to evaluate the total cost that the intervention would generate in Equation (31). We then compare the ACER values of each strategy, and the one with the least value saves cost. Therefore, the cost-effective intervention is considered as the strategy with the least ACER value. This is illustrated below.

From Table 2, control strategy 1, the implementation of public education only has the least value of ACER, hence saving cost. This is not enough to choose a strategy; we further explore other approaches.

The incremental cost-effectiveness ratio (ICER)

We define the incremental cost-effectiveness ratio (ICER) of implementing a strategy as follows Equation (32):

$$ICER = \frac{\textit{The cost difference generated by strategies } x \textit{ and } y}{\textit{Difference in the total number of infections averted in strategies } x \textit{ and } y}. \quad (32)$$

The total cost function Q, stated in (24), would be used to estimate the total cost that the intervention would generate. It is worth knowing that the averted total number of infections is the difference between the initial values of E_x, I_x, where $x = st, rt, c, stc, rtc$, without control(s) and with controls. The outcomes are tabulated below in infection averted increasing order.

The ICER in Table 3 is calculated as follows:

$$ICER\,(3) = \frac{1.6016 \times 10^4 - 0}{5.4017 \times 10^5 - 0} = 0.0296,$$

$$ICER\,(2) = \frac{3.1531 \times 10^3 - 1.6016 \times 10^4}{2.3485 \times 10^6 - 5.4017 \times 10^5} = -0.0071,$$

$$ICER\,(4) = \frac{3.3031 \times 10^4 - 3.1531 \times 10^3}{2.3177 \times 10^8 - 2.3485 \times 10^6} = 1.3023 \times 10^{-4},$$

$$ICER\,(7) = \frac{4.9047 \times 10^4 - 3.3031 \times 10^4}{2.3231 \times 10^8 - 2.3177 \times 10^8} = 0.0297,$$

TABLE 3 Strategies' ICER values with their total infection averted and total cost involved.

Strategies	Total infection averted	Total cost involved	ICER value
Strategy 3	5.4017×10^5	1.6016×10^4	0.0296
Strategy 2	2.3485×10^6	3.1531×10^3	−0.0071
Strategy 4	2.3177×10^8	3.3031×10^4	1.3023×10^{-4}
Strategy 7	2.3231×10^8	4.9047×10^4	0.0297
Strategy 1	2.7545×10^8	6.3063×10^3	-9.9074×10^{-4}
Strategy 6	2.7566×10^8	9.4594×10^3	0.0150
Strategy 5	3.2339×10^8	5.8506×10^4	0.0010

TABLE 4 Strategies' ICER values with their total infection averted and total cost involved.

Strategies	Total infection averted	Total cost involved	ICER value
Strategy 2	2.3485×10^6	3.1531×10^3	0.0013
Strategy 4	2.3177×10^8	3.3031×10^4	1.3023×10^{-4}
Strategy 7	2.3231×10^8	4.9047×10^4	0.0297
Strategy 1	2.7545×10^8	6.3063×10^3	-9.9074×10^{-4}
Strategy 6	2.7566×10^8	9.4594×10^3	0.0150
Strategy 5	3.2339×10^8	5.8506×10^4	0.0010

TABLE 5 Strategies' ICER values with their total infection averted and total cost involved.

Strategies	Total infection averted	Total cost involved	ICER value
Strategy 4	2.3177×10^8	3.3031×10^4	1.4252×10^{-4}
Strategy 7	2.3231×10^8	4.9047×10^4	0.0297
Strategy 1	2.7545×10^8	6.3063×10^3	-9.9074×10^{-4}
Strategy 6	2.7566×10^8	9.4594×10^3	0.0150
Strategy 5	3.2339×10^8	5.8506×10^4	0.0010

$$ICER\,(1) = \frac{6.3063 \times 10^3 - 4.9047 \times 10^4}{2.7545 \times 10^8 - 2.3231 \times 10^8} = -9.9074 \times 10^{-4},$$

$$ICER\,(6) = \frac{9.4594 \times 10^3 - 6.3063 \times 10^3}{2.7566 \times 10^8 - 2.7545 \times 10^8} = 0.0150,$$

$$ICER\,(5) = \frac{5.8506 \times 10^4 - 9.4594 \times 10^3}{3.2339 \times 10^8 - 2.7566 \times 10^8} = 0.0010.$$

Assessing strategy 3 and strategy 2 in Table 3, it is noticed from the ICER that strategy 3 is expensive to deploy in a resource-limited setting; hence, strategy 3 is removed from the list of possible controls, and the ICER is calculated again. This is presented in Table 4.

Assessing strategy 2 and strategy 4 in Table 4, it is noticed from the ICER that strategy 2 is expensive to deploy in a resource-limited setting; hence, strategy 2 is removed from the list of possible controls, and the ICER is calculated again. This is presented in Table 5.

Assessing strategy 4 and strategy 7 in Table 5, it is noticed from the ICER that strategy 7 is expensive to deploy in a resource-limited setting; hence, strategy 7 is removed from the list of possible controls, and the ICER is calculated again. This is presented in Table 6.

TABLE 6 Strategies' ICER values with their total infection averted and total cost involved.

Strategies	Total infection averted	Total cost involved	ICER value
Strategy 4	2.3177×10^8	3.3031×10^4	1.4252×10^{-4}
Strategy 1	2.7545×10^8	6.3063×10^3	-6.1183×10^{-4}
Strategy 6	2.7566×10^8	9.4594×10^3	0.0150
Strategy 5	3.2339×10^8	5.8506×10^4	0.0010

TABLE 7 Strategies' ICER values with their total infection averted and total cost involved.

Strategies	Total infection averted	Total cost involved	ICER value
Strategy 1	2.7545×10^8	6.3063×10^3	2.2895×10^{-5}
Strategy 6	2.7566×10^8	9.4594×10^3	0.0150
Strategy 5	3.2339×10^8	5.8506×10^4	0.0010

TABLE 8 Strategies' ICER values with their total infection averted and total cost involved.

Strategies	Total infection averted	Total cost involved	ICER value
Strategy 1	2.7545×10^8	6.3063×10^3	2.2895×10^{-5}
Strategy 5	3.2339×10^8	5.8506×10^4	0.0011

Assessing strategy 4 and strategy 1 in Table 6, it is noticed from the ICER that strategy 4 is expensive to deploy in a resource-limited setting; hence, strategy 4 is removed from the list of possible controls, and the ICER is calculated again. This is presented in Table 7.

Assessing strategy 1 and strategy 6 in Table 7, it is noticed from the ICER that strategy 6 is expensive to deploy in a resource-limited setting; hence, strategy 6 is removed from the list of possible controls, and the ICER is calculated again. This is presented in Table 8.

Finally, assessing strategy 1 and strategy 5 in Table 8, it is noticed from the ICER that strategy 5 is expensive to deploy in a resource-limited setting; hence, strategy 5 is removed from the list of possible controls. Therefore, we conclude that strategy 1 is

the most cost-effective strategy to use among the several strategies under study here. From the above analysis, it is obvious that strategy 1, thus, public education is the intervention that saves cost.

Conclusion

We have designed a new epidemiological co-infection vaccination model involving two strains of TB and COVID-19 to explore the transmission dynamics of tuberculosis (TB) and COVID-19 using data from Ghana. We have estimated the model's parameters and analyzed their effects on the two diseases' transmission through numerical and graphical illustrations. Again, we have exhibited the threshold dynamics of the basic reproduction number R_0 by evaluating the reproduction numbers of the two streams of the model, thus, TB and COVID-19 streams. It was found that the reproduction number of the TB stream with two strains: the drug-sensitive (DS) strain of TB, $R_{st} = 0.55$, and the reproduction number of the drug-resistant (DR) strain of TB, $R_{rt} = 1.47$. The reproduction number of the COVID-19 stream is $R_{0c} = 2.21$. This signifies that ∼82.8% of TB and COVID-19 co-infection cases are drug-resistant (DR) strains of TB-induced, while 17.2% are drug-sensitive (DS) strains of TB-induced. The treatment of TB is not easy due to ineffective vaccines, as stated in [4, 5], which has also been demonstrated in this study. It was observed that the number of drug-resistant (DR) strains of TB and COVID-19 co-infection is higher in all cases (see Figures 5E–11E).

Our goal is to study the co-infection of tuberculosis (TB) and COVID-19 and devise strategies that save costs to mitigate the transmission; therefore, we have formulated optimal control strategies together with the cost-effectiveness analysis that consider control measures involving both pharmaceutical and non-pharmaceutical interventions to control TB and COVID-19 co-infection. We implemented the strategies (see Figures 5–11), and it was observed that public education and vaccination to prevent TB and COVID-19 should be intensified and reach ∼25% of the population from the beginning and intensify in subsequent days. Vaccination should be enhanced up to ∼25% of the population from the start and reach ∼75% within 100 days of implementation, case holding, and case finding, as explained in [39], need ∼75% enforcement within 100 days because they are helpful in controlling the spread of TB. This indicates that although vaccination is good, it largely depends on the rise of drug-resistant (DR) strain infections if treatment failure of individuals infectious with drug-sensitive (DS) strain occurs and also the inefficacy of vaccines. We therefore encourage the health service to enhance the mechanism for TB diagnosis by following the recommendation in [40] because it is difficult to treat TB.

It is also worth knowing that public education saves cost per the cost-effectiveness analysis compared to the other strategies raised in this study. This intervention can minimize TB and/or COVID-19, as illustrated in Figure 5. This intervention should reach about 25% of the population from the beginning and intensify up to 75% in the subsequent days to realize the results of strategy 1 (see Figure 5F). However, it is imperative to check the effectiveness and cost of all the strategies raised in this study when choosing a control measure.

The outcomes of the findings imply that both pharmaceutical and non-pharmaceutical measures are very important in controlling the transmission of TB and COVID-19 co-infection. These control measures should always be vigorous to create public awareness of TB and COVID-19, as illustrated in Figures 5F–11F, to reduce the effective contact rates and rates of acquiring TB and/or COVID-19, as illustrated in Figure 4. Pharmaceutical measures such as vaccination against TB and COVID-19 are important; however, they should be implemented with vigilance because of the existence of drug-resistant (DR) strains of TB; therefore, the control measure should be mild in the beginning, as illustrated in all the PRCCs of this study (see Figure 3).

Although we have demonstrated the co-infection dynamics of TB and COVID-19, this study is focused on the homogeneity of the population; we hope to extend this study to explore the transmission of TB and COVID-19 co-infection by considering the heterogeneity of the population, such as age and sex. We encourage the Ghana health service to be keen on observing the drug-resistant (DR) strain of TB since it has a higher infection rate compared to the drug-sensitive (DS) strain of TB, leading to a high co-infection rate of drug-resistant (DR) strain of TB and COVID-19 which is difficult to treat. In addition, individuals with TB and/or COVID-19 are encouraged to complete their prophylaxis, especially for TB, to help halt the transmission of TB and COVID-19.

Data availability statement

The original contributions presented in the study are included in the article/supplementary material, further inquiries can be directed to the corresponding authors.

Author contributions

RA: Conceptualization, Data curation, Formal analysis, Investigation, Methodology, Writing – original draft, Writing – review & editing. ZJ: Funding acquisition, Supervision, Writing – review & editing. JY: Formal analysis, Supervision, Writing – review & editing. JA: Formal analysis, Investigation, Writing – review & editing. YW: Formal analysis, Investigation, Validation, Writing – review & editing.

Funding

The author(s) declare financial support was received for the research, authorship, and/or publication of this article. This research was supported by National Natural Science Foundation of China grants 12231012, 61873154.

Conflict of interest

The authors declare that the research was conducted in the absence of any commercial or financial relationships that could be construed as a potential conflict of interest.

Publisher's note

References

1. Adebisi YA, Agumage I, Sylvanus TD, Nawaila IJ, Ekwere WA, Nasiru M, et al. Burden of tuberculosis and challenges facing its eradication in West Africa. *Int J Infect*. (2019) 6:3. doi: 10.5812/iji.92250

2. World Health Organization. *World Health Statistics 2015*. Geneva: World Health Organization (2015).

3. World Health Organization. *Global Tuberculosis Report 2016*. Geneva : World Health Organization (2016).

4. Chaulet P. *Treatment of Tuberculosis: Case Holding Until Cure, WHO/TB/83*. Geneva: World Health Organization (1983). p. 141.

5. Reichman LB, Hersh Field ES. *Tuberculosis: a Comprehensive International Approach*, New York: Dekker. (2000).

6. Chen Y, Wang Y, Fleming J, Yu Y, Gu Y, Liu C, et al. Active or latent tuberculosis increases susceptibility to COVID-19 and disease severity. *MedRxiv*. (2020). doi: 10.1101/2020.03.10.20033795

7. Salman AM, Ahmed I, Mohd MH, Jamiluddin MS, Dheyab MA. Scenario analysis of COVID-19 transmission dynamics in Malaysia with the possibility of reinfection and limited medical resources scenarios. *Comput Biol Med*. (2021) 133:104372. doi: 10.1016/j.compbiomed.2021.104372

8. Zamir M, Nadeem F, Alqudah MA, Abdeljawad T. Future implications of COVID-19 through Mathematical modelling. *Results Phys*. (2022) 33:105097. doi: 10.1016/j.rinp.2021.105097

9. Worldometers. *Reported Cases and Deaths by Country or Territory*. Available online at: https://www.worldometers.info/coronavirus/#countries (accessed April 30, 2022).

10. Zegarra MAA, Infante SD, Carrasco DB, Liceaga DO. COVID-19 optimal vaccination policies: A modeling study on efficacy, natural and vaccine-induced immunity responses. *Math Biosci*. (2021) 337:108614. doi: 10.1016/j.mbs.2021.108614

11. Alanagreh L, Alzoughool F, Atoum M. The human corona virus disease COVID-19: its origin, characteristics, and insights into potential drugs and its mechanisms. *Pathogens*. (2020) 9:331. doi: 10.3390/pathogens9050331

12. Singh HP, Khullar V, Sharma M. Estimating the impact of COVID-19 outbreak on high risk age group population in India. *Augment Human Res*. (2020) 5:18. doi: 10.1007/s41133-020-00037-9

13. Lustig Y, Zuckerman N, Nemet I, Atari N, Kliker L, Regev-Yochay G, et al. Eurosurveillance | neutralizing capacity against delta (b.1.617.2) and other variants of concern following comirnaty (BNT162b2, BioNTech/pfizer) vaccination in health care workers, Israel. *Euro Surveil*. 26:2100557. doi: 10.2807/1560-7917.ES.2021.26.26.2100557

14. Nasreen S, Chung H, He S, Brown K, Gubbay JB, Buchan SA, et al. Effectiveness of COVID-19 vaccines against variants of concern in Ontario, Canada. *MedRxiv*. doi: 10.1101/2021.06.28.21259420

15. Katella, Omicron K, Delta, Alpha, and More: What to Know About the Coronavirus Variants. (2022). Available online at: https://www.yalemedicine.org/news/covid-19-variants-of-concern-omicron (accessed 30 Apr, 2022).

16. Bernal J, Gower AN, Gallagher CE. Effectiveness of COVID-19 vaccines against the b.1.617.2 (delta) variant. *N Engl J Med*. (2021) 385:585–594. doi: 10.1056/NEJMoa2108891

17. Cherian S, Potdar V, Jadhav S, Yadav P, Gupta N, Das G, et al. Convergent evolution of SARS-CoV-2 spike mutations, l452r, e484q and p681r, in the second wave of COVID-19 in Maharashtra, India. *BioRxiv*. doi: 10.1101/2021.04.22.440932

18. Takashita E, Kinoshita N, Yamayoshi S, Fujisaki S, Ito M, Chiba S, et al. Efficacy of antibodies and antiviral drugs against covid-19 omicron variant *N Engl J Med*.. 386:995–998. doi: 10.1056/NEJMc2119407

19. Sarkar S, Khanna P, Singh AK. Impact of COVID- 19 in patients with concurrent co- infections: a systematic review and meta- analyses. *J Med Virol*. (2021) 93:2385–95. doi: 10.1002/jmv.26740

20. Gao Y, Liu M, Chen Y, Shi S, Geng J, Tian J. Association between tuberculosis and COVID- 19 severity and mortality: a rapid systematic review and meta-analysis. *J Med Virol*. (2021) 93:194–6. doi: 10.1002/jmv.26311

21. Tadolini M. García-García J-M, Blanc FX, Borisov S, Goletti D, Motta I, et al. On tuberculosis and COVID-19 co-infection. *EurRespir J*. (2020) 56:2002328. doi: 10.1183/13993003.02328-2020

22. Visca D, Ong CWM, Tiberi S, Centis R, D'Ambrosio L, Chen B, et al. Tuberculosis and COVID- 19 interaction: a review of biological, clinical and public health effects. *Pulmonology*. (2021) 27:151–65. doi: 10.1016/j.pulmoe.2020.12.012

23. Mousquer GT, Peres A, Fiegenbaum M. Pathology of TB/COVID- 19 co- infection: the phantom menace. *Tuberculosis*. (2021) 126:102020. doi: 10.1016/j.tube.2020.102020

24. Yang H, Lu S. COVID- 19 and tuberculosis. *J Transl Int Med*. (2020) 8:59–65. doi: 10.2478/jtim-2020-0010

25. van den Driessche P, James W, Reproduction numbers and sub-threshold endemic eqilibria for compartmental models of disease transmission. *Math Biosci*. (2002) 180:29–48. doi: 10.1016/S0025-5564(02)00108-6

26. World Health Organization. Global Tuberculosis Report. In: *Incidence of Tuberculosis (per 100,000 People) - Ghana | Data*. Geneva: World Health Organization. Available online at: worldbank.org (2023).

27. Our World in Data. *COVID-19 cases*. Available online at: https://ourworldindata.org/covid-cases (assessed 16 Dec, 2023).

28. Li MY, Muldowney JS. Global stability for the seir model in epidemiology. *Mathemat Biosci*. (1995) 125:155–64. doi: 10.1016/0025-5564(95)92756-5

29. Dontwi I, Obeng-Denteh W, Andam E. A mathematical model to predict the prevalence and transmissiondynamics of tuberculosis in Amansie West district, Ghana. *Br J Mathemat Comp Sci*. (2014) 4:402–25. doi: 10.9734/BJMCS/2014/4681

30. Tchoumi S, Diagne M, Rwezaura H, Tchuenche J. Malaria and COVID-19 co-dynamics: a mathematical model and optimal control. *Appl Mathemat Model*. (2021) 99:294e327. doi: 10.1016/j.apm.2021.06.016

31. Omame A, Abbas M, Onyenegecha C. A fractional-order model for COVID-19 and tuberculosis co-infection using atanganaebaleanu derivative. *Chaos, Solitons Fract*. (2021) 153:111486. doi: 10.1016/j.chaos.2021.111486

32. Rwezaura H, Diagne M, Omame A, de Espindola A, Tchuenche J. Mathematical modeling and optimal control of SARS-CoV-2 and tuberculosis co-infection: a case study of Indonesia. *Model Earth Syst Environm*. (2022) 8:5493e5520. doi: 10.1007/s40808-022-01430-6

33. Khan MA, Atangana A. Mathematical modeling and analysis of COVID-19: a study of new variant omicron. *Physica A*. (2022) 599:127452. doi: 10.1016/j.physa.2022.127452

34. WHO. *Global tuberculosis Programme, treatment of tuberculosis: Guidelines for National Programmes (3rd ed.)*. (2020). Available online at: https://apps.who.int/iris/handle/10665/67890 (accessed January 12, 2024).

35. Osei E, Amu H, Kye-Duodu G, Kwabla MP, Danso E, Binka FN, et al. Impact of COVID-19 pandemic on Tuberculosis and HIV services in Ghana: An interrupted time series analysis. *PLoS ONE*. (2023) 18:e0291808. doi: 10.1371/journal.pone.0291808

36. Asamoah JKK, Owusu MA, Jin Z, Oduro FT, Abidemi A, Gyasi EO. Global stability and cost-effectiveness analysis of COVID-19 considering the impact of the environment: using data from Ghana. *Chaos, Solitons Fractals*. (2020) 140:110103. doi: 10.1016/j.chaos.2020.110103

37. Agusto F, Leite M. Optimal control and cost-effective analysis of the meningitis outbreak in Nigeria. *Infect Dis Model*. (2017) 4:161–87. doi: 10.1016/j.idm.2019.05.003

38. Asamoah JKK, Okyere E, Abidemi A, Moore SE, Sun G, Jin Z, Acheampong E, Gordon JF. Optimal control and comprehensive cost-effectiveness analysis for COVID-19. *Results Phys*. (2022) 33:105177. doi: 10.1016/j.rinp.2022.105177

39. Asamoah JKK, Jin Z, Sun G. Non-seasonal and seasonal relapse model for Q fever disease with comprehensive cost-effectiveness analysis. *Results Phys*. (2021) 22:103889. doi: 10.1016/j.rinp.2021.103889

40. CDC. *Latent Tuberculosis Infection: A Guide for Primary Health Care Providers*. Atlanta, GA: CDC (2014).

Frontiers in
Applied Mathematics and Statistics

Investigates both applied and applicable mathematics and statistical techniques

Explores how the application of mathematics and statistics can drive scientific developments across data science, engineering, finance, physics, biology, ecology, business, medicine, and beyond

---

Discover the latest Research Topics

See more →

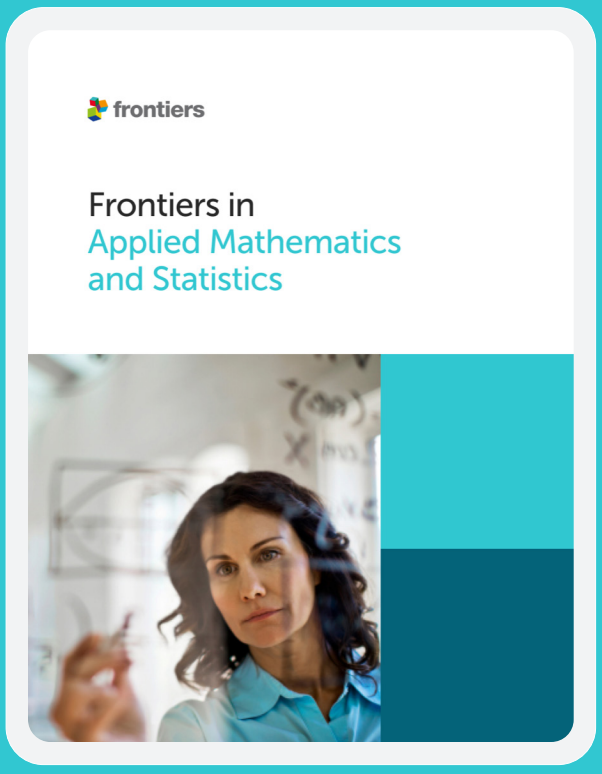

Frontiers

Avenue du Tribunal-Fédéral 34
1005 Lausanne, Switzerland
frontiersin.org

Contact us

+41 (0)21 510 17 00
frontiersin.org/about/contact